Dissertation
submitted to the
Combined Faculty of Mathematics, Engineering, and Natural Sciences
of Heidelberg University, Germany
for the degree of
Doctor of Natural Sciences

Put forward by
Simon Warnach
born in: Berlin, Germany
Oral examination: 11 July 2022

Bromine monoxide in volcanic plumes – A global survey of volcanic plume composition and chemistry derived from Sentinel-5 Precursor/TROPOMI data

Referees: Prof. Dr. Thomas Wagner

Prof. Dr. Thomas Leisner

Brommonoxid in Vulkanfahnen – Eine globale Untersuchung der Zusammensetzung und Chemie von Vulkanfahnen anhand von Sentinel-5 Precursor/TROPOMI Daten

Das Radikal Brommonoxid (BrO) beeinflusst viele chemische Prozesse der Atmosphäre, insbesondere die Konzentration von Ozon. Sein molares Verhältnis zu Schwefeldioxid im Vulkangas ist eine wichtige Kenngröße für die Magmazusammensetzung und kann unter Umständen zur genaueren Vorhersage von Eruptionen beitragen.
In dieser Arbeit wird die Verteilung von SO_2, BrO und des BrO/SO_2 Verhältnisses in Vulkan-fahnen über einen Zeitraum von vier Jahren (2018 - 2021) mit Hilfe der Differentiellen Optischen Absorptionsspektroskopie (DOAS) anhand von Spektraldaten des Satelliten S-5P/TROPOMI global untersucht. Dank seiner hohen räumlichen Auflösung (von bis zu $3.5 \times 5.5\,km^2$) und täglichen Abdeckung der Erdoberfläche, gelingt mit TROPOMI die Bestimmung des BrO/SO_2 Verhältnises auch für schwache Vulkanausbrüche erfolgreich bestimmen. 4323 Vulkanfahnen wurden global und automatisch durch einen Fahnenalgorithmus identifiziert, von denen in 1449 BrO zweifelsfrei nachgewiesen ist. 3063 Vulkanfahnen lassen sich 43 Vulkanen zuordnen und daraus das mittlere BrO/SO_2 Verhältnisse ermitteln. Damit steigt die Anzahl der Vulkane, für die ein BrO/SO_2 Verhältnis bestimmt ist, von 28 auf 60. Erstmalig sind auch für Hot Spot Vulkanen ein BrO/SO_2 Verhältnise berechnet - welches für alle niedriger ($\approx 5 \times 10^{-5}$) ist als an den Subduktionsvulkanen ($2 - 16 \times 10^{-5}$ in dieser Arbeit). Die gemessenen BrO/SO_2 Verhältnisse stimmen gut mit Bodengestützten Messungen überein.
Beobachtete räumliche Gradienten hin zur Fahnenmitte bei starken Eruptionen lassen sich erfolgreich mit niedrigen O_3 Konzentrationen in der Fahnenmitte erklären. Sowohl ein konzeptionelles als auch ein empirisches Modell bestätigt dies. Die Tatsache, dass sich der Rückgang im BrO/SO_2 Verhältnis zur Fahnenmitte in Entfernungen bis zu 1000 km beobachten lässt, verdeutlicht den starken Einfluss von Halogenradikalen vulkanischen Ursprungs auf die Atmosphäre.

Bromine monoxide in volcanic plumes – A global survey of volcanic plume composition and chemistry derived from Sentinel-5 Precursor/TROPOMI data

Bromine monoxide (BrO) is a radical which influences chemical processes in the atmosphere, in particular the abundance of ozone. Furthermore, the molar bromine to sulphur ratio in volcanic gas emissions is a proxy for the magmatic composition of a volcano and potentially an eruption forecast parameter.
In this thesis, the distribution of SO_2, BrO and the BrO/SO_2 ratio in volcanic gas plumes is surveyed globally over a four-year period (2018 - 2021) using Differential Optical Absorption Spectroscopy (DOAS) and spectral data of the S-5P/TROPOMI satellite instrument. TROPOMI's high spatial resolution (up to $3.5 \times 5.5\,km^2$) and its daily global coverage yield BrO/SO_2 ratios even for minor eruptions and quiescent degassing. Plumes are automatically detected globally through a plume detection algorithm, leading to a total of 4323 volcanic plumes and a detection of BrO in 1449 of them. 3063 volcanic plumes can be clearly assigned to 43 volcanoes, for which subsequently the mean BrO/SO_2 ratio is calculated – increasing the global data-base of reported BrO/SO_2 ratios from 28 to 60 volcanoes. For the first time, BrO/SO_2 ratios were successfully determined for pure hot spot volcanoes – all of which yield low BrO/SO_2 ratios of $\approx 5 \times 10^{-5}$, in contrast to $2 - 16 \times 10^{-5}$ for arc volcanoes. The observed BrO/SO_2 ratios were in good agreement with ground-based measurements.
A spatial gradient of decreasing BrO/SO_2 ratio towards the plume's center within major volcanic plumes could be attributed to O_3 destruction in the plume's center both from a conceptual model and an empirical plume model. The decrease in the BrO/SO_2 towards the center was observed over 1000 km, indicating the strong chemical impact of reactive volcanic halogenes in the atmosphere.

Contents

Introduction **1**

I Scientific background **3**

1 Volcanism **5**
1.1 Volcanism and volcanoes . . . 5
1.1.1 Volcanic gases and impact on the Earth's climate . . . 6
1.2 Volcanic plume chemistry . . . 8
1.2.1 Volcanic sulphur dioxide – SO_2 . . . 9
1.2.2 Bromine chemistry inside a volcanic plume . . . 10
1.2.3 BrO/SO_2 ratio as a volcanic tracer . . . 13
1.2.4 Release of gases from the magma . . . 14

II Methods **17**

2 Differential Optical Absorption Spectroscopy **19**
2.1 Absorption Spectroscopy . . . 19
2.2 Beer-Lambert-law . . . 20
2.3 The DOAS principle . . . 20
2.3.1 The DOAS retrieval of trace gases . . . 21
2.3.2 DOAS Measurements with an instrument . . . 22
2.4 Additional DOAS effects . . . 23
2.4.1 ISRF response . . . 23
2.4.2 Saturation and I_0 effect . . . 23
2.4.3 Pukite terms . . . 24
2.4.4 Ring effect . . . 24
2.4.5 Shift and Stretch . . . 24
2.5 DOAS measurements of volcanic plumes from satellite . . . 25
2.5.1 Vertical column density (VCD) calculation . . . 26

3 TROPOMI instrument onboard Sentinel-5 Precursor **27**
3.1 TROPOMI instrument . . . 27
3.2 Scanning and coverage . . . 28
3.3 Satellite viewing geometry . . . 29

4 Satellite retrievals **31**
4.1 Selection of reference region . . . 31
4.2 SO_2 retrieval . . . 32
4.2.1 The multiple fit window approach . . . 33
4.3 BrO retrieval . . . 35
4.3.1 Investigation of systematic influences . . . 38
4.3.2 Cloud and Ozone correction scheme . . . 41
4.3.3 Influence of Formaldehyde . . . 47
4.3.4 Statistical uncertainties . . . 51
4.3.5 Overview of the statistical and systematic uncertainties . . . 53

5 Processing of the volcanic data **57**
5.1 Processing of daily data . . . 57
5.2 Automated plume detection algorithm . . . 58
5.2.1 Global SO_2 map . . . 58
5.2.2 Automated event selection . . . 61
5.2.3 Limitations of the plume detection algorithm . . . 65
5.2.4 Processing of an Event . . . 65
5.3 Calculation of the BrO/SO_2 molar ratio in previous studies . . . 66
5.4 Calculation of the BrO/SO_2 ratio in this thesis . . . 69
5.4.1 Categorizing of the linear BrO/SO_2 fit . . . 69
5.5 Alternative measures used in this thesis . . . 73
5.5.1 The fit error of the BrO/SO_2 ratio fit . . . 73
5.5.2 The detection of BrO inside a volcanic plume . . . 74
5.5.3 The non-linearity criterion . . . 75

III Results **77**

6 Global study of the BrO/SO_2 ratio **79**
6.1 Overview of the results . . . 79
6.1.1 Selection criteria for the BrO/SO_2 ratio . . . 81
6.2 Linear BrO/SO_2 cases . . . 82
6.2.1 Minor eruptions and quiescent degassing . . . 86
6.2.2 Medium and major eruptions . . . 88
6.3 Non-linear BrO-SO_2 relation . . . 91
6.3.1 Plume of Mt. Etna, Italy on 25 December 2018 . . . 93
6.3.2 Eruption of Raikoke volcano, Kuril islands, Russia on 22 June 2019 . . . 95
6.4 BrO/SO_2 ratio catalogue . . . 98
6.4.1 Overview . . . 104
6.4.2 Dependency of SO_2 and pixel number . . . 105
6.4.3 Dependency on solar zenith angle and latitude . . . 111
6.4.4 Volcano types . . . 112
6.5 Comparison to previous satellite data . . . 114
6.6 Comparison to ground-based data . . . 116
6.7 BrO/SO_2 ratio time-series . . . 120
6.8 Plume evolution over several days . . . 127
6.9 Summary . . . 129

7 Chemistry inside a volcanic plume – Etna's plume on 25 December 2018 133
7.1 Conceptual Model of the O_3 – BrO interaction in a volcanic plume 134
7.2 Empirical model of Mt. Etna's plume 138
7.2.1 Construction of the model 143
7.2.2 Model workflow 145
7.2.3 Model results 147
7.3 Summary 152

Conclusions and outlook 153

Appendix 159

A BrO/SO_2 Catalogue 159

List of Figures 187

List of Tables 191

Bibliography 193

Acknowledgements 209

Introduction

Volcanism shapes the Earth's system in multiple ways. Lava flows as well as pyroclastic flows, ejection of tephra, ash deposition and indirect effects such as flooding due to the melting of glaciers, pose an existential threat to life in the vicinity of volcanoes. In contrast, volcanic minerals fertilize the ground and deposit veins of highly concentrated minerals in the Earth's upper layers. Furthermore, volcanic eruptions emit large quantities of atmospheric trace gases, i. e. gases of an abundance of less than 0.1 %, which play an important role in many atmospheric processes.
The major trace gases in a volcanic gas plume are carbon dioxide (CO_2) and sulphur dioxide (SO_2) (Textor et al., 2004). The emission of volcanic gas into the atmosphere can have long-term climate impacts and alter the chemical state of the atmosphere – limited to the vicinity of the volcano during smaller eruptions, but also on global scale as the result of larger eruptions. The release of CO_2 does not have an immanent effect on the atmosphere. However, volcanic CO_2 closes the carbon cycle on geological timescales, accounting for the yearly 0.2 GtC, which would be otherwise removed through ocean sedimentation (Bakker et al., 2014). During large eruptions, volcanic sulfur species can reach the stratosphere and strongly influence the Earth's radiation budget. Globally, stratospheric sulfur causes net heating in the stratosphere and net cooling on the Earth's surface (Robock, 2000). This was for example observed at the eruption of Mount Pinatubo in 1991 which caused a global decrease of surface temperatures of 0.5 - 0.6° C over a period of two years (Self et al., 1993).

Equally important is the impact of volcanic halogens. Emitted in smaller amounts, their reactive radicals can nevertheless strongly influence the chemical state of the atmosphere, e. g. through their large O_3 destruction potential (Surl et al., 2021). For instance, reactive bromine species have been associated with ozone depletion inside the volcanic plume (Bobrowski et al., 2007; General et al., 2015; Surl et al., 2021). For eruptions injected into the tropical stratosphere, reduction of O_3 can last over a ten year period, with a hemispheric ozone hole condition in the first year and an Antarctic ozone hole condition up to six years (Brenna et al., 2019). Especially the first year ozone depletion occurring also in mid latitudes can lead to a doubling of UV radiation stress onto the biosphere (Brenna et al., 2019).
Another important aspect of quantifying the volcanic plume composition – particularly the halogen-to-sulphur ratio – is its relation to various volcanic properties. First, the chemical plume composition is a quantity specific to each volcano. Since the first detection of BrO inside a volcanic plume (Bobrowski et al., 2003), ground-based (Bobrowski and Platt, 2007; Gutmann et al., 2018) as well as satellite observations (Hörmann et al., 2013) reveal that the BrO/SO_2 ratio in volcanic plumes varies by three orders of magnitude for different volcanoes. This variation is mostly explained by differences in the magmatic composition (Platt and Bobrowski, 2015). Second, the halogen-to-sulphur ratio has been found to change in line with changes in the volcanic activity. The BrO/SO_2 ratio has been observed to be systematically correlated to changes in the volcanic activity in long-term time-series of Mt. Etna, Italy

(Bobrowski and Giuffrida, 2012), Nevado del Ruiz, Colombia (Lübcke et al., 2014), and Tungurahua, Ecuador (Warnach et al., 2019). These variations have been suggested to be linked to differences in the partitioning of bromine and sulphur from the magmatic melt, i. e. that bromine or sulphur is released in lower depth. However, the interpretation remains difficult, as the partitioning of bromine from the melt is not yet well-constrained.
Trace gas amounts in volcanic plumes can be quantified using the Differential Optical Absorption Spectroscopy (DOAS) technique (Platt and Stutz, 2008). DOAS makes use of the characteristic spectral absorption features of trace gas molecules to determine their concentrations along a light path.
Satellite missions measuring the Earth's spectral radiance with daily global coverage (e. g. TROPOMI) allow for the monitoring of volcanoes. The daily global coverage furthermore enables measurements at remote volcanoes and at volcanoes which are unexpectedly becoming active, such as the Tonga eruption in January 2022.
The high spatial resolution of the S-5P/TROPOMI instrument (up to $3.5 \times 5.5\,\mathrm{km}^2$) – operational since 2018 – and an adapted and refined spectral analysis furthermore offers the potential to detect BrO and its corresponding ratio with sulphur dioxide (BrO/SO_2) even during minor eruptions and for continuously passive degassing volcanoes.

This thesis aims to widen the understanding of (1) the BrO/SO_2 ratio as a volcanic parameter – a proxy for the magma composition – and (2) of BrO as a radical influencing the chemical processes inside a volcanic plume.
For this purpose, BrO and SO_2 column densities from TROPOMI over a four-year period (2018 - 2021) are derived by DOAS (Platt and Stutz, 2008). The retrieval of BrO is optimized for the global detection of BrO in volcanic plumes (see chapter 4).
A detection algorithm for volcanic plumes is employed based on previous work from Hörmann et al. (2013), identifying volcanic plumes globally using enhanced SO_2 columns as a plume tracer (chapter 5). SO_2 and BrO columns as well as the BrO/SO_2 ratio are derived for the individual plumes in chapter 6. Based on the plume dispersion and activity reports taken from the Global Volcanism Program (`volcano.si.edu/`, see bibliography at Global Volcanism Program), active volcanoes are identified globally. A catalogue listing the BrO/SO_2 ratios of the individual volcanoes is compiled. Mean BrO/SO_2 ratios are derived as a characteristic volcanic quantity and linked to volcanic parameters, such as volcano type and activity. Time-series are investigated and interpreted with respect to volcanic activity. Lastly, the obtained TROPOMI satellite data-set is compared to other data-bases from ground-based as well as other satellite measurements.

Spatial gradients of BrO inside a major volcanic plume of Mt. Etna are analyzed in chapter 7 and linked to in-plume chemical inhibition of the BrO concentration due to limited entrainment of O_3 using an empirical model. The model solely relies on measurement data and agrees well with former modelling studies on reactive halogen plume chemistry.

Part I

Scientific background

1 Volcanism and volcanic chemistry

This chapter summarizes the major processes from the Earth's mantle to gas in the atmosphere involved in volcanism. This chapter is based on the corresponding chapter in the author's master thesis (Warnach, 2015), but expanded to meet the different and more demanding scope of this thesis.[1]
Volcanism describes the phenomenon of the transport and release of molten rock from the Earth's mantle onto the surface. This release happens at ruptures in the Earth surface, called volcanoes.
In this chapter the different processes of volcanism happening inside and outside volcanoes are described with focus on gas emissions and chemistry. In section 1.1 a brief overview of the types and formation of volcanoes are given as well as an overview over the magmatic gas constituents. Section 1.2 describes the chemical evolution of volcanic trace gases inside the volcanic plume. The gases SO_2 and BrO and its potential as tracer for volcanic activity are discussed.

1.1 Volcanism and volcanoes

Volcanism is driven by the large amounts of energy inside the Earth. The bulk of the energy is produced by the decay of long-lived radioactive isotopes, but there is also remnant of the potential energy released during the Earth's formation by increasing gravitational pressure. If heat is transferred to the lithosphere (the uppermost 100 - 200 km of the Earth) and rises through the lithosphere, it can open a rupture in the earth surface forming a volcano. The lithosphere consists of the plates (oceanic and continental), which move due to heat convection in the underlying lower and upper mantle (20 - 2900 km depth).
Most types of volcanism occurs at plate boundaries (see figure 1.1). They can be distinguished by the type of boundary at which they occur: diverging or converging plates. If two plates diverge from each other (leading to the formation of new crust) mid-ocean ridge volcanism (for oceanic plates) or continental rift zone volcanism (for continental plates) occurs. If two plates converge, one of them will be subdued into the Earth's mantle. The occurring form of volcanism there is called subduction zone volcanism. One example for subduction zone volcanism are the Andes volcanoes. There, the oceanic Nazca plate descends below the south American continental plate, causing the formation of a volcanic belt.
Subduction zone volcanoes mostly consist of andesitic magma, but the interplay between oceanic lithosphere, continental lithosphere and upper mantle can produce basaltic, dacite or rhyolite magmas as well. Over the course of the subduction of a tectonic plate, volatiles and water stored in the sediments melt. These volatiles rise and are then incorporated into the magmatic melt in the overlying mantel causing the magma and ultimately the volcanic

[1] Mostly, section 1.2.2 is expanded to meet the investigation of the plume chemistry in chapter 7. The other sections are not changed significantly.

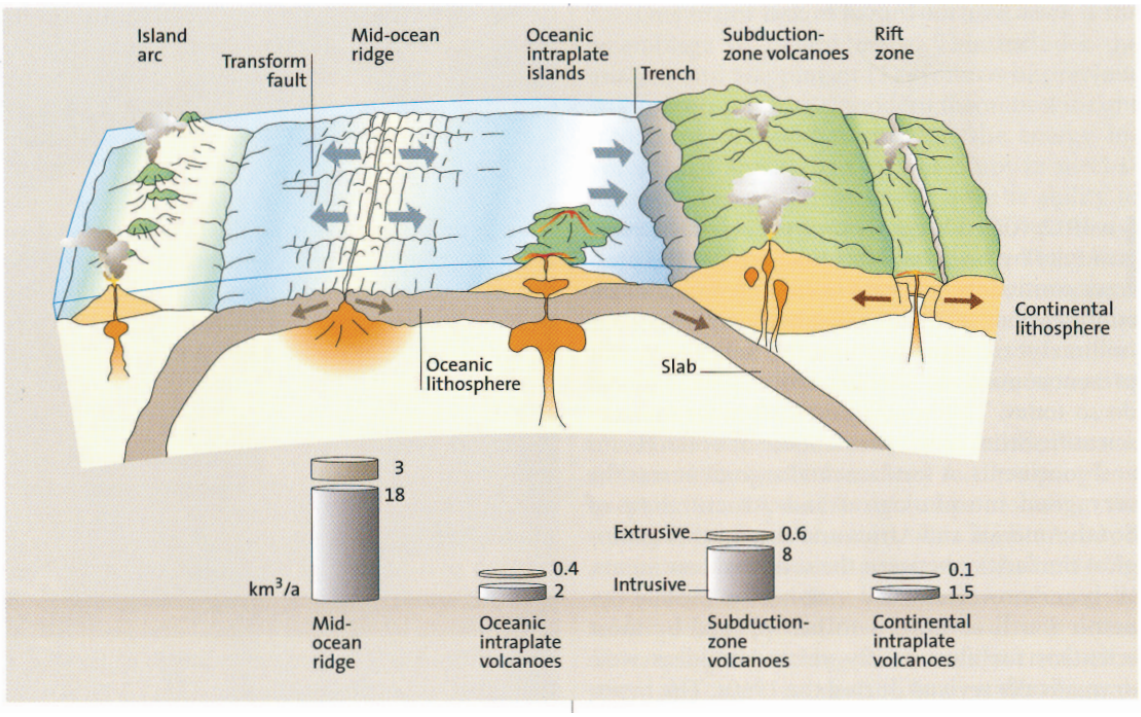


Figure 1.1: Summary of the different types of volcanism. Taken from Schmincke (2004). Diverging plates form rift volcanoes (continental plates) and mid-ocean ridge volcanism (oeanic plate). Subduction of an oceanic plate form subduction-zone volcanoes if submerged below a continental plate and island arc volcanism if submerged below an oceanic plate. Hot spot volcanism (Oceanic intraplate volcanoes) are independent of plate movement.

emission of subduction zone volcanoes to be enriched in water as well as volatile content compared to rift or ridge volcanoes.
Differing from these two forms of volcanism occurring at the margins of plates, the hot spot volcanism occurs in the middle of a tectonic plate. Hot spot volcanoes make up only 5 % of the world's volcanoes. Hot spot volcanism is caused by a hot spot on the core-mantle boundary causing material to rise. This process is independent of the movement of the plates. Over geological time scales a hot spot volcano thus changes its position on the plate forming a »track« from which the plates movement can be derived. One example for such a track is the Hawaiian-emperor-seamount-chain which is the track of the volcanism of the Hawaiian hot spot back up to 85 million years.
Inside a volcano edifice, magma rises depending on its boyancy. During the rise the pressure decreases. If the magma pressure falls below the partial pressure of a solved gas (through Henry's law proportional to the concentration) the gas will exsolve and form a bubble (see section 1.2.3). This can be a process leading to degassing of volcanic gases.

1.1.1 Volcanic gases and impact on the Earth's climate

Volcanoes emit gases into the atmosphere. This can happen through explosive eruptions or through quiescent degassing. The two modes of emission cause different influences on the atmosphere. While quiescent degassing will on a first order impact remain in the troposphere, major eruptions can inject volcanic gas into the stratosphere (Robock, 2000) having a larger impact on the Earth's atmosphere, because it has a longer lifetime.
In addition the origin of the gas differs for quiescent and explosive degassing. While quiescent

Table 1.1: Volcanic gas constituents at the emission vent and global estimated source strength. Adapted from Textor et al. (2004).

Species	H_2O	CO_2	SO_2	H_2S	COS	SC_2	HCl	HBr	HF
%/vol	50 - 90	1 - 40	1 - 25	1 - 10	10^{-4} - 10^{-2}	10^{-4} - 10^{-2}	1 - 10	?	$< 10^{-3}$
Tg/year	?	75	1.5 - 50	1 - 2.8	0.005 - 0.1	0.007 - 0.096	0.4 - 11	0.0078 - 0.1	0.06 - 6

degassing originates mostly from the shallow regions of the volcano, gas emission during eruptions have shown to form at deeper regions (at Stromboli the eruptions originated up to 3 km below the volcanic vent, see Burton et al., 2007, and also figure 1.6). Even though emission fluxes during eruptions are up to one order larger compared to quiescent degassing, the latter is estimated to contribute to 40 % of the accumulated SO_2 emissions during 1972 and 2000 (Halmer et al., 2002) and more recent data suggest that this is only 10 - 20 % (Carn et al., 2017).
Volcanoes mostly emit water (H_2O), carbon dioxide (CO_2) and the sulphur species SO_2 and H_2S (see table 1.1). In addition, small amounts of halogens are emitted in the form of their hydrogen species HBr, HCl and HF. Nevertheless, halogen emission from volcanoes are important, as their reactive radicals can strongly influence the chemical state of the air e. g. halogens can lead to significant changes in the ozone cycle.
Sulphur dioxide (SO_2) and bromine monoxide (BrO), which is formed inside the volcanic plume after release into the atmosphere, are the trace gases evaluated in this thesis. Plume chemistry will be discussed in section 1.2 with respect to both trace gases.

Climate influences

Global accumulated emissions of volcanic gases impact the Earth's climate. The largest impact is caused by the SO_2 emissions which are roughly 7.5 - 10.5 $TgS\,yr^{-1}$ (Halmer et al., 2002). This is still significant compared to the anthropogenic emission of 55 $TgS\,yr^{-1}$ (IPCC, 2013). Additionally, due to higher buoyancy of volcanic SO_2 emissions, they reach higher altitudes leading to a stronger impact on the climate.
Generally, sulphate aerosoles formed in the volcanic plume increases the backscattering of solar radiation and thus the Earth's albedo. In addition, in the troposphere, these can serve as cloud-condensation nuclei (CCN, see figure 1.2). This increases the number of cloud particles, leading to whiter clouds with an increased albedo. In regions with less than 100 $nuclei\,cm^{-2}$, which is the case for large areas over the ocean, the input of CCN can also initiate cloud formation, further increasing the Earth's albedo.
At large eruptions sulphur can also be injected into the stratosphere. The lifetime of sulphur species in the stratosphere is with 1 - 3 years much longer than the 1 - 3 weeks lifetime in the troposphere (Robock, 2000), thus increasing its back-scattering effect (see figure 1.2). Sulphate aerosols in the stratosphere cause stratospheric heating and net cooling on the ground over the time scale of years (Robock, 2000). In the aftermath of the 1991 eruption of Mount Pinatubo, Philippines, the global temperature decreased by 0.5 - 0.6° C during the two years succeeding the eruption (McCormick et al., 1995).
The net radiative forcing due to volcanic emissions is estimated to be -0.11 Wm^{-2} during the years 2008 and 2011 (IPCC, 2013). For comparison: the anthropogenic radiative forcing

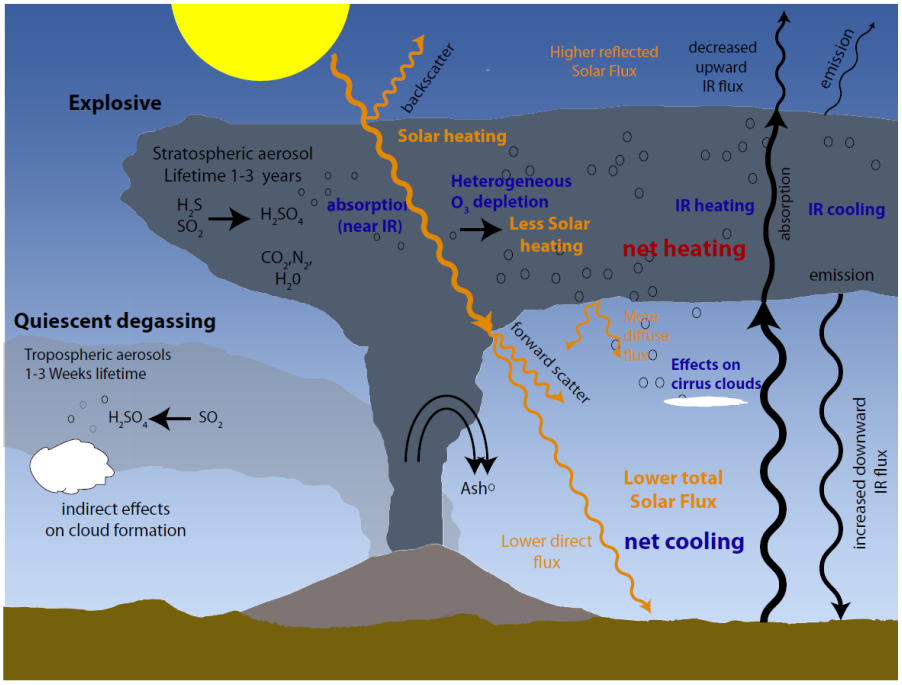


Figure 1.2: Influence of volcanic degassing on the Earth's climate. From Lübcke (2014) redrawn on the basis of Robock (2000).

of CO_2 is estimated as $1.68\,\mathrm{Wm}^{-2}$ during the same period.
Water emissions by volcanoes are negligible compared to the large water budget of the atmosphere and thus not influence the climate or atmosphere significantly.
Even though CO_2 is the second most abundant plume constituent, making up to 40 % vol. of the plume, the accumulated volcanic release of CO_2, estimated to 0.13 - 0.44 Gt (gigatons) per year in 2010, is two orders below the anthropogenic emissions of 35 Gt per year (Gerlach, 2011). Thus its influence on the climate is negligible.
However, on geological time scales the volcanic CO_2 emission is very important for the deep carbon cycle, since it accounts for the 0.2 $\mathrm{GtC\,yr}^{-1}$ ($\approx 0.73\,\mathrm{Gt}$ CO_2 Bakker et al., 2014), which is yearly deposited in sediments and would else be lost to the Earth's core.
Halogen species can also alter the atmosphere globally. Brenna et al. (2019) model the impact of halogen injection into the stratosphere in the aftermath of a plinian eruption in the tropics. They predict hemispheric depletion of ozone in the first years and antarctic ozone hole conditions up to six years after the eruption (Brenna et al., 2019). Furthermore, for such a decrease of O_3, UV radiation is predicted to double over the mid-latitudes of the northern hemisphere, impacting the biosphere (Brenna et al., 2019).

1.2 Volcanic plume chemistry

Upon release in the atmosphere the emitted volcanic gas rises forming a volcanic plume. Even though not always visible to the human eye the volcanic plume is a mixture of the various gases and many aerosol particles. The gas is emitted from volcanoes at a temperature above 500° C (Gerlach, 2004). While rising, the plume cools and mixes with ambient air, activating chemical processes that alter the plume constituents. Since the volcanic plume contains large quantities of aerosoles, volcanic plume chemistry is strongly influenced by

heterogeneous reactions.
In this section the plume constituents SO_2 and BrO, which are the trace gases observed in this thesis, are discussed and its chemical development inside the plume described.

1.2.1 Volcanic sulphur dioxide – SO_2

The sulphur species SO_2 and H_2S are the third and forth most abundant species emitted by volcanoes, contributing up to 35 % (see table 1.1). Upon release the H_2S develops to SO_2 through a series of reactions initiated by a reaction with OH ($H_2S + OH \rightarrow H_2O + SH \rightarrow H_2O + SH$) (for a more detailed description, see Bobrowski, 2005, and references therein).
SO_2 is mainly removed from the atmosphere through dry and wet depositions, leading to lifetimes of several days in the troposphere and in the order of 1 - 3 years in the stratosphere (Robock, 2000). On the time-scales of hours and the first days after emission it can be thus seen as inert and used as a tracer for the volcanic gas content.
Considering the ratio of another plume constituent with respect to SO_2 thus yields information about the evolution of this other plume constituent independent of plume dispersion.
The main sink of SO_2 in the gas phase is the formation of sulphuric acid H_2SO_4 via the following processes:

$$SO_2 + OH \rightarrow HSO_3 \quad \text{(R1)}$$
$$HSO_3 \rightarrow H_2O + SO_3 \quad \text{(R2)}$$
$$SO_3 + H_2O \rightarrow H_2SO_4 \quad \text{(R3)}$$

This process is slow under dry condition leading to estimated 0.43 % loss of SO_2 per hour (Lübcke, 2014). In clouds a different pathway is also possible:

$$SO_2 + H_2O \rightarrow H_2SO_3 \quad \text{(R4)}$$
$$H_2SO_3 + H_2O_2 \rightarrow H_2SO_4 + H_2O \quad \text{(R5)}$$

The sulphuric acid in turn condenses to form aerosols. These can serve as cloud condensation nuclei (CCN) in the troposphere and shield solar radiation in the stratosphere, cooling the Earth's surface over long periods (Robock, 2000).
Concentrations of SO_2 can well exceed 1 ppm (Oppenheimer, 2003), which is several orders of magnitude larger than the mean atmospheric background concentration. Thus, in remote sensing applications, plume-SO_2 is easily distinguishable from ambient SO_2 even if the plume is vertically small compared to the atmospheric vertical extent. In addition with its relative long life time the clear detection of SO_2 with remote sensing allows for the SO_2 content to be used as a tracer for the amount of volcanic gas and hence the SO_2 concentration can be used as a correction factor for the dispertion of volcanic gas.
The ratio of another plume constituent with respect to SO_2 will thus yield information independent of plume dispersion. I. e. the evolution of the X/SO_2 ratio will lead information about the evolution of X inside the volcanic gas.
One example is the plume profile of BrO. Bobrowski et al. (2007) observe higher BrO/SO_2 ratios at the edges of the plume in comparison to the center of the plume and deduce that the relative BrO content is smaller there. The authors suggest that this is due to insufficient mixing with ozone-rich ambient air inside the plume (see figure 1.3 and Bobrowski et al., 2007).

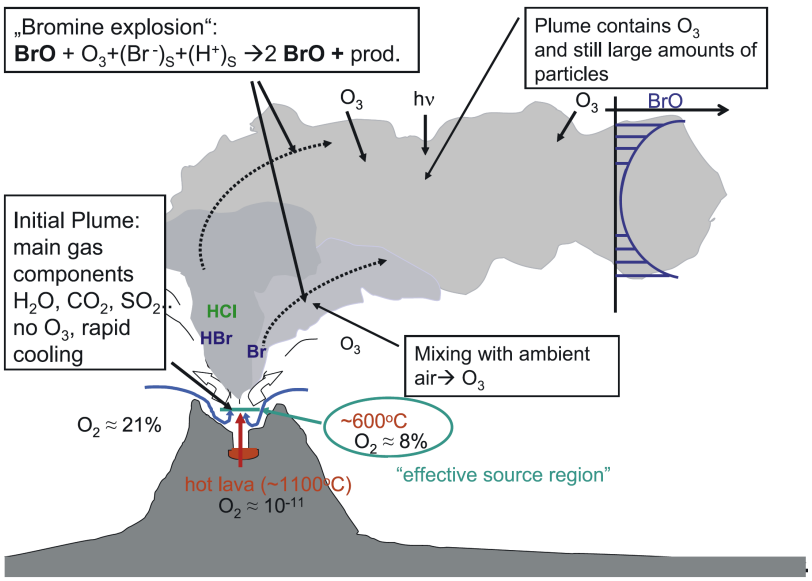


Figure 1.3: Bromine evolution inside the plume after release. Release of bromine at the volcanic vent in the form of HBr. First mixing with ambient air in the »effective source region« leads to Br formation. However the major part of HBr is transformed into BrO via the »bromine explosion« at ambient temperatures. Adapted from Bobrowski et al. (2007).

1.2.2 Bromine chemistry inside a volcanic plume

Bromine monoxide (BrO) was first detected in the volcanic plume of Soufriere Hills volcano (Montserrat) by Bobrowski et al. (2003). Since then many observations have followed with remote sensing DOAS instruments (e. g. Bobrowski and Platt, 2007; Bobrowski et al., 2007; Theys et al., 2009; Vogel, 2011; Hörmann et al., 2013; Lübcke et al., 2014).

However, BrO is not primarily emitted directly from the volcanic vent, but rather in the form of gaseous HBr. High-temperature model calculations suggest that small amounts of atomic Br can be found in emitted gas (Gerlach, 2004), but this is not enough to explain the observed BrO columns. In order to form BrO, the unreactive HBr has to be first converted to reactive radicals – like Br and BrO – in the process called »halogen activation« (Surl et al., 2021). The main driver for this is the so called »bromine explosion« (Bobrowski et al., 2007), which is described in analogy to the arctic bromine explosion (Platt and Lehrer, 1997; Wennberg, 1999).

Upon first high-temperature mixing with ambient air in the so called »effective source region« (see figure 1.3), the initial reactive bromine is believed to start the bromine explosion, by forming BrO (through reaction R10) and subsequently initial HOBr (see reaction R11)(Bobrowski et al., 2007).

At ambient temperature the so called »bromine explosion« then causes a non-linear formation of BrO, following an autocatalytic reaction scheme.

The Bromine explosion at volcanoes can be described by the following reaction cycle, which

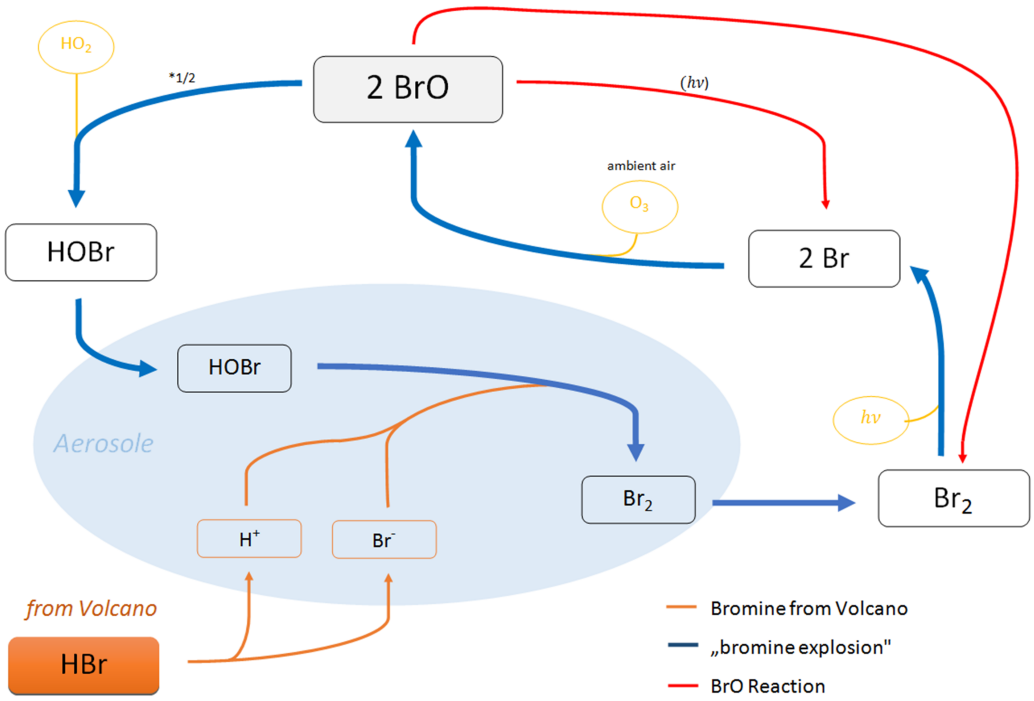


Figure 1.4: Bromine evolution inside a volcanic plume: Release of HBr at the volcanic vent (orange). Heterogeneous dissociation with HOBr inside aerosols forms Br_2, which is then photolytically split into single Br radicals. BrO is formed through a reaction with O_3 upon mixing with ambient air. Reaction with HO_2 forms HOBr, creating an autocatalytic cycle (blue lines, called »bromine explosion«).

is also illustrated in figure 1.4:

$$\mathrm{HBr_{gas}} \rightarrow \mathrm{Br^-_{aq}} + \mathrm{H^+_{aq}} \tag{R6}$$

$$\mathrm{HOBr_{aq}} + \mathrm{Br^-_{aq}} + \mathrm{H^+_{aq}} \rightarrow \mathrm{Br_{2,(aq)}} + \mathrm{H_2O} \tag{R7}$$

$$\mathrm{Br_{2,(aq)}} \rightarrow \mathrm{Br_{2,(gas)}} \tag{R8}$$

$$\mathrm{Br_2} + h\nu \rightarrow 2\,\mathrm{Br} \tag{R9}$$

$$2\,\mathrm{Br} + 2\,\mathrm{O_3} \rightarrow 2\,\mathrm{BrO} + 2\,\mathrm{O_2} \tag{R10}$$

$$\mathrm{BrO} + \mathrm{HO_2} \rightarrow \mathrm{HOBr} + \mathrm{O_2} \tag{R11}$$

$$\mathrm{HOBr_{gas}} \rightarrow \mathrm{HOBr_{aq}} \tag{R12}$$

$$\mathrm{BrO} + \mathrm{HBr} + (h\nu + 2\,\mathrm{O_3} + \mathrm{HO_2}) \rightarrow 2\,\mathrm{BrO} + (3\,\mathrm{O_2} + \mathrm{H_2O}) \tag{R13}$$

The gaseous HBr is taken up by aerosole particles and is split heterogeneously into Br^- and H^+ (reaction R6, orange line in figure 1.4). Inside the aerosole they react with the initial HOBr to form Br_2 (reaction R7), which is then released into the gas phase. The Br_2 is split photolytically into 2 Br (reaction R9), which then reacts with O_3 to form 2 BrO (reaction R10). In a last step one of the BrO forms HOBr (reaction R11), which closes the Bromine explosion cycle, which is also illustrated by the blue lines in figure 1.4. Looking at the sum of the whole reaction cycle (reaction R13), each iteration transforms BrO + HBr into 2 BrO. This means that the reaction rate is driven by the BrO content inside the plume resulting in the exponential, thus »explosive« increase in the BrO content.
The BrO concentration reaches a maximum in the first minutes after the gas is emitted

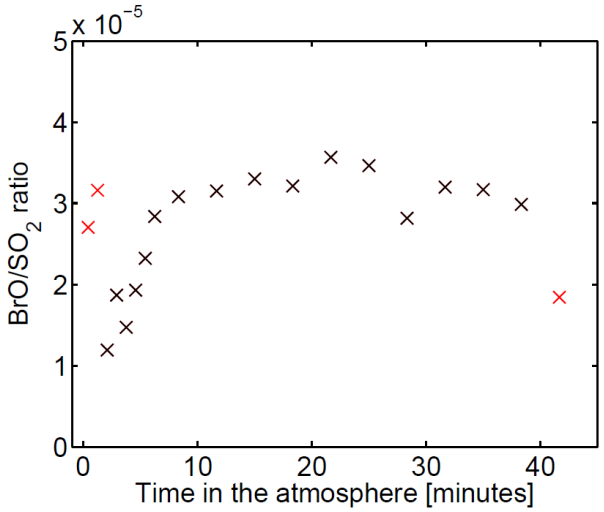


Figure 1.5: Time evolution of the BrO/SO_2 ratio inside the volcanic plume of Nevado del Ruiz, Colombia. Black crosses correspond to more than 20 scans while red crosses have fewer data points. Adapted from Lübcke (2014).

from the volcano and remains constant over at least the next 25 minutes (see figure 1.5 and Lübcke, 2014). BrO formation can be seen as completed, when this equilibrium is reached. This is in line with model studies, e. g. the one from Surl et al. (2021) modelling the complete bromine speciation in the plume of Mt. Etna. The results reveal that the BrO fraction remains constant after a certain initial formation time. This model and also Roberts et al. (2014) as well as measurements at Mt. Etna and Nyiragongo (Bobrowski et al., 2015) suggest that the BrO fraction varies for different emission scenarios.

Limited BrO formation

The exponential BrO formation is diminished by self reactions of the BrO molecules (red lines in figure 1.4):

$$BrO + BrO \rightarrow Br_2 \tag{R14}$$
$$BrO + BrO + h\nu \rightarrow 2Br \tag{R15}$$

These counteract the conversion to HOBr in reaction R11 and has two implications: In the early plume this might slow down the halogen activation, as both BrO atoms cannot activate another HBr. In addition, these reactions can lead to rapid O_3 destruction together with reaction R8 - R10 yielding the cycle:

$$BrO + BrO \rightarrow Br_2 \tag{R16}$$
$$Br_2 + h\nu \rightarrow 2\,Br \tag{R17}$$
$$2\,Br + 2\,O_3 \rightarrow 2\,BrO + 2\,O_2 \tag{R18}$$
$$h\nu + 2\,O_3 \rightarrow 3\,O_2 \tag{R19}$$

In contrast to the bromine explosion pathway, which depends linear on the BrO concentration, this reaction cycle depends on the square of the [BrO] concentration. Hence it will have a larger impact in the dense center of the plume compared to the dispersed edges of the plume.

The slower BrO formation in the plume center caused by lack of O_3 was first measured, modeled and described by Bobrowski et al. (2007). These findings are confirmed by airborne measurements by (General et al., 2015), observing a lower BrO/SO_2 ratio in the center of the plume compared to the edges in the first 10 km of the plume independent of the plume size. Direct measurements of a decrease in O_3 in the center of Mt. Etna's plume is also observed in the early plume of the Br-rich plume of Mt. Etna (Surl et al., 2021).
It must be noted, that the initialization of the bromine explosion requires HOx radicals (to form HOBr in equation R12). In the »effective source region« the formation of OH and HO_2 originates from assuming thermal equilibrium (TE) in the emitted gas (Gerlach, 2004), which predicts significant amounts of released HOx radicals. However, recent models suggest that the plume does not remain in TE during the first seconds after release (Kuhn, 2022), but is rather determined by reaction rates and emission dynamics. This puts a question mark onto the assumptions. Furthermore, this also raises the question if HOx might be the limiting factor in bromine explosion instead of O_3.

Reservoir species of bromine

As the plume disperses BrO will decrease. However, there is no observational evidence about the late stages of bromine speciation. Models suggest that the pathways into $BrNO_2$ and HOBr might be a sink for reactive bromine species and eventually halt the BrO formation. Nevertheless, BrO in the very large plume of Kasatotchi eruption in 2008, is detected up to five days after release (Theys et al., 2009; Hörmann et al., 2013).

1.2.3 BrO/SO_2 ratio as a volcanic tracer

The Br/S ratio is a quantity of the volcanic system. It depends foremost on the magmatic mineral composition. While the BrO/SO_2 ratio at one volcano can change over time, there is also a general difference between different volcanoes (Bobrowski and Platt, 2007), i. e. Nevado del Ruiz, Colombia (Lübcke et al., 2014) and Tungurahua volcano, Ecuador (Warnach et al., 2019) have ratios of 10^{-5}, while Etna, Italy, has ratios in the order of several 10^{-4} (Bobrowski and Giuffrida, 2012). These are mostly dependent on the different magmatic composition (Platt and Bobrowski, 2015) and a quantity specific to the volcano.
This leads to a large range in observed BrO/SO_2 ratios of several orders of magnitudes between 10^{-6} and 10^{-3} (Bobrowski and Platt, 2007; Gutmann et al., 2018).
Overlaid on this general BrO/SO_2 »footprint« of each volcano, long-term observations (on the scale of up to ten years) of the BrO/SO_2 ratio have revealed changes over time in the degassing signature of single volcanoes. These changes have been attributed to changes in volcanic activity. For Mt. Etna (Bobrowski and Giuffrida, 2012), larger BrO/SO_2 ratios are calculated during non-erupting periods compared to eruptive periods and a decrease over the course of the eruptions is reported.
A similar relation is found for one eruption of Nevado del Ruiz (Lübcke et al., 2014), where the BrO/SO_2 ratio decreased three month prior to a major eruption.
At Tungurahua volcano, a lower BrO/SO_2 ratio during the high explosive activity at the onset of eruptive phases is followed by an increase in the ratio as the activity subsides – discovered for 13 eruptive phases over a ten-year time-series obtained from NOVAC[2] spectra.(Warnach et al., 2019)
The changes of the BrO/SO_2 ratio in line with changes of volcanic activity is attributed to different melt-fluid partitioning of bromine and SO_2 (Bobrowski and Giuffrida, 2012;

[2]Network for the Observation of Volcanic and Atmospheric Change (Galle et al., 2010)

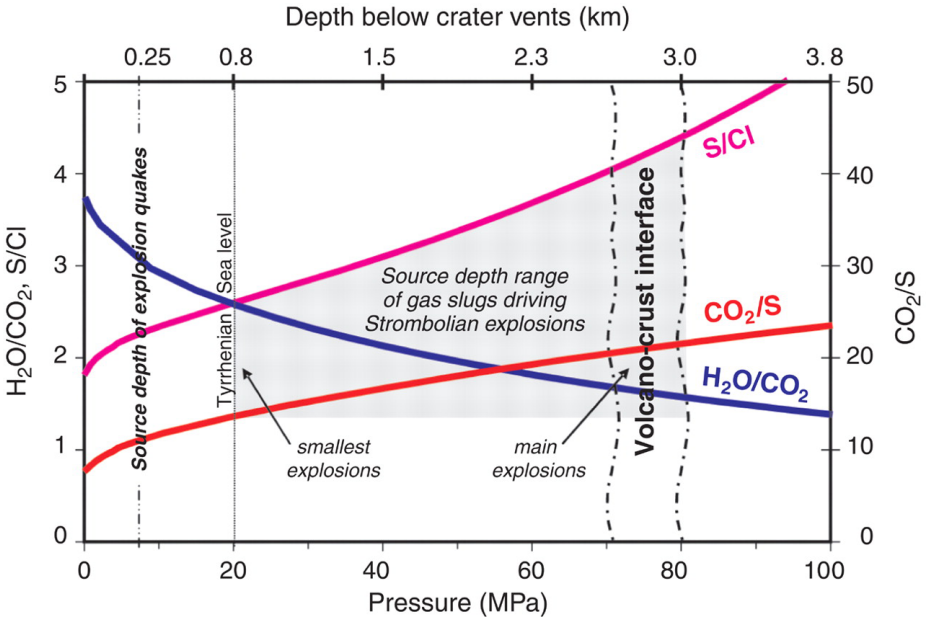


Figure 1.6: Evolution with depth of the ratios of different volcanic gases at Stromboli volcano. Taken from Burton et al. (2007).

Warnach et al., 2019).
Different degassing depths will yield different degassing ratios, i. e. input of fresh magma from deeper regions resulting in first deep degassing will lead to more pronounced signal of species with a higher melt-fluid partitioning, while species with lower partitioning will be released only when the magma has reached shallow depth.

1.2.4 Release of gases from the magma

Inside the volcano the volatiles like the sulphur and halogene species are in solution in the magmatic melt. A gas solute – i. e. a magmatic gas constituent – forms gaseous bubbles if its partial pressure[3] exceeds the pressure of its surrounding solvent – i. e. the magmatic melt. The gas formation stops when the partial pressure of the gas remaining in solution is below the surrounding pressure. The partial pressure p of a gas in equilibrium with a solution is defined by Henry's law:

$$p = K_H c \tag{1.1}$$

Where p is the equilibrium partial pressure, c is the concentration of the solute and K_H is the Henry-constant which is anti-proportional to the solubility α (i. e. $\alpha = K_H^{-1}$). The solubility and thus the Henry constant depends on the temperature of the solution as well as the chemical composition of the solute (i. e. the gas at question) as well as the solvent (i. e. the magmatic melt).
The pressure in the magmatic chamber below the volcanic vent increases with depth. This means that gases will start exsolving at a certain depth, depending on their partial pressure, i. e. on their concentration and solubility in the magma. Further rising will lead to increased gas formation. Thus for each gas the percentage of the gas that is exsolved changes with depth.

[3] In a gas mixture the partial pressure of one gas constituent is defined as the hypothetical pressure if the gas constituent alone occupies the volume of the mixture.

At a certain depth the percentage that is exsolved will be different for different gases. This means that gas formed at different depths will have a different composition of the various constituents. Thus the ratio between two gases contains information about its originating source depth.

Volcanic eruptions are caused by the rising of magma from the mantle. The rising magma will start exsolving gas. Since the gas is usually less dense than the magmatic melt it can rise to the surface prior to the eruption, leading to an increase in gas emission (Malinconico, 1979). This was for instance observed at Santa Ana volcano, where an increase of SO_2 emissions was detected prior to the eruption in 2005 (Olmos et al., 2007). In addition, changes in the composition of the gas are expected as a result of rising magma during or before eruptions, because the ratio of the different constituents change with degassing source depth (see figure 1.6) due to their different melt-fluid partitioning coefficients. Especially the halogen-to-sulphur ratio is interesting, because the ambient air concentrations of both gases are negligible. One of the early reports of a change in the halogen-to-sulphur ratio is by Noguchi and Kamiya (1963), who observe a decrease in the Cl/S ratio prior to an eruption.

A lower Cl/S ratio during eruptive periods compared to non-eruptive periods is also reported by Pennisi and Cloarec (1998) at Mt. Etna. Burton et al. (2007) have measured various gases at Stromboli and find CO_2/SO_2 and the SO_2/HCl ratios to be 3 - 5 times higher during explosions compared to quiescent degassing. The authors compare these data to gas formation simulations for different degassing source depths (see figure 1.6). They conclude that these eruptions are driven by gas slugs originating from deeper levels, where the ratios are higher, while the gas emitted during quiescent degassing originates from shallow magma.

For chlorine and flourine, melt fluid partitioning with respect to sulphur has been studied extensively (e. g. Spilliaert et al., 2006; Burton et al., 2007). Chlorine is found to have a lower melt-fluid partitioning coefficient compared to sulphur, i. e. sulphur is released more pronounced at deep degassing compared to clorine (Carroll and Webster, 1994; Spilliaert et al., 2006; Aiuppa, 2009; Webster et al., 2009). Melt fluid coefficients are reported to range between 0.3 - 50 (Alletti et al., 2009; Webster et al., 2009; Zajacz et al., 2012), which is much lower compared to 3 and 236 for sulphur (Beermann et al., 2015). Aiuppa (2009) report roughly a factor of 9 to be representative for most volcanoes. This is in line with observed Cl/S ratios, where an increase with degassing source depth is found for Stromboli (Burton et al., 2007). At Mt. Etna, measurements suggest that chlorine is predominantly released at shallow depths below 2 km (Allard et al., 2005; Spina et al., 2015).

For bromine, the melt-fluid partitioning is still debated. Cadoux et al. (2018) derive melt-fluid coefficients for bromine between 3.8 - 20.8 from natural silicate glasses. Similar partitioning coefficients are estimated from melt inclusion (0.3 - 21 Kutterolf et al., 2015). Melts produced artificially in an experimental setup show similar partitioning between 2.18-9.2 and 17.5 (Bureau et al., 2000, 2010). These findings suggest that bromine has a lower melt-fluid partitioning coefficient compared to sulphur and thus would show a similar behaviour as chlorine.

However, a direct link to observational gas data and a model curve, like the ones shown in figure 1.6, is not yet available for the BrO/SO_2 ratio. Changes in the BrO/SO_2 ratio are detected at Etna (Bobrowski and Giuffrida, 2012). They observed multiple eruptions between 2006 and 2009 and find the highest ratios two to three months prior to the eruptions, when the magma rises inside the volcano. The ratio then decreases and the lowest values are measured during the eruption, when the magma reaches the volcano vent. Bobrowski and Giuffrida (2012) deduce that bromine is exsolved earlier at lower depths than sulphur. Lübcke (2014) finds a decrease of the BrO/SO_2 ratio at Nevado del Ruiz 5 month prior to

the eruption in 2012. This can also be attributed to an earlier exsolution of bromine during rising magma. Both these interpretations suggest a higher bromine melt-fluid partitioning compared to sulphur, which is conflicting with the finding from Cadoux et al. (2018).
Based on a pattern in BrO/SO_2 found for 11 eruptive phases at Tungurahua (Warnach et al., 2019) and with the findings from Cadoux et al. (2018), Warnach et al. (2019) deduced a conceptual model, which can explain the observed pattern. However, the study does not solve the question of the partitioning of bromine. Firstly as no BrO/SO_2 ratio could be detected during non-eruptive periods and secondly there was no information on the degassing source depth.
Even though a solubility curve is not yet available, investigating the BrO/SO_2 ratio has a great potential for investigating of magmatic processes. Firstly, both gases can be measured with remote sensing by DOAS instruments (e. g. ground-based by Bobrowski et al. (2003, 2007); Vogel (2011); Lübcke et al. (2014); Warnach (2015); Warnach et al. (2019), airplane measurements (General et al., 2015), and satellite based by Hörmann et al. (2013); Beirle et al. (2014) and this study). This enables measurements also during eruptions, where in-situ measurements are not always possible. In addition, the mixing ratio of both gases is found to remain constant between 5 until at least 30 minutes after release (Lübcke, 2014). Bobrowski et al. (2007) also report constant BrO/SO_2 ratios 5 to 20 km off the volcano (see figure 1.5). These results indicate that inter-comparability for data recorded at different distances from the volcano or under varying conditions. Secondly, the remote sensing scanning DOAS instruments allow continuous measurements over long periods. This allows long-term studies of the BrO/SO_2 ratio needed for a detailed understanding of its correlation to magmatic processes.

Part II

Methods

2 Differential Optical Absorption Spectroscopy

This chapter describes the basics of the underlying spectroscopic theory. This chapter is taken from the corresponding chapter in the author's master thesis (Warnach, 2015), but expanded to meet the different and more demanding scope of this thesis.[1]
Differential Optical Absorption Spectroscopy (DOAS) is a widely used method for the retrieval of atmospheric trace gases. First described by Perner and Platt (1979), it utilizes the fact that trace gases are distinguishable by the way they interact with electromagnetic radiation and thus different trace gases can be measured simultaneously using only a single spectrum. Thus, DOAS yields the opportunity to accurately resolve the composition of different parts of the atmosphere.
There are two types of DOAS instruments: passive and active (Platt and Stutz, 2008). Active instruments use a specific light source, which is either implemented into the instrument and cast back to the detector via a reflector (Platt and Stutz, 2008), or can be installed outside. While an active setup has the advantage, that it can be used on any day and night and allows for an easy determination of the light path, it requires a more complex setup and a robust power supply.
Passive instruments use natural light sources, almost always the sun, but also moon-light DOAS measurements have been successfully performed (e. g. Wagner et al., 2000; Zielcke, 2010). This requires no light-source and is thus a less complex setup, but measurements are limited to daytime. Furthermore, the light path is not well constrained, and a calculation of concentration is difficult, requiring knowledge about the radiative transfer. Lastly, the light intensity is limited by the solar spectrum, e. g. limiting the sensitivity of UV and short UV measurements.
Satellite DOAS measurements are so far solely passive DOAS measurements. They measure solar irradiance, which is scattered back in the atmosphere or on the Earth's surface (see figure 2.2).

2.1 Absorption Spectroscopy

The two major processes of the interaction between radiation and the molecules as well as atoms in the atmosphere are absorption through excitation and scattering. For longer wavelength emission can additionally play a role.
Photons can excite molecules into a state of higher energy, being absorbed in the process. This excitation can change either the energetic state of an electron or the rotational or vibrational state of the complete molecule. The energy required for these processes is specific

[1] Section 2.4 and section 2.5 are added completely. The other sections are expanded both with more detailed explanations and additional topics as well as satellite specific information.

for each molecule. The absorption can be described by a wavelength-dependent absorption cross section σ, which is unique for each molecule.
The most important scattering processes are Rayleigh and Mie scattering. Rayleigh scattering describes elastic scattering on particles much smaller than the wavelength of the incident light (i. e. $< 0.1\,\mu m$ for solar radiation). This holds true for most molecules in the atmosphere and small particles. The wavelength dependence of Rayleigh scattering is proportional to λ^{-4} (van de Hulst, 1958). Mie scattering on the other hand describes scattering on particles which have a size in the order of or above the wavelength of the incident light (i. e. $\approx 1\,\mu m$ for solar radiation). In the atmosphere and especially at volcanoes Mie scattering happens on cloud droplets, aerosols and ash particles. Mie scattering shows a weak wavelength dependence proportional to $\lambda^{-\alpha}$, where α is the size dependent Ångström coefficient. The Ångström coefficient is estimated at 1.3 for the general atmosphere (van de Hulst, 1958), while the ash-containing volcanic plume is best represented by an Ångström coefficient of 1.2 (Spinetti and Buongiorno, 2007).

2.2 Beer-Lambert-law

The attenuation of radiation passing through an absorbing medium due to scattering and absorption is described by the Beer-Lambert law:

$$I(\lambda, L) = I_0(\lambda) \cdot exp\left(-\int_0^L \epsilon_R(\lambda, l) + \epsilon_M(\lambda, l) + \sum_i \sigma_i(\lambda, p, T)\, c_i(l)\, dl\right) \tag{2.1}$$

Where I_0 is the initial intensity, ϵ_M, ϵ_R are the scattering coefficients for Rayleigh and Mie scattering, σ and c the absorption cross section and the concentration of the absorbing molecules along the light path L.

2.3 The DOAS principle

In order to utilize the differential absorption features of molecules, the DOAS principle separates broad-band absorption processes and narrow-band (differential) absorption, rewriting equation 2.1 to:

$$I(\lambda, L) = \overbrace{I_0(\lambda) \cdot exp\left(-\int_0^L \epsilon_R(\lambda, l) + \epsilon_M(\lambda, l) + \sum_j \sigma_{b,j}(\lambda)\, c_j(l) dl\right)}^{=:I_0'(\lambda)} \cdot exp\left(\sum_i \sigma_{d,i}(\lambda)\, c_i(l) dl\right) \tag{2.2}$$

The broad band effects including Rayleigh and Mie scattering as well as other broad-band absorber given by $\sigma_{b,j}$ are combined into a new initial intensity $I_0'(\lambda)$, while the absorption on molecules which have narrow band absorption features given by $\sigma_{d,i}$ are separated from $I_0'(\lambda)$. Comparing the broad-band part $I_0'(\lambda)$ with the measured intensity $I(\lambda)$ leads to a differential optical density τ':

$$\tau' = ln\left(\frac{I_0'(\lambda)}{I(\lambda)}\right) = \sum_i \sigma_{d,i}(\lambda) \cdot \int_L c_i(l)\, dl = \sum_i \sigma_{d,i}(\lambda) \cdot S_i \tag{2.3}$$

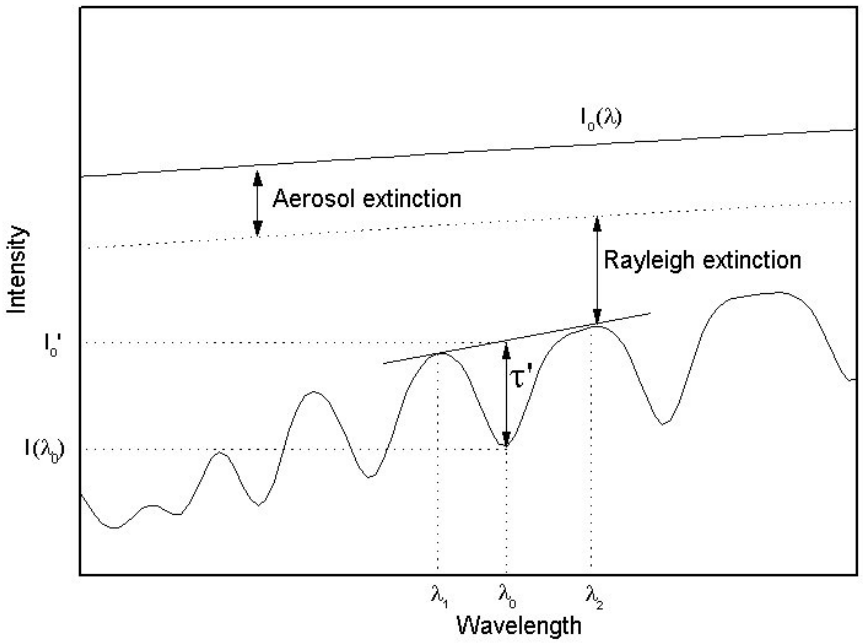


Figure 2.1: Attenuation of light intensity in the atmosphere. Broad band extinction caused by Aerosoles and Rayleigh scattering attenuate I_0 to I'_0. Measured intensity $I(\lambda)$ is formed by attenuation due to differential absorption structures of the trace gas with differential optical density τ'. Taken from Kern (2009).

where the slant column density (SCD) $S_i = \int_L c_i(l)\, dl$ is defined as the integrated column of the absorber i along the light path L. figure 2.1 illustrates the different effects on the light intensity described in equation 2.2. The initial intensity I_0 is attenuated by atmospheric scattering – mostly Mie scattering on aerosoles and Rayleigh scattering. These broad band absorption features are included in I'_0. It deviates from the measured intensity $I(\lambda)$ only by the differential absorption structures. The differential optical density τ' of a trace gas is then obtained by comparing I'_0 with the measured intensity.
Thus, in an ideal case the intensity I is the intensity including the investigated trace gases and I'_0 is the intensity passing through the same path in the atmosphere but seeing no absorbing trace gas.

2.3.1 The DOAS retrieval of trace gases

In a typical DOAS measurement a so called »reference« spectrum is recorded as an approximation for a trace gas free intensity I'_0. The retrieved differential slant column density (dSCD) is defined by the difference in the trace gas between the reference spectrum intensity I_R and the measured spectrum intensity I_M:

$$\tau' = ln\left(\frac{I_R(\lambda)}{I_M(\lambda)}\right) = \sum_i \sigma_i(\lambda) \cdot (S_M - S_R) \tag{2.4}$$

The total slant column density along the light path is thus obtained only if the reference spectrum can be assumed to a have negligible trace gas content in its light path compared to the measurement spectrum or if the column of the reference spectrum S_R is known.
Ideally, the reference spectrum I'_0 is the intensity passing through the same path in the atmosphere void of the absorbers in question. In reality this can never be achieved and

the reference spectrum is measured in a different viewing direction, at a different time or over a different area (in the case of airplane or satellite measurements). Thus, the reference spectrum has a different light path through the atmosphere and will have different Rayleigh and Mie scattering terms. Especially for volcanic plumes with a possibly large aerosol density the different light path can cause a major difference in broad band absorption. However, since these are broad band features they can be accounted for in the DOAS retrieval by adding a polynomial. It can be easily seen that multiplying I'_0 in equation 2.3 by a polynomial $P(\lambda)$ will lead to an added polynomial in the optical density space:

$$\tau' = ln\left(\frac{I'_0(\lambda)}{I(\lambda)}\right) + P(\lambda) = \sum_i \sigma_{d,i}(\lambda) \cdot S_i + P(\lambda) \tag{2.5}$$

Rewriting equation 2.5 and replacing $I(\lambda)$ and $I'_0(\lambda)$ with the measurement and reference spectrum $I_M(\lambda)$ and $I_R(\lambda)$ respectively, the DOAS model function $F(\lambda)$ that resembles the measured intensity $I_M(\lambda)$ can be written as:

$$ln(I_M(\lambda)) \approx F(\lambda) = ln(I_R(\lambda)) + P(\lambda) + \sum_i \sigma_i(\lambda) \cdot S_i \tag{2.6}$$

The DOAS retrieval historically uses a combination of a standard least-squares fit and a Levenberg-Marquard algorithm, varying the polynomial $P(\lambda)$ and the slant column densities S_i, to minimize the deviation from the logarithm of the measured spectra $ln\,(I_M(\lambda))$. A more detailed description of the algorithm can be found in Kraus (2006); Platt and Stutz (2008). For satellite applications the DOAS fit is performed using a standard least-squared fit only following Beirle et al. (2013). This is achieved by a linearisation of the shift and stretch term in the DOAS algorithm (both are included as a pseudo absorber in the fit, derived from a taylor expansion, see section 2.4.5 and Beirle et al., 2013).

2.3.2 DOAS Measurements with an instrument

The intensities described in the previous section are recorded by an instrument. Its finite optical and spectral resolution varies the spectral structures depending on the instruments spectral response function (ISRF). The spectrum $I^*(\lambda)$ arriving at the detector can be thus described by a convolution of the incident spectrum $I(\lambda)$ with the ISRF described by $H(\lambda)$.

$$I^*(\lambda) = I(\lambda) * H(\lambda) = \int I(\lambda - \lambda') \cdot H(\lambda, \lambda')\, d\lambda' \tag{2.7}$$

Using recorded literature absorption cross section typically recorded with a higher resolution, they too have to be convolved with the ISRF:

$$\sigma_i^* = \sigma_i * H(\lambda)$$

The instrument response funtion $H(\lambda)$ can be obtained by measuring the lines of a mercury lamp. Since the spectral width of these lines are only a few pm they can be assumed to be a delta peak compared to typical spectrometer resolutions. However, the ISRF might change over time, e. g. due to temperature variations, and an initial measurement of the ISRF might lose representative. While this can be resolved by renewed measurements of the ISRF, this is not always feasible, e. g. in low-cost autonomous monitoring stations such as NOVAC instruments (Galle et al., 2010) the instrument line function is not remeasured (Lübcke, 2014; Warnach et al., 2019).
For satellites, the instrument is typically not accessible after launch. Significant changes in the ISRF has been observed over time, e. g. for GOME-2 (Munro et al., 2016), which lead

to the need to derive the ISRF directly from daily irradiance in the case of Formaldehyde and Ozone retrieval (e. g. De Smedt et al., 2012; Miles et al., 2015).

2.4 Additional DOAS effects

2.4.1 ISRF response

Changes in the ISRF can also be parametrised and included in the DOAS retrieval as pseudo absorbers (Beirle et al., 2017). For this the ISRF is parametrised using a super-Gaussian (SG):

$$S(x) = A(\omega, k) \cdot e^{-\left|\frac{x}{\omega}\right|^k} \tag{2.8}$$

Where ω corresponds to the width of the super-Gaussian and k to its shape.[2] For TROPOMI the ISRF is determined directly by comparing a high-resolution solar spectrum (Kurucz et al., 1984) with the daily reference solar spectrum (Beirle et al., 2017). A Taylor expansion for each parameter returns spectra, which simulate the influence of a small deviation with respect to the original parameter. These can be included in the DOAS fit as pseudo-absorber in order to model potential changes between reference and measured spectra. For a more detailed description, see Beirle et al. (2017).

2.4.2 Saturation and I_0 effect

There are two effects, which originate from the convolution with the instrument response function as described in equation 2.7: The saturation and the I_0 effect.

The saturation effect and I_0 correction originates from the fact that the convolution and the logarithm do not commute (Wagner et al., 2001). Combining equation 2.3 and equation 2.7, we get:

$$ln\left(\frac{I_0'(\lambda)}{I(\lambda)}\right) * H(\lambda) = \sum_i \sigma_{d,i}(\lambda) * H(\lambda) \cdot S_i \tag{2.9}$$

However, we do not measure the convolution of the logarithm, but the convolved spectra $I_0'^*(\lambda) = I_0'(\lambda) * H(\lambda)$ and $I^*(\lambda) = I(\lambda) * H(\lambda)$ and thus the measured optical thickness τ_{meas} deviates from the modeled optical thickness $\sum_i \sigma_{d,i}(\lambda) * H(\lambda) \cdot S_i$:

$$\tau_{meas} = ln\left(\frac{I_0'(\lambda)}{I(\lambda)} * H(\lambda)\right) \neq ln\left(\frac{I_0'(\lambda)}{I(\lambda)}\right) * H(\lambda) = \sum_i \sigma_{d,i}(\lambda) * H(\lambda) \cdot S_i \tag{2.10}$$

This effect will increase with optical thickness (Wagner et al., 2001), and it is important to ensure that the optical thickness of the trace gas in question has a small optical thickness in the fit range in question ($<$0.1). The optical thickness of SO_2 will exceed 0.1 for strong volcanic plumes in the standard fit range (312 - 324 nm). This can be avoided by fitting in a wavelength range with smaller SO_2 absorption and hence smaller optical thickness, giving rise to the multiple fit window approach in the SO_2 DOAS retrieval, where fit ranges with different absorption strengths are combined depending on the optical thickness (see section 4.2).

[2] For k=2, the function is a normal Gaussian.

The I_0 effect originates from the fact that the ratio does not commute with the convolution, i. e. that:

$$\frac{I_0'(\lambda) * H(\lambda)}{I(\lambda) * H(\lambda)} \neq ln\frac{I_0'(\lambda)}{I(\lambda)} * H(\lambda) \tag{2.11}$$

and thus dividing the convolved spectra instead of the unconvolved spectra will not completely remove the Fraunhofer lines (Wagner et al., 2001). This can be corrected by an I_0 correction of the cross-section σ following Johnston (1996); Wagner et al. (2001):

$$\sigma_{corrected}(\lambda, S) = \frac{ln\left(\frac{I^*(\lambda,S)}{I_0^*(\lambda)}\right)}{S} \tag{2.12}$$

where S is the slant column in the atmosphere. For S either typical maximum values can be assumed (Aliwell et al., 2002) or an iterative approach using the measured slant column itself. An I_0 correction can also be needed to reduce interference of a strong absorber onto a weak absorber, e. g. Aliwell et al. (2002) found a 30% change in the BrO columns in mid latitude summer after applying the I_0 correction onto the O_3 cross section.
In this thesis, the O_3 cross sections are I_0 corrected in order to prevent the interference both onto SO_2 and BrO.

2.4.3 Pukite terms

In the DOAS algorithm the optical density definition $\tau = S \cdot \sigma = \sigma(\lambda) \cdot c \cdot L$ assumes that the light path is independent of the wavelength. For strong absorption, such as LIMB O_3 measurements (Puķīte et al., 2010), however, this assumption does not hold true and the light path is depending on the wavelength. Essentially, the strong absorption reduces the light path more strongly at wavelengths with high absorption compared to wavelengths with lower absorption strength. This effect can be corrected by a Taylor expansion of the relation $\tau = S \cdot \sigma$, leading to $\tau = S \cdot \sigma + S \cdot \lambda\sigma + S \cdot \sigma^2$ (Puķīte et al., 2010), where $\lambda\sigma$ and σ^2 are the so called »Pukite-terms«, which can be added to the DOAS fit as pseudo-absorber.
This is important for O_3, but has also been applied to SO_2 (pers. comm. Nicolas Theys, BIRA). In this thesis the Pukite terms are applied for O_3 and included in both BrO as well as SO_2 fits.

2.4.4 Ring effect

Apart from the elastic scattering, i. e. Rayleigh and Mie scattering, inelastic Raman scattering also influences the measured intensity $I(\lambda)$. In difference to elastic scattering, inelastic scattering on atoms and molecules changes the energy and thus the wavelength of a photon. The propability of Raman scattering is in first order proportional to the intensity. Intensity minima in the solar spectrum caused by the Fraunhofer lines will thus be »filled in« because it is less likely that a photon energy will be moved into this wavelength than the opposite (Grainger and Ring, 1962). This effect is today known as »Ring effect« and has to be included in the DOAS retrieval as a spectrum that is calculated from the solar spectrum $I_0(\lambda)$, following Wagner et al. (2009).

2.4.5 Shift and Stretch

In a DOAS measurement the measurement spectrum can have a wavelength shift as well as a stretched in wavelength with respect to the reference spectrum. While traditional DOAS retrievals use a non-linear fit separated from the actual DOAS fit (which is linear) to estimate

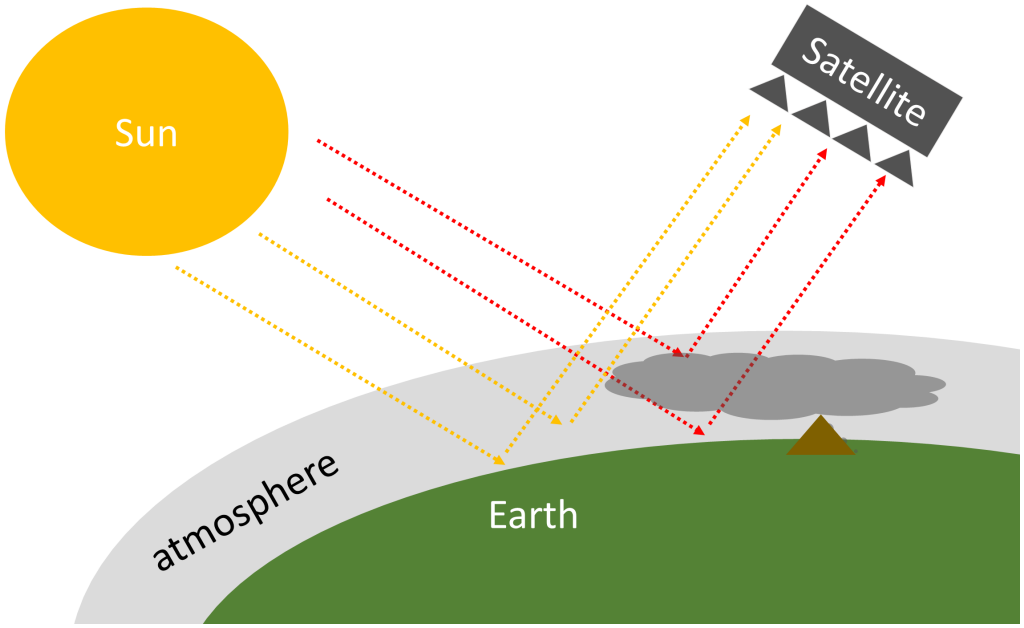


Figure 2.2: Schematic view of a satellite measurement of a volcanic plume. Sun irradiance scattered into the satellite is marked by yellow (not traversing the volcanic plume) and red lines (traversing the volcanic plume).

the shift and stretch, the effect of a small shift and stretch can be estimated by a spectrum derived from a taylor expansion (Beirle et al., 2013). This spectrum can be included in the DOAS fit as pseudo-absorber, making the retrieval purely linear. For satellites, which produce 2×10^7 measurements per day, this enhances the processing speed drastically, and this method of accounting for shift and stretch is used throughout this thesis.

2.5 DOAS measurements of volcanic plumes from satellite

DOAS requires a light source emitting light in the wavelength region in question.

In equation 2.4 it can be seen that the DOAS is done by comparing a reference spectrum and a measurement spectrum, which ideally see the same background atmosphere.

This is achieved by selecting a spectrum void of the absorber in question. For satellite measurements of volcanic plumes, this is effectuated by looking into a direction where there is no volcanic plume is. Thus, the satellite observes light passing through the plume and light not traversing the plume separately, which are then used as the measurement and the reference spectrum respectively. The selection of the reference spectrum and the method of how to derive the slant column of the volcanic plume is written in section 4.1. Ideally, the reference region is measured directly next to the volcanic plume. However, for a global volcanic plume retrieval from satellite, this is not feasible. Instead one global reference spectrum is used (see section 4.1) and the dSCD of the background around the volcano is subtracted from both volcanic and background data afterwards (see section 5.2.4), essentially leading to the equivalent column as using a reference spectrum close to the volcano.

2.5.1 Vertical column density (VCD) calculation

The DOAS retrieval results in the SCD, e. g. the integrated column along the slant light path. Apart from the amount of gas, i. e. the the gas concentration as well as its dispersion, the light path and thus the SCD is strongly depending on the viewing geometry. The viewing geometry of a satellite irradiance measurement can be defined by three angles: The solar zenith angle (SZA), the viewing zenith angle (VZA) and the relative azimuth angle (RAA). A detailed description of satellite geometry is given in section 3.3.

A quantity independent of the viewing geometry is the vertical column density (VCD), defined as the integrated column along the vertical light path. The SCD can be connected to the VCD via the so called air mass factor (AMF):

$$VCD = \frac{SCD}{AMF} \tag{2.13}$$

While accurate estimation of the AMF has to be done using radiative transfer models, e. g. MCArtim (Deutschmann et al., 2011) or VLIDORT (Spurr, 2006), a geometrical approximation – valid for stratospheric absorber and SZA$< 80°$ – is used in this thesis:

$$AMF_{geo} = \frac{1}{\cos(SZA)} + \frac{1}{\cos(VZA)} \tag{2.14}$$

3 TROPOMI instrument onboard Sentinel-5 Precursor

Sentinel-5 Precursor (S-5P) – launched on 13 October 2017 – is a low-earth orbit (LEO) polar satellite, build and operated by the European Space Agency (ESA). S-5P's mission is to provide long-term data for the analysis of the atmospheric composition and variation.
The only instrument onboard S-5P is the TROPOspheric Monitoring Instrument (TROPOMI). TROPOMI is a hyperspectral imaging spectrometer measuring radiance spectra via four different detectors each in different wavelength regions: The Ultra-Violet detector (UV, 270 - 320 nm), the UV-visible detector (UVIS, 310 - 500 nm), the Near-InfraRed detector (NIR, 675 - 775 nm) and the Short-Wave-InfraRed detector (SWIR, 2305 - 2385 nm). A detailed overview of the spectral characteristica for each detector is given in figure 3.1 and Veefkind et al. (2012).
In this thesis, TROPOMI's UVIS radiances are used to detect SO_2 and BrO vertical column densities using the DOAS technique (see chapter 2 for a description of the DOAS algorithm and chapter 4 for a description of the fit settings).
In the following, a few characteristics of the TROPOMI instrument and its measurement parameter are introduced focusing on the UVIS channel.

3.1 TROPOMI instrument

Sentinel-5 Precursor and thus TROPOMI is flying in a low Earth orbit at an altitude of roughly 824 km. Its orbit is sun-synchronous with an equator crossing time at roughly 13:30 h mean local solar time, i. e. the complete Earth's surface will have a similar solar angle and similar local time. Every day S-5P covers 14 orbits with an orbital repeat cycle of 16 days (in total 227 orbits in one orbit cycle, i. e. 3 days of this cycle will have 15 orbits). Orbital inclination is 98.7° with respect to the equator, leading a near-polar orbit.

Table 1
TROPOMI spectral bands.

Detector	UV		UVIS		NIR		SWIR
Band	1	2	3	4	5	6	7
Spectral range [nm]	270–300	300–320	310–405	405–500	675–725	725–775	2305–2385
Spectral resolution [nm]	1.0	0.5	0.55	0.55	0.5	0.5	0.25
Spectral sampling [nm]	0.065	0.065	0.2	0.2	0.1	0.1	<0.1
Spatial sampling [km^2]	21×28	7×7	7×7	7×7	7×7	7 (1.8)[c]	7×7
Detector binning factor	16	4	4	4	4	4 (1)	1
Minimum signal-to-noise	100–800[a]	90–700[a]	800–1000[a]	800–1000[a]	100–500[a]	100–500[a]	100–120[b]

[a] The minimum signal to noise is specified for a scene with an albedo of 2% and the Sun in zenith.
[b] The minimum signal to noise is specified for a scene with an albedo of 5% and solar zenith angle of 70°.
[c] The spatial sampling of Band 6 can be reduced to improve the spatial co-registration with the other bands.

Figure 3.1: Spectral range, resolution, sampling, spatial sampling, and minimum signal-to-noise given for the four TROPOMI detectors. Taken from Veefkind et al. (2012).

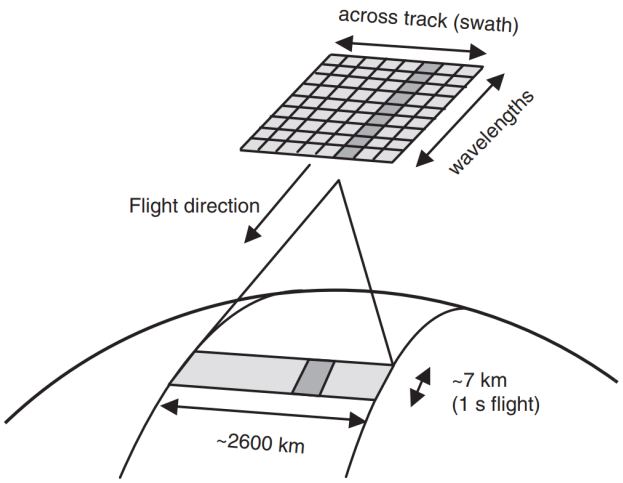


Figure 3.2: Overview of the TROPOMI Scanning procedure. The earthshine radiance of a 2600 km wide and 7 km (5.5 km after 6 August 2019) long swath is projected onto a 2d CCD. Taken from Veefkind et al. (2012).

3.2 Scanning and coverage

TROPOMI scans the Earth with a push-broom method. This means that the surface is scanned by pushing a swath of a certain width over it. This »broom« is then pushed orthogonal to the swath direction in order to scan the area of interest. In the case of TROPOMI, each orbit will thus scan an area of the swath width along the orbit. TROPOMI has an opening angle of 108° leading to a ground swath of approx. 2 600 km. In turn, the 14 daily orbits result in daily global coverage (with the exception for a small area between 7° S and 7° N where almost complete coverage is achieved). Vice versa, for high latitude regions a large area will have multiple overpasses over one day and the poles will be covered 14 times each day. The push-broom-scanning is achieved by projecting the different incoming angles (i. e. the different positions along the swath) onto the first dimension of a 2d-CCD detector array. Wavelength is resolved via a grating spectrometer, which splits the light along the other dimension of the detector array (see figure 3.2).

The pixel along the swath are called across-track pixel and the pixel along the flight direction are called along-track pixel.

The pixel size across track is defined by the sampling of the one direction of the CCD detector. For the UVIS band of TROPOMI the across-track spatial sampling at nadir (see figure 3.4) is 3.5 km, which increases up to 14.4 km for larger viewing angles.

The along-track pixel size was originally 7 km (corresponding to $\approx$ 1 s flight) and was reduced to 5.5 km on 6 August 2019. Since then the maximal spatial resolution is thus $5.5 \times 3.5\,\mathrm{km}^2 = 19.25\,\mathrm{km}^2$.

This yields a drastic improvement in the detection of small scale structures and gradients compared to the other atmospheric trace gas sensors with similar capabilities. Compared to the Ozone Monitoring Instrument (OMI) wich has a pixel footprint of $24 \times 13\,\mathrm{km}^2 = 312\,\mathrm{km}^2$, which is operating from 2005 - today, this is an improvement of a factor 16. A factor of 166 in pixel area is achieved compared to GOME-2 (in operation from 2008 - today), which has a pixel area of $80 \times 40\,\mathrm{km}^2 = 3\,200\,\mathrm{km}^2$. The older satellites SCIAMACHY onboard ENVISAT ($60 \times 30\,\mathrm{km}^2 = 1\,800\,\mathrm{km}^2$, 2002 - 2012) and GOME ($320 \times 40\,\mathrm{km}^2 = 12\,800\,\mathrm{km}^2$) have a pixel area factor of 94 and 665 respectively. A comparison of the pixel area of the

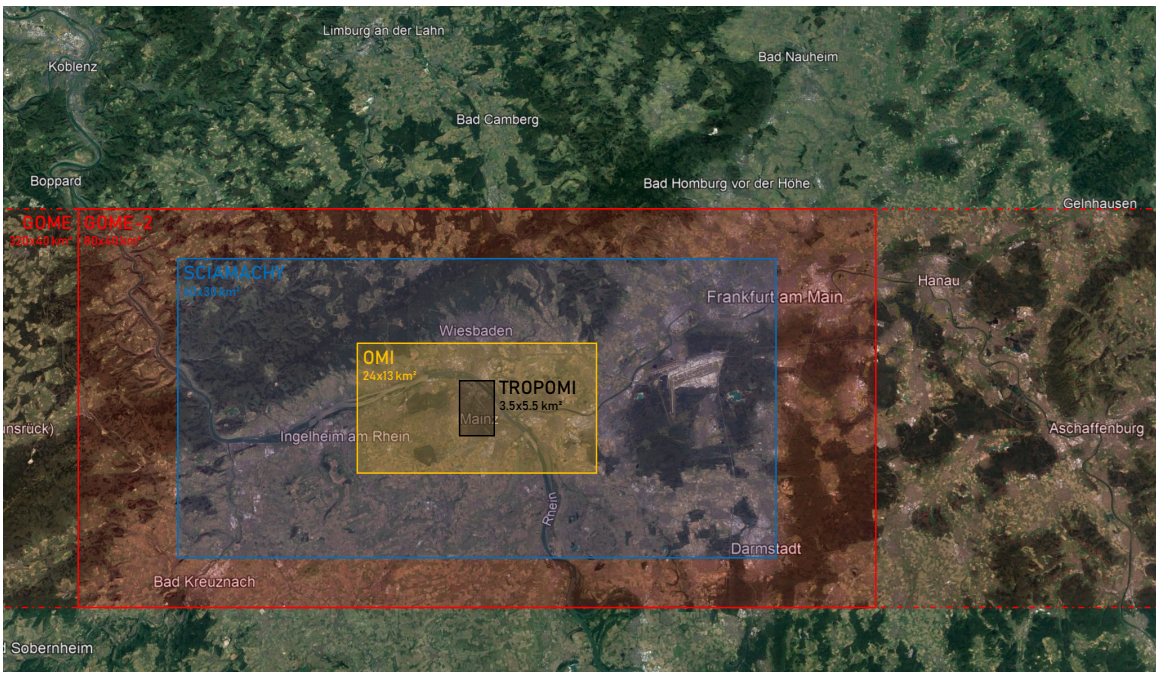


Figure 3.3: Comparison of the pixel area of different satellite instruments over the Rhein-Main region. Background map taken from Google Earth.

different instruments is shown in figure 3.3 over the Rhein-Main region. It can be seen that the TROPOMI pixel size is small enough to separate neighbouring cities, such as Mainz and Wiesbaden, while the footprint of the next larger instrument (OMI) is larger than the distance between Mainz and Wiesbaden. Especially the improvement to the previous ESA satellite GOME-2 is significant, as one GOME-2 pixel covers the complete Rhein-Main region encompassing 4 large cities, while TROPOMI will ideally yield a detailed image of 166 pixel in the same area.

3.3 Satellite viewing geometry

TROPOMI is a nadir looking instrument. The nadir is the direction from the satellite to the Earth's center, i.e. it is approximately perpendicular to the Earth's surface (see figure 3.4). The zenith is defined as the line perpendicular to the surface of the Earth at the point of measurement. Neglecting the Earth's curvature, it is parallel to nadir. The solar irradiance line connects the sun with the point of measurement (yellow line in figure 3.4), while the satellite radiance line connects the point of measurement with the satellite (blue line in figure 3.4).
There are three angles, which describe the satellite's viewing geometry with respect to the sun:

- The solar zenith angle (SZA) θ is defined as the angle between the solar irradiance line and the zenith.
- The viewing zenith angle (VZA) ϕ is defined as the angle between the satellite radiance line and the zenith.
- The relative azimuth angle (RAA) is defined as the angle between the solar plane (yellow shaded area in figure 3.4) and the viewing plane (blue shaded area in figure 3.4).

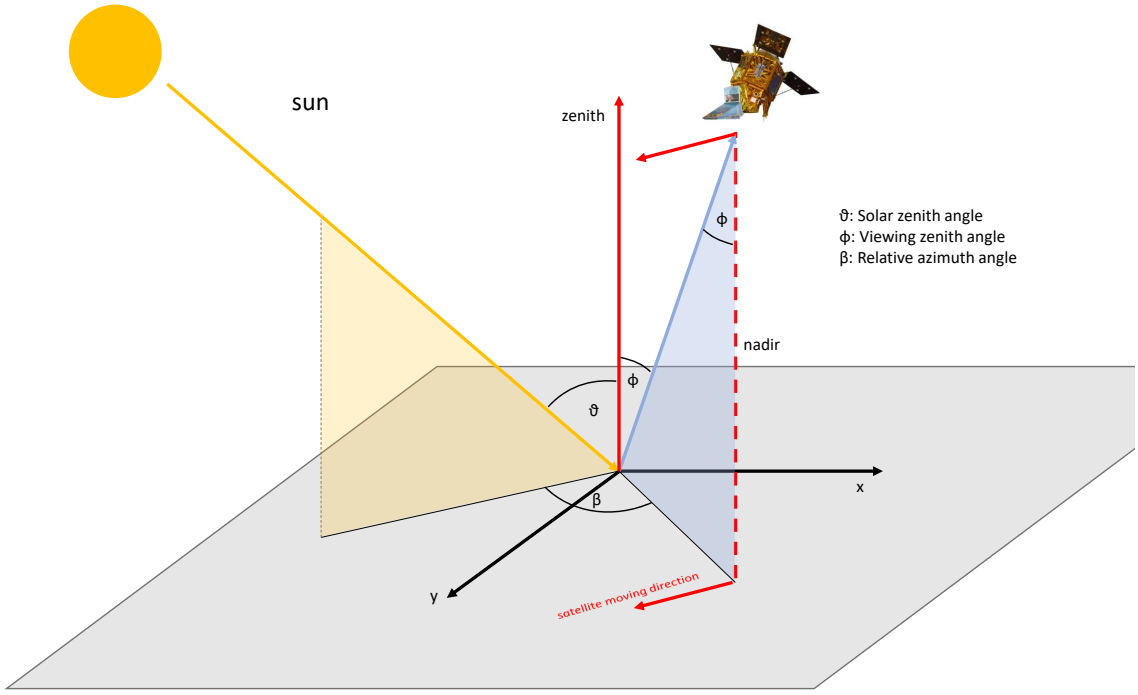


Figure 3.4: Satellite viewing geometry: Viewing zenith angle ϕ and relative azimuth angle β are the angles between the satellite's viewing plane (blue shaded area, orthogonal to the satellite moving direction) and the zenith and anlge between the satellite's viewing plane and the solar plane (yellow shaded area) respectively. Solar zenith angle θ is the angle between the solar viewing plane and the zenith.

4 Satellite retrievals

The selection of the DOAS fit parameters and the wavelength range depend mainly on the application, i. e. the optical density (OD) of the trace gas in question as well as other trace gases. Thus, the same trace gas can have very different optimal fit settings for different applications.
In this chapter the optimal retrieval settings for volcanic applications for BrO and SO_2 are explored. This includes the investigation of DOAS fit setting best suited for the retrieval of global volcanic events as well as the correction and discussion of potential spectral influences. The main focus is laid on the BrO retrieval, as its signal-to-noise is several orders below the one of SO_2 for typical volcanic plumes.

4.1 Selection of reference region

Traditionally, DOAS retrievals from satellites use the direct solar spectrum recorded each day as a reference spectrum. This ensures that the DOAS retrieval can yield absolute slant columns of the respective trace gas. However, the direct solar spectra are obtained through a different optical input channel and traverses different optical parts. Thus, differences in the sensitivity of individual CCD pixel will cause stripes in the across-track direction. While this can be corrected via so called »destriping« (e. g. Hörmann et al., 2016), in recent times an earthshine spectrum has been used as reference spectrum for the retrieval (Theys et al., 2017; Seo et al., 2019). Ideally, such an earthshine spectrum is calculated from radiances obtained at regions, where the respective trace gas is not abundant. Thus, regions over the equatorial pacific are used (Sihler et al., 2012; Hörmann et al., 2013; Seo et al., 2019), far off potential anthropogenic pollution sources and remote from potential volcanoes. In this thesis, an earthshine spectrum is calculated similarly, however the equatorial reference region (20° S to 20° N) is extended to the whole latitude band from 180° W to 180° E.
For SO_2, the assumption that remaining SO_2 is negligible holds true for this case under normal circumstances[1] and is implemented for example in the algorithm of the TROPOMI SO_2 operational product (Theys et al., 2021).
For BrO however, there is a significant stratospheric background signal over the equatorial region with VCDs of roughly 3.5×10^{13} molecules cm^{-2}, as stated by Richter et al. (2002) and also found for this data-set. Thus, using the earthshine reference will yield differential SCDs instead of absolute SCDs. However, a potential contamination signal or the stratospheric signal will introduce an offset in the resulting slant column densities, which is only slowly changing in spatial direction. In this thesis, the focus is on local volcanic plumes. Volcanic plumes are singular events, whose (1) spatial patterns have a high contrast compared to the background, (2) spatial extend is almost always of a much smaller scale w. r. t. stratospheric

[1] There have been cases, where major eruptions of volcanoes, whose plume can stretch several thousand kilometres, induce a signal inside this reference region (pers. communication Nicolas Theys, BIRA).

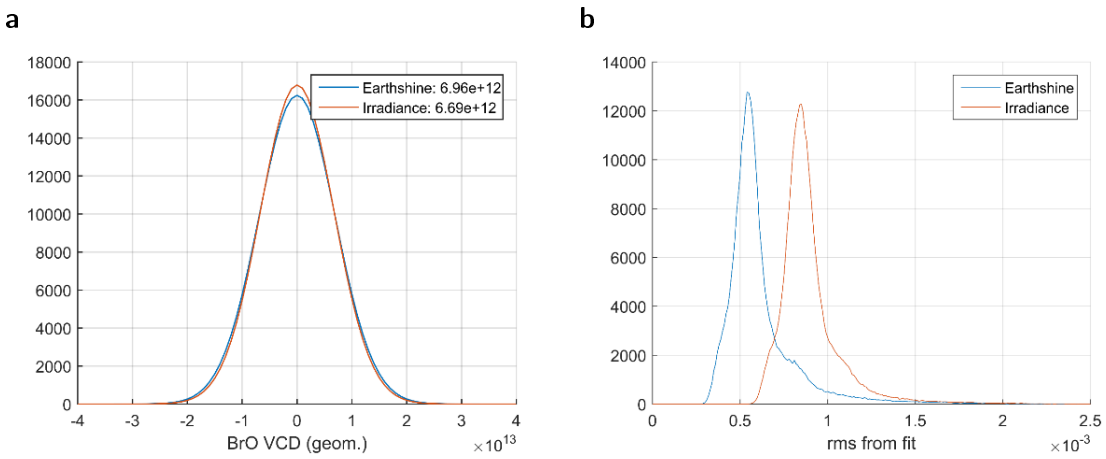


Figure 4.1: **a** Distribution of the RMS and **b** the BrO VCD for both the irradiance and earthshine retrieval for the pacific region [±20°N, 135-105°W] on 1 October 2018.

patterns, and (3) dispersion is independent from the latter. Thus, any stratospheric can be removed by performing a local background correction SO_2 and BrO (see section 5.2.4).
The earthshine reference spectra are calculated in the following way: Firstly, all radiances within the global latitude band [180° W to 180° E] around the equator [20° S to 20° N] are selected. In a second step, the radiances are normalized with respect to their maximum intensity in order to prevent that scenes or geometries which result in a brighter backscatter radiation, e. g. cloudy scenes, to be systematically weighted stronger. In the last step, the mean of the normalized radiances is taken as the daily reference spectrum in the DOAS analysis.
This process is done separately for each of the 450 across-track detectors of the TROPOMI instrument and for each day. A comparison of both results using the earthshine as well as the direct solar spectrum for a fit for the pacific region [±20°N, 135 - 105°W] on 1 October 2018 is shown in figure 4.1. It can be seen that the retrieved VCD shows no difference (here the stratospheric influence in the irradiance data is eliminated for comparison by subtracting the mean BrO VCD). The fit root-mean-square (RMS), however, is about 25% lower for the earthshine fit.

4.2 SO_2 retrieval

DOAS SO_2 retrievals from satellites are performed starting with the launch of the Global Ozone Monitoring Experiment (GOME) in 1995 (Eisinger and Burrows, 1998; Thomas et al., 2005; Khokhar et al., 2005); later DOAS retrievals are implemented also for the SCanning Imaging Absorption SpectroMeter for Atmospheric CHartographY (SCIAMACHY) (Afe et al., 2004), GOME-2 (Rix et al., 2012; Hörmann et al., 2013), the Ozone Monitoring Instrument (OMI) (Theys et al., 2015) and most recently for TROPOMI (Theys et al., 2017).
While for GOME and SCIAMACHY the SO_2 retrieval was initially only performed in one wavelength range (typically 315 - 327 nm), the observation of large volcanic plumes like the Kasatotchi eruption in 2008, lead to more sophisticated retrieval schemes. Both Hörmann et al. (2013) and Theys et al. (2015) introduced a scheme using multiple fits in different wavelength ranges, allowing optimal and accurate SO_2 detection at different order of magnitudes of SO_2 columns. For increased sensitivity to small SO_2 columns such as minor volcanic

Table 4.1: Selection criteria and formula for the combined SO_2 SCD for the four SO_2 fits SR, MR, AR, and LR. The respective slant column S is indexed with the respective abbreviation.

No.	selection criteria	combined SO_2 SCD
1	$S_{SR} < 3 \times 10^{17}$	S_{SR}
2	$3 \times 10^{17} < S_{SR} < 8 \times 10^{17}$ & $S_{MR} < 2 \times 10^{18}$	$S_{SR} \cdot \left(1 - \frac{S_{SR} - 3\times10^{17}}{8\times10^{17} - 3\times10^{17}}\right)$ + $S_{MR} \cdot \left(\frac{S_{SR} - 3\times10^{17}}{8\times10^{17} - 3\times10^{17}}\right)$
3	$8 \times 10^{17} < S_{SR}$ & $S_{MR} < 2 \times 10^{18}$	S_{MR}
4	$3 \times 10^{17} < S_{MR} < 4.6 \times 10^{18}$ & $S_{AR} < 6 \times 10^{18}$	$S_{MR} \cdot \left(1 - \frac{S_{MR} - 2\times10^{18}}{4.6\times10^{18} - 2\times10^{18}}\right)$ + $S_{AR} \cdot \left(\frac{S_{MR} - 2\times10^{18}}{4.6\times10^{18} - 2\times10^{18}}\right)$
5	$4.6 \times 10^{18} < S_{MR}$ & $S_{AR} < 6 \times 10^{18}$	S_{AR}
6	$6 \times 10^{18} < S_{AR} < 8 \times 10^{18}$	$S_{AR} \cdot \left(1 - \frac{S_{AR} - 6\times10^{18}}{8\times10^{18} - 6\times10^{18}}\right)$ + $S_{LR} \cdot \left(\frac{S_{AR} - 6\times10^{18}}{8\times10^{18} - 6\times10^{18}}\right)$
7	$8 \times 10^{18} < S_{AR}$	S_{LR}

eruption and anthropogenic sources the fit ranges starting at 312 nm and ending at 324 nm (Hörmann et al., 2013) and 326 nm (Theys et al., 2015) is used. While in principle even lower wavelengths would further increase the sensitivity, the steep decrease in solar irradiance as well as the increased O_3 absorption in this wavelength range limits this. A lower boundary of 310.5 nm was tested by Theys et al. (2015), yielding only very minor improvements. For SO_2 columns exceeding 1×10^{18} – as can be found in large volcanic eruptions – however, the optical depth of SO_2 will increase. In such cases the linear assumption made in the DOAS procedure is no longer given, leading to a saturation effect, i. e. a diminished response to an increase in column density. Therefore, additional DOAS fits in higher wavelength ranges are added (Hörmann et al., 2013; Theys et al., 2015), where the SO_2 absorption strength is weaker and large SO_2 columns can be accurately determined.

4.2.1 The multiple fit window approach

In preparation for the TROPOMI instrument onboard Sentinel-5 Precursor, analysis in three fit windows were developed for the verification algorithm (by C. Hörmann, MPIC, Mainz) as well as the operational algorithm (by N. Theys, BIRA, Brussels) and compared in the verification exercise (Richter and the S5-P/TROPOMI verification team, 2015; Theys et al., 2017).

The heritage of the retrieval scheme used in this thesis is the verification algorithm developed by Christoph Hörmann (Richter and the S5-P/TROPOMI verification team, 2015). The algorithm employs three DOAS fits with different fit ranges: The standard range (SR: 312.1-324 nm) used if the SR SCDs are below 4×10^{17} molecules cm^{-2}, the medium range (MR:

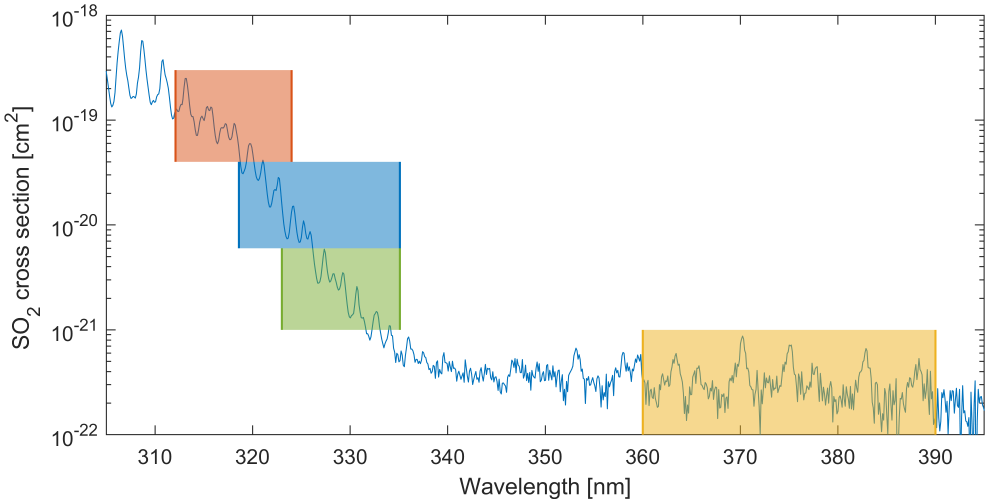


Figure 4.2: Absorption cross section of SO_2 (Bogumil et al., 2003) from 305 - 395 nm. The four fit ranges are shaded: Standard range (SR, red), medium range (MR,blue), alternative range (AR, green), and large range (LR, yellow).

318.6 - 335.1 nm) used for MR SCDs between 9×10^{17} and 2.4×10^{18} molecules cm^{-2}, and the alternative range (AR: 323.1 - 335.1 nm) for AR SCDs above 4.6×10^{18} molecules cm^{-2}. In between the SCDs from neighbouring fit ranges were interpolated linearly between the neighbouring fit ranges. In this thesis, this approach was tested on S-5P/TROPOMI data within the SO_2 verification for the upcoming Sentinel-5 mission (van Roozendael and the Sentinel 5 Verification team) as well as on synthetic spectra within the SO_2 verification for the upcoming Sentinel-4 mission (Wagner and the Sentinel 4 Verification team). In both cases the performance of the results were compared to the results of the S-5P/TROPOMI operational algorithm (Theys et al., 2017). While the three fit ranges were not changed, small refinements in the boundaries for the different fits were done. In addition, two very large eruptions with SO_2 SCDs exceeding 1×10^{19} molecules cm^{-2} (Raikoke, Kuril islands, Russia in June 2019, and La Palma, Canary islands, Spain in September 2021) require the inclusion of a fourth fit range from 360 - 390 nm – Large range(LR), as proposed by Bobrowski et al. (2010) and also used in Theys et al. (2017)) – which is employed only when AR SO_2 SCDs exceed 8×10^{18} molecules cm^{-2}.

Thus, four fit ranges are used:

- Standard range (SR): 312.0 - 324.0 nm
- Medium range (MR): 318.6 - 335.1 nm
- Alternative range (AR): 323.0 - 335.1 nm
- Large range (LR): 360.0 - 390.0 nm

The absorption cross section of SO_2 varies by almost three orders of magnitude from 10^{-19} cm^{-2} (SR) to 10^{-22} cm^{-2} (LR) as shown in figure 4.2. The SCDs of each fit are combined based on their respective SCD. The selection criteria and the respective calculated combined SCD are listed in table 4.1. Larger SO_2 SCDs induce the selection of a higher wavelength range. For an odd selection criteria number the resulting SCD will be simply

Table 4.2: Fit settings for the four SO_2 DOAS retrievals: Standard range (SR), Medium range (MR), Alternative range (AR) and Long range (LR). The asteriks (*) indicates that a cross section is included.

Reference spectrum:		daily earthshine spectrum from equator region [20° S – 20° N; 180° W – 180° E] (see section 4.1)				
Fit name		SR	MR	AR	LR	
lower wavelength		312.0	318.6	323.0	360.0	
upper wavelength		324.0	335.1	335.1	390.0	
unit		nm	nm	nm	nm	
Absorption cross-sections:						Reference
O_3	223 K	*	*	*	*	Serdyuchenko et al. (2014)
O_3	243 K	*	*	*	*	Serdyuchenko et al. (2014)
SO_2	203 K	*	*	*	*	Bogumil et al. (2003)
BrO	223 K				*	Fleischmann et al. (2004)
OClO	293 K				*	Bogumil et al. (2003)
NO_2	220 K				*	Vandaele et al. (1998)
O_4	203 K				*	Thalman and Volkamer (2013)
Pseudo absorber:						
Ring, norm	230 K	*	*	*	*	Wagner et al. (2009)
Ring, λ	230 K	*	*	*	*	Wagner et al. (2009)
Pukite, $O_3 \cdot \lambda$	223 K	*	*	*	*	Puķīte et al. (2010)
Pukite, ${O_3}^2$	223 K	*	*	*	*	Puķīte et al. (2010)
ISRF	w, aw, k	*	*	*	*	Beirle et al. (2017)
Shift & stretch		*	*	*	*	Beirle et al. (2013)
polynomial order:		5	5	5	5	

the SCD from one fit range (i. e. if the SCD of the SR fit is below 3×10^{17} molecules cm^{-2} the first criterion is fulfilled and the combined SCD is just the SCD from the SR fit). In between (defined in the even selection criteria numbers) the combined SCD is a linear interpolation between the neighbouring fits (i. e. if the SCD of the SR fit is between 3 and 8×10^{17} molecules cm^{-2} the SR and MR SCDs will be interpolated linearly, where SR SCD is weighted by 100 % if SR SCD is 3×10^{17} molecules cm^{-2} and MR SCD is weighted 100 % if SR SCD is 8×10^{17} molecules cm^{-2}). The complete formula is given in table 4.1.

4.3 BrO retrieval

DOAS retrievals of BrO from satellites have varied over time both w. r. t. the wavelength fit range as well as the other fit settings. The first detection of tropospheric BrO from the GOME instrument by Wagner and Platt (1998), employs a wavelength range of 345 - 359.5 nm. Other studies use almost identical fit ranges for spectra from GOME (Richter et al., 1998; Hegels et al., 1998; Chance, 1998; Richter et al., 2002) and for spectra from OMI Chance (2002). For SCIAMACHY and GOME-2 measurements, the lower limit of the fit range was lowered to 336 nm, and the upper limit varied between 347 nm (Afe et al.,

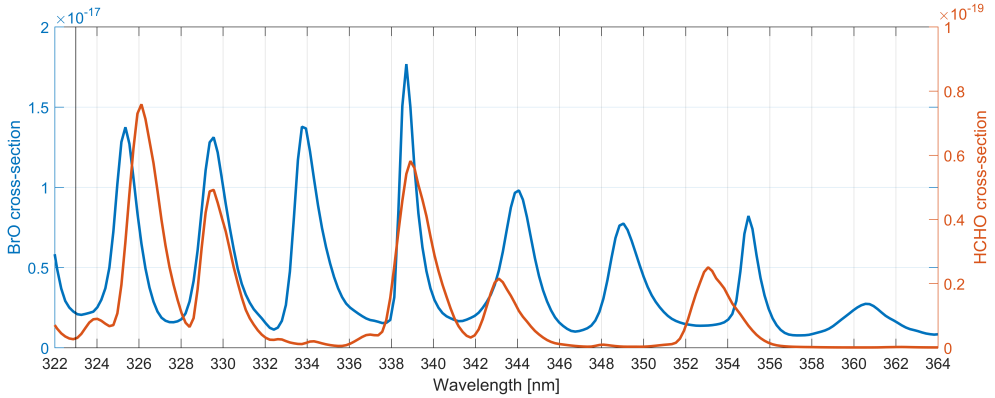


Figure 4.3: Absorption cross section of BrO (blue) and HCHO (red) convolved with a typical TROPOMI ISRF.

2004; Begoin et al., 2010), 351 - 352 nm (Valks et al., 2009; Theys et al., 2009), and 360 nm (Heue et al., 2011; Sihler et al., 2012; Hörmann et al., 2013). For recent global studies of GOME-2 (Theys et al., 2011) and TROPOMI (Seo et al., 2019) the lower boundary was further lowered and a fit range of 332 - 359 nm was chosen.

The DOAS BrO fit used in this thesis is based on Sihler et al. (2012). This fit routine was developed for the retrieval of BrO in arctic regions. There, a fit range from 336 - 360 nm was chosen. The omission of shorter wavelengths was mainly attributed to the large ozone column at high latitudes (and thus large SZA), causing strong absorption in the UV.

For the global investigation of volcanic plumes, which mainly occur at lower latitudes, the ozone columns are usually considerably lower, allowing to perform the BrO retrieval at lower wavelengths benefitting from an improved signal-to-noise ratio.

Another question is whether the formaldehyde (HCHO) absorption cross-section should be included in the DOAS retrieval. The structure of the absorption cross-section of BrO and HCHO are very similar (see figure 4.3). Especially the fact, that the largest absorption peak of BrO overlaps with a major absorption peak of HCHO at 339 nm, can cause a spectral interference between both trace gases. For arctic applications, like in Wagner and Platt (1998), Richter et al. (1998), but also for the more recent study by Sihler et al. (2012), the inclusion of HCHO in the DOAS retrieval is not needed, because HCHO is almost not abundant in arctic regions. However, in equatorial regions, where HCHO can reach large columns due to biomass burning, interference with HCHO potentially has to be considered. HCHO is therefore included within the DOAS analysis of the global BrO detection algorithms from GOME-2 by Theys et al. (2011) and the TROPOMI algorithm by Seo et al. (2019). Interferences between BrO and HCHO are observed for equatorial regions by Theys et al. (2011). Using 332 nm compared to 336 nm as the lower fit boundary reduces these interferences (Theys et al., 2011). Hence both Theys et al. (2011) and Seo et al. (2019) employ a fit range starting at 332 nm.

The interference can also be observed in HCHO retrievals (De Smedt et al., 2012, 2018). There, the interference is much more critical, so that the BrO SCD in the HCHO-fit needs to be fixed using a pre-fit in a different wavelength range in order to retrieve meaningful HCHO columns. In the following section, different wavelength ranges are investigated. The performance with respect to sensitivity, systematic influences and HCHO interference is checked by looking at four fit ranges, where the upper fit range boundary is unchanged and the same as in Sihler et al. (2012), while the lower fit range boundary is varied:

Table 4.3: Fit settings for the eight BrO DOAS retrievals. The asteriks (*) indicates that a cross section is included.

Wavelength ranges:	323 - 360 nm 323 –328.5 & 332 - 360 nm 332 - 360 nm 336 - 360 nm		
Polynomial order:	5		
Reference spectrum:	earthshine spectrum from equator region [20° S – 20° N; 180° W – 180° E] (see section 4.1)		
Absorption cross-section:	Fit type SR	HCHO	Reference
O_3 (223 K)	*	*	Serdyuchenko et al. (2014)
O_3 (243 K)	*	*	Serdyuchenko et al. (2014)
SO_2 (203 K)	*	*	Bogumil et al. (2003)
BrO (223 K)	*	*	Fleischmann et al. (2004)
O_4 (203 K)	*	*	Thalman and Volkamer (2013)
OClO (293 K)	*	*	Bogumil et al. (2003)
NO_2 (220 K)	*	*	Vandaele et al. (1998)
HCHO (298 K)		*	Meller and Moortgat (2000)
Pseudo absorber:			
Ring, norm	*	*	Wagner et al. (2009)
Ring, λ	*	*	Wagner et al. (2009)
Pukite, $O_3 \cdot \lambda$	*	*	Puķīte et al. (2010)
Pukite, ${O_3}^2$	*	*	Puķīte et al. (2010)
Shift & stretch	*	*	Beirle et al. (2013)
ISRF (w, aw, k)	*	*	Beirle et al. (2017)

- *336 - 360 nm*: This smallest fit range includes four BrO absorption bands (see figure 4.3) and is the baseline wavelength range used by Sihler et al. (2012); Hörmann et al. (2013, 2016).
- *332 - 360 nm*: This wavelength range is chosen, because it adds one more BrO absorption band compared to the baseline, while adding no additional HCHO absorption features (see figure 4.3). This lower wavelength is also used in Theys et al. (2011) (GOME-2) and Seo et al. (2019) (S-5P/TROPOMI). Theys et al. (2011) found that including this additional absorption band reduces the interference with HCHO.
- *323 - 360 nm*: The largest fit range was chosen, such that it includes seven BrO absorption bands while avoiding interference with very strong O_3 or SO_2 bands. It was not used in satellite measurements so far due to the strong O_3 absorption.
- *323 - 328.5 & 332 - 360 nm*: The same largest wavelength range, but the HCHO absorption band around 329 nm, which overlaps with a BrO absorption band, is skipped in order to suppress HCHO interference (see figure 4.3).

All four wavelength ranges are implemented with two different fit types, including and excluding the HCHO absorption cross section, leading to a total set of eight different fits. The

fits including the HCHO absorption cross section are labeled »HCHO«, the ones excluding HCHO are labeled »SR«, i. e. the fit *HCHO 332 - 360 nm* is evaluated from 332 nm to 360 nm and has the HCHO absorption cross section included, while the fit labeled *SR 332 - 360 nm* is the same fit just without the absorption cross sections included. These labels will be used throughout this chapter. The overview over the DOAS fit settings, and the included absorption cross-sections for both *SR* and *HCHO* fits are listed in table 4.3.

4.3.1 Investigation of systematic influences

The global BrO VCD map for 1 October 2018 is shown in figure 4.4. The major structures of enhanced BrO occur at high latitudes and are caused by variations in the stratospheric signal, related to variations in the tropopause height (Sihler et al., 2012). Hence, they are linked to the Ozone column, which in turn can be used as a proxy for the strength of the stratospheric column (Sihler et al., 2012). On this day there might also be enhanced tropospheric BrO events occuring at southern high latitude polar spring. In addition, it can be seen that in the equatorial region there are also spatial patterns not originating from volcanic plumes, which could be caused by radiative transfer influences linked to clouds.
In this section, influences onto the BrO retrieval are investigated for eight different BrO fit settings. Firstly, potential systematic influences of both major BrO pattern, polar and cloud, onto the volcanic BrO data are investigated (section 4.3.1), minimized (section 4.3.2) and quantified (figure 4.3.2). Furthermore, the question of spectral interference of HCHO is investigated and also quantified (section 4.3.3). Lastly, statistical uncertainties of the fits are quantified.
Based on both the statistical and systematic uncertainties an optimal fit range is chosen. In addition, the combined fit uncertainty are quantified for various scenarios.

Influence of Clouds

In order to investigate the effect of clouds onto the retrieved trace gas columns, the data is sorted by cloud top height (CTH) and cloud fraction (CF). The cloud top heights are calculated from cloud pressure determined by FRESCO provided in the NO_2 operational product (van Geffen et al., 2021; NO2, 2021). The cloud fraction is taken from the MICRU algorithm (Sihler et al., 2020). The maps of a pacific equatorial region ([±20° N, 160° - 100° W]) of both CTH and CF as well as the BrO VCD for fit *SR 323 - 360 nm* are shown in figure 4.5a, b, and c respectively.
It can be seen that the patterns in the BrO are correlated to the cloud patterns and even negative BrO VCDs are retrieved in the presence of clouds. The impact of large cloud fraction and high cloud top height (e. g. around 15° N, 110° W) seems different compared to large cloud fraction and low cloud top height (e. g. arround -15° N, 110° W).
This suggests that both cloud fraction (which is a measure for the fraction of a pixel covered by a cloud) as well as the height of said cloud is influencing the spectroscopic response and cause a different BrO VCD response.
In order to investigate this potentially systematic effect of clouds on the BrO retrieval, the pixels are sorted in bins of 0.05 cloud fraction and 500 m cloud top height (CTH-CF bins) for the complete equatorial latitude band ([±20° N, ±180° E]). The strength of the BrO response is quantified by taking the mean BrO VCD of all pixels in each bin respectively.
The mean BrO VCD is systematically decreasing both for increasing CTH and increasing CF for all eight fit settings (see figure 4.6). The relation is stronger for larger fit ranges (left side) and seems also slightly increased for fits including HCHO (bottom row). The response is weakest for the fits with wavelength range 323 - 360 nm both for *SR* and *HCHO* fits. The

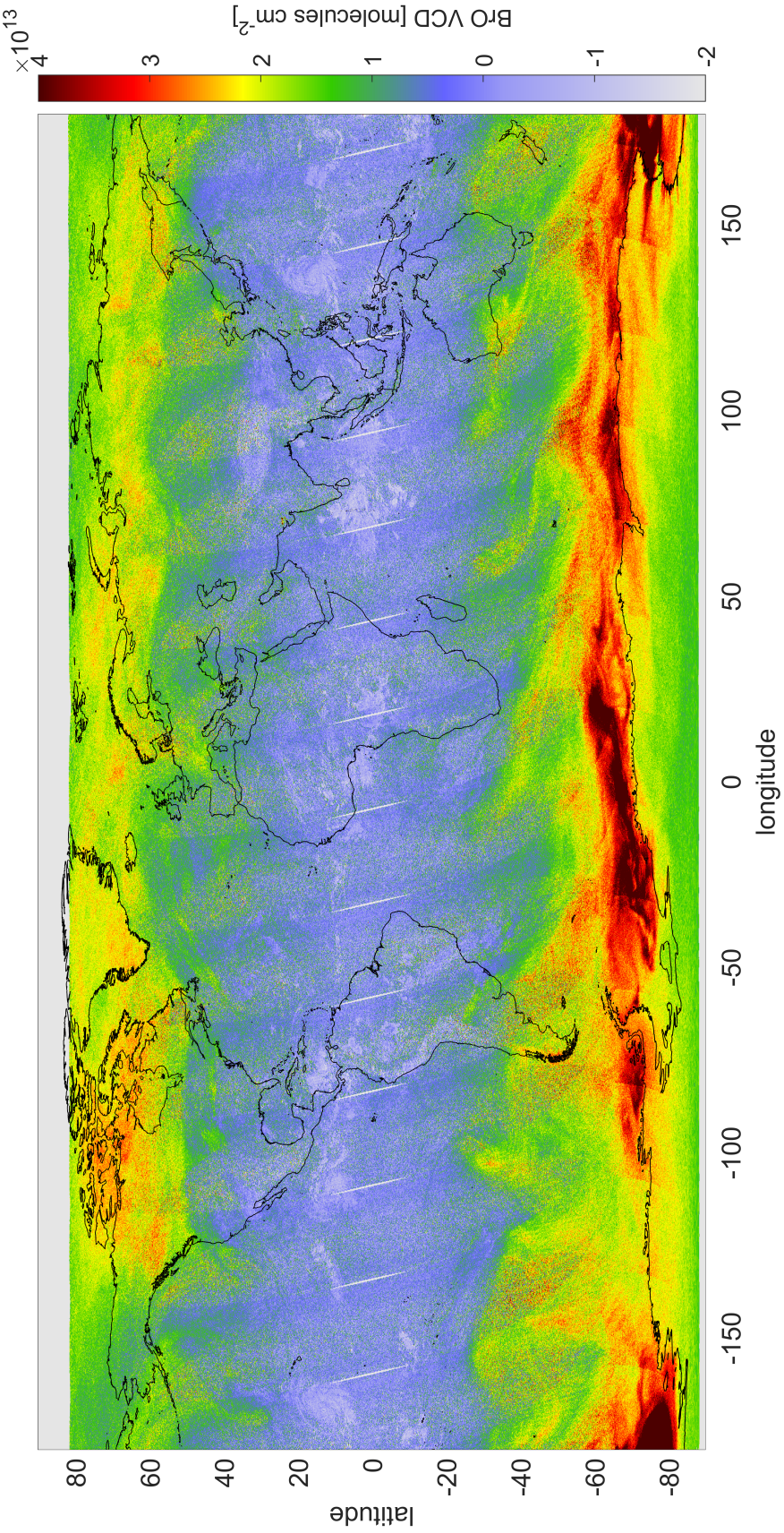


Figure 4.4: Global map of the BrO geometric VCD retrieved using the fit range *SR 323-360 nm* on 1 October 2018.

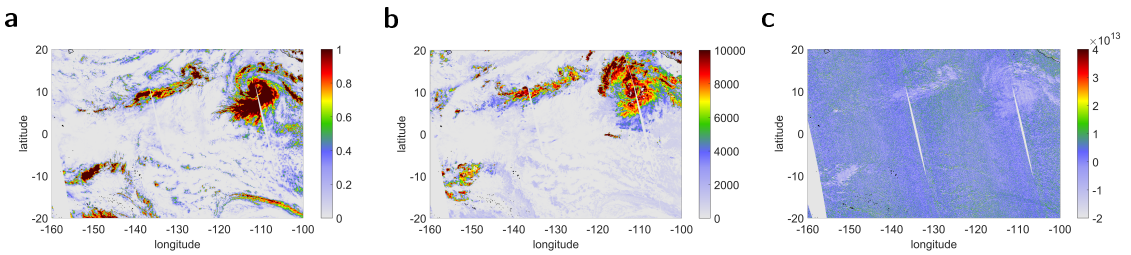


Figure 4.5: **a** MICRU cloud fraction, **b** FRESCO cloud top height, and **c** BrO VCD from fit *SR 323 - 360 nm* over the equatorial region [±20° N, 160° - 100° W] on 1 October 2018.

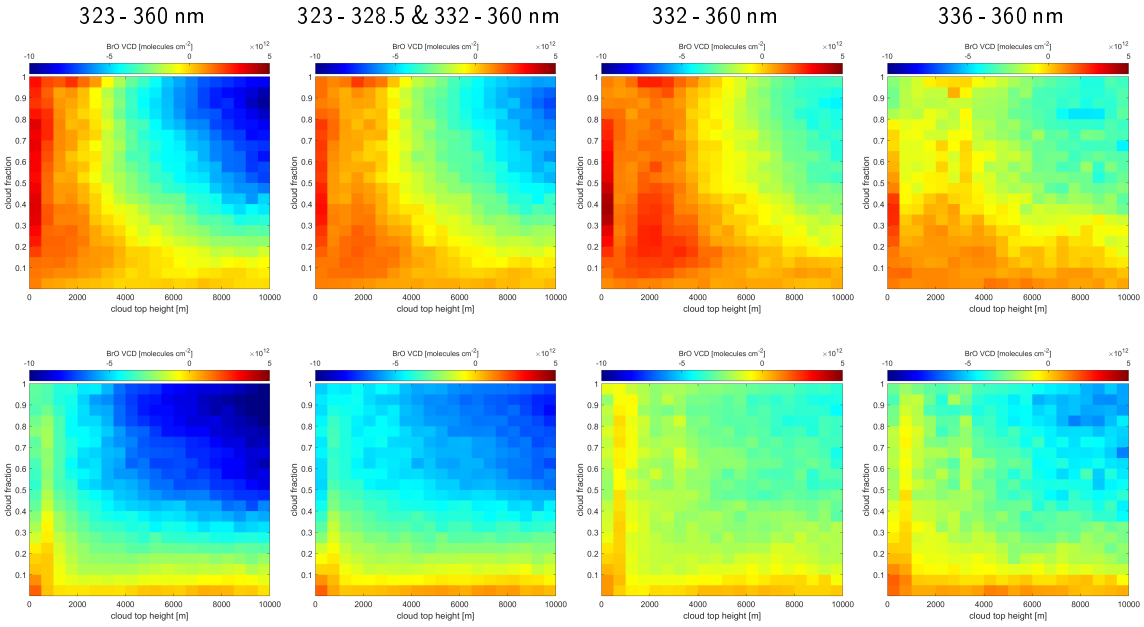


Figure 4.6: Mean BrO VCD dependency on the cloud top height – cloud fraction bins for the equatorial region [±20° N, ±180° E] for the eight different BrO fits. Top row: Fits not including HCHO absorption cross section (*SR*), fit ranges: *323-360 nm*, *323-328.5 & 332-360 nm*, *332-360 nm*, *336-360 nm* (f. l. t. r). Bottom row: Fits including the HCHO absorption cross section (*HCHO*), for each fit range from the top row respectively.

relation both to CTH and CF seems linear allowing to derive a correction term, which will be investigated in section 4.3.2.

While the cloud influence is very strong and rather linear for the equatorial region, there are also systematic structures in mid- and high latitudes (compare figure 4.4), which could also be caused by clouds, but might as well be influenced by other parameters. In order to investigate this, the same CTH-CF binning is performed for 20° latitude bands over the whole globe, which are shown in figure 4.7 for the fit *SR 323 - 360 nm*. The linear dependency of CTH and CF observed for the equator case is dominant for latitude bands from 30° S to 30° N. For mid- to high latitudes north and south, this dependency of BrO on CTH and CF is changing and/or is overlayed by other features.

While the general CTH dependency (higher clouds, lower BrO) is prevailing for high latitudes, the CF dependency is changing its sign, so that it is inverted for 70° N - 90° N, i. e. a lower cloud fraction leads to a lower BrO VCD. In addition, there is a positive BrO signal overlayed for cloud top heights between 1000 and 5000 m independent of cloud fraction. It

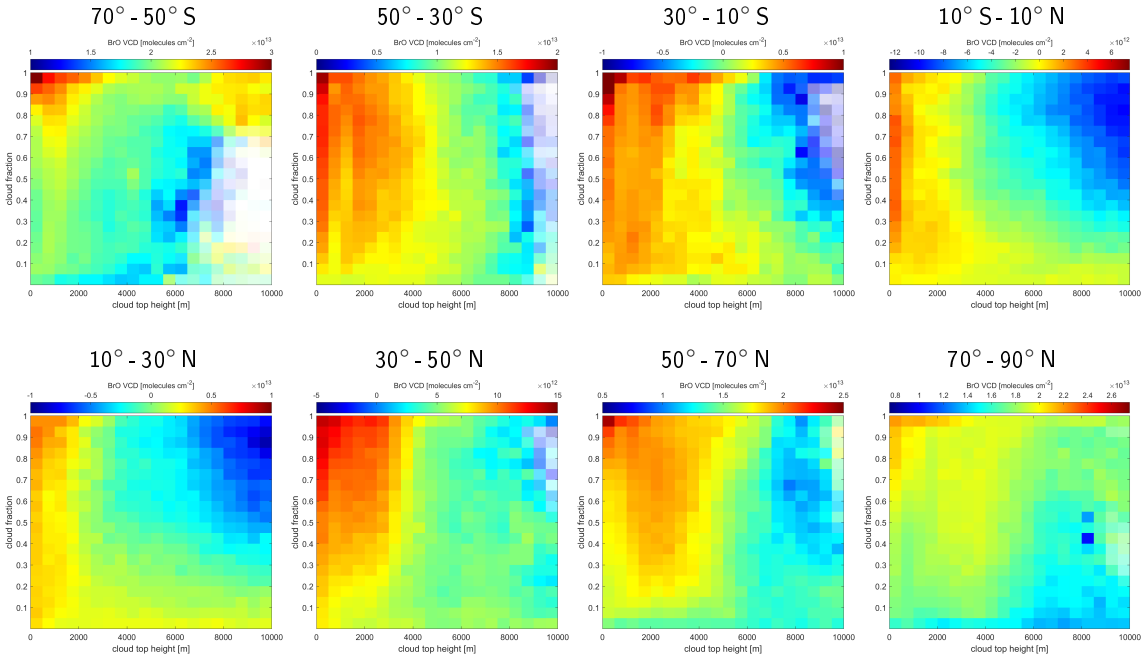


Figure 4.7: Mean BrO VCD of the cloud top height - cloud fraction bins for the *SR 323-360 nm* fit for different latitude bands in 20° steps from 70° S (upper left) to 90° N (lower right).

is clearly visible for northern latitudes (30° N - 90° N), and seems to shift to higher cloud top heights towards higher latitudes. These structures in the CTH-CF plot are most likely caused by other large scale structures independent of clouds. Since this appears at high latitudes only this could be caused by an increase in the stratospheric column (due to the high SZA at high latitudes).

In order to correct for these systematic effects on the BrO VCDs different correction approaches are investigated in the next section (section 4.3.2). Since the dependency on cloud parameters is latitudinal dependent, the correction approach is applied to different latitude bands independently. Furthermore, since the systematic structures in high latitudes might be correlated to the stratospheric column, the inclusion of the O_3 VCD in the correction scheme as a first order indicator for the extent of the stratospheric column is tested.

4.3.2 Cloud and Ozone correction scheme

In order to investigate and correct the effects of the three parameters cloud fraction, cloud top height, and ozone VCD onto the BrO VCDs, three multidimensional polynomial fitting schemes are tested on the BrO VCDs of the data from 1 October 2018.

The three correction schemes are: »ozone«, »latitude«, and »ozone latitude« (see table 4.4). All schemes include the two cloud parameters cloud fraction (MICRU, Sihler et al., 2020), and the cloud top height (from the FRESCO product Compernolle et al., 2021; NO2, 2021). In addition, the schemes »ozone« and »ozone latitude« also include the O_3 VCD, taken from the BrO fit. Since there are two absorption cross-sections and two so called »Pukite«-pseudo absorbers included in the fit (see table 4.3) to account for the spectral signal of O_3, the contributions of each retrieved slant column S are combined to the complete slant column following Puķīte and Wagner (2016):

Table 4.4: Cloud/O_3 correction schemes.

Name	latitude region	Fitted parameter	polynomial degree
Ozone	70° S to 70° N	cloud top height	2
		cloud fraction	2
		O_3 VCD	2
latitude	20° bands from 90° S to 90° N	cloud top height	2
		cloud fraction	2
ozone latitude	20° bands from 90° S to 90° N	cloud top height	2
		cloud fraction	2
		O_3 VCD	2

$$S_{O_3} = S_{O_3,223K} + S_{O_3,243K} + S_{O_3,\lambda}\,\lambda + S_{O_3,\sigma}\,\sigma_{O_3} \tag{4.1}$$

where the slant columns $S_{O_3,223K}$, and $S_{O_3,243K}$ correspond to the cross sections for two temperatures while the two last terms $S_{O_3,\lambda}$, $S_{O_3,\sigma}$ correspond to the two Pukite-term pseudo-absorbers (Puķīte et al., 2010), λ to the wavelength, and σ_{O_3} to the ozone absorption cross-sections. For simplicity this was taken only for one wavelength cross-section pair and this was chosen at the maximum of the absorption cross section closest to the lower wavelength bound (e. g. for the fit wavelength range 323,–360 nm: $\lambda = 325.0\,\text{nm}$ and $\sigma_{O_3} = 1.5 \times 10^{-20}\ \text{cm}^2\,\text{molecule}^{-1}$).
The fitted multidimensional polynomial P comprising of p fitted parameter $x_1 \dots x_p$ and their corresponding polynomial degrees $n_1 \dots n_p$ is defined by in the following way:

$$P = \sum_{i_1=0}^{n_1} \dots \sum_{i_p=0}^{n_p} c_{i_1,\dots,i_p} \cdot x_1^{i_1} \dots x_p^{i_p} \tag{4.2}$$

where $c_{i_1,\dots,i_p}$ are the resulting fitted coefficients describing the dependency of the fitted quantity (in our case the BrO VCD) to the fitting parameters (in our case cloud parameters). This means for example, that for the correction scheme »latitude« (see table 4.4), where the fitted parameters are the cloud top height (CTH) and the cloud fraction (CF) with polynomial degree of two for both parameter. Thus, the equation looks like:

$$P = \sum_{i,j=0}^{2} c_{i,j} \cdot [\text{CTH}]^i\,[\text{CF}]^j \tag{4.3}$$

$$P = \quad c_{0,0} \qquad + c_{1,0}\,[\text{CTH}]^1 \qquad + c_{2,0}\,[\text{CTH}]^2 \tag{4.4}$$

$$+ c_{0,1}\,[\text{CF}]^1 \qquad + c_{1,1}\,[\text{CTH}]^1\,[\text{CF}]^1 \qquad + c_{2,1}\,[\text{CTH}]^2\,[\text{CF}]^1 \tag{4.5}$$

$$+ c_{0,2}\,[\text{CF}]^2 \qquad + c_{1,2}\,[\text{CTH}]^1\,[\text{CF}]^2 \qquad + c_{2,2}\,[\text{CTH}]^2\,[\text{CF}]^2 \tag{4.6}$$

The principle output of this fit are the coefficients $c_{i_1,\dots,i_p}$. In this section the polynomial P is then applied to the complete data-set. However, for the result discussed in part III, only parts of the globe are looked at. The correction coefficients are calculated on the complete latitude band, but only applied to a subset of the data: a region inside this latitude band.

Afterwards the polynomial P is subtracted from the uncorrected BrO VCDs forming the corrected BrO VCDs.

In the following, this procedure will be applied and discussed for the fit *SR 323 - 360 nm* only. The correction scheme shows similar results for the other fits, but the fit *SR 323 - 360 nm* will show the best performance with respect to HCHO influence (see section 4.3.3) and statistical uncertainties (see section 4.3.4) and is therefore chosen as the best fit in the end.

The original uncorrected global map, as well as the corrected map – after applying the correction schemes »latitude« and »ozone latitude« – are schown in figure 4.8 for the settings *SR 323 - 360 nm* (excluding HCHO). Note that the scale for the uncorrected and the corrected maps is different.

In the equator region all the systematic structures are no longer visible in both corrected global maps for the »latitude« and »ozone latitude« schemes. However, in mid- to high-latitude there are still structures visible. These structures are reduced for the »ozone latitude« scheme. However, even for this most sofisticated scheme very strong BrO signals in the antarctic region uncorrelated with O_3 remain. These are propably tropospheric signals in the polar spring (compare Wagner and Platt, 1998; Sihler et al., 2012). In addition there are jumps in the BrO VCD on the edges of the latitude bands visible for both »latitude« and »ozone latitude« schemes. These vanish in the »ozone latitude« scheme for low and mid-latitudes compared to the »latitude« scheme.

In order to quantify the efficacy of the different correction schemes, the mean of the corrected BrO VCD is calculated for each CTH-CF bin. Ideally, there should be no or little dependency on the cloud parameters remaining and no additional structures appearing. The CTH-CF bin plots are shown in figure 4.9, where the dependency of the cloud parameter on the BrO VCD is shown prior and after correction for each correction scheme and each latitude band.

All three correction schemes reduce the cloud dependency.[2]

It can be seen that the correction schemes working on each latitude band separately (»latitude« and »ozone latitude«) are much better at reducing the dependencies both on cloud fraction as well as cloud top height compared to the global »ozone« scheme, which produces new CTH-CF gradients in equator regions.[3] The »latitude« correction reduces most cloud dependencies for latitude bins between 90° N to 50° S. However, cloud independent signals remain for high latitudes. The inclusion of ozone in the correction scheme (»ozone latitude«) is further reducing the cloud dependencies but most importantly drastically reduces the cloud independent structures. For this scheme maximal differences in the CTH-CF plots is typically 3×10^{12} molecules cm^{-2} for latitudes between 90° N to 50° S and 5×10^{12} molecules cm^{-2} for latitudes south of 50° S.

Thus, including ozone in the correction scheme shows the best correction both in consistency in the global map (see figure 4.8) and in the CTH-CF bin plots (see figure 4.9) , and therefore this correction scheme is chosen for this study.

From now on, all BrO VCDs used in this thesis will be by default corrected BrO VCD using the »ozone latitude« correction scheme. The quantification of the remaining systematic cloud effects is done for the fit *SR 323 - 360 nm*.

[2] Note that the color-scale of the uncorrected plots is two times as large as the corrected ones.

[3] Note that the gradients are not larger than the gradients of the uncorrected plots, as the color-scale for the corrected subplots covers a much smaller scale compared to the uncorrected plots.

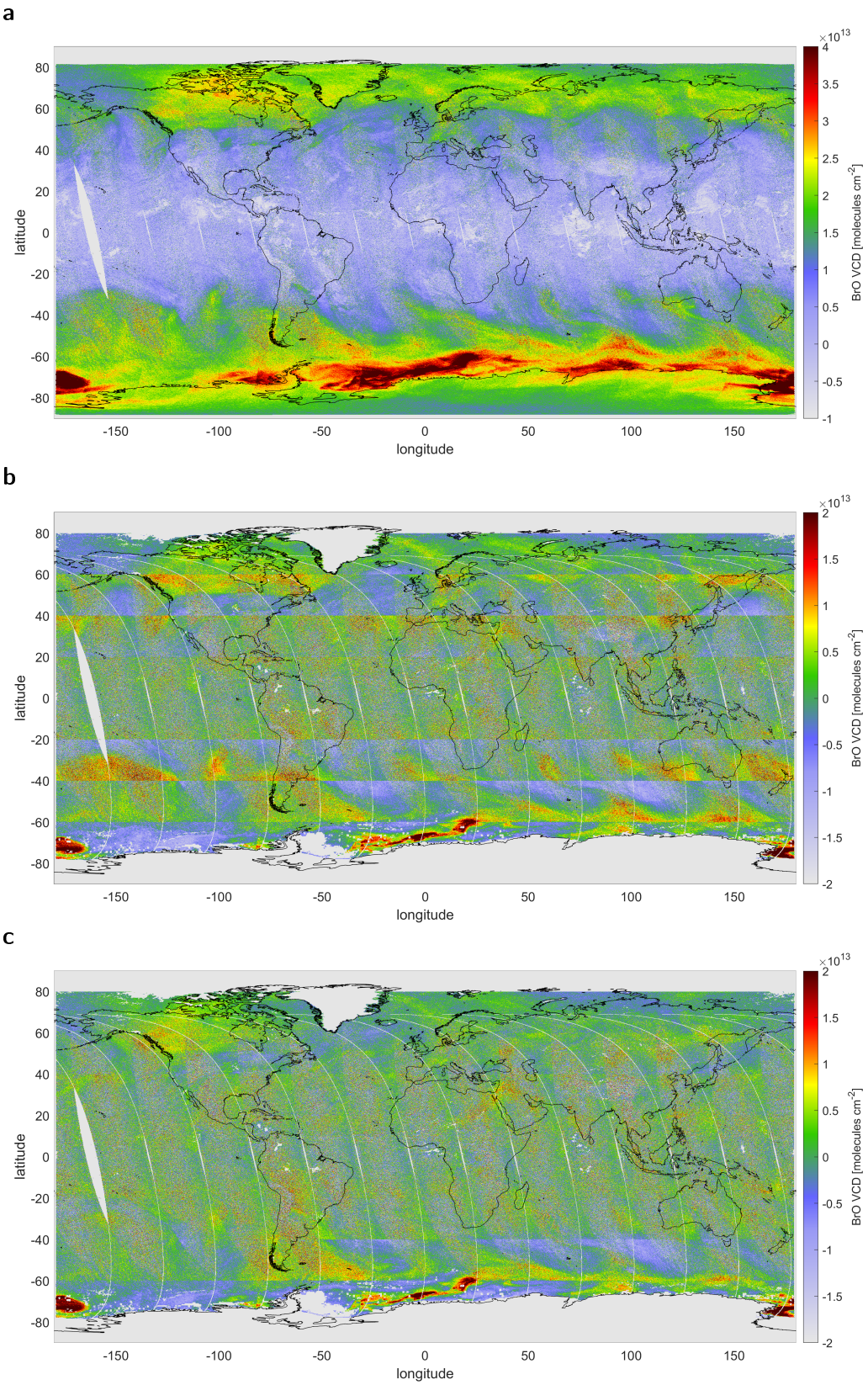


Figure 4.8: Global map of the BrO VCDs of the *SR 323 - 360 nm* fit **a** without correction, **b** with CF and CTH »latitude« correction only, and **c** CTH, CF, and O_3 »ozone latitude« correction.

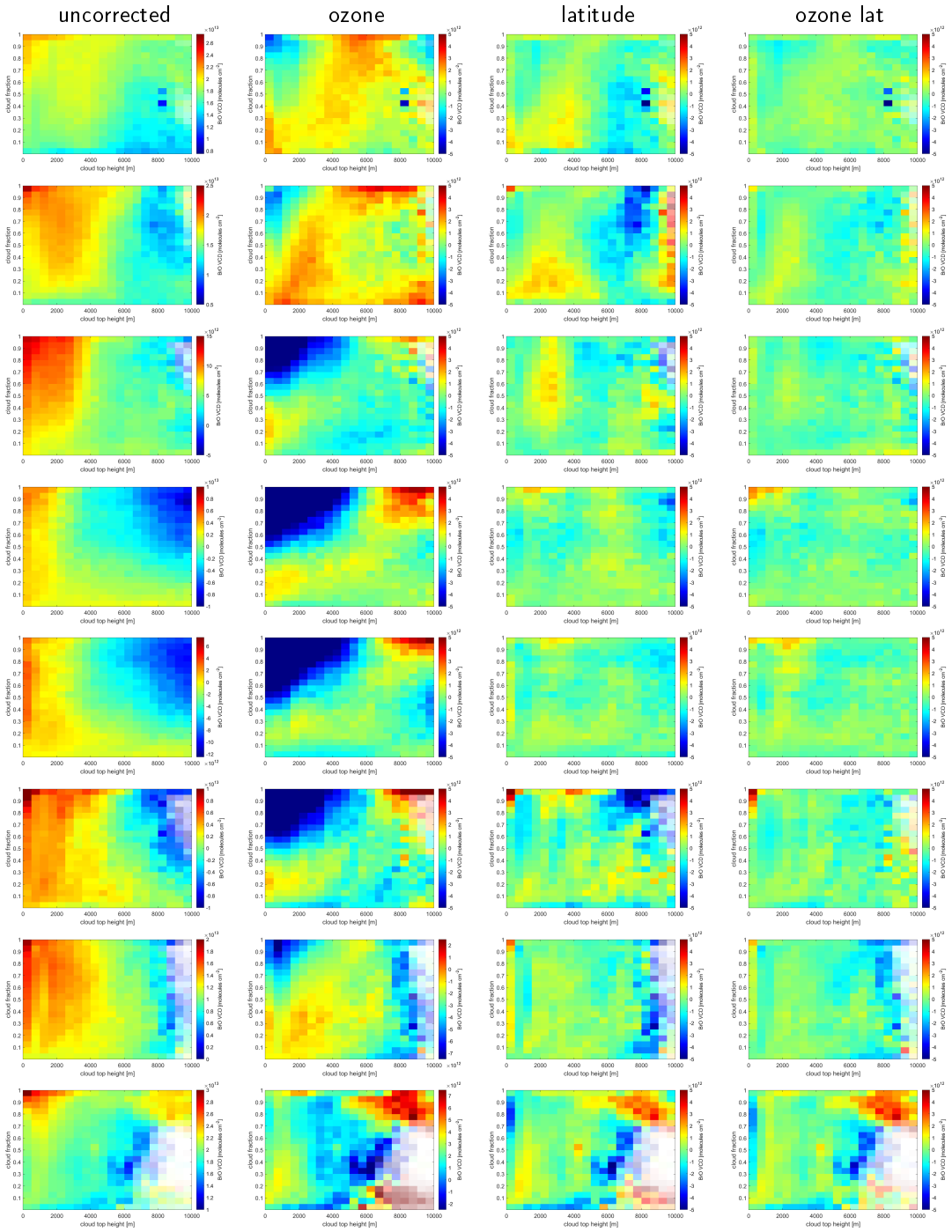


Figure 4.9: Mean BrO VCD as a function of the cloud top height - cloud fraction bins for different latitude bands and correction schemes. From top to bottom: latitude bands from north to south: 90° - 70° N, 70° - 50° N, 50° - 30° N, 30° - 10° N, 10° N - 10° S, 10° - 30° S, 30° - 50° S, 50° - 70° S. Columns indicate the different correction schemes: the uncorrected BrO VCD (first column), and corrected BrO VCDs using ozone (second column), latitude (third column), and ozone latitude correction scheme (fourth column).

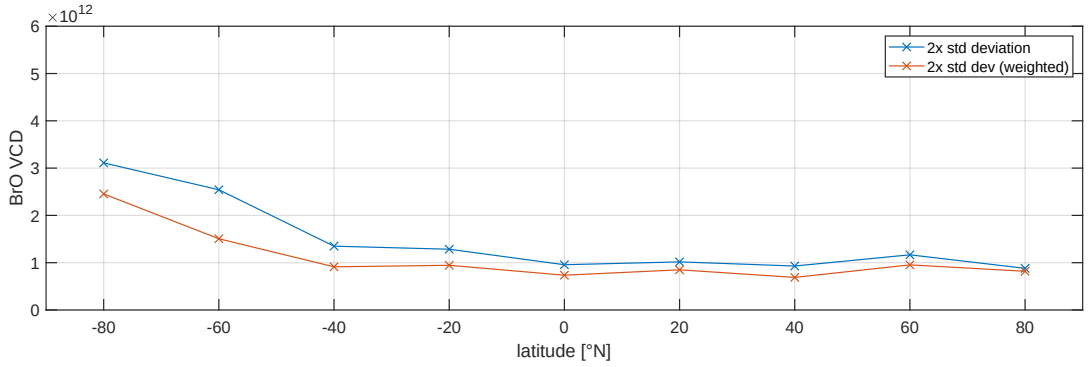


Figure 4.10: The standard deviation of the data for all CTH-CF bins for the seven different latitude bands unweighted (blue) and weighted by the number of pixels included in each CTH-CF bin (red).

Quantifying the systematic influence

Here, the remaining potential systematic influence of clouds and other systematic structures onto the retrieval is investigated, i. e. the potential »false« signal which could be created by clouds, ozone or other sytematic pattern. For this the BrO VCD (after the correction with the »ozone latitude« correction scheme) is investigated for the fit *SR 323 - 360 nm*.
For this a two-fold approach is chosen, by looking at the CTH-CF bins and by averaging pixel:

Estimation using CTH-CF bins The first approach is to look at the corrected CTH-CF bins as seen in figure 4.9. The systematic influence would be then related to the variance between the different CTH-CF bins, e. g. what would be the potential systematic difference between two pixels which happen to have different cloud top height and cloud fraction. To estimate this, the standard deviation of the different mean BrO VCD in the CTH-CF plot, weighted by the number of pixels in each bin, is calculated. This is done for each latitude band separately.
The resulting standard deviation is plotted in figure 4.10. Here for each latitude bin the double standard deviation of all the CTH-CF bins is calculated without weights (blue line) and weighted by the number of pixels in each CTH-CF bin (red line) is plotted for each latitude. Both are roughly 1×10^{12} molecules cm^{-2} except for the latitudes of 60° and 80° S, where it is 1.5 to 3×10^{12} molecules cm^{-2}. These are the regions where springtime tropospheric BrO might interfere, thus these data points are only representative for these conditions. In conclusion, this would mean that remaining possible systematic influences from clouds are 1×10^{12} molecules cm^{-2} except for high-latitude spring cases, where it is rather $2 - 3 \times 10^{12}$ molecules cm^{-2}.

Estimation by averaging of pixels Another approach to estimate the systematic influence is by looking at the variation after spatially averaging over many pixels. The variation of any data-set is comprised of overlapping statistical and systematic variations. By averaging over neighbouring pixels the statistical variation is gradually reduced and the remaining variation can be attributed to systematic effects. In difference to the approach described in the previous paragraph (figure 4.3.2), this is not limited to cloud influences, but also other spatially non-uniformally distributed systematic influences. The statistical variation is quantified by the standard deviation of the BrO VCD distribution calculated from a Gauss

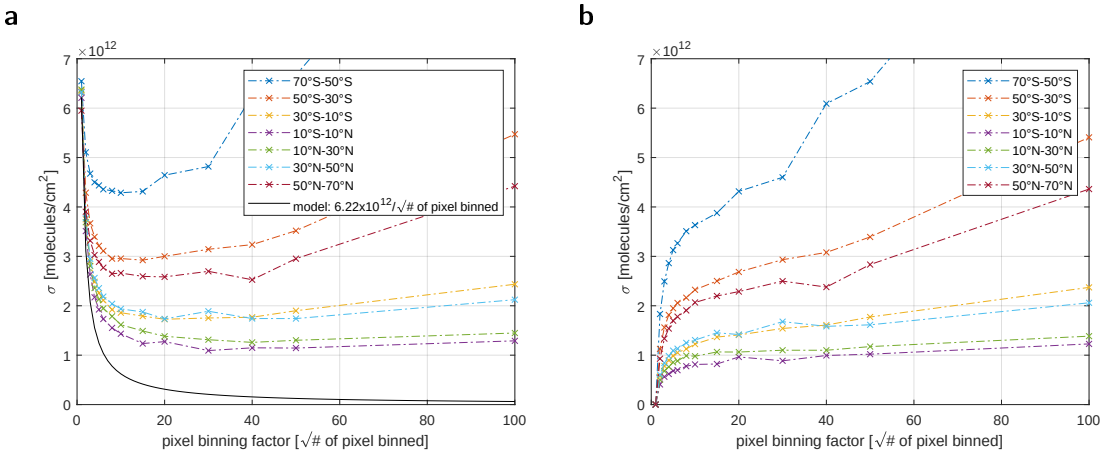


Figure 4.11: **a** The standard deviation of the BrO VCD distribution for different binnings for the seven latitude bands (colored lines) and the model if the total variation would be statistically distributed ($\frac{1}{\sqrt{N}}$, black line). **b** The difference to the statistical model for the seven latitude bands.

fit over the BrO distribution of the binned pixels. This Gauss fit is performed separately for each latitude band as well as for each binning factor and the resulting standard deviation are plotted in figure 4.11.

It can be seen in figure 4.11 that the decrease for larger binning factors in the standard deviation is significantly lower compared to the purely statistical model (black line in figure 4.11). For binning factors of more than 20 (i. e. more than 400 pixels are binned together) the statistical model predicts a standard deviation of less than 5×10^{11} molecules cm^{-2}, while the measured data shows a standard deviation between 1 and 6×10^{12} molecules cm^{-2} depending on the latitude. Thus, this remaining variance can be attributed to systematic effects. This strongly varies with latitude. For the latitude bands at the equator (10° S and 10° N, violet squares) the remaining standard deviation is almost 1×10^{12} molecules cm^{-2}, for the bands around the equator from 30° S to 50° N (squares and light blue diamonds) the systematic standard deviation is still below 2×10^{12} molecules cm^{-2}. For the higher latitudes both north of 50° N and south of 30° S, the systematic effects increase to 3×10^{12} molecules cm^{-2} for 50°-70° N and 30°-50° S, and further to 5×10^{12} molecules cm^{-2} for 50°-70° S.

It is noteworthy that for high latitude bands of 70° S–50° S 50° S–30° S and 50° S–70° N there is an increase in the standard deviation visible for binning factors larger than 20. This is due to the lower number of total pixel in this region. This is because there is partially no light in these regions (solar zenith angle $> 90°$), which will lead to an even smaller number of data-points after binning. This can be seen for all latitudes for the very high binning factor of 100 (i. e. 10000 pixel binned), where a slight increase can be seen for all latitude bands.

4.3.3 Influence of Formaldehyde

Formaldehyde (HCHO) is an organic compound emitted into the atmosphere mostly in the wake of biogenic combustion. Highest columns are observed in tropical regions (De Smedt et al., 2018). Since the cross-sections of BrO and HCHO in the UV range are very similar (see figure 4.3), atmospheric HCHO absorptions can cause strong systematic interference within the DOAS BrO retrieval.

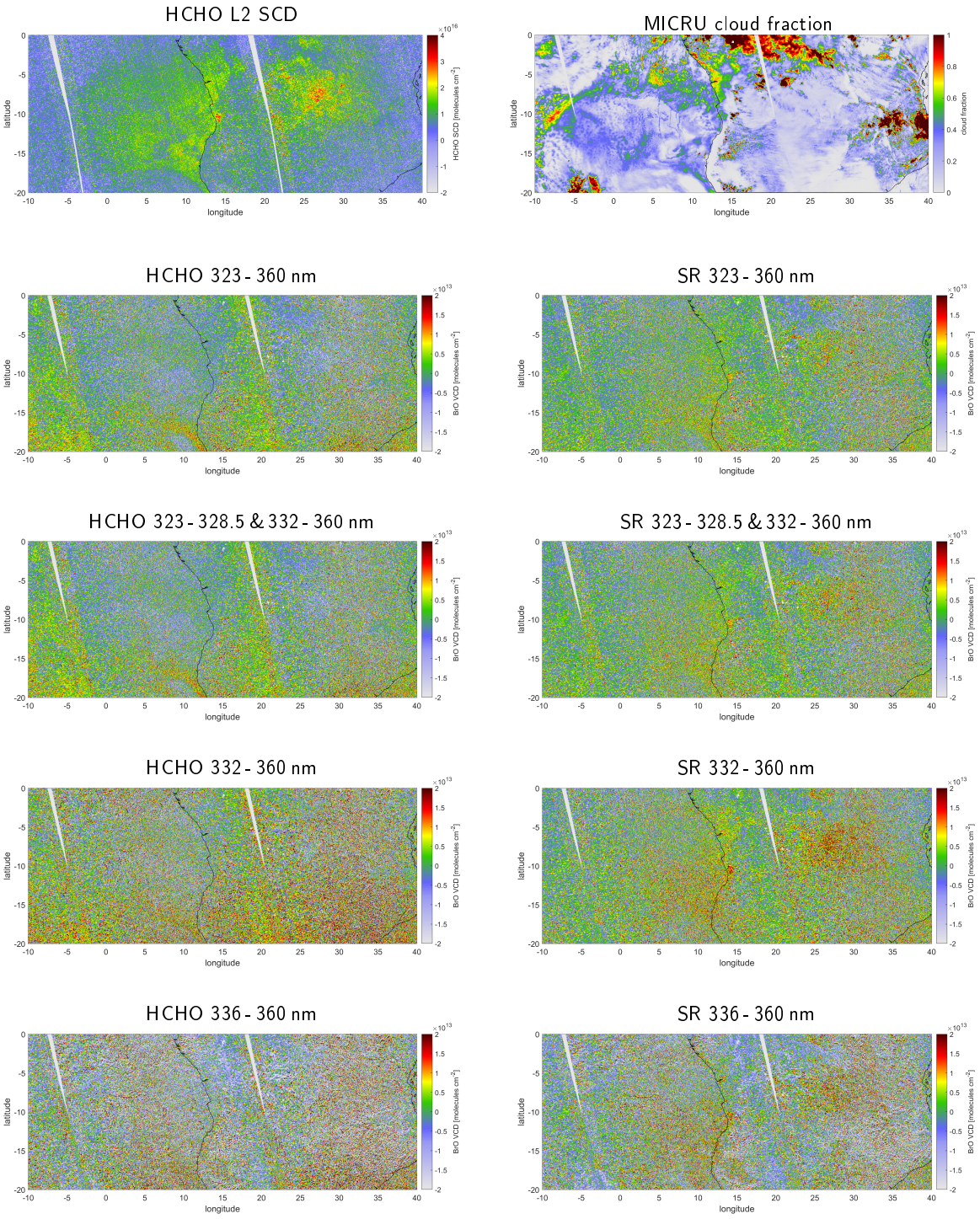


Figure 4.12: Maps of the auxiliary data and the BrO VCD for the eight fits over the African biomass burning region on 1 October 2018. *Topmost row, auxiliary data:* Operational S-5P/TROPOMI HCHO SCD (left) and MICRU cloud fraction (right). *Below, BrO VCD:* BrO VCDs for the eight different fit ranges. The four fit wavelength ranges are listed from second top row to bottom row: *323 - 360 nm*, *323 - 328.5 & 332 - 360 nm*, *332 - 360 nm*, and *336 - 360 nm*. *Left column*: fits including HCHO (*HCHO*); *right column*: fits excluding HCHO (*SR*).

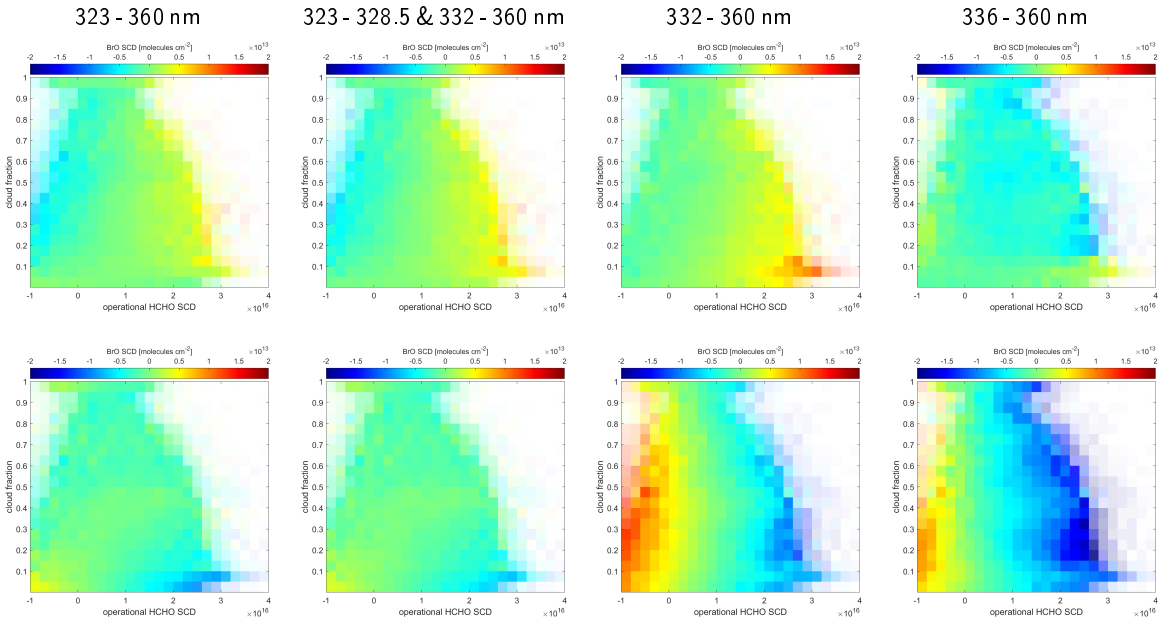


Figure 4.13: Mean BrO SCD as a function cloud fraction and HCHO SCD bins for the African biomass region on 1 October 2018 for the four different fit ranges (from left to right): *323 - 360 nm*, *323 - 328.5 & 332 - 360 nm*, *332 - 360 nm*, and *336 - 360 nm*. *Upper row*: fits excluding HCHO (*SR*); *lower row*: fits including HCHO (*HCHO*).

This section is looking at the interference between HCHO and BrO for the eight BrO DOAS fits (defined in section 4.3). The response of the different BrO fits to atmospheric HCHO is investigated on the example of a biomass burning region in Africa between 0° – 20° S and 10° W – 40° E on 1 October 2018. The main questions is if the inclusion of HCHO in the fit is necessary, i.e. whether the exclusion of HCHO in the fit introduce a systematic offset in BrO, in presence of HCHO. One reason why it would be advantageous not to include the HCHO absorption cross-section is that the analysis yields a larger noise in the retrieved BrO SCDs if HCHO is included (as shown in section 4.3.4). Furthermore, the question is which fit range results in the lowest systematic influence of HCHO onto the BrO VCD and how large a potential false BrO signal could be.

As information on the atmospheric HCHO column, the HCHO SCDs from the operational S-5P/TROPOMI HCHO L2 product (De Smedt et al., 2018) are used. The cloud information (cloud fraction and cloud top height) is taken from MICRU and FRESCO respectively as in the previous sections.

The HCHO SCD derived from the operational S-5P/TROPOMI HCHO L2 product for the selected region is plotted in figure 4.12 (noted »HCHO L2 SCD«, topmost left). There is a region of high HCHO columns exceeding 3×10^{16} molecules cm^{-2} inside the African continent around 5° S and 29° E. Most importantly, this region is mostly cloud free (see figure 4.12 (noted »MICRU cloud fraction«, topmost right), ensuring minimal influence of clouds.

The BrO VCDs are corrected using the latitude dependent ozone cloud correction scheme described in section 4.3.2. The corresponding maps for the eight fits are plotted in figure 4.12. While it is difficult to judge from a map with a relatively large random variation, the maps of the fits including HCHO (*HCHO*, figure 4.12 left column) do not reveal a distinct positive BrO VCD signal in the region of the HCHO event. To the contrary, there rather seems to be a systematic negative offset in this region, most visible for the fits *HCHO 323 - 360 nm* and *HCHO 323 - 328.5 & 332 - 360 nm*. The fits excluding HCHO (*SR*, figure 4.12 right column),

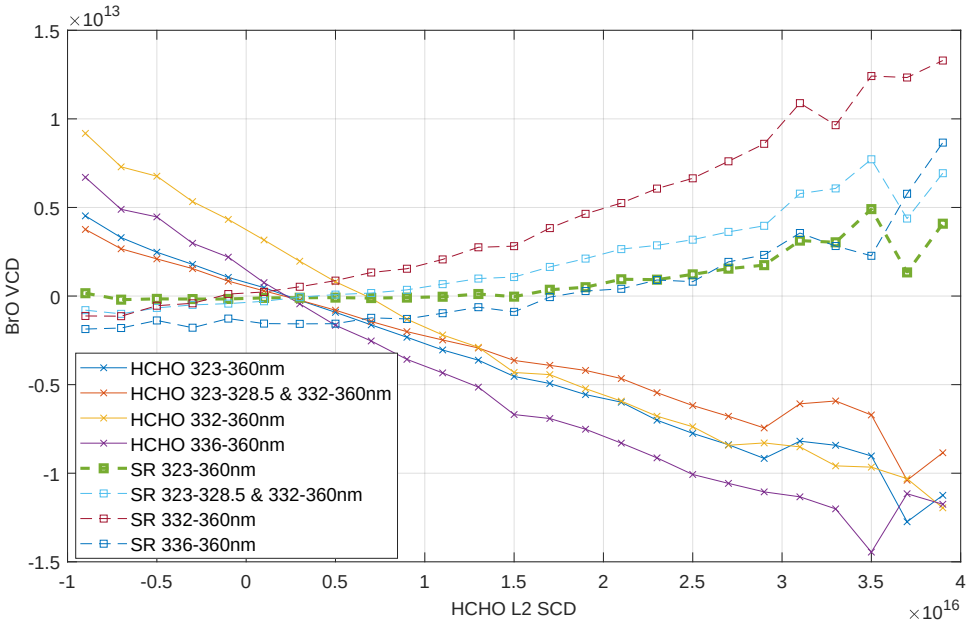


Figure 4.14: Mean BrO VCD as a function of HCHO SCD for the African biomass region on 1 October 2018 for the eight different fits including HCHO (*HCHO*) and excluding HCHO (*SR*). Only cloud free pixels (cloud fraction <0.1) are considered.

show a positive offset in the region of high HCHO SCDs. This is most prominent for the fit range *SR 323 - 360 nm* (third from top), where the BrO VCDs exceed 1×10^{13} over a large area.

In order to investigate the potential systematic response of the BrO retrieval onto HCHO, the pixels are separated into bins of HCHO SCD and cloud fraction. For each HCHO-CF bin the mean BrO SCD is calculated. The corresponding plots for the eight fits are shown in figure 4.13, where the four fit ranges are plotted from left to right and the fits excluding HCHO are in the upper row, while the fits including HCHO are plotted in the lower row.

It can be seen that the fits excluding HCHO (upper row) show a positive response to HCHO, i. e. BrO SCDs increase for higher HCHO SCDs. This is most dominant for the fit range *SR 332 - 360 nm*, where BrO SCDs exceed 2×10^{13} molecules cm^{-2}, whereas this is much less pronounced for the other fit ranges, where maximal BrO SCDs do not exceed 1×10^{13} molecules cm^{-2}. More importantly, for low HCHO SCDs below 2×10^{16} molecules cm^{-2}, the BrO SCDs are close to zero for all fit ranges apart from bins with large cloud fractions. The fits including HCHO (lower row) show the opposite behavior. BrO SCDs are anticorrelated to the HCHO SCDs, i. e. negative HCHO SCDs are found together with positive BrO SCDs which decrease linearly towards higher HCHO SCDs. Here also the fit range *HCHO 332 - 360 nm* shows the strongest influence of HCHO.

In order to separate the HCHO effect from potential cloud influence (which is also an error source in the operational HCHO fit), only cloud free pixels are considered, i. e. cloud fractions below 0.1. The resulting mean BrO VCDs for the different HCHO bins for all eights fits are shown in figure 4.14. Both effects, the decreasing of BrO SCDs with increasing HCHO SCDs for the fits including HCHO (*HCHO*, solid lines in figure 4.14) as well as the opposite behavior for the fits not including HCHO (*SR*, dashed lines in figure 4.14) is clearly visible. However, the fits including HCHO (*HCHO*) show a continuous decrease over the complete range of HCHO SCDs. In contrast, the fits not including HCHO (*SR*) have a large range of

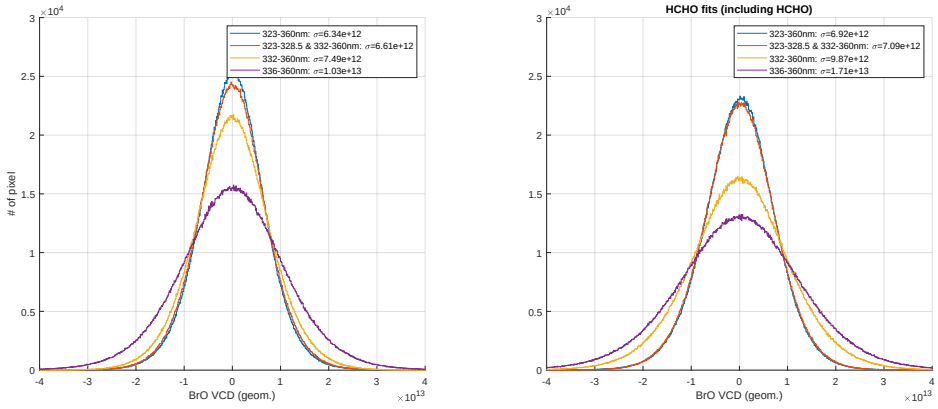


Figure 4.15: Statistical uncertainty of the eight BrO fits. Distribution of BrO VCDs for the four fits excluding HCHO (*SR*, left) and including HCHO (*HCHO*, right). All pixels in the equator band between 20° S and 20° N over the whole longitude band are considered.

HCHO SCDs for which they change only very slightly. This is most prominent for the fit range *SR 323 - 360 nm* (green dashed line). Here the BrO VCDs are zero for HCHO SCDs below 1.5×10^{16} molecules cm^{-2}. For higher HCHO SCDs, BrO VCDs slowly increase, reaching around 5×10^{13} molecules cm^{-2} for maximal HCHO SCDs. Interestingly the fit range *SR 323 - 328.5 & 332 - 360 nm*, in which an overlapping BrO/HCHO absorption band is left out, shows a higher false positive signal.
It can be thus concluded, that the inclusion of HCHO in the BrO DOAS retrieval is not necessary. Even though there can be a systematic false positive BrO response produced by very large HCHO columns, this effect is very low for the fit range *SR 323 - 360nm*, with no response below 1.5×10^{16} molecules cm^{-2} and a response not exceeding 5×10^{13} molecules cm^{-2} for very large columns. Columns above 1.5×10^{16} molecules cm^{-2} are only observed for tropical biomass burning events, mostly ocurring around the equator, i. e. the systematic impact of HCHO on the BrO retrieval is for most cases negligible.

4.3.4 Statistical uncertainties

In order to investigate the general performance of the respective fits, the distribution of BrO VCDs in the equator region [±20° N, 180° W - 180° E] for all eight fits (see figure 4.15) is examined. The distributions are separated into the fits excluding HCHO (*SR*, left), and including HCHO (*HCHO*, right) so that the same fit ranges have the same colors in both subplots. Increasing the fit wavelength range leads to a significant decrease in statistical variation for both fit settings. For the *SR* fits the smallest fit range (*SR 336 - 360 nm*, which is the heritage fit range for arctic BrO from Sihler et al. (2012)) shows a distribution of the data in equator region [±20° N, 180° W - 180° E] with a standard deviation σ of 1.03×10^{13} molecules cm^{-2}, which subsequently decreases to 7.49×10^{12} molecules cm^{-2} (*SR 332 - 360 nm*) and finally 6.34×10^{12} molecules cm^{-2} (*SR 323 - 360 nm*) when the wavelength range is expanded. This is to be expected as a larger wavelength range increases the information content for the least-squared fit of the DOAS retrieval.
In comparison to the *SR* fits, the *HCHO* fits have a larger standard deviation for all wavelength ranges, leading to a minimal σ of 6.92×10^{12} molecules cm^{-2} (compared to 6.34×10^{12} molecules cm^{-2} for the corresponding *SR* fit) and a maximum σ of 1.71×10^{13} molecules cm^{-2}.

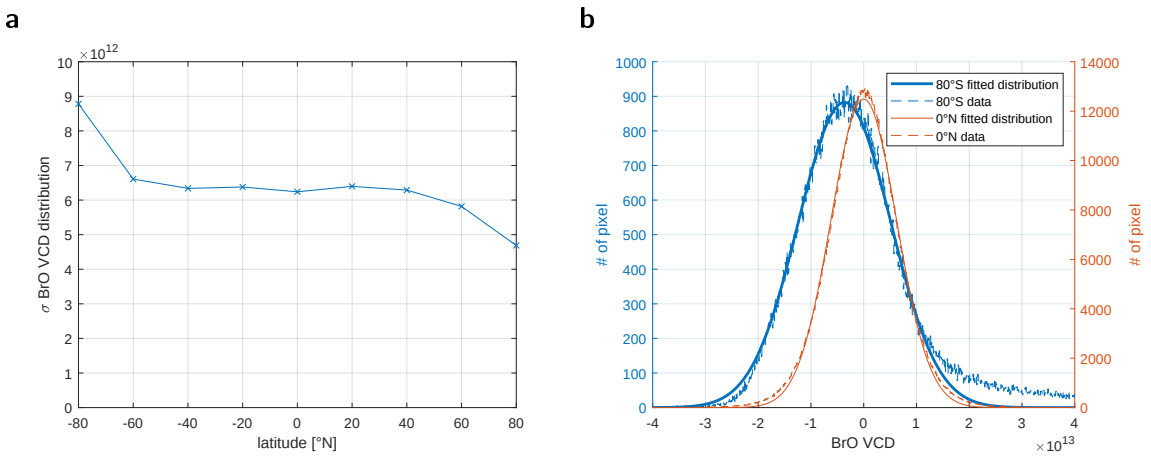


Figure 4.16: Latitudinal variation of the statistical uncertainty. **a** Standard deviation σ of the distribution of the BrO VCD of fit *SR 323 - 360 nm* for different latitude bands on 1 October 2018. **b** BrO VCD distribution of fit *SR 323 - 360 nm* for 80° S and 0° S (right).

Thus, in order to achieve the lowest statistical variation, the largest fit wavelength range possible should be chosen and the *SR* fits (excluding HCHO) are most advantageous. This means from a purely statistical argument, the fit *SR 323 - 360 nm* should be selected.

Looking at the whole globe for the fit range *SR 323 - 360 nm* shows that the standard deviation is around 6.5×10^{12} for the mid-low latitude band between 70° S and 50° N (see figure 4.16a). In the Antarctic region the standard deviation increases strongly to 8.9×10^{12}. However, the distribution in this region is highly affected by systematically enhanced BrO VCDs caused by BrO tropospheric polar spring events (see figure 4.16b). Surprisingly, the standard deviation is gradually decreasing towards high northern latitudes.

Concluding, the statistical variation of the fit *SR 323 - 360 nm* can be best estimated by a standard deviation of 6.5×10^{12} molecules cm^{-2} for all latitudes except for the case of polar spring, where 8.5×10^{12} molecules cm^{-2} should be assumed.

Selection of fit settings

The investigation of the eight different fits can be summarized by the following:

- The statistical uncertainty is lower if (1) the wavelength range of the fit is increased and (b) HCHO is not included as an absorber in the DOAS fit settings.
- The systematic influence of clouds and O_3 can be successfully corrected by the correction scheme described in section 4.3.1 for all eight fits. Thus, there is no preference for a fit range or fit setting.
- Influence of HCHO is lowest for the fit *SR 323 - 360 nm*. It shows no response for moderate HCHO columns and the lowest response for very high HCHO columns.

Thus, the fit range *SR 323 - 360 nm* is chosen as BrO DOAS fit in this thesis, since it shows the lowest statistical variation and is least susceptible to HCHO interference. The complete overview of the DOAS fit settings for this fit is listed in table 4.5.

Table 4.5: Fit settings for the selected BrO DOAS retrieval.

Wavelength range:		323 - 360 nm
Polynomial order:		5
Reference spectrum:		daily earthshine spectrum from equator region [20° S – 20° N; 180° W – 180° E] (see section 4.1)
Absorption cross-section:		Reference
O_3	223 K	Serdyuchenko et al. (2014)
O_3	243 K	Serdyuchenko et al. (2014)
SO_2	203 K	Bogumil et al. (2003)
BrO	223 K	Fleischmann et al. (2004)
O_4	203 K	Thalman and Volkamer (2013)
OClO	293 K	Bogumil et al. (2003)
NO_2	220 K	Vandaele et al. (1998)
Pseudo absorber:		
Ring, norm	230 K	Wagner et al. (2009)
Ring, λ	230 K	Wagner et al. (2009)
Pukite, $O_3 \cdot \lambda$	223 K	Puķīte et al. (2010)
Pukite, ${O_3}^2$	223 K	Puķīte et al. (2010)
ISRF	w, aw, k	Beirle et al. (2017)
Shift & stretch		Beirle et al. (2013)

4.3.5 Overview of the statistical and systematic uncertainties

In this section, the error estimations from the previous sections are summarised for all the different cases identified throughout these sections and the combined error is calculated. The main cases are separated by latitude, where three regions are selected: Equator is the latitude band between 20° S and 20° N, mid-latitudes stretch from the equator region to 50° N and 50° S, and high latitudes are further north/south. In addition, there are two special cases distinquished: The polar spring in high latitudes and the biomass burning case at the equator. Since biomass burning can seldomly also occur in mid-latitude or boreal summer, these cases are included as well.
Finally, for each of these cases the statistical uncertainty and the systematic uncertainties are added quadratically:

$$\sigma_{combined} = \sqrt{\left(\sum \sigma_{systematic}\right)^2 + (\sigma_{statistical})^2} \tag{4.7}$$

The systematic uncertainties are the general systematic uncertainties derived in figure 4.3.2 (depicted in figure 4.10) for each latitude region and the systematic uncertainties caused by large HCHO columns, derived in section 4.3.3 (depicted in figure 4.14). The statistical uncertainty is derived for each latitude region in section 4.3.4 (depicted in figure 4.16).
The added systematic, statistical, and the combined uncertainty are shown for all cases in table 4.6. Under normal conditions, the combined uncertainty is between 6.6 and 6.8×10^{12} molecules cm^{-2}. These cover most of the volcanoes, e. g. the island volcanoes in the equatorial region (Galapagos, Vanuatu, Mayon) but also all mid- as well as high-latitude volcanoes

such as Etna, Kilauea, and La Palma as well as Kamchatka, Iceland and Aleut volcanic regions. While the latter mid- to high-latitude volcanic regions can also be affected by high HCHO columns which would increase the uncertainty by roughly 1×10^{12} molecules cm^{-2}, this is expected only under very rare circumstances.
Other volcanoes with a risk of a general influence of biomass burning are the African rift valley volcanoes Nyiragongo/Nyamuragira, the northern Andes volcanoes – e. g. Nevado del Ruiz – and the Central American volcanic Arc volcanoes – e. g. Masaya and Fuego. Here an uncertainty of 7.4×10^{12} molecules cm^{-2} has to be assumed.

Table 4.6: Overview of the different systematic influence contributions.

Error class	systematic		statistical	combined	affected volcano/
Error origin	general	HCHO			volcanic region
molecules cm^{-2}	$\times 10^{12}$	$\times 10^{12}$	$\times 10^{12}$	$\times 10^{12}$	
Equator:					
normal	1.0	–	6.5	6.6	Island volcanoes: Ambrym, Agung, Yasur, Galapagos island, Sufriere hills, Hunga Tonga, Mayon, Ana Krakatau, Piton de la fournaise
biomass burning	1.0	2.5	6.5	7.4	Nyiragongo/Nyamuragira, Central American Volcanic Arc: Fuego, Masaya; Andes: Nevado del Ruiz, Sangay, Tungurahua
Mid-latitudes:					
normal	1.5	–	6.5	6.7	Etna, Kilauea, La Palma, Japan
biomass burning	1.5	2.5	6.5	7.6	–
High-latitudes:					
normal	2.0	–	6.5	6.8	Aleuten, Kamtchatka, Iceland
polar spring	4.0	–	8.5	9.3	–
biomass burning	4.0	2.5	8.5	10.7	–

5 Processing of the volcanic data

This section describes the processing of the BrO and SO_2 VCD data derived in chapter 4. Firstly, section 5.1 defines to which day the data is assigned. The automated plume algorithm is described in section 5.2, where the global SO_2 VCD map of each day (see section 5.2.1) is scanned and plume events are automatically defined as areas with elevated SO_2 signals (see section 5.2.2). The BrO and SO_2 processing of these events is explained in section 5.2.4. The resulting calculation of the BrO/SO_2 ratio is given in sections 5.3 and 5.4.

5.1 Processing of daily data

The S-5P/TROPOMI data is sorted by days, each consisting of 14 to 15 orbits. Each orbit starts when the ascending node begins. An orbit is assigned to a specific day based on its starting time in UTC, i.e. if the orbit starts after 00:00 h UTC it is assigned to the corresponding day. Since the local time on ascending node is 13:35 h [1], at 00:00 h UTC the satellite is slightly east of the dateline. Thus, the first orbit of each day will typically cross the dateline and the last orbit can also cross the dateline, leading to the overlap or neighbouring of pixels with very different time stamps (see figure 5.1, top). Especially the first orbit – starting at 150° W – does not fit into the UTC global map projection of [180° W - 180° E] longitude.[2]
To overcome this »misplacement« of parts of some orbits, a correction is applied as described in the following:

Early pixels: pixels with a timestamp earlier than 9:00 h UTC and west of 60° W are shifted to the east by 360°.

Late pixels: pixels with a timestamp later than 15:00 h UTC and east of 60° E are shifted to the west by 360°.

The resulting map is shown in figure 5.1 (bottom). The black rectangle then shows the boundaries of the data assigned to the day (in this case 25 December 2018). This already reveals that a significant portion of the data is no longer assigned to this day. The data east of the boundary is then assigned to the preceding day (24 December 2018), while the data west is assigned to the succeeding day (26 December 2018). Since this is done for each day, each day will receive some data originally assigned to its preceding and some data originally assigned to its succeeding day. Thus, the global map of 25 December 2018 will have mostly data originally assigned to 25 December 2018 (figure 5.2, top, inside the black rectangle),

[1] Taken from `https://directory.eoportal.org/web/eoportal/satellite-missions/c-missions/copernicus-sentinel-5p`

[2] This is a convention and the cut-off of the global map projection could be also chosen at any longitude.

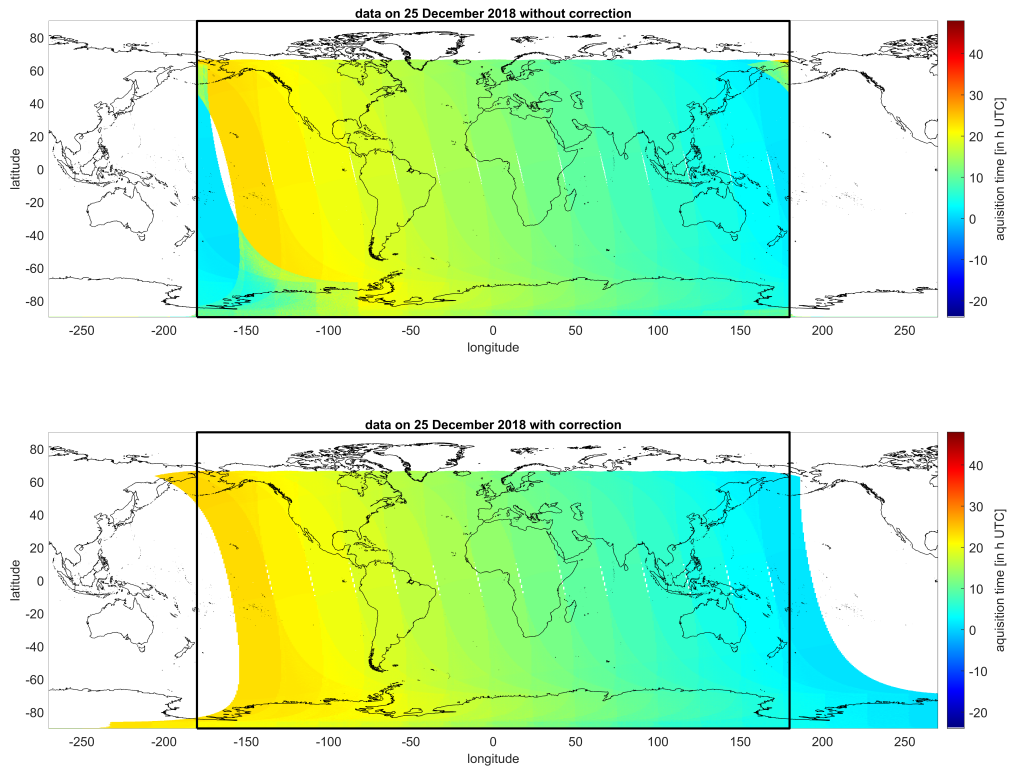


Figure 5.1: Aquisition time in h UTC for the orbits on the 25 December 2018. *Top:* longitude input taken as stored in the Level-1 files. *Bottom:* after shifting early pixel east and late pixel west. The area corresponding to one global map is marked by the black rectangle.

but also some data from 24 and 26 December 2018 (figure 5.2, middle, inside the black rectangle), resulting in a homogeneous map both in space and time (figure 5.2, bottom).

5.2 Automated plume detection algorithm

An automated plume detection algorithm was developed which identifies, locates and extracts volcanic plumes on a global scale. It is designed to capture the extent of the complete plume based on the SO_2 signal. For this first the daily SO_2 maps are created and then systematically scanned for elevated SO_2 signals, which are then combined to volcanic events.

5.2.1 Global SO_2 map

In a first step, a global map of the derived SO_2 VCD is created on a daily basis. For this the data derived from the SO_2 standard fit (312 - 324 nm, compare section 4.2) is chosen, since it is most sensitive to detect also small volcanic columns. The data for the global map are selected based on the procedure described in section 5.1.

Only measurements with a solar zenith angle (SZA) smaller than 70° are considered. This is to prevent strong interference of SO_2 from O_3 in the DOAS retrieval. The SO_2 slant columns are converted to vertical columns using geometric Air Mass Factors (AMF, see section 2.5.1). The resulting geometric VCDs are shown in figure 5.3 for 25 December 2018.

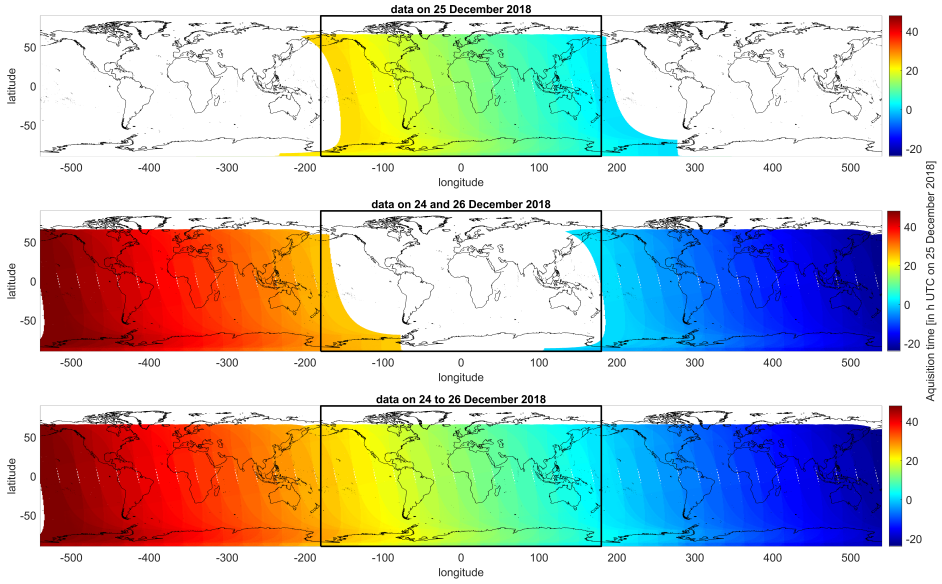


Figure 5.2: Acquisition time in h UTC of 25 December 2018 for the orbits of 24 to26 December 2018. *Top:* Data originally assigned to 25 December 2018 *Middle:* Data originally assigned to 26 and 24 December 2018. *Bottom:* Data of all three days combined. The area assigned to the global map of 25 December 2018 is marked by the black rectangle.

Latitudinal correction of SO_2

In order to correct for the spectral interference with O_3, which induces in first order approximation a systematic latitudinal bias on the SO_2 VCDs, a latitudinal correction is applied. For this, the global maps are scanned in 1° steps from 90° S to 90° N. For each latitude the median SO_2 VCD of all pixels within this latitude step is calculated and then used as a correction for said pixels. While this correction term tends to be typically in the order of 10^{15} molecules cm^{-2} – which is one order of magnitude lower than the statistical variation of the fit result – there could be some cases where the effect is larger. In such cases, the correction of the O_3 interference becomes especially important. The global map of the corrected SO_2 VCD is depicted in figure 5.3.

Excluded areas

In order to prevent the detection of anthropogenic SO_2 sources as volcanic events, areas with large anthropogenic sources are excluded in the automatic plume detection. These are China and the Highveld region, South Africa, both affected by industrial emissions, the region around Norilsk, Russia, where SO_2 is produced by a large copper smelter, as well as the Arabian Penninsula, where fossil fuel processing produces a detectable SO_2 signal. Furthermore, to prevent erroneous measurements caused by enhanced cosmic radiation the South Atlantic Anomaly zone is also excluded. All excluded regions are listed in table 5.1 and shaded in figure 5.3.

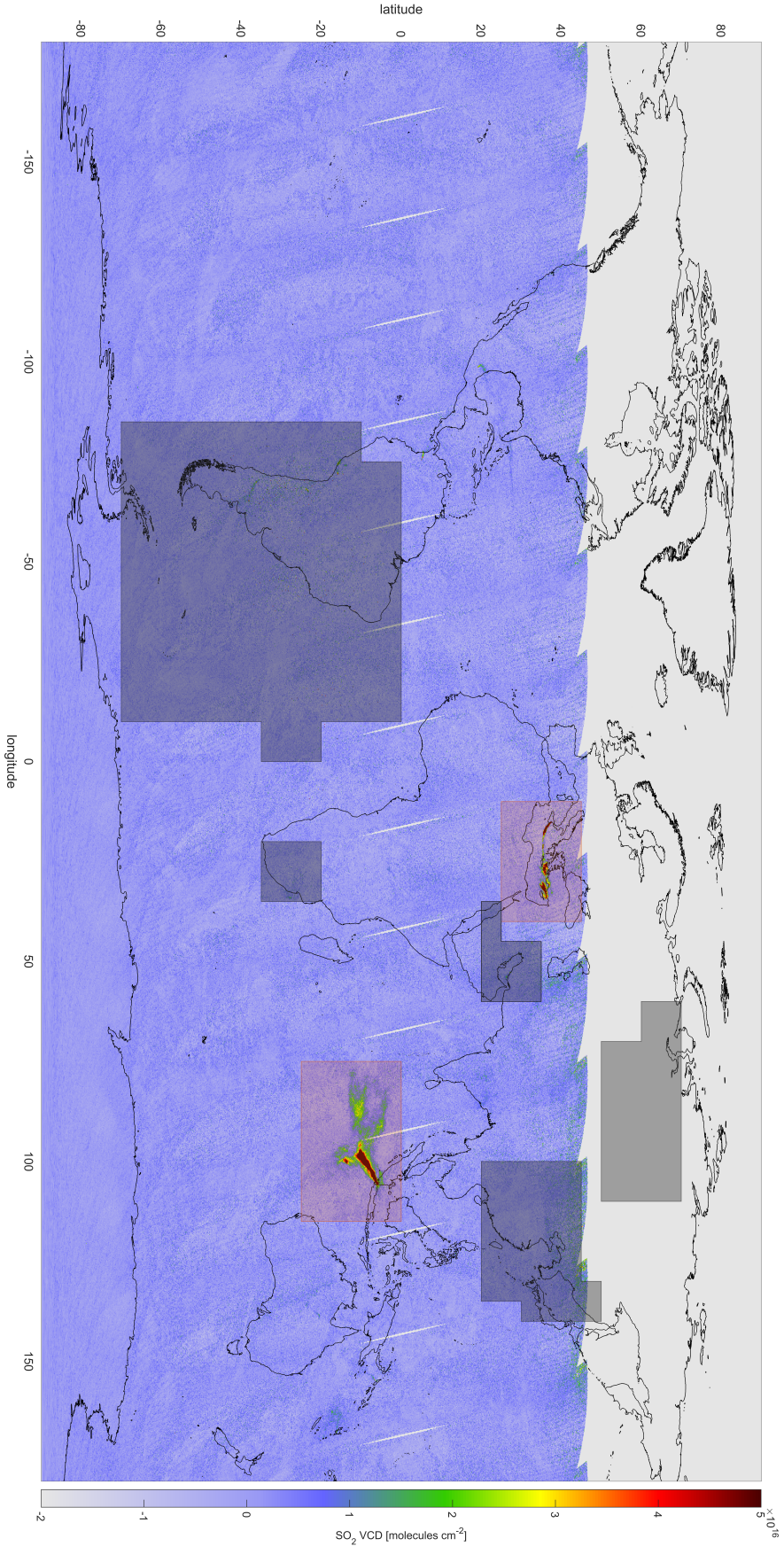


Figure 5.3: Resulting global SO_2 VCD (geom.) on 25 December 2018 after the latitudinal correction. The areas excluded in the automated plume algorithm are marked as grey polygons. The area of the two events detected by the plume algorithm around Mt. Etna, Italy and Anak Krakatau volcano, Indonesia are marked by red polygons.

Table 5.1: List of the latitude and longitude boundaries of the different exclusion areas.

Area name	Latitude bounds	Longitude bounds	Cause for exclusion
Highveld, South Africa	35° S - 20° S	20° E - 35° E	Coal power plants
Arabian penninsula	20° N - 25° N 20° N - 35° N	35° E - 45° E 45° E - 60° E	Fossil fuel processing
China	20° N - 45° N 45° N - 50° N 30° N - 50° N	100° E - 135° E 130° E - 135° E 135° E - 140° E	Anthropogenic signals
Norilsk, Russia	60° N - 80° N 50° N - 80° N	60° E - 70° E 70° E - 110° E	Copper smelter
South atlantic anomaly (SAA)	70° S - 10° S 70° S - 0° S 35° S - 20° S	85° W - 75° W 75° W - 10° W 10° W - 0° W	Cosmic radiation

5.2.2 Automated event selection

In a second step, the corrected global SO_2 data is taken to automatically identify and extract volcanic plume events for each day. A volcanic plume event is defined as a continuous distribution of enhanced SO_2 columns (plume) visible on the daily satellite map created by emissions of a volcanic source.

When volcanic gas emission is ongoing, the volcanic plume is usually directly at or close to the volcano. Thus, for continuously emitting or moderately erupting volcanoes, scanning the area around the volcano will ensure to pick up a potential volcanic plume signal. However, automatically scanning the area in the vicinity of known volcanoes proves not to be efficient for monitoring the whole globe for multiple reasons. For instance, there are many volcanoes where the plume signal is above the detection limit only for a limited time during the observation period of this thesis (2018 to 2021). Scanning this area on days where the volcanic signal is not detectable is hence not efficient. More importantly, there are also cases where the signal of the volcanic plume is not located close to the originating volcano. This can be the case if the eruption has ceased and the plume was advected away from the vent until its detection by the daily satellite overpass. Another difficulty can be an intermittent eruption, where older parts of the plume are spatially separated from young parts of the plume close to the volcanic vent. For earlier satellites, e.g. GOME-2 with a rather coarse resolution, the separation of different plume parts could only be resolved in very few cases of large eruptions. However, the high spatial resolution and high sensitivity of the S-5P/TROPOMI instrument yields a spatial separation even for small interruptions during an eruptive period. In order to include all of these cases and include all parts of a single plume, an automatic detection algorithm was employed, which is based on the algorithm developed by Hörmann (2013), adapted to the specifications of TROPOMI.

Separation into $5° \times 5°$ grid boxes and classification

In a first step, the global SO_2 data is seperated into »grid boxes« of $5° \times 5°$, comprising roughly 5000 - 10000 individual TROPOMI pixels.

Each grid box is classified either as »primary«, »secondary« or »background« grid box, based on the following specifications.

Primary event grid boxes are defined, if the following criteria are fulfilled:

1. at least 10 pixels exceed the SO_2 VCD threshold of $5x10^{16}$ molecules cm^{-2}.
2. there is at least one pixel, which:
   - has at least 10 pixels SO_2 VCD larger than $5x10^{16}$ molecules cm^{-2} and
   - has at least 4 of its 8 direct neighbour pixels have an SO_2 VCD larger than $3x10^{16}$ molecules cm^{-2}.

The first criterion ensures that events that are of low statistical significance due to a low number of pixels are not considered, while the second criterion ensures that singular erroneous pixels cannot create an event.

Secondary event grid boxes are defined, if:

1. at least 30 pixels exceed the SO_2 VCD threshold of $3x10^{16}$ molecules cm^{-2}.

These are grid boxes, which still might include dispersed parts of a volcanic plume, but not enough to constitute an event of its own. Thus they will only be used complementary to primary event boxes to ensure that there are no plume parts left out.

Background grid boxes are all grid boxes that are neither primary nor secondary events. Hence, they can be directly adjacent to primary as well as secondary event grid boxes. These grid boxes are assumed to be free of volcanic gas and are used to calculate background corrections and statistics.

Defining a volcanic event

The primary, secondary and background event grid boxes are then put together in the following manner to form a volcanic event.
The starting point for a volcanic event is an arbitrary primary box.
Firstly, all primary event grid boxes, which are adjacent (directly as well as diagonally) to the initial box are added to the event. This is repeated iteratively for the new set of primary event grid boxes, until no adjacent primary grid box is found. On the event on 25 December 2018 (see figure 5.5), this leads to a cluster of five primary event grid boxes which form the primary event cluster (PEC). These primary boxes will then not be used as starting points of new events.
Secondly, all secondary event boxes surrounding the PEC are included as secondary event grid boxes to this event. This is also done iteratively until no adjacent secondary box is found, which is not already included in the event. In the example event in figure 5.5 there are six secondary boxes found. As can be seen, they are all west and south of the PEC. The combination of both types of boxes forms the event cluster. This data is used to calculate the BrO/SO_2 ratio of the event.
Lastly, the next adjacent background grid boxes around the event cluster are added to this event as background grid boxes of this event. This constitutes the spatial extend of the event, i. e. the background grid boxes will add 5° in each direction. Background grid boxes are added until the event has a rectangular shape on the lat-lon map. In the example in figure 5.5 this leads to an event extent from 75° E to 115° E and 25° S to 0° S. The background event boxes are assumed to be void of volcanic gases. They are used to calculate the background statistic specific to this event, i. e. the median of SO_2 as a first

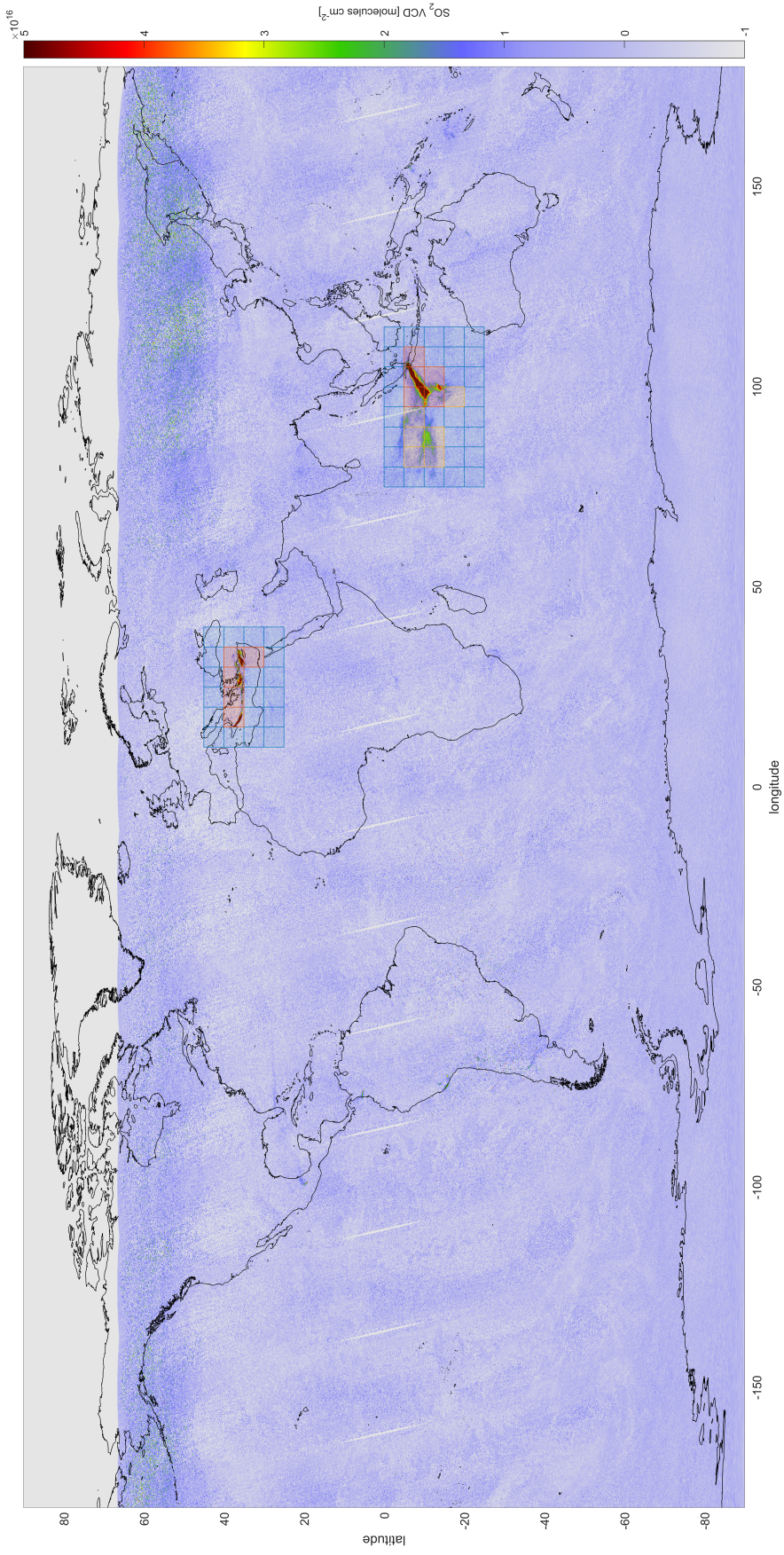


Figure 5.4: Global map of SO_2 VCD on 25 December 2018 and the events grid boxes for the two volcanic events. Primary event boxes (red), secondary event boxes (yellow), and background boxes (blue) assigned to each event are shaded.

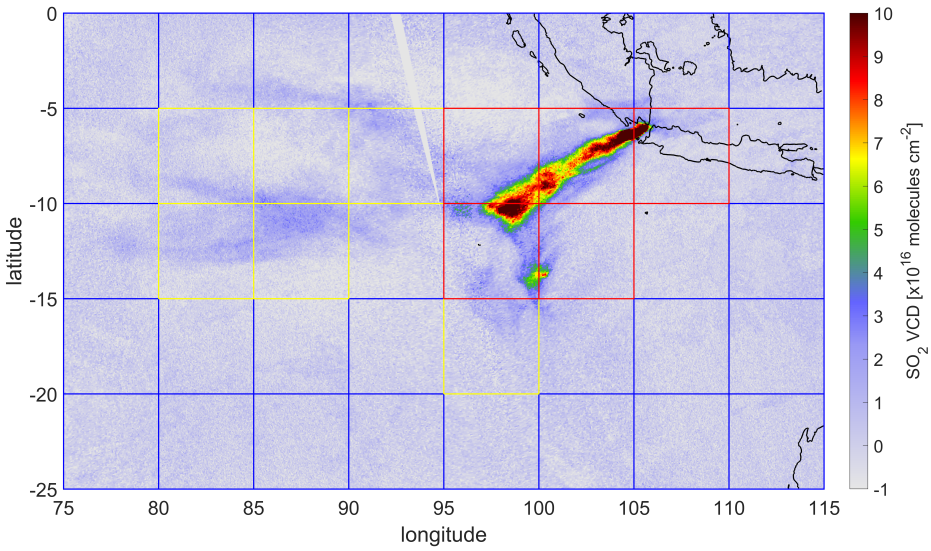


Figure 5.5: Example of the automatic event selection on the case of Anak Krakatau on 25 December 2018. The event is selected based on the SO_2 VCD on a 5°x5° grid. The event comprises of: 1. Primary event grid boxes (red): Grid boxes with clusters of at least ten S-5P/TROPOMI pixels with SO_2 VCDs exceeding $5x10^{16}$ molecules cm^{-2}. 2. Secondary event grid boxes (yellow): Grid boxes adjacent to a primary event grid box or a secondary event grid box, which contain at least 20 S-5P/TROPOMI pixels with SO_2 VCDs exceeding $3x10^{16}$ molecules cm^{-2}. 3. Background grid boxes (blue): The grid boxes directly surrounding primary and secondary event grid boxes are assigned to the event as background grid boxes.

correction (see section 5.2.4) and the standard deviation of SO_2 used as the threshold in the BrO/SO_2 calculation (see section 5.3). Furthermore the complete event domain including the background event grid boxes is used to calculate the spatial background polynomial correction (see section 5.2.4 for the implementation in processing the event and section 5.2.4 for a description of the spatial polynomial).
A map of all the event grid boxes of one example event on 25 December 2018 can be seen in figure 5.5. There are five primary event grid boxes (marked in red) encompassing the major parts of the plume from 95° E to 110° E and 5° S and 15° S. It can be seen that in the two boxes 15° to 10° S and 95° to 105° E there is a strong plume part spatially separated from the rest of the plume, which is also included in this scheme.

Treatment of events crossing the dateline

The definition of an event in section 5.2.2 is only based on the global SO_2 map of one day. Thus, events crossing the dateline would be considered as two separate events of two separate days, even though they are located next to each other and are measured at the same time. In order to consider these events only as a single event, the data west of the dateline (i. e. data assigned to the following day) are also considered and potential primary or secondary event grid boxes are also considered. I. e. if a primary event cluster (see figure 5.2.2) reaches the dateline during its iterative formation, it will also look past the dateline and incorporate the grid boxes from the next day if they fulfill the criteria as primary event grid boxes. These grid boxes will then not be included when defining events on the following day.

5.2.3 Limitations of the plume detection algorithm

One limitation is that plumes close to each other can not always be separated into two events. The high spatial resolution of S-5P/TROPOMI allows for the separation of volcanic plumes of volcanoes closer than 100 km, as can be seen at Ambrym/Ambae. The coarse grid of event boxes however – chosen on a $5° \times 5°$ grid so that intermittent plume parts are not taken as several events – counteract this, meaning that simultaneous erupting volcanoes within a 500 km distance will most likely be clustered as one event and their plume composition signature will be mixed.
Another difficulty for this algorithm is the coverage of very large events spanning over one complete hemisphere. Such an event occurred once in the three years of data looked at here (the eruption of Raikoke, Russia, on 22 June 2018). While the algorithm in principle is able to detect such an event, the way it starts from a single event box and then iteratively adds adjacent boxes is not designed for a large number of event boxes, thus the algorithm will take quite a lot of time for such an event.

5.2.4 Processing of an Event

The data of the complete event domain (including the background grid boxes) of one event as defined in figure 5.2.2 are then processed in multiple steps.
Firstly, the SO_2 and BrO VCDs are calculated using the DOAS settings and respective corrections described in section 4.2 and section 4.3.
For SO_2 the SCDs from the DOAS fits of all four fit windows are included. Afterwards, the median background is calculated for each fit window using the data of the background event boxes (blue grid boxes in figure 5.5). The four fit ranges are then combined depending on their SCDs as described in section 4.2.1.
For BrO the VCD derived from the DOAS fit is corrected using the ozone latitudinal correction (see section 4.3.2). The ozone latitude correction for BrO (see section 4.3.2) is calculated based on the latitude boundaries of the event domain. I. e. for the example event shown in figure 5.5, the correction term would be calculated using the data between 25° S and 0° S and the whole longitude range of this day.
Both data-sets are then corrected using the stratospheric background polynomial scheme (see subsection »Spatial polynomial correction«, below). For this the complete event data including the data from the background grid boxes are used.
Lastly, the BrO/SO_2 ratio is calculated based on the corrected VCDs as described in section 5.3. The ratio calculation is done for all pixels with an SO_2 VCD exceeding four times the standard deviation calculated from the background grid boxes.

Spatial polynomial correction

In order to correct for a potential remaining spatial pattern in the background distribution of SO_2 as well as BrO, a spatial polynomial correction is applied. This was implemented already in Hörmann (2013). Even though the BrO and SO_2 retrieval and correction scheme presented in this thesis is much less affected by background gradients due to the inclusion of Pukite-Terms for O_3 and the aforementioned BrO correction scheme, there are still potential small spatial patterns remaining, which should be further reduced.
The retrieved VCD V_m can thus be decomposed into the background VCD V_b and the volcanic VCD V_v:

$$V_m = V_b + V_v \tag{5.1}$$

The spatial polynomial correction scheme makes use of the fact that volcanic plumes can usually be considered as a localized phenomenon of several 100 km extent within a large scale background distribution pattern on the scale of 1000 km for both BrO and SO_2. Furthermore, both volcanic and background distributions are independent from each other. Thus, it can be assumed that the background is smooth with respect to the scale of the volcanic plume and background information gathered spatially around the plume can be interpolated over the plume region.
The background VCD V_b for each pixel k is modeled by two-dimensional polynomial of degree three:

$$[V_b]_k = \sum_{i,j=0}^{3} c_{i,j} \cdot x_k^i \cdot y_k^j \tag{5.2}$$

where x is the pixel latitude and y the longitude corrected by a latitudinal dependent squeeze:

$$[V_b]_k = \sum_{i,j=0}^{3} c_{i,j} \cdot [\text{lat}]_k^i \cdot [\text{lon} \cdot \cos(\text{lat})]_k^j \tag{5.3}$$

In order to calculate the polynomial first the volcanic plume is masked. For this a SO_2 VCD threshold is chosen, above which a pixel is masked as influenced by the volcanic plume. This is typically chosen as four times the standard deviation of SO_2 (typically in the range of 2×10^{16} molecules cm^{-2}). The polynomial coefficients $c_{i,j}$ are then determined for this subset of data for both BrO and SO_2 independently and applied to each pixel of the complete data-set, leading to the background VCD. The resulting (volcanic) VCD is obtained by subtracting the background VCD V_b from the retrieved VCD V_m.

5.3 Calculation of the BrO/SO_2 molar ratio in previous studies

Ideally, the calculation of the BrO/SO_2 ratio is just the division of two numbers – in our case the BrO VCD of one pixel divided by the SO_2 VCD of the same pixel.
However, in a volcanic plume, detected from satellites, there is only a small fraction of the pixels, where the signal-to-noise ratio of a single BrO VCD measurement is above one. For ground-based measurements this is similar (Warnach et al., 2019; Lübcke et al., 2014). Thus, BrO/SO_2 ratios are typically calculated based on a multitude of pixels / datapoints.
In previous studies, the BrO/SO_2 ratio calculation from DOAS measurements has been done in several different ways depending on two measures – the method to calculate the ratio and the (sub)set of data used for the calculation. In the following these different methods are introduced. The method used in this thesis is described in section 5.4.

The linear regression method of both BrO and SO_2 VCD data-sets is the most common method used to calculate the BrO/SO_2 ratio. This method was employed in the first detection with DOAS in volcanic plumes (Bobrowski et al., 2003), and a study comparing the ratios of the plumes of several volcanoes (Bobrowski and Platt, 2007), as well as in the satellite study of Hörmann et al. (2013).
For ground-based measurements (Bobrowski et al., 2003; Bobrowski and Platt, 2007; Warnach et al., 2019) the method was applied to complete data-sets, whereas only a subset of a data-set was used for the linear regression in the satellite study (Hörmann et al., 2013). For satellite only datapoints inside the plumes are selected and not the complete covered

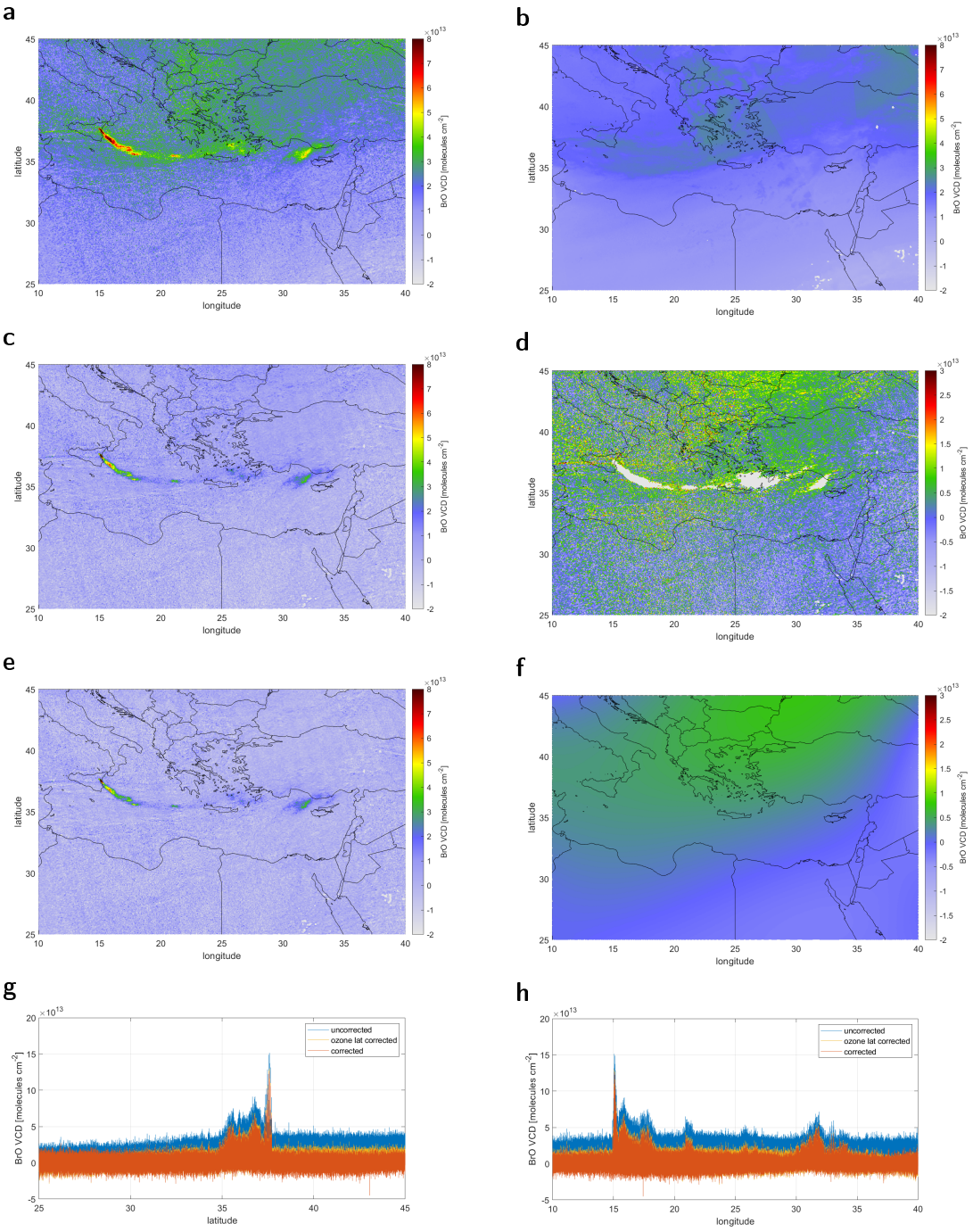


Figure 5.6: Overview of the processing of the BrO VCD for a volcanic event: The uncorrected data (**a**) is first corrected using the lat ozone correction term (**b**) to yield the lat ozone corrected VCD (**c**). For the calculation of the spatial polynomial correction the plume is masked (**d**) and a third order spatial polynomial term is retrieved (**f**). The final corrected data is shown in **e**. The intersections in latitude (**g**) and longitude direction (**h**) are also included.

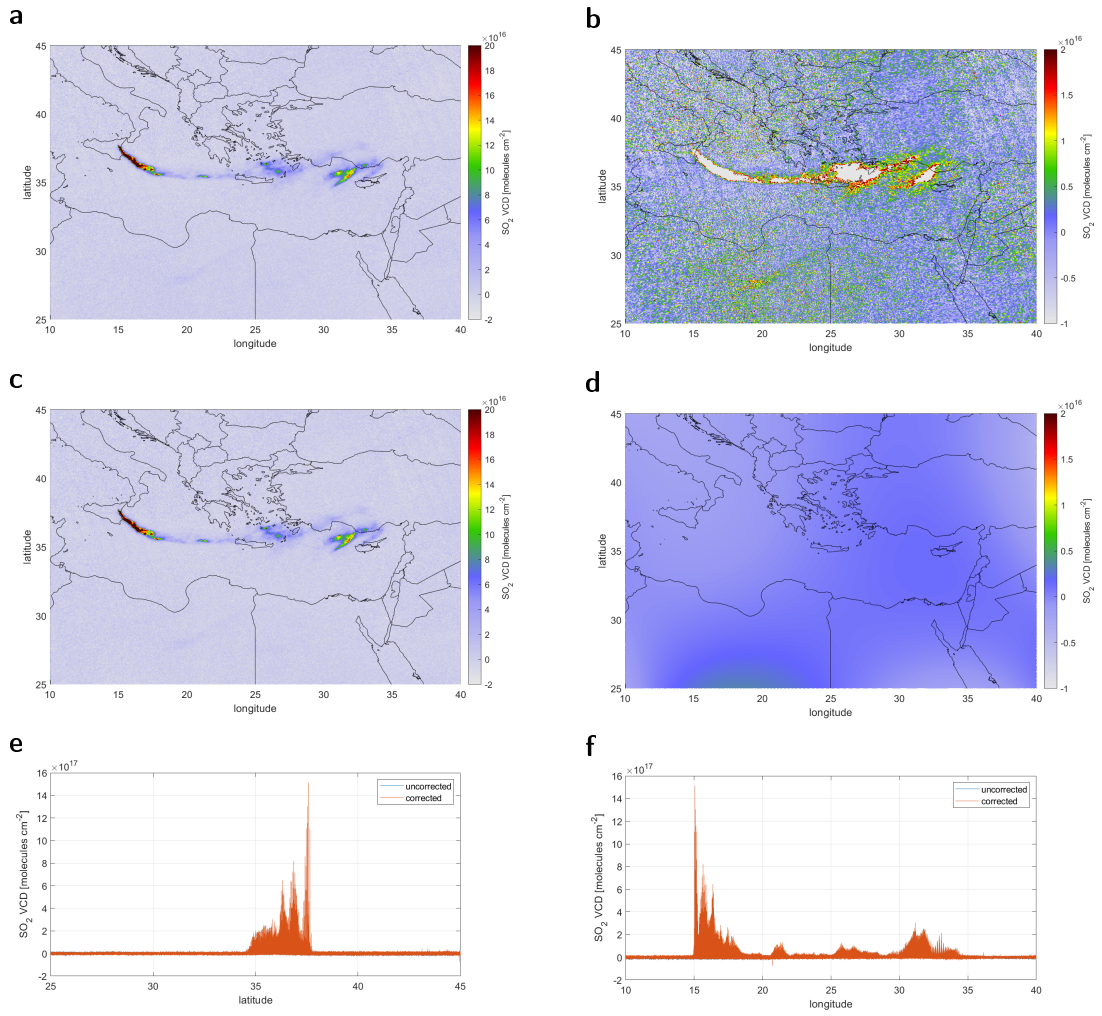


Figure 5.7: Overview of the processing of the SO_2 VCD for a volcanic event. From the uncorrected data (**a**) the plume is masked (**b**). Based on this data the spatial polynomial term is retrieved (**d**) used to calculate the corrected VCD (**c**). The intersections in latitude (**e**) and longitude direction (**f**) are plotted below.

data-set (which in the case of GOME-2 and TROPOMI encompasses the whole globe). Ground-based instruments on the other hand are placed in a way, that most of the measurements are inside of the volcanic plume. Thus, in a way the data-set of a ground-based measurement is selective by design and in a sense already a subset of a complete picture.

The daily weighted average method is another method to calculate the BrO/SO_2 ratio. It is calculated by a weighted average of all the individual ratios, where the weight is calculated from the error of both DOAS retrievals. This method was employed first on the NOVAC data of Nevado del Ruiz, Colombia (Lübcke et al., 2014), and of Cotopaxi, Ecuador (Dinger et al., 2018). Warnach et al. (2019) applied both approaches onto the same NOVAC data-set of Tungurahua. They found very good agreement between both methods. However, the average mean method was only applied to a subset of data.

Selection of the data-set If a subset of data is used, it is the data which can be clearly assigned to the volcanic plume. For the average weighted mean method this is determined by

an SO_2 VCD threshold above which a data point is above the SO_2 detection limit as well as being in the range of the BrO detection limit. It is obvious that the latter is not necessarily the case as it depends on the underlying BrO/SO_2 ratio. For example, for NOVAC data (Lübcke et al., 2014; Warnach et al., 2019), this SO_2 threshold was chosed at an SO_2 VCD of 7×10^{17} molecules cm^{-2}. Assuming a BrO/SO_2 ratio of 5×10^{-5} (typical for volcanoes in the Andes) this leads to a BrO threshold of 3.5×10^{13} molecules cm^{-2}, which is only slightly lower than the detection limit of 4.8×10^{13} molecules cm^{-2} (Warnach et al., 2019).
For the case of satellite measurements, i. e. Hörmann et al. (2013), the linear regression method was used and applied only to data above a threshold of SO_2 VCD larger than 3 times the standard deviation of SO_2 SCD.

5.4 Calculation of the BrO/SO_2 ratio in this thesis

For this study, the linear regression method is used and applied to a subset of the data of a specific area. It is applied only to data exceeding four times the standard deviation of the SO_2 VCD, which can be as low as four times 5×10^{15} molecules cm^{-2}, i. e. 2×10^{16} molecules cm^{-2}.
The linear regression between x=SO_2 and y=BrO is done by the following function:

$$y = m \cdot x \tag{5.4}$$

$$BrO = \frac{BrO}{SO_2} \cdot SO_2 \tag{5.5}$$

where the slope m of the fit corresponds to the BrO/SO_2 ratio. In contrast to previous works (e. g. Hörmann et al., 2013), there is no parameter included for a y-offset, i. e. the linear regression assumes that there is no BrO offset. While in principle, the inclusion of such a variable allows for the correction of an potential remaining offset, there are two reasons, why it is not to include in this thesis. Firstly, the rigorous background correction (compare section 4.3.2) ensures that potential offsets are removed almost for all cases, yielding potentially significant offsets only for very special cases (biomass burning events overlapping spatially with the volcanic plume). Thus it can be assumed, that there are no offsets present. Secondly, the data at SO_2 VCD = 0 is excluded for the fit. Thus, a linear fit with a free y-intersect is not bound to the actual y-intersect, but would just yield another free parameter. E. g. in the non-linear case of Mt. Etna on 25 December 2018 figure 5.16c, the fit results a large positive offset in order to better deal with the non-linearity of the data-set. Thus, the y-intersect yields an unrealistic value, which is neither representative of the actual y-intersect nor has any other physical meaning.
The uncertainty of the BrO/SO_2 ratio is given as the 95% confidence interval of the slope.

5.4.1 Categorizing of the linear BrO/SO_2 fit

Hörmann (2013) classified the eruption based on the accuracy of the calculation of the BrO/SO_2 ratio. The two main criteria were the coefficient of determination (R^2) of the BrO/SO_2 fit as well as the maximal BrO VCD. In the Hörmann (2013) thesis the R^2 value defined if a correlation between BrO and SO_2 was linear. If it exceeded 0.5, Hörmann (2013) defined the correlation as clearly linear, while values below 0.25 were considered as a non-linear BrO/SO_2 relation. The value in between was counted as weak linear. In addition, he only accounted events with a significant detection of BrO. For this a threshold of two times the standard deviation of the BrO VCD was selected in the case of the linear correlation, and four times the standard deviation in the case of the non-linear correlation.

While the R^2 value is widely used as a measure of a fitted line, it has some limitations and drawbacks. In the following, the representativeness of the R^2 value as a measure both for fit quality and linearity of the BrO-SO_2 distribution is discussed with respect to S-5P/TROPOMI data and other measures are introduced.

Representativeness of the R^2 value

The general definition of the R^2 is the following:

$$R^2 = 1 - \frac{\sum (y_i - \hat{y}_i)^2}{\sum (y_i - \bar{y})^2} = 1 - \frac{SQE}{SQT} = 1 - \frac{\text{deviation from fitted line}}{\text{deviation from mean of y}} \tag{5.6}$$

where y_i represent the single BrO VCD measurements, $\hat{y}_i$ the y-values (in this case the BrO VCD) of the model function (in this case the linear regression between SO_2 and BrO VCD) and $\bar{y}$ the mean of the measured y-data. The R^2 is thus one subtracted by a quotient. The nominator is the so called »**S**um of S**q**uares **E**xplained« (SQE), while the denominator is the so called »**S**um of S**q**uares **T**otal« (SQT). In a more profound way, SQE can be seen as the deviation of the data-set from the fitted line and the SQT as the deviation of the mean BrO.
The quotient is thus a measure for the deviation of the R^2 from 1. It can be directly seen that the SQE will increase if the uncertainty is increasing, e. g. a larger random deviation of BrO will lead to a larger nominator, while the SQT is much less affected by this. Thus, larger random variation will lower the R^2, meaning a larger scatter representing a larger uncertainty will lead to a lower R^2. And in this sense the R^2 is a measure for the uncertainty.
However, both the underlying BrO/SO_2 ratio as well as the maximum SO_2 will lower the mean BrO of a distribution, which in turn will change the SQT, the deviation from the mean BrO.
In a handwaving argument, the mean BrO can be seen as the following product:

$$\overline{\text{BrO}} = \frac{\text{SO}_{2,\text{max}}}{2} \cdot \frac{\text{BrO}}{\text{SO}_2} \tag{5.7}$$

and thus, it is clear that the SQT, which can be seen as the deviation from the mean BrO, is depending on both the maximal SO_2 as well as the underlying BrO/SO_2 ratio.
This calls for the need to investigate and identify potential inherent dependencies of the R^2 on the underlying BrO/SO_2, the maximum SO_2. Furthermore, the number of data points as well as the random variation of the BrO is included in the investigation.
Various synthetic data-sets are created, with different random variation of the BrO signal (σ_{BrO}), the BrO/SO_2 ratio, the maximum SO_2 VCD and the number of points (the different values for the data-sets are given in table 5.2). The data-sets are created by first taking a Gaussian distribution of BrO VCDs, with $\sigma = \sigma_{\text{BrO}}$ and $\mu = 0$. An SO_2 VCD is assigned to these values as a random distribution between zero and the maximum SO_2 VCD. To simulate the statistical variation a random Gaussian distribution with $\sigma = 5 \times 10^{15}$ (the typical statistical uncertainty found in TROPOMI data). This is done for each σ_{BrO}, maximum SO_2 VCD and No. of points given in table 5.2.
In a second step a BrO/SO_2 ratio is added to these data-sets, by adding a term $SO_2 \times \left[\frac{BrO}{SO2}\right]_{ratio}$ to the random distributed BrO. This is done for 17 different BrO/SO_2 ratios as given in table 5.2. In total this yields 1088 BrO-SO_2 distributions. An example of distributions for the different σ_{BrO} and five selected BrO/SO_2 ratios are shown in figure 5.8.
The BrO uncertainty is given by the σ_{BrO}. In the TROPOMI data this is typically 6 - 7 $\times 10^{12}$. A lower variation in BrO should lead to a larger R^2. Both SQE and SQT should

Table 5.2: Variables used to calculate synthetic BrO-SO_2 distributions. The nodes typical for TROPOMI are marked in bold.

Variable	σ_{BrO} [$\times 10^{12}$]	BrO/SO_2	max SO_2 [$\times 10^{17}$]	No. of points
Values	$1, 3, \mathbf{5}, 10$	$1, 2, 5 \times 10^{-7}$	$1, 2, 5, \mathbf{10}$	$100, 500$
		$1, 2, 3, 5, 7 \times 10^{-6}$		$\mathbf{1000}, 5000$
		$\mathbf{1, 2, 3, 5, 7} \times 10^{-5}$		
		$\mathbf{1, 2, 3, 5} \times 10^{-4}$		

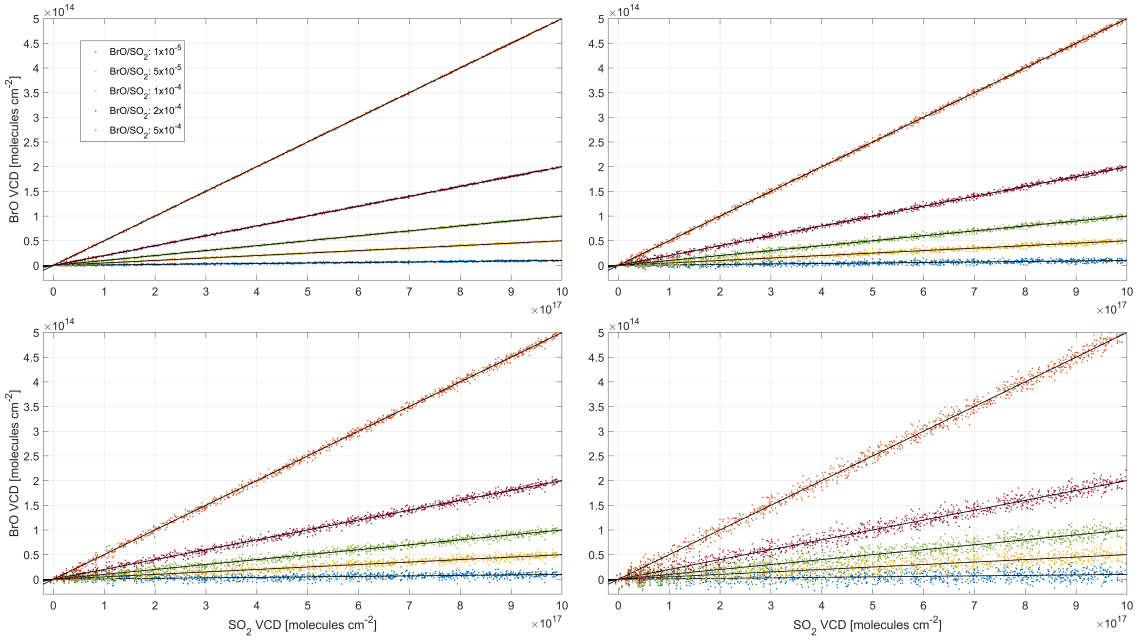


Figure 5.8: Modelled BrO-SO_2 data-sets for different σ_{BrO} and BrO/SO_2 ratios, N = 1000. **a**: $\sigma_{BrO} = 1 \times 10^{12}$, **b**: $\sigma_{BrO} = 3 \times 10^{12}$, **c**: $\sigma_{BrO} = 5 \times 10^{12}$, **d**: $\sigma_{BrO} = 1 \times 10^{13}$.

decrease, but the SQT should decrease less, thus leading to a larger R^2. This effect is visible in figure 5.8.

It can be seen that a lower BrO/SO_2 ratio will lead to a lower R^2. This dependency on the BrO/SO_2 ratio is independent from the other parameter and originates solely in the dependency of the SQT on the BrO/SO_2 ratio, while the SQE is independent on the BrO/SO_2 ratio (see figure 5.9, figure 5.10, and figure 5.11).

It can be seen that lowering the random variation of BrO σ_{BrO} will lead to a larger R^2 (see figure 5.9), because the SQE decreases with lower σ_{BrO}, while the SQT is unaffected or less affected, except for BrO/SO_2 ratios, where the R^2 is already almost zero. This effect, that the R^2 will increase if the deviation from the fitted line is smaller, is desired and shows that the R^2 has some meaning in interpreting the fit quality.

Another desirable relation is the dependency of the maximal SO_2. A larger maximal SO_2 increases the R^2 independent of the BrO/SO_2 ratio (see figure 5.10). If the distribution has a larger extend in SO_2 direction the fit should be more certain. As expected, the SQE is unaffected by the change in maximal SO_2 - since the SQE is only depending on the deviation from the fitted line.

However, the SQT is increasing with increasing maximal SO_2 VCD. Lastly, the R^2 is almost

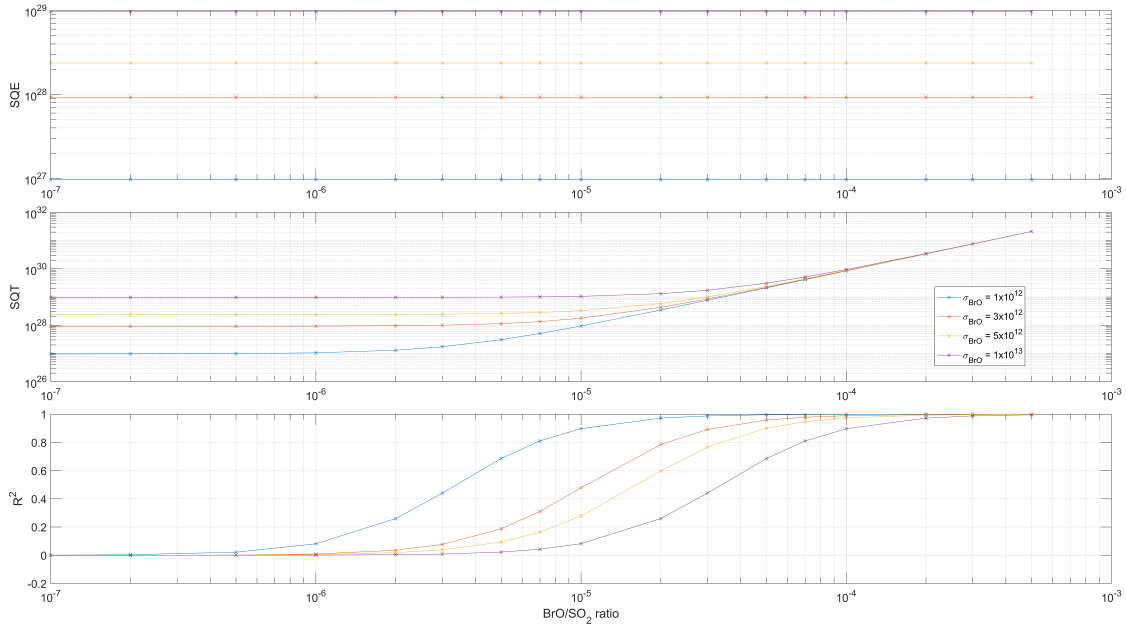


Figure 5.9: SQE (top), SQT (middle), and R^2 (bottom) as a function of the BrO/SO_2 ratio for different σ_{BrO}.

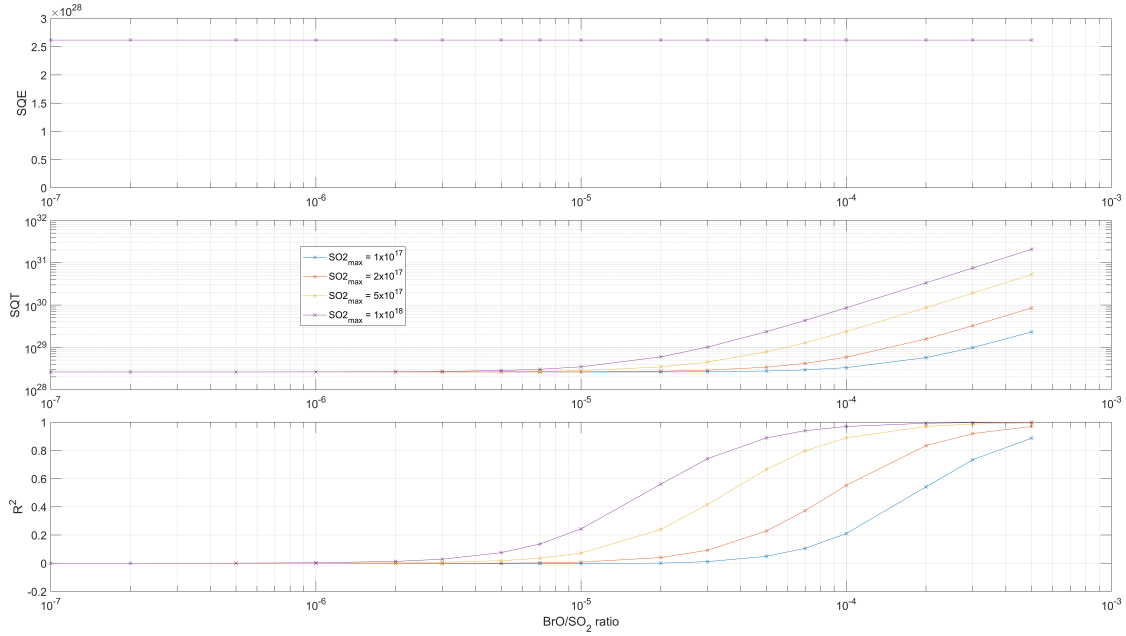


Figure 5.10: SQE (top), SQT (middle), and R^2 (bottom) as a function of the BrO/SO_2 ratio for different maximal SO_2.

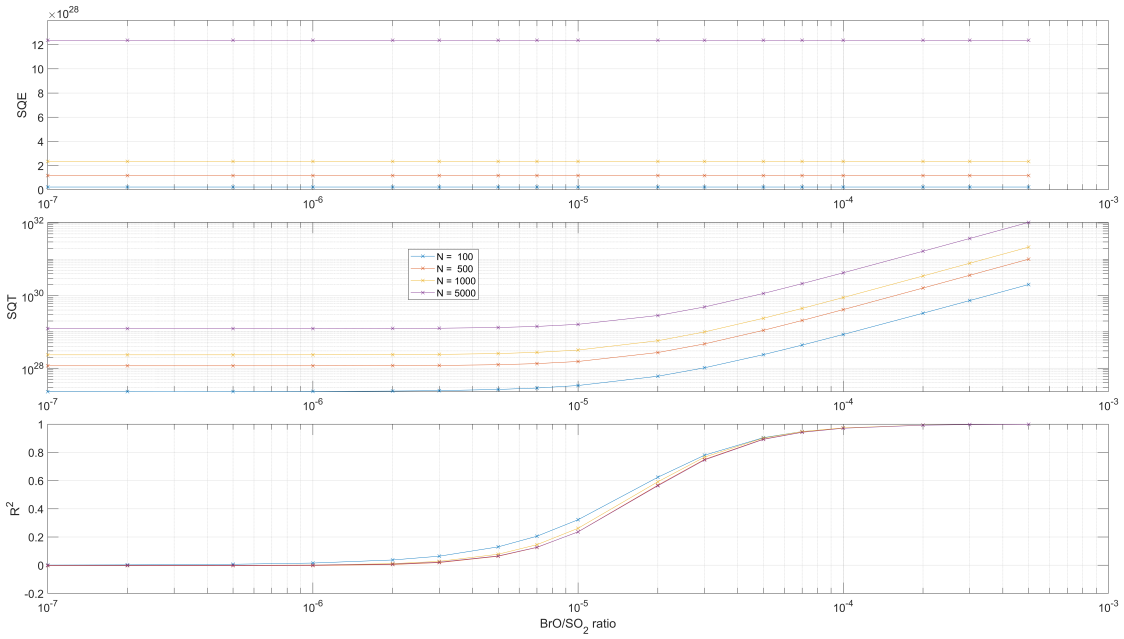


Figure 5.11: SQE (top), SQT (middle), and R^2 (bottom) as a function of the BrO/SO_2 ratio for different number of points.

independent on the number of data points. Increasing the number of data-points should lead to an increase in certainty of the BrO-SO_2 relation. However, the R^2 is only minimally changed by an increase in data-points from 100 to 5000 (see figure 5.11).
Thus, it can be seen that the R^2 might be a decent quantity to determine the accuracy of a fit for high BrO/SO_2 ratios, but fails to do so for low BrO/SO_2 ratios.

5.5 Alternative measures used in this thesis

Therefore, the need arises to employ alternative measures to both quantify the uncertainty as well as the linearity of the BrO-SO_2 fit.

5.5.1 The fit error of the BrO/SO_2 ratio fit

A different measure for the fit accuracy and thus for the accuracy of the retrieved BrO/SO_2 ratio is the fit error. This measure proves to be independent of the BrO/SO_2 ratio - except for a very weak increase in the fit error observed for ratios larger than 1×10^{-4} for some settings (see figure 5.12 - figure 5.14).
The absolute error decreases if the random variation (parametrised by σ_{BrO}) decreases (see figure 5.12). The relation between σ_{BrO} and the absolute fit error is linear (see figure 5.15a). The relative fit error is below 10 % even for $\sigma_{BrO} = 1 \times 10^{13}$, which is larger than the observed σ_{BrO} for BrO/SO_2 ratios larger than 1×10^{-5} (see figure 5.12).
A decrease in the maximum SO_2 leads to a larger absolute fit error, as expected (see figure 5.13). The relation between the maximum SO_2 and the absolute fit error follows a 1/(maximum of SO_2)-line (see figure 5.15b, black line). The relative fit error is typically below 10 %, except for maximum SO_2 below 2×10^{17}, where the relative error exceeds 10 % if the ratio is smaller than 3×10^{-5}.

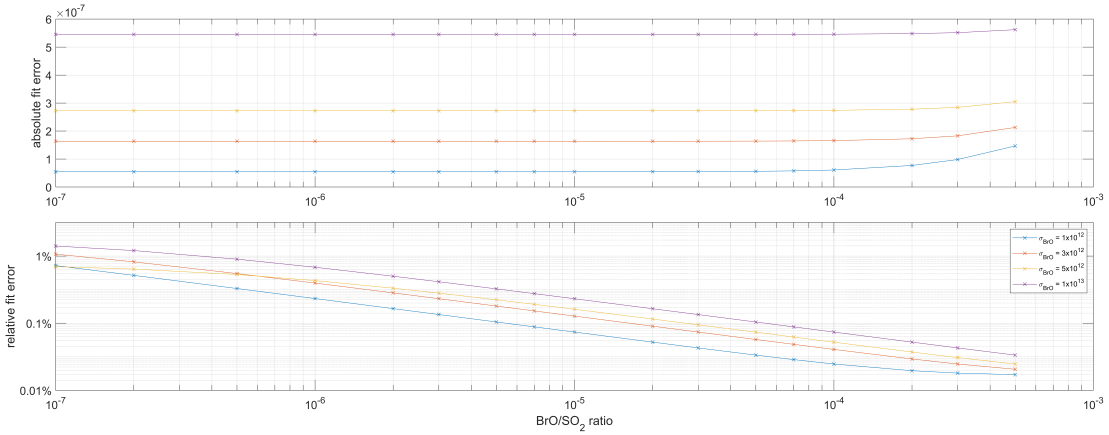


Figure 5.12: Absolute (top) and relative (bottom) fit error for different σ_{BrO} and $\mathrm{BrO}/\mathrm{SO}_2$ ratios.

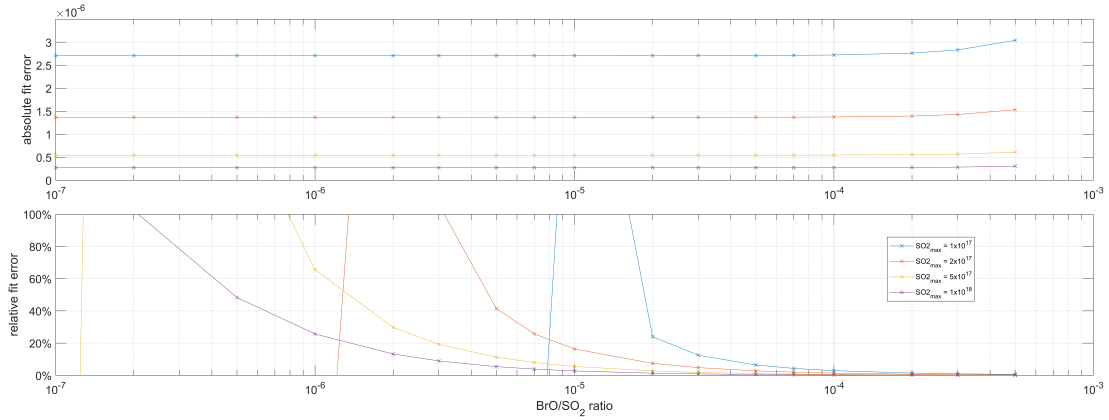


Figure 5.13: Absolute (top) and relative (bottom) fit error for different maximal SO_2 and $\mathrm{BrO}/\mathrm{SO}_2$ ratios.

An increase in data points (see figure 5.14) results in a lower absolute fit error following a $1/\sqrt{N}$ relation (see figure 5.15c, black line), as expected from increasing the number of points in a random distribution.
Thus, the fit error is a quantity which shows in this model data-set all expected features, i. e. a linear increase with relation to the σ_{BrO}, a $1/\sqrt{N}$ relation and a decrease if the maximal SO_2 is increased, while not depending on the $\mathrm{BrO}/\mathrm{SO}_2$ ratio. The fit error therefore proves to be a much suitable measure to determine the absolute and relative uncertainty of a BrO-SO_2 fitted line than the R^2. Thus, it will be used in this study, in difference to the study by Hörmann (2013).

5.5.2 The detection of BrO inside a volcanic plume

Another criterion to select a meaningful $\mathrm{BrO}/\mathrm{SO}_2$ ratio is the BrO VCD inside the volcanic plume. A successful detection of BrO is defined if there are at least 5 pixel in a 3×3 pixel cluster inside the plume exceeding two times the standard deviation of BrO VCD. The standard deviation of BrO is derived from the BrO distribution in the background, i. e. outside of the volcanic plume.

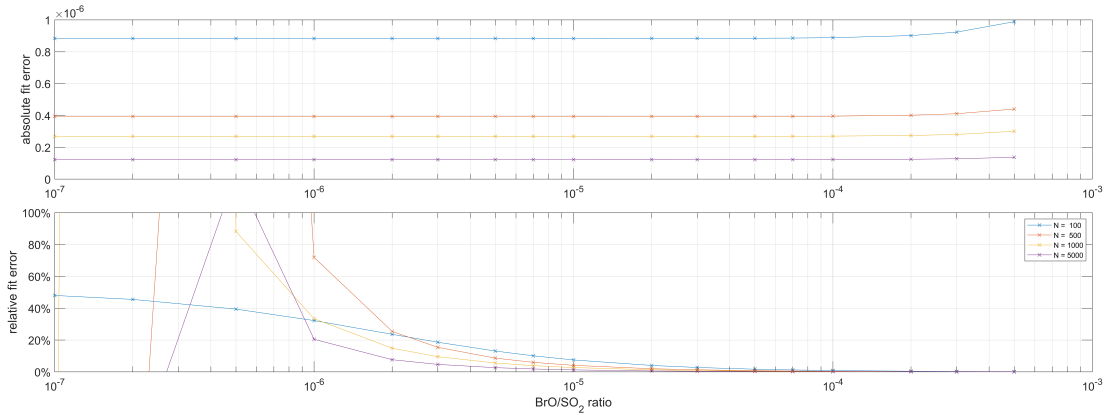


Figure 5.14: Absolute (top) and relative (bottom) fit error for different number of points and BrO/SO_2 ratios.

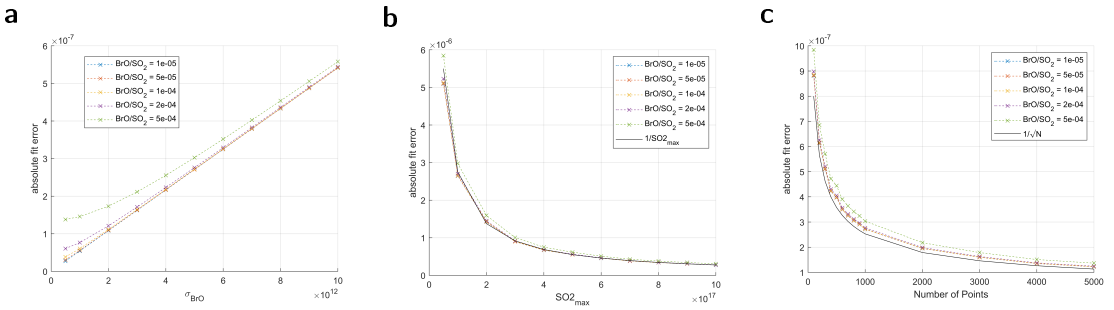


Figure 5.15: Dependency of the fit error on the variation of **a** the BrO, **b** the maximal SO_2, and **c** the Number of points for different BrO/SO_2 ratios (marked by colors). for maximal SO_2 a $1/(\text{maximal } SO_2)$ line is plotted in **b** and for the number of points a $1/\sqrt{N}$ line is included in black.

5.5.3 The non-linearity criterion

While the fit error of a linear regression will in principle increases if a distribution of two quantities is non-linear, its main dependency is on the number of points. Thus a distribution with a large number of pixels (large plumes can include 10 000 S-5P/TROPOMI pixels) will have a low fit error even if it is highly non-linear (e. g. figure 5.16c). This requires a new measure to detect non-linearity of a BrO-SO_2 distribution. In order for this, two linear regressions are compared: firstly the fixed linear regression without an y-intercept, e. g. following $y = m \cdot x$ and the unfixed linear regression including an y-intercept, e. g. following $y = m \cdot x + b$. If the relation between x and y is linear, then both fits will yield the same m. In the non-linear case, both fits cannot perfectly represent the x-y relation, and since the unfixed has one more free variable, the chosen parameter will differ from each other. An example for this is shown in figure 5.16c. In this case the BrO response is lower for high SO_2 leading to a high non-linearity. While neither the fixed nor the unfixed fit can represent this non-linear relation, the unfixed tries to better represent this through a lower slope in combination with an unrealistic large y-intersect of 7.79×10^{12} molecules cm^{-2}. The slopes of both fits do not agree within their 95% confidence interval.
The agreement of the slopes of the two linear regression lines is quantified by the Slope Coefficient SCF, which is the quotient of the absolute difference between the fixed slope Sl_f and the unfixed slope Sl_u and the added uncertainty given by the sum of the errors E_f and

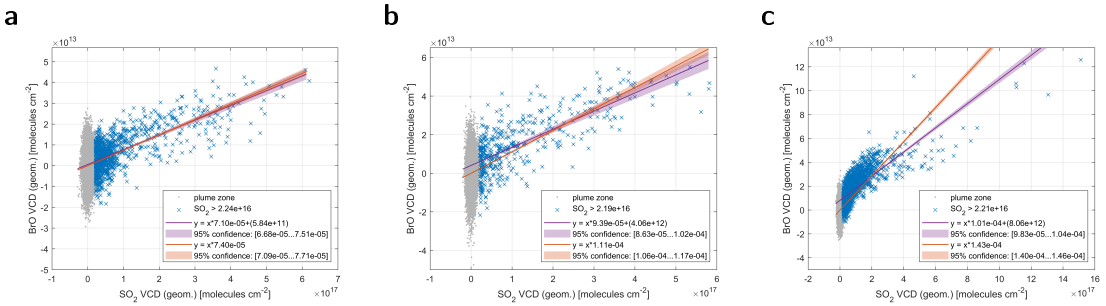


Figure 5.16: Distribution of the BrO VCD and SO_2 VCD of different linearity for different events of Mt. Etna. **a** example for a linear relation (slope coefficient 0.41), detected on 7 July 2021. **b** example for a weak non-linear relation (slope coefficient 1.30), detected on 2 June 2021. The relation is linear only for $SO_2 < 4 \times 10^{17}$ molecules cm^{-2}. *right:* example for a highly non-linear relation (slope coefficient 6.88), detected on 25 December 2021. Similar to the weak non-linear example (**b**) there is a linear relation for $SO_2 < 4 \times 10^{17}$ molecules cm^{-2}. In addition there is a different linear relation for $SO_2 > 6 \times 10^{17}$ molecules cm^{-2}. The fitted line of the unfixed linear regression (purple line) and the fixed linear regression (red line) are plotted. The respective 95% confidence interval of the slope is indicated by the shaded area in the respective color.

E_u:

$$SCF = \frac{|Sl_f - Sl_u|}{E_f + E_u} = \frac{\text{absolute difference between fixed and unfixed slopes}}{\text{added uncertainty of unfixed and fixed slopes}} \tag{5.8}$$

There are three classifications:

linear: All events with a slope coefficient <= 1, i. e. if both slopes agree within their uncertainties. Here, the linear assumption is valid for the complete data-set and the slopes can be seen as a valid representation of the BrO/SO_2 ratio. An example for such a distribution with a slope coefficient of 0.39 is shown in figure 5.16a.

weakly non-linear: All events with 1 < slope coefficient <= 2 are defined as weakly non-linear. While the linear assumption is no longer valid for the complete distribution, there are still strong linear parts. An example for such a distribution with a slope coefficient of 1.30 is shown in figure 5.16b. It can be seen that the distribution is linear for $SO_2 < 4 \times 10^{17}$ molecules cm^{-2} and only deviated for the small fraction of $SO_2 > 4 \times 10^{17}$ molecules cm^{-2}, where the BrO response to an increase in SO_2 is much lower. Since the major part of the data-set can be attributed to a linear part, the fitted regression line (purple) is in this case a decent estimate for this linear part. However, this is not necessarily always the case for distributions identified as weakly non-linear.

highly non-linear: All events with a slope coefficient > 2 are completely non-linear. An example for such a distribution with a slope coefficient of 6.85 is shown in figure 5.16c. It can be seen that the distribution consists of multiple parts with different BrO/SO_2 ratios. Similar to the weakly non-linear example, there is a linear part for $SO_2 < 4 \times 10^{17}$ molecules cm^{-2}. For higher SO_2 another, very different BrO/SO_2 relation can be seen, for $SO_2 > 6 \times 10^{17}$ molecules cm^{-2}. This strong non-linearity is well reflected in the high slope coefficient of 6.85. It can be seen that the slope of the fitted regression line (purple) does not match either of the different parts of the distribution. Thus it will not yield a meaningful BrO/SO_2 ratio.

Part III

Results

6 Global study of the BrO/SO_2 ratio

In this chapter a global survey of the BrO/SO_2 ratios observed in volcanic plume is unfolded. Volcanic plumes are detected systematically from spectral data of S-5P/TROPOMI over a four-year period from January 2018 to December 2021 using the automated plume detection algorithm described in section 5.2. The result is a global data-set of volcanic events (as defined in section 5.2). For each event the SO_2 VCD map, BrO VCD map as well as the BrO/SO_2 ratio are derived and calculated following section 5.2 and the BrO/SO_2 ratio is classified into linear, weakly non-linear and non-linear as described in section 5.5.3.
The data-set is discussed showcasing different SO_2 emission strengths corresponding to different types of volcanic activity, i. e. quiescent degassing until major eruptions. Furthermore, the events are categorized based on the BrO-to-SO_2 relations, i. e. linear and non-linear (for the definition, see section 5.4.1). Events with linear BrO/SO_2 ratios are assigned to 43 volcanoes and cataloged, leading to a data-base of BrO/SO_2 ratios for these volcanoes. The results are discussed with respect to volcanic parameters and compared to other measurements of volcanic BrO/SO_2. Lastly, information of the effective Lifetime of reactive bromine are derived for Mt. Etna.

6.1 Overview of the results

In total, 4323 SO_2 events have been detected. For 90.9 % of these events (3845) the SO_2 VCD does not exceed 5×10^{17} molecules cm^{-2}.[1] These events can be sub-categorized into events below and above SO_2 VCD of 1×10^{17} molecules cm^{-2}. The former loosely corresponds to quiescent degassing while the latter corresponds to a minor eruption. There are roughly 1185 events, i. e. 28.0 % of the complete data-set, which then correspond to quiescent degassing. Minor eruptions then make up 2660 events (62.9 %). The remaining 9.1 % – which have maximal SO_2 VCDs larger than 5×10^{17} molecules cm^{-2} – can be divided into medium size eruptions – assumed to have maximal SO_2 VCDs below 1×10^{18}, 242 events or 5.7 % – and major eruptions with maximal SO_2 VCDs above 1×10^{18} molecules cm^{-2} (145 events, i. e. 3.4 %) (see figure 6.1a). The number of events for each of these categories is given in table 6.1.
The largest SO_2 VCDs are recorded during the Raikoke eruption on 22 June 2019 and during the La Palma eruption in September 2021. Both eruptions have SO_2 VCDs exceeding 1×10^{19} molecules cm^{-2}. Apart from these two eruptions, the major eruptions in 2018 originate mainly from Ambrym/Ambae, Vanuatu, for both of which multiple major eruptions are observed throughout 2018. Furthermore, Kilauea, USA, and Fernandina, Ecuador, were both active in June/July 2018 with several major eruptions observed each. In 2020 SO_2 VCDs exceed 2×10^{18} molecules cm^{-2} for three eruptions: namely one from Taal, Philippines

[1] It is noteworthy, that events are only detected if the SO_2 VCD exceeds 5×10^{16} molecules cm^{-2} (see section 5.2), i. e. one order of magnitude lower.

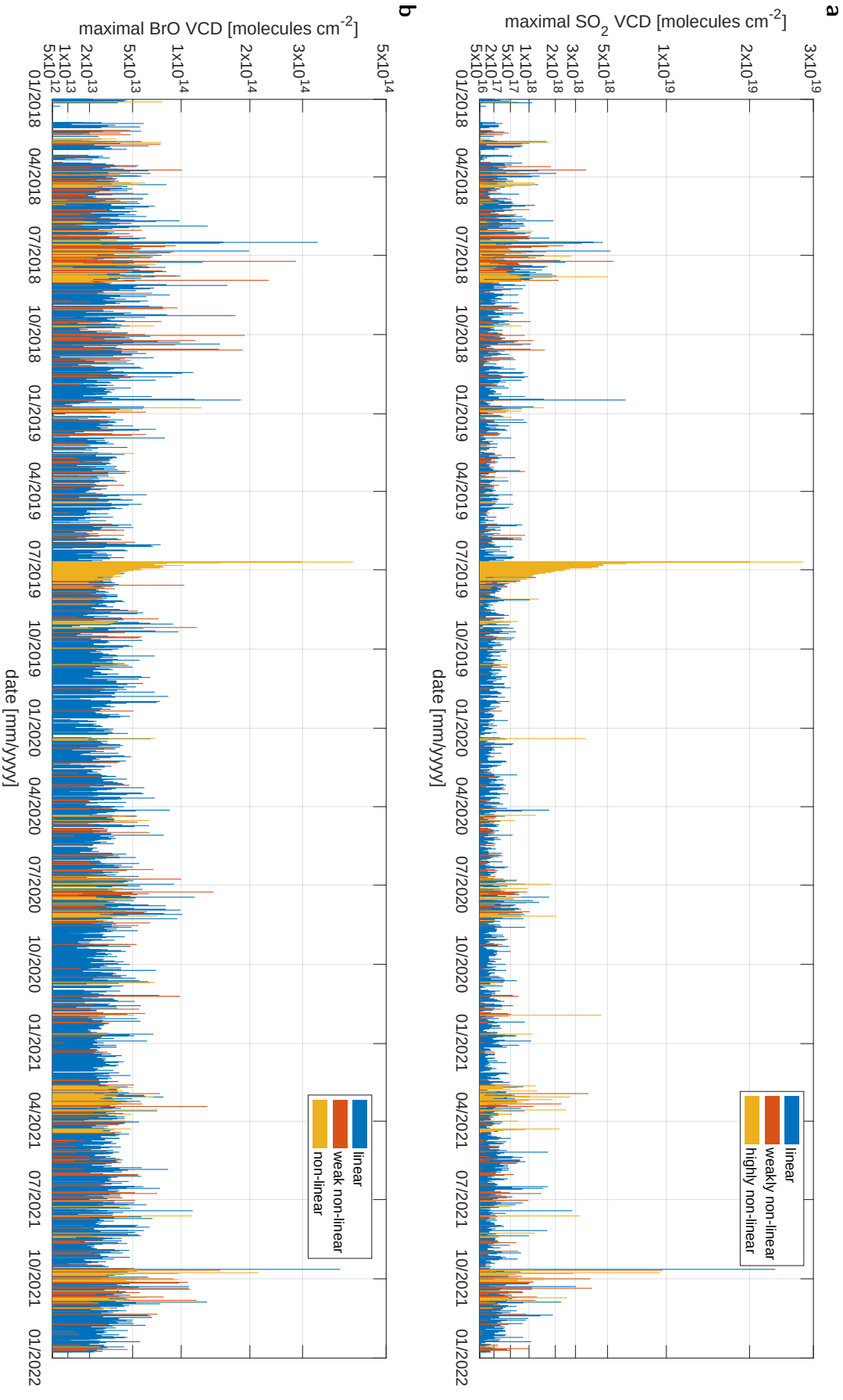


Figure 6.1: Overview of **a** the maximum SO_2 VCD, and **b** the maximum BrO VCD of the volcanic plume events over the four-year time-series.

Table 6.1: Overview of the events detected by the automated plume algorithm categorized by their maximal SO_2 VCD which is related to the eruption type. The number of events is given both without any error criterion, with an error criterion, and for significant detection of BrO.

Eruption type	maximum SO_2 VCD	events total	rel. error <20%	significant BrO
All data	$[5 \times 10^{16} \dots 3 \times 10^{19}]$	4232	1634	1449
... quiescent degasing	$[5 \times 10^{16} \dots 1 \times 10^{17}]$	1185	250	150
... minor eruption	$]1 \times 10^{17} \dots 5 \times 10^{17}]$	2660	1008	943
... medium eruption	$]5 \times 10^{17} \dots 1 \times 10^{18}]$	242	231	212
... major eruption	$]1 \times 10^{18} \dots 3 \times 10^{19}]$	145	145	144

on 13 January 2020, one from Nishinoshima, Japan, which was active in July/August 2020, and one from Lewotolok, Indonesia, on 29 November 2020. In the first half of 2021 multiple major eruptions of Mt. Etna can be seen throughout February and July as well as the La Soufriere, St. Vincents eruption on 22 April 2021.
There are 341 events with BrO VCDs exceeding 5×10^{13} (see figure 6.1b), 43 of which even exceed 1×10^{14}. The largest BrO VCDs do not necessarily correspond to events with the largest SO_2 values. Highest BrO VCDs in the range of $2 - 4 \times 10^{14}$ molecules cm^{-2} are observed for Raikoke and La Palma eruption, but also for the major eruptions of Fernandina volcano, Galapagos in June/July 2018, where maximal SO_2 VCDs are one order of magnitude lower. This is not surprising, since the BrO/SO_2 can vary more than one order of magnitude between different volcanoes.

6.1.1 Selection criteria for the BrO/SO_2 ratio

In order to derive meaningful BrO/SO_2 ratios of the volcanic events, there are two selection criteria: the linearity of the BrO-SO_2 relation and the quality of the fit. The former criterion is determined by the slope coefficient, described and discussed in section 5.5.3, distinguishing between »linear«, »weakly non-linear«, and »highly non-linear«. The latter criterion is subdivided into two criteria. One is the relative error of the BrO/SO_2 ratio, which is defined by the 95% confidence interval of the BrO-SO_2 fitted slope. A meaningful BrO/SO_2 ratio is found, if the relative uncertainty is less than 20% (see section 5.5.1 for a detailed description). The other criterion is whether there is at least one 5-pixel cluster for which BrO VCDs exceed the detection limit of two times the standard deviation of the background BrO (see section 5.5.2 for a detailed description). The number of events of the different criteria are listed in table 6.2.
Roughly 84.6% of events have a linear BrO/SO_2 ratio. This percentage is reduced to 69.0 % and 70.4 % by introducing the error criterion and the BrO criterion respectively. 1634 Events fulfill the error criterion (see table 6.2). 1126 of these are linear, 310 weakly non-linear, while 198 are classified as highly non-linear. Interestingly, there are only relatively few (6 of 204) highly non-linear events which do not fulfill the error criterion. The most likely explanation is that highly non-linear events are almost always found for large plumes with a large number of pixels. Since the uncertainty of the slope decreases with the number of pixels (see figure 5.15) generally lower uncertainties are found in this sample. For the events with significant BrO detection (BrO criterion) this is less strong as there are only 178 of 204 highly non-linear events. In total there are 1449 events with significant BrO detection, 1020 of which are linear, 251 with a weakly non-linear correlation.

Table 6.2: Overview of the events detected by the automated plume algorithm categorized by the classification. The number of events is given both without any error criterion, with an error criterion, and for significant detection of BrO.

Classification	slope coefficient	events	rel error <20%	significant BrO
All data	[0 ... 29.73]	4232	1634	1449
... linear	[0 ... 1]	3581	1126	1020
... weakly non-linear	]1 ... 2]	447	310	251
... highly non-linear	]2 ... 29.73]	204	198	178

All events are plotted for all three classifications: linear (figure 6.2), weakly non-linear (figure 6.3), and highly non-linear (figure 6.4). Each circle represents one event on one day. The color as well as the size of the dots correspond to the value of the BrO/SO_2 ratio (note that the color scale is logarithmic, the size however scales linear). The location of the circles corresponds to the location of the maximal SO_2 VCD of the corresponding event. The map of the events with the linear BrO-SO_2 relation includes most data points, which are clustered indicating the presence of an active volcano. The major active volcanoes however, such as Mt. Etna, Ambrym/Ambae, the Kamchatka region, La Palma, Kilauea, and the northern Andes volcanoes have events in all three categories.

In the following section, different examples of all three classifications are introduced and discussed to point out the wide range of events found in the S-5P/TROPOMI data-set.

6.2 Linear BrO/SO_2 cases

In total, there are 3581 events which are classified as linear, of which 1126 (31.4 %) and 1020 (28.5 %) have a relative error of the slope below 20 % or have a 5-pixel cluster with BrO $> 2\sigma$ (see table 6.2 and section 5.5.1 for the definition of the slope error and BrO cluster criteria). For these events the linear assumption between BrO and SO_2 can be assumed and the slope is equivalent to the mean BrO/SO_2 molar ratio inside the plume. The 3581 events are plotted in figure 6.2, where each circle corresponds to one event and is located above the pixel with maximal SO_2 VCD of the event. The map displays events located at the major degassing volcanoes and volcanic regions like Etna (Italy), the Andes volcanic region (South America) and the Central American Volcanic Arc (CAVA, Central America), Indonesia, Vanuatu, Iceland, and the Nyiaragongo/Nyamuragira volcanoes (DR Congo). Most notably, there are also events detected at the hot spot volcanoes Kilauea (USA), La Palma (Spain), Piton det la fournaise (Reunion, France). There are many volcanoes for which more than one event is found. In addition, there is a significant number of events which are not located in the vicinity of the volcano, but downwind. For instance, events located over the east mediterranean sea and central asia (from 10° to 90° E and 20° to 50° N) can be traced back to Mt. Etna in Italy, with plume ages of up to two days.

It should not be omitted, that despite excluding major regions influenced by anthropogenic sources (see figure 5.2.1), there are still events, which most likely are of anthropogenic origin, i. e. the agglomeration of events located at the eastern part as well as on the south tip of India indicate sources not of volcanic origin. They are excluded in the systematic survey in section 6.4.

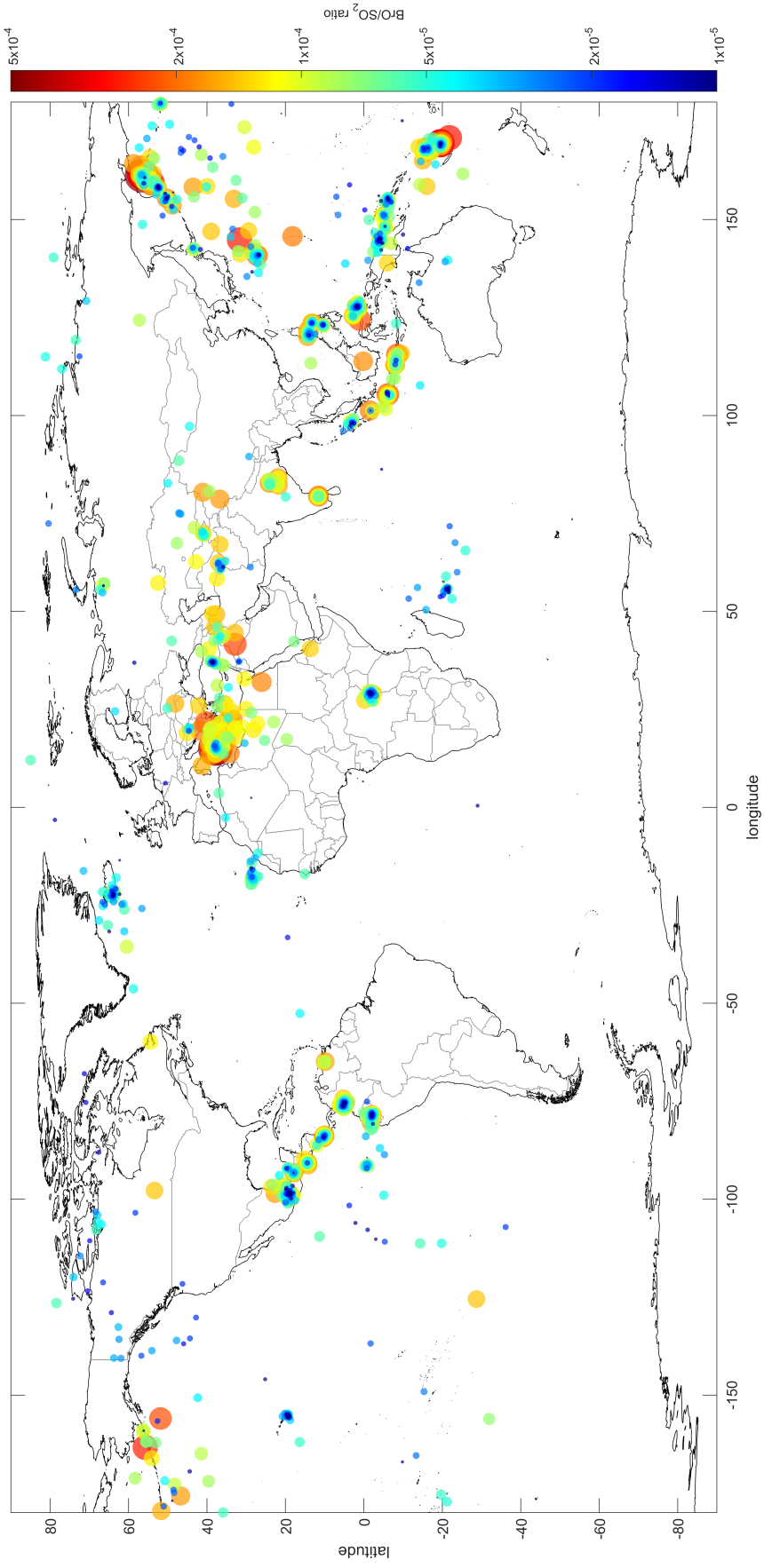


Figure 6.2: Global map of the BrO/SO_2 ratios for all events derived by the plume algorithm which have a linear BrO-SO_2 relation. Each circle represents one event on one day. The color as well as the size of the dots correspond to the value of the BrO/SO_2 ratio. The location of the circles correspond to the location of the maximal SO_2 VCD of the corresponding event.

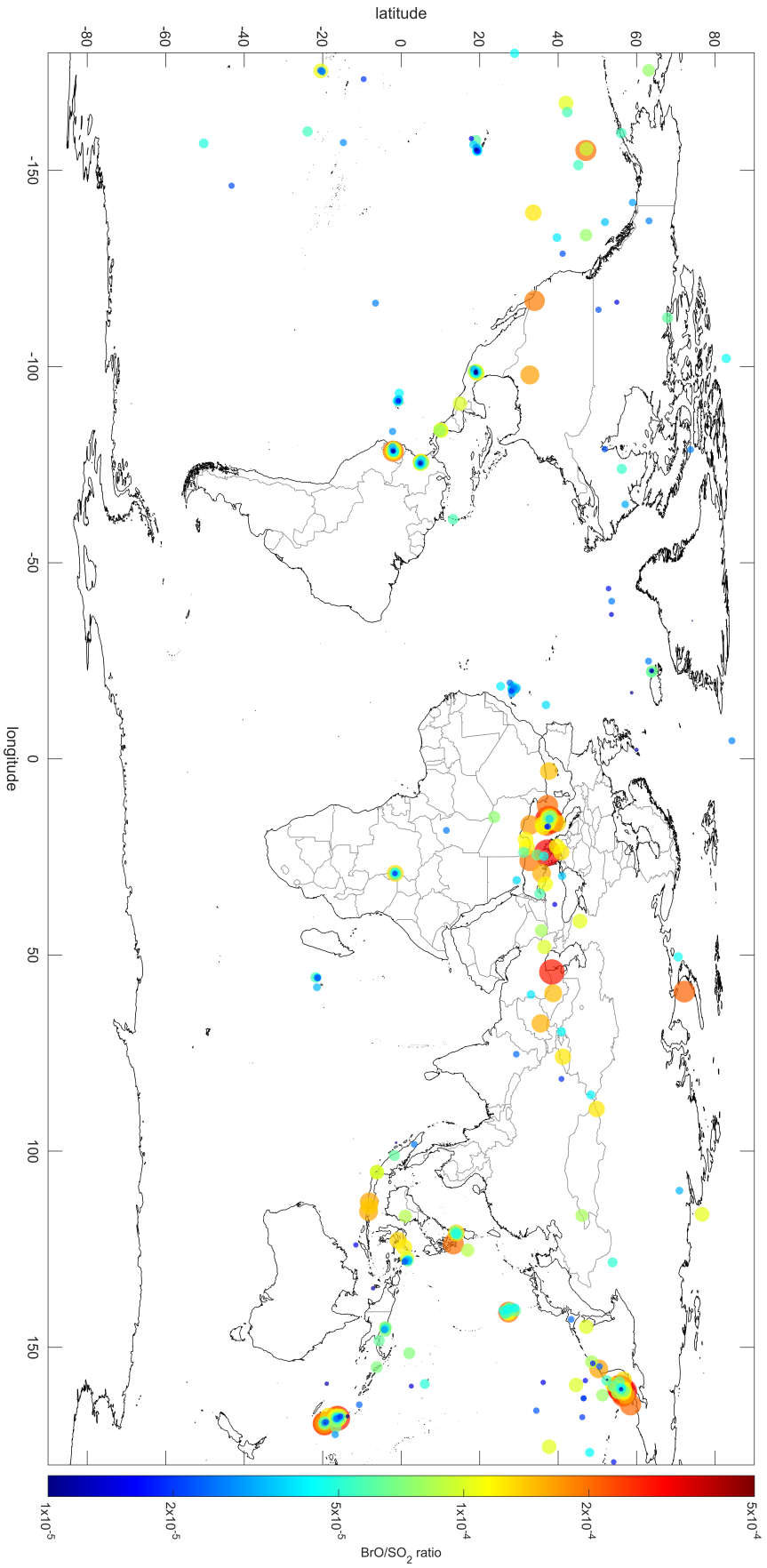


Figure 6.3: Global map of the BrO/SO_2 ratios for all events derived by the plume algorithm which have a weakly non-linear $BrO\text{-}SO_2$ relation. Each circle represents one event on one day. The color as well as the size of the dots correspond to the value of the BrO/SO_2 ratio. The location of the circles correspond to the location of the maximal SO_2 VCD of the corresponding event.

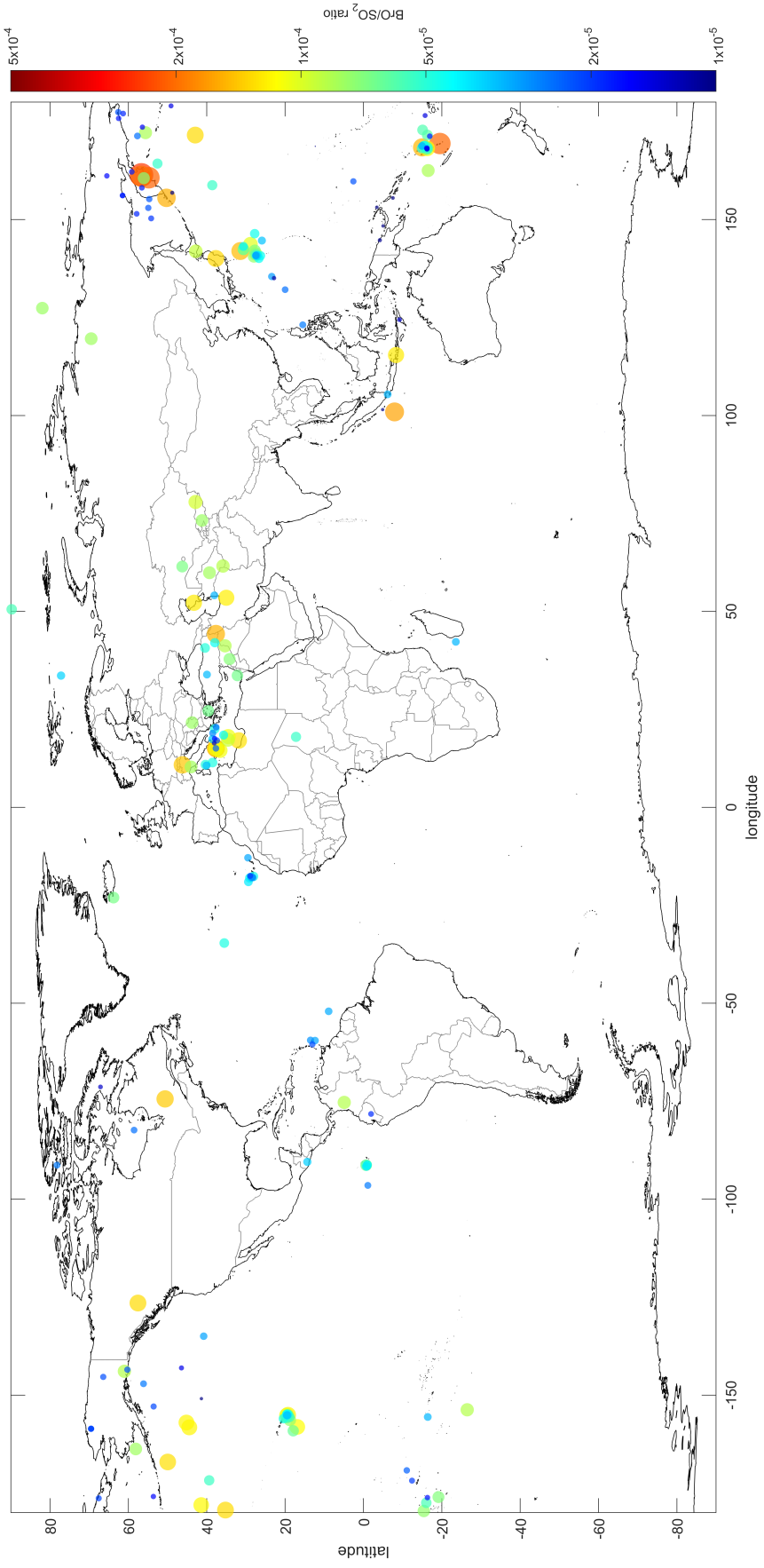


Figure 6.4: Global map of the BrO/SO_2 ratios for all events derived by the plume algorithm which have a highly non-linear BrO-SO_2 relation. Each circle represents one event on one day. The color as well as the size of the dots correspond to the value of the BrO/SO_2 ratio. The location of the circles correspond to the location of the maximal SO_2 VCD of the corresponding event.

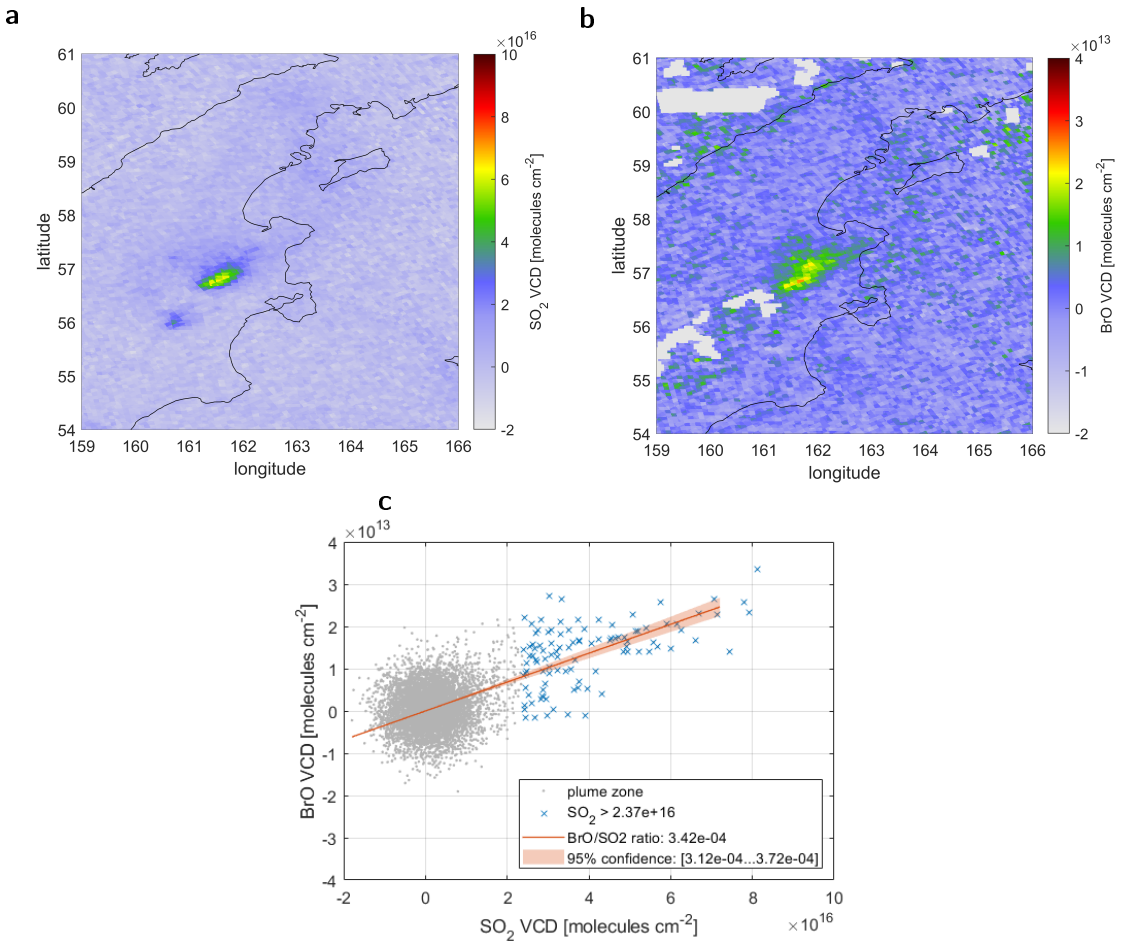


Figure 6.5: Eruption of Sheveluch, Kamchatka, Russia, on 18 April 2019. **a** the SO_2 VCD map, **b** the BrO VCD map, and **c** the BrO-SO_2 scatter plot with the linear fit. The plume pixels exceeding the $4\sigma_{SO_2} = 2.37 \times 10^{16}$ molecules cm^{-2} are marked as blue dots.

6.2.1 Minor eruptions and quiescent degassing

The high spatial resolution of TROPOMI ($3.5 \times 5.5\,km^2$) allows to spatially resolve localized plumes, ensuring sufficient statistics to calculate a BrO/SO_2 ratio for quiescent degassing (assumed to correspond to maximal SO_2 VCD $< 1 \times 10^{17}$ molecules cm^{-2}) and minor eruptions (1×10^{17} <SO_2 VCD $< 5 \times 10^{17}$ molecules cm^{-2}), whose plumes have a sufficient gas signal only in a small area in the vicinity of the volcano. There are even successful derivations of a BrO/SO_2 ratio for plumes where the maximum SO_2 VCD does not exceed 6×10^{16} molecules cm^{-2}, which is almost at the limit of detection of an event – as only SO_2-plumes with at least 5×10^{16} molecules cm^{-2} are considered by the algorithm. In total, 1063 linear events have a maximal SO_2 VCD below 1×10^{17} molecules cm^{-2}, which can be seen as quiescent degassing. 2313 linear events correspond to minor eruptions where SO_2 is between 1 and 5×10^{17} molecules cm^{-2}. Thus, 94.3 % of the 3581 linear events fall in these two activity classes. As passive degassing accounts for roughly 80 % of emitted SO_2 (Carn et al., 2017), the majority of events would be expected to be passive degassing. In the following, three quiescent degassing/minor eruptions cases from Sheveluch (Kamtchatka, Russia), Mt. Etna (Italy), and Ambrym (Vanuatu) are showcased.

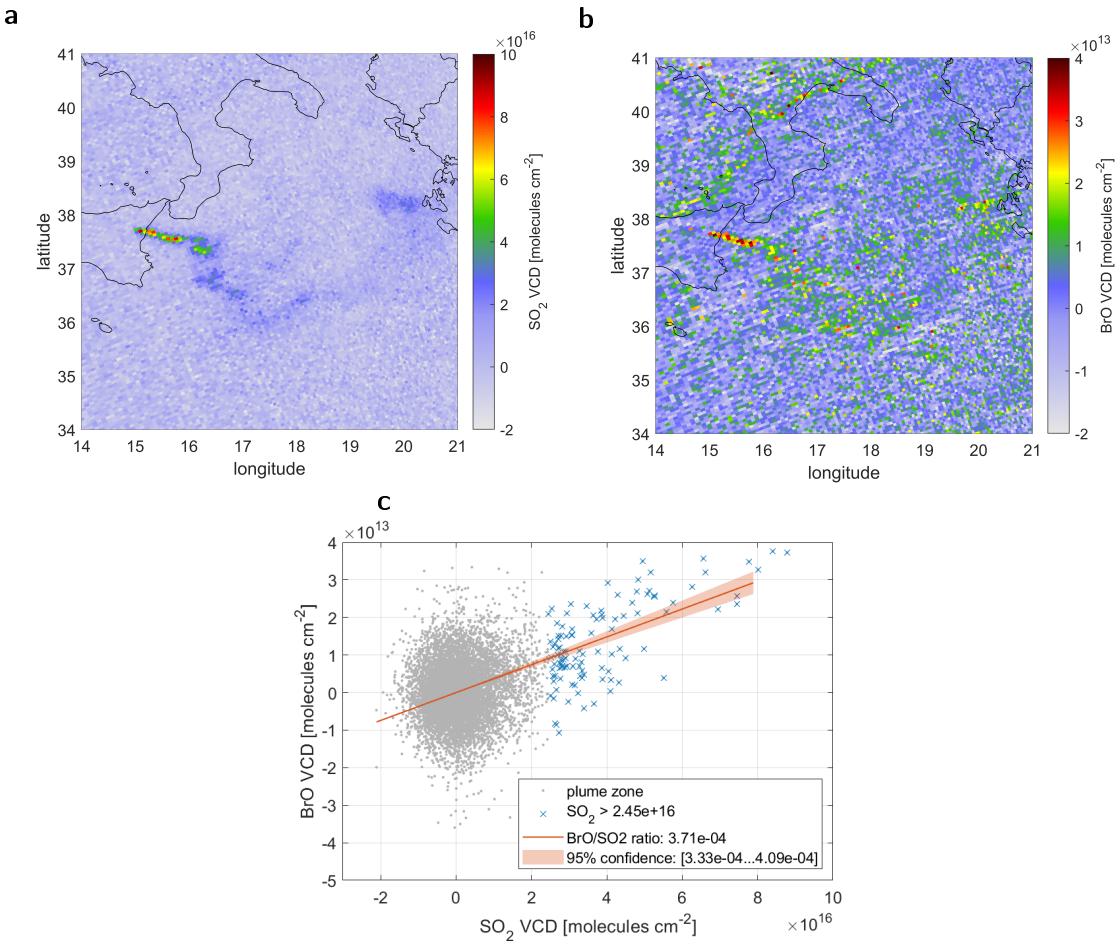


Figure 6.6: Eruption of Mt. Etna, Italy, on 23 March 2020. **a** the SO_2 VCD map, **b** the BrO VCD map, and **c** the BrO-SO_2 scatter plot with the linear fit. The plume pixels exceeding the $4\sigma_{SO_2} = 2.45 \times 10^{16}$ molecules cm^{-2} are marked as blue dots.

Eruption of Sheveluch, Kamchatka, Russia on 18 April 2019

An example of a small scale event is the plume of Sheveluch, Kamtchatka on 18 April 2019. While only low SO_2 VCDs are observed – not exceeding 8×10^{16} molecules cm^{-2} – there is still a large number of pixels (102) exceeding the 4σ-SO_2 threshold (see figure 6.5c, blue dots). In addition, a clear and significant BrO VCD of up to 3×10^{13} molecules cm^{-2} can be seen in the BrO VCD map as well as the BrO-SO_2 scatter plot (see figure 6.5b,c), leading to large BrO/SO_2 ratio of 3.42×10^{-4}. The linear relation between BrO and SO_2 is visible. Also the SO_2 VCDs below the 4σ-SO_2 threshold follow the fitted line (grey data points in figure 6.5c).

Eruption of Mt. Etna, Italy on 23 March 2020

A similar case of a minor degassing of a BrO-rich volcano is the eruption of Etna on 23 March 2020. 109 pixels exceed the 4σ-SO_2 threshold, while maximum VCDs is below 1×10^{17} molecules cm^{-2}, BrO is clearly visible inside the SO_2 plume (see figure 6.6), leading to a BrO/SO_2 ratio of 3.71×10^{-4}.

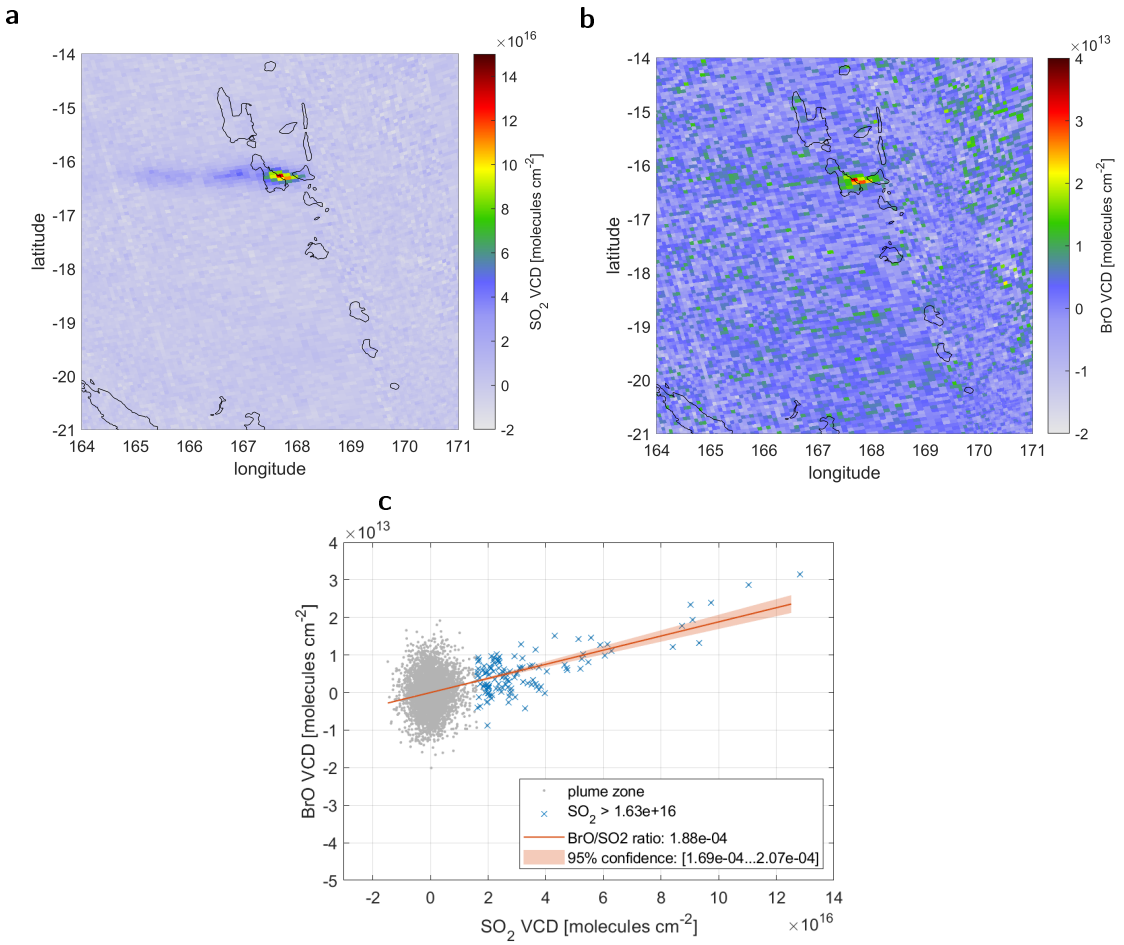


Figure 6.7: Eruption of Ambrym volcano, Vanuatu, on 30 September 2018. **a** the SO_2 VCD map, **b** the BrO VCD map, and **c** the BrO-SO_2 scatter plot with the linear fit. The plume pixels exceeding the $4\sigma_{SO_2} = 1.63 \times 10^{16}$ molecules cm^{-2} are marked as blue dots.

Eruption of Ambrym volcano, Vanuatu on 30 September 2018

Another minor eruption with a clear linear correlation is the eruption of Ambrym volcano on 30 September 2018 (see figure 6.7). While the SO_2 signal can be detected over several 100 km, maximum SO_2 columns do not exceed 1.5×10^{17} molecules cm^{-2}, which constitutes a minor eruption according to the SO_2 criteria applied in this thesis. Nevertheless, BrO VCDs exceed 3×10^{13} molecules cm^{-2} indicating that the plume is rich in BrO and the fitted BrO/SO_2 ratio is 1.9×10^{-4}.

Concluding, these three examples emphasize, that the high spatial resolution of TROPOMI can yield a BrO VCD signal clearly above detection and the BrO/SO_2 ratio even from a quiescent degassing and a minor eruption for BrO-rich volcanic plumes.

6.2.2 Medium and major eruptions

SO_2 VCDs above 5×10^{17} molecules cm^{-2} correspond to medium eruptions, and eruptions with a maximal SO_2 VCD exceeding 1×10^{18} molecules cm^{-2} can be seen as major eruptions. There are 242 medium and 145 major eruptions found in the TROPOMI data-set (see table 6.1), 147 and 58 of which have a linear BrO/SO_2 relation respectively. Major eruptions

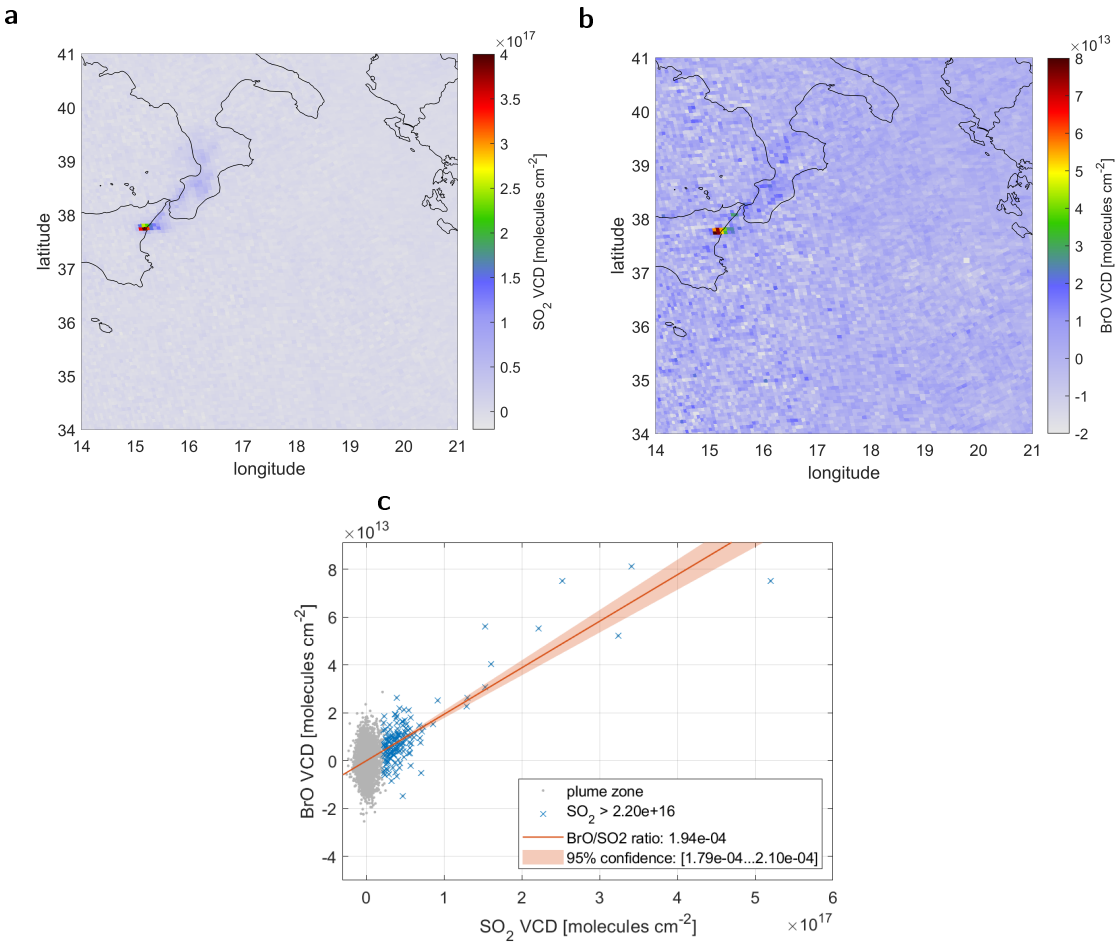


Figure 6.8: Eruption of Mount Etna, Italy, on 29 January 2019. **a** the SO_2 VCD map, **b** the BrO VCD map, and **c** the BrO-SO_2 scatter plot with the linear fit. The plume pixels exceeding the $4\sigma_{SO_2} = 2.20 \times 10^{16}$ molecules cm^{-2} are marked as blue dots.

typically lead to plumes extending over a large area stretching up to 1000 km downwind from the crater. However, if the satellite captures the plume shortly after the onset of an eruptive event, the plume can also be of small spatial extent.

Eruption of Mt. Etna, Italy on 29 January 2019

An example for a medium eruption, with a very localized volcanic plume is the Mt. Etna eruption on 29 January 2019 (see figure 6.8). This eruption is part of a phase of eruptive activity which started with weak degassing in December 2018 culminating in a major VEI-2 eruption on 24 December 2018 (Calvari et al., 2020) which resulted in a lava flow (GVP, 2019b). Activity subsided to strombolian activity throughout January and February 2019 (GVP, 2019b). The eruptive event on 29 January 2019 falls within a week of increased activity during the last week of January (GVP, 2019b). The event is a medium eruption, with maximum SO_2 VCD of 5×10^{17} molecules cm^{-2}, but with a very localized plume. SO_2 VCDs exceeding 1×10^{17} molecules cm^{-2} only occur within the first 50 km downwind from the volcano. A clear BrO signal of up to 8×10^{13} molecules cm^{-2} is also only observed in this area around the volcano. Further downwind only a very faint positive BrO signal can be seen. The BrO/SO_2 scatter plot display a clear linear correlation between BrO and SO_2.

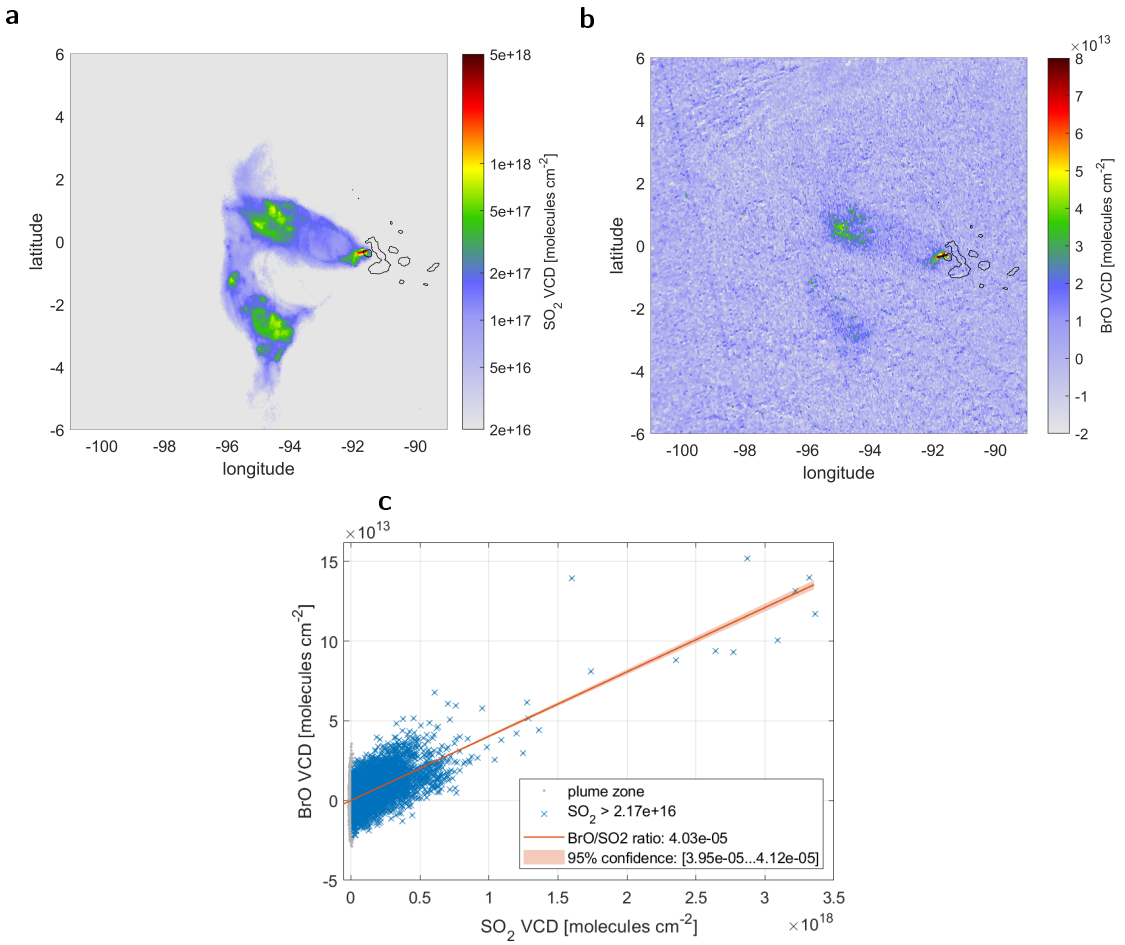


Figure 6.9: Eruption of Fernandina, Galapagos, Ecuador, on 17 June 2018. **a** the SO_2 VCD map (logarithmic color scale), the **b** BrO VCD map, and **c** the BrO-SO_2 scatter plot with the linear fit. The plume pixels exceeding the $4\sigma_{SO_2} = 1.75 \times 10^{16}$ molecules cm^{-2} are marked as blue dots.

The fitted line retrieves a BrO/SO_2 ratio of 1.85×10^{-4}.

Eruption of Fernandina volcano, Galapagos, Ecuador on 17 June 2018

Fernandina volcano experienced a strong and short eruptive episode from 16 to 18 June 2018 (see figure 6.9), started by seismic tremors and strong SO_2 degassing (GVP, 2018c). TROPOMI observed a plume spread over 500 to 1000 km off Fernandina island, Galapagos on 17 June 2018, containing the accumulated emissions during the afternoon of 16 June and morning of 17 June. Maximal SO_2 VCDs at the volcanic vent exceed $3{\times}10^{18}$ molecules cm^{-2}. Significant BrO VCDs can be observed throughout the whole plume with a maximal value of 1.5×10^{14} molecules cm^{-2} reached at the volcano. A linear BrO/SO_2 relation is found, and the slope yields a ratio of 4.01×10^{-5}.

Eruption of Ambrym, Vanuatu on 15 & 16 December 2018

The event of the Ambrym plume on 16 December 2018 is the result of a major flank eruption starting on 15 December 6:00 h local time (GVP, 2019a). The flank fissure leads to lava fountains throughout 16 December until 17 December. Ash and gas emissions are reported

with plume elevation estimated at 8 km (GVP, 2019a). In the process of the eruption, the lava lake persisting throughout 2018 was drained (Hamling et al., 2019). Furthermore, the eruption was the end of a one-year eruptive period which started on 7 December 2017 (GVP, 2019a). There is an event with linear BrO/SO_2 ratio detected for both 15 and 16 December 2018. SO_2 VCD, BrO VCD and the BrO-SO_2 scatter plot for both days are plotted in figure 6.10.
On 15 December there is a distinct SO_2 plume with columns reaching $1.5{\times}10^{18}$ molecules cm^{-2} extending several 100 km and 758 pixels exceeding the 4σ-SO_2 threshold. As the eruption started at 6:00 h local time (GVP, 2019a), the eruption was already ongoing for almost 8 hours at the satellite overpass time at 13:48 h local time. A strong BrO plume can be seen close to the volcano with a maximal BrO VCD of 1.2×10^{14} molecules cm^{-2}. The calculated BrO/SO_2 ratio is 5.64×10^{-5}.
On 16 December the plume extended already over more than 1000 km, but maximum SO_2 VCDs were still located at the volcano. This is in line with the report of continuous degassing on both days and suggests that the plume visible on 16 December consists of gas emitted during both days (i e. parts of the plume may be older than one day). Maximum SO_2 VCDs are four times larger than the VCDs on 15 December, reaching 6×10^{18} molecules cm^{-2}. There is a strong BrO plume visible reaching 1.2×10^{14} molecules cm^{-2}. Downwind there is a faint BrO plume with BrO VCDs between $2 - 3 \times 10^{13}$ molecules cm^{-2} visible even at 1 000 km distance. The BrO/SO_2 ratio is determined at 3.00×10^{-5}, which is significantly lower compared to the previous day. The higher SO_2 VCDs might suggest an increasing eruptive strength which in turn could have affected the gas release.

6.3 Non-linear BrO-SO_2 relation

A non-linear relation between BrO and SO_2 inside a volcanic plume can have two origins: the plume can (1) is comprised of a mixture of parts which have a different degassing source composition or (2) have a gradient in BrO/SO_2 ratio due to different chemical states of parts of the plume. There are two mechanism, which can produce a plume with mixed degassing source composition. First, different parts of the plume seen by the satellite instrument can correspond to different ejection times, i. e. different parts of large extended plumes can be emitted over more than one day (compare figure 6.2.2). If the emitted bromine/sulphur ratio changes over the course of this ongoing eruption, the different plume parts will have a different composition, and hence a diverging – i. e. non-linear – BrO to SO_2 relation. Secondly, a mixture of different bromine/sulphur sources can also occur if the plumes of neighbouring volcanoes with different bromine/sulphur emission ratios mix or are identified as one event (see also section 5.2.3). This is seen often for the Vanuatu volcanoes Ambrym and Ambae, who are roughly 100 km apart, some of the Kamchatka volcanoes, some of the Latin American volcanoes, and also Nyiragongo and Nyamuragira. In principle, the Aeolian volcanoes Etna, Vulcano & Stromboli, can also be mixed into one event, however, the degassing plume of Vulcano is always below the SO_2 detection limit and even the eruption of Stromboli with significant SO_2 emissions on 3 July 2019 was not detected by TROPOMI and did not coincide with an event from Mt. Etna. In general, the mixing of different plume signatures can also occur, when bromine and sulphur diverge spatially even if they are ejected at the same time. This could occur if bromine and sulphur are released in different heights with diverging wind patterns. Such a case was documented for instance by Hörmann et al. (2013) for the Sarychev eruption (15/16 June 2009), where BrO and SO_2 diverged spatially were suspected at different heights. Another incidence of diverging BrO and SO_2 patterns was reported in the wake of the Tonga eruption in January 2022, where

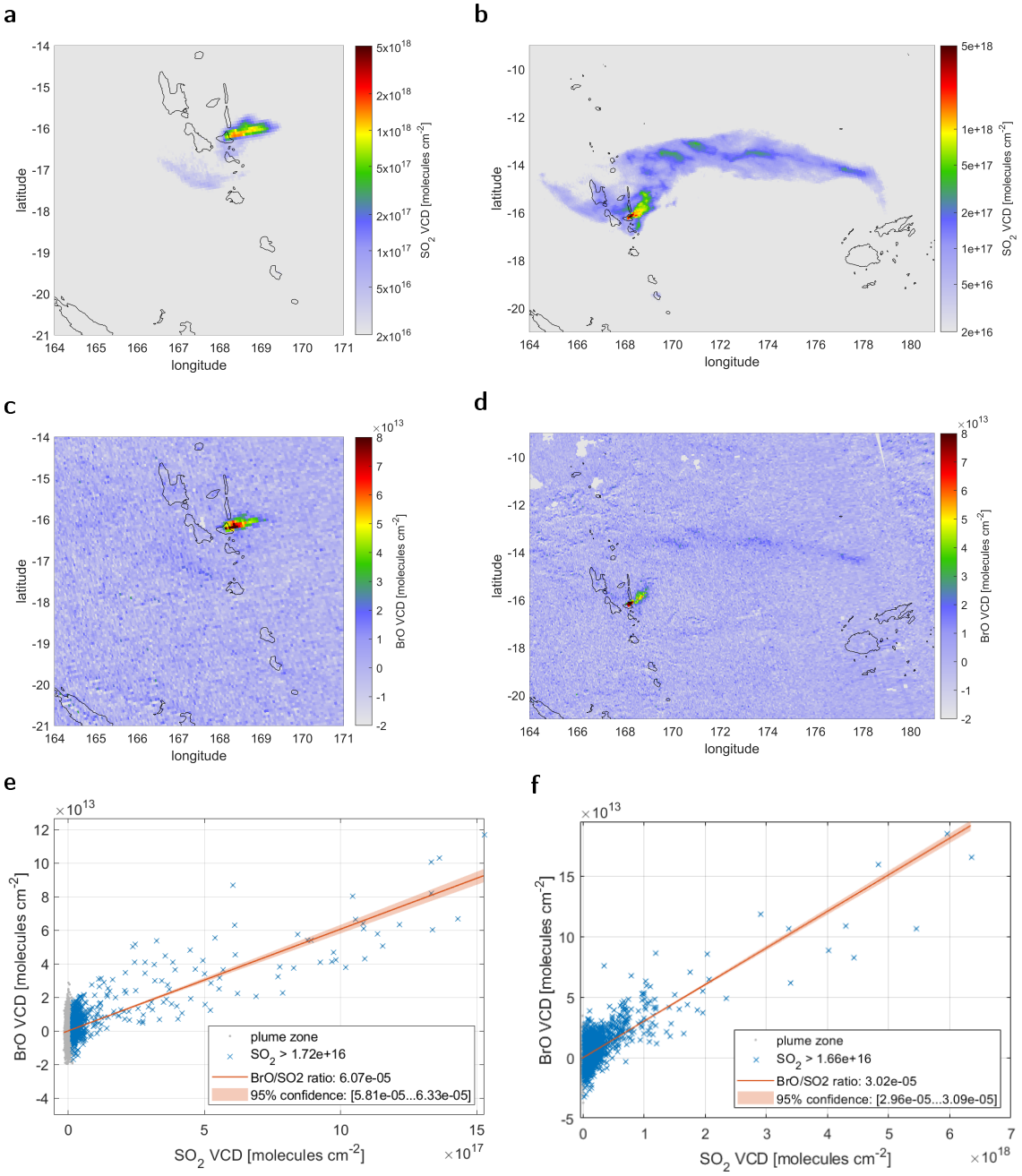


Figure 6.10: Eruption of Ambrym, Vanuatu, on 15 December 2018 (left column) and 16 December 2018 (right column). **a/b** the SO_2 VCD maps (logarithmic scale), **c/d** the BrO VCD maps, and **e/f** the BrO-SO_2 scatter plots with the linear fit respectively. The plume pixels exceeding the $4\sigma_{SO_2} = 1.72 \times 10^{16}$ and 1.66×10^{16} molecules cm^{-2} respectively are marked as blue dots.

preliminary measurements suggest a divergent tropospheric plume of BrO in addition to the main stratospheric plume of SO_2 and BrO (personal communication Andreas Richter, IUP Bremen).
A chemically induced gradient in the BrO/SO_2 ratio can occur, if the formation of BrO is enhanced/inhibited chemically. As BrO is a secondary species, diverging efficacy of its chemical formation in different plume parts can also result in a non-linear BrO/SO_2 relation. The need for an influx of ambient O_3 can especially lead to inhibition of BrO formation in parts of the plume with high density in volcanic gas compared parts with lower gas density. In the following two examples of gradients which are potentially caused by different bromine chemistry are showcased: The plume of Mt. Etna on 25 December 2018 and the plume of Raikoke, Kuril islands (Russia) on 22 June 2019. A detailed discussion of limited BrO formation in the Mt. Etna plume and an empirical model, which aims to reproduce the observed gradients in the BrO/SO_2 ratio is conducted in chapter 7.

6.3.1 Plume of Mt. Etna, Italy on 25 December 2018

One example of a large plume, where different parts correspond to different BrO-formation efficiencies is the plume of Mount Etna on 25 December 2018. The major eruption started on 24 December, where also an event is detected, and continued throughout the night and day of 25 December (GVP, 2019b), which results in a widespread plume visible at S-5P/TROPOMI's overpass. SO_2 VCDs reach up to 1.5×10^{18} molecules cm^{-2} and BrO VCDs 1×10^{14} molecules cm^{-2} (see figure 6.11a,b). The BrO/SO_2 linear fit suggests a BrO/SO_2 ratio of 1.15×10^{-4}. However, looking at the BrO-SO_2 scatter plot (figure 6.11**d**), it is clearly visible that BrO and SO_2 do not have a linear relation for the complete plume. There are two parts, which can be separated based on the SO_2 VCDs. The first part is made up of of the pixels with SO_2 VCDs below 4×10^{17} molecules cm^{-2}. Here, the pixels are significantly above the fitted line. This corresponds to a larger BrO/SO_2 ratio. The deviation from the fitted line is strongest for SO_2 VCDs up to 2×10^{17} molecules cm^{-2} and then gradually decreases. For SO_2 VCDs larger than 4×10^{17} molecules cm^{-2} the values are almost all below the fitted line, and thus have an individual BrO/SO_2 ratio below 1×10^{-4}. This effect becomes more dominant for SO_2 VCDs larger than 6×10^{17} molecules cm^{-2}, where there are no pixels above the fitted line.
The map of individual BrO/SO_2 ratios (figure 6.11c) reveals that the lower BrO/SO_2 ratios are located in the center of the plume, where SO_2 VCDs are highest. A large SO_2 VCD is equivalant to a dense plume, i. e. a high concentration of volcanic gas.
In order to separate the center – where SO_2 VCDs are high – and outer plume pixels, an orthogonal regression is done separately for the data of SO_2 below 2.5 (see figure 6.11e red points and line) and above 5×10^{17} molecules cm^{-2} (see figure 6.11e blue points and line). The fitted lines match the corresponding points well, revealing that the lower SO_2 VCD data-set is represented well by a BrO/SO_2 ratio of 2.17×10^{-4}, while the higher SO_2 VCD data-set is represented by a ratio of 8.51×10^{-5}.
Since the decrease of the BrO/SO_2 ratio towards the center of the plume is clearly seen throughout the complete main plume part west of 20° E independent of the distance from the crater (figure 6.11c), the gradient in the BrO/SO_2 ratios cannot be caused by a change in degassing composition. Hence, the volcanic source gas composition can be assumed similar for the complete plume and the different BrO/SO_2 ratio is caused by limited BrO formation in the center regions compared to the edge regions of the plume. The most simple explanation is that influx of ambient O_3 is not large enough to sustain the BrO formation in the very core, i. e. O_3 is used up more rapidly in the BrO formation process as is mixed in

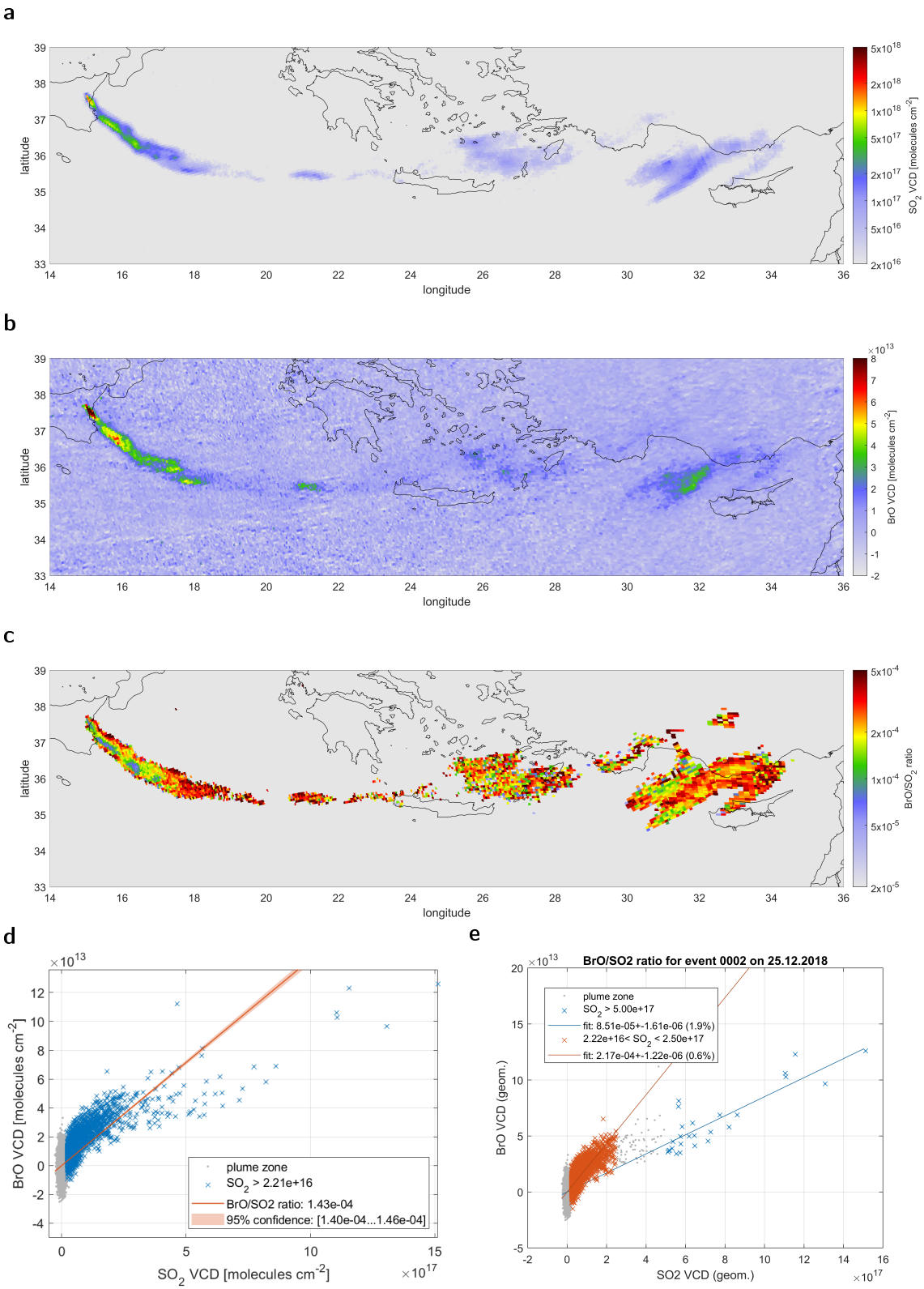


Figure 6.11: Eruption of Mount Etna, Italy, on 25 December 2018. **a** SO_2 VCD map (logarithmic scale), **b** BrO VCD map, and **c** map of the BrO/SO_2 ratio calculated for each pixel (logarithmic scale). **d** BrO-SO_2 scatter plots with the linear fit for all data and **e** with two seperate fits for SO_2 VCDs $< 2.5 \times 10^{17}$ molecules cm^{-2} (red) and SO_2 VCDs $> 5 \times 10^{17}$ molecules cm^{-2} (blue).

from the outside and the core is void of O_3. This does not mean that there are pixels with no zero BrO VCDs, since the BrO VCD in one pixel is the vertically integrated column, i. e. the integration of the vertical »plume edges« and the center part of the plume.
This decrease in BrO concentration in the center is tried to model conceptually and empirically in chapter 7, where a detailed discussion of the plume chemistry at play is also given.

6.3.2 Eruption of Raikoke volcano, Kuril islands, Russia on 22 June 2019

Raikoke volcano erupted on the morning of 22 June 2019 with massive amounts of gas reaching the stratosphere (plume heights were reported reaching 10 - 20 km altitude: Hedelt et al., 2019; GVP, 2019g). Observed SO_2 VCDs exceed 2×10^{19} molecules cm^{-2}, comparable only to VCDs observed in the plume of La Palma Cumbra Vieja eruption in September 2021 and the Kasatotchi volcanic plume in 2008 (Hörmann et al., 2013). BrO VCDs reach up to 4×10^{14} molecules cm^{-2}.
The SO_2 VCD map (figure 6.12a) as well as the BrO VCD map (figure 6.12b) reveals a very dense plume with SO_2 VCDs larger than 1×10^{19} molecules cm^{-2} and BrO VCDs exceeding 1×10^{14} molecules cm^{-2} stretching over the first 500 km east. a strong plume with SO_2 VCDs larger than 5×10^{17} molecules cm^{-2} and BrO VCDs larger than 2×10^{13} molecules cm^{-2} are still detected more than 2000 km east of the volcano.
The BrO/SO_2 scatter plot (see figure 6.12d), displays a branched distributions. Three branches can be identified. There are two main branches, comprising of the data with SO_2 larger than 5×10^{18} molecules cm^{-2}. These branches are hence inside the main part of the plume and named »upper main branch«(the one with larger BrO VCD) and »lower main branch«(the one with lower BrO VCD). The third branch consists of very low SO_2 VCDs, but high BrO VCDs. It is not inside the main SO_2 plume and therefore named »side branch«. The three branches are separated in figure 6.13 and color-coded in the BrO-SO_2 scatter plot (figure 6.13i). The pixels belonging to each branch are plotted in separate SO_2 and BrO maps (figure 6.13c-h). It can be seen that the two main branches are clearly separated: The lower main branch is made up of pixels stretching from the volcano until 156° E, whereas the upper main branch is composed of older plume parts from 156 to 158° E. Therefore, the lower main branch is located closer to the volcano and thus its plume age is lower. Thus, the upper main branch contains the initial gas from the onset of the explosion, while the lower main branch is made up of of the continuous degassing after the initial explosion.
The main upper, older branch is following a clear linear trend in the BrO-SO_2 scatter plot with BrO/SO_2 ratios around 2×10^{-5}. The lower main branch on the other hand includes lower BrO VCDs reaching only 2×10^{14} molecules cm^{-2} and subsequently a ratio below 1×10^{-5}.
There are two possible explanations for the different BrO/SO_2 signatures of the older and younger branch. First, the Br/S emissions of the initial blast and the subsequent degassing could differ. Bromine could partition more easily and be over-represented in the initial eruption compared to the later degassing.
A second explanation could be, that the formation of BrO in the older branch is more effective compared to the younger one. The BrO formation in large plumes is limited mainly by the intake of O_3 from the ambient air, i. e. BrO forms at the edges of the plume first and only later in the center of the plume. The time it takes for the BrO to be formed in the entire plume cross section depends on the gas concentration (which is related to the SO_2 column) as well as the plume diameter (which is in first order also related to the SO_2 flux, i. e. the SO_2 column) as well as the transport time (which is correlated to the distance

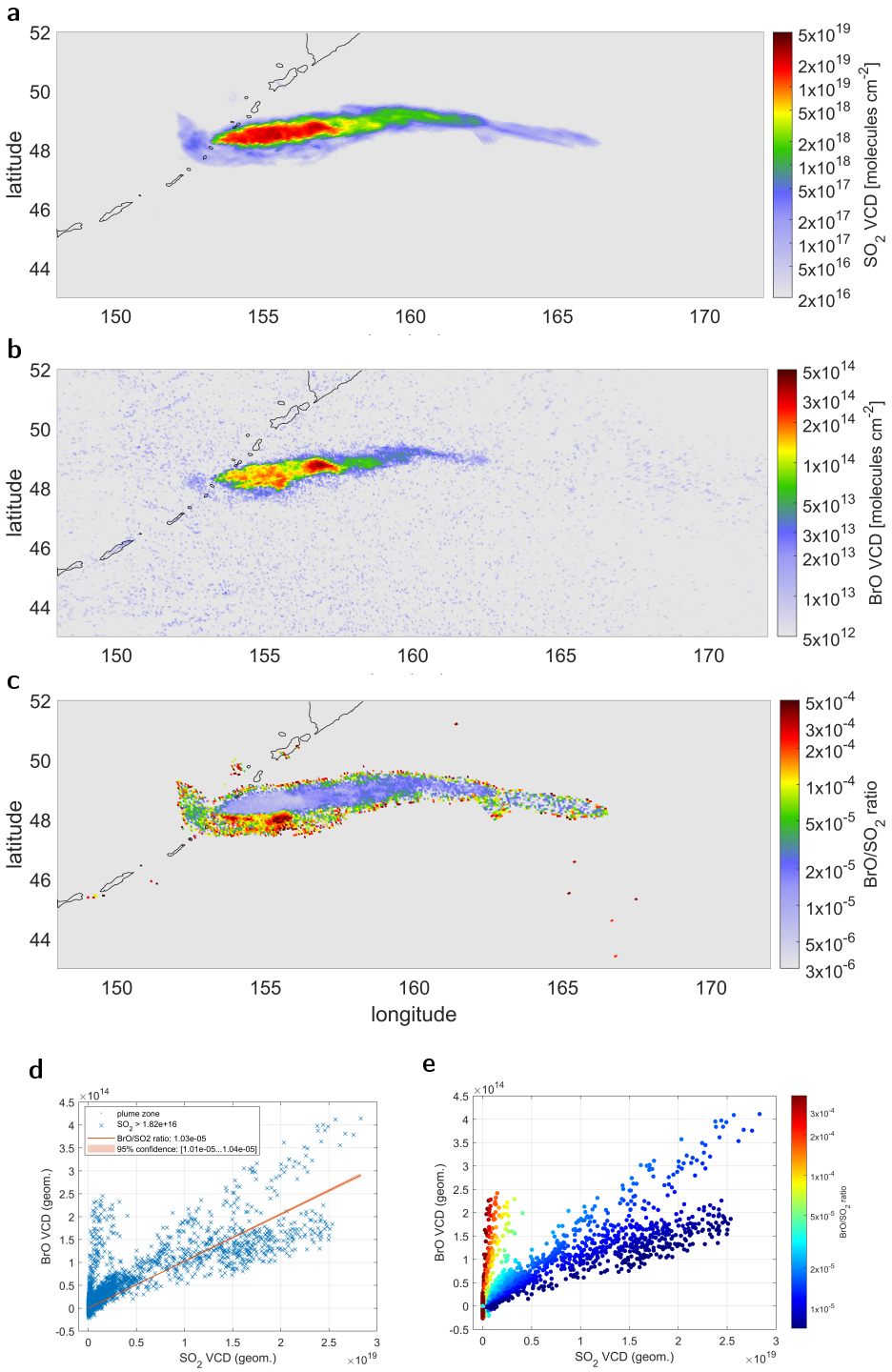


Figure 6.12: Eruption of Raikoke volcano, Kuril islands, Russia, on 22 June 2019. **a** SO_2 VCD map, **b** BrO VCD map, and **c** map of the BrO/SO_2 ratio calculated for each pixel exceeding the $4\sigma_{SO_2}$-threshold. **d** The BrO-SO_2 scatter plot with the linear fit for all data as well as **e** color scaled by the singular BrO/SO_2 ratio.

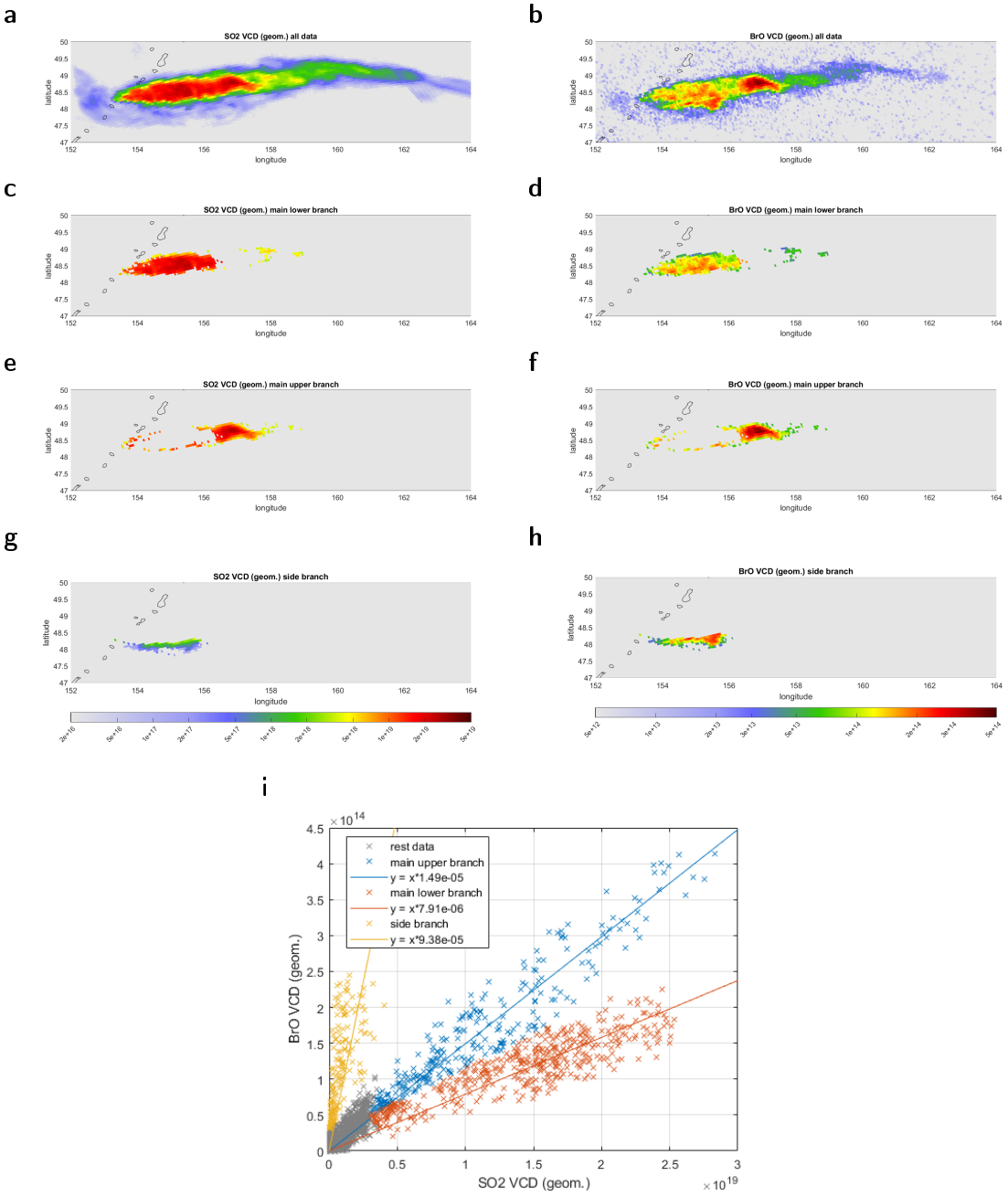


Figure 6.13: Plume of Raikoke volcano, Kuril islands, Russia, on 22 June 2019, separated into different branches. Left column: SO_2 VCD of **a** the complete plume, **c** the upper main branch, **e** the lower main branch and **g** the side branch. Right column **b,d,f,h**: BrO VCD for the respective branches. **i**: BrO-SO_2 scatter plot. The branches and the corresponding fitted BrO/SO_2 ratios for the branches are color coded.

from the volcano). Hence, BrO formation is expected in first order to be lower for high SO_2 columns and for smaller distances from the volcano. This relation can be seen for the young branch. The BrO response decreases with larger SO_2 VCDs. For lower SO_2 the data converge with the fitted line towards the older branch (blue dots in figure 6.13i).

The older branch however, does not exhibit this non-linear relation of BrO and SO_2. The fitted line represents the complete distribution of this branch well (blue dots and line in

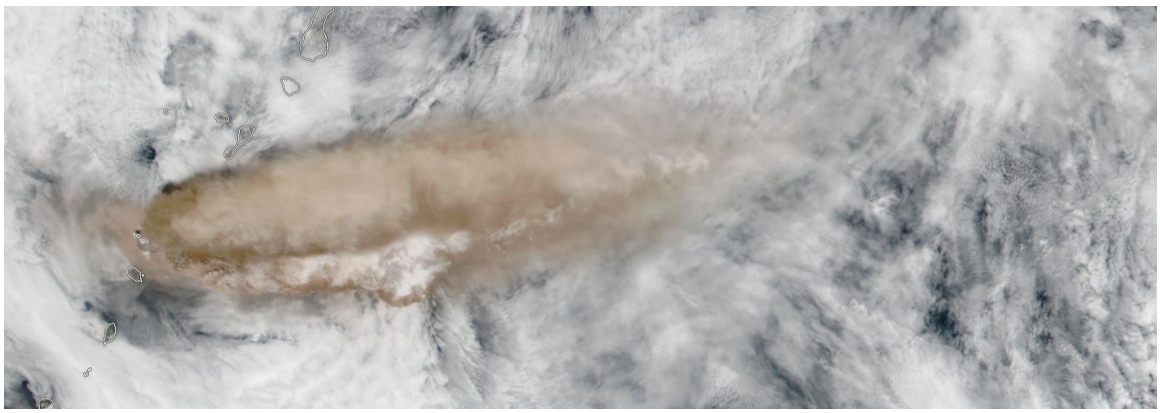


Figure 6.14: RGB image of the Raikoke plume recorded by VIIRS onboard Soumi-NPP satellite on 22 June 2019, observing the scene 5 minutes prior to the S-5P/TROPOMI overpass, taken from `zoom.earth/#view=48.48,156.3348,8z/date=2019-06-22,pm/layers=daily`.

figure 6.13i). Furthermore, the fitted line also matches the data not assigned to either branch (grey data-points in figure 6.13i). This data at low SO_2 is probably much less limited by O_3 intake and is thus more representative for the BrO/SO_2 ratio unaffected by chemical inhibition.
This indicates that the lower young branch is limited in BrO formation compared to the older branch and there is not yet enough ozone mixed into the plume compared to the older part.
As the eruption of Raikoke occurred around 18:00 h UTC on 21 June 2019 (Rashidov et al., 2019), the satellite captured the plume 8 h afterwards (satellite overpass was at 2:21 h UTC on 22 June 2019). This means that the young lower main branch is younger than 8 h.
The third branch does not fit into this scheme, as its BrO/SO_2 ratio differs largely from the other branches and it is also a young plume part. It is completely located south of the young branch on the south flank of the volcanic plume. It comprises only of relatively low SO_2 VCDs below 2×10^{18} molecules cm^{-2}, but very high BrO VCDs of up to 2×10^{18} molecules cm^{-2}. This means, that the BrO plume extends south beyond the SO_2 plume. Looking at the BrO/SO_2 ratio for each individual pixel (see figure 6.12e), it can be seen that these correspond to BrO/SO_2 ratios of $8 - 30 \times 10^{-5}$, thus one order of magnitude larger than the BrO/SO_2 ratio of the other branches.
In the visual picture of the scene (see figure 6.14), the southern edge is also distinguishable from the main plume. The main plume branches are a brown ash plume, while the side branch (southern edge) is white at the top with a brown edge. This might suggest that the southern edge corresponds to a lower altitude. If that would be the case, the higher BrO/SO_2 ratio could indicate the bromine was predominantly released at a different altitude compared to SO_2. However, until validation from trajectories are performed, this remains speculation.

6.4 BrO/SO_2 ratio catalogue

In this section, the events and their calculated BrO/SO_2 ratios are assigned to volcanoes and a catalogue of a mean BrO/SO_2 ratio is created for the volcanoes, where at least one BrO/SO_2 ratio is detected.
For the events, where the BrO/SO_2 relations are classified as linear, the slope of the BrO-

SO_2 scatter plot represents the mean BrO/SO_2 ratio of the plume. Furthermore, for these cases, BrO formation can be assumed to be not significantly affected by chemistry, i. e. the BrO/SO_2 ratio can be assumed representative for the bromine/sulphur content emitted from the volcano. Thus, they can be seen as a measurement of the BrO/SO_2 of the volcano on the respective day.

Since the maximum SO_2 VCD is typically located close to the emission source, the global map of the linear events (figure 6.15) already reveals the locations of the most active volcanoes/volcanic regions (i. e. Etna on Sicily, Kilauea, Hawaii, the Kamchatka region, Russia, Indonesia, and Vanuatu in Oceania).

A zoom into several regions is depicted in figure 6.16. It can be seen that the events are clustered around the volcanoes. e. g. for the Andes (figure 6.16a) the corresponding volcanoes can be identified easily by the location of clusters of events. From North to south they are: Popocatepetl (Mexico), Fuego (Guatemala), Poas (Costa Rica), Nevado del Ruiz (Colombia), Sangay (Ecuador) and Galapagos Island (Ecuador). On Galapagos island the events can be separated onto two islands, corresponding to Fernandina volcano (small island north west of the main island) and Sierra Negra volcano (on the south west tip of the main island). This already indicates that volcanoes close to each other can be distinguished based on the location of the maximal SO_2 VCD. Neighbouring volcanoes can also be separated for the Vanuatu region (figure 6.16c), where three clusters of events are found: Ambae (small cluster in the north), Ambrym (large cluster in the center of the map) and Yasur (small island in the south). However, while the clusters for Ambae and Ambrym are centered at different locations, there is significant overlap. The map of Kamchatka shows also several locations of volcanoes (figure 6.16b). A multitude of volcanoes can be identified in South East Asia (figure 6.16d).

The data-set of events with a linear BrO/SO_2 relation is systematically scanned and assigned to volcanoes. In a first step, a list of volcanoes and their location is created based on the global map of the events with linear BrO/SO_2 relationships (figure 6.15) and the information on active volcanoes during the measurement period. The plume origin is derived from the individual SO_2 VCD maps of the events and the activity reports from the website of the Global volcanism Program (Global Volcanism Program, `https://volcano.si.edu/`).

In total 43 volcanoes were identified, for which at least one event was found. The names along with their locations are listed in table 6.3. For one cluster of events located in southern Kamchatka, Russia (at 159° E, 54° N, see figure 6.16b), no volcano could be identified. There are multiple volcanoes located in the area, but no clear report of activity for any of them. Since this is a remote location, which is not monitored by a local observatory, and additionally these events are of minor SO_2 content only, it is not necessarily surprising that there are no reports available. In the list, this location is called »South Kamchatka«. The most likely candidates are Mutnowsky volcano or Gorely volcano, which have been reported to be active over the last decade.

In a second step the events in the vicinity of the volcanoes are assigned to the volcano. For this assignment, the distance of each event to each volcano is calculated and each event is assigned to the volcano closest to the location of its maximal SO_2 VCD. However, an assignment is done only if the distance to the volcano is less than 300 km. If the activity of a volcano can be limited to a specific period of time, only events during this time are assigned to this volcano to prevent assignment of long-distance transported plumes from neighbouring volcanoes, e. g. Yasur volcano in Vanuatu is not active in 2018. However, the neighbouring volcanoes Ambrym and Ambae were active in this period and there is one occasion in 2018 where a plume originating from Ambrym drifted directly over Yasur volcano during TROPOMI overpass and would otherwise have been falsely associated with

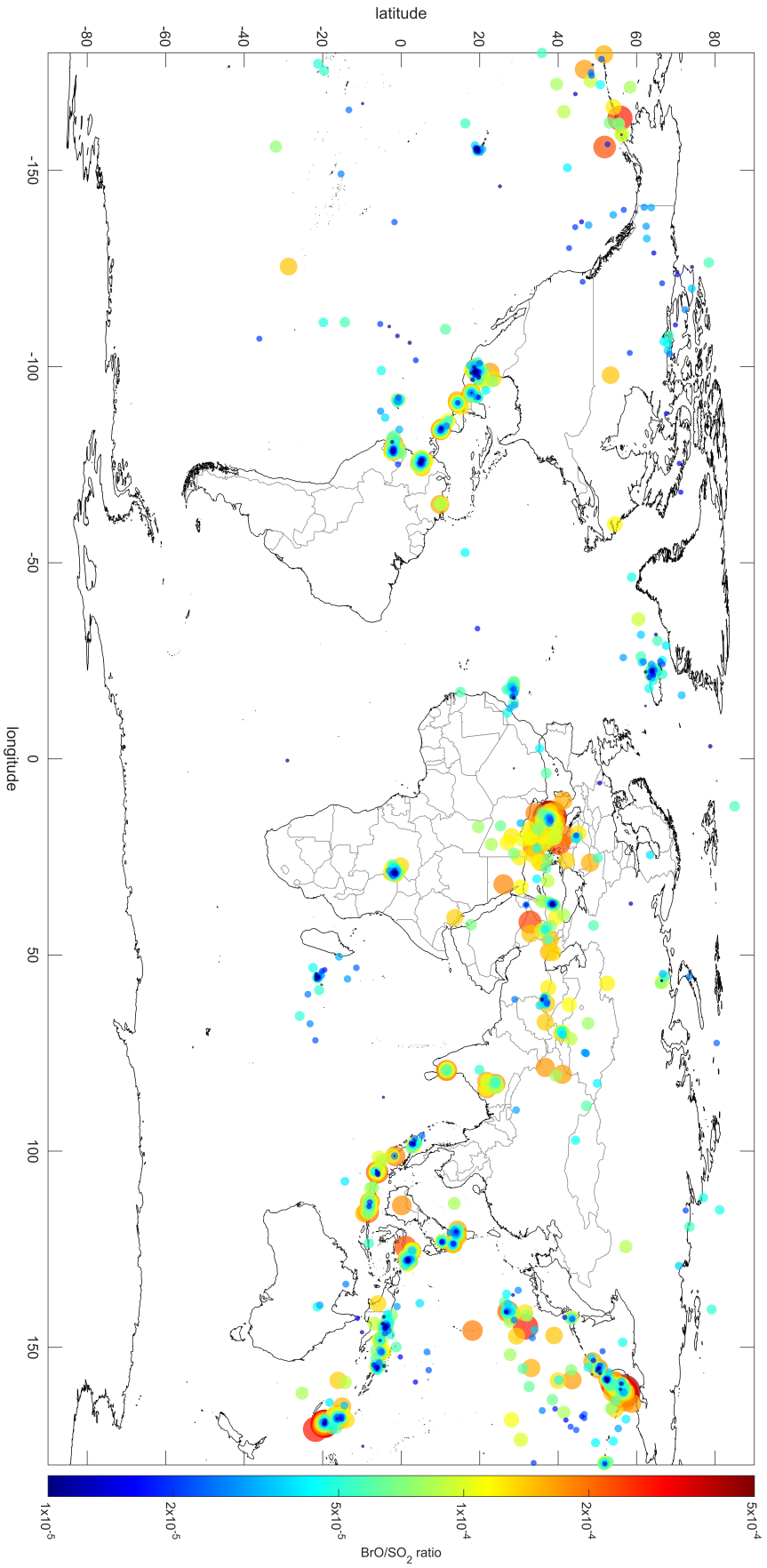


Figure 6.15: Global map of the BrO/SO_2 ratio for all events derived by the plume algorithm which have a linear BrO-SO_2 relation. Each circle represents one event on one day. The color as well as the size of the dots correspond to the value of the BrO/SO_2 ratio. The location of the circles correspond to the location of the maximal SO_2 VCD of the corresponding event.

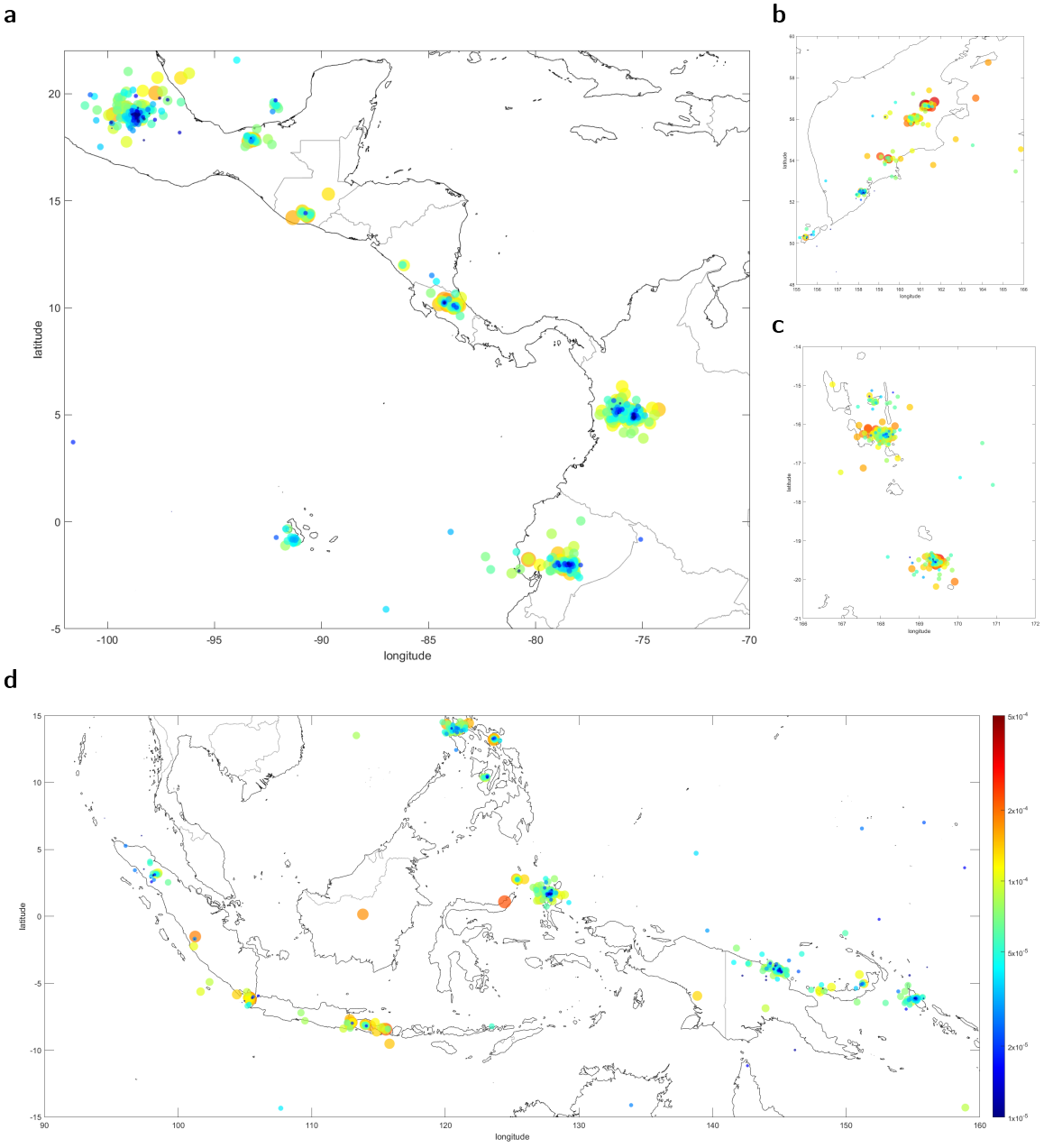


Figure 6.16: Map of events with linear BrO/SO_2 ratios for major volcanic regions:**a** Middle- and South America, **b** Kamchatka penninsula, Russia, **c** Vanuatu, Oceania, and **d** South east Asia.

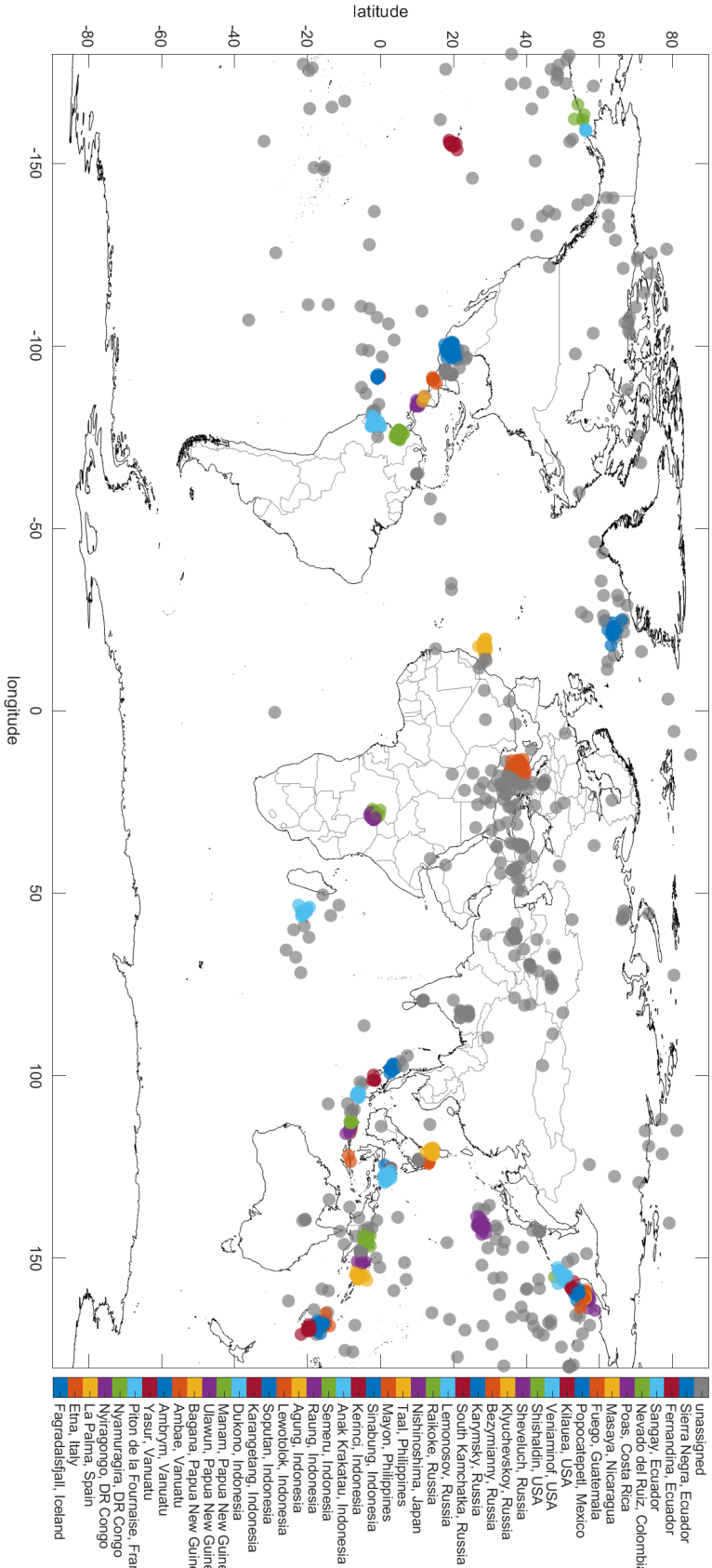


Figure 6.17: Map of the assignment to volcanoes within the BrO/SO_2 ratio catalogue. Events within 300 km of a volcano are assigned to a volcano and colored respectively. The colors are recurring in order to yield a high contrast between neighbouring volcanoes. Events further away from the volcano are marked as grey.

Table 6.3: List of the 43 volcanoes of the BrO/SO_2 catalogue. Name, country, location, as well as the number of events within 300 km distance are listed. Additionally the number of events who have a rel. BrO/SO_2 error below 20 % or who have a clear detection of BrO are given.

Volcano	Country	Latitude	Longitude	No. of all events	No. of events with error filter	No. of events with BrO filter
Fagradalsfjall	Iceland	22.27° W	63.91° N	59	25	24
Etna	Italy	15.00° E	37.75° N	231	143	137
La Palma	Spain	17.84° W	28.57° N	48	41	34
Nyiragongo	DR Congo	29.25° E	1.52° S	168	4	8
Nyamuragira	DR Congo	29.20° E	1.41° S	49	6	8
Piton de la Fournaise	France	55.72° E	21.23° S	48	12	6
Yasur	Vanuatu	169.45° E	19.53° S	133	34	62
Ambrym	Vanuatu	168.12° E	16.25° S	152	124	119
Ambae	Vanuatu	167.83° E	15.39° S	24	21	18
Bagana	PNG†	155.19° E	6.14° S	52	2	4
Ulawun	PNG†	151.33° E	5.05° S	9	4	3
Manam	PNG†	145.03° E	4.08° S	114	30	21
Dukono	Indonesia	127.88° E	1.70° N	199	1	18
Karangetang	Indonesia	125.40° E	2.78° N	7	0	1
Soputan	Indonesia	124.73° E	1.11° N	1	1	1
Lewotolok	Indonesia	123.50° E	8.27° S	2	1	1
Agung	Indonesia	116.01° E	8.34° S	5	2	3
Raung	Indonesia	114.05° E	8.12° S	17	3	4
Semeru	Indonesia	112.92° E	8.11° S	13	0	3
Anak Krakatau	Indonesia	105.42° E	6.10° S	19	10	6
Kerinci	Indonesia	101.26° E	1.70° S	5	2	2
Sinabung	Indonesia	98.39° E	3.17° N	20	3	3
Mayon	Philippines	123.69° E	13.26° N	15	4	5
Taal	Philippines	120.99° E	14.00° N	57	8	8
Nishinoshima	Japan	140.87° E	27.25° N	37	29	19
Raikoke	Russia	153.24° E	48.29° N	1	1	1
Lemonosov	Russia	155.43° E	50.25° N	24	6	4
South Kamchatka	Russia	158.27° E	52.49° N	47	3	5
Karymsky	Russia	159.45° E	54.05° N	20	9	11
Bezymianny	Russia	160.59° E	55.98° N	37	14	18
Klyuchevskoy	Russia	160.64° E	56.06° N	29	13	16
Sheveluch	Russia	161.36° E	56.65° N	30	15	19
Shishaldin	USA	163.97° W	54.76° N	5	2	2
Veniaminof	USA	159.39° W	56.20° N	3	1	1
Kilauea	USA	155.29° W	19.42° N	110	46	28
Popocatepetl	Mexico	98.62° W	19.03° N	467	50	84
Fuego	Guatemala	90.88° W	14.47° N	18	1	5
Masaya	Nicaragua	86.15° W	11.98° N	2	1	1
Poas	Costa Rica	84.23° W	10.20° N	69	18	27
Nevado del Ruiz	Colombia	75.32° W	4.88° N	467	110	113
Sangay	Ecuador	78.34° W	2.00° S	230	92	55
Fernandina	Ecuador	91.55° W	0.37° S	2	2	2
Sierra Negra	Ecuador	91.17° W	0.83° S	18	16	16

†PNG = Papua New Guinea

Yasur volcano.

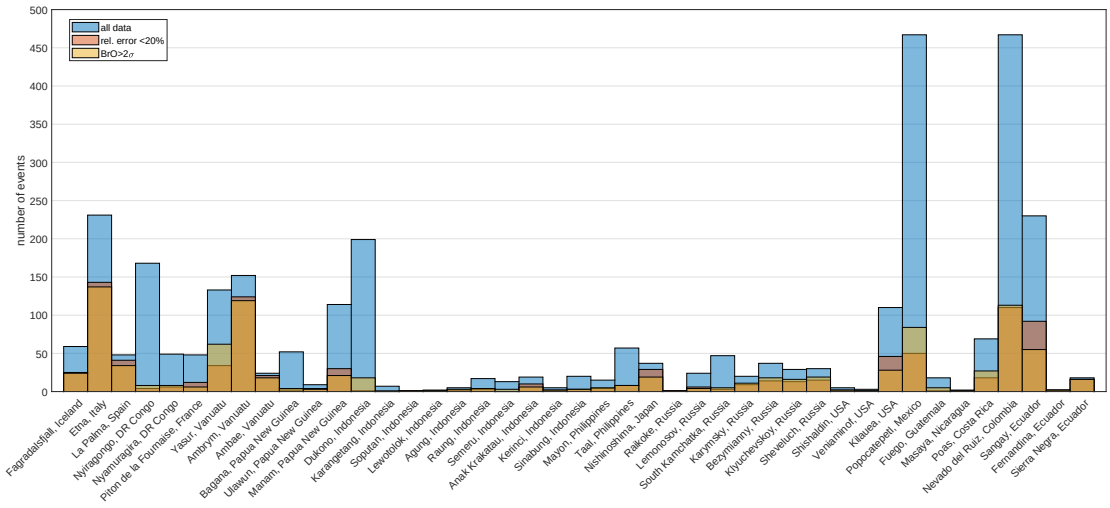


Figure 6.18: Number of events for each volcano of the catalogue. Color-coded for all data (blue), data with a BrO/SO_2 ratio error below 20 % (red) and a clear BrO detection (yellow). The data is also listed in table 6.3.

Wrongfully assigned plumes

Applying the above described algorithm, there is the risk of a wrongful assignment of an event to a volcano. A large plume of one volcano could drift over another volcano and be thus assigned to a false volcano. As 78 % of the events assigned to volcanoes are closer than 50 km to the respective volcano, a relevant risk of a plume drifting towards another volcano is only existing for volcanoes close to each other. For instance the volcanoes in the Andes (see figure 6.16a), who – apart from the neighbour volcanoes on Galapagos – have at least 800 km distance between each other, can be clearly separated and the risk of wrong assignment is almost non-existing. However, on the Kamchatka penninsula (see figure 6.16b) volcanoes are much closer, from 9 km (Klyuchevskoy/Bezymianny) to maximal 226 km (Karymsky/Bezymianny) distance from each other. The pair Klyuchevskoy/Bezymianny can thus not be distinguished. A similar argument has to be made for the pair Nyiaragongo/Nyamuragira, DR Congo, who are 13 km apart. Event though the pair Ambrym/Ambae, Vanuatu (100 km distance) can be clearly separated on the map (figure 6.16d), they are also at risk of being missmatched, as they have both multiple major eruptions with large plume extend. The Indonesian volcanoes Semeru, Raung, and Agung, who are 124 km (Semeru/Raung) and 216 km (Raung/Agung) distant from each other, also have a risk of wrongfull assigned plumes.

6.4.1 Overview

In total, 3482 of the total 4232 events are located within 300 km of one of these volcanoes. For the catalogue only the 3581 events with a linear BrO/SO_2 ratio are considered, of which 3063 are located within 300 km of one of the 43 volcanoes. These 3063 events are considered for the catalogue. Of the 1126 linear events with a relative BrO/SO_2 error of the BrO/SO_2 ratio below 20%, 910 can be assigned to one of the 43 volcanoes. The 3063 events comprising the catalogue are in detail also listed in Appendix A.
926 events of the 1020 linear events with a clear detection of BrO (i. e. a cluster of 5-pixels where BrO VCD exceeds twice the standard deviation of the BrO background distribution)

are located within 300 km distance of these 43 volcanoes. Thus, the catalogue covers a large portion of the detected volcanic plumes.
The number of events assigned to each volcano are included in table 6.3 and the 3581 linear events are plotted in figure 6.17, where the 3063 events assigned to a volcano are marked in the color respective of the volcano. The remaining events, which are further than 300 km away from the volcanoes are marked in grey.
The largest amounts of individual events are found for Nevado del Ruiz (Colombia) and Popocatepetl (Mexico), both having 467 events assigned, and Mt. Etna, Italy (231), and Sangay, Ecuador (230). The number of events for each volcano is plotted in figure 6.18. In total there are ten volcanoes with more than 100 events and only 11 volcanoes with less than ten events associated to.
The weighted mean BrO/SO_2 ratio is calculated using the inverse error of the BrO/SO_2 fitted line as weights. The mean BrO/SO_2 for the 43 volcanoes are plotted onto the global map in figure 6.19.
The weighted mean BrO/SO_2, the standard deviation and the 5-95-percentile range of the events of the 43 volcanoes are plotted in figure 6.20. The same plot is done only considering events with a relative error of the BrO/SO_2 of 20 % (figure 6.21) as well as only considering events with significant detection of BrO. (figure 6.22). The volcanoes are sorted based on their Volcano type.
For the data-set including all data (figure 6.20) BrO/SO_2 ratios vary between 2.1×10^{-5} (Bagana and Sinabung) up to almost 5×10^{-4}. There are significant differences between different volcanoes. While Sinabung, Indonesia has only two events with the lowest BrO/SO_2 ratio of 6.33×10^{-6}, the largest mean BrO/SO_2 ratio is observed for Yasur, Vanuatu, with a mean BrO/SO_2 ratio of 2×10^{-4} and no BrO/SO_2 ratio below 1×10^{-4}.
The mean BrO/SO_2 ratio derived from the different data-sets are compared in figure 6.23. It can be seen that including all data lowers the BrO/SO_2 ratio for many volcanoes, especially for the ones, that have a high mean BrO/SO_2 ratio if the data is filtered.
This raises the question, if applying any of the filter criteria yields a systematic positive bias onto the BrO/SO_2 ratio.

6.4.2 Dependency of SO_2 and pixel number

Both, selecting only events with BrO exceeding the detection limit as well as selecting events based on an rel. error could be selective to certain BrO/SO_2 ratios and systematically biase the BrO/SO_2 ratio catalogue.
The distribution of the BrO/SO_2 ratio with relation to its maximum SO_2 VCD is plotted for both criteria in figure 6.24 for the error filter (a, red dots) and the BrO filter (b, red dots). The complete data-set without any filter is included in both a and b as blue dots. It can be seen that both criteria discard events which have a low maximum SO_2 VCD and a low BrO/SO_2 ratio. For the error criterion this is less strict, whereas for the BrO criterion the dependency of SO_2 is more strict.
This is not surprising, as applying a strict BrO limit, will lead to an effective detection limit of the BrO/SO_2 ratio which then becomes depending inherently on the maximum SO_2 VCD:

$$\left[\frac{BrO}{SO_2}\right]_{\text{detection limit}} = \frac{BrO_{\text{detection limit}}}{max.\, SO_2\, VCD} \tag{6.1}$$

A similar, however less strict relation holds true for the rel. error criterion (see figure 6.24a). This is not surprising, as the combination of low BrO/SO_2 and low SO_2 VCDs will lead to a low maximum BrO VCD and the relative error of this fit will increase. However, the error

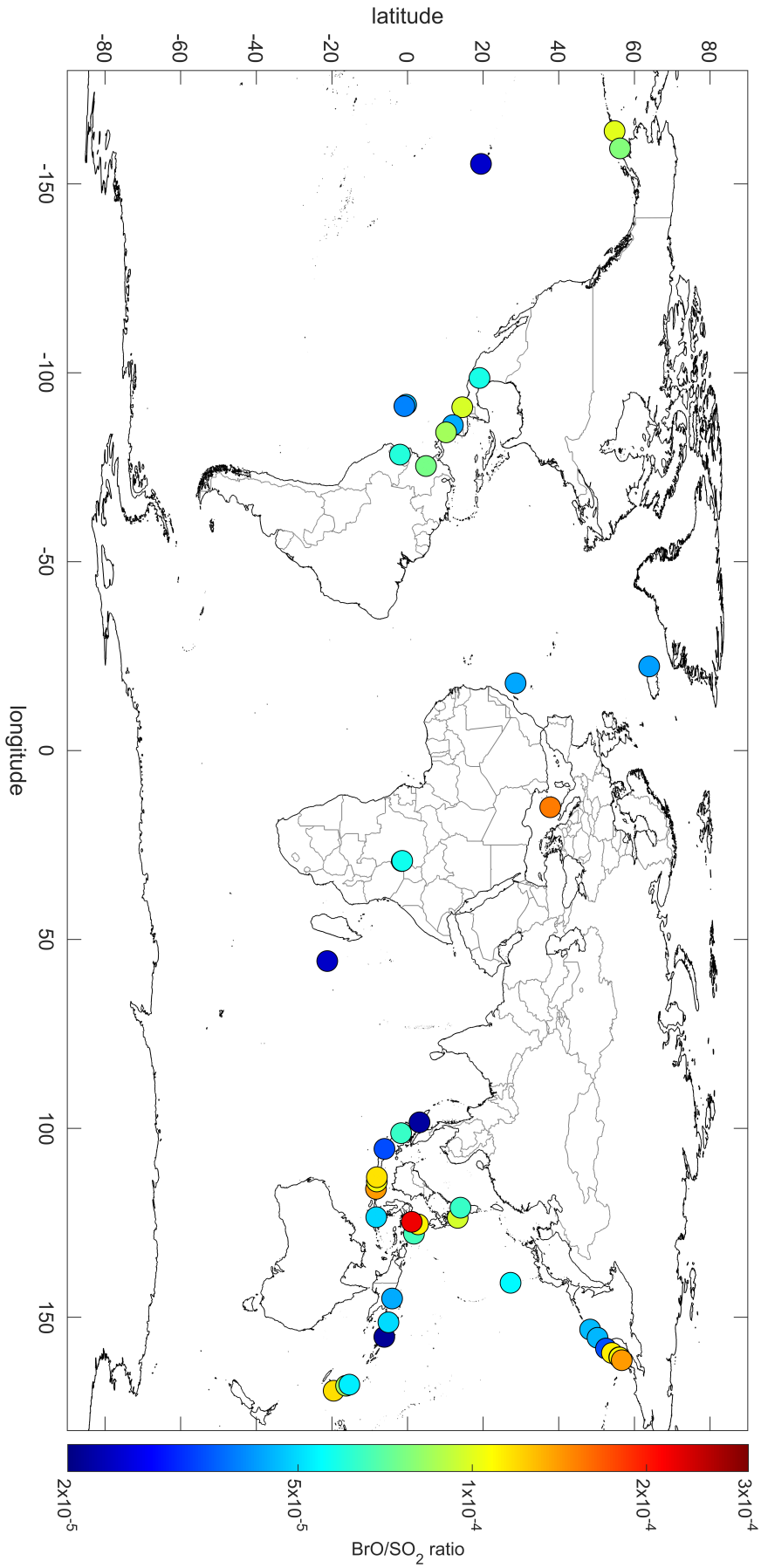


Figure 6.19: Global map of the mean BrO/SO_2 ratio for the 43 volcanoes of the catalogue. The mean BrO/SO_2 ratio is calculated as the weighted mean of all events within 300 km of the respective volcano. The BrO/SO_2 ratio is color coded.

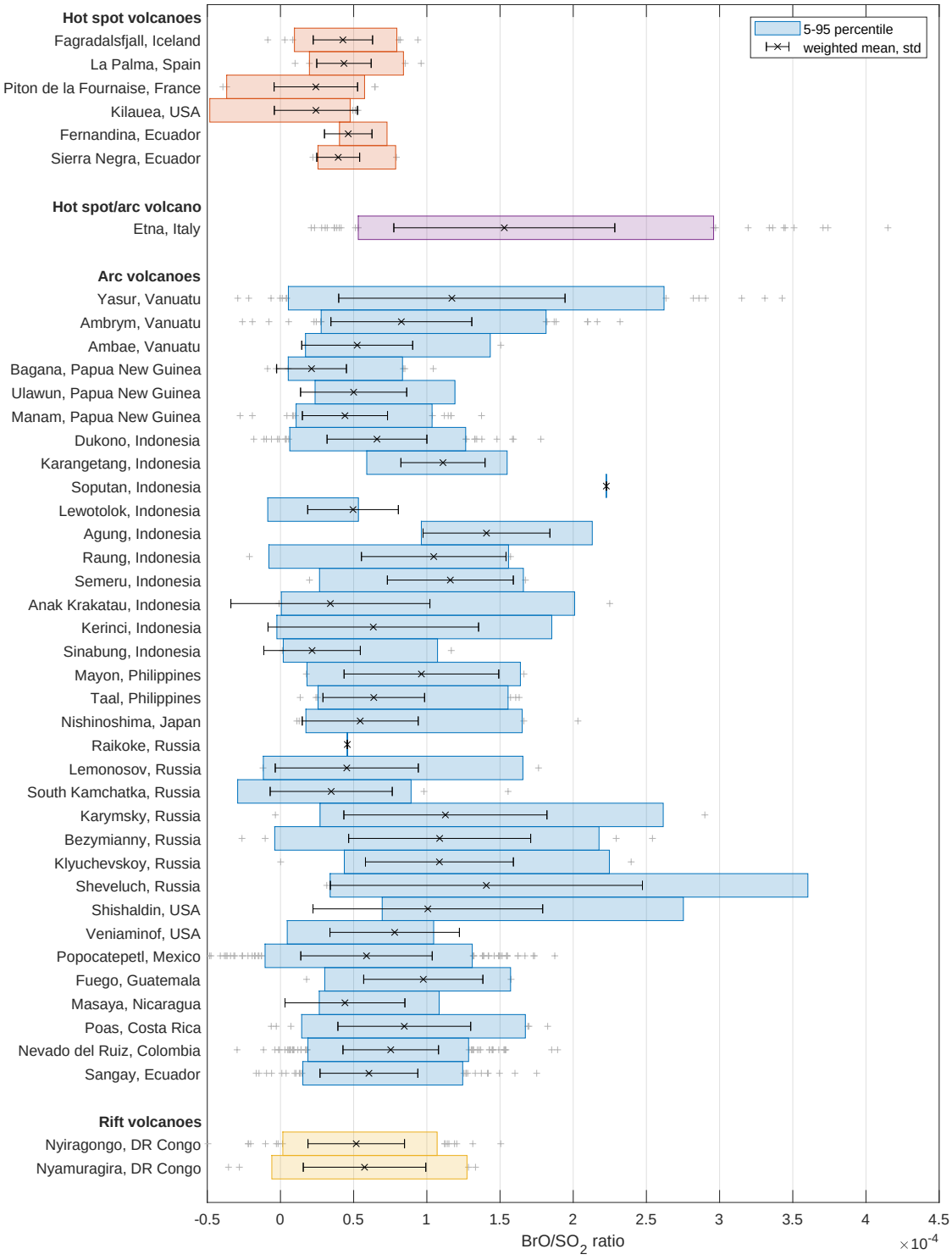


Figure 6.20: Mean BrO/SO_2 ratio of the 43 volcanoes of the catalogue considering all data. The range of the individual BrO/SO_2 ratios are shaded, the mean and the standard deviation are plotted as x and error bars respectively. Colors correspond to different volcanism type: Hot spot volcanism (red), arc volcanism (blue), and rift volcanoes (yellow).

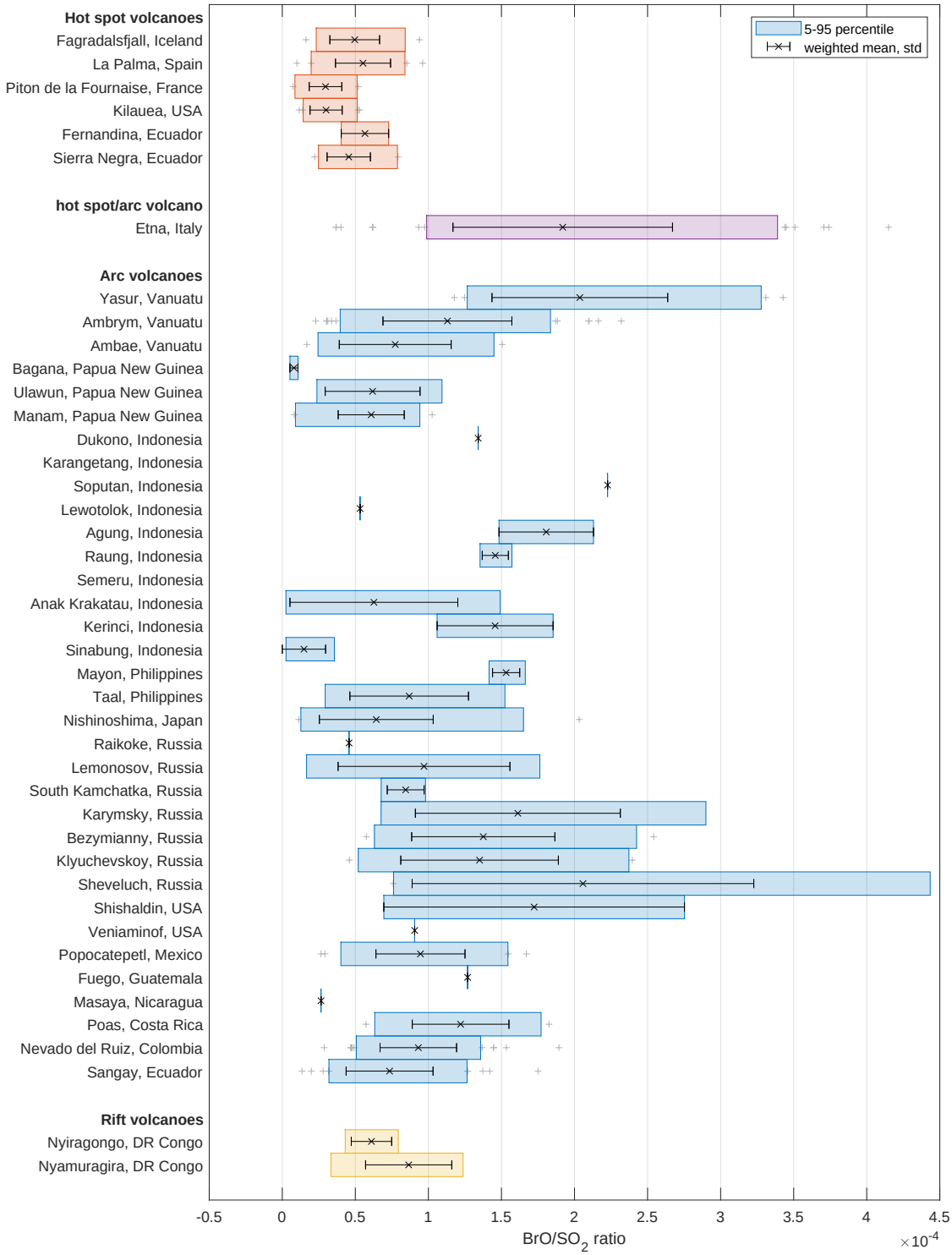


Figure 6.21: Mean BrO/SO_2 ratio of the 43 volcanoes of the catalogue considering only events with a rel. error of the BrO/SO_2 ratio below 20 %. The range of the individual BrO/SO_2 ratios are shaded, the mean and the standard deviation are plotted as x and error bars respectively. Colors correspond to different volcanism type: Hot spot volcanism (red), arc volcanism (blue), and rift volcanoes (yellow).

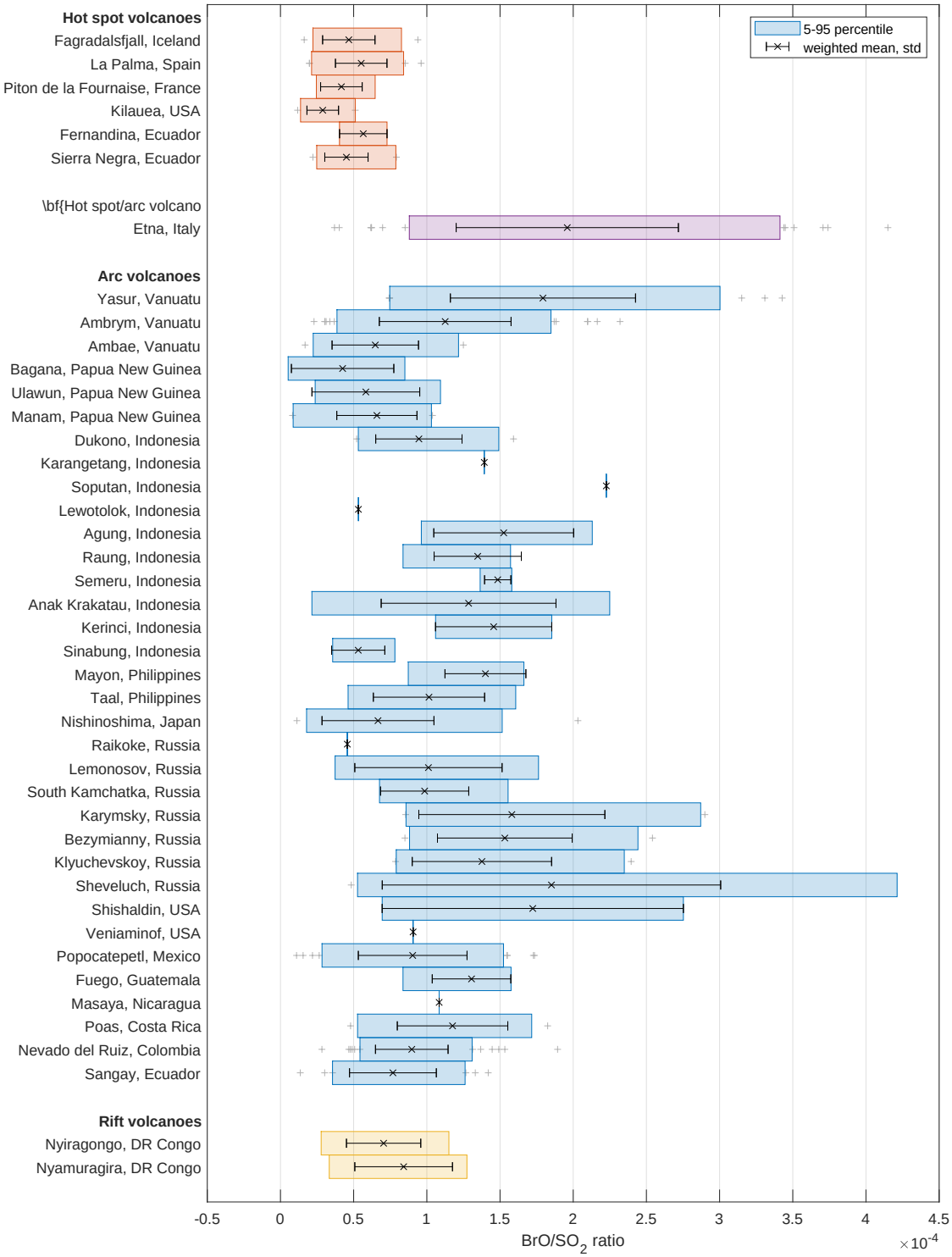


Figure 6.22: Mean BrO/SO_2 ratio of the 43 volcanoes of the catalogue considering only events, where a clear BrO signal is detected. The range of the individual BrO/SO_2 ratios are shaded, the mean and the standard deviation are plotted as x and error bars respectively. Colors correspond to different volcanism type: Hot spot volcanism (red), arc volcanism (blue), and rift volcanoes (yellow).

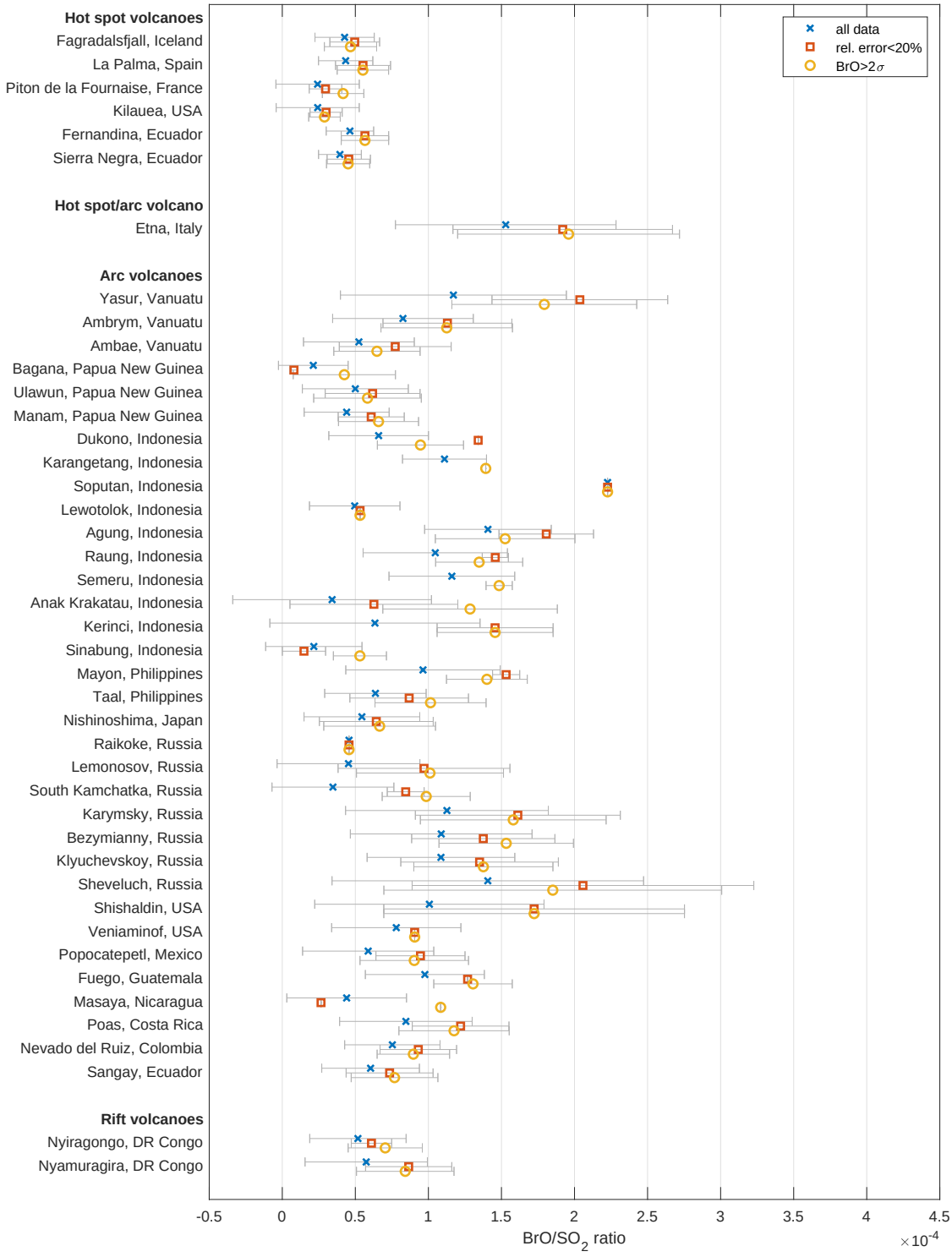


Figure 6.23: Mean BrO/SO_2 ratio of the 43 volcanoes of the catalogue for all three datasets: including all events within 300 km of the volcano (blue x), events with a rel. BrO/SO_2 error below 20 % (red square), and events with detectable BrO (yellow circle). The standard deviation is marked by the error bar. The volcanoes are sorted by their volcanism type: Hot spot volcanism (top section), arc volcanism (middle section), and rift volcanoes (bottom section).

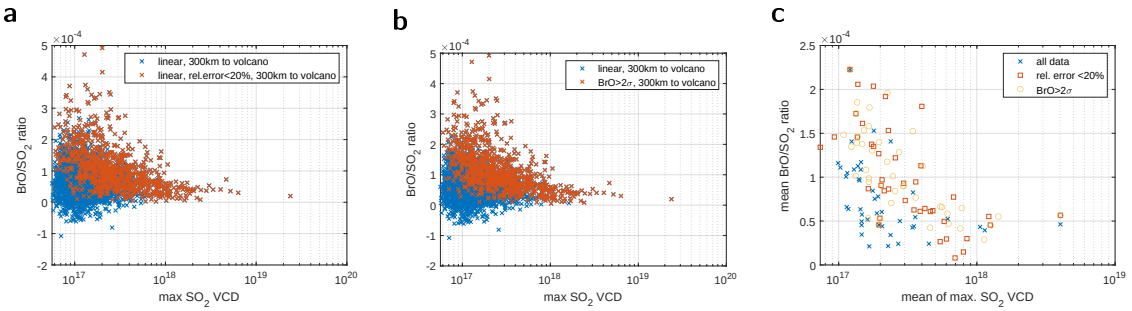


Figure 6.24: Dependencies of the BrO/SO_2 ratio on the max. SO_2 VCD for the linear BrO/SO_2 ratio events within 300 km of the 43 volcanoes. Comparison of all data (blue dots) with **a** the data fulfilling the 20 % rel. error criterion (red dots) and **b** the data with clear detection of BrO (red dots). **c** Comparison of the mean for the 43 volcanoes including all data (blue crosses), only data fulfilling the error criterion (red squares) or the BrO criterion (yellow circles).

is also depending strongly on the number of pixels included in an event. Hence, for events with a large number of pixels, a low SO_2 and low BrO/SO_2 can still lead to a relative error $< 20\,\%$. Thus, there is not a clear boundary in the BrO/SO_2 ratio as a funtion of the SO_2 VCD.

This shows that employing either criterion will lead to a systematic overestimation of the BrO/SO_2 for minor degassing volcanoes with low SO_2 VCDs. Hence, for the BrO/SO_2 catalogue the mean BrO/SO_2 ratio is calculated from all events without any filter criterion. The mean BrO/SO_2 ratio for the volcanoes are plotted in figure 6.20.

6.4.3 Dependency on solar zenith angle and latitude

The BrO/SO_2 ratio could also be affected by the viewing geometry or different geo-parameters. In order to investigate this, the BrO/SO_2 ratio of the catalogue is plotted as a function of solar zenith angle (SZA), viewing zenith angle (VZA) and the latitude in figure 6.25.

While there is no dependency for latitude (figure 6.25c) and VZA (figure 6.25b), the BrO/SO_2 ratio increases slightly for $SZA > 50°$ (figure 6.25a). This could be caused by a larger uncertainty of the BrO VCD at high SZA, which in turn will pronounce higher BrO/SO_2 ratios.

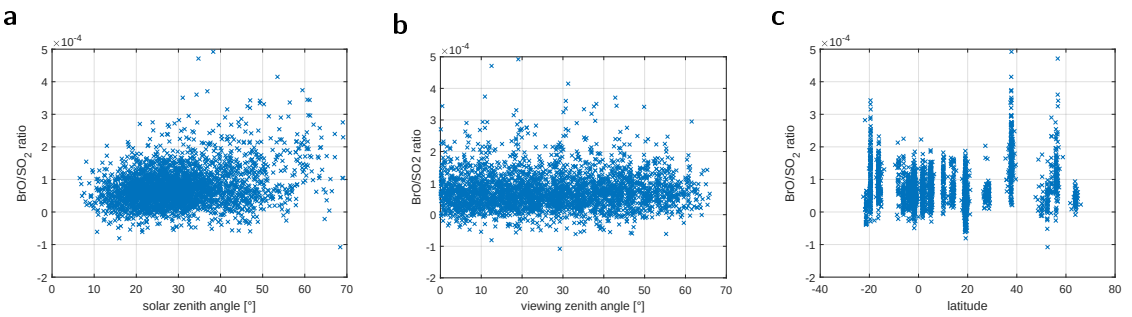


Figure 6.25: BrO/SO_2 ratio as a function of **a** the solar zenith angle, **b** the viewing zenith angle, and **c** the latitude for the BrO/SO_2 ratios within the catalogue.

6.4.4 Volcano types

In the following the different volcanoes are discussed based on their volcano type. There are three major volcano types: Hot spot, arc volcanoes, and rift volcanoes.

Hot spot volcanoes

Hot spot volcanism – also known as intraplate volcanism – originates from updrafts of hot magma within the asthenosphere which in turn partially melts the lithospheric plates and leads to volcanoes at the location of the updraft. Hence, their volcanic activity is not linked to plate tectonics. Over time a hot spot will thus produce a chain of volcanic remnants on the tectonic plate as it moves above the hot spot. One prominent example of such a chain is the »Hawaiian–Emperor seamount chain« stretching from the edge of the pacific plate in Kamchatka, Russia to the Hawaiian islands, where the hot spot is located today.
For hot spot volcanoes BrO/SO_2 ratios are all below 1×10^{-4} with mean BrO/SO_2 ratios between 2.41×10^{-5} (Piton de la Fournaise, Reunion, France) and 4.63×10^{-5} (Fernandina, Galapagos), even though they are located all over the world.
Mt. Etna can also be seen as a hot spot from a seismic (Anderson and Jackson, 1987) as well as a chemical point (Schiano et al., 2001, and references therein). Nevertheless, there has been long debates as to whether such a clear distinction can be made for Etna as its magmatic composition is similar to a volcanic arc volcano (Clarke, 2001; Schiano et al., 2001). Hence it is categorized into the category »hot spot/arc«. As the magma composition is the origin of the degassing composition, the »arc-like« magma signature could explain, that the observed BrO/SO_2 ratio differs from the hot spot volcanoes. BrO/SO_2 ratios observed for Etna are mostly between $1 - 2 \times 10^{-4}$ and a mean ratio of 1.53×10^{-4}, which is three times the maximal ratio reported for the hot spot volcanoes. BrO/SO_2 ratios matching the ones observed here, have been reported for Etna over the last 15 years (Bobrowski and Giuffrida, 2012; Hörmann et al., 2013, a detailed comparison is given in section 6.5 and section 6.6 respectively). This strongly indicates that Etnas plume composition is not that of a hot spot.

Arc volcanoes

Arc volcanoes originate from subduction of tectonic plates. Generally, observed BrO/SO_2 ratios are larger for arc volcanoes compared to hot spot volcanoes. Furthermore, arc volcanoes show a much more diverse BrO/SO_2 relation compared to hot spot volcanoes. The lowest ratios are at observed for Bagana (Papua New Guinea) and Sinabung (Indonesia) with 2.12×10^{-5} and 2.16×10^{-5} respectively, but BrO/SO_2 ratios exceeding 1×10^{-4} are observed for ten volcanoes in Indonesia and on the Kamchatka penninsula, Russia. The largest BrO/SO_2 ratio is 2.23×10^{-4} found for Soputan volcano, Indonesia. However, there is only one event assigned to this volcano, the highest mean BrO/SO_2 ratios for volcanoes with multiple events detected events are 1.41×10^{-4} observed for Mt. Agung, Indonesia as well as Sheveluch, Kamtchaka, Russia.
Generally, for each arc volcano, the range of different BrO/SO_2 is much larger compared to the hot spot volcanoes, ranging from -1.1×10^{-4} to 4.9×10^{-4} for example for Sheveluch volcano, Russia.

Oceania and Indonesian Arc

The Vanuatu volcanoes Ambae, Ambrym and Yasur show very different BrO/SO_2 ratios. Yasur, the southermost volcano, shows consistently high BrO/SO_2 ratios up to 3.5×10^{-4}.

Ambrym and Ambae – located 400 km further north – are relatively close to each other. Thus, separation of the plumes is not always ensured. Nevertheless, the emitted BrO/SO_2 ratio differs. While the mean BrO/SO_2 ratio for Ambae is below 5.2×10^{-5} single BrO/SO_2 ratios do not exceed 1.5×10^{-4}, Ambrym, has a mean BrO/SO_2 ratio of 8.3×10^{-5} and BrO/SO_2 ratios exceeding 2×10^{-4}.
Papua New Guinean volcanoes Bagana, Ulawun and Manam all have a mean BrO/SO_2 ratio below 5×10^{-5} and no single BrO/SO_2 ratio above 1.5×10^{-4}.
Indonesian and Philippians volcanoes show a large variety of BrO/SO_2 ratios. Sinabung and Kerinci (both Sumatra), Anak Krakatau, Semeru and Raung (both Java) and Agung (Bali) are all located on the Java and Sunda trench – i. e. the border between the Indian-Australian plate and the Eurasian plate (Muraoka et al., 2005). While the volcanoes on the Sunda trench have low mean BrO/SO_2 ratios (from north to south Sinabung: 2.16×10^{-5}, Kerinci: 6.34×10^{-5}, and Anak Krakatau: 3.41×10^{-5}) the volcanoes located on the Java trench – stretching east from Anak Krakatau all have ratios above 1×10^{-4} (from west to east Semeru: 1.16×10^{-4}, Raung: 1.05×10^{-4}, and Agung: 1.41×10^{-4}).

Northern Pacific Arc

The northern pacific arc includes the Russian Kuril islands, Kamchatka and the Aleutian trench (in figure 6.20 from »Raikoke, Russia« to »Veniaminof, USA«). The Kuril Island volcanoes Raikoke and Lemonosov as well as the neighbouring »South Kamchatka« have ratios of $3.5 - 5 \times 10^{-5}$, while the Kamchatka volcanoes Karymsky, Bezymianny, Klyuchevskoy, and Sheveluch have larger ratios between $1 - 1.4 \times 10^{-4}$.
Raikoke is a special case, since firstly there was only a paroxysmal singular large eruption in the measurement period. As the BrO/SO_2 ratio can be dependent on the eruption strength (Bobrowski and Giuffrida, 2012; Warnach et al., 2019), the BrO/SO_2 ratio of this eruption might be not representable to the magmatic composition. Secondly, the events assigned to the volcano is from a 18 day old plume parts, which passed again over the volcano, and hence have to be seen as drifted plume, whose BrO/SO_2 signature could have been altered by BrO life time in the atmosphere and hence the link between measured and released BrO/SO_2 ratio is not really valid.

Central and South American Volcanic Arc

In central and South America, there are six arc volcanoes with detected plumes: Popocatepetl (Mexico), Fuego (Guatemala), Masaya (Nicaragua), and Poas (Costa Rica) are located on the Central American Volcanic Arc (CAVA), while Nevado del Ruiz (Colombia) and Sangay (Ecuador) are located on the northern volcanic zone of the Andean volcanic belt.
Masaya has only two events, and hence the interpretation of the BrO/SO_2 is limited. For the other five volcanoes BrO/SO_2 ratios are between -1×10^{-4} reaching up to 2×10^{-4}. Mean BrO/SO_2 ratios are all between $5 - 10 \times 10^{-5}$, with the lowest calculated at 5.88×10^{-5} (Popocatepetl, Mexico) and the highest 9.76×10^{-5} (Fuego, Guatemala). This is larger than for the hotspot.

Rift volcanoes Nyiragongo & Nyamuragira

The only rift volcanoes active within the measurement period are Nyiragongo & Nyamuragira volcano, both located off Goma in the Democratic Republic of Congo. Mean BrO/SO_2 ratio are 5.18×10^{-5} (Nyiragongo) and 5.74×10^{-5} (Nyamuragira) with single BrO/SO_2 ratios of up to 1.5×10^{-4}.

Interpretation

Hot spot volcanoes show systematic lower BrO/SO_2 ratios compared to arc volcanoes, which is also emphasized by the histogram of the single event BrO/SO_2 ratios (figure 6.26). The calculated mean BrO/SO_2 of each distribution is 7.1×10^{-5} for the arc volcanoes, but only 3.5×10^{-5} for the hot spot volcanoes. Furthermore, in plumes of hot spot volcanoes there are no BrO/SO_2 ratios above 1×10^{-4} observed. It should be noted, that there are larger BrO/SO_2 ratios reported in the plume of volcanoes which are categorized as hot spot volcanoes in Gutmann et al. (2018): Eyjafjallajökull, Iceland (Hörmann et al., 2013) and Mt. Erebus, Antarctica (Boichu et al., 2011), both with BrO/SO_2 ratios above 1×10^{-4}. However, Eyjafjallajökull is classified as a rift volcano in the Global Volcanism Program (GVP, 2013a, `https://volcano.si.edu/volcano.cfm?vn=372020`). A similar argument can be made for Mt. Erebus, which is located along the West Antarctic Rift System (Behrendt et al., 1991), even though the Global Volcanism Program lists it as intra-plate volcanism (GVP, 2013b). This could indicate that the larger BrO/SO_2 ratio observed for these two volcanoes is caused by the rift nature of their respective volcanic systems.
The lower BrO/SO_2 ratios observed in this thesis for the five pure hot spot volcanoes indicate that the magmatic source of hot spot volcanoes is less Br-rich compared to arc volcanoes. There are several indications collected in Webster et al. (2018), that hot spot volcanoes have a lower bromine abundance compared to arc volcanoes. Br mixing ratio is reported to be much larger in subduction zone melt inclusions compared to hot spot melt inclusions (Webster et al., 2018, and references therein). Furthermore, degassing Br/S ratio is reported one order of magnitude larger for subduction zone volcanoes compared to hot spot and rift volcanoes (Webster et al., 2018, and references therein). However, both the lower Br mixing ratio in hot spot melt inclusions and Br/S degassing signature in is based on very few measurements in hot spot volcanoes (Webster et al., 2009).
Thus, the first detections of the BrO/SO_2 ratios in the plumes of five pure hot spot volcanoes in this thesis add valuable data points to understanding the gas origin of hot spot volcanoes and strengthen the hypothesis.
Another difference between arc and non-arc volcanoes is that the Br/Cl ratio is reported to differ (Webster et al., 2018). Non-arc volcanoes seem to be depleted in Br with respect to Cl, which could be an indication, that the lower BrO/SO_2 ratios observed for hot spot volcanoes originates not in a lower abundance of halogens with respect to sulphur, but of bromine only.

In the following, the BrO/SO_2 catalogue is compared to other data-set both satellite and ground-based observations.

6.5 Comparison to previous satellite data

The only study which also calculated BrO/SO_2 ratios from satellite data is by Hörmann et al. (2013), who used GOME-2 measurements between 2007 and 2011, thus also comprising of four years of data.
For GOME-2 the total amount of SO_2 events (772) as well as the amount of events with significant BrO (64) is significantly lower compared to 4323 and 1449 in this study. The percentage of events where BrO VCDs exceed the detection limit is thus 8.2 % in the GOME-2 study (Hörmann et al., 2013), which is four times lower compared to the 34.2 % found for TROPOMI in this thesis. This is expected by the 167 times better spatial resolution of TROPOMI (see section 3.2), which could in theory result in an observed BrO VCD up to 167 times higher compared to GOME-2. In addition, the signal-to-noise ratio of TROPOMI

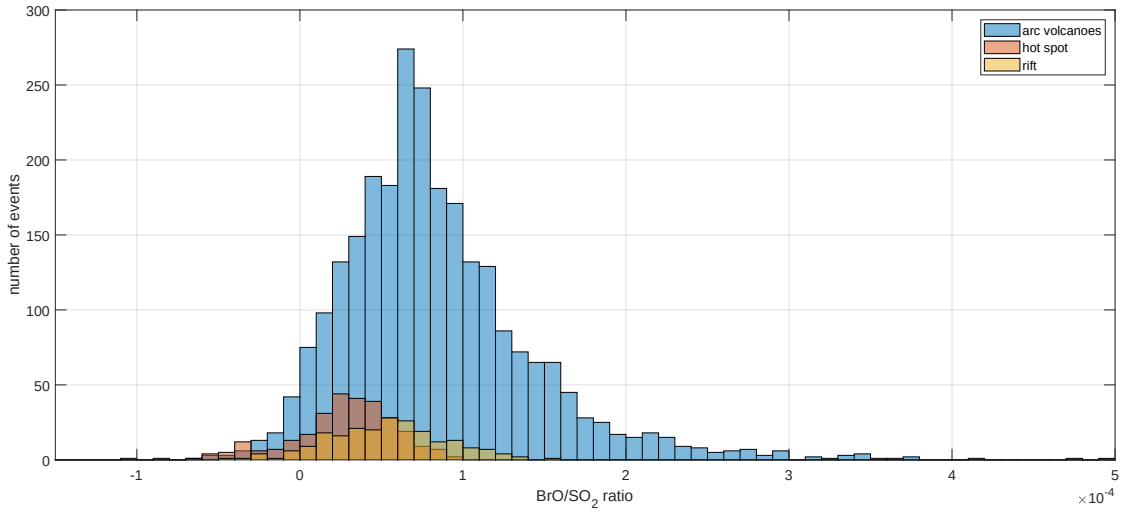


Figure 6.26: Histogram of the BrO/SO_2 ratios of the individual events of the catalogue separated by volcano type: arc volcanoes (blue, weighted mean: 7.1×10^{-5}), hot spot volcanoes (red, weighted mean: 3.5×10^{-5}) and rift volcanoes (yellow, weighted mean: 5.3×10^{-5}).

is improved compared to GOME-2. Further factors are the improvements in the BrO DOAS fit in this study, such as the larger wavelength window and the inclusion of additional fit parameter, as well as the more sophisticated background correction. This lead to the decrease of statistical variation by 40 % (compare figure 4.15 and section 4.3.4) and will lead to more significant BrO detections.
There are five volcanoes, for which both this study and Hörmann et al. (2013) calculated BrO/SO_2 ratios: Mt. Etna (Italy), Ambrym (Vanuatu), Bezymianny, Klyuchevskoy, and Karymsky (all Kamchatka, Russia) (see figure 6.27).
Generally, this study (TROPOMI) has much more data points for each of the five volcanoes. Most of the GOME-2 data-points lie within the range of BrO/SO_2 ratios found for TROPOMI. However, low BrO/SO_2 ratios observed by TROPOMI are not detected by GOME-2. The main reason for the lack of low BrO/SO_2 ratios in the GOME-2 data set is most likely the lower spatial resolution. As the resolution of TROPOMI is 167 times better, there will be less spatial averaging over a plume and hence the maximal SO_2 VCD will increase dramatically for local, small plumes compared to GOME-2. Furthermore, the data-set of GOME-2 only considers events, where BrO exceeds the detection limit, effectively leading to a BrO/SO_2 lower threshold depending on the maximum SO_2 VCD for each event. The dependency of the lower threshold on the BrO detection limit and the maximal SO_2 VCD can be formulated by the following equation:

$$\left[\frac{BrO}{SO_2}\right]_{thresh} = \frac{BrO_{detectionlim}}{SO_{2,max}} \tag{6.2}$$

Taking the typical BrO detection limit of at least 2×10^{13} molecules cm^{-2} [2] and maximal SO_2 VCD of 2×10^{17} molecules cm^{-2} will reject any BrO/SO_2 ratio below 1×10^{-4} or 5×10^{-5} if the SO_2 VCD is 4×10^{17} molecules cm^{-2}. Hence, small BrO/SO_2 ratios in the order of 2×10^{-5} require maximal SO_2 VCDs of at least 1×10^{18} molecules cm^{-2}, which is only rarely reached.

[2] This number is estimated by the author of this thesis, as it is not explicitly stated in Hörmann et al. (2013).

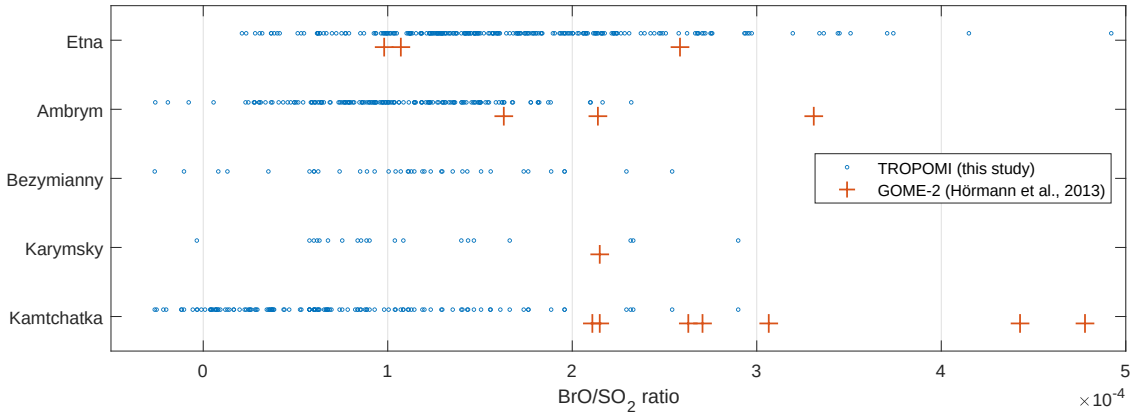


Figure 6.27: Comparison of BrO/SO_2 ratios of the catalogue with BrO/SO_2 ratio derived from GOME-2 satellite. Plotted are the BrO/SO_2 ratios found in this study (blue circles) and BrO/SO_2 ratio found in Hörmann et al. (2013) (red +).

One additional factor is that Hörmann et al. (2013) consider only BrO/SO_2 distributions with a coefficient of distribution $R^2>0.5$. As mentioned in section 5.4.1, lower BrO/SO_2 ratios will have a lower R^2, hence lower BrO/SO_2 ratios will be more likely to be discarded and the data-set from Hörmann et al. (2013) will by design contain more high BrO/SO_2 ratios. Both factors inherent to the satellite differences and data selection thus tend to suppress low BrO/SO_2 ratios in GOME-2 data-set compared to the data-set presented in this thesis and the bias towards high BrO/SO_2 ratios in the GOME-2 data set (see figure 6.27) can be attributed to these effects.

For Mt. Etna, there were three BrO/SO_2 ratios found with GOME-2, compared to 231 ratios from TROPOMI in this thesis (see figure 6.27). The BrO/SO_2 ratios from GOME-2 lie within the range of TROPOMI. Also two of the BrO/SO_2 ratios observed by GOME-2 are as low as 1×10^{-4}. These two ratios are found for very high SO_2 SCDs of at least exceeding 1×10^{18} molecules cm^{-2} (deduced from the plots of the corresponding thesis Hörmann, 2013). For Ambrym, BrO/SO_2 ratios found in the thesis presented here are generally lower compared to Hörmann et al. (2013). The data from TROPOMI yield a BrO/SO_2 ratio of 1.18×10^{-4} in this thesis, while GOME-2 data show no BrO/SO_2 ratio below 1.5×10^{-4}. In contrast to Mt. Etna, there are no large SO_2 SCDs found for Ambrym in the GOME-2 study (Hörmann, 2013), which could explain the lack of low BrO/SO_2 ratios compared to TROPOMI.
A similar effect is present for the Kamchatka volcanoes. While most BrO/SO_2 ratios observed with GOME-2 lie within the range of the BrO/SO_2 ratios found in this thesis, the low BrO/SO_2 ratios smaller than 2×10^{-4} are not found in the Hörmann et al. (2013) study. This holds true for all three Kamchatka volcanoes, for which both studies find plumes, but also for the distribution of all Kamchatka volcanoes, which additionally includes the Sheveluch (only found with TROPOMI) and the Kizimen (only found with GOME-2).

6.6 Comparison to ground-based data

Comparison with ground-based data is difficult. Similar as for satellite measurements, there are no simultaneous ground-based DOAS data available. The only exception is Manam, where measurements were performed in May 2019 (Liu et al., 2020). A compilation of every

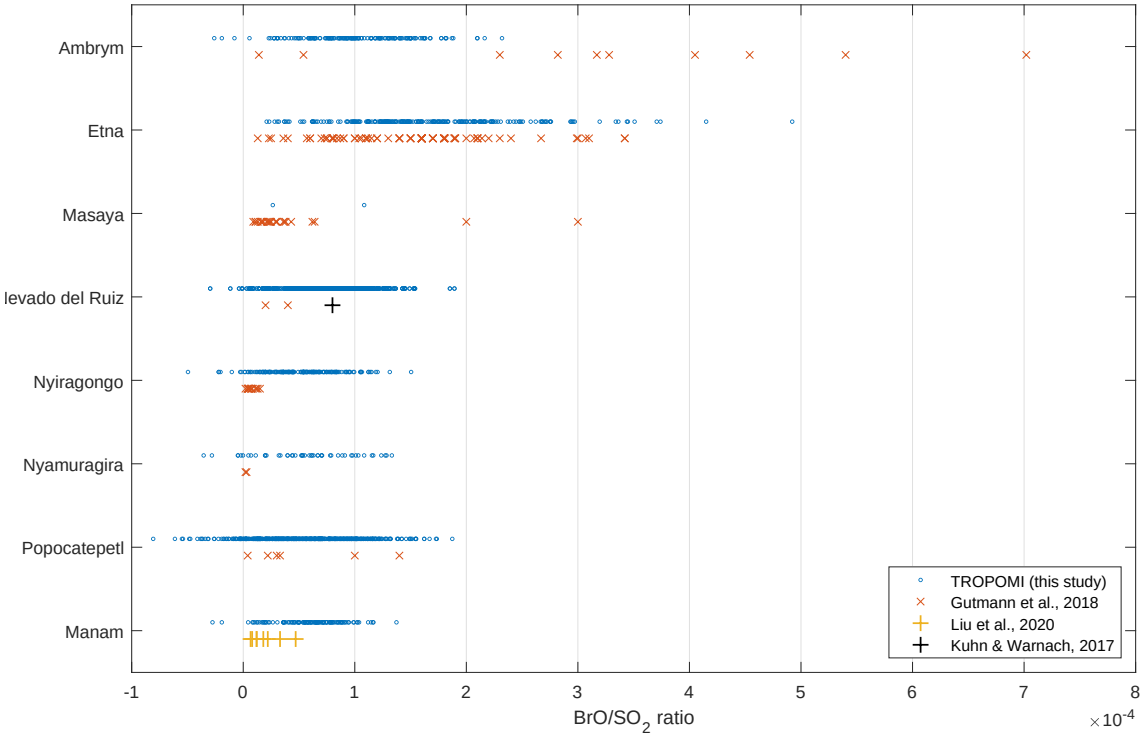


Figure 6.28: Comparison of BrO/SO_2 ratios of the catalogue with BrO/SO_2 ratio derived from ground-based measurements. Plotted are the BrO/SO_2 ratios found in this study (blue circles) and measured from ground-based measurements (red crosses) combined in Gutmann et al. (2018) (see references therein for source of the data). More recent measurements at Manam, Papua New Guinea, by Liu et al. (2020) are included (yellow crosses) as well as unpublished BrO/SO_2 ratio measurements in November 2017 derived by Jonas Kuhn and the author at Nevado del Ruiz, Colombia (black cross).

ground-based BrO/SO_2 ratio for the period 2003 – 2015 is collected by Gutmann et al. (2018). Hence, the comparison is done under the assumption that the magmatic Br/S ratio of each volcano has not changed between this period and the TROPOMI measurement period (2018 – 2021). There are eight volcanoes in the TROPOMI catalogue, for which ground-based measurements are reported: Ambrym (Vanuatu), Etna (Italy), Masaya (Nicaragua), Nevado del Ruiz (Colombia), Nyiragongo, Nyamuragira (both DR Congo), Popocatepetl (Mexico), and Manam.

For Ambrym, Vanuatu, ground-based measurements found BrO/SO_2 ratios similar and higher compared to the TROPOMI data, but no data between 0.6 and 2×10^{-4}, where most BrO/SO_2 ratios detected by TROPOMI lie. Highest ratios reported from ground-based measurements of up to 7×10^{-4} are roughly three times the highest BrO/SO_2 ratio reported from TROPOMI (2.3×10^{-4}). However, the three BrO/SO_2 ratios above 4.5×10^{-4} are all reported on a single day during a measurement campaign in 2007 (Bani et al., 2009), so they might be associated with a specific eruptive activity. Overall, there seems not to be any general bias between the two data-set, and the overall range of BrO/SO_2 ratios show an overlap.

For Etna, Italy, both data-sets have a large amount of data points (ground-based: 88;

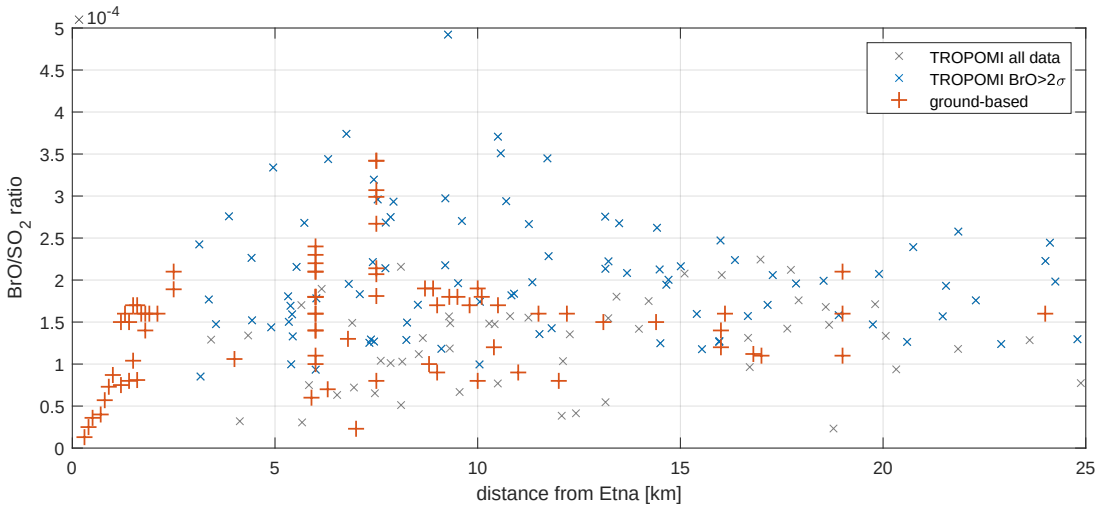


Figure 6.29: The BrO/SO_2 ratios as a function of the distance from the vent of Mt. Etna measured from ground-based instruments (red crosses, as reported in Gutmann et al., 2018, see references therein) and from TROPOMI (this study, grey dots all data and blue dots data with BrO above the detection limit).

TROPOMI: 231) and both BrO/SO_2 ratio distributions seem to have a similar range, where a majority of measurements yield BrO/SO_2 ratios between 0.5 and 2×10^{-4}. TROPOMI BrO/SO_2 ratios seem slightly higher compared to the ground-based measurements. However, the mean BrO/SO_2 ratio is similar with 1.53×10^{-4} (TROPOMI) and 1.51×10^{-4} (ground-based). The fact that there are less BrO/SO_2 ratios below 1×10^{-4} might indicate that TROPOMI is still less sensitive to these low BrO/SO_2 ratios. Indeed, three of the five lowest BrO/SO_2 ratios from TROPOMI correspond to the highest SO_2 columns ($> 1 \times 10^{18}$ molecules cm^{-2}), which suggest that there might be a bias. However, four of five ground-based BrO/SO_2 ratios below 5×10^{-5} are less than 1 km distance from the volcanic vent (see figure 6.29), i. e. at a distance where BrO formation is still limited (Bobrowski et al., 2007, as can also be seen by the linear increase in BrO/SO_2 ratio in figure 6.29 from distance 0 – 1 km, and described in the publication the data is taken from). Between 4 - 20 km both data-set agree well (see figure 6.29).
For Masaya, Nicaragua, the two data points detected by TROPOMI in this study agree with the ground-based data. Low BrO/SO_2 ratios reported from ground-based are partially closer than 1 km distance from the volcano (distances taken from the supplementary materials of Gutmann et al., 2018) and might thus be affected by incomplete BrO formation.
For Nevado del Ruiz, the reported BrO/SO_2 ratios from ground-based measurements in Gutmann et al. (2018) (red crosses in figure 6.28) are on the lower part of the distribution of the satellite measurements. However, the ground-based measurements included here are obtained from fixed stations at less roughly 3 km distance from the volcano. Other measurements done at distances between 1 and 30 km in 2017 (unpublished data performed by the author, Jonas Kuhn and Nicole Bobrowski and evaluated by Jonas Kuhn, included as a black cross in figure 6.28)) show that BrO/SO_2 ratio reached a plateau of 8×10^{-5} after the initial BrO formation (which took roughly 10 minutes). This is in good agreement with the range of the TROPOMI mean BrO/SO_2 ratio of $7.53 \pm 3.26 \times 10^{-5}$.
For Nyiragongo and Nyamuragira the reported ground-based BrO/SO_2 ratios do not exceed 1.5×10^{-5} while TROPOMI detects ratios of up to 1.5×10^{-4}. However, the ground-based data reported by Gutmann et al. (2018) are all measured 0.5 km from the volcanic vent,

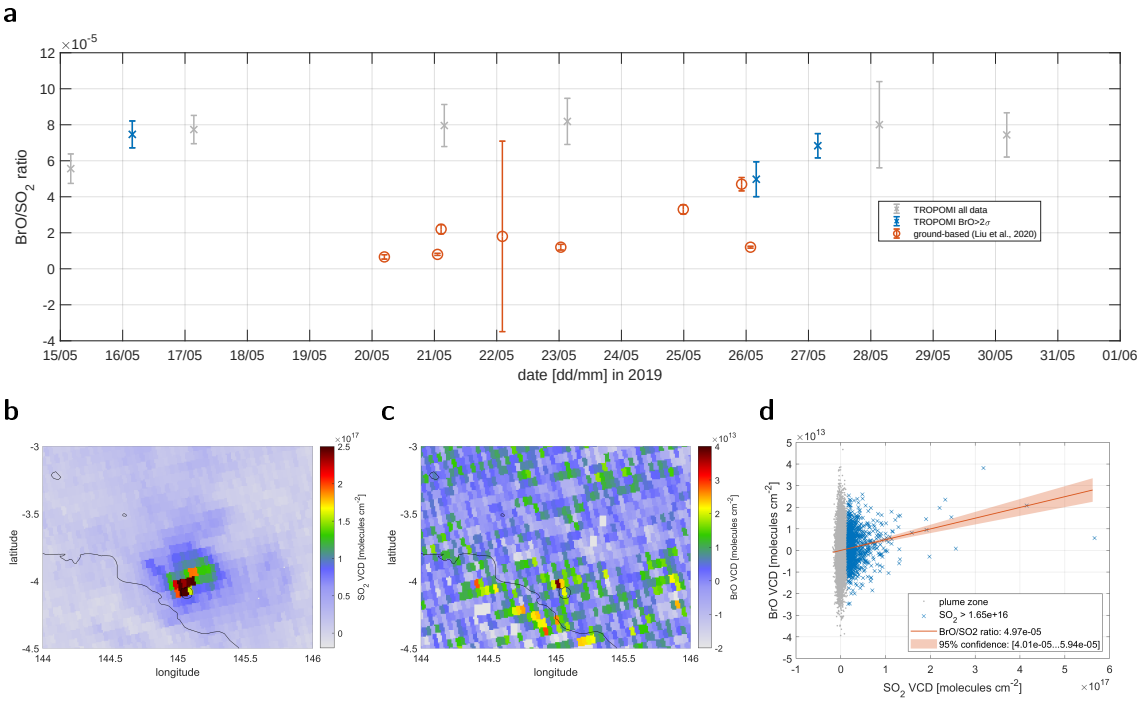


Figure 6.30: Comparison of simultaneous measurements of the BrO/SO_2 ratio from TROPOMI (this study) and ground-based instruments (Liu et al., 2020). **a** The BrO/SO_2 ratios from ground-based instruments (red circles, as reported in Liu et al., 2020) and from TROPOM (this study, grey dots all data and blue dots data with BrO above the detection limit). Map of the **b** SO_2 VCD, **c** SO_2 VCD, and **d** the BrO-SO2 scatter plot for the TROPOMI event of Manam on 26 May 2019.

thus they might be systematically lower.

A similar result can be seen for Popocatepetl, Mexico. There are several BrO/SO_2 ratios observed from ground-based measurements, which are on the low end of the distribution TROPOMI observes. However, these BrO/SO_2 were measured within 1 km distance to the volcanic vent, most likely affected by incomplete BrO formation. There are also BrO/SO_2 ratios of 1×10^{-4} measured, which is in agreement with the TROPOMI data. These were recorded at distances of around 5 km. In total the comparison for Popocatepetl suggests, that the plume composition determined from ground-based measurements is similar to the one determined from space.

Manam volcano is the only volcano for which ground-based measurements are reported during the measurement period of this thesis. They were obtained during a measurement campaign in May 2019 by Liu et al. (2020). However, the ground-based measurements could only be performed in 500 m distance as Manam island is small. Both data-sets are plotted in figure 6.30a. Generally, BrO/SO_2 ratios from ground-based measurements are much smaller compared to TROPOMI BrO/SO_2 ratios. There are three days, for which coinciding TROPOMI and ground-based measurements are found: 21, 23 and 26 May 2019. The TROPOMI event on 26 May 2019 is the only one where BrO is above the detection limit. Furthermore, its BrO/SO_2 ratio of $4.98 \pm 0.97 \times 10^{-5}$ agrees with and the early ground-based measurements of the day which report a BrO/SO_2 ratio of $4.7 \pm 0.37 \times 10^{-5}$ (taken from the supplementary material of Liu et al., 2020). The SO_2 and BrO VCD map as well as the BrO/SO_2 scatter plot of the TROPOMI event on 26 May 2019 is plotted in figure 6.30b-d. It can be seen that the plume is directly at the volcano and is furthermore

dispersing towards the direction of the ground-based DOAS measurement site. The distance of the maximal SO_2 VCD is found at 0.5 km, i. e. it is almost directly above the measurement site. Thus, for these measurements on the 26 May 2019 good spatio-temporal coincidence can be assumed.

In conclusion, the data-set from TROPOMI in this thesis shows BrO/SO_2 ratios which are similar to BrO/SO_2 ratios observed from ground-based DOAS retrievals. No systematic biases, such as that the satellite only detects major eruptions which might have a biased high/low BrO/SO_2 ratio, which would jeopardize the validity of the data, were found. For one occasion an overlapping measurement of ground-based and satellite observations was found and BrO/SO_2 ratios were in agreement.
Especially in comparison with the previous study from GOME-2 (Hörmann et al., 2013), this highlights that the improved spatial resolution of TROPOMI and improved retrieval in this thesis allows for a meaningful BrO/SO_2 ratio in volcanic plumes, representative to the degassing composition of the volcano in question.

6.7 BrO/SO_2 ratio time-series

Time-series of volcanic degassing offer the potential to link changes in the BrO/SO_2 ratio to a change in volcanic parameters. For the BrO/SO_2 ratio this has been demonstrated for time-series derived from spectral data of NOVAC (Network for the Observation of Volcanic and Atmospheric Change, Galle et al. (2010)), where changes in the BrO/SO_2 ratios could be linked to different recurring eruptive stages during 13 eruptive phases (Warnach et al., 2019) and for a change in the BrO/SO_2 ratio prior to major eruption (Lübcke et al., 2014). The latter was also observed for a time-series of Mt. Etna (Bobrowski and Giuffrida, 2012). In this section time-series are derived for a series of volcanoes from the BrO/SO_2 catalogue and potential agreement with volcanic parameters are reported and discussed.
The BrO/SO_2 data-set derived in the BrO/SO_2 catalogue (see section 6.4) includes several volcanoes, where a large number of events were found. This enables to derive time-series of BrO/SO_2 ratio for individual volcanoes. As a meaningful time-series requires a large amount of data points, volcanoes with a small number of events are not considered in the following.

Fagradalsfjall, Iceland showed only one eruptive period lasting several month. No trend can be observed. The time-series is plotted in figure 6.31a.

Mt. Etna, Italy has the largest and most complete time-series. Mt. Etna shows gas emissions for the complete 4 year period, as reported from the Global Volcanism Program (Global Volcanism Program). A large number of BrO/SO_2 detection can be seen from August 2018 to February 2019 and October to December 2019 (see figure 6.31b). Changes in the BrO/SO_2 are seen throughout the data-set. During the first half of 2018 the BrO/SO_2 ratio decreases from 3.3×10^{-4} down to 1.2×10^{-4}. In August 2018 many BrO/SO_2 ratios are low (close to 1×10^{-4}), which are then rising to 2×10^{-4} throughout August and September. From October through December 2018 BrO/SO_2 ratio remain high a around 2×10^{-4} up unto a major VEI 2 eruption on 24 December 2018 (Calvari et al., 2020). Following the eruption the BrO/SO_2 ratio decreases over the whole of January 2019 back to 1.2×10^{-4}. This might suggest that the BrO/SO_2 ratio is larger prior to an eruption and is subsequently lowered during this eruptive episode. A comparable result was found by Bobrowski and Giuffrida (2012), a multi-year ground-based survey of Etna's plume from 2004 to 2009. They observed a lower BrO/SO_2 ratios of roughly $1.1 - 1.4 \times 10^{-4}$ during

eruptive phases compared to $1.8 - 2.1 \times 10^{-4}$ during non-eruptive phases. Comparable to the 2018 eruption, there is also a decrease in the BrO/SO_2 ratio observed over the course of the eruption from July to December 2006 and the eruption from May 2008 to June 2009. In difference to the December 2018 eruption captured by TROPOMI, Bobrowski and Giuffrida (2012) observed that the decrease already started prior to the eruptions.
After January 2019, there are only few data-points until August/September 2019, where many BrO/SO_2 ratios are detected, most around 1.4×10^{-4}, but also ratios as high as 3.5×10^{-4}. From October 2019 to December an increase in BrO/SO_2 from below 1×10^{-4} (end of September) to 3×10^{-4} (November 2019) can be found. In 2020 and 2021 detections of BrO/SO_2 ratios are less frequent. BrO/SO_2 ratios are between 5×10^{-5} and 3.2×10^{-4}, but no real trend can be observed.

Nyiragongo, DR Congo shows many data-points with a very large error. No trend can be observed (figure 6.31c).

Piton de la Fournaise, France shows consistently low BrO/SO_2 ratios. No trend can be observed (figure 6.31d).

Yasur, Vanuatu was reported active for the whole measurement period (Global Volcanism Program), but gas emissions were only reported starting 2019 (GVP, 2019j) prevailing until the end of the measurement period and today (Global Volcanism Program). BrO/SO_2 ratios are detected first during the second half of 2019 with only a few data points until the beginning of 2020 (figure 6.32a). A larger number of BrO/SO_2 ratios are observed in 2020 as well as 2021. BrO/SO_2 ratios are below 5×10^{-5} at the beginning of 2020 and the beginning of 2021. During the remainder of 2020 BrO/SO_2 ratios are at 1.5×10^{-4}. Over the course of 2021 the BrO/SO_2 ratio increases to 2.5×10^{-4} in mid 2021 and a steep decrease to 5×10^{-5} in October 2021 prevailing until the end of 2021. There are no volcanic patterns reported fitting this increase or decrease. The multi-year pattern suggests a seasonality, as BrO/SO_2 ratios are larger during the southern hemisphere winter month and smaller during the summer month.

Ambrym, Vanuatu was active only during 2018. Degassing and the presence of a lava lake was reported throughout 2018 (Global Volcanism Program) ending with a flank eruption on 15 December 2018, which drained the lava lake (Hamling et al., 2019). No activity was reported after 17 December 2018 (GVP, 2019a). BrO/SO_2 ratios are detected over the complete course of 2018 (figure 6.32b). Data show an increase in the BrO/SO_2 ratio from 7×10^{-5} to 1.7×10^{-4} over the first half of 2018 and a subsequent decrease back to 7×10^{-5} until December 2018. This could indicate a general change in volcanic parameter prior to the eruption, but there are no correlating volcanic parameter reported. The trend is in line with the seasonality of the neighbouring Yasur volcano. Limiting the informative value is the fact that the other neighbouring volcano Ambae (also Vanuatu) was also active in 2018 for which a lower BrO/SO_2 ratio (see figure 6.20) is reported. This could mean that a portion of the BrO/SO_2 ratios assigned to Ambrym could actually originate from or are heavily influence by gas from Ambae, Vanuatu.

Bagana and Manam, Papua New Guinea as well as Dukono, Indonesia all have BrO/SO_2 ratios below 1×10^{-4}, but no trend can be observed (see figure 6.32c & d and figure 6.33a).

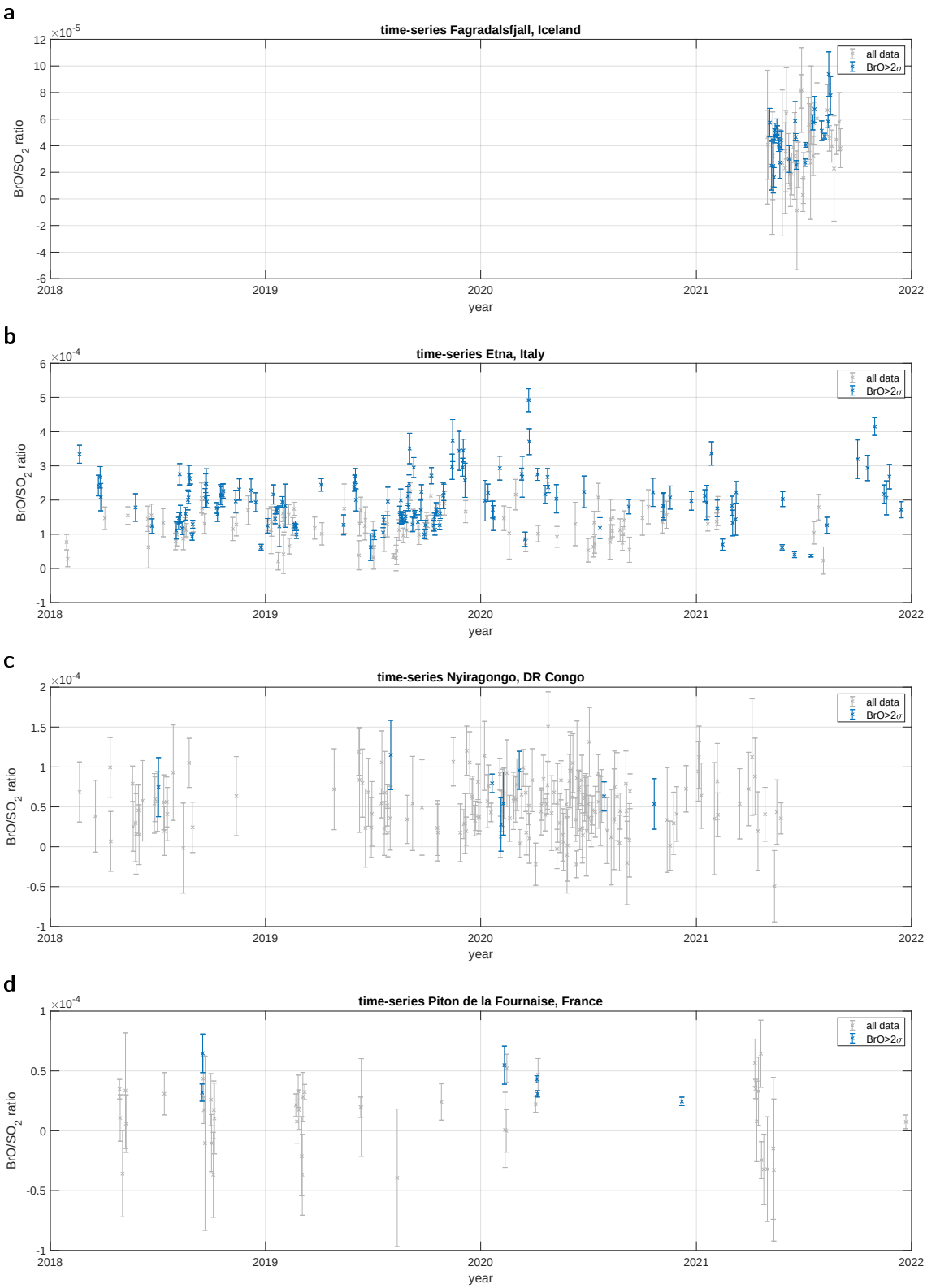


Figure 6.31: Time series of the BrO/SO_2 ratio for **a** Fagradalsfjall, Iceland, **b** Mt. Etna, Italy, **c** Nyiragongo, DR Congo, and **d** Piton de la Fournaise, France. Events, where BrO is above detection, are marked in blue.

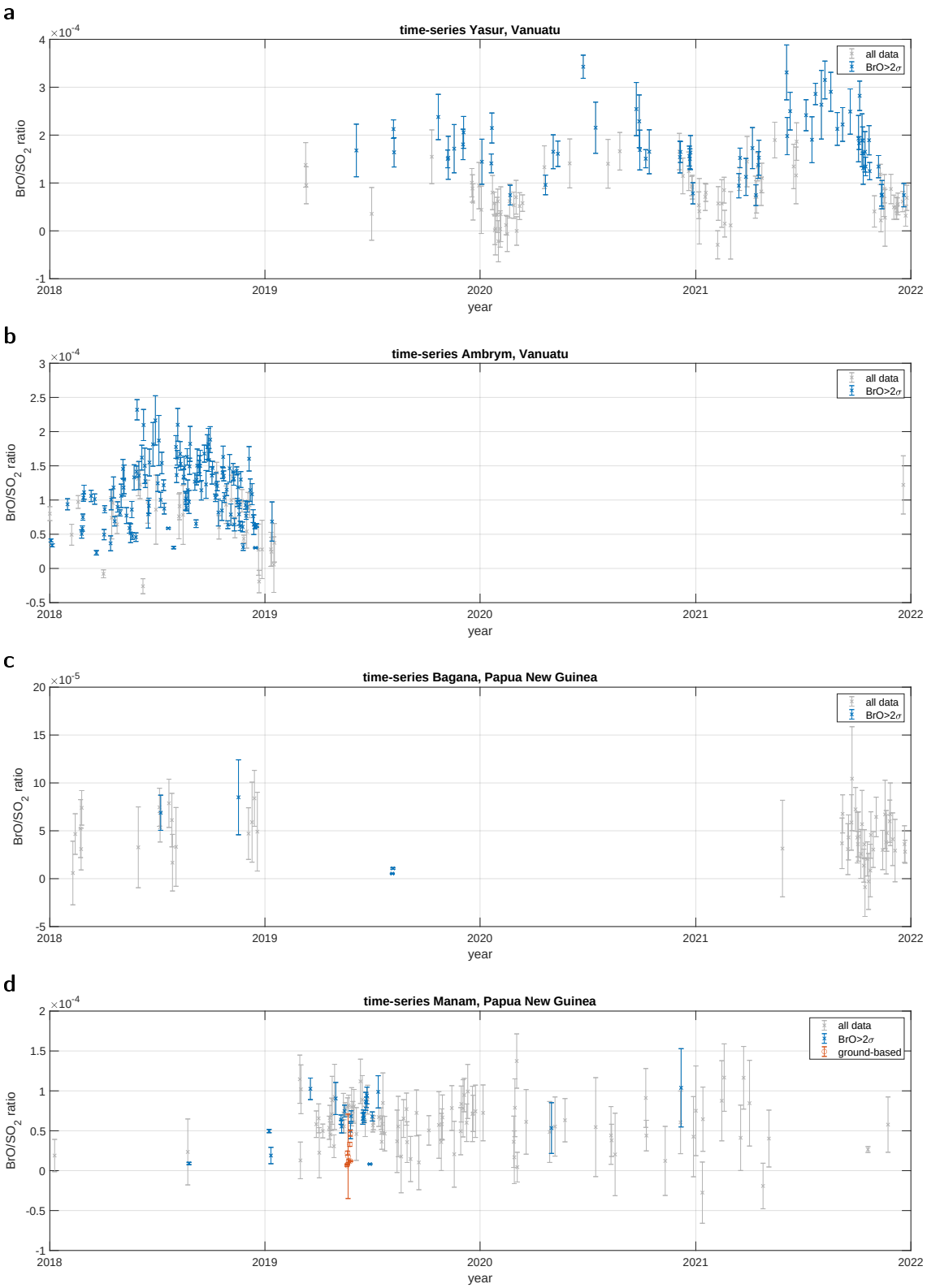


Figure 6.32: Time series of the BrO/SO_2 ratio for **a** Yasur, **b** Ambrym, both Vanuatu, **c** Bagana, and **d** Manam, both Papua New Guinea. Events, where BrO is above detection, are marked in blue.

Anak Krakatau, Indonesia has only 19 BrO/SO_2 ratios detected (see figure 6.33b). BrO/SO_2 ratios are between $1 - 2 \times 10^{-4}$ in 2018 and 2021, but are almost zero during December 2018. There was a strong shallow-water Surtseyan eruption from 22 to 29 December 2018 leading to a partial collapse of the volcanic island (GVP, 2019e). TROPOMI detects BrO/SO_2 ratios of $0 - 2 \times 10^{-5}$ during this eruption. While this could be an indication that similar to Mt. Etna the BrO/SO_2 ratio is lower during major eruptions, the reduction is much stronger. The fact that this coincides a dome collapse and the intrusion of water could indicate that this decrease in BrO/SO_2 ratio might be affected by these changes in the volcanic system.

Nishinoshima, Japan only had one eruption detected by TROPOMI in the time period: from March 2020 to August 2020 (GVP, 2020b). Activity in March through June was dominated by Lava flows, but little gas/ash emissions. Increasing ash and gas emission were reported during June 2020 persisting until 19 August 2020 (GVP, 2020b). BrO/SO_2 shows a decrease over the course of the eruption from 8×10^{-5} during the second half of June and first days of July to 5×10^{-5} during the end of July and throughout August 2020 (see figure 6.33d). This could indicate that BrO degases first and the BrO in the magma reservoir is thus depleted faster compared to SO_2.

Nevado del Ruiz, Colombia was also active throughout the complete time-series with intermittent ash and gas emission reported (Global Volcanism Program). BrO/SO_2 ratios are detected throughout the complete time-series varying between 3×10^{-5} and 1.9×10^{-4} (see figure 6.34b). There is a clear decrease in the BrO/SO_2 ratio from 1.4×10^{-4} to 7×10^{-5} starting in September 2018 and lasting until May 2019. A weaker and less pronounced decrease can be found on the turn of the years 2020/2021, where BrO/SO_2 ratios decrease from 1×10^{-4} in October 2020 to 6.5×10^{-5} in March 2021. For the rest of the measurement period, no trends can be observed. However, there is variation in the BrO/SO_2 ratio of more than 5×10^{-5}, which could imply changes on short time-scales not deducible from this data-set.

Sangay, Ecuador had a short phase of activity in the second half of 2018 (Global Volcanism Program) as well as a long reported activity phase from March 2019 until the end of the measurement period, with stronger activity in 2020 and 2021 (Global Volcanism Program). BrO/SO_2 ratio are found only during the second activity phase (figure 6.32c). In 2019 and 2020 BrO/SO_2 were at 1.1×10^{-4}. A subsequent slow decrease is observed until April 2021 with increased frequency of BrO/SO_2 detections, where it reaches BrO/SO_2 ratios as low as 4×10^{-5}. Finally, BrO/SO_2 ratios increase in the second half of 2021. The higher activity in 2021 thus coincides with lower BrO/SO_2 ratios, which could indicate that BrO is less efficiently released during more explosive activity. This is similar to the findings from the neighbouring Tungurahua volcano (Warnach et al., 2019), where high explosive activity coincided with a low BrO/SO_2 ratio between $2 - 6 \times 10^{-5}$ and low explosive activity was accompanied by higher BrO/SO_2 ratios in the range of $4 - 17 \times 10^{-5}$.

Taal, Philippines has several BrO/SO_2 ratios between 5×10^{-5} and 1.5×10^{-4}, but no trend can be observed (see figure 6.33c).

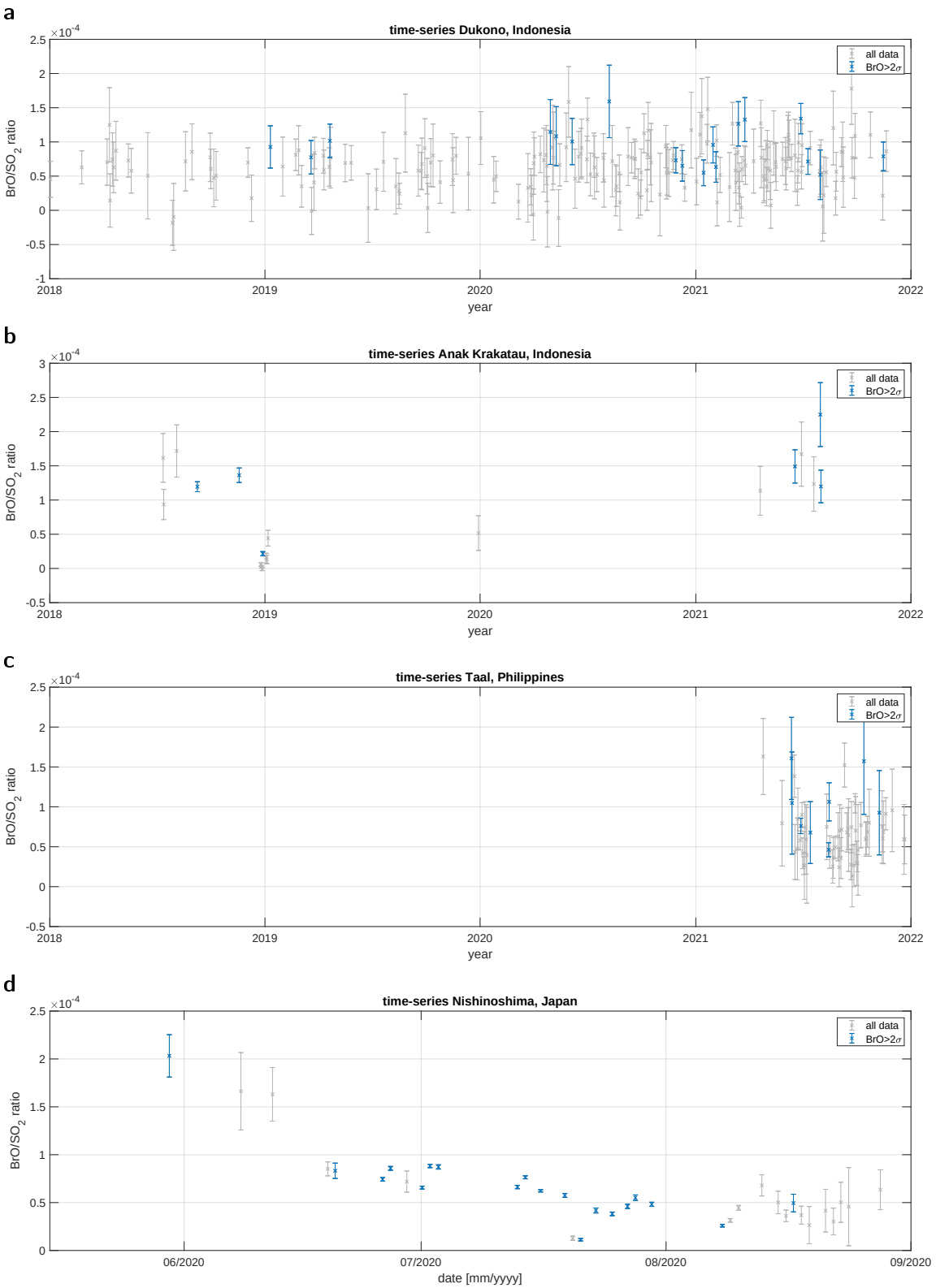


Figure 6.33: Time series of the BrO/SO_2 ratio for **a** Dukono, **b** Anak Krakatau, both Indonesia, **c** Taal, Philippines, and **d** Nishinoshima, Japan. Events, where BrO is above detection, are marked in blue.

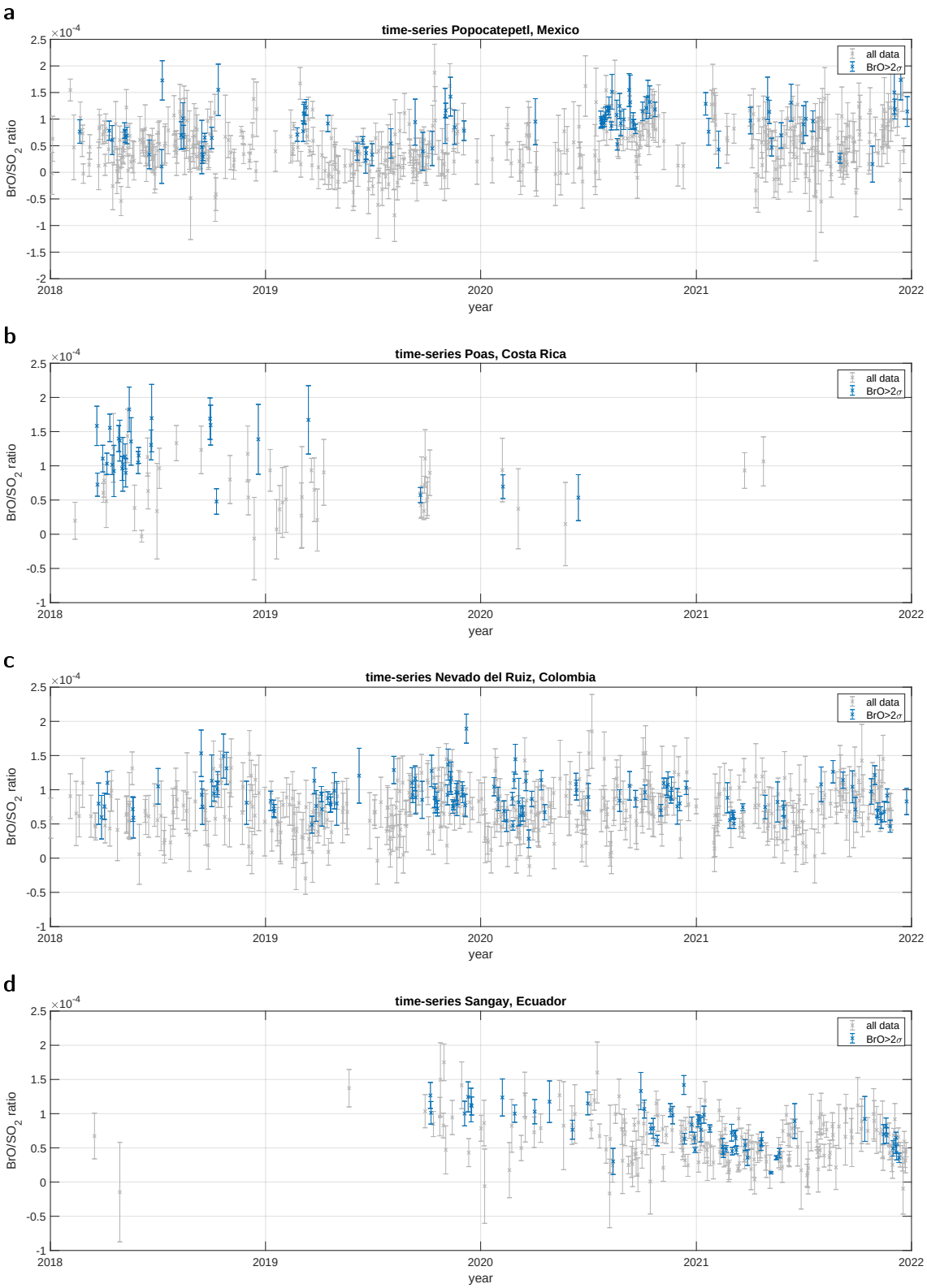


Figure 6.34: Time series of the BrO/SO_2 ratio for **a** Popocatepetl, Mexico, **b** Poas, Costa Rica, **c** Nevado del Ruiz, Colombia, and **d** Sangay, Ecuador. Events, where BrO is above detection, are marked in blue.

The Kamtchatka volcanoes, Russia and Kilauea, USA show no trend (see figure 6.35a-c).

There were several time series which offer information about changes in the BrO/SO_2 ratio over time. However, interpretation is very limited as there are many factors which can influence the interpretation. This originates from the fact that clear gradients in the BrO/SO_2 ratio are mostly observed for a part of the time-series. Furthermore, for most volcanoes volcanic parameter are not existing or hard to compare with the gas data.

Concluding, time-series reveal that the BrO/SO_2 catalogue offers the potential for several volcanoes to study the BrO/SO_2 ratio in comparison with volcanological parameter on long-term as well as and short-term variations. In addition TROPOMI successfully derived time-series for remote volcanoes, such as Yasur, where ground-based monitoring is difficult to set up.

6.8 Plume evolution over several days

In the previous sections only volcanic plumes in the vicinity (maximum SO_2 VCD < 300 km away from volcano) of the respective volcanoes where investigated, i. e. plumes with a mean plume age of typically less than several hours.[3] However, also older plumes can be observed, for instances plumes emitted ten hours prior to the satellite overpass as well as plumes which are observed over multiple consecutive days. These plumes are excluded from the previous data-sets, as they might be in a different chemical state compared to young plumes, close to the volcanic vent.

The comparison of the BrO/SO_2 ratio in plumes of different ages might offer insights into the depletion of BrO over time. The volcano with the most events is Mt. Etna, whose plumes can be tracked over several thousand kilometers even until Nepal, the Tibet region and Mongolia (see figure 6.2a), corresponding to plume ages of more than 2 days and up to 7000 km distance from the volcano. Assuming that the SO_2 is chemically stable on the time-scale of days, a depletion in the BrO/SO_2 ratio mostly corresponds to a depletion in BrO.

The BrO/SO_2 ratio is plotted against the distance in figure 6.36. It can be seen that the BrO/SO_2 ratio is highest very close to the volcano (8 - 10 km), where it is in the mean 2×10^{-4} and decreases reaching roughly 1.5×10^{-4} at 100 km distance. BrO/SO_2 ratio reaches 1.0×10^{-4} at rouhgly 1000 km and is only slightly lowering for larger distances. This suggests that BrO is decreasing faster in young plumes and slower in old plumes. However, BrO/SO_2 ratios are found at young plumes, hence there could be another reason that old plumes have lower BrO/SO_2 ratios. The TROPOMI data agree with the BrO/SO_2 ratios from ground-based measurements. The ground-based measurements also indicate the increase in BrO in the first 7 km, which is due to the initial BrO formation.

Concluding, there are two findings: BrO in plumes can be found in plumes of Mt. Etna of several days of age, i. e. radical bromine is recycled over a long time. Furthermore, reactive bromine content gets reduced more rapidly in the first hours compared to later stages. However, the measurements at far distances will predominantly correspond to events with a larger gas emission, i. e. stronger eruptive events. Thus a surpressed bromine release in strong events could the lower BrO/SO_2 ratio of plumes observed at far distances.

[3] Assuming a wind speed of 15 m/s the plume age at 300 km would be 5 1/2 hours.

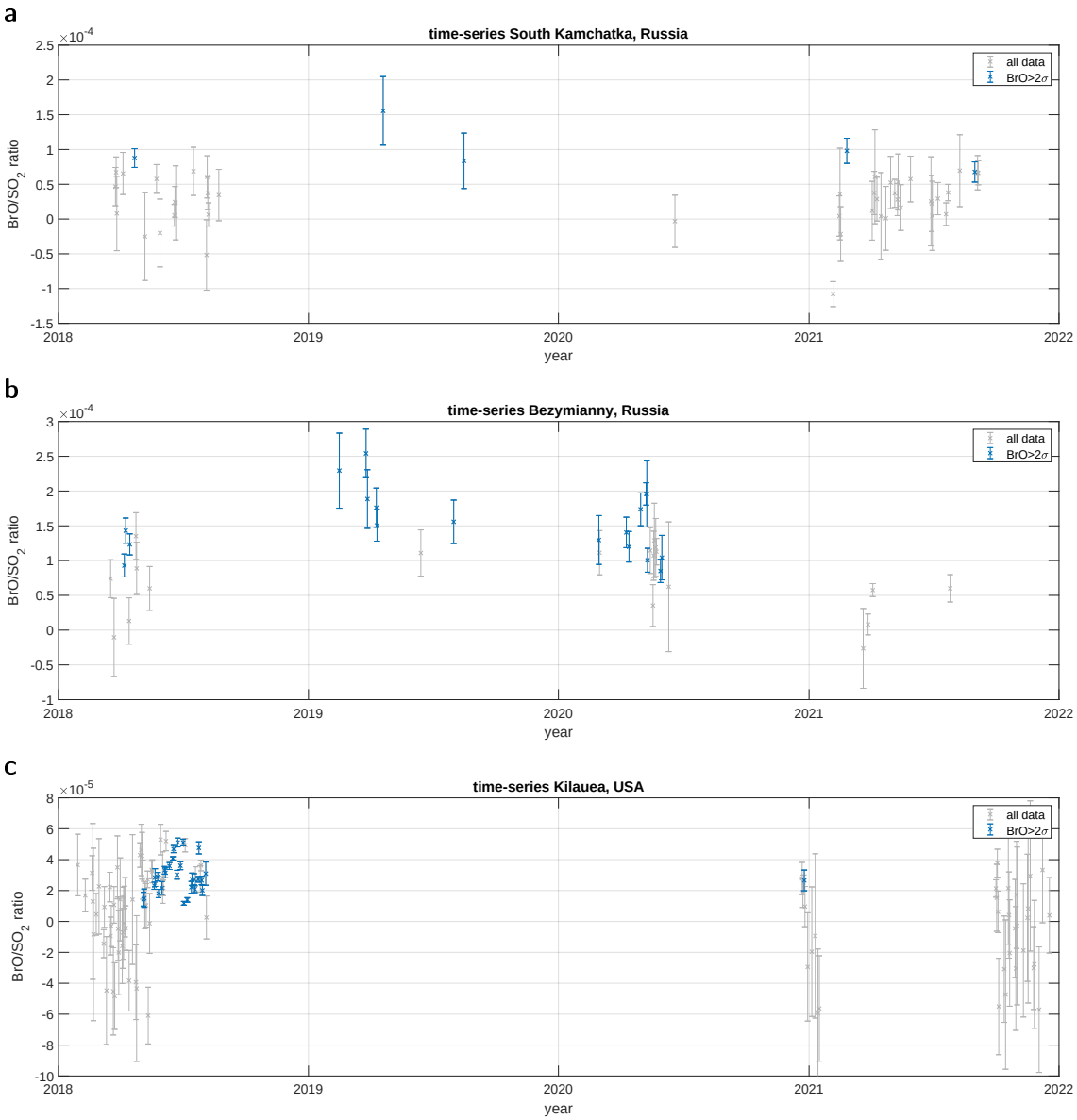


Figure 6.35: Time series of the BrO/SO_2 ratio for **a** »South Kamchatka«, **b** Bezymianny, both Russia, and **c** Kilauea, USA. Events, where BrO is above detection, are marked in blue.

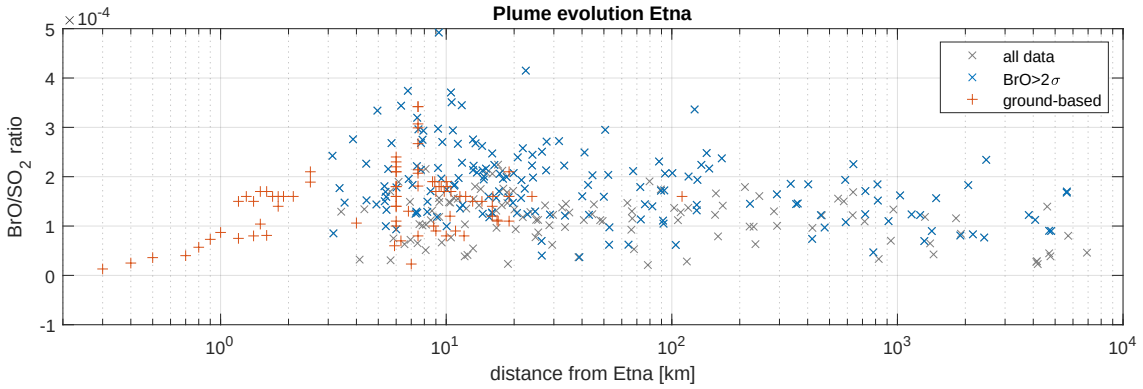


Figure 6.36: BrO/SO_2 ratios as a function of distance of the maximal SO_2 VCD from the volcanic vent for all events attributed to Mt. Etna. Events, where BrO exceeds the detection limit, are marked in blue. Ground-based data taken from Gutmann et al. (2018) are included (red +).

Other volcanoes

For other volcanoes there is not enough statistics to confirm or discard this finding. There are three volcanoes, for which drifting plumes can be observed up to 1000 km: Nishinoshima (Japan), Sierra Negra (Ecuador), and Fagradalsfjall (Iceland) (see figure 6.37). However, they either have a low number of events (Sierra Negra and Fagradalsfjall), or no significant decrease can be observed (Nishinoshima). In contrast to Mount Etna, the BrO/SO_2 ratio is roughly 5×10^{-5} for all three volcanoes and thus much lower. This further decreases the possibility to observe a significant change with distance.
There is also Ambrym and Ambae volcano (both Vanuatu, see figure 6.38), for which BrO/SO_2 ratio is lower for plume distances larger than 300 km. However, it is not clear if these plumes originate from Ambrym or Ambae, who have a different BrO/SO_2 signature. Hence no conclusion can be drawn.

6.9 Summary

Concluding, the automated plume algorithm detected more than 4000 plumes (events) and 1414 events with a clear detection of BrO. This can be attributed to the high spatial resolution and good spectral performance of TROPOMI, which allowed for a large number of detection of small, localized plumes. For 3581 events a linear BrO-SO_2 relation is found and a BrO/SO_2 ratio representative of the plume composition could be derived. Most of the events are located in the vicinity of volcanoes.
There are 43 volcanoes identified for which at least one event could be assigned to. 3063 of the 3581 events with a linear BrO/SO_2 ratio (85.5 %) had maximal SO_2 VCDs in less than 300 km distance from the volcanoes, with most of them (2780) being less than 100 km distant from the volcano. This allowed for the derivation of a catalogue of weighted mean BrO/SO_2 for each of the 43 volcanoes. Mean BrO/SO_2 ratios varied by almost one order of magnitude with ratios observed as low as 2.12×10^{-5} up to 1.53×10^{-4}. For hot spot volcanoes consistently low BrO/SO_2 ratios between $2 - 5 \times 10^{-5}$ where observed, while arc volcanoes show a large range of BrO/SO_2 ratios.
The data-set allowed time-series for many volcanoes. There are long and short term trends visible in the data-set. While the interpretation with respect to volcanic parameters is

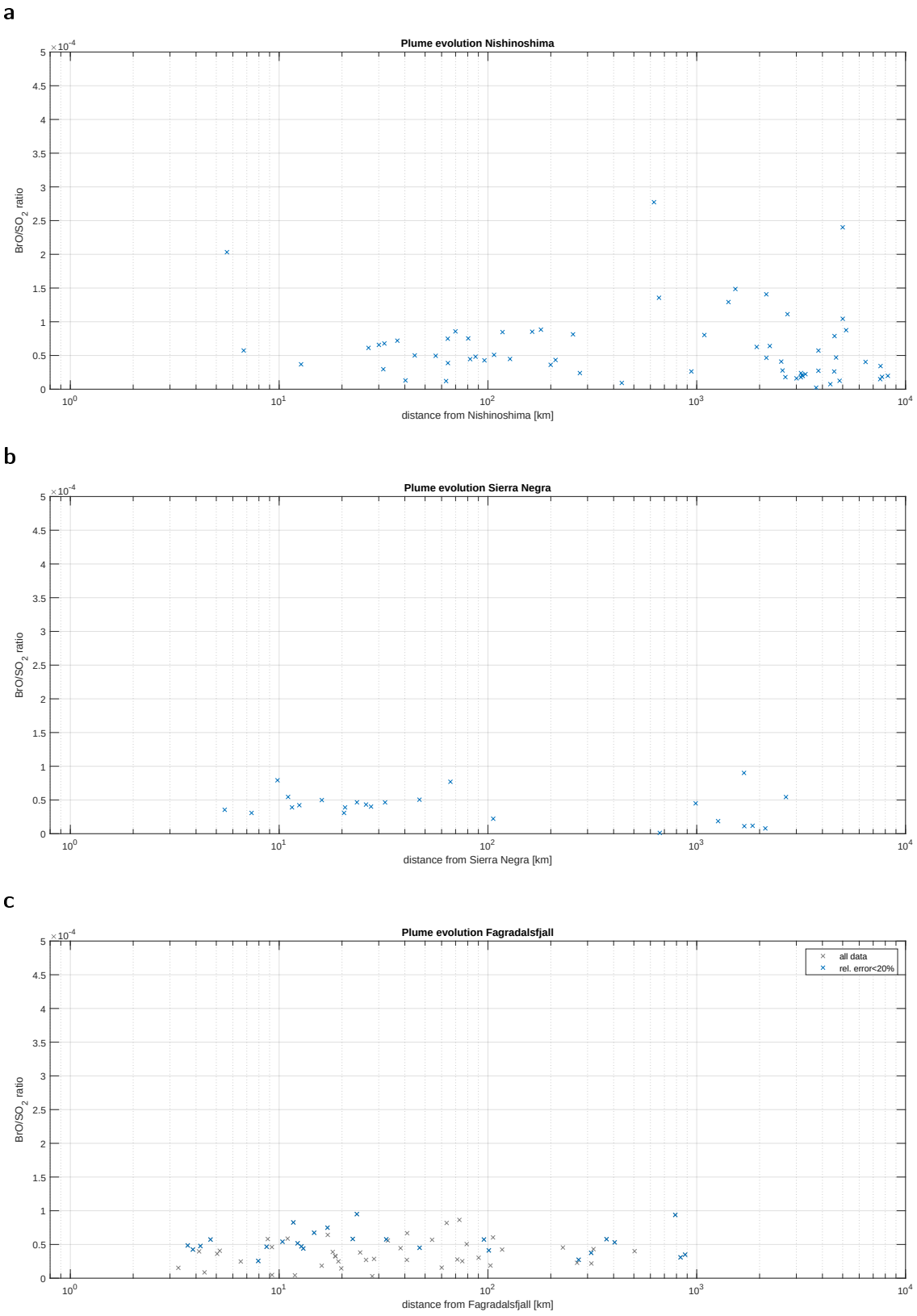


Figure 6.37: BrO/SO_2 ratios as a function of distance of the maximal SO_2 VCD from the volcanic vent for all events attributed to **a** Nishinoshima (Japan), **b** Sierra Negra (Ecuador), and **c** Fagradalsfjall (Iceland). Events, where BrO exceeds the detection limit, are marked in blue.

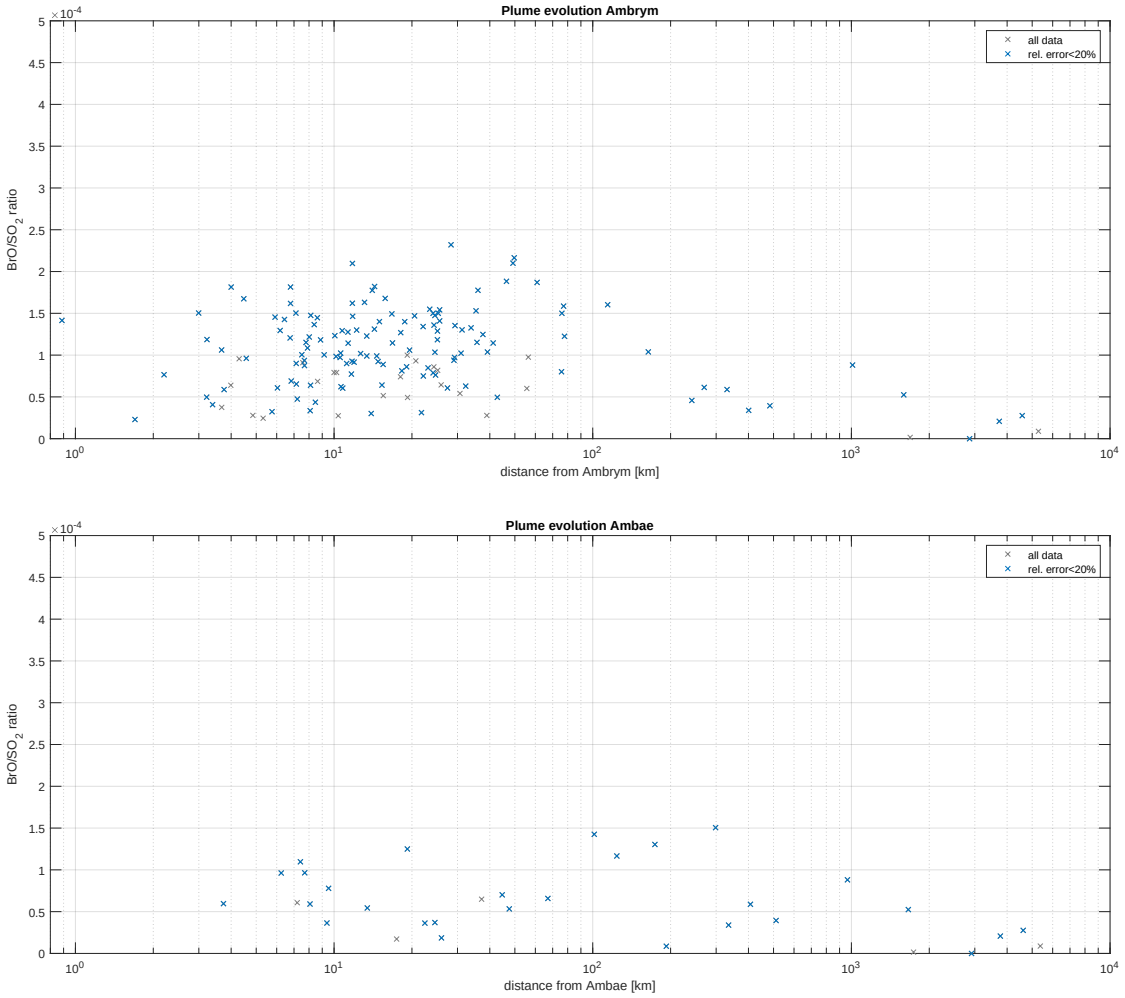


Figure 6.38: BrO/SO_2 ratios as a function of distance of the maximal SO_2 VCD from the volcanic vent for all events attributed to **a** Ambrym, and **b** Ambae, both Vanuatu. Events, where BrO exceeds the detection limit, are marked in blue.

limited, there are some hints of a decrease in BrO/SO_2 ratios during eruptions for Etna (Italy) and Nishinoshima (Japan). Some hints to seasonality are found for the Vanuatu volcanoes Yasur and Ambrym.
The BrO/SO_2 ratios agrees well with ground-based data and there was one day, for which a direct agreement with a ground-based measurement could be achieved. Comparison with previous satellite data (Hörmann et al., 2013), reveals a less positive bias of TROPOMI, which can be attributed to the better spatial resolution and signal-to-noise ratio of TROPOMI as well as improvements in the BrO-DOAS retrieval.

7 Chemistry inside a volcanic plume – Etna's plume on 25 December 2018

In chapter 6, 204 volcanic plumes (events) were detected, for which the BrO/SO_2 relation was determined to be highly non-linear.[1] One major factor for the non-linearity is the chemical evolution of bromine inside the plume (see section 1.2.2). The formation of BrO requires the inflow of ozone from ambient air. Furthermore, the BrO self-reaction continuously leads to the destruction of ozone. Both mechanisms mean that insufficient mixing-in of ozone can yield a decrease in the BrO concentration towards the center of the plume (Bobrowski et al., 2007). While this has been observed on multiple accounts (Bobrowski et al., 2007; General et al., 2015) and was confirmed by chemical model studies (Surl et al., 2021), these measurements were limited to the first 20 km downwind from the crater. For distances of several 100 km the volcanic plume was assumed to be completely mixed with ambient air and that BrO formation in such plumes would thus not be limited by ozone.

However, in the global plume survey there are two large eruptions described (Mt. Etna on 25 December 2018 and Raikoke eruption on 22 June 2019, see section 6.3), where a decrease in the BrO/SO_2 ratio was observed in the center of the plume compared to the edges even at distances up to 1000 km downwind from the crater. As the chemical reduction of SO_2 is much slower, SO_2 can be assumed chemically inert w. r. t. BrO in the first 1000 km downwind. Hence, it can be seen as a tracer for the amount of volcanic gas and the BrO/SO_2 ratio is proportional to the BrO mixing ratio inside the volcanic gas independent of the plume dispersion. Hence, the observed decrease in the BrO/SO_2 ratio towards the center is representative of a decrease in the BrO mixing ratio of the volcanic gas in the plume center, strongly suggesting that in plumes of large eruptions the bromine chemistry in volcanic plume is limited by the mixing in of O_3 even at distances where it should be completely mixed.

In this chapter the decrease in the observed BrO/SO_2 ratio towards the plume center is investigated in the context of plume chemistry. Firstly, a simplistic conceptual plume model of older dispersed plume parts is developed in section 7.1, based purely on chemical and physical parameters. The underlying idea is to determine how the concentration of multiple components (BrO and O_3), will evolve inside the plume considering only the interplay between physical mixing-in and chemical destruction of one component (O_3). A volcanic plume is then parametrized based on these conceptual findings in section 7.2, and an empirical model is constructed, which is used to reproduce the measured TROPOMI data observed in the Etna plume and deconstructs the components responsible for the limiting formation of BrO.

[1] A detailed list of the number of events that were determined to have a linear, weakly non-linear, and highly non-linear $BrO\text{-}SO_2$ relation is given in table 6.2.

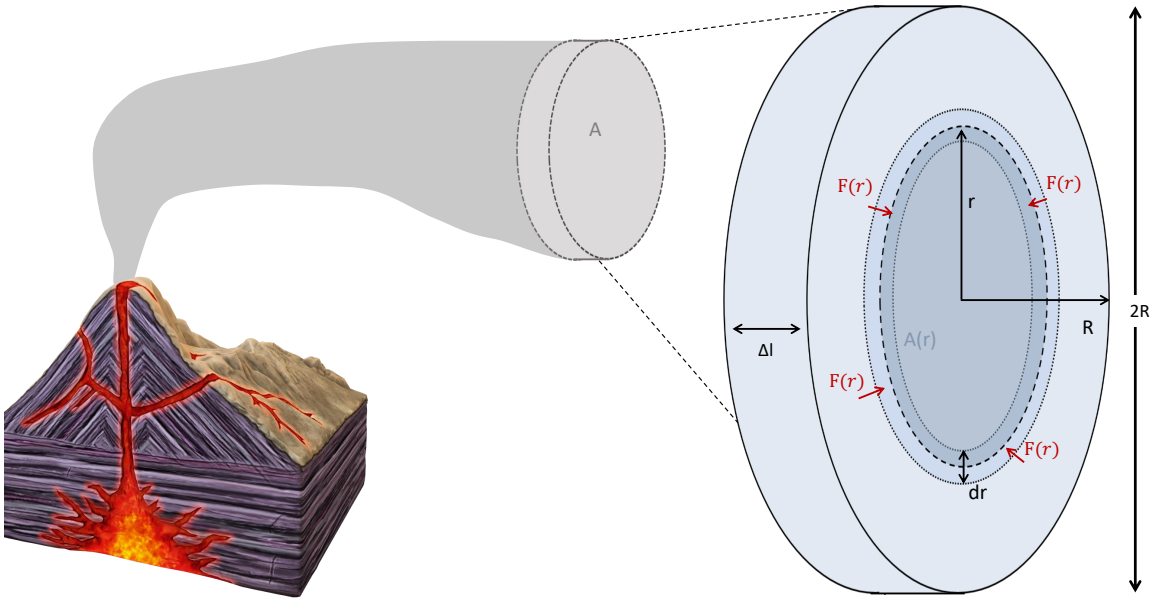


Figure 7.1: Sketch of the conceptual model. A volcanic plume slice of length Δl, radius R, and cross section A is taken. The plume slice is assumed to be in steady state for every shell cylinder with radius $r < R$ and depth of dr, which is subject to an O_3 flux F(r) (red arrows) entering the shell cylinder from the outer surface.

7.1 Conceptual Model of the O_3 – BrO interaction in a volcanic plume

The exponential BrO formation in the volcanic plume (detailed information is given in section 1.2.2) is diminished by self reactions of BrO molecules (red lines in figure 1.4):

$$\mathrm{BrO} + \mathrm{BrO} \rightarrow \mathrm{Br_2} \tag{R20}$$
$$\mathrm{BrO} + \mathrm{BrO} + \mathrm{h}\nu \rightarrow 2\mathrm{Br} \tag{R21}$$

In the early plume this will slow down the bromine activation (»initial BrO-formation«), as BrO atoms cannot activate another HBr. In addition, these reactions can lead to rapid O_3 destruction together with reaction R8 - R10 yielding the cycle:

$$\mathrm{BrO} + \mathrm{BrO} \rightarrow \mathrm{Br_2} \tag{R22}$$
$$\mathrm{Br_2} + \mathrm{h}\nu \rightarrow 2\,\mathrm{Br} \tag{R23}$$
$$2\,\mathrm{Br} + 2\,\mathrm{O_3} \rightarrow 2\,\mathrm{BrO} + 2\,\mathrm{O_2} \tag{R24}$$
$$\mathrm{h}\nu + 2\,\mathrm{O_3} \rightarrow 3\,\mathrm{O_2} \tag{R25}$$

In an evolved plume (i. e. where the »initial BrO formation« in the bromine explosion – see cycle reaction R13 – is not dominant any more), the self-reaction of BrO is the main driver of the BrO and O_3 interaction (reaction R25) through the following cycle (for a more detailed description, see subsection »limited BrO formation« in section 1.2.2):
The destruction of O_3 can thus be described by:

$$\frac{d}{dt}[\mathrm{O_3}] = -2k[\mathrm{BrO}]^2 \tag{7.1}$$

where k is the reaction constant for the reaction BrO + BrO (reaction R22). Since the time constants of reactions R20 and R21 (i.e. the time required to convert BrO to Br or Br_2) from the reaction BrO + BrO is roughly 20 s, while the back-reaction Br + O_3 (reaction R24) converts Br into BrO within roughly 1 s (at a typical O_3 concentration of 40 ppb), reactive bromine will predominately exist as BrO (rather than Br or Br_2). Therefore, the back-reaction R24 can be neglected in equation 7.1. This holds true as long as O_3 is sufficiently abundant, i. e. the reaction Br + O_3 is only limited by Br. Typical concentrations of Br inside a plume, which is several minutes old, are in the range of < 1 ppb, while O_3 concentrations in the ambient atmosphere at normal pressure is ≈ 40 ppb. Hence, neglecting the back-reaction R24 in equation 7.1 is reasonable and only invalid if O_3 is depleted to several ppb.
In a dense plume, with a high BrO concentration the reaction cycle R25 can lead to very fast and efficient O_3 destruction. Hence, BrO formation is limited, if the reaction cycle R25 is destroying O_3 faster than the in-flux of O_3.

A conceptual model is proposed, based on the assumptions, that:

- the plume is steady state at any stage and location of the plume. More specific, every part of the plume is in chemical equilibrium based on equation 7.1.
- ambient ozone is the only source of ozone. Thus, the in-flux of ozone is only governed by the ambient ozone concentration and diffusion.
- for the sake of simplicity the bromine concentration inside the plume is assumed to be constant.

Thus, the ozone concentration inside the plume is governed by the interplay of the mixing-in of ambient ozone and the counteracting destruction of ozone depending on the BrO concentration.
For the conceptual model a thin slice orthogonal to the direction of propagation of the plume is considered. This slice can be assumed to be a cylinder with radius R and length Δl in direction of the plume propagation. As the processes are radially symmetric, it is convenient to use a radial parameter r and the cylinder can be separated into different shell cylinder of width dr (see figure 7.1).
The in-flux of O_3 (in molecules per second) into this shell cylinder is then defined as:

$$F_{O_3}(r) = -D_T \cdot \frac{d}{dr}[O_3(r)] \cdot S(r) \tag{7.2}$$

where $[O_3(r)]$ is the ozone concentration at radius r, D_T the turbulent diffusion coefficient, and S(r) the surface of the cylinder shell $S(r) = 2\pi r \Delta l$.
In equilibrium, the in-flux of O_3 $F_{O_3}(r)$ must be equal to the destruction of O_3 in each cylinder shell:

$$F_{O_3}(r) = \frac{d}{dt}O_3(r) \tag{7.3}$$

The destruction (in molecules per second) inside the cylinder shell during the time interval dt is determined from equation 7.1 expanded to:

$$\frac{d}{dt}O_3(r) = \frac{d}{dt}[O_3(r)] \cdot V(r) = -2k[BrO]^2 \cdot A(r) \cdot \Delta l \tag{7.4}$$

with the cylinder volume $V(r) = A(r) \cdot \Delta l$ and the cylinder cross section area $A(r) = \pi r^2$.
Inserting equation 7.2 and equation 7.4 into equation 7.3, yields:

$$F(r) = \frac{d}{dt}\mathrm{O_3}(r) \tag{7.5}$$

$$\Rightarrow -D_T \cdot \frac{d}{dr}[\mathrm{O_3}(r)] \cdot 2\pi r \cdot \Delta l = -2k \cdot [\mathrm{BrO}(r)]^2 \cdot \pi r^2 \cdot \Delta l \quad | \ (-1)\ \frac{1}{\pi r \Delta l} \tag{7.6}$$

$$\Leftrightarrow D_T \cdot \frac{d}{dr}[\mathrm{O_3}(r)] \cdot 2 = 2k \cdot [\mathrm{BrO}(r)]^2 \cdot r \quad | \ \frac{1}{2D_T} \tag{7.7}$$

$$\Leftrightarrow \frac{d}{dr}[\mathrm{O_3}(r)] = \frac{2k \cdot [\mathrm{BrO}(r)]^2 \cdot r}{2D_T} \quad | \ K = \frac{k}{D_T} \tag{7.8}$$

$$\Leftrightarrow \frac{d}{dr}[\mathrm{O_3}(r)] = K \cdot [\mathrm{BrO}(r)]^2 \cdot r \tag{7.9}$$

Where $K = \frac{k}{D_T}$ is the ratio of the BrO + BrO reaction rate k and the turbulent diffusion coefficient D_T.
The O_3 concentration $[O_3](r)$ can then be formulated depending on a boundary conzentration $[O_3](R)$ at radius R in the following way and then specified using equation 7.9:

$$[\mathrm{O_3}](r) = [\mathrm{O_3}](R) - \int_r^R \frac{d}{dr'}[\mathrm{O_3}](r')dr' \tag{7.10}$$

$$= [\mathrm{O_3}](R) - K \int_r^R [\mathrm{BrO}(r')]^2 \cdot r' dr' \tag{7.11}$$

The boundary condition is that the O_3 concentration at the plume edge is the ambient air concentration, i. e. $[O_3(R)] = O_{3,ambient}$. Furthermore, the radius $R_0 \in [0, R]$ can be defined as the radius where the ozone concentration is zero, i. e. $[O_3](R_0) = 0$. This is the radius at which the destruction of O_3 exceeds the local in-flux of O_3.

$$0 = [\mathrm{O_3}](R_0) = [\mathrm{O_3}](R) - K \int_{R_0}^R [\mathrm{BrO}(r')]^2 \cdot r' dr' \tag{7.12}$$

$$\Rightarrow [\mathrm{O_3}](R) = K \int_{R_0}^R [\mathrm{BrO}(r')]^2 \cdot r' dr' \tag{7.13}$$

$$\Rightarrow [\mathrm{O_3}](R) = \frac{k}{D_T} \int_{R_0}^R [\mathrm{BrO}(r')]^2 \cdot r' dr' \tag{7.14}$$

If $R_0 = 0$, then BrO chemistry is not limited by O_3 throughout the complete plume. However, if $0 < R_0 < R$ then the plume center from 0 to R_0 will be depleted both in O_3 (and possibly also in BrO). The fraction of the plume where BrO chemistry is not limited by O_3, can then be defined as $f_0 = \frac{R-R0}{R} = 1 - \frac{R_0}{R}$ or $R_0 = R - f_m \cdot R = R \cdot (1 - f_m)$, $f_m \in [0, 1]$:

$$[\mathrm{O_3}](R) = \frac{k}{D_T} \int_{R \cdot (1-f_m)}^R [\mathrm{BrO}(r')]^2 \cdot r' dr' \tag{7.15}$$

Assuming a constant [BrO] concentration (i. e. independent of r) for radii, where BrO is not limited by O_3 (i. e. for $r \in [R(1 - f_m), R]$), the integral in equation 7.12 can be calculated as:

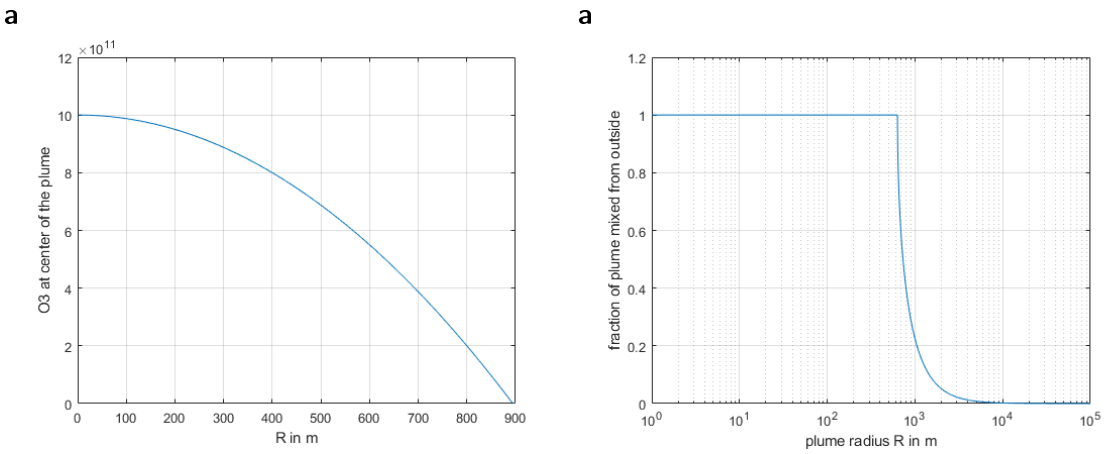


Figure 7.2: Results of the conceptual model: **a** O_3 concentration at the center of the plume and **b** the radial fraction of the mixed plume as a function of the plume radius.

$$[O_3](R) = \frac{k[BrO]^2}{D_T} \int_{R\cdot(1-f_m)}^{R} r' dr' \tag{7.16}$$

$$\Rightarrow [O_3](R) = \frac{k[BrO]^2}{D_T} \frac{1}{2} \left[R^2 - (R\cdot(1-f_m))^2\right] \tag{7.17}$$

$$\Rightarrow [O_3](R) = \frac{k[BrO]^2}{D_T} \frac{R^2}{2} \left[1 - (1-f_m)^2\right] \tag{7.18}$$

$$\Rightarrow 1 - (1-f_m)^2 = \frac{2[O_3](R) D_T}{k[BrO]^2 R^2} \tag{7.19}$$

$$\Rightarrow f_m = 1 - \sqrt{1 - \frac{2[O_3](R) D_T}{k[BrO]^2 R^2}} \tag{7.20}$$

Hence, $f_m = 1$, i. e. the complete plume is not limited by O_3 mixing-in, if:

$$\frac{2[O_3](R) D_T}{k[BrO]^2 R^2} = 1 \tag{7.21}$$

and the plume is partially limited by O_3 mixing-in if $f_m < 1$, i. e.

$$\frac{2[O_3](R) D_T}{k[BrO]^2 R^2} < 1 \tag{7.22}$$

Inserting ambient O_3 concentration at $[O_3](R) = 10^{12}\,cm^{-3}$, $D_T = 10^5\,cm$, k= $2.5 \times 10^{-13}\,cm^3\,s^{-1}$ and a BrO concentration of $10^{10}\,cm^{-3}$ yields, that O_3 is not depleted in the center of the plume for a plume radius below roughly 900 m. The dependency of the O_3 concentration at the plume center with the plume radius is plotted in figure 7.2a. The factor f_m is plotted in figure 7.2b. It shows that the fraction of the radius where O_3 is mixed in, decreases sharply for $R > 900\,m$ and almost no O_3 is mixed in for plumes of the size of 10 km.
For this plot however, the BrO concentration is assumed constant, i. e. a larger plume means that the total bromine inside the plume is increasing. Thus, the increase with radius does not reflect the temporal evolution of a dispersing plume, where the mass is conserved.

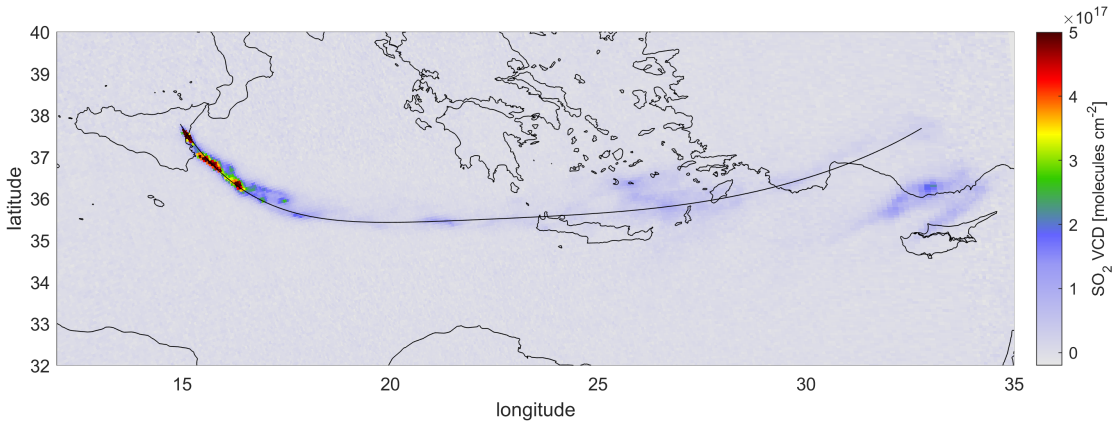


Figure 7.3: Map of SO_2 VCD of the eruption of Mount Etna on 25 December 2018. Black line: trajectory of the plume center along the plume direction based on the maximum SO_2 VCDs.

It must be noted that this is a conceptual approach. It assumes that the O_3 concentration is large enough to maintain the reaction cycle reaction R16. As BrO concentrations in typical volcanic plume is maximal 1 ppb, this can be assumed to occur at similar O_3 concentrations (i. e. at less than 2.5 % of ambient O_3 concentrations). If this is the case, the equilibration equation 7.5 will become non-linear. However, this is occurring very close to R_0, hence this will only affect a very small portion of the plume and will neither change the qualitative nor the quantitative result.

Evolution over time: So far a static plume slice was modeled. From a lagrangian perspective, the evolution in time of a volcanic plume can be described by the evolution of time of each slice. Over time the plume will diffuse following the dispersion coefficient D_T. The diffusion coefficient is different in horizontal and lateral direction. Thus, over time the plume radius R will increase and can be described by R(t). The assumption of a steady state of the plume can still be made for plume slices where the expansion in radius is smaller than the time it takes the plume to re-equilibrate.

7.2 Empirical model of Mt. Etna's plume

In order to investigate the data from the Etna eruption on 25 December 2018, a change of basis from lat-lon coordinates to plume coordinates has to be done. These plume coordinates are: (1) the direction along the plume's advection direction (from now on called »along plume dimension«) and (2) the direction perpendicular to the plume's advection direction (from now on called »across plume dimension«).
Firstly, the trajectory of the center of the plume is calculated. The center of the plume is assumed where SO_2 is maximal. The pixels with maximum SO_2 VCDs on the lat-lon grid are interpolated by a 6^{th} order polynomial. The resulting trajectory is plotted as a black line in figure 7.3. The trajectory is then the first dimension (along plume dimension) of the new bases, whereas the second base is then calculated by the line locally perpendicular to the trajectory (across plume dimension). Both new coordinates are sampled on a $0.01° \approx 1.1$ km grid. The resulting SO_2 VCD, BrO VCD, and BrO/SO_2 ratios for the first 1000 km downwind from the volcano are plotted in figure 7.4.

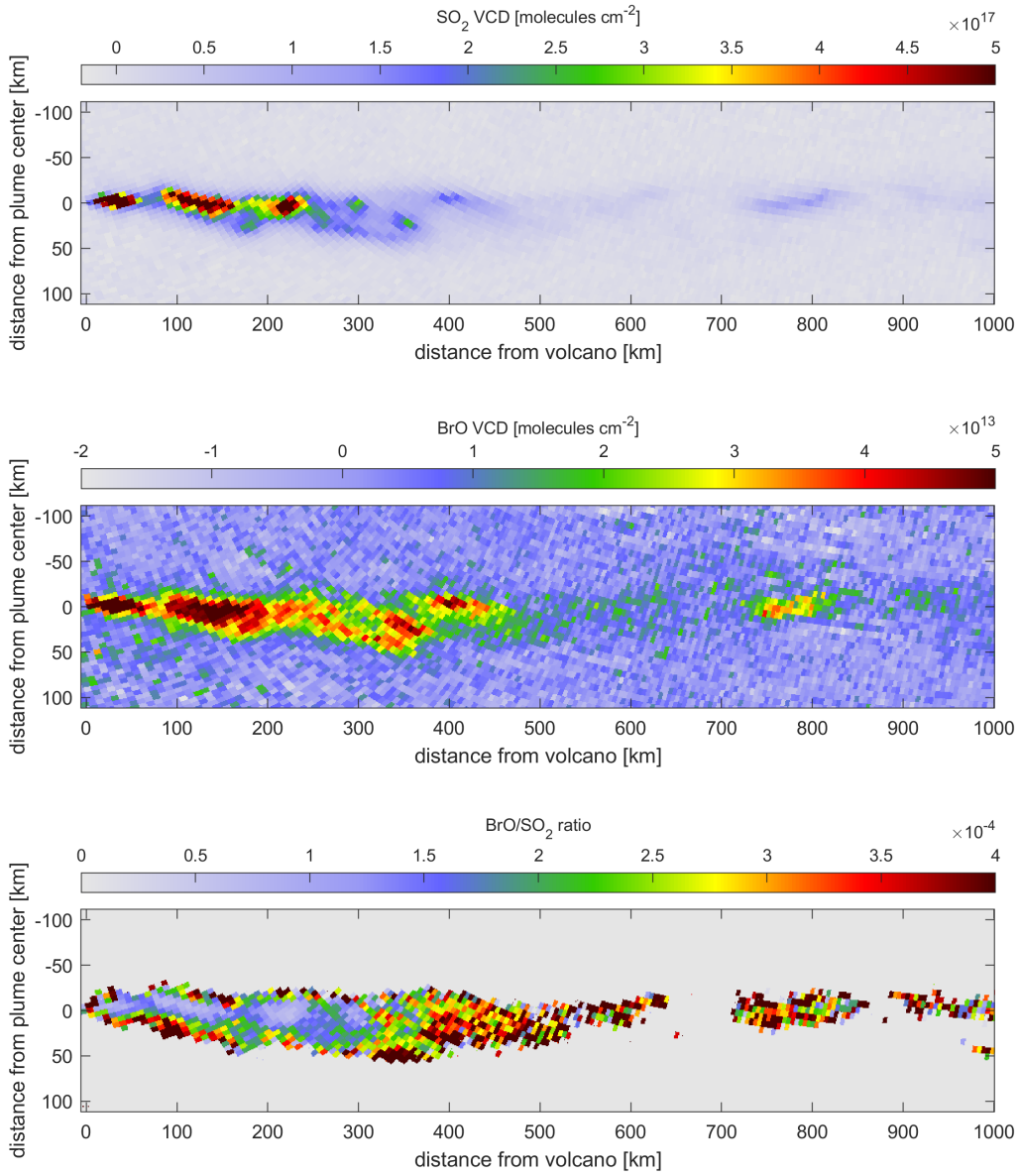


Figure 7.4: Rotated maps of the eruption of Mount Etna on 25 December 2018 on the bases along and perpendicular to the plume. *Top:* SO_2 VCD, *middle:* BrO VCD, and *bottom:* BrO/SO_2 ratio for pixels where SO_2 VCD exceeds 2×10^{16} molecules cm^{-2}.

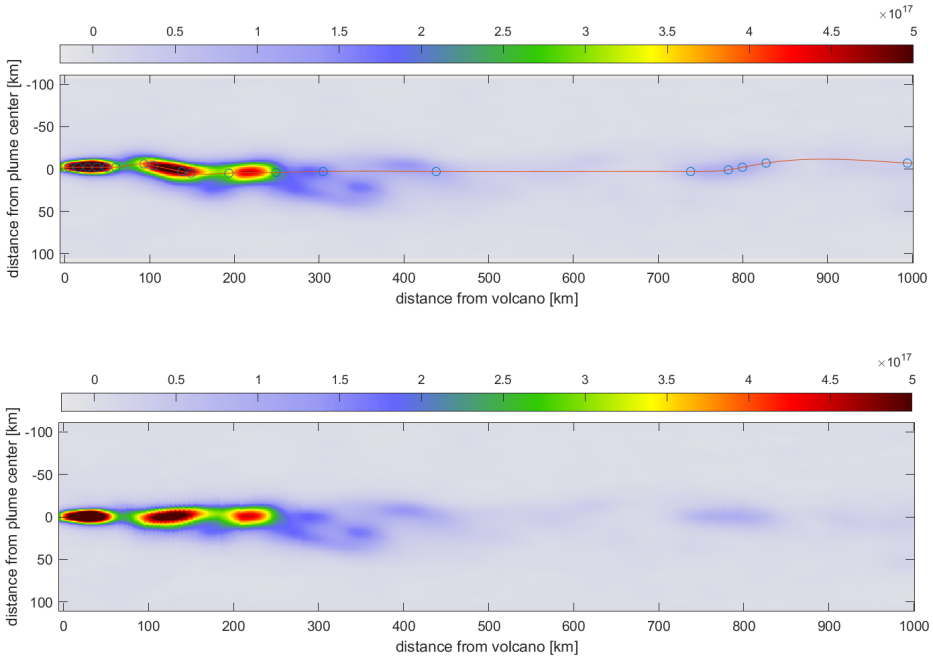


Figure 7.5: Rotated maps of SO_2 VCDs of the eruption of Mount Etna on 25 December 2018. The data are averaged over 20 km along the plume direction and 5.6 km perpendicular to the plume direction. *Top:* SO_2 VCD, inputs into the local spline correction (blue circles) ans the resulting spline (red line) *bottom:* SO_2 VCD map after the spline correction.

In a second step, the rotated gridded data are averaged with 20 km along the plume direction and 5.6 km across the plume direction. The latter corresponds to the mean size of the pixel dimensions of TROPOMI, so that the resolution across the plume direction is not lowered by averaging. The resulting SO_2 VCD, BrO VCD, and BrO/SO_2 ratio for the first 1000 km downwind from the volcano are shown in figure 7.6. In this process, local small deviations of the maximal SO_2 VCDs from the plume center are corrected by a spline (see figure 7.5). The resulting data-set, depicted in figure 7.6 is thus a collection of slices similar to the one sketched in figure 7.1, each at a different plume along dimension (plume propagation direction). TROPOMI is scanning the slice and it only measures the vertically integrated column, i. e. there is no information on the vertical distribution inside the plume inherent in the data. Nevertheless, in the following, an empirical model of the 2-dimensional plume slice is developed based purely on this data-set of vertical columns of SO_2 and BrO.

For the empirical model of the plume slices, the following assumptions are made:

- The SO_2 concentration can be described by a 2-dimensional gaussian distribution.
- The plume is fully mixed on the outside, i. e. the BrO/SO_2 ratio on the outside is not limited by chemistry.
- Inside the plume O_3 gradually decreases and the BrO/SO_2 ratio can also decrease.
- The BrO concentration can be described by the product of the SO_2 concentration and a term describing the effectiveness of mixing (i. e. the BrO/SO_2)

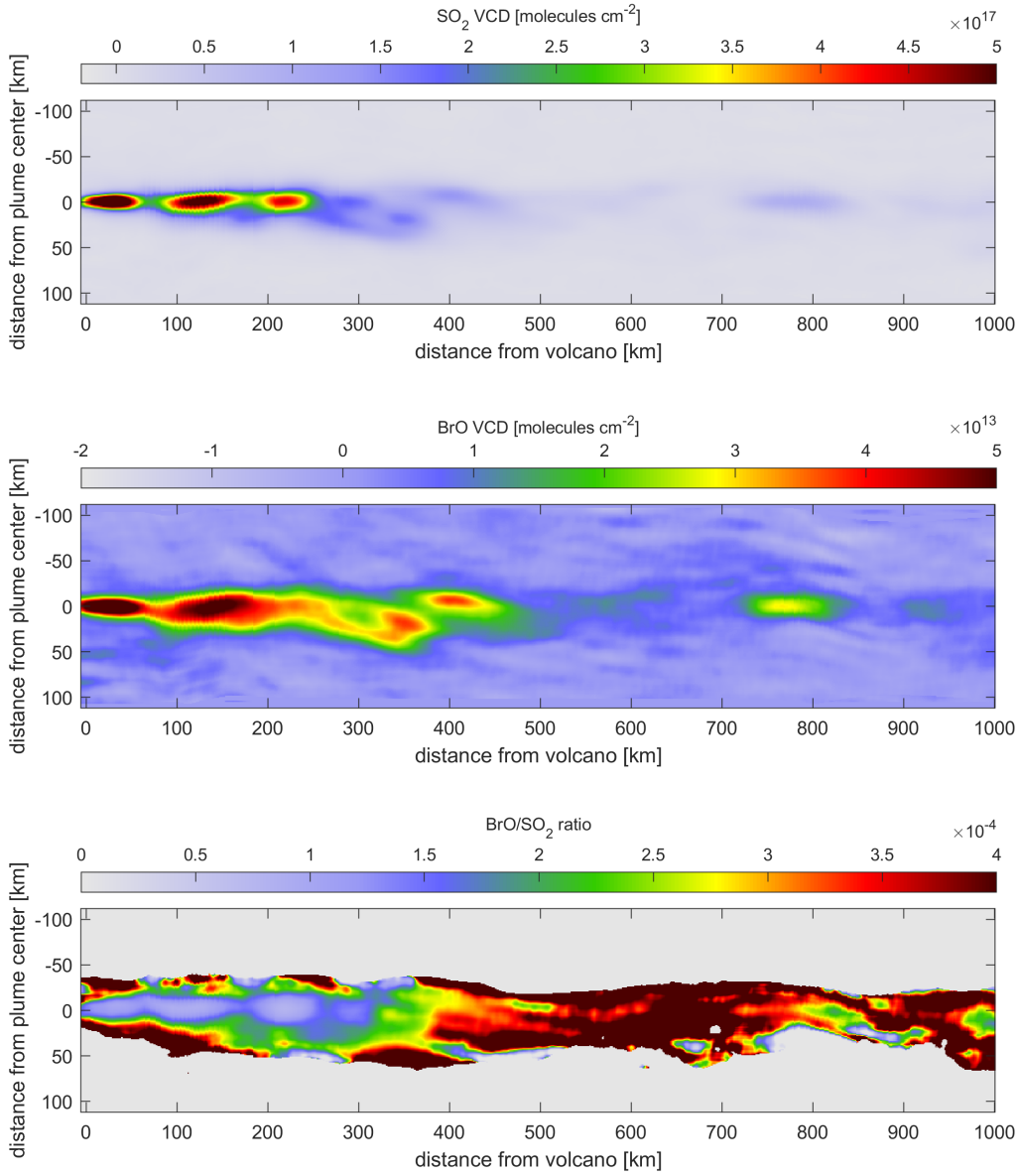


Figure 7.6: Rotated averaged maps of the eruption of Mount Etna on 25 December 2018. The data are averaged over 20 km along the plume direction and 5.6 km perpendicular to the plume direction. *Top:* SO_2 VCD, *middle:* BrO VCD, and *bottom:* BrO/SO_2 ratio for pixels where SO_2 VCD exceeds 2×10^{16} molecules cm^{-2}.

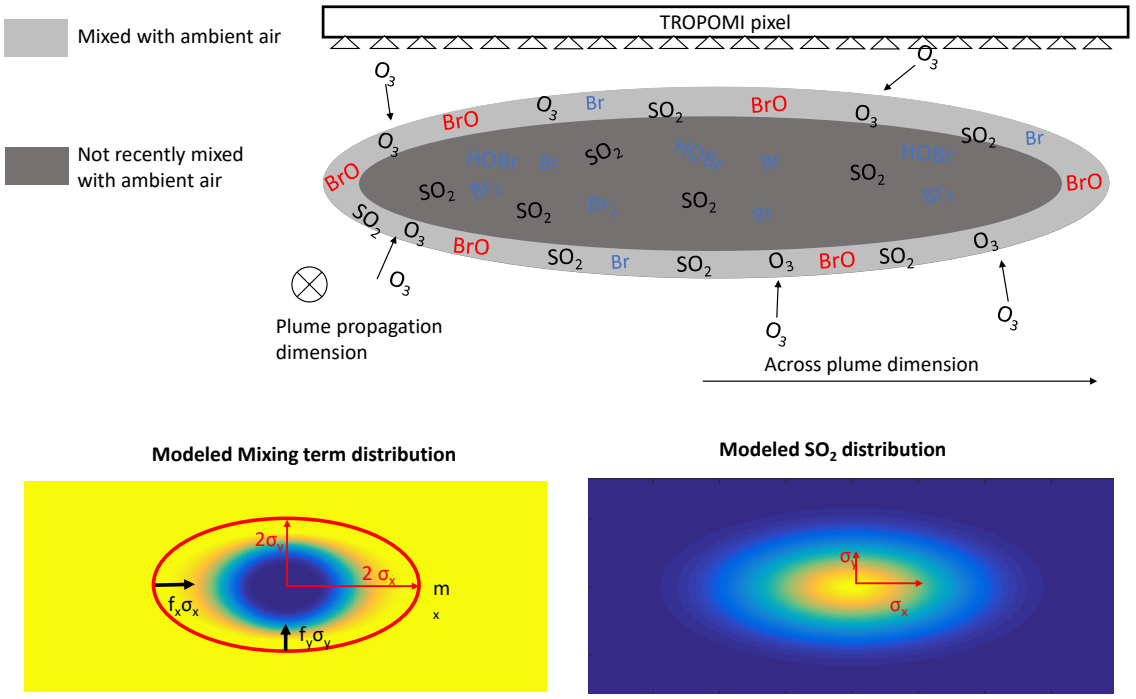


Figure 7.7: Sketch of the plume cross-section (slice). The plume cross-section can be seen as an ellipse, which is filled with SO_2 and bromine. O_3 is mixed in, and gets destroyed forming BrO. Thus, it will only reach a certain distance from outside. This outer layer (light grey), will contain BrO, while the part not recently mixed with ambient air (dark gray) does not. TROPOMI observes the integrated column. This can be reproduced by assuming a 2d-Gaussian SO_2 concentration representative of the gas concentration (parameterized by σ_x, σ_y) and a mixing term, which describes the reduction of BrO plume mixing ratio relative to the outside. The mixing term is 1 on a ellipse with axis $2\sigma_x$ and $2\sigma_y$ and the reduction towards the center is parameterized by f_x and f_y.

7.2.1 Construction of the model

The idea behind the empirical model is to reconstruct the measured BrO VCD based on the distribution of the *BrO concentration*, the *SO_2 concentration*, a *mixing term* – which describes how much BrO production is allowed by O_3 – and the *BrO/SO_2 ratio on the plume edge*. The SO_2 distribution is described by a 2d-Gaussian distribution with horizontal and vertical plume extent σ_x and σ_y. The mixing term is constructed based on σ_x, σ_y and the mixing parameters f_x and f_y.

The BrO concentration is modeled as the product of the SO_2 concentration, a mixing term M, and the BrO/SO_2 ratio under mixed conditions:

$$[BrO](x,y) = [\mathrm{SO_2}](x,y) \cdot \mathrm{M}(x,y) \cdot \left(\frac{\mathrm{BrO}}{\mathrm{SO_2}}\right)_{\mathrm{mixed}} \tag{7.23}$$

The SO_2 concentration accounts for the concentration of volcanic gas. The product with the mixed BrO/SO_2 ratio would yield the BrO concentration if BrO chemistry is not limited by the mixing-in of ambient air. Hence, the mixing term should be defined as one at the plume edge and decrease towards the center of the plume.

The SO_2 distribution – and hence the gas concentration – is assumed to be a 2d-elliptical Gaussian distribution, parametrised in the following way:

$$[\mathrm{SO_2}](x,y) = \frac{A}{2\pi\sigma_x\sigma_y} \cdot e^{-\frac{1}{2}\left(\frac{x^2}{\sigma_x^2}+\frac{y^2}{\sigma_y^2}\right)} \tag{7.24}$$

with the horizontal standard deviation σ_x and the vertical standard deviation σ_y and the amplitude A.

The mixing term M(x,y) should be one outside of the elliptical plume, and should decrease towards the center of the ellipse. This is parametrised as a Gaussian decrease of elliptical shape. The Gaussian decrease strength is determined by a sigma parameter σ_m, which should be different in x-and-y direction. σ_m is parametrized by the two mixing length m_x and m_y. It should be defined in a way so that it varies with the angular component ν of the ellipse, and does not change if the radial component u is changes (see figure 7.8 on how the elliptical coordinates are defined). Thus σ_m should depend only on ν and is defined in the following:

$$\sigma_{mixing}(\nu) = \sigma_m(\nu) = m_y \cdot sin(\nu)^2 + m_x \cdot cos(\nu)^2 \tag{7.25}$$

using trigonometric equation $1 = \sin(\nu)^2 + \cos(\nu)^2$:

$$\sigma_{mixing}(\nu) = \sigma_m(\nu) = sin(\nu)^2 \cdot (m_y - m_x) + m_x \tag{7.26}$$

This means that the σ_m will be constant along the hyperbolical elliptical coordinate u (see figure 7.8), i.e. the equivalent to the radial coordinate in a circle, and will change with ν, the equivalent to the angular component.
The extent of the plume is assumed to be an ellipse with the semi-major axes $a_x = 2\sigma_x$ and the semi-minor axis $a_y = 2\sigma_y$. The Mixing term M(x,y) should decrease from this (a_x, a_y)-ellipse towards its center. This decrease is defined as a gaussian shape based on σ_{mixing}. The mixing term M(x,y) is then defined by a linear Gaussian distribution $M(x,y) =$

$G(f(x,y),\sigma_m)$, with the scaling σ_m, where f(x,y) is defined in a way, that it has its maximum at the ellipse and decreases towards the center:

$$M(x,y) = \exp\left(-\frac{f(x,y)}{2\sigma_m(\nu)^2}\right) \tag{7.27}$$

f(x,y) thus has to be a a function which is 0 at the (a_x, a_y)-ellipse and decreases towards the center. This is achieved by a modification of the ellipse function:

$$f(x,y) = \sqrt{\left(\frac{x}{a_x}\right)^2 + \left(\frac{y}{a_y}\right)^2} - 1 \tag{7.28}$$

f(x,y) is 0 on the (a_x, a_y)-ellipse and will decrease to -1 in the center of the ellipse. Thus, M(x,y) can be defined as a Gaussian field G(f(x,y)):

$$M(x,y) = \exp\left(-\frac{\left(\left(\frac{x}{a_x}\right).^2 + \left(\frac{y}{a_y}\right)^2 - 1\right)^2}{2\sigma_m(\nu)^2}\right) \tag{7.29}$$

yielding a field which is 1 at the (a_x, a_y)-ellipse and will decrease towards the center based on the sigma-field $\sigma_m(\nu)$:

$$M(x,y) = \exp\left(-\frac{\left(\left(\frac{x}{a_x}\right).^2 + \left(\frac{y}{a_y}\right)^2 - 1\right)^2}{2sin(\nu)^2 \cdot (m_y - m_x) + m_x}\right) \tag{7.30}$$

Lastly, $\sigma_m(\nu)$ must be transformed into cartesian coordinates. For this first the focal point c of the ellipse is defined as the difference of the squares of the axis of the ellipse, i. e.

$$c = \sqrt{(a_x)^2 - (a_y)^2} = \sqrt{(2\sigma_x)^2 - (2\sigma_y)^2} \tag{7.31}$$

Furthermore, a substitute variable $s = \frac{x^2+y^2-c^2}{2}$ is defined.
The elliptical coordinate ν is depending on the focal point c of the ellipse and the substitute variable s in the following way:

$$\sin(\nu) = \sqrt{\frac{-s + \sqrt{s^2 + c^2 \cdot y^2}}{c^2}} \tag{7.32}$$

This relation can be derived, a derivation can be found for instance in (Sun, 2017).
The resulting mixing term is then:

$$M(x,y) = \exp\left(-\frac{\left(\left(\frac{x}{a_x}\right).^2 + \left(\frac{y}{a_y}\right)^2 - 1\right)^2}{2 \cdot \left(\frac{-s+\sqrt{s^2+c^2 \cdot y^2}}{c^2}\right) \cdot (m_y - m_x) + m_x}\right) \tag{7.33}$$

Lastly, to prevent values <1 outside of the (a_x, a_y)-ellipse, i. e. all values with:

$$\sqrt{\left(\frac{x}{a_x}\right)^2 + \left(\frac{y}{a_y}\right)^2} > 1 \tag{7.34}$$

are set to 1.

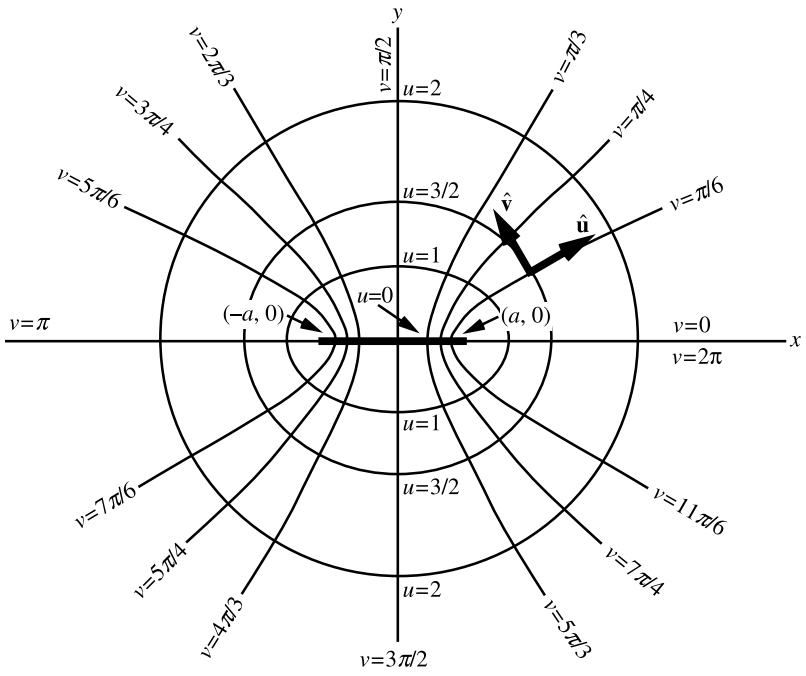


Figure 7.8: Sketch of the elliptical coordinate system. The elliptical coordinates ν and u and focal point a. The base ellipse is defined for $u = 1$. Graphic taken from `https://mathworld.wolfram.com/EllipticCylindricalCoordinates.html`.

SO_2 and BrO VCD: In a last step the modeled SO_2 and BrO VCDs can be calculated by the integration of the SO_2 and the BrO concentration respectively in y-direction.

7.2.2 Model workflow

The empirical model is done independently for each slice along the plume propagation. The model workflow is depicted in figure 7.9. The only information used is the SO_2 as well as the BrO VCD distribution of this slice, i. e. the distribution along the across plume dimesion (perpendicular to the plume propagation direction). These are depicted in the yellow field in figure 7.9).
The input parameters are:

- The horizontal plume extent σ_x
- The maximal SO_2 VCD
- The across plume dimension.

The horizontal plume extend as well as the maximal SO_2 VCD are derived as the σ and the amplitude A of a Gauss pre-fit of the SO_2 VCD distribution. In principle this pre-fit could be included also in the main model fit. However, for this first test, it is done separately.
The model fits both SO_2 VCD as well as BrO VCD to the modeled SO_2 and BrO VCD. The fit parameters for the model are:

- The vertical plume extent σ_y
- The horizontal mixing parameter f_x

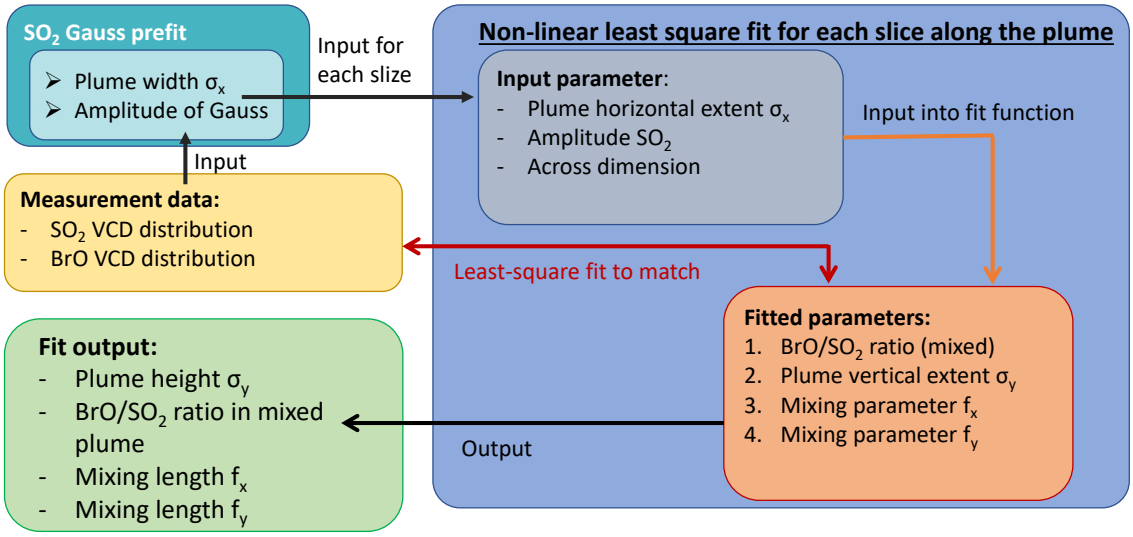


Figure 7.9: Workflow of the empirical model.

- The vertical mixing parameter f_y
- The BrO/SO_2 ratio under mixed conditions

These parameters are varied in a least-square fit to best match the measured SO_2 and BrO VCD distribution in the across plume dimension.
The result will be then the parameters σ_y, f_x, f_y, from which the BrO concentration, the mixing term, which ideally is an indicator for the O_3 concentration in the plume, and most importantly the BrO/SO_2 ratio excluding the plume chemistry influence can be calculated.

SO_2 Gauss prefit: (turquois field in figure 7.9) As the gas is dispersed trough diffusion, the gas distribution – and hence the SO_2 VCD – will have a Gaussian shape perpendicular to its propagation. TROPOMI observes the integrated column into vertical (y-) direction. Hence, the shape of the SO_2 VCD should follow a Gaussian shape in horizontal (x-) direction. In a Gaussian pre-fit, the SO_2 VCD is modeled by a Gaussian 1d distribution, retrieving the standard deviation σ_x as well as the amplitude A:

$$SO_2(x)_{modeled} \frac{A}{\sqrt{2\pi}\sigma_x} \cdot \exp\left(-\frac{x^2}{2\sigma_x^2}\right) \tag{7.35}$$

Initialization: The initial parameters, the boundaries and the normalization factor for the four model parameter of the least-square fit are given in table 7.1. Initial parameters are selected as typical expected values, the lower and upper boundary is each a factor of ten different from the initial parameter. One exception is the upper boundary for the σ_y, which should not be larger that the horizontal plume extent σ_x, as the focal points of of the ellipse would else be imaginary. Furthermore a vertical plume stretching 10 - 20 km (which is a typical horizontal plume extend in the Etna plume) is not physical. The range for the BrO/SO_2 ratio is also not a factor of ten different from initial parameter. The upper boundary is set to 2×10^{-3}, in order to be a factor of 2 above the highest detected BrO/SO_2 ratio (1×10^{-3} Gutmann et al., 2018) and the lower boundary is set to zero.

Table 7.1: Initialization of the four input parameter of the least-square fit of the empirical model. The initial parameters, lower and upper boundaries as well as the normalization is given.

Parameter	Initial parameter	lower boundary	upper boundary	normalization factor
σ_y	$\sigma_x/2$	$\sigma_x/20$	σ_x	1
f_x	0.1	0.01	1	0.1
f_y	0.1	0.01	1	0.1
$[BrO/SO_2]_{mixed}$	1×10^{-4}	0	2×10^{-3}	1×10^{-4}

The normalization is chosen so that all parameters are input in the order of magnitude of one. This is needed, as the BrO/SO_2 ratio is four orders of magitude below the mixing parameters. The same is done with the input parameter, i. e. the SO_2 amplitude is scaled by a factor of 1×10^{-17} so that the amplitude is in the range of 0.1...10.

7.2.3 Model results

The modeled SO_2 VCD, BrO VCD and the resulting BrO/SO_2 ratio for the first 1000 km are plotted in figure 7.10 (right column) as well as the measured data (left column) respectively. The SO_2 VCD distribution as well as the BrO VCD distribution show good agreements for plume regions with SO_2 center columns exceeding 3×10^{17}. For the other regions, the model plume is much more dispersed. The fact that the SO_2 VCD also shows this effect means that the Gauss prefit did not succeed in fitting the plume slice accurately.
The BrO/SO_2 pattern is generally also modeled quite well. The lower ratios below 1×10^{-4} in the center of the plume corresponding to the high SO_2 VCDs from 0 - 240 km are reproduced well. The BrO/SO_2 ratio on the edges is similar to the ones observed, both reaching above 4×10^{-4}. However, the gradient from the center BrO/SO_2 ratio is much steeper in the modeled distribution compared to the measured distribution. Additionally, the maximum BrO/SO_2 ratio of the modeled plume reaches slightly further towards the center. This indicates that the model predicts that mixing is unperturbed further towards the center and then a steeper decrease from the unperturbed edges to the perturbed center.
The parameters resulting from the fit are plotted in figure 7.11. The red line in each plot corresponds to the initial parameter, the blue line to the resulting parameter and the grey lines represent the boundaries. It can be seen that there are many regions where the first three fitting parameters jump to extreme values. This means that the fit did not work there, i. e. for distances above 850 km or for 160 - 190 km. While the maximal SO_2 VCD for the region of 850 km distance is very low, i. e. the signal is too weak for the fit to work, the region 160 - 190 has maximal SO_2 VCDs of more than 3×10^{17} molecules cm^{-2}. However, it can be seen that the SO_2 distribution is not well represented by the initial Gauss pre-fit figure 7.10. Hence, the SO_2 distribution is not correctly modeled.
For the other regions, it can be seen that the horizontal mixing parameter f_x is always at the lower boundary. This means that the horizontal gradient in the BrO/SO_2 ratio is very steep, as can be seen in the BrO/SO_2 distribution.
The mixed BrO/SO_2 ratio ranges between $2 - 5 \times 10^{-4}$ for the regions where the fit worked. This is in the region where it would be expected.
One example slice of the plume close to the volcanic vent (in 26.7 km distance) is plotted in figure 7.12. The comparison of the measured and modelled SO_2 VCD, BrO VCD and the

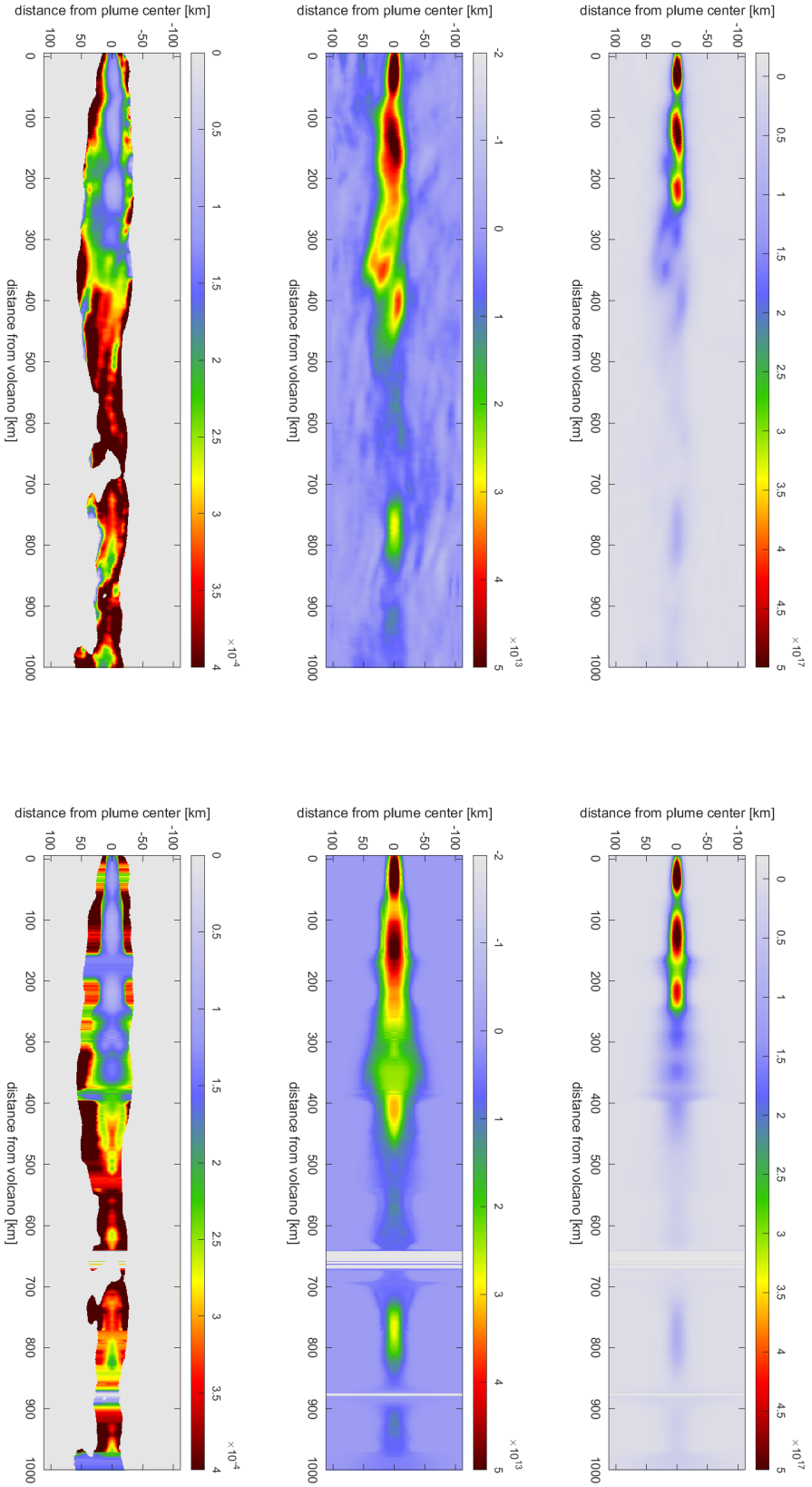


Figure 7.10: Results of the empirical model. SO_2 VCD (top), BrO VCD (middle), and the BrO/SO_2 ratio (bottom). The input data (left column) and the model results (right column). The BrO/SO_2 ratio is calculated only for pixel where the SO_2 VCD exceeds 1×10^{16}.

BrO/SO_2 ratio show good agreement. While the general U-shape of the measured BrO/SO_2 ratio is matched well by the model, it does not reproduce the very high BrO/SO_2 ratios of the measured data. However, these very high ratios are potentially influenced by a systematic offset in the BrO VCD (see also the subsection »Potential influence by systematic BrO« below and figure 7.14), and thus might be a better estimate of the BrO/SO_2 ratio at the unmixed plume edge.

The concentration distribution (figure 7.12, right column) reveals a strong decrease in the mixing term, which almost directly decreases to zero. This is stronger in the x-direction (as reflected in the very low f_x values). This yields a somewhat unlikely distribution of the BrO concentration (figure 7.12, lower right). This is most likely caused by the fact that the SO_2 distribution is not completely matching the measured VCD distribution (as the SO2 distribution is prescribed in the fit, it cannot reduce differences between model and measurement). The model fit tries to account for these minor differences by modifying the mixing term (as it cannot modify the SO_2 concentration) and thus yields the unlikely distribution of the BrO concentration. Nevertheless, the mixed BrO/SO_2 ratio is potentially less affected by this.

Another example is the slice at 793.9 km distance figure 7.13. There the difference between the BrO/SO_2 ratio in the center and the edge is much weaker. The BrO distribution and the center BrO/SO_2 ratio is well reproduced by the model (figure 7.13, left column). However, the increase in the BrO/SO_2 ratio towards the edges in underestimated by the model. The mixing term and the BrO concentration (figure 7.13, right column), indicate a plume which is well mixed, with minimal mixing terms of 0.6 predicted. Both examples show that the proposed model can reproduce the measured BrO VCD and BrO/SO_2 ratio in plume slices with different mixing status. However, there are large uncertainties remaining.

Potential influence by systematic BrO

A systematic offset in the BrO VCDs could in principle produce an increase in the BrO/SO_2 towards the edges, as the BrO column would increase relatively more for lower columns. While systematic influences in the BrO VCDs were investigated and minimized (see section 4.3.1), such influences cannot be ruled out.

In order to determine this effect, the BrO VCD is systematically lowered for a plume cross section at 26 km distance from the volcano (see figure 7.14). This slice is selected, as it shows elevated BrO VCDs which are not reproduced in the modeled BrO VCD distribution.

It can be seen that the measured BrO/SO_2 ratio is increasing steadily to the edges. As expected, the increase towards the edges is diminished when subtracting a constant BrO column. However, the decrease at the very center of the plume prevails, even when reducing the BrO column by 5×10^{12} molecules cm^{-2}. Potential systematic influences exceed 3×10^{12} molecules cm^{-2} only for polar spring ozone depletion events, which have not been observed in correspondence with volcanic plumes, and are mostly in the range of $1 - 2.5 \times 10^{12}$ molecules cm^{-2} (see table 4.6).

This implies that parts of the observed increase in the BrO/SO_2 ratio towards the edges could be caused by systematic influences onto the BrO VCDs, but the observed gradient towards the center cannot be caused by systematic influences. The model (plotted by the black line in figure 7.14) recreates the BrO/SO_2 center gradient quite well, but not the outer gradient. This is caused by the assumption in the model that the BrO/SO_2 is constant for distances of more than $2\sigma_x$ from the center of the plume.

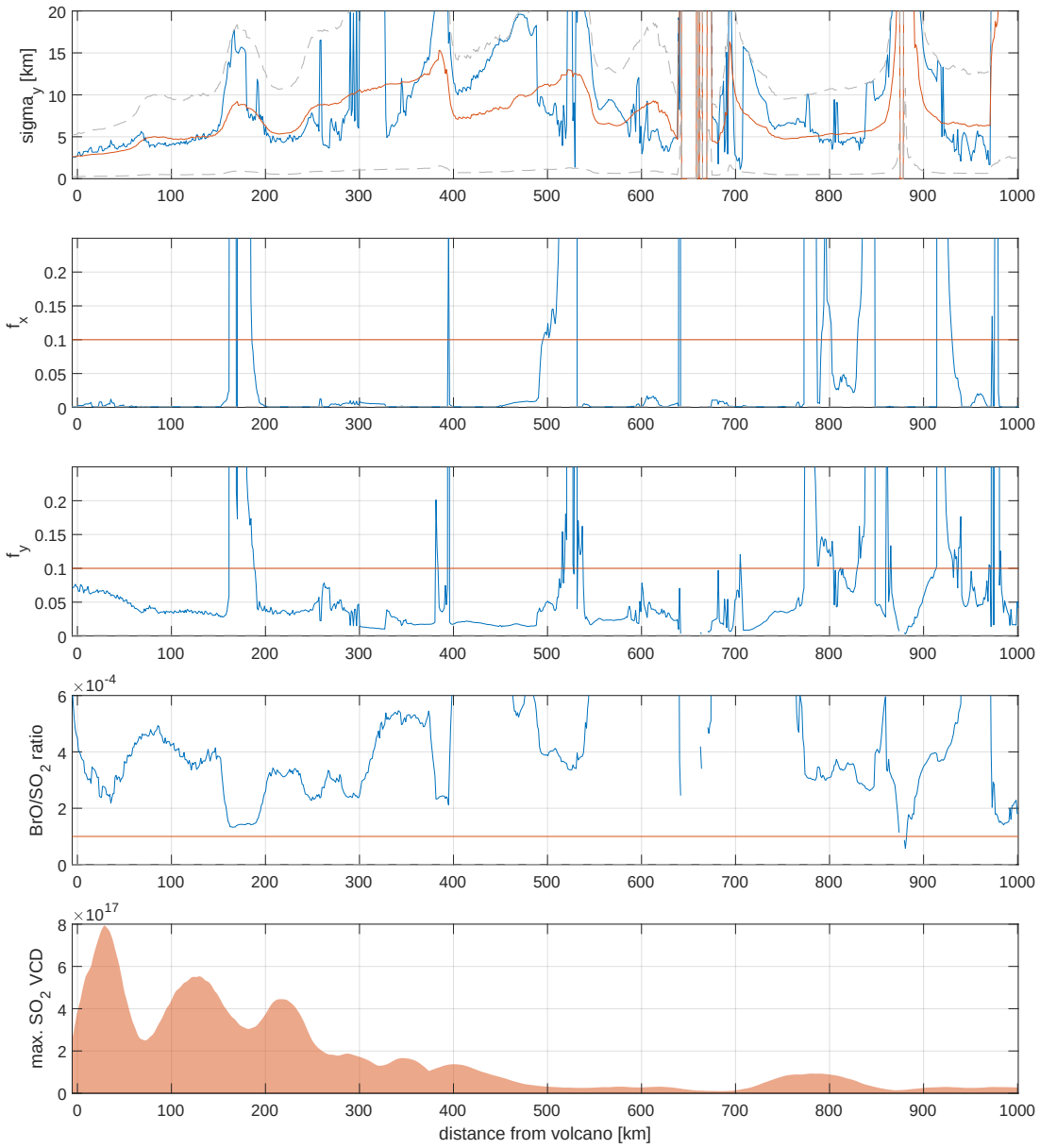


Figure 7.11: Output of the empirical model parameter σ_y, f_x,f_y, and the mixed BrO/SO_2 ratio (from top to bottom). The resulting parameter (blue line), the initialization (red line) as well as the boundaries (grey lines) are included. The maximum SO_2 VCD is not an output parameter, but included in the bottom.

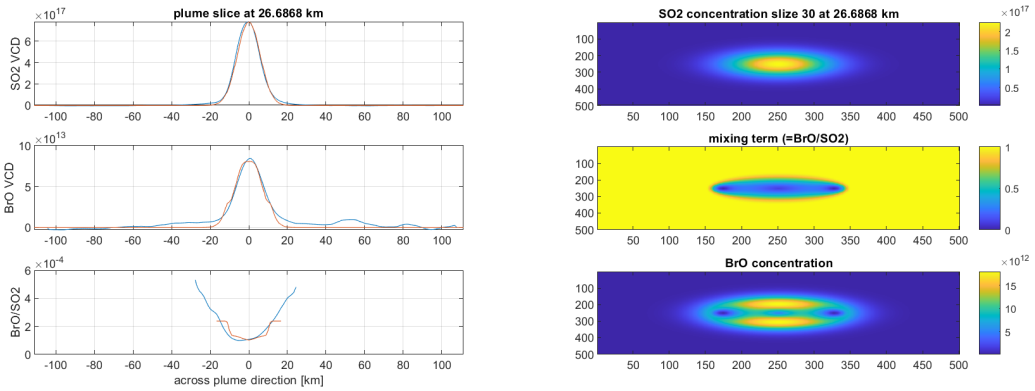


Figure 7.12: Comparison of the model results for slice 30 at 26.7 km distance from Etna. *Left column:* the measured (blue line) and modeled (red line) SO_2 VCD (top), BrO VCD (middle) and BrO/SO_2 ratio (bottom) along the across-plume dimension. *Reft column:* the modelled SO_2 concentration (top), the mixing term (middle), and the BrO concentration (bottom) in units of σ_x and σ_y.

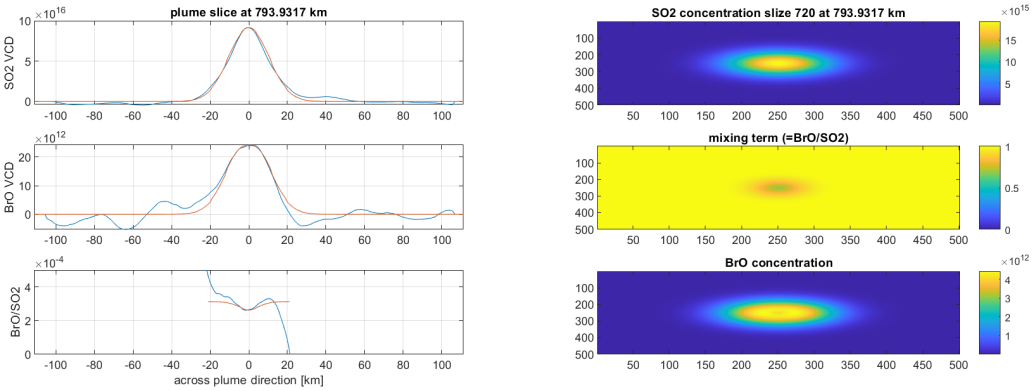


Figure 7.13: Comparison of the model results for slice 200 at 793.9 km distance from Etna. *Left column:* the measured (blue line) and modeled (red line) SO_2 VCD (top), BrO VCD (middle) and BrO/SO_2 ratio (bottom) along the across-plume dimension. *Reft column:* the modelled SO_2 concentration (top), the mixing term (middle), and the BrO concentration (bottom) in units of σ_x and σ_y.

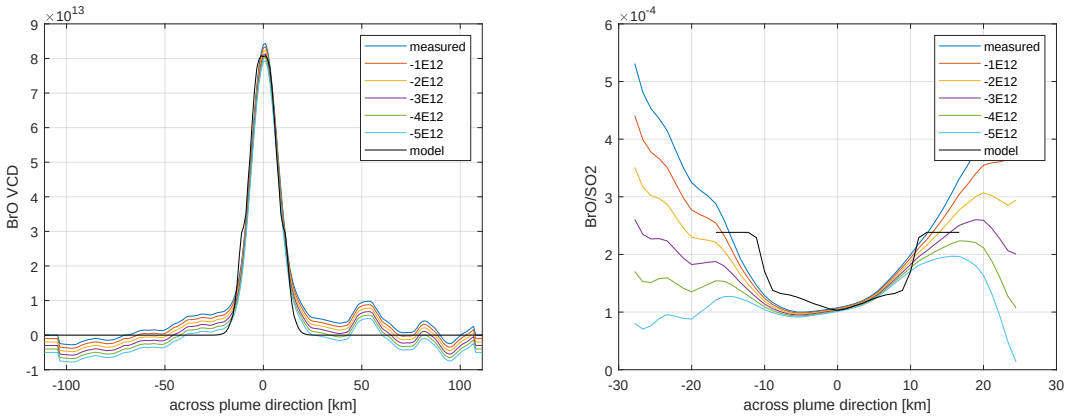


Figure 7.14: The measured BrO VCD (left) and the BrO/SO_2 ratio (right) distribution for a slice at 26 km distance from the volcano. The measured BrO VCD (blue line) is systematically lowered by 1,2...5$\times 10^{-12}$ molecules cm^{-2}. The modeled data is included as a black line.

7.3 Summary

Overall, the case of the plume of Mt. Etna on 25 December 2018 shows that there is a change in the chemical state in parts of the plume and that this can be observed with the high spatial resolution of TROPOMI.
An empirical model purely based on the assumption of limited mixing-in of a chemical component, which in turn limits the BrO formation in the center of the plume, could reproduce the observed decrease in the BrO/SO_2 ratio towards the center of the plume. The model implies that the BrO/SO_2 ratio under mixed conditions is in the range of $2 - 4 \times 10^{-4}$, which is in agreement with the observed BrO/SO_2 ratio at the edge and within the range of BrO/SO_2 ratios derived in the catalogue, but slightly above the mean BrO/SO_2 ratio from the catalogue (1.53×10^{-4}, see section 6.4 and figure 6.23 therein).
Accompanying this, a conceptual model of a plume could reproduce the depletion of BrO and O_3 in the center of the plume. The conceptual model assumes that physical mixing-in of O_3 as the driver of BrO formation is counteracted only by the O_3 destruction of BrO. While this is a very conceptual view on the physical and chemical processes inside a volcanic plume, which are much better reproduced by state of the art models, such as WRF-CHEM (Surl et al., 2021), it allows to reproduce the observed main dependencies quite well and directly relates them to the most important underlying processes.

Conclusions and outlook

Conclusions

This thesis investigates the composition of volcanic plumes from satellite-based observations, specifically the distribution of bromine monoxide (BrO) and sulphur dioxide (SO_2) and their ratio.
BrO and SO_2 column densities in volcanic plumes are derived using Differential Optical Absorption Spectroscopy (DOAS). Spectral radiances from the TROPospheric Monitoring Instrument (TROPOMI), which has a daily global coverage, are analyzed over a four year time period (2018 - 2021).
An improved BrO DOAS fit is developed, optimized for the specific measurements of volcanic BrO from TROPOMI. Expanding the wavelength range of the BrO DOAS fit to 323 - 360 nm yields a reduction in statistical noise by a factor of two, without adding any systematic influence. Remaining systematic influences where investigated, quantified and partially corrected based on various sensitivity studies. These improvements result in a detection limit of BrO vertical columns of typically 1.5×10^{13} molecules cm^{-2} for a single pixel measurement.
An automated plume detection algorithm is employed for TROPOMI based on Hörmann et al. (2013). In total, 4323 volcanic plume events are detected, 3581 with an almost linear relation between BrO and SO_2. A majority (94.3 %) of these events had SO_2 VCD strengths corresponding to minor eruptions or small degassing scenarios. This demonstrates, that with the high spatial resolution of TROPOMI ($3.5 \times 5.5\,\mathrm{km}^2$), satellite observations of the BrO/SO_2 ratio are not limited to large eruptions. BrO was successfully detected – i. e. five neighbouring pixel above the detection limit – for 1449 events.
Volcanic plumes could be successfully assigned to 43 active volcanoes. A Catalogue is created comprising of the 3063 plumes which are within 300 km of the 43 volcanoes and for which a linear BrO/SO_2 relation is determined. For each volcano a mean BrO/SO_2 ratio is calculated. For 32 volcanoes a BrO/SO_2 ratio was measured for the first time, doubling the global data-set of volcanoes for which at least one measurement exists (from 28 to 60). For the first time, BrO/SO_2 ratios are derived in the plume of five classical hot spot volcanoes. All hot spot volcanoes have low mean BrO/SO_2 ratios of $2-5 \times 10^{-5}$, which suggests a similar magmatic composition and hence magmatic source. For arc volcanoes, mean BrO/SO_2 ratios vary between 1×10^{-5} and 2×10^{-4}, implying that the gas composition is dependent on multiple parameter specific to each volcanoes. While a comparison between magmatic composition is not undertaken as part of this thesis, the most likely interpretation is that magmatic composition is the main driver of the differences in the BrO/SO_2 ratio between the different volcanic arc systems (Platt and Bobrowski, 2015). Additionally, plume chemistry can alter the observed BrO/SO_2 ratio. As BrO is a secondarily formed species in volcanic plumes, the chemistry of its formation has to be considered as well. While models predict that roughly 20-40 % of the total bromine inside a plume is converted to BrO (Roberts et al., 2014; Surl et al., 2021), differences in the effectiveness of this process have also been

observed between Mt. Etna and Nyiragongo (Bobrowski et al., 2015).

Lastly, a decrease in the BrO/SO_2 ratio at the center of a plume of Mt. Etna could be detected over several 100 km for a strong eruption. A conceptual model is developed purely on the assumption that the plume is in a steady state, that BrO is formed only if O_3 is mixed in and that O_3 decreases towards the center of the plume due to reaction with BrO. The observation of the plume of Mt. Etna could be explained qualitatively and quantitatively by the model, yielding significant depletion of BrO in the center of the plume. An estimation of the theoretical BrO/SO_2 ratio unaffected by O_3 could be derived. While O_3 limited BrO formation has been observed already close to volcanoes (Bobrowski et al., 2007; General et al., 2015), this was only observed and expected in the first 50 - 100 km. Hence, the gradient in BrO/SO_2 observed in this thesis at up to 1000 km reveals that reactive bromine can affect the atmospheric chemical state over much larger distances.
Concluding, this thesis demonstrates that satellites can be used to systematically monitor volcanic plumes globally as satellite observations from TROPOMI are (1) no longer limited to major eruptions and (2) can resolve and constrain plume chemistry effects inside large volcanic plumes.

Outlook

This thesis highlights the capabilities of satellites as a monitoring tool of volcanic plume composition. There are several points, which could be further done to improve and constrain uncertainties:

- The threshold for BrO/SO_2 ratios could be reduced to even weaker degassing volcanoes by averaging over measurements of multiple days. There are several volcanoes in this study where BrO is below the detection limit. Averaging the plume pixels over several days can reduce the uncertainty in the BrO/SO_2 ratio for these periods. This could improve the quality of time-series and enable monitoring from space to further volcano.

- Applying this evaluation and algorithm to upcoming missions such as Sentinel-5 (sun-synchronous orbit, yielding global daily coverage) as well as the geostationary Sentinel-4 mission can answer additional science questions. Sentinel-5, which is measuring during the morning compared to the mid-day/afternoon overpass of TROPOMI, would add a measurement every day, which would allow to better track volcanic plumes. Sentinel-4 will yield hourly observations of the plumes of European volcanoes like Mt. Etna, Italy. This could allow to observe the evolution of bromine inside a plume with much higher temporal resolution and corresponding distances.

- The general good agreement with ground based observations indicates that the differences in measurement geometry and sensitivity might not systematically influence the measured BrO/SO_2 ratio. However, the satellite and ground based data sets compared in this study covered different time periods. An inter-comparison with a state-of-the art ground-based instrument, which is placed for a long time period at a volcano, could (1) give insights into potential systematic differences between satellite and ground based observations, (2) determine under which volcanic, chemical or meteorological conditions the satellite/ground-based instrument successfully derives a BrO/SO_2 ratio, and thus (3) derive a more complete time-series of the BrO/SO_2 ratio.

Furthermore, the volcanic and chemical interpretations in the thesis can be improved by the following aspects:

- This thesis demonstrates that the plume chemistry in large plumes can be spatially resolved with TROPOMI. However, the employed conceptual model is rather simple and should be further improved. Furthermore, a comparison with full chemistry models might enable to further constrain the chemistry of BrO formation.
- In order to connect this vast and growing data-set of BrO/SO_2 ratios to the magmatic composition, there is the need to quantify the BrO conversion for different eruption cases. Reducing the uncertainties is crucial to accurately deduce volcanic information from the presented BrO/SO_2 data.
- For the comparison of observed changes in the BrO/SO_2 ratio with volcanic parameters, such as seismicity, petrological data of changes in the magmatic composition and intrusions, there is the need to obtain these parameters even at remote volcanoes.

Appendix

A BrO/SO_2 Catalogue

In the following all events of the BrO/SO_2 ratio catalogue (see section 6.4) are listed. The list is sorted into sections for each volcano of the catalogue. Each section is initiated by an overview of the volcano, namely, the name, country, latitude longitude, the number of events (total and with significant detections of BrO), as well as the mean BrO/SO_2 ratio, the standard deviation of the BrO/SO_2 ratios, the mean maximal SO_2 VCD, and the mean maximal BrO VCD. Furthermore a small world map where the volcano is marked as well as a zoom into the region of the volcano. In the zoom plot all events are marked based on the location of maximal SO_2 VCD and color coded based on the BrO/SO_2 ratio. In each section every event assigned to the volcano is listed, including date, maximal SO_2 and BrO VCD, fitted BrO/SO_2 ratio, and the uncertainty of the fitted BrO/SO_2 ratio. The volcanoes are also listed below in the order of appearance as an orientation in the list:

Volcano	Country	latitude	longitude	volcano type	no. of Events	no. of Events error	no. of Events BrO
Fagradalsfjall	Iceland	22.27° W	63.91° N	hot spot	59	25	24
Etna	Italy	15.00° E	37.75° N	hot spot/arc	231	143	137
La Palma	Spain	17.84° W	28.57° N	hot spot	48	41	34
Nyiragongo	DR Congo	29.25° E	1.52° S	rift	168	4	8
Nyamuragira	DR Congo	29.20° E	1.41° S	rift	49	6	8
Piton de la Fournaise	France	55.72° E	21.23° S	hot spot	48	12	6
Yasur	Vanuatu	169.45° E	19.53° S	arc	133	34	62
Ambrym	Vanuatu	168.12° E	16.25° S	arc	152	124	119
Ambae	Vanuatu	167.83° E	15.39° S	arc	24	21	18
Bagana	PNG†	155.19° E	6.14° S	arc	52	2	4
Ulawun	PNG†	151.33° E	5.05° S	arc	9	4	3
Manam	PNG†	145.03° E	4.08° S	arc	114	30	21
Dukono	Indonesia	127.88° E	1.70° N	arc	199	1	18
Karangetang	Indonesia	125.40° E	2.78° N	arc	7	0	1
Soputan	Indonesia	124.73° E	1.11° N	arc	1	1	1
Lewotolok	Indonesia	123.50° E	8.27° S	arc	2	1	1
Agung	Indonesia	116.01° E	8.34° S	arc	5	2	3
Raung	Indonesia	114.05° E	8.12° S	arc	17	3	4
Semeru	Indonesia	112.92° E	8.11° S	arc	13	0	3
Anak Krakatau	Indonesia	105.42° E	6.10° S	arc	19	10	6
Kerinci	Indonesia	101.26° E	1.70° S	arc	5	2	2
Sinabung	Indonesia	98.39° E	3.17° N	arc	20	3	3
Mayon	Philippines	123.69° E	13.26° N	arc	15	4	5
Taal	Philippines	120.99° E	14.00° N	arc	57	8	8
Nishinoshima	Japan	140.87° E	27.25° N	arc	37	29	19
Raikoke	Russia	153.24° E	48.29° N	arc	1	1	1
Lemonosov	Russia	155.43° E	50.25° N	arc	24	6	4
South Kamchatka	Russia	158.27° E	52.49° N	arc	47	3	5
Karymsky	Russia	159.45° E	54.05° N	arc	20	9	11
Bezymianny	Russia	160.59° E	55.98° N	arc	37	14	18
Klyuchevskoy	Russia	160.64° E	56.06° N	arc	29	13	16
Sheveluch	Russia	161.36° E	56.65° N	arc	30	15	19
Shishaldin	USA	163.97° W	54.76° N	arc	5	2	2
Veniaminof	USA	159.39° W	56.20° N	arc	3	1	1
Kilauea	USA	155.29° W	19.42° N	hot spot	110	46	28
Popocatepetl	Mexico	98.62° W	19.03° N	arc	467	50	84
Fuego	Guatemala	90.88° W	14.47° N	arc	18	1	5
Masaya	Nicaragua	86.15° W	11.98° N	arc	2	1	1
Poas	Costa Rica	84.23° W	10.20° N	arc	69	18	27
Nevado del Ruiz	Colombia	75.32° W	4.88° N	arc	467	110	113
Sangay	Ecuador	78.34° W	2.00° S	arc	230	92	55
Fernandina	Ecuador	91.55° W	0.37° S	hot spot	2	2	2
Sierra Negra	Ecuador	91.17° W	0.83° S	hot spot	18	16	16

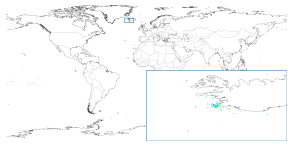
†PNG = Papua New Guinea

Fagradalsfjall, Iceland

date	SO_2 VCD max. [molecules cm^{-2}]	BrO VCD	BrO/SO_2 fitted	BrO/SO_2 error

Fagradalsfjall, Iceland

Type:	hot spot
longitude:	22.27° W
latitude:	63.91° N
Events:	59
$BrO > 2\sigma$:	24
BrO/SO_2:	$4.3x10^{-5}$
std. dev.:	$2.0x10^{-5}$
mean SO_2:	$3.4x10^{17}$
mean BrO:	$3.1x10^{13}$



1 May 2021	$1.2x10^{17}$	$4.0x10^{13}$	$4.6x10^{-5}$	$5.0x10^{-5}$
2 May 2021	$2.7x10^{17}$	$3.1x10^{13}$	$4.1x10^{-5}$	$2.6x10^{-5}$
5 May 2021	$4.3x10^{17}$	$3.6x10^{13}$	$5.7x10^{-5}$	$1.1x10^{-5}$
8 May 2021	$2.0x10^{17}$	$2.7x10^{13}$	$2.5x10^{-5}$	$1.8x10^{-5}$
9 May 2021	$8.0x10^{16}$	$3.2x10^{13}$	$8.4x10^{-6}$	$3.5x10^{-5}$
10 May 2021	$8.6x10^{16}$	$2.3x10^{13}$	$3.2x10^{-5}$	$3.3x10^{-5}$
11 May 2021	$2.6x10^{17}$	$3.9x10^{13}$	$2.5x10^{-5}$	$2.0x10^{-5}$
12 May 2021	$5.6x10^{17}$	$3.3x10^{13}$	$1.6x10^{-5}$	$7.3x10^{-6}$
13 May 2021	$8.1x10^{17}$	$3.5x10^{13}$	$4.8x10^{-5}$	$5.5x10^{-6}$
14 May 2021	$5.3x10^{17}$	$3.7x10^{13}$	$5.2x10^{-5}$	$5.3x10^{-6}$
17 May 2021	$7.3x10^{17}$	$3.7x10^{13}$	$5.4x10^{-5}$	$6.1x10^{-6}$
18 May 2021	$8.9x10^{17}$	$3.9x10^{13}$	$5.0x10^{-5}$	$5.5x10^{-6}$
20 May 2021	$6.5x10^{17}$	$3.4x10^{13}$	$4.1x10^{-5}$	$5.1x10^{-6}$
21 May 2021	$1.9x10^{17}$	$3.0x10^{13}$	$4.5x10^{-5}$	$7.0x10^{-6}$
22 May 2021	$4.5x10^{17}$	$4.1x10^{13}$	$2.7x10^{-5}$	$1.2x10^{-5}$
24 May 2021	$4.5x10^{17}$	$3.9x10^{13}$	$4.4x10^{-5}$	$7.2x10^{-6}$
26 May 2021	$9.8x10^{16}$	$1.7x10^{13}$	$2.7x10^{-5}$	$5.5x10^{-5}$
31 May 2021	$1.3x10^{17}$	$2.5x10^{13}$	$2.3x10^{-5}$	$3.4x10^{-5}$
1 June 2021	$9.1x10^{16}$	$2.8x10^{13}$	$3.6x10^{-5}$	$3.1x10^{-5}$
2 June 2021	$2.1x10^{17}$	$2.9x10^{13}$	$6.4x10^{-5}$	$3.4x10^{-5}$
6 June 2021	$1.3x10^{17}$	$3.3x10^{13}$	$3.0x10^{-5}$	$1.9x10^{-5}$
7 June 2021	$4.4x10^{17}$	$3.1x10^{13}$	$3.0x10^{-5}$	$1.0x10^{-5}$
8 June 2021	$3.7x10^{17}$	$2.3x10^{13}$	$1.9x10^{-5}$	$1.1x10^{-5}$
9 June 2021	$1.1x10^{17}$	$1.8x10^{13}$	$1.1x10^{-5}$	$1.7x10^{-5}$
11 June 2021	$1.2x10^{17}$	$2.7x10^{13}$	$1.9x10^{-5}$	$1.6x10^{-5}$
14 June 2021	$2.3x10^{17}$	$2.5x10^{13}$	$3.9x10^{-5}$	$1.1x10^{-5}$
16 June 2021	$9.0x10^{16}$	$1.5x10^{13}$	$3.2x10^{-5}$	$3.3x10^{-5}$
17 June 2021	$5.4x10^{17}$	$4.7x10^{13}$	$5.9x10^{-5}$	$1.5x10^{-5}$
18 June 2021	$1.5x10^{18}$	$7.6x10^{13}$	$4.6x10^{-5}$	$2.7x10^{-6}$
19 June 2021	$8.0x10^{17}$	$3.8x10^{13}$	$2.6x10^{-5}$	$3.3x10^{-6}$
20 June 2021	$7.6x10^{16}$	$2.4x10^{13}$	$5.8x10^{-6}$	$4.5x10^{-5}$
22 June 2021	$1.2x10^{17}$	$2.4x10^{13}$	$2.6x10^{-5}$	$1.7x10^{-5}$
27 June 2021	$1.1x10^{17}$	$2.1x10^{13}$	$8.1x10^{-5}$	$1.3x10^{-5}$
28 June 2021	$7.7x10^{16}$	$1.6x10^{13}$	$8.2x10^{-5}$	$3.2x10^{-5}$
30 June 2021	$2.3x10^{17}$	$1.3x10^{13}$	$3.0x10^{-6}$	$1.2x10^{-5}$
1 July 2021	$1.2x10^{17}$	$2.0x10^{13}$	$1.6x10^{-5}$	$1.9x10^{-5}$
4 July 2021	$2.3x10^{17}$	$2.5x10^{13}$	$2.7x10^{-5}$	$2.7x10^{-6}$
5 July 2021	$8.1x10^{17}$	$5.2x10^{13}$	$4.1x10^{-5}$	$1.8x10^{-6}$
10 July 2021	$2.0x10^{17}$	$3.9x10^{13}$	$5.6x10^{-5}$	$2.0x10^{-5}$
11 July 2021	$1.6x10^{17}$	$2.8x10^{13}$	$5.1x10^{-5}$	$2.1x10^{-5}$
13 July 2021	$1.3x10^{17}$	$2.5x10^{13}$	$2.7x10^{-5}$	$4.3x10^{-5}$
14 July 2021	$9.0x10^{16}$	$1.6x10^{13}$	$7.1x10^{-5}$	$2.9x10^{-5}$
17 July 2021	$4.0x10^{17}$	$3.5x10^{13}$	$5.8x10^{-5}$	$5.7x10^{-6}$
18 July 2021	$1.5x10^{17}$	$1.6x10^{13}$	$3.2x10^{-5}$	$1.5x10^{-5}$
19 July 2021	$1.3x10^{17}$	$3.4x10^{13}$	$5.7x10^{-5}$	$1.6x10^{-5}$
20 July 2021	$9.2x10^{17}$	$5.7x10^{13}$	$6.7x10^{-5}$	$9.8x10^{-6}$
24 July 2021	$1.2x10^{17}$	$1.6x10^{13}$	$6.0x10^{-5}$	$2.7x10^{-5}$
1 Aug 2021	$3.7x10^{17}$	$2.8x10^{13}$	$5.1x10^{-5}$	$7.4x10^{-6}$
6 Aug 2021	$1.7x10^{18}$	$6.0x10^{13}$	$4.7x10^{-5}$	$2.1x10^{-6}$
11 Aug 2021	$1.2x10^{17}$	$2.9x10^{13}$	$6.7x10^{-5}$	$1.9x10^{-5}$
12 Aug 2021	$9.9x10^{17}$	$5.7x10^{13}$	$5.8x10^{-5}$	$4.6x10^{-6}$
13 Aug 2021	$1.2x10^{17}$	$2.4x10^{13}$	$9.4x10^{-5}$	$1.7x10^{-5}$
14 Aug 2021	$1.7x10^{17}$	$2.7x10^{13}$	$4.5x10^{-5}$	$9.6x10^{-6}$
16 Aug 2021	$2.2x10^{17}$	$2.2x10^{13}$	$7.8x10^{-5}$	$1.4x10^{-5}$
18 Aug 2021	$2.6x10^{17}$	$1.5x10^{13}$	$4.0x10^{-5}$	$1.2x10^{-5}$
22 Aug 2021	$6.1x10^{16}$	$2.2x10^{13}$	$2.3x10^{-5}$	$4.0x10^{-5}$
26 Aug 2021	$3.0x10^{17}$	$1.9x10^{13}$	$4.5x10^{-5}$	$1.1x10^{-5}$
31 Aug 2021	$1.6x10^{17}$	$2.2x10^{13}$	$5.8x10^{-5}$	$2.2x10^{-5}$
2 Sept 2021	$1.1x10^{17}$	$2.6x10^{13}$	$3.8x10^{-5}$	$1.5x10^{-5}$

Etna, Italy

date	SO_2 VCD max. [molecules cm^{-2}]	BrO VCD	BrO/SO_2 fitted	BrO/SO_2 error

Etna, Italy

Type:	hotspot/arc
longitude:	15.00° E
latitude:	37.75° N
Events:	231
$BrO > 2\sigma$:	137
BrO/SO_2:	$1.5x10^{-4}$
std. dev.:	$7.5x10^{-5}$
mean SO_2:	$1.8x10^{17}$
mean BrO:	$3.8x10^{13}$



28 Jan 2018	$2.2x10^{17}$	$2.7x10^{13}$	$7.7x10^{-5}$	$2.2x10^{-5}$
30 Jan 2018	$7.1x10^{16}$	$1.3x10^{13}$	$2.8x10^{-5}$	$2.3x10^{-5}$
19 Feb 2018	$1.7x10^{17}$	$5.8x10^{13}$	$3.3x10^{-4}$	$2.6x10^{-5}$
23 Mar 2018	$1.3x10^{17}$	$3.8x10^{13}$	$2.4x10^{-4}$	$3.0x10^{-5}$
26 Mar 2018	$1.8x10^{17}$	$4.8x10^{13}$	$2.7x10^{-4}$	$3.1x10^{-5}$
27 Mar 2018	$1.1x10^{17}$	$3.1x10^{13}$	$2.1x10^{-4}$	$4.0x10^{-5}$
3 April 2018	$8.5x10^{16}$	$2.4x10^{13}$	$1.5x10^{-4}$	$3.3x10^{-5}$
12 May 2018	$7.0x10^{16}$	$2.6x10^{13}$	$1.5x10^{-4}$	$2.6x10^{-5}$
25 May 2018	$1.9x10^{17}$	$4.9x10^{13}$	$1.8x10^{-4}$	$4.0x10^{-5}$
15 June 2018	$1.0x10^{17}$	$2.6x10^{13}$	$1.5x10^{-4}$	$3.7x10^{-5}$
16 June 2018	$1.2x10^{17}$	$2.1x10^{13}$	$6.2x10^{-5}$	$6.1x10^{-5}$
21 June 2018	$1.2x10^{17}$	$2.5x10^{13}$	$1.6x10^{-4}$	$3.3x10^{-5}$
22 June 2018	$1.9x10^{17}$	$2.8x10^{13}$	$1.2x10^{-4}$	$2.1x10^{-5}$
11 July 2018	$1.1x10^{17}$	$2.2x10^{13}$	$1.3x10^{-4}$	$4.1x10^{-5}$
1 Aug 2018	$9.7x10^{16}$	$1.9x10^{13}$	$7.9x10^{-5}$	$2.4x10^{-5}$
2 Aug 2018	$9.0x10^{16}$	$3.3x10^{13}$	$1.1x10^{-4}$	$2.5x10^{-5}$
3 Aug 2018	$9.2x10^{16}$	$2.2x10^{13}$	$9.9x10^{-5}$	$3.3x10^{-5}$
6 Aug 2018	$1.7x10^{17}$	$3.2x10^{13}$	$1.3x10^{-4}$	$1.8x10^{-5}$
7 Aug 2018	$3.6x10^{17}$	$5.1x10^{13}$	$1.5x10^{-4}$	$1.5x10^{-5}$
8 Aug 2018	$1.7x10^{17}$	$7.0x10^{13}$	$2.8x10^{-4}$	$3.1x10^{-5}$
9 Aug 2018	$1.4x10^{17}$	$2.7x10^{13}$	$1.6x10^{-4}$	$2.5x10^{-5}$
12 Aug 2018	$1.5x10^{17}$	$2.9x10^{13}$	$1.2x10^{-4}$	$1.9x10^{-5}$
14 Aug 2018	$8.8x10^{16}$	$2.9x10^{13}$	$8.7x10^{-5}$	$3.2x10^{-5}$
17 Aug 2018	$1.4x10^{17}$	$3.0x10^{13}$	$1.2x10^{-4}$	$3.0x10^{-5}$
18 Aug 2018	$2.5x10^{17}$	$6.2x10^{13}$	$1.6x10^{-4}$	$1.8x10^{-5}$
19 Aug 2018	$1.5x10^{17}$	$4.0x10^{13}$	$1.1x10^{-4}$	$1.9x10^{-5}$
22 Aug 2018	$8.8x10^{16}$	$2.7x10^{13}$	$2.0x10^{-4}$	$2.9x10^{-5}$
23 Aug 2018	$2.0x10^{17}$	$6.4x10^{13}$	$2.1x10^{-4}$	$1.8x10^{-5}$
24 Aug 2018	$1.5x10^{17}$	$5.7x10^{13}$	$2.7x10^{-4}$	$2.9x10^{-5}$
25 Aug 2018	$1.1x10^{17}$	$3.6x10^{13}$	$2.6x10^{-4}$	$1.6x10^{-5}$
29 Aug 2018	$5.3x10^{17}$	$6.5x10^{13}$	$9.3x10^{-5}$	$1.1x10^{-5}$
30 Aug 2018	$4.7x10^{17}$	$7.9x10^{13}$	$1.3x10^{-4}$	$1.2x10^{-5}$
31 Aug 2018	$1.2x10^{17}$	$2.3x10^{13}$	$1.2x10^{-4}$	$1.6x10^{-5}$
14 Sept 2018	$6.9x10^{16}$	$3.0x10^{13}$	$2.1x10^{-4}$	$4.4x10^{-5}$
15 Sept 2018	$1.2x10^{17}$	$3.8x10^{13}$	$1.8x10^{-4}$	$2.3x10^{-5}$
19 Sept 2018	$1.0x10^{17}$	$3.0x10^{13}$	$1.3x10^{-4}$	$2.8x10^{-5}$
20 Sept 2018	$1.3x10^{17}$	$4.1x10^{13}$	$2.1x10^{-4}$	$2.8x10^{-5}$
21 Sept 2018	$1.6x10^{17}$	$4.7x10^{13}$	$2.5x10^{-4}$	$2.7x10^{-5}$
22 Sept 2018	$8.0x10^{16}$	$3.6x10^{13}$	$2.5x10^{-4}$	$4.4x10^{-5}$
23 Sept 2018	$1.6x10^{17}$	$4.0x10^{13}$	$2.0x10^{-4}$	$1.8x10^{-5}$
10 Oct 2018	$6.0x10^{17}$	$9.9x10^{13}$	$1.8x10^{-4}$	$1.6x10^{-5}$
11 Oct 2018	$1.9x10^{17}$	$3.6x10^{13}$	$1.6x10^{-4}$	$2.1x10^{-5}$
16 Oct 2018	$1.1x10^{17}$	$3.7x10^{13}$	$2.2x10^{-4}$	$2.9x10^{-5}$
17 Oct 2018	$2.0x10^{17}$	$4.1x10^{13}$	$2.1x10^{-4}$	$2.6x10^{-5}$
20 Oct 2018	$1.3x10^{17}$	$3.5x10^{13}$	$2.1x10^{-4}$	$3.3x10^{-5}$
21 Oct 2018	$9.9x10^{16}$	$5.4x10^{13}$	$2.3x10^{-4}$	$2.1x10^{-5}$
6 Nov 2018	$7.9x10^{16}$	$2.1x10^{13}$	$1.2x10^{-4}$	$3.4x10^{-5}$
11 Nov 2018	$1.4x10^{17}$	$3.3x10^{13}$	$2.0x10^{-4}$	$3.2x10^{-5}$
12 Nov 2018	$8.3x10^{16}$	$2.3x10^{13}$	$1.3x10^{-4}$	$3.3x10^{-5}$
17 Nov 2018	$1.2x10^{17}$	$4.6x10^{13}$	$2.3x10^{-4}$	$3.1x10^{-5}$
2 Dec 2018	$9.1x10^{16}$	$2.8x10^{13}$	$1.7x10^{-4}$	$4.2x10^{-5}$
7 Dec 2018	$1.9x10^{17}$	$3.4x10^{13}$	$2.3x10^{-4}$	$3.3x10^{-5}$
15 Dec 2018	$1.2x10^{17}$	$3.1x10^{13}$	$1.9x10^{-4}$	$2.8x10^{-5}$
24 Dec 2018	$1.1x10^{18}$	$6.0x10^{13}$	$6.2x10^{-5}$	$8.3x10^{-6}$
4 Jan 2019	$3.2x10^{17}$	$3.4x10^{13}$	$1.2x10^{-4}$	$2.1x10^{-5}$
5 Jan 2019	$8.6x10^{16}$	$3.3x10^{13}$	$1.4x10^{-4}$	$3.2x10^{-5}$
10 Jan 2019	$7.8x10^{16}$	$2.8x10^{13}$	$1.1x10^{-4}$	$6.9x10^{-5}$
11 Jan 2019	$8.3x10^{16}$	$2.2x10^{13}$	$1.4x10^{-4}$	$4.3x10^{-5}$
14 Jan 2019	$1.2x10^{17}$	$3.5x10^{13}$	$2.2x10^{-4}$	$2.8x10^{-5}$
16 Jan 2019	$9.7x10^{16}$	$2.4x10^{13}$	$1.5x10^{-4}$	$2.1x10^{-5}$

Etna, Italy

date	SO_2 VCD max. [molecules cm^{-2}]	BrO VCD	BrO/SO_2 fitted	BrO/SO_2 error
17 Jan 2019	$9.4x10^{16}$	$2.6x10^{13}$	$1.5x10^{-4}$	$1.4x10^{-5}$
19 Jan 2019	$3.9x10^{17}$	$7.2x10^{13}$	$1.7x10^{-4}$	$9.7x10^{-6}$
20 Jan 2019	$4.3x10^{17}$	$5.6x10^{13}$	$1.7x10^{-4}$	$9.7x10^{-6}$
22 Jan 2019	$1.1x10^{17}$	$1.7x10^{13}$	$2.1x10^{-5}$	$2.5x10^{-5}$
24 Jan 2019	$1.4x10^{17}$	$2.5x10^{13}$	$1.2x10^{-4}$	$6.0x10^{-5}$
29 Jan 2019	$5.2x10^{17}$	$8.1x10^{13}$	$1.9x10^{-4}$	$1.6x10^{-5}$
30 Jan 2019	$9.2x10^{16}$	$2.9x10^{13}$	$1.6x10^{-4}$	$2.4x10^{-5}$
31 Jan 2019	$8.6x10^{16}$	$1.8x10^{13}$	$4.1x10^{-5}$	$5.6x10^{-5}$
1 Feb 2019	$6.8x10^{16}$	$2.9x10^{13}$	$1.3x10^{-4}$	$2.1x10^{-5}$
3 Feb 2019	$7.3x10^{16}$	$3.2x10^{13}$	$1.8x10^{-4}$	$6.3x10^{-5}$
9 Feb 2019	$2.5x10^{17}$	$4.6x10^{13}$	$1.6x10^{-4}$	$2.9x10^{-5}$
10 Feb 2019	$1.0x10^{17}$	$2.5x10^{13}$	$6.5x10^{-5}$	$2.3x10^{-5}$
16 Feb 2019	$1.3x10^{17}$	$3.4x10^{13}$	$1.2x10^{-4}$	$2.6x10^{-5}$
18 Feb 2019	$6.6x10^{16}$	$2.0x10^{13}$	$1.7x10^{-4}$	$1.9x10^{-5}$
19 Feb 2019	$1.4x10^{17}$	$2.3x10^{13}$	$1.2x10^{-4}$	$1.0x10^{-5}$
20 Feb 2019	$2.0x10^{17}$	$3.8x10^{13}$	$1.3x10^{-4}$	$9.1x10^{-6}$
21 Feb 2019	$2.2x10^{17}$	$3.8x10^{13}$	$1.2x10^{-4}$	$7.5x10^{-6}$
22 Feb 2019	$1.6x10^{17}$	$3.4x10^{13}$	$1.0x10^{-4}$	$1.2x10^{-5}$
25 Mar 2019	$7.9x10^{16}$	$2.0x10^{13}$	$1.2x10^{-4}$	$3.2x10^{-5}$
5 April 2019	$1.1x10^{17}$	$2.7x10^{13}$	$2.4x10^{-4}$	$1.8x10^{-5}$
6 April 2019	$2.0x10^{17}$	$2.1x10^{13}$	$1.0x10^{-4}$	$3.3x10^{-5}$
13 May 2019	$3.0x10^{17}$	$5.1x10^{13}$	$1.3x10^{-4}$	$2.9x10^{-5}$
14 May 2019	$7.8x10^{16}$	$2.7x10^{13}$	$1.7x10^{-4}$	$7.2x10^{-5}$
31 May 2019	$9.8x10^{16}$	$3.1x10^{13}$	$2.4x10^{-4}$	$1.3x10^{-5}$
1 June 2019	$1.7x10^{17}$	$4.4x10^{13}$	$2.5x10^{-4}$	$2.2x10^{-5}$
2 June 2019	$2.2x10^{17}$	$7.7x10^{13}$	$2.7x10^{-4}$	$2.2x10^{-5}$
3 June 2019	$7.4x10^{16}$	$2.8x10^{13}$	$2.0x10^{-4}$	$3.2x10^{-5}$
8 June 2019	$1.9x10^{17}$	$3.2x10^{13}$	$3.8x10^{-5}$	$4.3x10^{-5}$
9 June 2019	$9.6x10^{16}$	$8.4x10^{13}$	$1.3x10^{-4}$	$3.6x10^{-5}$
11 June 2019	$7.4x10^{16}$	$2.4x10^{13}$	$1.7x10^{-4}$	$3.7x10^{-5}$
18 June 2019	$1.0x10^{17}$	$3.2x10^{13}$	$1.2x10^{-4}$	$4.1x10^{-5}$
19 June 2019	$8.7x10^{16}$	$2.7x10^{13}$	$1.4x10^{-4}$	$3.8x10^{-5}$
28 June 2019	$1.1x10^{17}$	$2.9x10^{13}$	$6.2x10^{-5}$	$3.9x10^{-5}$
30 June 2019	$7.7x10^{16}$	$2.3x10^{13}$	$6.3x10^{-5}$	$3.3x10^{-5}$
2 July 2019	$7.1x10^{16}$	$1.9x10^{13}$	$9.8x10^{-5}$	$4.0x10^{-5}$
3 July 2019	$1.9x10^{17}$	$1.8x10^{13}$	$3.2x10^{-5}$	$3.4x10^{-5}$
4 July 2019	$2.1x10^{17}$	$3.4x10^{13}$	$9.7x10^{-5}$	$1.3x10^{-5}$
19 July 2019	$1.1x10^{17}$	$2.4x10^{13}$	$1.0x10^{-4}$	$1.4x10^{-5}$
20 July 2019	$2.2x10^{17}$	$3.6x10^{13}$	$1.4x10^{-4}$	$1.2x10^{-5}$
21 July 2019	$8.0x10^{16}$	$2.7x10^{13}$	$9.4x10^{-5}$	$4.4x10^{-5}$
26 July 2019	$1.4x10^{17}$	$3.2x10^{13}$	$1.3x10^{-4}$	$3.7x10^{-5}$
27 July 2019	$1.1x10^{17}$	$3.2x10^{13}$	$2.0x10^{-4}$	$4.2x10^{-5}$
6 Aug 2019	$9.7x10^{16}$	$3.2x10^{13}$	$3.7x10^{-5}$	$6.7x10^{-6}$
10 Aug 2019	$1.1x10^{17}$	$2.8x10^{13}$	$3.1x10^{-5}$	$3.7x10^{-5}$
11 Aug 2019	$7.9x10^{16}$	$2.5x10^{13}$	$5.1x10^{-5}$	$4.0x10^{-5}$
15 Aug 2019	$7.1x10^{16}$	$2.5x10^{13}$	$1.1x10^{-4}$	$3.0x10^{-5}$
16 Aug 2019	$1.0x10^{17}$	$3.6x10^{13}$	$1.6x10^{-4}$	$2.5x10^{-5}$
18 Aug 2019	$9.6x10^{16}$	$2.3x10^{13}$	$2.0x10^{-4}$	$3.3x10^{-5}$
19 Aug 2019	$1.6x10^{17}$	$3.3x10^{13}$	$1.4x10^{-4}$	$1.5x10^{-5}$
20 Aug 2019	$2.3x10^{17}$	$6.0x10^{13}$	$1.5x10^{-4}$	$1.3x10^{-5}$
21 Aug 2019	$2.8x10^{17}$	$5.4x10^{13}$	$1.4x10^{-4}$	$1.1x10^{-5}$
22 Aug 2019	$1.7x10^{17}$	$3.2x10^{13}$	$9.6x10^{-5}$	$2.2x10^{-5}$
25 Aug 2019	$9.9x10^{16}$	$2.3x10^{13}$	$1.4x10^{-4}$	$2.5x10^{-5}$
26 Aug 2019	$3.7x10^{17}$	$4.1x10^{13}$	$1.5x10^{-4}$	$1.7x10^{-5}$
28 Aug 2019	$2.0x10^{17}$	$4.2x10^{13}$	$1.1x10^{-4}$	$2.2x10^{-5}$
30 Aug 2019	$7.7x10^{16}$	$3.8x10^{13}$	$2.1x10^{-4}$	$2.7x10^{-5}$
31 Aug 2019	$3.0x10^{17}$	$5.5x10^{13}$	$1.8x10^{-4}$	$1.0x10^{-5}$
1 Sept 2019	$6.6x10^{16}$	$3.7x10^{13}$	$2.5x10^{-4}$	$2.6x10^{-5}$
2 Sept 2019	$2.4x10^{17}$	$9.0x10^{13}$	$3.5x10^{-4}$	$4.5x10^{-5}$
3 Sept 2019	$7.5x10^{16}$	$2.4x10^{13}$	$2.2x10^{-4}$	$2.6x10^{-5}$
7 Sept 2019	$1.5x10^{17}$	$3.7x10^{13}$	$1.3x10^{-4}$	$2.1x10^{-5}$
8 Sept 2019	$7.9x10^{16}$	$3.2x10^{13}$	$1.4x10^{-4}$	$3.1x10^{-5}$
9 Sept 2019	$1.0x10^{17}$	$3.1x10^{13}$	$2.9x10^{-4}$	$2.9x10^{-5}$
10 Sept 2019	$3.4x10^{17}$	$7.1x10^{13}$	$1.6x10^{-4}$	$9.1x10^{-6}$
11 Sept 2019	$6.3x10^{17}$	$9.7x10^{13}$	$1.6x10^{-4}$	$1.1x10^{-5}$
16 Sept 2019	$1.9x10^{17}$	$3.1x10^{13}$	$1.4x10^{-4}$	$2.1x10^{-5}$
18 Sept 2019	$9.6x10^{16}$	$2.3x10^{13}$	$9.9x10^{-5}$	$2.9x10^{-5}$
21 Sept 2019	$1.9x10^{17}$	$5.9x10^{13}$	$1.7x10^{-4}$	$2.9x10^{-5}$
22 Sept 2019	$1.6x10^{17}$	$3.1x10^{13}$	$2.2x10^{-4}$	$2.1x10^{-5}$
27 Sept 2019	$3.2x10^{17}$	$4.7x10^{13}$	$1.0x10^{-4}$	$1.3x10^{-5}$
28 Sept 2019	$1.5x10^{17}$	$3.1x10^{13}$	$1.1x10^{-4}$	$2.2x10^{-5}$

Etna, Italy

date	SO_2 VCD max. [molecules cm^{-2}]	BrO VCD	BrO/SO_2 fitted	BrO/SO_2 error
29 Sept 2019	$1.9x10^{17}$	$4.2x10^{13}$	$1.3x10^{-4}$	$1.3x10^{-5}$
30 Sept 2019	$9.4x10^{16}$	$2.5x10^{13}$	$1.0x10^{-4}$	$1.9x10^{-5}$
1 Oct 2019	$1.5x10^{17}$	$3.9x10^{13}$	$1.5x10^{-4}$	$1.6x10^{-5}$
2 Oct 2019	$1.0x10^{17}$	$3.4x10^{13}$	$1.4x10^{-4}$	$1.7x10^{-5}$
8 Oct 2019	$8.6x10^{16}$	$2.9x10^{13}$	$2.1x10^{-4}$	$5.6x10^{-5}$
9 Oct 2019	$3.1x10^{17}$	$7.1x10^{13}$	$2.7x10^{-4}$	$2.4x10^{-5}$
12 Oct 2019	$1.2x10^{17}$	$2.7x10^{13}$	$1.3x10^{-4}$	$1.7x10^{-5}$
13 Oct 2019	$2.5x10^{17}$	$3.8x10^{13}$	$1.3x10^{-4}$	$1.6x10^{-5}$
14 Oct 2019	$3.2x10^{17}$	$5.6x10^{13}$	$1.5x10^{-4}$	$1.2x10^{-5}$
15 Oct 2019	$1.7x10^{17}$	$3.0x10^{13}$	$1.1x10^{-4}$	$1.6x10^{-5}$
17 Oct 2019	$1.9x10^{17}$	$3.6x10^{13}$	$1.7x10^{-4}$	$1.8x10^{-5}$
18 Oct 2019	$1.3x10^{17}$	$2.9x10^{13}$	$1.6x10^{-4}$	$1.2x10^{-5}$
22 Oct 2019	$1.1x10^{17}$	$3.9x10^{13}$	$1.9x10^{-4}$	$2.3x10^{-5}$
23 Oct 2019	$1.7x10^{17}$	$2.9x10^{13}$	$1.3x10^{-4}$	$1.4x10^{-5}$
24 Oct 2019	$9.5x10^{16}$	$3.2x10^{13}$	$1.6x10^{-4}$	$1.4x10^{-5}$
29 Oct 2019	$8.5x10^{16}$	$2.9x10^{13}$	$2.1x10^{-4}$	$3.8x10^{-5}$
30 Oct 2019	$1.6x10^{17}$	$4.1x10^{13}$	$2.2x10^{-4}$	$2.4x10^{-5}$
31 Oct 2019	$9.4x10^{16}$	$3.0x10^{13}$	$1.9x10^{-4}$	$3.4x10^{-5}$
13 Nov 2019	$8.0x10^{16}$	$3.8x10^{13}$	$3.0x10^{-4}$	$3.7x10^{-5}$
14 Nov 2019	$1.3x10^{17}$	$5.3x10^{13}$	$3.7x10^{-4}$	$6.2x10^{-5}$
25 Nov 2019	$2.5x10^{17}$	$8.5x10^{13}$	$3.4x10^{-4}$	$5.7x10^{-5}$
1 Dec 2019	$2.5x10^{17}$	$7.6x10^{13}$	$3.0x10^{-4}$	$2.6x10^{-5}$
2 Dec 2019	$1.9x10^{17}$	$7.3x10^{13}$	$3.4x10^{-4}$	$3.3x10^{-5}$
5 Dec 2019	$7.9x10^{16}$	$2.6x10^{13}$	$2.6x10^{-4}$	$5.0x10^{-5}$
6 Dec 2019	$7.7x10^{16}$	$2.1x10^{13}$	$1.7x10^{-4}$	$3.2x10^{-5}$
8 Jan 2020	$8.8x10^{16}$	$3.1x10^{13}$	$2.0x10^{-4}$	$5.9x10^{-5}$
13 Jan 2020	$3.6x10^{17}$	$6.7x10^{13}$	$2.2x10^{-4}$	$2.5x10^{-5}$
21 Jan 2020	$8.9x10^{16}$	$2.7x10^{13}$	$1.7x10^{-4}$	$2.5x10^{-5}$
22 Jan 2020	$8.0x10^{16}$	$3.1x10^{13}$	$1.5x10^{-4}$	$3.6x10^{-5}$
2 Feb 2020	$1.0x10^{17}$	$4.3x10^{13}$	$2.9x10^{-4}$	$3.5x10^{-5}$
9 Feb 2020	$6.8x10^{16}$	$2.1x10^{13}$	$1.5x10^{-4}$	$3.6x10^{-5}$
18 Feb 2020	$6.6x10^{16}$	$2.7x10^{13}$	$1.0x10^{-4}$	$7.6x10^{-5}$
29 Feb 2020	$1.7x10^{17}$	$4.5x10^{13}$	$2.2x10^{-4}$	$4.5x10^{-5}$
10 Mar 2020	$3.6x10^{17}$	$6.0x10^{13}$	$2.8x10^{-4}$	$1.7x10^{-5}$
11 Mar 2020	$1.1x10^{17}$	$3.6x10^{13}$	$2.7x10^{-4}$	$6.0x10^{-5}$
16 Mar 2020	$2.6x10^{17}$	$5.8x10^{13}$	$8.5x10^{-5}$	$2.1x10^{-5}$
17 Mar 2020	$3.7x10^{17}$	$3.6x10^{13}$	$6.7x10^{-5}$	$1.8x10^{-5}$
22 Mar 2020	$2.0x10^{17}$	$7.1x10^{13}$	$4.9x10^{-4}$	$3.4x10^{-5}$
23 Mar 2020	$8.8x10^{16}$	$3.8x10^{13}$	$3.7x10^{-4}$	$3.8x10^{-5}$
6 April 2020	$2.3x10^{17}$	$5.3x10^{13}$	$2.7x10^{-4}$	$1.7x10^{-5}$
7 April 2020	$1.9x10^{17}$	$2.7x10^{13}$	$1.0x10^{-4}$	$2.4x10^{-5}$
19 April 2020	$1.4x10^{17}$	$3.2x10^{13}$	$2.2x10^{-4}$	$2.6x10^{-5}$
23 April 2020	$2.3x10^{17}$	$6.5x10^{13}$	$2.7x10^{-4}$	$2.5x10^{-5}$
24 April 2020	$1.8x10^{17}$	$5.2x10^{13}$	$2.4x10^{-4}$	$1.6x10^{-5}$
8 May 2020	$9.4x10^{16}$	$3.7x10^{13}$	$2.0x10^{-4}$	$4.1x10^{-5}$
9 May 2020	$6.3x10^{16}$	$2.6x10^{13}$	$9.2x10^{-5}$	$3.0x10^{-5}$
9 June 2020	$7.8x10^{16}$	$2.8x10^{13}$	$1.3x10^{-4}$	$6.3x10^{-5}$
24 June 2020	$1.4x10^{17}$	$3.5x10^{13}$	$2.2x10^{-4}$	$4.6x10^{-5}$
1 July 2020	$8.3x10^{16}$	$2.2x10^{13}$	$5.3x10^{-5}$	$3.5x10^{-5}$
10 July 2020	$1.2x10^{17}$	$3.6x10^{13}$	$6.3x10^{-5}$	$3.0x10^{-5}$
11 July 2020	$1.5x10^{17}$	$2.6x10^{13}$	$1.3x10^{-4}$	$3.3x10^{-5}$
12 July 2020	$1.3x10^{17}$	$4.0x10^{13}$	$7.2x10^{-5}$	$2.8x10^{-5}$
18 July 2020	$9.8x10^{16}$	$2.7x10^{13}$	$2.1x10^{-4}$	$4.1x10^{-5}$
21 July 2020	$1.9x10^{17}$	$3.6x10^{13}$	$1.2x10^{-4}$	$3.0x10^{-5}$
7 Aug 2020	$1.0x10^{17}$	$3.4x10^{13}$	$7.7x10^{-5}$	$5.0x10^{-5}$
8 Aug 2020	$8.0x10^{16}$	$3.4x10^{13}$	$1.4x10^{-4}$	$5.8x10^{-5}$
11 Aug 2020	$1.4x10^{17}$	$2.9x10^{13}$	$1.1x10^{-4}$	$1.8x10^{-5}$
12 Aug 2020	$1.4x10^{17}$	$3.3x10^{13}$	$1.5x10^{-4}$	$2.2x10^{-5}$
24 Aug 2020	$1.1x10^{17}$	$2.8x10^{13}$	$1.1x10^{-4}$	$3.3x10^{-5}$
28 Aug 2020	$3.5x10^{17}$	$3.6x10^{13}$	$7.5x10^{-5}$	$2.2x10^{-5}$
29 Aug 2020	$8.2x10^{16}$	$2.8x10^{13}$	$1.0x10^{-4}$	$2.2x10^{-5}$
31 Aug 2020	$1.1x10^{17}$	$2.7x10^{13}$	$1.4x10^{-4}$	$2.7x10^{-5}$
8 Sept 2020	$2.8x10^{17}$	$4.7x10^{13}$	$1.8x10^{-4}$	$2.1x10^{-5}$
9 Sept 2020	$1.2x10^{17}$	$2.2x10^{13}$	$5.5x10^{-5}$	$3.7x10^{-5}$
1 Oct 2020	$1.1x10^{17}$	$3.5x10^{13}$	$1.5x10^{-4}$	$5.0x10^{-5}$
11 Oct 2020	$7.1x10^{16}$	$3.5x10^{13}$	$1.8x10^{-4}$	$5.0x10^{-5}$
19 Oct 2020	$8.3x10^{16}$	$3.1x10^{13}$	$2.2x10^{-4}$	$4.1x10^{-5}$
4 Nov 2020	$9.3x10^{16}$	$2.5x10^{13}$	$1.4x10^{-4}$	$3.2x10^{-5}$
5 Nov 2020	$9.5x10^{16}$	$2.8x10^{13}$	$1.8x10^{-4}$	$3.5x10^{-5}$
6 Nov 2020	$1.3x10^{17}$	$3.4x10^{13}$	$1.8x10^{-4}$	$3.9x10^{-5}$
11 Nov 2020	$1.6x10^{17}$	$2.8x10^{13}$	$1.6x10^{-4}$	$4.0x10^{-5}$

Etna, Italy

date	SO_2 VCD max. [molecules cm^{-2}]	BrO VCD	BrO/SO_2 fitted	BrO/SO_2 error
17 Nov 2020	$1.1x10^{17}$	$2.9x10^{13}$	$2.1x10^{-4}$	$3.4x10^{-5}$
23 Dec 2020	$1.8x10^{17}$	$5.2x10^{13}$	$2.0x10^{-4}$	$2.7x10^{-5}$
15 Jan 2021	$1.2x10^{17}$	$3.1x10^{13}$	$2.1x10^{-4}$	$1.7x10^{-5}$
18 Jan 2021	$1.1x10^{17}$	$3.0x10^{13}$	$1.9x10^{-4}$	$5.0x10^{-5}$
20 Jan 2021	$1.1x10^{17}$	$3.1x10^{13}$	$1.3x10^{-4}$	$2.0x10^{-5}$
26 Jan 2021	$8.0x10^{16}$	$3.9x10^{13}$	$3.4x10^{-4}$	$3.4x10^{-5}$
4 Feb 2021	$8.8x10^{16}$	$2.6x10^{13}$	$1.4x10^{-4}$	$2.4x10^{-5}$
5 Feb 2021	$6.9x10^{16}$	$3.2x10^{13}$	$1.8x10^{-4}$	$2.4x10^{-5}$
6 Feb 2021	$7.3x10^{16}$	$2.4x10^{13}$	$1.7x10^{-4}$	$4.3x10^{-5}$
14 Feb 2021	$1.3x10^{17}$	$3.4x10^{13}$	$7.0x10^{-5}$	$1.6x10^{-5}$
2 Mar 2021	$3.9x10^{17}$	$6.0x10^{13}$	$1.8x10^{-4}$	$2.8x10^{-5}$
3 Mar 2021	$1.1x10^{17}$	$3.6x10^{13}$	$1.3x10^{-4}$	$3.8x10^{-5}$
8 Mar 2021	$1.4x10^{17}$	$2.1x10^{13}$	$1.4x10^{-4}$	$4.7x10^{-5}$
9 Mar 2021	$9.8x10^{16}$	$4.5x10^{13}$	$2.2x10^{-4}$	$3.2x10^{-5}$
26 May 2021	$4.7x10^{17}$	$3.9x10^{13}$	$6.2x10^{-5}$	$7.7x10^{-6}$
27 May 2021	$3.2x10^{17}$	$8.5x10^{13}$	$2.0x10^{-4}$	$2.2x10^{-5}$
16 June 2021	$1.7x10^{18}$	$6.0x10^{13}$	$4.0x10^{-5}$	$8.4x10^{-6}$
14 July 2021	$2.8x10^{18}$	$1.1x10^{14}$	$3.7x10^{-5}$	$3.3x10^{-6}$
19 July 2021	$1.1x10^{17}$	$2.8x10^{13}$	$1.0x10^{-4}$	$3.3x10^{-5}$
27 July 2021	$7.2x10^{16}$	$2.4x10^{13}$	$1.8x10^{-4}$	$3.7x10^{-5}$
4 Aug 2021	$7.6x10^{16}$	$2.0x10^{13}$	$2.3x10^{-5}$	$4.0x10^{-5}$
10 Aug 2021	$1.8x10^{17}$	$4.1x10^{13}$	$1.3x10^{-4}$	$2.3x10^{-5}$
1 Oct 2021	$1.4x10^{17}$	$5.4x10^{13}$	$3.2x10^{-4}$	$5.6x10^{-5}$
18 Oct 2021	$9.1x10^{16}$	$4.2x10^{13}$	$2.9x10^{-4}$	$3.7x10^{-5}$
30 Oct 2021	$2.0x10^{17}$	$7.6x10^{13}$	$4.1x10^{-4}$	$2.6x10^{-5}$
15 Nov 2021	$2.8x10^{17}$	$6.8x10^{13}$	$2.2x10^{-4}$	$2.6x10^{-5}$
19 Nov 2021	$8.6x10^{16}$	$3.2x10^{13}$	$2.1x10^{-4}$	$5.0x10^{-5}$
24 Nov 2021	$3.0x10^{17}$	$6.2x10^{13}$	$2.7x10^{-4}$	$3.6x10^{-5}$
14 Dec 2021	$1.0x10^{17}$	$3.0x10^{13}$	$1.7x10^{-4}$	$2.4x10^{-5}$

La Palma, Spain

Type: hot spot
longitude: 17.84° W
latitude: 28.57° N
Events: 48
$BrO > 2\sigma$: $4.3x10^{-5}$
BrO/SO_2: $1.9x10^{-5}$
std. dev.: $1.1x10^{18}$
mean SO_2: $4.9x10^{13}$
mean BrO:



20 Sept 2021	$2.4x10^{19}$	$3.8x10^{14}$	$2.0x10^{-5}$	$3.1x10^{-7}$
22 Sept 2021	$3.7x10^{17}$	$3.8x10^{13}$	$7.9x10^{-5}$	$4.5x10^{-6}$
23 Sept 2021	$7.6x10^{17}$	$4.6x10^{13}$	$6.6x10^{-5}$	$1.6x10^{-6}$
29 Sept 2021	$4.5x10^{17}$	$6.3x10^{13}$	$3.5x10^{-5}$	$1.9x10^{-6}$
7 Oct 2021	$9.9x10^{17}$	$4.7x10^{13}$	$2.7x10^{-5}$	$8.5x10^{-7}$
8 Oct 2021	$4.1x10^{17}$	$2.7x10^{13}$	$2.0x10^{-5}$	$2.0x10^{-6}$
10 Oct 2021	$3.0x10^{18}$	$1.1x10^{14}$	$5.3x10^{-5}$	$1.6x10^{-6}$
13 Oct 2021	$1.1x10^{18}$	$1.1x10^{14}$	$5.3x10^{-5}$	$3.3x10^{-6}$
14 Oct 2021	$2.4x10^{17}$	$2.8x10^{13}$	$6.3x10^{-5}$	$3.5x10^{-6}$
20 Oct 2021	$5.3x10^{17}$	$6.2x10^{13}$	$6.6x10^{-5}$	$2.7x10^{-6}$
24 Oct 2021	$5.4x10^{17}$	$4.5x10^{13}$	$6.6x10^{-5}$	$3.3x10^{-6}$
25 Oct 2021	$3.5x10^{17}$	$4.2x10^{13}$	$6.8x10^{-5}$	$3.8x10^{-6}$
27 Oct 2021	$4.2x10^{17}$	$3.7x10^{13}$	$4.4x10^{-5}$	$3.7x10^{-6}$
28 Oct 2021	$2.3x10^{18}$	$1.3x10^{14}$	$4.8x10^{-5}$	$2.5x10^{-6}$
29 Oct 2021	$8.3x10^{17}$	$5.3x10^{13}$	$5.5x10^{-5}$	$4.5x10^{-6}$
30 Oct 2021	$2.5x10^{17}$	$2.8x10^{13}$	$6.8x10^{-5}$	$5.7x10^{-6}$
1 Nov 2021	$4.5x10^{17}$	$4.8x10^{13}$	$3.6x10^{-5}$	$2.1x10^{-6}$
2 Nov 2021	$6.4x10^{17}$	$4.3x10^{13}$	$4.5x10^{-5}$	$2.0x10^{-6}$
5 Nov 2021	$3.5x10^{17}$	$2.7x10^{13}$	$5.0x10^{-5}$	$3.3x10^{-6}$
6 Nov 2021	$3.1x10^{17}$	$3.4x10^{13}$	$4.0x10^{-5}$	$5.5x10^{-6}$
7 Nov 2021	$6.6x10^{17}$	$4.5x10^{13}$	$7.0x10^{-5}$	$5.7x10^{-6}$
9 Nov 2021	$4.9x10^{17}$	$2.4x10^{13}$	$6.1x10^{-5}$	$7.9x10^{-6}$
10 Nov 2021	$2.0x10^{17}$	$2.5x10^{13}$	$6.6x10^{-5}$	$8.1x10^{-6}$
12 Nov 2021	$1.9x10^{18}$	$6.4x10^{13}$	$4.2x10^{-5}$	$3.1x10^{-6}$
13 Nov 2021	$1.4x10^{18}$	$6.7x10^{13}$	$4.9x10^{-5}$	$4.1x10^{-6}$
14 Nov 2021	$2.8x10^{17}$	$2.2x10^{13}$	$5.6x10^{-5}$	$1.0x10^{-5}$
15 Nov 2021	$9.0x10^{16}$	$1.7x10^{13}$	$8.2x10^{-5}$	$1.4x10^{-5}$
16 Nov 2021	$9.7x10^{17}$	$3.9x10^{13}$	$4.6x10^{-5}$	$5.0x10^{-6}$
17 Nov 2021	$1.2x10^{17}$	$2.8x10^{13}$	$4.2x10^{-5}$	$1.4x10^{-5}$
18 Nov 2021	$9.1x10^{17}$	$4.5x10^{13}$	$3.4x10^{-5}$	$4.7x10^{-6}$
19 Nov 2021	$3.0x10^{17}$	$3.4x10^{13}$	$3.6x10^{-5}$	$7.0x10^{-6}$

La Palma, Spain

date	SO_2 VCD max. [molecules cm^{-2}]	BrO VCD	BrO/SO_2 fitted	BrO/SO_2 error
20 Nov 2021	$1.1x10^{17}$	$1.9x10^{13}$	$1.0x10^{-5}$	$9.8x10^{-6}$
21 Nov 2021	$7.3x10^{16}$	$1.8x10^{13}$	$6.9x10^{-5}$	$1.5x10^{-5}$
22 Nov 2021	$8.1x10^{17}$	$5.1x10^{13}$	$6.1x10^{-5}$	$5.1x10^{-6}$
27 Nov 2021	$3.9x10^{17}$	$3.7x10^{13}$	$7.0x10^{-5}$	$6.9x10^{-6}$
28 Nov 2021	$3.6x10^{17}$	$4.2x10^{13}$	$6.5x10^{-5}$	$7.9x10^{-6}$
29 Nov 2021	$1.0x10^{17}$	$2.3x10^{13}$	$5.7x10^{-5}$	$2.0x10^{-5}$
30 Nov 2021	$4.0x10^{17}$	$4.6x10^{13}$	$9.6x10^{-5}$	$1.3x10^{-5}$
1 Dec 2021	$1.3x10^{17}$	$3.0x10^{13}$	$8.3x10^{-5}$	$1.0x10^{-5}$
2 Dec 2021	$2.7x10^{17}$	$3.0x10^{13}$	$5.7x10^{-5}$	$8.6x10^{-6}$
3 Dec 2021	$1.4x10^{17}$	$3.0x10^{13}$	$8.0x10^{-5}$	$1.6x10^{-5}$
4 Dec 2021	$1.2x10^{17}$	$2.4x10^{13}$	$8.0x10^{-5}$	$2.0x10^{-5}$
5 Dec 2021	$6.6x10^{16}$	$1.8x10^{13}$	$4.8x10^{-5}$	$3.5x10^{-5}$
7 Dec 2021	$7.9x10^{16}$	$1.7x10^{13}$	$4.0x10^{-5}$	$3.8x10^{-5}$
8 Dec 2021	$8.3x10^{17}$	$4.3x10^{13}$	$6.1x10^{-5}$	$6.8x10^{-6}$
9 Dec 2021	$8.8x10^{16}$	$3.0x10^{13}$	$8.4x10^{-5}$	$2.5x10^{-5}$
12 Dec 2021	$2.7x10^{17}$	$2.6x10^{13}$	$8.5x10^{-5}$	$9.8x10^{-6}$
13 Dec 2021	$1.1x10^{18}$	$5.7x10^{13}$	$5.5x10^{-5}$	$6.4x10^{-6}$

Nyiragongo, DR Congo

Type: rift
longitude: 29.25° E
latitude: 1.52° S
Events: 168
$BrO > 2\sigma$: 8
BrO/SO_2: $5.2x10^{-5}$
std. dev.: $3.3x10^{-5}$
mean SO_2: $1.6x10^{17}$
mean BrO: $2.9x10^{13}$



19 Feb 2018	$7.5x10^{16}$	$2.0x10^{13}$	$6.9x10^{-5}$	$3.8x10^{-5}$
18 Mar 2018	$9.3x10^{16}$	$3.3x10^{13}$	$3.8x10^{-5}$	$4.5x10^{-5}$
12 April 2018	$1.3x10^{17}$	$2.7x10^{13}$	$9.9x10^{-5}$	$3.7x10^{-5}$
13 April 2018	$8.2x10^{16}$	$2.6x10^{13}$	$6.7x10^{-6}$	$3.7x10^{-5}$
20 May 2018	$2.3x10^{17}$	$3.3x10^{13}$	$7.9x10^{-5}$	$2.2x10^{-5}$
21 May 2018	$8.5x10^{16}$	$3.0x10^{13}$	$2.5x10^{-5}$	$3.1x10^{-5}$
25 May 2018	$1.3x10^{17}$	$1.7x10^{13}$	$3.0x10^{-5}$	$4.9x10^{-5}$
26 May 2018	$1.4x10^{17}$	$1.8x10^{13}$	$1.6x10^{-5}$	$5.0x10^{-5}$
30 May 2018	$2.3x10^{17}$	$1.8x10^{13}$	$4.6x10^{-5}$	$3.2x10^{-5}$
31 May 2018	$1.5x10^{17}$	$3.3x10^{13}$	$1.5x10^{-5}$	$3.8x10^{-5}$
6 June 2018	$1.0x10^{17}$	$2.7x10^{13}$	$5.8x10^{-5}$	$5.0x10^{-5}$
26 June 2018	$1.8x10^{17}$	$2.1x10^{13}$	$5.4x10^{-5}$	$3.7x10^{-5}$
27 June 2018	$2.3x10^{17}$	$1.8x10^{13}$	$6.0x10^{-5}$	$2.8x10^{-5}$
1 July 2018	$1.5x10^{17}$	$1.8x10^{13}$	$5.7x10^{-5}$	$3.7x10^{-5}$
3 July 2018	$2.7x10^{17}$	$2.2x10^{13}$	$7.5x10^{-5}$	$3.7x10^{-5}$
12 July 2018	$1.1x10^{17}$	$2.0x10^{13}$	$5.6x10^{-5}$	$3.4x10^{-5}$
13 July 2018	$1.0x10^{17}$	$2.1x10^{13}$	$2.0x10^{-5}$	$3.0x10^{-5}$
17 July 2018	$1.3x10^{17}$	$1.9x10^{13}$	$5.6x10^{-5}$	$3.1x10^{-5}$
18 July 2018	$1.6x10^{17}$	$4.5x10^{13}$	$4.1x10^{-5}$	$3.3x10^{-5}$
28 July 2018	$1.0x10^{17}$	$2.7x10^{13}$	$9.3x10^{-5}$	$6.0x10^{-5}$
14 Aug 2018	$7.8x10^{16}$	$1.7x10^{13}$	$1.1x10^{-6}$	$5.6x10^{-5}$
24 Aug 2018	$8.1x10^{16}$	$2.0x10^{13}$	$1.1x10^{-4}$	$3.1x10^{-5}$
30 Aug 2018	$2.7x10^{17}$	$2.7x10^{13}$	$2.4x10^{-5}$	$3.2x10^{-5}$
12 Nov 2018	$1.0x10^{17}$	$3.1x10^{13}$	$6.3x10^{-5}$	$5.0x10^{-5}$
27 April 2019	$1.0x10^{17}$	$3.1x10^{13}$	$7.2x10^{-5}$	$5.1x10^{-5}$
8 June 2019	$3.0x10^{17}$	$4.4x10^{13}$	$1.2x10^{-4}$	$2.9x10^{-5}$
9 June 2019	$9.7x10^{16}$	$3.3x10^{13}$	$8.4x10^{-5}$	$6.6x10^{-5}$
14 June 2019	$1.2x10^{17}$	$2.2x10^{13}$	$8.0x10^{-5}$	$4.3x10^{-5}$
19 June 2019	$1.1x10^{17}$	$2.8x10^{13}$	$2.4x10^{-5}$	$4.9x10^{-5}$
24 June 2019	$1.1x10^{17}$	$3.6x10^{13}$	$6.8x10^{-5}$	$4.3x10^{-5}$
29 June 2019	$1.2x10^{17}$	$2.5x10^{13}$	$2.4x10^{-5}$	$3.8x10^{-5}$
30 June 2019	$1.3x10^{17}$	$1.4x10^{13}$	$4.1x10^{-5}$	$4.1x10^{-5}$
16 July 2019	$2.3x10^{17}$	$3.6x10^{13}$	$5.4x10^{-5}$	$1.8x10^{-5}$
17 July 2019	$7.1x10^{16}$	$2.1x10^{13}$	$1.1x10^{-4}$	$4.0x10^{-5}$
21 July 2019	$1.6x10^{17}$	$2.8x10^{13}$	$2.3x10^{-5}$	$3.4x10^{-5}$
22 July 2019	$1.4x10^{17}$	$2.5x10^{13}$	$6.8x10^{-5}$	$5.2x10^{-5}$
26 July 2019	$2.9x10^{17}$	$2.2x10^{13}$	$5.2x10^{-5}$	$2.6x10^{-5}$
27 July 2019	$2.2x10^{17}$	$1.4x10^{13}$	$1.8x10^{-5}$	$3.0x10^{-5}$
31 July 2019	$9.7x10^{16}$	$1.5x10^{13}$	$3.6x10^{-5}$	$4.0x10^{-5}$
1 Aug 2019	$1.1x10^{17}$	$2.7x10^{13}$	$1.2x10^{-4}$	$4.3x10^{-5}$
29 Aug 2019	$1.5x10^{17}$	$2.0x10^{13}$	$3.4x10^{-5}$	$3.0x10^{-5}$
7 Sept 2019	$1.4x10^{17}$	$2.5x10^{13}$	$5.4x10^{-5}$	$5.9x10^{-5}$
23 Sept 2019	$1.4x10^{17}$	$2.4x10^{13}$	$4.9x10^{-5}$	$6.0x10^{-5}$

Nyiragongo, DR Congo

date	SO_2 VCD max. [molecules cm^{-2}]	BrO VCD	BrO/SO_2 fitted	BrO/SO_2 error
19 Oct 2019	$1.2x10^{17}$	$4.3x10^{13}$	$2.3x10^{-5}$	$3.4x10^{-5}$
20 Oct 2019	$9.2x10^{16}$	$2.5x10^{13}$	$1.8x10^{-5}$	$3.6x10^{-5}$
15 Nov 2019	$1.1x10^{17}$	$3.2x10^{13}$	$1.1x10^{-4}$	$3.0x10^{-5}$
27 Nov 2019	$8.0x10^{16}$	$1.8x10^{13}$	$1.8x10^{-5}$	$3.6x10^{-5}$
3 Dec 2019	$1.2x10^{17}$	$1.6x10^{13}$	$2.8x10^{-5}$	$1.8x10^{-5}$
5 Dec 2019	$1.0x10^{17}$	$1.7x10^{13}$	$2.9x10^{-5}$	$3.7x10^{-5}$
7 Dec 2019	$2.9x10^{17}$	$2.8x10^{13}$	$2.0x10^{-5}$	$1.8x10^{-5}$
8 Dec 2019	$8.9x10^{16}$	$2.1x10^{13}$	$1.2x10^{-4}$	$3.1x10^{-5}$
13 Dec 2019	$6.1x10^{16}$	$2.9x10^{13}$	$1.1x10^{-4}$	$3.9x10^{-5}$
17 Dec 2019	$1.3x10^{17}$	$4.9x10^{13}$	$6.3x10^{-5}$	$2.2x10^{-5}$
18 Dec 2019	$2.0x10^{17}$	$4.8x10^{13}$	$6.1x10^{-5}$	$2.7x10^{-5}$
22 Dec 2019	$2.0x10^{17}$	$2.9x10^{13}$	$3.3x10^{-5}$	$1.9x10^{-5}$
23 Dec 2019	$4.5x10^{17}$	$3.4x10^{13}$	$3.9x10^{-5}$	$1.8x10^{-5}$
27 Dec 2019	$1.9x10^{17}$	$2.7x10^{13}$	$8.1x10^{-5}$	$2.2x10^{-5}$
28 Dec 2019	$9.9x10^{16}$	$2.9x10^{13}$	$3.6x10^{-5}$	$2.0x10^{-5}$
29 Dec 2019	$2.5x10^{17}$	$3.2x10^{13}$	$3.8x10^{-5}$	$1.8x10^{-5}$
7 Jan 2020	$1.6x10^{17}$	$4.6x10^{13}$	$1.1x10^{-4}$	$4.3x10^{-5}$
12 Jan 2020	$8.1x10^{16}$	$3.7x10^{13}$	$5.7x10^{-5}$	$3.3x10^{-5}$
14 Jan 2020	$1.4x10^{17}$	$3.4x10^{13}$	$7.6x10^{-5}$	$2.6x10^{-5}$
18 Jan 2020	$1.8x10^{17}$	$3.2x10^{13}$	$4.3x10^{-5}$	$1.2x10^{-5}$
20 Jan 2020	$5.4x10^{17}$	$4.0x10^{13}$	$7.9x10^{-5}$	$1.2x10^{-5}$
2 Feb 2020	$1.2x10^{17}$	$2.9x10^{13}$	$9.1x10^{-5}$	$2.0x10^{-5}$
3 Feb 2020	$2.0x10^{17}$	$3.2x10^{13}$	$1.2x10^{-5}$	$2.6x10^{-5}$
4 Feb 2020	$9.5x10^{16}$	$3.4x10^{13}$	$2.8x10^{-5}$	$3.4x10^{-5}$
5 Feb 2020	$1.2x10^{17}$	$1.9x10^{13}$	$4.5x10^{-5}$	$2.6x10^{-5}$
7 Feb 2020	$9.9x10^{16}$	$2.5x10^{13}$	$6.1x10^{-5}$	$3.6x10^{-5}$
8 Feb 2020	$1.6x10^{17}$	$3.5x10^{13}$	$5.4x10^{-5}$	$4.0x10^{-5}$
9 Feb 2020	$2.2x10^{17}$	$4.9x10^{13}$	$6.7x10^{-5}$	$3.2x10^{-5}$
14 Feb 2020	$2.0x10^{17}$	$3.4x10^{13}$	$9.2x10^{-5}$	$4.2x10^{-5}$
19 Feb 2020	$1.4x10^{17}$	$4.0x10^{13}$	$3.6x10^{-5}$	$2.9x10^{-5}$
25 Feb 2020	$1.4x10^{17}$	$2.9x10^{13}$	$5.7x10^{-5}$	$3.6x10^{-5}$
26 Feb 2020	$1.9x10^{17}$	$3.7x10^{13}$	$6.2x10^{-5}$	$2.7x10^{-5}$
29 Feb 2020	$1.0x10^{17}$	$3.2x10^{13}$	$5.9x10^{-5}$	$2.8x10^{-5}$
2 Mar 2020	$6.5x10^{16}$	$3.1x10^{13}$	$7.8x10^{-5}$	$3.2x10^{-5}$
6 Mar 2020	$3.6x10^{17}$	$4.3x10^{13}$	$9.6x10^{-5}$	$2.4x10^{-5}$
7 Mar 2020	$4.1x10^{17}$	$3.4x10^{13}$	$4.1x10^{-6}$	$1.7x10^{-5}$
10 Mar 2020	$9.1x10^{16}$	$2.7x10^{13}$	$6.5x10^{-5}$	$2.9x10^{-5}$
13 Mar 2020	$9.5x10^{16}$	$2.4x10^{13}$	$9.9x10^{-5}$	$2.3x10^{-5}$
17 Mar 2020	$1.3x10^{17}$	$4.3x10^{13}$	$6.8x10^{-5}$	$2.4x10^{-5}$
18 Mar 2020	$1.0x10^{17}$	$1.2x10^{13}$	$1.8x10^{-5}$	$2.8x10^{-5}$
22 Mar 2020	$1.2x10^{17}$	$2.5x10^{13}$	$5.2x10^{-5}$	$2.4x10^{-5}$
23 Mar 2020	$1.4x10^{17}$	$3.7x10^{13}$	$1.1x10^{-5}$	$3.1x10^{-5}$
28 Mar 2020	$8.7x10^{16}$	$2.3x10^{13}$	$8.3x10^{-5}$	$3.9x10^{-5}$
3 April 2020	$7.4x10^{16}$	$2.4x10^{13}$	$1.5x10^{-5}$	$2.6x10^{-5}$
12 April 2020	$1.3x10^{17}$	$2.9x10^{13}$	$4.4x10^{-5}$	$2.9x10^{-5}$
13 April 2020	$2.1x10^{17}$	$3.0x10^{13}$	$5.2x10^{-5}$	$1.9x10^{-5}$
16 April 2020	$1.2x10^{17}$	$1.9x10^{13}$	$8.5x10^{-5}$	$3.0x10^{-5}$
19 April 2020	$1.4x10^{17}$	$2.7x10^{13}$	$4.0x10^{-5}$	$2.0x10^{-5}$
22 April 2020	$2.9x10^{17}$	$2.6x10^{13}$	$5.4x10^{-5}$	$1.2x10^{-5}$
23 April 2020	$1.4x10^{17}$	$3.5x10^{13}$	$7.7x10^{-5}$	$3.0x10^{-5}$
24 April 2020	$1.2x10^{17}$	$4.9x10^{13}$	$1.5x10^{-4}$	$4.4x10^{-5}$
30 April 2020	$1.9x10^{17}$	$2.8x10^{13}$	$4.2x10^{-5}$	$4.7x10^{-5}$
4 May 2020	$5.5x10^{17}$	$5.7x10^{13}$	$6.8x10^{-5}$	$1.4x10^{-5}$
9 May 2020	$3.1x10^{17}$	$3.0x10^{13}$	$1.9x10^{-6}$	$2.5x10^{-5}$
10 May 2020	$8.3x10^{16}$	$3.0x10^{13}$	$5.5x10^{-5}$	$4.9x10^{-5}$
14 May 2020	$1.8x10^{17}$	$3.1x10^{13}$	$3.0x10^{-5}$	$3.7x10^{-5}$
16 May 2020	$2.0x10^{17}$	$2.3x10^{13}$	$8.3x10^{-5}$	$2.4x10^{-5}$
19 May 2020	$1.7x10^{17}$	$2.6x10^{13}$	$1.5x10^{-5}$	$3.3x10^{-5}$
20 May 2020	$2.3x10^{17}$	$4.1x10^{13}$	$6.2x10^{-6}$	$3.6x10^{-5}$
25 May 2020	$3.3x10^{17}$	$6.0x10^{13}$	$5.3x10^{-5}$	$1.8x10^{-5}$
26 May 2020	$9.7x10^{16}$	$2.7x10^{13}$	$0.7x10^{-5}$	$4.8x10^{-5}$
27 May 2020	$1.4x10^{17}$	$1.2x10^{13}$	$1.6x10^{-6}$	$4.5x10^{-5}$
30 May 2020	$1.8x10^{17}$	$5.3x10^{13}$	$8.2x10^{-5}$	$3.4x10^{-5}$
31 May 2020	$1.3x10^{17}$	$3.0x10^{13}$	$9.5x10^{-5}$	$4.9x10^{-5}$
1 June 2020	$1.2x10^{17}$	$2.3x10^{13}$	$9.5x10^{-5}$	$4.4x10^{-5}$
4 June 2020	$1.4x10^{17}$	$2.3x10^{13}$	$6.2x10^{-5}$	$3.8x10^{-5}$
5 June 2020	$1.4x10^{17}$	$2.4x10^{13}$	$1.0x10^{-4}$	$3.7x10^{-5}$
10 June 2020	$2.0x10^{17}$	$2.4x10^{13}$	$3.4x10^{-5}$	$2.7x10^{-5}$
11 June 2020	$1.5x10^{17}$	$1.4x10^{13}$	$1.5x10^{-5}$	$1.7x10^{-5}$
12 June 2020	$9.4x10^{16}$	$3.2x10^{13}$	$8.6x10^{-5}$	$7.2x10^{-5}$
15 June 2020	$1.1x10^{17}$	$2.6x10^{13}$	$7.1x10^{-5}$	$2.5x10^{-5}$

Nyiragongo, DR Congo

date	SO_2 VCD max. [molecules cm^{-2}]	BrO VCD	BrO/SO_2 fitted	BrO/SO_2 error
16 June 2020	$2.4x10^{17}$	$3.5x10^{13}$	$7.4x10^{-5}$	$2.0x10^{-5}$
17 June 2020	$2.0x10^{17}$	$3.1x10^{13}$	$2.1x10^{-5}$	$2.5x10^{-5}$
20 June 2020	$1.3x10^{17}$	$2.3x10^{13}$	$8.3x10^{-5}$	$3.1x10^{-5}$
21 June 2020	$8.1x10^{16}$	$2.6x10^{13}$	$2.3x10^{-5}$	$4.4x10^{-5}$
22 June 2020	$1.0x10^{17}$	$2.5x10^{13}$	$1.4x10^{-5}$	$2.8x10^{-5}$
25 June 2020	$2.1x10^{17}$	$1.9x10^{13}$	$6.1x10^{-5}$	$2.9x10^{-5}$
26 June 2020	$3.3x10^{17}$	$2.8x10^{13}$	$6.5x10^{-5}$	$2.2x10^{-5}$
27 June 2020	$1.1x10^{17}$	$3.5x10^{13}$	$6.6x10^{-5}$	$2.6x10^{-5}$
28 June 2020	$8.8x10^{16}$	$2.1x10^{13}$	$2.0x10^{-5}$	$5.7x10^{-5}$
1 July 2020	$8.7x10^{16}$	$1.9x10^{13}$	$5.4x10^{-5}$	$3.5x10^{-5}$
2 July 2020	$2.0x10^{17}$	$2.6x10^{13}$	$3.6x10^{-5}$	$2.8x10^{-5}$
3 July 2020	$1.2x10^{17}$	$2.8x10^{13}$	$1.3x10^{-4}$	$4.3x10^{-5}$
6 July 2020	$1.8x10^{17}$	$2.0x10^{13}$	$3.1x10^{-5}$	$3.1x10^{-5}$
7 July 2020	$1.9x10^{17}$	$3.0x10^{13}$	$3.6x10^{-5}$	$2.0x10^{-5}$
8 July 2020	$3.7x10^{17}$	$3.6x10^{13}$	$4.6x10^{-5}$	$1.8x10^{-5}$
13 July 2020	$2.6x10^{17}$	$4.1x10^{13}$	$4.4x10^{-5}$	$3.2x10^{-5}$
18 July 2020	$2.0x10^{17}$	$2.4x10^{13}$	$9.2x10^{-5}$	$2.3x10^{-5}$
19 July 2020	$1.2x10^{17}$	$1.6x10^{13}$	$5.6x10^{-5}$	$3.3x10^{-5}$
22 July 2020	$1.3x10^{17}$	$1.8x10^{13}$	$4.5x10^{-5}$	$4.3x10^{-5}$
24 July 2020	$1.1x10^{17}$	$2.3x10^{13}$	$6.4x10^{-5}$	$3.3x10^{-5}$
28 July 2020	$2.4x10^{17}$	$3.7x10^{13}$	$6.3x10^{-5}$	$1.8x10^{-5}$
2 Aug 2020	$1.6x10^{17}$	$2.3x10^{13}$	$2.0x10^{-5}$	$4.1x10^{-5}$
9 Aug 2020	$6.3x10^{16}$	$1.5x10^{13}$	$1.2x10^{-5}$	$6.0x10^{-5}$
14 Aug 2020	$9.8x10^{16}$	$2.6x10^{13}$	$3.4x10^{-5}$	$6.3x10^{-5}$
15 Aug 2020	$7.8x10^{16}$	$1.7x10^{13}$	$7.5x10^{-5}$	$4.5x10^{-5}$
19 Aug 2020	$1.2x10^{17}$	$2.7x10^{13}$	$6.3x10^{-5}$	$5.5x10^{-5}$
23 Aug 2020	$1.3x10^{17}$	$1.8x10^{13}$	$4.7x10^{-6}$	$3.5x10^{-5}$
24 Aug 2020	$2.3x10^{17}$	$3.3x10^{13}$	$4.5x10^{-5}$	$2.3x10^{-5}$
3 Sept 2020	$1.6x10^{17}$	$2.3x10^{13}$	$7.9x10^{-5}$	$4.1x10^{-5}$
4 Sept 2020	$1.2x10^{17}$	$2.6x10^{13}$	$4.5x10^{-5}$	$3.4x10^{-5}$
5 Sept 2020	$1.5x10^{17}$	$2.3x10^{13}$	$1.4x10^{-5}$	$5.2x10^{-5}$
9 Sept 2020	$1.2x10^{17}$	$3.1x10^{13}$	$8.1x10^{-6}$	$4.6x10^{-5}$
10 Sept 2020	$4.7x10^{17}$	$4.8x10^{13}$	$7.0x10^{-5}$	$2.2x10^{-5}$
21 Oct 2020	$1.4x10^{17}$	$2.8x10^{13}$	$5.4x10^{-5}$	$3.2x10^{-5}$
12 Nov 2020	$6.0x10^{16}$	$3.9x10^{13}$	$3.3x10^{-5}$	$6.6x10^{-5}$
17 Nov 2020	$2.0x10^{17}$	$2.6x10^{13}$	$1.4x10^{-6}$	$3.1x10^{-5}$
23 Nov 2020	$1.7x10^{17}$	$2.2x10^{13}$	$2.9x10^{-5}$	$3.9x10^{-5}$
28 Nov 2020	$1.9x10^{17}$	$2.4x10^{13}$	$4.1x10^{-5}$	$3.4x10^{-5}$
14 Dec 2020	$3.2x10^{17}$	$2.5x10^{13}$	$7.3x10^{-5}$	$2.9x10^{-5}$
4 Jan 2021	$1.8x10^{17}$	$2.4x10^{13}$	$9.4x10^{-5}$	$3.7x10^{-5}$
5 Jan 2021	$1.8x10^{17}$	$3.5x10^{13}$	$1.1x10^{-4}$	$3.9x10^{-5}$
9 Jan 2021	$9.7x10^{16}$	$2.1x10^{13}$	$6.4x10^{-5}$	$4.1x10^{-5}$
31 Jan 2021	$1.4x10^{17}$	$3.0x10^{13}$	$3.5x10^{-5}$	$7.0x10^{-5}$
5 Feb 2021	$9.2x10^{16}$	$3.8x10^{13}$	$8.2x10^{-5}$	$4.8x10^{-5}$
6 Feb 2021	$2.4x10^{17}$	$2.5x10^{13}$	$4.0x10^{-5}$	$2.7x10^{-5}$
15 Mar 2021	$1.3x10^{17}$	$2.3x10^{13}$	$5.4x10^{-5}$	$4.4x10^{-5}$
30 Mar 2021	$1.6x10^{17}$	$3.4x10^{13}$	$7.2x10^{-5}$	$4.6x10^{-5}$
5 April 2021	$9.0x10^{16}$	$4.2x10^{13}$	$1.1x10^{-4}$	$7.3x10^{-5}$
10 April 2021	$1.4x10^{17}$	$2.5x10^{13}$	$8.8x10^{-5}$	$4.8x10^{-5}$
15 April 2021	$1.2x10^{17}$	$3.4x10^{13}$	$2.0x10^{-5}$	$4.9x10^{-5}$
27 April 2021	$3.7x10^{17}$	$3.5x10^{13}$	$4.1x10^{-5}$	$3.4x10^{-5}$
13 May 2021	$1.2x10^{17}$	$2.8x10^{13}$	$3.3x10^{-5}$	$4.5x10^{-5}$
17 May 2021	$1.2x10^{17}$	$4.6x10^{13}$	$4.3x10^{-5}$	$4.0x10^{-5}$
24 May 2021	$1.1x10^{17}$	$3.1x10^{13}$	$3.6x10^{-5}$	$1.9x10^{-5}$

Nyamuragira, DR Congo

Type:	rift
longitude:	29.20° E
latitude:	1.41° S
Events:	49
BrO > 2σ:	8
BrO/SO_2:	$5.7x10^{-5}$
std. dev.:	$4.2x10^{-5}$
mean SO_2:	$1.5x10^{17}$
mean BrO:	$3.0x10^{13}$



3 Jan 2018	$8.1x10^{16}$	$1.1x10^{13}$	$2.0x10^{-5}$	$3.3x10^{-5}$
17 Mar 2018	$1.7x10^{17}$	$3.1x10^{13}$	$1.3x10^{-4}$	$3.0x10^{-5}$
16 June 2018	$7.9x10^{16}$	$1.9x10^{13}$	$1.9x10^{-5}$	$4.5x10^{-5}$
23 May 2019	$1.2x10^{17}$	$2.2x10^{13}$	$7.1x10^{-5}$	$5.1x10^{-5}$
1 Sept 2019	$2.0x10^{17}$	$2.8x10^{13}$	$6.7x10^{-5}$	$1.3x10^{-5}$
31 Oct 2019	$5.7x10^{16}$	$1.6x10^{13}$	$7.0x10^{-6}$	$4.3x10^{-5}$

Nyamuragira, DR Congo

date	SO_2 VCD max. [molecules cm^{-2}]	BrO VCD	BrO/SO_2 fitted	BrO/SO_2 error
21 Nov 2019	$1.0x10^{17}$	$3.2x10^{13}$	$1.2x10^{-4}$	$3.9x10^{-5}$
26 Nov 2019	$3.9x10^{17}$	$3.0x10^{13}$	$5.3x10^{-5}$	$1.6x10^{-5}$
1 Dec 2019	$1.2x10^{17}$	$2.8x10^{13}$	$3.2x10^{-5}$	$1.8x10^{-5}$
2 Dec 2019	$2.2x10^{17}$	$3.5x10^{13}$	$6.2x10^{-5}$	$1.5x10^{-5}$
6 Dec 2019	$1.5x10^{17}$	$3.1x10^{13}$	$1.2x10^{-4}$	$2.5x10^{-5}$
11 Dec 2019	$1.5x10^{17}$	$2.0x10^{13}$	$5.5x10^{-5}$	$1.5x10^{-5}$
12 Dec 2019	$8.4x10^{16}$	$4.5x10^{13}$	$5.2x10^{-5}$	$3.2x10^{-5}$
16 Dec 2019	$8.3x10^{16}$	$2.9x10^{13}$	$9.8x10^{-5}$	$1.9x10^{-5}$
24 Dec 2019	$1.5x10^{17}$	$3.7x10^{13}$	$5.3x10^{-5}$	$2.4x10^{-5}$
2 Jan 2020	$1.1x10^{17}$	$3.5x10^{13}$	$7.8x10^{-5}$	$3.5x10^{-5}$
3 Jan 2020	$9.1x10^{16}$	$1.9x10^{13}$	$1.0x10^{-4}$	$4.3x10^{-5}$
13 Jan 2020	$2.3x10^{17}$	$4.1x10^{13}$	$8.9x10^{-5}$	$1.6x10^{-5}$
23 Jan 2020	$1.6x10^{17}$	$2.6x10^{13}$	$5.3x10^{-5}$	$1.6x10^{-5}$
24 Jan 2020	$1.5x10^{17}$	$2.5x10^{13}$	$2.0x10^{-5}$	$1.3x10^{-5}$
25 Jan 2020	$1.8x10^{17}$	$3.6x10^{13}$	$1.2x10^{-4}$	$2.0x10^{-5}$
13 Feb 2020	$1.6x10^{17}$	$1.6x10^{13}$	$2.1x10^{-5}$	$2.8x10^{-5}$
18 Feb 2020	$9.8x10^{16}$	$2.7x10^{13}$	$4.4x10^{-5}$	$3.3x10^{-5}$
1 Mar 2020	$3.6x10^{17}$	$4.0x10^{13}$	$8.5x10^{-5}$	$2.1x10^{-5}$
11 Mar 2020	$3.3x10^{17}$	$4.3x10^{13}$	$1.1x10^{-4}$	$1.4x10^{-5}$
12 Mar 2020	$2.5x10^{17}$	$3.9x10^{13}$	$7.9x10^{-5}$	$2.1x10^{-5}$
16 Mar 2020	$7.5x10^{16}$	$3.4x10^{13}$	$4.0x10^{-5}$	$1.8x10^{-5}$
21 Mar 2020	$9.4x10^{16}$	$2.9x10^{13}$	$5.9x10^{-5}$	$2.1x10^{-5}$
1 April 2020	$8.6x10^{16}$	$4.3x10^{13}$	$7.0x10^{-5}$	$2.9x10^{-5}$
2 April 2020	$1.3x10^{17}$	$2.6x10^{13}$	$3.2x10^{-6}$	$2.7x10^{-5}$
7 April 2020	$2.3x10^{17}$	$4.0x10^{13}$	$4.0x10^{-5}$	$1.7x10^{-5}$
8 April 2020	$9.0x10^{16}$	$3.7x10^{13}$	$4.6x10^{-6}$	$4.2x10^{-5}$
18 April 2020	$7.3x10^{16}$	$3.1x10^{13}$	$9.7x10^{-5}$	$3.1x10^{-5}$
29 April 2020	$8.8x10^{16}$	$1.3x10^{13}$	$3.1x10^{-6}$	$3.0x10^{-5}$
5 May 2020	$1.2x10^{17}$	$2.1x10^{13}$	$2.4x10^{-5}$	$4.0x10^{-5}$
12 July 2020	$1.0x10^{17}$	$3.8x10^{13}$	$1.1x10^{-5}$	$6.3x10^{-5}$
13 Aug 2020	$1.9x10^{17}$	$2.9x10^{13}$	$4.4x10^{-5}$	$2.0x10^{-5}$
30 Aug 2020	$8.3x10^{16}$	$4.4x10^{13}$	$6.1x10^{-5}$	$5.5x10^{-5}$
25 Sept 2020	$6.6x10^{16}$	$2.9x10^{13}$	$9.1x10^{-5}$	$3.6x10^{-5}$
30 Sept 2020	$9.1x10^{16}$	$3.7x10^{13}$	$1.3x10^{-4}$	$2.9x10^{-5}$
11 Oct 2020	$1.6x10^{17}$	$2.8x10^{13}$	$1.5x10^{-7}$	$3.2x10^{-5}$
16 Nov 2020	$2.1x10^{17}$	$2.7x10^{13}$	$6.7x10^{-5}$	$2.7x10^{-5}$
18 Nov 2020	$1.4x10^{17}$	$2.1x10^{13}$	$1.3x10^{-6}$	$4.3x10^{-5}$
9 Dec 2020	$1.2x10^{17}$	$2.4x10^{13}$	$1.3x10^{-4}$	$4.1x10^{-5}$
15 Dec 2020	$1.4x10^{17}$	$2.8x10^{13}$	$6.3x10^{-5}$	$6.6x10^{-5}$
25 Dec 2020	$1.2x10^{17}$	$3.0x10^{13}$	$7.0x10^{-5}$	$4.4x10^{-5}$
10 Jan 2021	$9.6x10^{16}$	$2.8x10^{13}$	$1.0x10^{-4}$	$3.0x10^{-5}$
7 Feb 2021	$9.8x10^{16}$	$1.4x10^{13}$	$4.7x10^{-5}$	$4.8x10^{-5}$
23 May 2021	$3.6x10^{17}$	$3.8x10^{13}$	$3.3x10^{-5}$	$4.2x10^{-6}$

Piton de la Fournaise, France

Type: hot spot
longitude: 55.72° E
latitude: 21.23° S
Events: 48
$BrO > 2\sigma$: 6
BrO/SO_2: $2.4x10^{-5}$
std. dev.: $2.9x10^{-5}$
mean SO_2: $2.7x10^{17}$
mean BrO: $2.5x10^{13}$



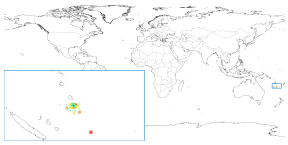
28 April 2018	$2.7x10^{17}$	$2.1x10^{13}$	$3.5x10^{-5}$	$8.2x10^{-6}$
29 April 2018	$1.9x10^{17}$	$2.1x10^{13}$	$1.1x10^{-5}$	$1.9x10^{-5}$
3 May 2018	$9.8x10^{16}$	$1.6x10^{13}$	$2.4x10^{-5}$	$3.6x10^{-5}$
8 May 2018	$8.1x10^{16}$	$2.9x10^{13}$	$3.4x10^{-5}$	$4.8x10^{-5}$
9 May 2018	$2.0x10^{17}$	$2.6x10^{13}$	$6.0x10^{-6}$	$2.4x10^{-5}$
13 July 2018	$1.2x10^{17}$	$2.1x10^{13}$	$3.1x10^{-5}$	$1.8x10^{-5}$
15 Sept 2018	$4.6x10^{17}$	$2.5x10^{13}$	$3.2x10^{-5}$	$7.2x10^{-6}$
16 Sept 2018	$3.6x10^{17}$	$3.6x10^{13}$	$6.5x10^{-5}$	$1.6x10^{-5}$
17 Sept 2018	$9.9x10^{16}$	$1.5x10^{13}$	$4.3x10^{-5}$	$1.9x10^{-5}$
18 Sept 2018	$9.6x10^{16}$	$1.9x10^{13}$	$1.7x10^{-5}$	$1.1x10^{-5}$
20 Sept 2018	$1.3x10^{17}$	$3.6x10^{13}$	$0.7x10^{-5}$	$7.3x10^{-5}$
30 Sept 2018	$3.2x10^{17}$	$2.6x10^{13}$	$2.6x10^{-5}$	$2.2x10^{-5}$
1 Oct 2018	$3.4x10^{17}$	$3.3x10^{13}$	$0.7x10^{-5}$	$2.4x10^{-5}$
4 Oct 2018	$1.3x10^{17}$	$1.4x10^{13}$	$2.5x10^{-5}$	$3.5x10^{-5}$
5 Oct 2018	$1.6x10^{17}$	$2.0x10^{13}$	$1.7x10^{-5}$	$2.4x10^{-5}$
6 Oct 2018	$2.2x10^{17}$	$3.2x10^{13}$	$1.0x10^{-5}$	$3.0x10^{-5}$
21 Feb 2019	$6.1x10^{17}$	$2.8x10^{13}$	$2.1x10^{-5}$	$9.5x10^{-6}$

Piton de la Fournaise, France

date	SO_2 VCD max. [molecules cm^{-2}]	BrO VCD	BrO/SO_2 fitted	BrO/SO_2 error
23 Feb 2019	$1.3x10^{17}$	$1.7x10^{13}$	$7.7x10^{-6}$	$1.8x10^{-5}$
25 Feb 2019	$1.2x10^{17}$	$2.7x10^{13}$	$3.3x10^{-5}$	$1.4x10^{-5}$
26 Feb 2019	$1.6x10^{17}$	$1.7x10^{13}$	$1.8x10^{-5}$	$1.7x10^{-5}$
3 Mar 2019	$1.1x10^{17}$	$1.4x10^{13}$	$1.4x10^{-5}$	$3.3x10^{-5}$
4 Mar 2019	$7.9x10^{16}$	$1.7x10^{13}$	$2.5x10^{-5}$	$3.4x10^{-5}$
5 Mar 2019	$1.3x10^{17}$	$1.4x10^{13}$	$2.8x10^{-5}$	$2.0x10^{-5}$
8 Mar 2019	$7.4x10^{17}$	$2.7x10^{13}$	$3.2x10^{-5}$	$6.4x10^{-6}$
11 June 2019	$1.9x10^{17}$	$1.7x10^{13}$	$2.0x10^{-5}$	$8.5x10^{-6}$
12 June 2019	$8.9x10^{16}$	$1.8x10^{13}$	$2.0x10^{-5}$	$4.1x10^{-5}$
12 Aug 2019	$1.1x10^{17}$	$1.7x10^{13}$	$2.6x10^{-5}$	$5.8x10^{-5}$
26 Oct 2019	$3.3x10^{17}$	$3.6x10^{13}$	$2.4x10^{-5}$	$1.5x10^{-5}$
10 Feb 2020	$3.2x10^{17}$	$2.6x10^{13}$	$5.5x10^{-5}$	$1.6x10^{-5}$
11 Feb 2020	$6.9x10^{16}$	$1.1x10^{13}$	$7.7x10^{-7}$	$3.1x10^{-5}$
13 Feb 2020	$3.1x10^{17}$	$2.2x10^{13}$	$5.6x10^{-8}$	$1.8x10^{-5}$
14 Feb 2020	$2.5x10^{17}$	$2.4x10^{13}$	$5.2x10^{-5}$	$1.2x10^{-5}$
3 April 2020	$4.3x10^{17}$	$2.7x10^{13}$	$2.2x10^{-5}$	$6.7x10^{-6}$
5 April 2020	$1.7x10^{18}$	$8.7x10^{13}$	$4.3x10^{-5}$	$2.9x10^{-6}$
6 April 2020	$7.9x10^{17}$	$4.6x10^{13}$	$3.1x10^{-5}$	$2.6x10^{-6}$
7 April 2020	$9.5x10^{16}$	$2.9x10^{13}$	$4.7x10^{-5}$	$1.3x10^{-5}$
7 Dec 2020	$8.7x10^{17}$	$3.6x10^{13}$	$2.5x10^{-5}$	$3.6x10^{-6}$
10 April 2021	$1.4x10^{17}$	$3.3x10^{13}$	$5.7x10^{-5}$	$2.0x10^{-5}$
11 April 2021	$6.2x10^{17}$	$3.6x10^{13}$	$3.5x10^{-5}$	$8.1x10^{-6}$
13 April 2021	$6.5x10^{16}$	$1.4x10^{13}$	$7.9x10^{-6}$	$3.4x10^{-5}$
16 April 2021	$1.7x10^{17}$	$2.0x10^{13}$	$3.3x10^{-5}$	$2.9x10^{-5}$
20 April 2021	$1.8x10^{17}$	$3.9x10^{13}$	$6.4x10^{-5}$	$2.8x10^{-5}$
21 April 2021	$1.3x10^{17}$	$1.6x10^{13}$	$1.6x10^{-5}$	$1.5x10^{-5}$
25 April 2021	$7.9x10^{16}$	$2.4x10^{13}$	$2.2x10^{-5}$	$3.0x10^{-5}$
1 May 2021	$1.4x10^{17}$	$2.5x10^{13}$	$2.1x10^{-5}$	$4.4x10^{-5}$
11 May 2021	$1.1x10^{17}$	$1.6x10^{13}$	$1.0x10^{-5}$	$5.9x10^{-5}$
12 May 2021	$1.1x10^{17}$	$2.0x10^{13}$	$2.2x10^{-5}$	$5.9x10^{-5}$
22 Dec 2021	$2.6x10^{17}$	$2.9x10^{13}$	$7.4x10^{-6}$	$5.7x10^{-6}$

Yasur, Vanuatu

Type: arc
longitude: 169.45° E
latitude: 19.53° S
Events: 133
$BrO > 2\sigma$: 62
BrO/SO_2: $1.2x10^{-4}$
std. dev.: $7.7x10^{-5}$
mean SO_2: $1.5x10^{17}$
mean BrO: $3.4x10^{13}$



11 Mar 2019	$7.2x10^{16}$	$2.0x10^{13}$	$1.4x10^{-4}$	$4.7x10^{-5}$
12 Mar 2019	$1.3x10^{17}$	$3.4x10^{13}$	$9.5x10^{-5}$	$3.9x10^{-5}$
5 June 2019	$8.5x10^{16}$	$2.7x10^{13}$	$1.7x10^{-4}$	$5.5x10^{-5}$
1 July 2019	$1.0x10^{17}$	$1.9x10^{13}$	$3.5x10^{-5}$	$5.5x10^{-5}$
7 Aug 2019	$1.7x10^{17}$	$4.3x10^{13}$	$2.1x10^{-4}$	$1.9x10^{-5}$
8 Aug 2019	$1.6x10^{17}$	$3.6x10^{13}$	$1.6x10^{-4}$	$3.1x10^{-5}$
11 Oct 2019	$9.8x10^{16}$	$3.5x10^{13}$	$1.5x10^{-4}$	$5.6x10^{-5}$
22 Oct 2019	$1.1x10^{17}$	$5.0x10^{13}$	$2.4x10^{-4}$	$4.7x10^{-5}$
7 Nov 2019	$2.4x10^{17}$	$3.7x10^{13}$	$1.5x10^{-4}$	$1.9x10^{-5}$
8 Nov 2019	$1.9x10^{17}$	$3.7x10^{13}$	$1.5x10^{-4}$	$4.5x10^{-5}$
18 Nov 2019	$9.4x10^{16}$	$3.8x10^{13}$	$1.7x10^{-4}$	$5.0x10^{-5}$
3 Dec 2019	$1.2x10^{17}$	$4.2x10^{13}$	$1.8x10^{-4}$	$3.2x10^{-5}$
4 Dec 2019	$1.4x10^{17}$	$3.0x10^{13}$	$2.1x10^{-4}$	$3.3x10^{-5}$
18 Dec 2019	$6.9x10^{16}$	$1.8x10^{13}$	$1.0x10^{-4}$	$3.0x10^{-5}$
19 Dec 2019	$1.8x10^{17}$	$3.6x10^{13}$	$8.9x10^{-5}$	$2.9x10^{-5}$
20 Dec 2019	$1.1x10^{17}$	$3.1x10^{13}$	$6.0x10^{-5}$	$3.8x10^{-5}$
30 Dec 2019	$7.3x10^{16}$	$3.4x10^{13}$	$9.4x10^{-5}$	$4.8x10^{-5}$
3 Jan 2020	$7.3x10^{16}$	$2.3x10^{13}$	$4.4x10^{-5}$	$4.9x10^{-5}$
4 Jan 2020	$9.4x10^{16}$	$3.4x10^{13}$	$1.4x10^{-4}$	$4.7x10^{-5}$
20 Jan 2020	$1.7x10^{17}$	$3.6x10^{13}$	$1.4x10^{-4}$	$2.0x10^{-5}$
21 Jan 2020	$1.6x10^{17}$	$4.2x10^{13}$	$2.1x10^{-4}$	$3.1x10^{-5}$
22 Jan 2020	$8.6x10^{16}$	$2.3x10^{13}$	$8.0x10^{-5}$	$3.6x10^{-5}$
25 Jan 2020	$1.2x10^{17}$	$2.3x10^{13}$	$5.8x10^{-5}$	$2.3x10^{-5}$
26 Jan 2020	$2.1x10^{17}$	$3.3x10^{13}$	$1.2x10^{-6}$	$3.0x10^{-5}$
27 Jan 2020	$1.1x10^{17}$	$1.7x10^{13}$	$4.3x10^{-6}$	$5.5x10^{-5}$
30 Jan 2020	$1.0x10^{17}$	$2.7x10^{13}$	$3.3x10^{-5}$	$3.7x10^{-5}$
31 Jan 2020	$1.4x10^{17}$	$3.9x10^{13}$	$6.2x10^{-5}$	$2.6x10^{-5}$
1 Feb 2020	$9.8x10^{16}$	$1.5x10^{13}$	$1.4x10^{-5}$	$4.3x10^{-5}$
4 Feb 2020	$7.9x10^{16}$	$2.0x10^{13}$	$3.9x10^{-6}$	$3.8x10^{-5}$

Yasur, Vanuatu

date	SO_2 VCD max. [molecules cm^{-2}]	BrO VCD max. [molecules cm^{-2}]	BrO/SO_2 fitted	BrO/SO_2 error
5 Feb 2020	$8.9x10^{16}$	$4.1x10^{13}$	$3.5x10^{-5}$	$5.7x10^{-5}$
14 Feb 2020	$9.1x10^{16}$	$1.5x10^{13}$	$1.2x10^{-5}$	$2.0x10^{-5}$
16 Feb 2020	$1.3x10^{17}$	$2.4x10^{13}$	$4.3x10^{-6}$	$3.7x10^{-5}$
20 Feb 2020	$6.7x10^{16}$	$2.2x10^{13}$	$6.2x10^{-5}$	$3.5x10^{-5}$
21 Feb 2020	$1.2x10^{17}$	$2.6x10^{13}$	$7.5x10^{-5}$	$2.1x10^{-5}$
27 Feb 2020	$2.7x10^{17}$	$3.5x10^{13}$	$5.4x10^{-5}$	$2.7x10^{-5}$
2 Mar 2020	$7.7x10^{16}$	$2.7x10^{13}$	$7.0x10^{-5}$	$3.5x10^{-5}$
3 Mar 2020	$1.6x10^{17}$	$3.5x10^{13}$	$1.5x10^{-7}$	$3.0x10^{-5}$
8 Mar 2020	$6.1x10^{16}$	$2.6x10^{13}$	$5.2x10^{-5}$	$2.8x10^{-5}$
13 Mar 2020	$1.7x10^{17}$	$2.8x10^{13}$	$5.8x10^{-5}$	$1.7x10^{-5}$
19 April 2020	$8.1x10^{16}$	$2.3x10^{13}$	$1.3x10^{-4}$	$4.5x10^{-5}$
21 April 2020	$1.9x10^{17}$	$2.9x10^{13}$	$9.6x10^{-5}$	$2.0x10^{-5}$
4 May 2020	$9.3x10^{16}$	$2.0x10^{13}$	$1.7x10^{-4}$	$3.5x10^{-5}$
12 May 2020	$1.3x10^{17}$	$3.0x10^{13}$	$1.6x10^{-4}$	$2.7x10^{-5}$
1 June 2020	$7.1x10^{16}$	$2.0x10^{13}$	$1.4x10^{-4}$	$5.1x10^{-5}$
24 June 2020	$1.5x10^{17}$	$6.6x10^{13}$	$3.4x10^{-4}$	$2.4x10^{-5}$
15 July 2020	$9.1x10^{16}$	$3.2x10^{13}$	$2.2x10^{-4}$	$5.3x10^{-5}$
5 Aug 2020	$1.9x10^{17}$	$2.8x10^{13}$	$1.4x10^{-4}$	$5.1x10^{-5}$
25 Aug 2020	$1.0x10^{17}$	$2.6x10^{13}$	$1.7x10^{-4}$	$3.9x10^{-5}$
22 Sept 2020	$8.4x10^{16}$	$3.8x10^{13}$	$2.5x10^{-4}$	$5.5x10^{-5}$
27 Sept 2020	$1.4x10^{17}$	$3.6x10^{13}$	$2.3x10^{-4}$	$5.5x10^{-5}$
28 Sept 2020	$2.3x10^{17}$	$4.3x10^{13}$	$1.7x10^{-4}$	$4.2x10^{-5}$
8 Oct 2020	$4.1x10^{17}$	$7.2x10^{13}$	$1.5x10^{-4}$	$1.9x10^{-5}$
14 Oct 2020	$1.4x10^{17}$	$4.5x10^{13}$	$1.7x10^{-4}$	$4.6x10^{-5}$
4 Dec 2020	$1.0x10^{17}$	$2.1x10^{13}$	$1.7x10^{-4}$	$3.8x10^{-5}$
5 Dec 2020	$1.1x10^{17}$	$2.8x10^{13}$	$1.5x10^{-4}$	$3.3x10^{-5}$
6 Dec 2020	$2.0x10^{17}$	$5.7x10^{13}$	$1.6x10^{-4}$	$2.2x10^{-5}$
10 Dec 2020	$8.2x10^{16}$	$3.6x10^{13}$	$1.1x10^{-4}$	$3.7x10^{-5}$
20 Dec 2020	$1.5x10^{17}$	$2.5x10^{13}$	$1.2x10^{-4}$	$4.0x10^{-5}$
21 Dec 2020	$2.3x10^{17}$	$6.9x10^{13}$	$1.6x10^{-4}$	$2.1x10^{-5}$
22 Dec 2020	$3.9x10^{17}$	$4.7x10^{13}$	$1.5x10^{-4}$	$2.1x10^{-5}$
23 Dec 2020	$2.0x10^{17}$	$4.3x10^{13}$	$1.6x10^{-4}$	$3.6x10^{-5}$
25 Dec 2020	$1.0x10^{17}$	$1.9x10^{13}$	$9.4x10^{-5}$	$2.0x10^{-5}$
26 Dec 2020	$1.8x10^{17}$	$3.7x10^{13}$	$9.1x10^{-5}$	$2.5x10^{-5}$
27 Dec 2020	$1.9x10^{17}$	$2.4x10^{13}$	$7.8x10^{-5}$	$2.2x10^{-5}$
6 Jan 2021	$7.7x10^{16}$	$2.7x10^{13}$	$5.3x10^{-5}$	$2.8x10^{-5}$
7 Jan 2021	$8.1x10^{16}$	$2.4x10^{13}$	$4.1x10^{-5}$	$6.8x10^{-5}$
17 Jan 2021	$1.0x10^{17}$	$3.3x10^{13}$	$7.1x10^{-5}$	$2.8x10^{-5}$
18 Jan 2021	$1.8x10^{17}$	$2.7x10^{13}$	$8.0x10^{-5}$	$1.8x10^{-5}$
7 Feb 2021	$2.4x10^{17}$	$1.9x10^{13}$	$1.9x10^{-5}$	$2.9x10^{-5}$
8 Feb 2021	$1.0x10^{17}$	$3.2x10^{13}$	$5.7x10^{-5}$	$3.5x10^{-5}$
14 Feb 2021	$1.0x10^{17}$	$2.3x10^{13}$	$5.7x10^{-5}$	$5.0x10^{-5}$
18 Feb 2021	$1.7x10^{17}$	$3.4x10^{13}$	$8.5x10^{-5}$	$2.7x10^{-5}$
19 Feb 2021	$2.4x10^{17}$	$3.2x10^{13}$	$1.5x10^{-5}$	$2.8x10^{-5}$
1 Mar 2021	$7.5x10^{16}$	$4.3x10^{13}$	$1.1x10^{-5}$	$7.0x10^{-5}$
15 Mar 2021	$1.4x10^{17}$	$2.3x10^{13}$	$9.4x10^{-5}$	$2.5x10^{-5}$
16 Mar 2021	$2.2x10^{17}$	$3.6x10^{13}$	$1.1x10^{-4}$	$2.4x10^{-5}$
17 Mar 2021	$1.6x10^{17}$	$3.6x10^{13}$	$1.5x10^{-4}$	$2.0x10^{-5}$
27 Mar 2021	$2.0x10^{17}$	$4.3x10^{13}$	$1.1x10^{-4}$	$3.9x10^{-5}$
29 Mar 2021	$1.1x10^{17}$	$3.8x10^{13}$	$1.4x10^{-4}$	$5.3x10^{-5}$
7 April 2021	$1.1x10^{17}$	$3.7x10^{13}$	$1.7x10^{-4}$	$4.3x10^{-5}$
12 April 2021	$9.0x10^{16}$	$2.7x10^{13}$	$7.0x10^{-5}$	$4.4x10^{-5}$
13 April 2021	$2.6x10^{17}$	$4.2x10^{13}$	$7.5x10^{-5}$	$2.2x10^{-5}$
14 April 2021	$1.0x10^{17}$	$1.6x10^{13}$	$7.1x10^{-5}$	$3.4x10^{-5}$
16 April 2021	$9.1x10^{16}$	$2.3x10^{13}$	$1.3x10^{-4}$	$2.9x10^{-5}$
17 April 2021	$1.2x10^{17}$	$3.9x10^{13}$	$1.4x10^{-4}$	$2.8x10^{-5}$
18 April 2021	$9.8x10^{16}$	$3.7x10^{13}$	$1.5x10^{-4}$	$3.7x10^{-5}$
22 April 2021	$2.4x10^{17}$	$2.6x10^{13}$	$8.2x10^{-5}$	$2.9x10^{-5}$
23 April 2021	$1.3x10^{17}$	$3.1x10^{13}$	$1.1x10^{-4}$	$3.1x10^{-5}$
15 May 2021	$1.1x10^{17}$	$2.9x10^{13}$	$1.9x10^{-4}$	$3.7x10^{-5}$
4 June 2021	$1.6x10^{17}$	$5.7x10^{13}$	$3.3x10^{-4}$	$5.7x10^{-5}$
5 June 2021	$1.2x10^{17}$	$3.8x10^{13}$	$2.0x10^{-4}$	$3.9x10^{-5}$
10 June 2021	$1.5x10^{17}$	$4.7x10^{13}$	$2.5x10^{-4}$	$3.9x10^{-5}$
16 June 2021	$1.4x10^{17}$	$5.1x10^{13}$	$1.3x10^{-4}$	$4.6x10^{-5}$
20 June 2021	$9.1x10^{16}$	$3.1x10^{13}$	$1.2x10^{-4}$	$5.9x10^{-5}$
21 June 2021	$1.2x10^{17}$	$3.9x10^{13}$	$1.9x10^{-4}$	$3.9x10^{-5}$
7 July 2021	$2.4x10^{17}$	$6.3x10^{13}$	$2.4x10^{-4}$	$3.2x10^{-5}$
17 July 2021	$9.8x10^{16}$	$3.0x10^{13}$	$1.9x10^{-4}$	$4.8x10^{-5}$
23 July 2021	$2.2x10^{17}$	$6.8x10^{13}$	$2.9x10^{-4}$	$2.2x10^{-5}$
2 Aug 2021	$1.4x10^{17}$	$6.5x10^{13}$	$2.6x10^{-4}$	$7.2x10^{-5}$
8 Aug 2021	$1.4x10^{17}$	$5.2x10^{13}$	$3.2x10^{-4}$	$3.9x10^{-5}$

Yasur, Vanuatu

date	SO_2 VCD max. [molecules cm^{-2}]	BrO VCD max. [molecules cm^{-2}]	BrO/SO_2 fitted	BrO/SO_2 error
18 Aug 2021	$1.1x10^{17}$	$4.1x10^{13}$	$2.9x10^{-4}$	$4.1x10^{-5}$
29 Aug 2021	$2.0x10^{17}$	$4.7x10^{13}$	$2.1x10^{-4}$	$3.4x10^{-5}$
7 Sept 2021	$9.7x10^{16}$	$2.7x10^{13}$	$2.2x10^{-4}$	$3.5x10^{-5}$
20 Sept 2021	$1.3x10^{17}$	$4.5x10^{13}$	$2.5x10^{-4}$	$4.7x10^{-5}$
4 Oct 2021	$1.2x10^{17}$	$3.4x10^{13}$	$1.9x10^{-4}$	$4.8x10^{-5}$
5 Oct 2021	$2.3x10^{17}$	$6.1x10^{13}$	$1.8x10^{-4}$	$1.3x10^{-5}$
6 Oct 2021	$6.8x10^{16}$	$3.7x10^{13}$	$2.8x10^{-4}$	$3.1x10^{-5}$
10 Oct 2021	$1.2x10^{17}$	$4.8x10^{13}$	$1.9x10^{-4}$	$5.5x10^{-5}$
11 Oct 2021	$2.2x10^{17}$	$5.5x10^{13}$	$1.9x10^{-4}$	$2.9x10^{-5}$
12 Oct 2021	$3.3x10^{17}$	$3.7x10^{13}$	$1.3x10^{-4}$	$3.4x10^{-5}$
15 Oct 2021	$1.2x10^{17}$	$3.9x10^{13}$	$1.7x10^{-4}$	$4.2x10^{-5}$
16 Oct 2021	$3.3x10^{17}$	$4.4x10^{13}$	$1.3x10^{-4}$	$1.9x10^{-5}$
22 Oct 2021	$1.1x10^{17}$	$2.8x10^{13}$	$1.9x10^{-4}$	$3.0x10^{-5}$
23 Oct 2021	$1.3x10^{17}$	$2.8x10^{13}$	$1.2x10^{-4}$	$1.8x10^{-5}$
31 Oct 2021	$7.3x10^{16}$	$2.5x10^{13}$	$4.1x10^{-5}$	$3.3x10^{-5}$
7 Nov 2021	$2.3x10^{17}$	$3.9x10^{13}$	$1.3x10^{-4}$	$2.3x10^{-5}$
10 Nov 2021	$1.1x10^{17}$	$1.7x10^{13}$	$1.2x10^{-4}$	$2.1x10^{-5}$
11 Nov 2021	$2.0x10^{17}$	$2.4x10^{13}$	$2.2x10^{-5}$	$2.4x10^{-5}$
12 Nov 2021	$2.4x10^{17}$	$3.6x10^{13}$	$7.4x10^{-5}$	$2.2x10^{-5}$
13 Nov 2021	$2.2x10^{17}$	$3.5x10^{13}$	$7.6x10^{-5}$	$3.0x10^{-5}$
16 Nov 2021	$2.1x10^{17}$	$3.2x10^{13}$	$5.0x10^{-5}$	$2.0x10^{-5}$
17 Nov 2021	$1.5x10^{17}$	$3.9x10^{13}$	$8.8x10^{-5}$	$3.0x10^{-5}$
18 Nov 2021	$8.5x10^{16}$	$2.9x10^{13}$	$2.7x10^{-5}$	$5.9x10^{-5}$
28 Nov 2021	$6.7x10^{16}$	$2.9x10^{13}$	$8.7x10^{-5}$	$3.1x10^{-5}$
3 Dec 2021	$2.1x10^{17}$	$2.6x10^{13}$	$4.9x10^{-5}$	$2.5x10^{-5}$
7 Dec 2021	$2.0x10^{17}$	$2.6x10^{13}$	$4.7x10^{-5}$	$2.3x10^{-5}$
8 Dec 2021	$2.0x10^{17}$	$3.4x10^{13}$	$3.8x10^{-5}$	$1.4x10^{-5}$
9 Dec 2021	$2.1x10^{17}$	$3.6x10^{13}$	$5.4x10^{-5}$	$1.5x10^{-5}$
10 Dec 2021	$1.2x10^{17}$	$2.6x10^{13}$	$5.6x10^{-5}$	$2.3x10^{-5}$
18 Dec 2021	$5.8x10^{16}$	$1.4x10^{13}$	$6.1x10^{-5}$	$2.1x10^{-5}$
20 Dec 2021	$1.5x10^{17}$	$3.2x10^{13}$	$7.5x10^{-5}$	$2.4x10^{-5}$
23 Dec 2021	$9.8x10^{16}$	$2.1x10^{13}$	$3.2x10^{-5}$	$2.2x10^{-5}$
25 Dec 2021	$1.1x10^{17}$	$2.3x10^{13}$	$6.9x10^{-5}$	$2.6x10^{-5}$

Ambrym, Vanuatu

Type:	arc
longitude:	168.12° E
latitude:	16.25° S
Events:	152
BrO > 2σ:	119
BrO/SO_2:	$8.3x10^{-5}$
std. dev.:	$4.8x10^{-5}$
mean SO_2:	$3.5x10^{17}$
mean BrO:	$4.2x10^{13}$



1 Jan 2018	$1.1x10^{17}$	$1.9x10^{13}$	$8.0x10^{-5}$	$1.0x10^{-5}$
3 Jan 2018	$4.7x10^{17}$	$4.3x10^{13}$	$4.1x10^{-5}$	$2.3x10^{-6}$
5 Jan 2018	$1.1x10^{18}$	$3.8x10^{13}$	$3.4x10^{-5}$	$2.3x10^{-6}$
31 Jan 2018	$2.8x10^{17}$	$3.6x10^{13}$	$9.4x10^{-5}$	$8.1x10^{-6}$
7 Feb 2018	$1.5x10^{17}$	$2.0x10^{13}$	$4.9x10^{-5}$	$1.5x10^{-5}$
18 Feb 2018	$1.3x10^{17}$	$2.0x10^{13}$	$9.7x10^{-5}$	$9.3x10^{-6}$
24 Feb 2018	$3.7x10^{17}$	$2.5x10^{13}$	$5.0x10^{-5}$	$6.1x10^{-6}$
25 Feb 2018	$7.6x10^{17}$	$3.4x10^{13}$	$5.8x10^{-5}$	$3.9x10^{-6}$
26 Feb 2018	$5.8x10^{17}$	$5.1x10^{13}$	$7.5x10^{-5}$	$4.5x10^{-6}$
27 Feb 2018	$2.1x10^{17}$	$3.4x10^{13}$	$1.0x10^{-4}$	$5.2x10^{-6}$
28 Feb 2018	$2.7x10^{17}$	$4.5x10^{13}$	$1.1x10^{-4}$	$1.0x10^{-5}$
12 Mar 2018	$9.0x10^{16}$	$2.2x10^{13}$	$1.1x10^{-4}$	$8.3x10^{-6}$
18 Mar 2018	$2.6x10^{17}$	$3.5x10^{13}$	$1.0x10^{-4}$	$7.5x10^{-6}$
21 Mar 2018	$4.1x10^{17}$	$3.5x10^{13}$	$2.3x10^{-5}$	$3.4x10^{-6}$
2 April 2018	$1.6x10^{17}$	$2.6x10^{13}$	$5.3x10^{-6}$	$5.8x10^{-6}$
3 April 2018	$3.6x10^{17}$	$2.9x10^{13}$	$4.9x10^{-5}$	$7.5x10^{-6}$
4 April 2018	$3.3x10^{17}$	$3.8x10^{13}$	$8.7x10^{-5}$	$5.2x10^{-6}$
14 April 2018	$1.6x10^{17}$	$4.1x10^{13}$	$3.7x10^{-5}$	$1.1x10^{-5}$
15 April 2018	$3.1x10^{17}$	$4.8x10^{13}$	$1.0x10^{-4}$	$1.5x10^{-5}$
16 April 2018	$1.2x10^{17}$	$3.2x10^{13}$	$7.4x10^{-5}$	$3.1x10^{-5}$
18 April 2018	$1.1x10^{17}$	$1.6x10^{13}$	$9.6x10^{-5}$	$2.0x10^{-5}$
19 April 2018	$1.3x10^{17}$	$2.6x10^{13}$	$1.2x10^{-4}$	$1.5x10^{-5}$
21 April 2018	$7.1x10^{17}$	$6.4x10^{13}$	$6.9x10^{-5}$	$6.9x10^{-6}$
25 April 2018	$1.3x10^{17}$	$2.2x10^{13}$	$6.4x10^{-5}$	$1.3x10^{-5}$
26 April 2018	$4.3x10^{17}$	$5.9x10^{13}$	$9.0x10^{-5}$	$7.5x10^{-6}$
30 April 2018	$5.5x10^{17}$	$5.5x10^{13}$	$8.1x10^{-5}$	$4.5x10^{-6}$
2 May 2018	$3.5x10^{17}$	$3.2x10^{13}$	$1.1x10^{-4}$	$1.7x10^{-5}$

Ambrym, Vanuatu

date	SO_2 VCD max. [molecules cm^{-2}]	BrO VCD	BrO/SO_2 fitted	BrO/SO_2 error
5 May 2018	$2.6x10^{17}$	$7.1x10^{13}$	$1.5x10^{-4}$	$1.4x10^{-5}$
6 May 2018	$3.9x10^{17}$	$6.5x10^{13}$	$1.2x10^{-4}$	$1.2x10^{-5}$
7 May 2018	$1.8x10^{17}$	$4.4x10^{13}$	$1.3x10^{-4}$	$2.1x10^{-5}$
11 May 2018	$1.5x10^{17}$	$5.4x10^{13}$	$7.7x10^{-5}$	$1.2x10^{-5}$
16 May 2018	$4.1x10^{17}$	$4.8x10^{13}$	$5.9x10^{-5}$	$7.4x10^{-6}$
18 May 2018	$2.4x10^{17}$	$3.1x10^{13}$	$5.2x10^{-5}$	$1.4x10^{-5}$
20 May 2018	$2.2x10^{17}$	$2.9x10^{13}$	$8.6x10^{-5}$	$1.2x10^{-5}$
21 May 2018	$5.2x10^{17}$	$5.2x10^{13}$	$4.7x10^{-5}$	$4.9x10^{-6}$
24 May 2018	$7.9x10^{16}$	$2.7x10^{13}$	$1.3x10^{-4}$	$1.8x10^{-5}$
27 May 2018	$3.3x10^{17}$	$3.6x10^{13}$	$4.6x10^{-5}$	$6.2x10^{-6}$
28 May 2018	$8.8x10^{17}$	$1.3x10^{14}$	$1.4x10^{-4}$	$8.2x10^{-6}$
29 May 2018	$2.5x10^{17}$	$5.6x10^{13}$	$2.3x10^{-4}$	$1.5x10^{-5}$
31 May 2018	$1.2x10^{17}$	$3.3x10^{13}$	$1.3x10^{-4}$	$2.5x10^{-5}$
1 June 2018	$8.0x10^{16}$	$2.2x10^{13}$	$1.4x10^{-4}$	$2.0x10^{-5}$
3 June 2018	$6.9x10^{16}$	$2.0x10^{13}$	$1.2x10^{-4}$	$2.0x10^{-5}$
6 June 2018	$2.0x10^{17}$	$3.4x10^{13}$	$1.6x10^{-4}$	$1.8x10^{-5}$
8 June 2018	$5.8x10^{16}$	$9.8x10^{12}$	$1.7x10^{-5}$	$1.1x10^{-5}$
9 June 2018	$1.4x10^{17}$	$2.6x10^{13}$	$2.1x10^{-4}$	$2.3x10^{-5}$
11 June 2018	$1.5x10^{17}$	$2.4x10^{13}$	$1.5x10^{-4}$	$2.6x10^{-5}$
12 June 2018	$5.8x10^{17}$	$5.6x10^{13}$	$1.3x10^{-4}$	$9.3x10^{-6}$
16 June 2018	$7.1x10^{16}$	$2.0x10^{13}$	$9.8x10^{-5}$	$3.1x10^{-5}$
17 June 2018	$1.4x10^{17}$	$3.6x10^{13}$	$7.9x10^{-5}$	$2.0x10^{-5}$
18 June 2018	$5.2x10^{17}$	$5.1x10^{13}$	$9.2x10^{-5}$	$1.1x10^{-5}$
19 June 2018	$1.7x10^{17}$	$3.0x10^{13}$	$1.5x10^{-4}$	$2.0x10^{-5}$
25 June 2018	$8.4x10^{16}$	$2.4x10^{13}$	$1.8x10^{-4}$	$3.2x10^{-5}$
29 June 2018	$1.1x10^{17}$	$3.2x10^{13}$	$2.2x10^{-4}$	$3.6x10^{-5}$
30 June 2018	$8.0x10^{16}$	$1.7x10^{13}$	$8.6x10^{-5}$	$5.1x10^{-5}$
3 July 2018	$1.4x10^{17}$	$3.7x10^{13}$	$1.2x10^{-4}$	$1.2x10^{-5}$
5 July 2018	$8.3x10^{16}$	$2.8x10^{13}$	$1.9x10^{-4}$	$3.7x10^{-5}$
8 July 2018	$1.3x10^{17}$	$4.5x10^{13}$	$1.0x10^{-4}$	$1.1x10^{-5}$
10 July 2018	$2.8x10^{17}$	$5.1x10^{13}$	$1.5x10^{-4}$	$1.6x10^{-5}$
13 July 2018	$1.3x10^{17}$	$2.6x10^{13}$	$1.2x10^{-4}$	$7.8x10^{-6}$
14 July 2018	$6.2x10^{17}$	$5.8x10^{13}$	$8.7x10^{-5}$	$7.9x10^{-6}$
21 July 2018	$9.9x10^{17}$	$6.7x10^{13}$	$5.9x10^{-5}$	$1.1x10^{-6}$
30 July 2018	$6.2x10^{17}$	$7.7x10^{13}$	$3.0x10^{-5}$	$1.7x10^{-6}$
3 Aug 2018	$1.5x10^{17}$	$3.0x10^{13}$	$1.8x10^{-4}$	$1.7x10^{-5}$
4 Aug 2018	$6.1x10^{17}$	$8.3x10^{13}$	$1.4x10^{-4}$	$1.1x10^{-5}$
5 Aug 2018	$9.0x10^{17}$	$1.6x10^{14}$	$1.6x10^{-4}$	$1.1x10^{-5}$
6 Aug 2018	$2.0x10^{17}$	$5.4x10^{13}$	$2.1x10^{-4}$	$2.4x10^{-5}$
8 Aug 2018	$8.9x10^{16}$	$1.4x10^{13}$	$7.6x10^{-5}$	$3.3x10^{-5}$
9 Aug 2018	$1.9x10^{17}$	$2.3x10^{13}$	$9.1x10^{-5}$	$2.0x10^{-5}$
10 Aug 2018	$1.7x10^{17}$	$3.9x10^{13}$	$1.7x10^{-4}$	$1.8x10^{-5}$
11 Aug 2018	$3.3x10^{17}$	$5.3x10^{13}$	$1.5x10^{-4}$	$9.1x10^{-6}$
15 Aug 2018	$6.8x10^{16}$	$2.9x10^{13}$	$7.8x10^{-5}$	$4.3x10^{-5}$
16 Aug 2018	$6.9x10^{17}$	$8.7x10^{13}$	$1.3x10^{-4}$	$1.1x10^{-5}$
17 Aug 2018	$3.4x10^{17}$	$4.0x10^{13}$	$1.5x10^{-4}$	$1.7x10^{-5}$
19 Aug 2018	$2.1x10^{17}$	$2.5x10^{13}$	$9.9x10^{-5}$	$1.4x10^{-5}$
20 Aug 2018	$3.1x10^{17}$	$3.6x10^{13}$	$1.0x10^{-4}$	$8.0x10^{-6}$
21 Aug 2018	$3.4x10^{17}$	$4.4x10^{13}$	$8.9x10^{-5}$	$4.6x10^{-6}$
22 Aug 2018	$1.5x10^{17}$	$2.8x10^{13}$	$1.6x10^{-4}$	$1.2x10^{-5}$
23 Aug 2018	$2.1x10^{17}$	$3.0x10^{13}$	$1.1x10^{-4}$	$1.5x10^{-5}$
25 Aug 2018	$1.8x10^{17}$	$3.6x10^{13}$	$9.7x10^{-5}$	$1.7x10^{-5}$
26 Aug 2018	$2.2x10^{17}$	$4.5x10^{13}$	$1.5x10^{-4}$	$1.2x10^{-5}$
27 Aug 2018	$2.1x10^{17}$	$3.4x10^{13}$	$1.8x10^{-4}$	$2.6x10^{-5}$
4 Sept 2018	$1.3x10^{17}$	$3.5x10^{13}$	$1.3x10^{-4}$	$1.2x10^{-5}$
6 Sept 2018	$8.3x10^{17}$	$4.9x10^{13}$	$6.5x10^{-5}$	$5.6x10^{-6}$
7 Sept 2018	$3.5x10^{17}$	$4.4x10^{13}$	$1.3x10^{-4}$	$7.3x10^{-6}$
8 Sept 2018	$1.2x10^{17}$	$3.1x10^{13}$	$1.5x10^{-4}$	$2.4x10^{-5}$
11 Sept 2018	$3.1x10^{17}$	$6.1x10^{13}$	$1.5x10^{-4}$	$9.2x10^{-6}$
12 Sept 2018	$1.9x10^{17}$	$3.6x10^{13}$	$1.5x10^{-4}$	$1.5x10^{-5}$
13 Sept 2018	$1.1x10^{17}$	$2.4x10^{13}$	$1.5x10^{-4}$	$2.3x10^{-5}$
15 Sept 2018	$2.8x10^{17}$	$4.4x10^{13}$	$1.1x10^{-4}$	$1.4x10^{-5}$
20 Sept 2018	$1.2x10^{17}$	$3.3x10^{13}$	$1.7x10^{-4}$	$1.2x10^{-5}$
23 Sept 2018	$2.0x10^{17}$	$2.9x10^{13}$	$1.2x10^{-4}$	$2.0x10^{-5}$
25 Sept 2018	$8.6x10^{16}$	$1.5x10^{13}$	$1.8x10^{-4}$	$1.8x10^{-5}$
27 Sept 2018	$7.6x10^{16}$	$2.2x10^{13}$	$1.8x10^{-4}$	$2.3x10^{-5}$
28 Sept 2018	$8.3x10^{16}$	$2.8x10^{13}$	$1.6x10^{-4}$	$1.7x10^{-5}$
30 Sept 2018	$1.3x10^{17}$	$3.2x10^{13}$	$1.9x10^{-4}$	$1.9x10^{-5}$
3 Oct 2018	$2.9x10^{17}$	$6.6x10^{13}$	$1.4x10^{-4}$	$1.3x10^{-5}$
4 Oct 2018	$2.2x10^{17}$	$4.0x10^{13}$	$1.5x10^{-4}$	$9.6x10^{-6}$
9 Oct 2018	$6.8x10^{17}$	$7.4x10^{13}$	$1.0x10^{-4}$	$5.5x10^{-6}$

Ambrym, Vanuatu

date	SO_2 VCD max. [molecules cm^{-2}]	BrO VCD	BrO/SO_2 fitted	BrO/SO_2 error
10 Oct 2018	$2.1x10^{17}$	$3.4x10^{13}$	$1.2x10^{-4}$	$1.7x10^{-5}$
11 Oct 2018	$1.7x10^{17}$	$4.2x10^{13}$	$1.4x10^{-4}$	$1.5x10^{-5}$
12 Oct 2018	$1.1x10^{18}$	$1.5x10^{14}$	$1.2x10^{-4}$	$6.9x10^{-6}$
14 Oct 2018	$1.5x10^{17}$	$3.8x10^{13}$	$8.2x10^{-5}$	$2.0x10^{-5}$
15 Oct 2018	$1.6x10^{17}$	$1.7x10^{13}$	$6.0x10^{-5}$	$1.7x10^{-5}$
20 Oct 2018	$3.8x10^{17}$	$4.1x10^{13}$	$8.5x10^{-5}$	$1.4x10^{-5}$
21 Oct 2018	$2.6x10^{17}$	$3.7x10^{13}$	$1.4x10^{-4}$	$8.5x10^{-6}$
22 Oct 2018	$1.3x10^{17}$	$4.1x10^{13}$	$1.6x10^{-4}$	$1.6x10^{-5}$
23 Oct 2018	$3.2x10^{17}$	$6.2x10^{13}$	$1.4x10^{-4}$	$7.2x10^{-6}$
24 Oct 2018	$4.7x10^{17}$	$4.9x10^{13}$	$1.0x10^{-4}$	$7.2x10^{-6}$
27 Oct 2018	$8.0x10^{16}$	$1.4x10^{13}$	$9.3x10^{-5}$	$2.7x10^{-5}$
28 Oct 2018	$5.7x10^{17}$	$7.0x10^{13}$	$1.2x10^{-4}$	$8.6x10^{-6}$
30 Oct 2018	$6.1x10^{17}$	$4.0x10^{13}$	$6.4x10^{-5}$	$5.7x10^{-6}$
2 Nov 2018	$1.5x10^{17}$	$4.5x10^{13}$	$1.5x10^{-4}$	$2.0x10^{-5}$
4 Nov 2018	$2.4x10^{17}$	$5.1x10^{13}$	$7.9x10^{-5}$	$1.6x10^{-5}$
5 Nov 2018	$8.1x10^{16}$	$1.4x10^{13}$	$1.0x10^{-4}$	$3.6x10^{-5}$
8 Nov 2018	$2.8x10^{17}$	$5.7x10^{13}$	$1.4x10^{-4}$	$1.3x10^{-5}$
9 Nov 2018	$3.1x10^{17}$	$5.9x10^{13}$	$1.3x10^{-4}$	$9.7x10^{-6}$
10 Nov 2018	$6.2x10^{17}$	$4.2x10^{13}$	$6.4x10^{-5}$	$9.2x10^{-6}$
11 Nov 2018	$1.4x10^{17}$	$2.6x10^{13}$	$7.3x10^{-5}$	$2.9x10^{-5}$
14 Nov 2018	$8.5x10^{17}$	$1.2x10^{14}$	$1.4x10^{-4}$	$5.9x10^{-6}$
15 Nov 2018	$8.1x10^{17}$	$1.0x10^{14}$	$9.7x10^{-5}$	$6.1x10^{-6}$
16 Nov 2018	$1.3x10^{17}$	$2.1x10^{13}$	$1.2x10^{-4}$	$2.0x10^{-5}$
18 Nov 2018	$2.1x10^{17}$	$2.4x10^{13}$	$7.9x10^{-5}$	$1.6x10^{-5}$
19 Nov 2018	$9.7x10^{17}$	$9.0x10^{13}$	$9.4x10^{-5}$	$6.2x10^{-6}$
20 Nov 2018	$8.6x10^{17}$	$4.9x10^{13}$	$6.2x10^{-5}$	$6.9x10^{-6}$
21 Nov 2018	$3.1x10^{17}$	$3.9x10^{13}$	$1.3x10^{-4}$	$1.2x10^{-5}$
23 Nov 2018	$2.1x10^{17}$	$1.6x10^{13}$	$9.9x10^{-5}$	$1.6x10^{-5}$
24 Nov 2018	$3.0x10^{17}$	$2.4x10^{13}$	$6.1x10^{-5}$	$7.2x10^{-6}$
25 Nov 2018	$4.0x10^{17}$	$4.2x10^{13}$	$3.1x10^{-5}$	$4.8x10^{-6}$
26 Nov 2018	$2.7x10^{17}$	$3.3x10^{13}$	$4.3x10^{-5}$	$5.4x10^{-6}$
29 Nov 2018	$2.5x10^{17}$	$3.0x10^{13}$	$9.3x10^{-5}$	$6.1x10^{-6}$
30 Nov 2018	$3.8x10^{17}$	$3.9x10^{13}$	$7.7x10^{-5}$	$5.3x10^{-6}$
1 Dec 2018	$6.4x10^{16}$	$2.2x10^{13}$	$5.4x10^{-5}$	$2.4x10^{-5}$
2 Dec 2018	$4.7x10^{17}$	$4.9x10^{13}$	$9.0x10^{-5}$	$7.4x10^{-6}$
3 Dec 2018	$1.6x10^{17}$	$1.9x10^{13}$	$9.8x10^{-5}$	$1.3x10^{-5}$
5 Dec 2018	$1.0x10^{17}$	$2.9x10^{13}$	$1.6x10^{-4}$	$1.8x10^{-5}$
6 Dec 2018	$2.3x10^{17}$	$3.5x10^{13}$	$9.2x10^{-5}$	$1.8x10^{-5}$
7 Dec 2018	$2.3x10^{17}$	$3.1x10^{13}$	$1.1x10^{-4}$	$1.6x10^{-5}$
10 Dec 2018	$1.3x10^{17}$	$2.3x10^{13}$	$1.1x10^{-4}$	$1.5x10^{-5}$
12 Dec 2018	$8.7x10^{17}$	$6.8x10^{13}$	$7.6x10^{-5}$	$9.4x10^{-6}$
13 Dec 2018	$2.8x10^{17}$	$2.8x10^{13}$	$6.4x10^{-5}$	$1.4x10^{-5}$
15 Dec 2018	$1.5x10^{18}$	$1.2x10^{14}$	$6.1x10^{-5}$	$2.6x10^{-6}$
16 Dec 2018	$6.3x10^{18}$	$1.9x10^{14}$	$3.0x10^{-5}$	$6.6x10^{-7}$
17 Dec 2018	$1.9x10^{17}$	$3.1x10^{13}$	$6.3x10^{-5}$	$2.6x10^{-6}$
21 Dec 2018	$1.3x10^{17}$	$2.6x10^{13}$	$2.7x10^{-5}$	$3.7x10^{-5}$
22 Dec 2018	$1.5x10^{17}$	$2.3x10^{13}$	$1.3x10^{-5}$	$1.6x10^{-5}$
27 Dec 2018	$9.2x10^{16}$	$2.6x10^{13}$	$2.8x10^{-5}$	$4.3x10^{-5}$
11 Jan 2019	$2.5x10^{17}$	$1.8x10^{13}$	$2.8x10^{-5}$	$2.5x10^{-5}$
12 Jan 2019	$1.1x10^{17}$	$2.4x10^{13}$	$2.4x10^{-5}$	$2.1x10^{-5}$
13 Jan 2019	$1.3x10^{17}$	$2.2x10^{13}$	$6.9x10^{-5}$	$2.9x10^{-5}$
16 Jan 2019	$9.4x10^{16}$	$1.8x10^{13}$	$5.6x10^{-6}$	$4.1x10^{-5}$
17 Jan 2019	$2.3x10^{17}$	$3.1x10^{13}$	$3.7x10^{-5}$	$2.8x10^{-5}$
19 Dec 2021	$7.4x10^{16}$	$4.3x10^{13}$	$1.2x10^{-4}$	$4.3x10^{-5}$

Ambae, Vanuatu

Type:	arc
longitude:	167.83° E
latitude:	15.39° S
Events:	24
BrO > 2σ:	18
BrO/SO_2:	$5.2x10^{-5}$
std. dev.:	$3.8x10^{-5}$
mean SO_2:	$6.2x10^{17}$
mean BrO:	$4.5x10^{13}$



2 Jan 2018	$3.0x10^{17}$	$4.5x10^{13}$	$7.0x10^{-5}$	$5.2x10^{-6}$
13 Feb 2018	$7.5x10^{16}$	$2.5x10^{13}$	$1.4x10^{-4}$	$1.3x10^{-5}$
19 Mar 2018	$3.9x10^{17}$	$5.5x10^{13}$	$1.2x10^{-4}$	$3.9x10^{-6}$
25 Mar 2018	$1.3x10^{18}$	$6.4x10^{13}$	$3.7x10^{-5}$	$8.7x10^{-7}$
27 Mar 2018	$4.1x10^{17}$	$3.1x10^{13}$	$5.3x10^{-5}$	$2.6x10^{-6}$
28 Mar 2018	$2.0x10^{18}$	$6.6x10^{13}$	$3.6x10^{-5}$	$9.5x10^{-7}$

Ambae, Vanuatu

date	SO_2 VCD max. [molecules cm^{-2}]	BrO VCD	BrO/SO_2 fitted	BrO/SO_2 error
31 Mar 2018	$1.4x10^{18}$	$5.8x10^{13}$	$3.1x10^{-5}$	$1.5x10^{-6}$
1 April 2018	$1.1x10^{18}$	$3.8x10^{13}$	$1.7x10^{-5}$	$1.6x10^{-6}$
10 April 2018	$1.3x10^{18}$	$8.3x10^{13}$	$6.6x10^{-5}$	$1.0x10^{-6}$
28 April 2018	$2.4x10^{17}$	$2.7x10^{13}$	$9.6x10^{-5}$	$6.5x10^{-6}$
12 May 2018	$2.2x10^{17}$	$4.8x10^{13}$	$1.1x10^{-4}$	$1.4x10^{-5}$
17 May 2018	$8.0x10^{17}$	$6.2x10^{13}$	$5.9x10^{-5}$	$4.9x10^{-6}$
22 May 2018	$1.9x10^{18}$	$9.8x10^{13}$	$3.6x10^{-5}$	$1.7x10^{-6}$
21 June 2018	$1.6x10^{17}$	$1.5x10^{13}$	$6.5x10^{-5}$	$1.7x10^{-5}$
24 June 2018	$1.6x10^{17}$	$3.1x10^{13}$	$7.8x10^{-5}$	$1.5x10^{-5}$
27 June 2018	$1.9x10^{17}$	$2.1x10^{13}$	$6.1x10^{-5}$	$3.2x10^{-5}$
28 June 2018	$2.1x10^{17}$	$5.0x10^{13}$	$1.2x10^{-4}$	$9.8x10^{-6}$
4 July 2018	$2.1x10^{17}$	$2.7x10^{13}$	$9.6x10^{-5}$	$1.6x10^{-5}$
6 July 2018	$1.8x10^{17}$	$2.4x10^{13}$	$1.7x10^{-5}$	$2.0x10^{-5}$
11 July 2018	$8.7x10^{16}$	$2.0x10^{13}$	$1.3x10^{-4}$	$1.7x10^{-5}$
15 July 2018	$4.3x10^{17}$	$4.5x10^{13}$	$5.4x10^{-5}$	$5.1x10^{-6}$
16 July 2018	$5.6x10^{17}$	$3.1x10^{13}$	$6.0x10^{-5}$	$9.2x10^{-6}$
20 July 2018	$1.0x10^{18}$	$8.3x10^{13}$	$6.0x10^{-5}$	$1.7x10^{-6}$
4 Dec 2018	$6.5x10^{16}$	$2.2x10^{13}$	$1.5x10^{-4}$	$1.3x10^{-5}$

Bagana, Papua New Guinea

Type: arc
longitude: 155.19° E
latitude: 6.14° S
Events: 52
$BrO > 2\sigma$: 4
BrO/SO_2: $2.1x10^{-5}$
std. dev.: $2.4x10^{-5}$
mean SO_2: $1.7x10^{17}$
mean BrO: $2.6x10^{13}$



9 Feb 2018	$8.4x10^{16}$	$2.3x10^{13}$	$5.9x10^{-6}$	$3.3x10^{-5}$
13 Feb 2018	$1.9x10^{17}$	$2.3x10^{13}$	$4.7x10^{-5}$	$2.1x10^{-5}$
22 Feb 2018	$8.2x10^{16}$	$1.8x10^{13}$	$5.2x10^{-5}$	$3.0x10^{-5}$
23 Feb 2018	$1.1x10^{17}$	$4.3x10^{13}$	$3.1x10^{-5}$	$2.2x10^{-5}$
24 Feb 2018	$1.1x10^{17}$	$2.9x10^{13}$	$7.4x10^{-5}$	$1.8x10^{-5}$
31 May 2018	$1.0x10^{17}$	$1.7x10^{13}$	$3.3x10^{-5}$	$4.2x10^{-5}$
6 July 2018	$1.5x10^{17}$	$2.4x10^{13}$	$7.5x10^{-5}$	$2.0x10^{-5}$
7 July 2018	$2.1x10^{17}$	$3.1x10^{13}$	$5.4x10^{-5}$	$1.5x10^{-5}$
8 July 2018	$1.5x10^{17}$	$3.1x10^{13}$	$6.9x10^{-5}$	$1.8x10^{-5}$
22 July 2018	$1.2x10^{17}$	$2.6x10^{13}$	$7.9x10^{-5}$	$2.5x10^{-5}$
27 July 2018	$1.2x10^{17}$	$2.0x10^{13}$	$6.1x10^{-5}$	$2.8x10^{-5}$
28 July 2018	$6.7x10^{16}$	$2.6x10^{13}$	$1.7x10^{-5}$	$3.0x10^{-5}$
3 Aug 2018	$8.2x10^{16}$	$2.3x10^{13}$	$3.3x10^{-5}$	$4.1x10^{-5}$
17 Nov 2018	$2.9x10^{17}$	$3.4x10^{13}$	$8.5x10^{-5}$	$3.9x10^{-5}$
4 Dec 2018	$9.3x10^{16}$	$2.0x10^{13}$	$4.7x10^{-5}$	$2.7x10^{-5}$
10 Dec 2018	$6.0x10^{16}$	$1.4x10^{13}$	$5.9x10^{-5}$	$4.2x10^{-5}$
14 Dec 2018	$1.7x10^{17}$	$1.9x10^{13}$	$8.4x10^{-5}$	$2.9x10^{-5}$
19 Dec 2018	$1.1x10^{17}$	$3.2x10^{13}$	$4.9x10^{-5}$	$4.1x10^{-5}$
5 Aug 2019	$1.0x10^{18}$	$3.3x10^{13}$	$5.2x10^{-6}$	$4.6x10^{-7}$
6 Aug 2019	$3.7x10^{17}$	$5.5x10^{13}$	$1.1x10^{-5}$	$8.5x10^{-7}$
28 May 2021	$1.2x10^{17}$	$1.7x10^{13}$	$3.1x10^{-5}$	$5.0x10^{-5}$
6 Sept 2021	$1.4x10^{17}$	$3.0x10^{13}$	$3.7x10^{-5}$	$2.6x10^{-5}$
7 Sept 2021	$1.2x10^{17}$	$2.4x10^{13}$	$6.8x10^{-5}$	$2.0x10^{-5}$
16 Sept 2021	$9.8x10^{16}$	$2.1x10^{13}$	$3.1x10^{-5}$	$2.7x10^{-5}$
17 Sept 2021	$1.1x10^{17}$	$3.4x10^{13}$	$4.3x10^{-5}$	$2.4x10^{-5}$
22 Sept 2021	$6.3x10^{16}$	$3.2x10^{13}$	$5.9x10^{-5}$	$2.9x10^{-5}$
23 Sept 2021	$8.6x10^{16}$	$2.7x10^{13}$	$1.0x10^{-4}$	$5.4x10^{-5}$
29 Sept 2021	$9.3x10^{16}$	$1.8x10^{13}$	$7.2x10^{-5}$	$2.3x10^{-5}$
2 Oct 2021	$8.6x10^{16}$	$1.8x10^{13}$	$4.3x10^{-5}$	$2.6x10^{-5}$
3 Oct 2021	$1.7x10^{17}$	$3.0x10^{13}$	$3.6x10^{-5}$	$1.3x10^{-5}$
4 Oct 2021	$1.1x10^{17}$	$2.2x10^{13}$	$4.4x10^{-5}$	$2.6x10^{-5}$
8 Oct 2021	$9.4x10^{16}$	$2.3x10^{13}$	$2.6x10^{-5}$	$2.6x10^{-5}$
10 Oct 2021	$1.1x10^{17}$	$1.4x10^{13}$	$5.7x10^{-5}$	$3.5x10^{-5}$
13 Oct 2021	$2.5x10^{17}$	$2.5x10^{13}$	$1.4x10^{-5}$	$1.7x10^{-5}$
14 Oct 2021	$2.9x10^{17}$	$3.6x10^{13}$	$3.6x10^{-5}$	$1.5x10^{-5}$
15 Oct 2021	$1.4x10^{17}$	$2.4x10^{13}$	$5.9x10^{-6}$	$3.1x10^{-5}$
19 Oct 2021	$2.9x10^{17}$	$2.9x10^{13}$	$2.1x10^{-5}$	$1.8x10^{-5}$
21 Oct 2021	$1.1x10^{17}$	$1.9x10^{13}$	$1.9x10^{-6}$	$2.9x10^{-5}$
24 Oct 2021	$1.7x10^{17}$	$2.7x10^{13}$	$8.5x10^{-6}$	$2.7x10^{-5}$
25 Oct 2021	$8.6x10^{16}$	$2.4x10^{13}$	$4.6x10^{-5}$	$2.4x10^{-5}$
29 Oct 2021	$1.6x10^{17}$	$2.4x10^{13}$	$3.0x10^{-5}$	$1.9x10^{-5}$
3 Nov 2021	$2.9x10^{17}$	$2.5x10^{13}$	$6.4x10^{-5}$	$2.1x10^{-5}$

Bagana, Papua New Guinea

date	SO_2 VCD max. [molecules cm^{-2}]	BrO VCD	BrO/SO_2 fitted	BrO/SO_2 error
14 Nov 2021	$2.0x10^{17}$	$3.8x10^{13}$	$3.0x10^{-5}$	$2.1x10^{-5}$
18 Nov 2021	$7.0x10^{16}$	$1.5x10^{13}$	$6.7x10^{-5}$	$3.6x10^{-5}$
20 Nov 2021	$1.3x10^{17}$	$3.1x10^{13}$	$3.8x10^{-5}$	$3.3x10^{-5}$
21 Nov 2021	$2.5x10^{17}$	$2.8x10^{13}$	$4.8x10^{-5}$	$1.9x10^{-5}$
26 Nov 2021	$1.7x10^{17}$	$2.2x10^{13}$	$6.0x10^{-5}$	$2.2x10^{-5}$
27 Nov 2021	$7.4x10^{16}$	$1.7x10^{13}$	$6.7x10^{-5}$	$3.3x10^{-5}$
1 Dec 2021	$1.4x10^{17}$	$2.6x10^{13}$	$4.1x10^{-5}$	$2.8x10^{-5}$
5 Dec 2021	$1.4x10^{17}$	$1.7x10^{13}$	$2.9x10^{-5}$	$3.3x10^{-5}$
21 Dec 2021	$1.6x10^{17}$	$2.4x10^{13}$	$3.6x10^{-5}$	$1.9x10^{-5}$
22 Dec 2021	$4.3x10^{17}$	$3.0x10^{13}$	$2.8x10^{-5}$	$1.2x10^{-5}$

Ulawun, Papua New Guinea

Type: arc
longitude: 151.33° E
latitude: 5.05° S
Events: 9
$BrO > 2\sigma$: 3
BrO/SO_2: $5.0x10^{-5}$
std. dev.: $3.6x10^{-5}$
mean SO_2: $2.8x10^{17}$
mean BrO: $2.8x10^{13}$



20 Mar 2019	$1.2x10^{17}$	$3.8x10^{13}$	$1.1x10^{-4}$	$9.5x10^{-6}$
10 April 2019	$8.2x10^{16}$	$3.1x10^{13}$	$7.2x10^{-5}$	$1.3x10^{-5}$
25 June 2019	$8.4x10^{16}$	$1.1x10^{13}$	$5.5x10^{-5}$	$2.3x10^{-5}$
26 June 2019	$1.3x10^{18}$	$3.9x10^{13}$	$2.4x10^{-5}$	$3.1x10^{-6}$
1 Oct 2019	$1.5x10^{17}$	$2.0x10^{13}$	$3.6x10^{-5}$	$1.3x10^{-5}$
2 Oct 2019	$4.1x10^{17}$	$3.5x10^{13}$	$4.2x10^{-5}$	$6.7x10^{-6}$
3 Oct 2019	$7.6x10^{16}$	$2.3x10^{13}$	$1.1x10^{-4}$	$2.7x10^{-5}$
26 Jan 2021	$1.5x10^{17}$	$3.2x10^{13}$	$1.2x10^{-4}$	$4.7x10^{-5}$
25 Nov 2021	$1.1x10^{17}$	$2.1x10^{13}$	$2.4x10^{-5}$	$2.7x10^{-5}$

Manam, Papua New Guinea

Type: arc
longitude: 145.03° E
latitude: 4.08° S
Events: 114
$BrO > 2\sigma$: 21
BrO/SO_2: $4.4x10^{-5}$
std. dev.: $2.9x10^{-5}$
mean SO_2: $2.1x10^{17}$
mean BrO: $2.7x10^{13}$



9 Jan 2018	$1.1x10^{17}$	$2.1x10^{13}$	$1.9x10^{-5}$	$2.0x10^{-5}$
23 Aug 2018	$5.7x10^{16}$	$1.4x10^{13}$	$2.3x10^{-5}$	$4.1x10^{-5}$
25 Aug 2018	$7.0x10^{17}$	$2.3x10^{13}$	$9.0x10^{-6}$	$1.5x10^{-6}$
8 Jan 2019	$8.4x10^{17}$	$4.2x10^{13}$	$5.0x10^{-5}$	$2.1x10^{-6}$
11 Jan 2019	$9.2x10^{17}$	$3.7x10^{13}$	$1.9x10^{-5}$	$1.0x10^{-5}$
1 Mar 2019	$1.5x10^{17}$	$2.3x10^{13}$	$1.1x10^{-4}$	$3.0x10^{-5}$
2 Mar 2019	$1.4x10^{17}$	$2.2x10^{13}$	$1.3x10^{-5}$	$2.3x10^{-5}$
3 Mar 2019	$1.1x10^{17}$	$3.7x10^{13}$	$1.0x10^{-4}$	$3.1x10^{-5}$
19 Mar 2019	$2.1x10^{17}$	$3.5x10^{13}$	$1.0x10^{-4}$	$1.3x10^{-5}$
29 Mar 2019	$2.0x10^{17}$	$3.0x10^{13}$	$5.8x10^{-5}$	$1.7x10^{-5}$
2 April 2019	$1.0x10^{17}$	$1.8x10^{13}$	$6.6x10^{-5}$	$1.8x10^{-5}$
3 April 2019	$8.5x10^{16}$	$2.4x10^{13}$	$2.2x10^{-5}$	$3.1x10^{-5}$
9 April 2019	$2.4x10^{17}$	$2.8x10^{13}$	$5.0x10^{-5}$	$8.6x10^{-6}$
20 April 2019	$4.7x10^{17}$	$3.5x10^{13}$	$5.4x10^{-5}$	$1.5x10^{-5}$
21 April 2019	$1.2x10^{17}$	$1.8x10^{13}$	$6.6x10^{-5}$	$1.6x10^{-5}$
22 April 2019	$6.7x10^{16}$	$1.3x10^{13}$	$4.5x10^{-5}$	$1.6x10^{-5}$
24 April 2019	$1.2x10^{17}$	$2.4x10^{13}$	$7.1x10^{-5}$	$2.0x10^{-5}$
25 April 2019	$9.6x10^{16}$	$1.8x10^{13}$	$8.8x10^{-5}$	$3.0x10^{-5}$
28 April 2019	$1.1x10^{17}$	$2.1x10^{13}$	$3.1x10^{-5}$	$1.4x10^{-5}$
29 April 2019	$1.1x10^{17}$	$4.0x10^{13}$	$9.2x10^{-5}$	$4.1x10^{-5}$
1 May 2019	$2.4x10^{17}$	$3.5x10^{13}$	$9.0x10^{-5}$	$2.0x10^{-5}$
10 May 2019	$8.0x10^{17}$	$4.9x10^{13}$	$6.4x10^{-5}$	$5.8x10^{-6}$
11 May 2019	$6.5x10^{17}$	$4.1x10^{13}$	$5.5x10^{-5}$	$8.0x10^{-6}$
14 May 2019	$1.0x10^{17}$	$1.8x10^{13}$	$7.2x10^{-5}$	$2.5x10^{-5}$
15 May 2019	$2.2x10^{17}$	$2.6x10^{13}$	$5.6x10^{-5}$	$8.2x10^{-6}$
16 May 2019	$3.1x10^{17}$	$5.0x10^{13}$	$7.5x10^{-5}$	$7.5x10^{-6}$
17 May 2019	$1.6x10^{17}$	$2.3x10^{13}$	$7.7x10^{-5}$	$7.8x10^{-6}$
21 May 2019	$1.9x10^{17}$	$3.0x10^{13}$	$8.0x10^{-5}$	$1.2x10^{-5}$
23 May 2019	$1.2x10^{17}$	$2.2x10^{13}$	$8.2x10^{-5}$	$1.3x10^{-5}$
26 May 2019	$5.7x10^{17}$	$3.8x10^{13}$	$5.0x10^{-5}$	$9.7x10^{-6}$

Manam, Papua New Guinea

date	SO_2 VCD max. [molecules cm^{-2}]	BrO VCD max. [molecules cm^{-2}]	BrO/SO_2 fitted	BrO/SO_2 error
27 May 2019	$7.9x10^{17}$	$4.1x10^{13}$	$6.8x10^{-5}$	$6.7x10^{-6}$
28 May 2019	$7.0x10^{16}$	$2.4x10^{13}$	$8.0x10^{-5}$	$2.4x10^{-5}$
30 May 2019	$1.2x10^{17}$	$2.6x10^{13}$	$7.4x10^{-5}$	$1.2x10^{-5}$
1 June 2019	$8.9x10^{16}$	$2.5x10^{13}$	$8.1x10^{-5}$	$2.1x10^{-5}$
5 June 2019	$6.0x10^{16}$	$2.4x10^{13}$	$4.6x10^{-5}$	$3.3x10^{-5}$
12 June 2019	$1.3x10^{17}$	$3.0x10^{13}$	$1.1x10^{-4}$	$2.8x10^{-5}$
15 June 2019	$8.6x10^{16}$	$2.5x10^{13}$	$8.9x10^{-5}$	$3.0x10^{-5}$
16 June 2019	$5.7x10^{17}$	$3.1x10^{13}$	$6.5x10^{-5}$	$7.1x10^{-6}$
17 June 2019	$5.8x10^{17}$	$4.3x10^{13}$	$7.0x10^{-5}$	$6.4x10^{-6}$
18 June 2019	$5.3x10^{17}$	$3.3x10^{13}$	$6.7x10^{-5}$	$6.4x10^{-6}$
20 June 2019	$8.9x10^{16}$	$1.9x10^{13}$	$6.2x10^{-5}$	$1.9x10^{-5}$
21 June 2019	$1.4x10^{17}$	$2.1x10^{13}$	$8.7x10^{-5}$	$1.1x10^{-5}$
22 June 2019	$5.7x10^{17}$	$5.8x10^{13}$	$8.6x10^{-5}$	$6.5x10^{-6}$
23 June 2019	$1.6x10^{17}$	$2.6x10^{13}$	$9.4x10^{-5}$	$1.0x10^{-5}$
24 June 2019	$9.0x10^{16}$	$2.1x10^{13}$	$8.9x10^{-5}$	$1.8x10^{-5}$
28 June 2019	$2.4x10^{18}$	$3.8x10^{13}$	$8.2x10^{-6}$	$4.1x10^{-7}$
2 July 2019	$3.5x10^{17}$	$3.7x10^{13}$	$6.8x10^{-5}$	$5.7x10^{-6}$
3 July 2019	$2.6x10^{17}$	$3.3x10^{13}$	$5.7x10^{-5}$	$8.3x10^{-6}$
4 July 2019	$1.9x10^{17}$	$2.3x10^{13}$	$6.0x10^{-5}$	$8.7x10^{-6}$
12 July 2019	$1.1x10^{17}$	$2.1x10^{13}$	$9.9x10^{-5}$	$2.0x10^{-5}$
13 July 2019	$2.1x10^{17}$	$3.3x10^{13}$	$6.7x10^{-5}$	$1.2x10^{-5}$
17 July 2019	$1.5x10^{17}$	$2.7x10^{13}$	$6.5x10^{-5}$	$1.4x10^{-5}$
18 July 2019	$1.5x10^{17}$	$2.1x10^{13}$	$3.6x10^{-5}$	$9.5x10^{-6}$
19 July 2019	$3.5x10^{17}$	$2.8x10^{13}$	$5.9x10^{-5}$	$9.9x10^{-6}$
20 July 2019	$6.4x10^{16}$	$1.4x10^{13}$	$8.5x10^{-5}$	$3.8x10^{-5}$
23 July 2019	$1.1x10^{17}$	$2.7x10^{13}$	$4.6x10^{-5}$	$2.2x10^{-5}$
13 Aug 2019	$6.1x10^{16}$	$2.3x10^{13}$	$3.7x10^{-5}$	$3.9x10^{-5}$
15 Aug 2019	$1.1x10^{17}$	$1.9x10^{13}$	$5.5x10^{-5}$	$3.8x10^{-5}$
20 Aug 2019	$6.6x10^{16}$	$2.4x10^{13}$	$1.8x10^{-5}$	$4.5x10^{-5}$
24 Aug 2019	$1.1x10^{17}$	$2.5x10^{13}$	$6.5x10^{-5}$	$2.4x10^{-5}$
29 Aug 2019	$1.3x10^{17}$	$2.6x10^{13}$	$7.7x10^{-5}$	$2.0x10^{-5}$
30 Aug 2019	$6.1x10^{16}$	$3.1x10^{13}$	$3.6x10^{-5}$	$2.6x10^{-5}$
5 Sept 2019	$7.0x10^{16}$	$1.3x10^{13}$	$1.5x10^{-5}$	$2.8x10^{-5}$
15 Sept 2019	$9.2x10^{16}$	$2.5x10^{13}$	$7.2x10^{-5}$	$2.9x10^{-5}$
19 Sept 2019	$9.5x10^{16}$	$1.8x10^{13}$	$1.0x10^{-5}$	$3.4x10^{-5}$
6 Oct 2019	$1.7x10^{17}$	$2.1x10^{13}$	$5.0x10^{-5}$	$1.8x10^{-5}$
23 Oct 2019	$8.0x10^{16}$	$1.9x10^{13}$	$5.7x10^{-5}$	$4.2x10^{-5}$
27 Oct 2019	$6.6x10^{16}$	$2.8x10^{13}$	$3.6x10^{-5}$	$3.6x10^{-5}$
28 Oct 2019	$1.7x10^{17}$	$3.8x10^{13}$	$5.8x10^{-5}$	$1.9x10^{-5}$
29 Oct 2019	$8.1x10^{16}$	$2.6x10^{13}$	$6.7x10^{-5}$	$2.8x10^{-5}$
14 Nov 2019	$8.6x10^{16}$	$2.6x10^{13}$	$7.8x10^{-5}$	$2.8x10^{-5}$
18 Nov 2019	$1.5x10^{17}$	$2.9x10^{13}$	$2.1x10^{-5}$	$4.1x10^{-5}$
29 Nov 2019	$1.1x10^{17}$	$1.8x10^{13}$	$4.9x10^{-5}$	$3.0x10^{-5}$
30 Nov 2019	$2.0x10^{17}$	$1.9x10^{13}$	$8.4x10^{-5}$	$2.3x10^{-5}$
3 Dec 2019	$6.7x10^{16}$	$1.9x10^{13}$	$7.8x10^{-5}$	$3.6x10^{-5}$
5 Dec 2019	$1.5x10^{17}$	$2.9x10^{13}$	$9.5x10^{-5}$	$2.1x10^{-5}$
9 Dec 2019	$2.4x10^{17}$	$2.7x10^{13}$	$6.0x10^{-5}$	$2.4x10^{-5}$
11 Dec 2019	$1.4x10^{17}$	$1.9x10^{13}$	$9.9x10^{-5}$	$3.4x10^{-5}$
19 Dec 2019	$1.9x10^{17}$	$4.0x10^{13}$	$7.1x10^{-5}$	$3.5x10^{-5}$
20 Dec 2019	$1.4x10^{17}$	$2.7x10^{13}$	$7.2x10^{-5}$	$2.3x10^{-5}$
24 Dec 2019	$1.1x10^{17}$	$2.2x10^{13}$	$7.4x10^{-5}$	$3.3x10^{-5}$
6 Jan 2020	$2.4x10^{17}$	$2.4x10^{13}$	$7.2x10^{-5}$	$3.5x10^{-5}$
27 Feb 2020	$1.9x10^{17}$	$2.4x10^{13}$	$3.6x10^{-5}$	$3.2x10^{-5}$
28 Feb 2020	$1.2x10^{17}$	$2.4x10^{13}$	$1.7x10^{-5}$	$3.3x10^{-5}$
29 Feb 2020	$1.0x10^{17}$	$2.6x10^{13}$	$7.9x10^{-5}$	$3.6x10^{-5}$
3 Mar 2020	$8.4x10^{16}$	$2.7x10^{13}$	$1.4x10^{-4}$	$3.4x10^{-5}$
4 Mar 2020	$2.1x10^{17}$	$3.8x10^{13}$	$4.4x10^{-6}$	$1.9x10^{-5}$
19 Mar 2020	$9.7x10^{16}$	$2.5x10^{13}$	$6.1x10^{-5}$	$4.0x10^{-5}$
28 April 2020	$8.4x10^{16}$	$1.5x10^{13}$	$4.8x10^{-5}$	$3.8x10^{-5}$
1 May 2020	$1.6x10^{17}$	$2.5x10^{13}$	$5.3x10^{-5}$	$3.2x10^{-5}$
7 May 2020	$9.5x10^{16}$	$2.0x10^{13}$	$5.5x10^{-5}$	$3.7x10^{-5}$
24 May 2020	$1.3x10^{17}$	$2.3x10^{13}$	$6.3x10^{-5}$	$2.7x10^{-5}$
15 July 2020	$7.7x10^{16}$	$2.4x10^{13}$	$5.5x10^{-5}$	$6.2x10^{-5}$
10 Aug 2020	$9.6x10^{16}$	$2.3x10^{13}$	$4.4x10^{-5}$	$3.6x10^{-5}$
11 Aug 2020	$9.7x10^{16}$	$2.7x10^{13}$	$3.8x10^{-5}$	$2.0x10^{-5}$
17 Aug 2020	$8.5x10^{16}$	$1.6x10^{13}$	$2.0x10^{-5}$	$5.2x10^{-5}$
8 Oct 2020	$7.8x10^{16}$	$1.9x10^{13}$	$9.1x10^{-5}$	$3.7x10^{-5}$
9 Oct 2020	$1.4x10^{17}$	$2.4x10^{13}$	$4.4x10^{-5}$	$1.9x10^{-5}$
10 Nov 2020	$7.0x10^{16}$	$1.7x10^{13}$	$1.2x10^{-5}$	$4.3x10^{-5}$
6 Dec 2020	$8.5x10^{16}$	$3.2x10^{13}$	$6.1x10^{-5}$	$3.9x10^{-5}$
7 Dec 2020	$9.3x10^{16}$	$2.3x10^{13}$	$1.0x10^{-4}$	$4.9x10^{-5}$

Manam, Papua New Guinea

date	SO_2 VCD max. [molecules cm^{-2}]	BrO VCD max. [molecules cm^{-2}]	BrO/SO_2 fitted	BrO/SO_2 error
28 Dec 2020	$1.0x10^{17}$	$2.6x10^{13}$	$4.3x10^{-5}$	$5.0x10^{-5}$
1 Jan 2021	$1.0x10^{17}$	$2.7x10^{13}$	$7.5x10^{-5}$	$5.6x10^{-5}$
12 Jan 2021	$9.6x10^{16}$	$2.2x10^{13}$	$1.8x10^{-5}$	$3.8x10^{-5}$
13 Jan 2021	$9.6x10^{16}$	$2.8x10^{13}$	$6.4x10^{-5}$	$4.0x10^{-5}$
14 Feb 2021	$8.3x10^{16}$	$2.1x10^{13}$	$8.8x10^{-5}$	$5.0x10^{-5}$
18 Feb 2021	$1.1x10^{17}$	$2.6x10^{13}$	$1.2x10^{-4}$	$4.2x10^{-5}$
18 Mar 2021	$8.5x10^{16}$	$1.6x10^{13}$	$4.1x10^{-5}$	$4.1x10^{-5}$
23 Mar 2021	$1.2x10^{17}$	$4.2x10^{13}$	$1.2x10^{-4}$	$3.9x10^{-5}$
2 April 2021	$7.6x10^{16}$	$3.2x10^{13}$	$8.5x10^{-5}$	$5.4x10^{-5}$
25 April 2021	$8.4x10^{16}$	$2.1x10^{13}$	$1.3x10^{-5}$	$2.9x10^{-5}$
5 May 2021	$1.1x10^{17}$	$2.1x10^{13}$	$4.0x10^{-5}$	$3.6x10^{-5}$
20 Oct 2021	$3.3x10^{17}$	$3.0x10^{13}$	$2.7x10^{-5}$	$3.7x10^{-6}$
23 Nov 2021	$1.1x10^{17}$	$3.2x10^{13}$	$5.8x10^{-5}$	$3.5x10^{-5}$

Dukono, Indonesia

Type: arc
longitude: 127.88° E
latitude: 1.70° N
Events: 199
$BrO > 2\sigma$: 18
BrO/SO_2: $6.6x10^{-5}$
std. dev.: $3.4x10^{-5}$
mean SO_2: $1.1x10^{17}$
mean BrO: $2.8x10^{13}$



2 Jan 2018	$1.3x10^{17}$	$1.7x10^{13}$	$4.5x10^{-5}$	$2.6x10^{-5}$
24 Feb 2018	$9.8x10^{16}$	$2.5x10^{13}$	$6.3x10^{-5}$	$2.4x10^{-5}$
8 April 2018	$8.6x10^{16}$	$1.9x10^{13}$	$7.0x10^{-5}$	$3.4x10^{-5}$
12 April 2018	$8.9x10^{16}$	$2.4x10^{13}$	$1.2x10^{-4}$	$5.4x10^{-5}$
13 April 2018	$1.2x10^{17}$	$3.1x10^{13}$	$1.4x10^{-5}$	$3.9x10^{-5}$
17 April 2018	$8.3x10^{16}$	$1.4x10^{13}$	$7.4x10^{-5}$	$3.9x10^{-5}$
19 April 2018	$9.4x10^{16}$	$1.7x10^{13}$	$6.3x10^{-5}$	$3.7x10^{-5}$
23 April 2018	$1.3x10^{17}$	$2.4x10^{13}$	$8.7x10^{-5}$	$4.3x10^{-5}$
14 May 2018	$8.0x10^{16}$	$2.3x10^{13}$	$7.3x10^{-5}$	$2.4x10^{-5}$
19 May 2018	$7.1x10^{16}$	$1.9x10^{13}$	$5.8x10^{-5}$	$3.3x10^{-5}$
16 June 2018	$7.6x10^{16}$	$2.1x10^{13}$	$5.0x10^{-5}$	$6.3x10^{-5}$
28 July 2018	$1.8x10^{17}$	$1.7x10^{13}$	$1.2x10^{-5}$	$3.3x10^{-5}$
30 July 2018	$7.8x10^{16}$	$1.8x10^{13}$	$6.4x10^{-6}$	$4.9x10^{-5}$
19 Aug 2018	$9.8x10^{16}$	$1.9x10^{13}$	$7.2x10^{-5}$	$4.3x10^{-5}$
30 Aug 2018	$9.0x10^{16}$	$1.9x10^{13}$	$8.6x10^{-5}$	$4.1x10^{-5}$
30 Sept 2018	$8.8x10^{16}$	$2.0x10^{13}$	$7.7x10^{-5}$	$3.5x10^{-5}$
1 Oct 2018	$1.0x10^{17}$	$3.3x10^{13}$	$6.1x10^{-5}$	$2.9x10^{-5}$
6 Oct 2018	$7.0x10^{16}$	$6.0x10^{13}$	$4.7x10^{-5}$	$4.2x10^{-5}$
10 Oct 2018	$8.2x10^{16}$	$2.0x10^{13}$	$5.0x10^{-5}$	$3.6x10^{-5}$
3 Dec 2018	$1.0x10^{17}$	$3.0x10^{13}$	$7.0x10^{-5}$	$2.2x10^{-5}$
9 Dec 2018	$1.2x10^{17}$	$2.0x10^{13}$	$1.8x10^{-5}$	$3.4x10^{-5}$
10 Jan 2019	$1.8x10^{17}$	$3.2x10^{13}$	$9.3x10^{-5}$	$3.1x10^{-5}$
31 Jan 2019	$1.0x10^{17}$	$2.3x10^{13}$	$6.4x10^{-5}$	$4.3x10^{-5}$
22 Feb 2019	$2.7x10^{17}$	$2.8x10^{13}$	$8.1x10^{-5}$	$2.3x10^{-5}$
27 Feb 2019	$8.5x10^{16}$	$3.2x10^{13}$	$8.8x10^{-5}$	$3.6x10^{-5}$
4 Mar 2019	$8.8x10^{16}$	$3.1x10^{13}$	$3.5x10^{-5}$	$3.0x10^{-5}$
20 Mar 2019	$2.0x10^{17}$	$2.9x10^{13}$	$7.8x10^{-5}$	$2.4x10^{-5}$
21 Mar 2019	$1.1x10^{17}$	$1.7x10^{13}$	$6.3x10^{-7}$	$3.4x10^{-5}$
25 Mar 2019	$1.2x10^{17}$	$3.8x10^{13}$	$4.1x10^{-5}$	$4.1x10^{-5}$
26 Mar 2019	$1.1x10^{17}$	$2.3x10^{13}$	$8.4x10^{-5}$	$2.3x10^{-5}$
10 April 2019	$1.1x10^{17}$	$2.3x10^{13}$	$8.0x10^{-5}$	$2.5x10^{-5}$
11 April 2019	$9.2x10^{16}$	$1.7x10^{13}$	$5.9x10^{-5}$	$2.9x10^{-5}$
20 April 2019	$1.1x10^{17}$	$2.7x10^{13}$	$6.3x10^{-5}$	$2.8x10^{-5}$
21 April 2019	$1.6x10^{17}$	$3.4x10^{13}$	$1.0x10^{-4}$	$2.4x10^{-5}$
22 April 2019	$8.0x10^{16}$	$3.1x10^{13}$	$7.7x10^{-5}$	$4.5x10^{-5}$
17 May 2019	$8.6x10^{16}$	$2.5x10^{13}$	$6.9x10^{-5}$	$2.7x10^{-5}$
27 May 2019	$6.0x10^{16}$	$1.8x10^{13}$	$6.9x10^{-5}$	$2.5x10^{-5}$
25 June 2019	$6.7x10^{16}$	$1.4x10^{13}$	$3.4x10^{-6}$	$5.0x10^{-5}$
9 July 2019	$1.7x10^{17}$	$2.4x10^{13}$	$3.1x10^{-5}$	$3.0x10^{-5}$
21 July 2019	$1.0x10^{17}$	$2.0x10^{13}$	$7.1x10^{-5}$	$4.3x10^{-5}$
11 Aug 2019	$1.9x10^{17}$	$2.4x10^{13}$	$3.5x10^{-5}$	$4.1x10^{-5}$
16 Aug 2019	$1.5x10^{17}$	$2.5x10^{13}$	$2.9x10^{-5}$	$2.6x10^{-5}$
17 Aug 2019	$2.2x10^{17}$	$3.7x10^{13}$	$2.4x10^{-5}$	$1.5x10^{-5}$
27 Aug 2019	$7.2x10^{16}$	$3.0x10^{13}$	$1.1x10^{-4}$	$5.7x10^{-5}$
18 Sept 2019	$1.2x10^{17}$	$2.5x10^{13}$	$5.8x10^{-5}$	$3.7x10^{-5}$
23 Sept 2019	$1.1x10^{17}$	$2.5x10^{13}$	$5.8x10^{-5}$	$2.7x10^{-5}$
24 Sept 2019	$9.4x10^{16}$	$1.9x10^{13}$	$6.8x10^{-5}$	$3.8x10^{-5}$

Dukono, Indonesia

date	SO_2 VCD max. [molecules cm^{-2}]	BrO VCD	BrO/SO_2 fitted	BrO/SO_2 error
29 Sept 2019	$6.3x10^{16}$	$4.1x10^{13}$	$9.1x10^{-5}$	$4.3x10^{-5}$
3 Oct 2019	$1.2x10^{17}$	$4.1x10^{13}$	$5.0x10^{-5}$	$2.6x10^{-5}$
4 Oct 2019	$1.4x10^{17}$	$2.5x10^{13}$	$3.5x10^{-6}$	$3.6x10^{-5}$
9 Oct 2019	$7.8x10^{16}$	$2.3x10^{13}$	$7.0x10^{-5}$	$3.5x10^{-5}$
13 Oct 2019	$1.3x10^{17}$	$2.2x10^{13}$	$8.0x10^{-5}$	$4.6x10^{-5}$
25 Oct 2019	$1.2x10^{17}$	$3.4x10^{13}$	$4.1x10^{-5}$	$3.1x10^{-5}$
15 Nov 2019	$1.7x10^{17}$	$2.7x10^{13}$	$7.4x10^{-5}$	$3.8x10^{-5}$
16 Nov 2019	$8.0x10^{16}$	$2.4x10^{13}$	$4.4x10^{-5}$	$4.7x10^{-5}$
21 Nov 2019	$1.1x10^{17}$	$2.4x10^{13}$	$8.0x10^{-5}$	$2.7x10^{-5}$
12 Dec 2019	$1.1x10^{17}$	$4.1x10^{13}$	$5.4x10^{-5}$	$5.3x10^{-5}$
2 Jan 2020	$6.4x10^{16}$	$2.6x10^{13}$	$1.1x10^{-4}$	$3.9x10^{-5}$
24 Jan 2020	$1.4x10^{17}$	$2.6x10^{13}$	$4.5x10^{-5}$	$3.4x10^{-5}$
28 Jan 2020	$1.3x10^{17}$	$2.8x10^{13}$	$5.0x10^{-5}$	$2.2x10^{-5}$
6 Mar 2020	$1.6x10^{17}$	$4.1x10^{13}$	$1.3x10^{-5}$	$2.5x10^{-5}$
22 Mar 2020	$7.7x10^{16}$	$2.5x10^{13}$	$3.3x10^{-5}$	$5.0x10^{-5}$
27 Mar 2020	$2.0x10^{17}$	$2.7x10^{13}$	$3.4x10^{-5}$	$2.6x10^{-5}$
28 Mar 2020	$8.4x10^{16}$	$2.1x10^{13}$	$2.2x10^{-5}$	$2.9x10^{-5}$
31 Mar 2020	$8.5x10^{16}$	$1.8x10^{13}$	$4.1x10^{-6}$	$3.7x10^{-5}$
1 April 2020	$1.2x10^{17}$	$3.3x10^{13}$	$6.9x10^{-5}$	$4.6x10^{-5}$
2 April 2020	$1.1x10^{17}$	$2.4x10^{13}$	$7.9x10^{-5}$	$2.8x10^{-5}$
12 April 2020	$1.9x10^{17}$	$2.6x10^{13}$	$8.2x10^{-5}$	$2.7x10^{-5}$
18 April 2020	$6.9x10^{16}$	$2.1x10^{13}$	$7.3x10^{-5}$	$4.7x10^{-5}$
22 April 2020	$7.2x10^{16}$	$2.3x10^{13}$	$8.1x10^{-5}$	$4.3x10^{-5}$
23 April 2020	$1.1x10^{17}$	$3.2x10^{13}$	$6.5x10^{-5}$	$5.2x10^{-5}$
24 April 2020	$9.1x10^{16}$	$3.0x10^{13}$	$1.4x10^{-6}$	$5.1x10^{-5}$
29 April 2020	$9.8x10^{16}$	$3.7x10^{13}$	$1.1x10^{-4}$	$4.7x10^{-5}$
3 May 2020	$6.5x10^{16}$	$2.3x10^{13}$	$9.2x10^{-5}$	$6.2x10^{-5}$
4 May 2020	$1.5x10^{17}$	$2.7x10^{13}$	$7.7x10^{-5}$	$3.9x10^{-5}$
5 May 2020	$1.1x10^{17}$	$2.2x10^{13}$	$1.1x10^{-4}$	$3.9x10^{-5}$
9 May 2020	$1.4x10^{17}$	$3.7x10^{13}$	$1.1x10^{-4}$	$4.3x10^{-5}$
13 May 2020	$1.1x10^{17}$	$2.0x10^{13}$	$0.7x10^{-5}$	$4.1x10^{-5}$
15 May 2020	$1.0x10^{17}$	$4.5x10^{13}$	$6.6x10^{-5}$	$3.1x10^{-5}$
26 May 2020	$7.2x10^{16}$	$4.5x10^{13}$	$9.2x10^{-5}$	$5.0x10^{-5}$
30 May 2020	$1.2x10^{17}$	$3.2x10^{13}$	$1.6x10^{-4}$	$5.2x10^{-5}$
5 June 2020	$1.5x10^{17}$	$3.4x10^{13}$	$1.0x10^{-4}$	$3.4x10^{-5}$
10 June 2020	$1.3x10^{17}$	$2.3x10^{13}$	$4.6x10^{-5}$	$4.3x10^{-5}$
16 June 2020	$1.2x10^{17}$	$2.2x10^{13}$	$7.8x10^{-5}$	$3.7x10^{-5}$
20 June 2020	$9.9x10^{16}$	$2.9x10^{13}$	$8.3x10^{-5}$	$3.7x10^{-5}$
21 June 2020	$7.4x10^{16}$	$2.5x10^{13}$	$9.1x10^{-5}$	$4.2x10^{-5}$
30 June 2020	$1.1x10^{17}$	$2.5x10^{13}$	$7.4x10^{-5}$	$3.4x10^{-5}$
1 July 2020	$7.8x10^{16}$	$3.1x10^{13}$	$1.3x10^{-4}$	$3.1x10^{-5}$
6 July 2020	$9.6x10^{16}$	$2.6x10^{13}$	$5.3x10^{-5}$	$3.1x10^{-5}$
12 July 2020	$6.8x10^{16}$	$3.4x10^{13}$	$8.1x10^{-5}$	$3.2x10^{-5}$
13 July 2020	$7.3x10^{16}$	$1.8x10^{13}$	$6.3x10^{-5}$	$4.6x10^{-5}$
17 July 2020	$1.3x10^{17}$	$2.6x10^{13}$	$5.2x10^{-5}$	$2.5x10^{-5}$
28 July 2020	$1.1x10^{17}$	$3.3x10^{13}$	$7.7x10^{-5}$	$3.5x10^{-5}$
29 July 2020	$1.2x10^{17}$	$3.6x10^{13}$	$4.4x10^{-5}$	$3.9x10^{-5}$
7 Aug 2020	$8.0x10^{16}$	$3.3x10^{13}$	$1.6x10^{-4}$	$5.3x10^{-5}$
12 Aug 2020	$9.0x10^{16}$	$3.1x10^{13}$	$7.2x10^{-5}$	$5.2x10^{-5}$
18 Aug 2020	$1.3x10^{17}$	$2.6x10^{13}$	$3.0x10^{-5}$	$3.7x10^{-5}$
19 Aug 2020	$1.0x10^{17}$	$4.5x10^{13}$	$3.5x10^{-5}$	$3.0x10^{-5}$
24 Aug 2020	$9.8x10^{16}$	$2.7x10^{13}$	$5.4x10^{-5}$	$2.7x10^{-5}$
25 Aug 2020	$1.2x10^{17}$	$1.8x10^{13}$	$1.2x10^{-5}$	$4.1x10^{-5}$
8 Sept 2020	$1.1x10^{17}$	$2.2x10^{13}$	$7.9x10^{-5}$	$4.2x10^{-5}$
14 Sept 2020	$8.9x10^{16}$	$3.0x10^{13}$	$7.7x10^{-5}$	$2.2x10^{-5}$
19 Sept 2020	$1.5x10^{17}$	$3.5x10^{13}$	$7.5x10^{-5}$	$2.9x10^{-5}$
20 Sept 2020	$9.1x10^{16}$	$2.9x10^{13}$	$7.5x10^{-5}$	$2.6x10^{-5}$
25 Sept 2020	$7.9x10^{16}$	$2.0x10^{13}$	$2.5x10^{-5}$	$3.6x10^{-5}$
29 Sept 2020	$1.2x10^{17}$	$1.7x10^{13}$	$1.9x10^{-5}$	$2.6x10^{-5}$
30 Sept 2020	$1.4x10^{17}$	$2.9x10^{13}$	$5.5x10^{-5}$	$3.4x10^{-5}$
5 Oct 2020	$1.4x10^{17}$	$3.9x10^{13}$	$1.1x10^{-4}$	$2.8x10^{-5}$
10 Oct 2020	$6.7x10^{16}$	$2.6x10^{13}$	$2.9x10^{-5}$	$2.9x10^{-5}$
11 Oct 2020	$2.1x10^{17}$	$3.0x10^{13}$	$8.1x10^{-5}$	$2.1x10^{-5}$
12 Oct 2020	$1.2x10^{17}$	$3.7x10^{13}$	$1.2x10^{-4}$	$4.1x10^{-5}$
16 Oct 2020	$9.4x10^{16}$	$3.8x10^{13}$	$7.7x10^{-5}$	$4.0x10^{-5}$
17 Oct 2020	$7.8x10^{16}$	$2.9x10^{13}$	$7.0x10^{-5}$	$5.7x10^{-5}$
1 Nov 2020	$7.9x10^{16}$	$1.9x10^{13}$	$2.3x10^{-5}$	$6.0x10^{-5}$
11 Nov 2020	$8.8x10^{16}$	$3.6x10^{13}$	$9.3x10^{-5}$	$3.1x10^{-5}$
12 Nov 2020	$9.8x10^{16}$	$3.6x10^{13}$	$5.4x10^{-5}$	$3.8x10^{-5}$
13 Nov 2020	$6.8x10^{16}$	$1.8x10^{13}$	$6.0x10^{-5}$	$3.7x10^{-5}$
16 Nov 2020	$6.7x10^{16}$	$3.2x10^{13}$	$5.5x10^{-5}$	$3.4x10^{-5}$

Dukono, Indonesia

date	SO_2 VCD max. [molecules cm^{-2}]	BrO VCD	BrO/SO_2 fitted	BrO/SO_2 error
23 Nov 2020	$1.9x10^{17}$	$4.5x10^{13}$	$7.4x10^{-5}$	$1.8x10^{-5}$
24 Nov 2020	$8.7x10^{16}$	$2.1x10^{13}$	$8.0x10^{-5}$	$2.0x10^{-5}$
28 Nov 2020	$2.0x10^{17}$	$3.8x10^{13}$	$7.3x10^{-5}$	$1.8x10^{-5}$
8 Dec 2020	$1.7x10^{17}$	$3.5x10^{13}$	$7.5x10^{-5}$	$2.1x10^{-5}$
9 Dec 2020	$1.2x10^{17}$	$2.6x10^{13}$	$6.5x10^{-5}$	$2.2x10^{-5}$
13 Dec 2020	$1.7x10^{17}$	$2.2x10^{13}$	$3.3x10^{-5}$	$2.0x10^{-5}$
24 Dec 2020	$7.1x10^{16}$	$2.8x10^{13}$	$1.2x10^{-4}$	$5.5x10^{-5}$
2 Jan 2021	$8.0x10^{16}$	$1.7x10^{13}$	$4.2x10^{-5}$	$3.4x10^{-5}$
8 Jan 2021	$9.5x10^{16}$	$2.4x10^{13}$	$1.1x10^{-4}$	$3.2x10^{-5}$
11 Jan 2021	$8.2x10^{16}$	$2.8x10^{13}$	$1.4x10^{-4}$	$5.5x10^{-5}$
14 Jan 2021	$1.9x10^{17}$	$3.4x10^{13}$	$5.5x10^{-5}$	$1.9x10^{-5}$
20 Jan 2021	$1.2x10^{17}$	$3.0x10^{13}$	$9.7x10^{-5}$	$2.8x10^{-5}$
21 Jan 2021	$7.1x10^{16}$	$4.6x10^{13}$	$1.5x10^{-4}$	$4.7x10^{-5}$
30 Jan 2021	$1.3x10^{17}$	$2.1x10^{13}$	$9.6x10^{-5}$	$2.6x10^{-5}$
4 Feb 2021	$4.2x10^{17}$	$3.9x10^{13}$	$6.3x10^{-5}$	$2.2x10^{-5}$
5 Feb 2021	$7.5x10^{16}$	$2.8x10^{13}$	$1.0x10^{-4}$	$2.3x10^{-5}$
6 Feb 2021	$1.2x10^{17}$	$2.1x10^{13}$	$1.2x10^{-5}$	$3.4x10^{-5}$
11 Feb 2021	$1.0x10^{17}$	$2.9x10^{13}$	$5.2x10^{-5}$	$2.6x10^{-5}$
27 Feb 2021	$6.1x10^{16}$	$2.4x10^{13}$	$3.4x10^{-5}$	$5.0x10^{-5}$
4 Mar 2021	$1.0x10^{17}$	$4.5x10^{13}$	$1.3x10^{-4}$	$3.1x10^{-5}$
9 Mar 2021	$9.7x10^{16}$	$3.8x10^{13}$	$5.8x10^{-5}$	$3.3x10^{-5}$
10 Mar 2021	$7.4x10^{16}$	$2.4x10^{13}$	$4.1x10^{-5}$	$4.1x10^{-5}$
13 Mar 2021	$7.4x10^{16}$	$1.8x10^{13}$	$8.5x10^{-5}$	$4.3x10^{-5}$
14 Mar 2021	$1.4x10^{17}$	$3.6x10^{13}$	$1.3x10^{-4}$	$3.2x10^{-5}$
15 Mar 2021	$1.4x10^{17}$	$3.7x10^{13}$	$3.3x10^{-5}$	$2.4x10^{-5}$
16 Mar 2021	$6.7x10^{16}$	$3.1x10^{13}$	$2.3x10^{-5}$	$4.6x10^{-5}$
19 Mar 2021	$1.1x10^{17}$	$1.5x10^{13}$	$4.0x10^{-6}$	$1.5x10^{-5}$
20 Mar 2021	$2.5x10^{17}$	$4.0x10^{13}$	$6.0x10^{-5}$	$1.8x10^{-5}$
24 Mar 2021	$1.2x10^{17}$	$2.3x10^{13}$	$7.3x10^{-5}$	$2.2x10^{-5}$
25 Mar 2021	$1.2x10^{17}$	$3.1x10^{13}$	$1.3x10^{-4}$	$3.2x10^{-5}$
26 Mar 2021	$1.3x10^{17}$	$3.4x10^{13}$	$6.6x10^{-5}$	$2.8x10^{-5}$
9 April 2021	$6.6x10^{16}$	$2.9x10^{13}$	$7.2x10^{-5}$	$4.7x10^{-5}$
21 April 2021	$8.7x10^{16}$	$3.2x10^{13}$	$1.3x10^{-4}$	$3.4x10^{-5}$
22 April 2021	$1.0x10^{17}$	$2.6x10^{13}$	$7.7x10^{-5}$	$4.4x10^{-5}$
26 April 2021	$1.4x10^{17}$	$2.8x10^{13}$	$5.0x10^{-5}$	$3.9x10^{-5}$
27 April 2021	$1.7x10^{17}$	$1.8x10^{13}$	$4.4x10^{-5}$	$3.1x10^{-5}$
30 April 2021	$1.6x10^{17}$	$2.7x10^{13}$	$7.3x10^{-5}$	$2.9x10^{-5}$
1 May 2021	$1.7x10^{17}$	$3.4x10^{13}$	$3.5x10^{-5}$	$2.8x10^{-5}$
2 May 2021	$1.6x10^{17}$	$3.2x10^{13}$	$9.6x10^{-5}$	$2.1x10^{-5}$
3 May 2021	$1.0x10^{17}$	$1.8x10^{13}$	$6.0x10^{-5}$	$3.2x10^{-5}$
7 May 2021	$1.0x10^{17}$	$2.2x10^{13}$	$5.8x10^{-5}$	$4.3x10^{-5}$
8 May 2021	$8.7x10^{16}$	$1.8x10^{13}$	$7.2x10^{-6}$	$3.4x10^{-5}$
13 May 2021	$6.3x10^{16}$	$2.1x10^{13}$	$9.8x10^{-5}$	$4.7x10^{-5}$
16 May 2021	$1.3x10^{17}$	$2.2x10^{13}$	$7.1x10^{-5}$	$2.9x10^{-5}$
17 May 2021	$7.1x10^{16}$	$2.5x10^{13}$	$6.4x10^{-5}$	$3.4x10^{-5}$
28 May 2021	$3.3x10^{17}$	$4.1x10^{13}$	$7.5x10^{-5}$	$2.4x10^{-5}$
2 June 2021	$7.7x10^{16}$	$2.5x10^{13}$	$7.2x10^{-5}$	$3.4x10^{-5}$
3 June 2021	$8.6x10^{16}$	$3.1x10^{13}$	$6.1x10^{-5}$	$3.1x10^{-5}$
6 June 2021	$7.1x10^{16}$	$2.2x10^{13}$	$1.0x10^{-4}$	$3.8x10^{-5}$
7 June 2021	$9.5x10^{16}$	$4.0x10^{13}$	$1.1x10^{-4}$	$3.3x10^{-5}$
8 June 2021	$6.8x10^{16}$	$2.9x10^{13}$	$1.0x10^{-4}$	$2.9x10^{-5}$
12 June 2021	$1.3x10^{17}$	$2.7x10^{13}$	$7.7x10^{-5}$	$2.0x10^{-5}$
18 June 2021	$6.2x10^{16}$	$4.5x10^{13}$	$8.0x10^{-5}$	$5.3x10^{-5}$
22 June 2021	$1.2x10^{17}$	$3.6x10^{13}$	$2.9x10^{-5}$	$2.2x10^{-5}$
23 June 2021	$1.2x10^{17}$	$3.4x10^{13}$	$5.8x10^{-5}$	$1.8x10^{-5}$
24 June 2021	$1.0x10^{17}$	$3.2x10^{13}$	$9.9x10^{-5}$	$2.8x10^{-5}$
28 June 2021	$7.4x10^{16}$	$2.8x10^{13}$	$1.3x10^{-4}$	$2.2x10^{-5}$
29 June 2021	$1.6x10^{17}$	$4.3x10^{13}$	$5.6x10^{-5}$	$2.5x10^{-5}$
30 June 2021	$1.4x10^{17}$	$3.8x10^{13}$	$9.5x10^{-5}$	$3.1x10^{-5}$
10 July 2021	$2.8x10^{17}$	$3.2x10^{13}$	$7.1x10^{-5}$	$1.9x10^{-5}$
14 July 2021	$8.3x10^{16}$	$2.9x10^{13}$	$9.1x10^{-5}$	$2.4x10^{-5}$
30 July 2021	$1.9x10^{17}$	$2.6x10^{13}$	$5.7x10^{-5}$	$3.8x10^{-5}$
31 July 2021	$7.0x10^{16}$	$3.5x10^{13}$	$5.2x10^{-5}$	$3.6x10^{-5}$
1 Aug 2021	$1.0x10^{17}$	$2.3x10^{13}$	$6.3x10^{-5}$	$4.0x10^{-5}$
4 Aug 2021	$7.7x10^{16}$	$2.3x10^{13}$	$5.6x10^{-6}$	$5.1x10^{-5}$
6 Aug 2021	$1.0x10^{17}$	$3.3x10^{13}$	$2.2x10^{-5}$	$5.6x10^{-5}$
10 Aug 2021	$1.0x10^{17}$	$3.8x10^{13}$	$5.6x10^{-5}$	$2.1x10^{-5}$
22 Aug 2021	$7.4x10^{16}$	$3.2x10^{13}$	$1.2x10^{-4}$	$5.4x10^{-5}$
26 Aug 2021	$1.2x10^{17}$	$2.8x10^{13}$	$1.8x10^{-5}$	$2.5x10^{-5}$
27 Aug 2021	$1.2x10^{17}$	$4.0x10^{13}$	$5.6x10^{-5}$	$2.8x10^{-5}$
5 Sept 2021	$1.1x10^{17}$	$2.0x10^{13}$	$8.5x10^{-5}$	$2.1x10^{-5}$

Dukono, Indonesia

date	SO_2 VCD max. [molecules cm^{-2}]	BrO VCD	BrO/SO_2 fitted	BrO/SO_2 error
7 Sept 2021	$1.2x10^{17}$	$2.7x10^{13}$	$8.6x10^{-5}$	$4.3x10^{-5}$
8 Sept 2021	$6.9x10^{16}$	$2.1x10^{13}$	$4.9x10^{-5}$	$4.4x10^{-5}$
22 Sept 2021	$1.3x10^{17}$	$5.4x10^{13}$	$1.8x10^{-4}$	$5.2x10^{-5}$
23 Sept 2021	$1.5x10^{17}$	$3.5x10^{13}$	$7.7x10^{-5}$	$3.0x10^{-5}$
27 Sept 2021	$7.7x10^{16}$	$2.7x10^{13}$	$4.8x10^{-5}$	$3.0x10^{-5}$
28 Sept 2021	$8.8x10^{16}$	$2.4x10^{13}$	$1.1x10^{-4}$	$3.3x10^{-5}$
24 Oct 2021	$1.2x10^{17}$	$2.7x10^{13}$	$1.1x10^{-4}$	$3.3x10^{-5}$
14 Nov 2021	$1.0x10^{17}$	$2.2x10^{13}$	$2.1x10^{-5}$	$3.6x10^{-5}$
15 Nov 2021	$2.2x10^{17}$	$4.5x10^{13}$	$7.9x10^{-5}$	$2.1x10^{-5}$
20 Nov 2021	$7.8x10^{16}$	$4.9x10^{13}$	$8.6x10^{-5}$	$3.0x10^{-5}$

Karangetang, Indonesia

Type: arc
longitude: 125.40° E
latitude: 2.78° N
Events: 7
$BrO > 2\sigma$: 1
BrO/SO_2: $1.1x10^{-4}$
std. dev.: $2.9x10^{-5}$
mean SO_2: $1.0x10^{17}$
mean BrO: $2.6x10^{13}$



28 Nov 2018	$8.9x10^{16}$	$3.0x10^{13}$	$1.2x10^{-4}$	$4.3x10^{-5}$
3 Mar 2019	$1.0x10^{17}$	$1.9x10^{13}$	$5.9x10^{-5}$	$3.4x10^{-5}$
13 May 2019	$7.9x10^{16}$	$2.7x10^{13}$	$1.0x10^{-4}$	$3.0x10^{-5}$
26 July 2019	$1.2x10^{17}$	$2.9x10^{13}$	$1.5x10^{-4}$	$4.2x10^{-5}$
27 Sept 2019	$7.8x10^{16}$	$2.9x10^{13}$	$1.3x10^{-4}$	$4.5x10^{-5}$
6 Dec 2019	$1.2x10^{17}$	$2.4x10^{13}$	$1.0x10^{-4}$	$3.2x10^{-5}$
11 Dec 2019	$1.4x10^{17}$	$2.6x10^{13}$	$1.4x10^{-4}$	$4.5x10^{-5}$

Soputan, Indonesia

Type: arc
longitude: 124.73° E
latitude: 1.11° N
Events: 1
$BrO > 2\sigma$: 1
BrO/SO_2: $2.2x10^{-4}$
std. dev.: $NaNx10^{-Inf}$
mean SO_2: $1.2x10^{17}$
mean BrO: $2.6x10^{13}$



3 Oct 2018	$1.2x10^{17}$	$2.6x10^{13}$	$2.2x10^{-4}$	$3.2x10^{-5}$

Lewotolok, Indonesia

Type: arc
longitude: 123.50° E
latitude: 8.27° S
Events: 2
$BrO > 2\sigma$: 1
BrO/SO_2: $5.0x10^{-5}$
std. dev.: $3.1x10^{-5}$
mean SO_2: $1.5x10^{17}$
mean BrO: $3.1x10^{13}$



1 Dec 2020	$2.0x10^{17}$	$4.2x10^{13}$	$5.3x10^{-5}$	$3.4x10^{-6}$
23 Mar 2021	$9.5x10^{16}$	$2.0x10^{13}$	$5.8x10^{-6}$	$5.4x10^{-5}$

Agung, Indonesia

Type: arc
longitude: 116.01° E
latitude: 8.34° S
Events: 5
$BrO > 2\sigma$: 3
BrO/SO_2: $1.4x10^{-4}$
std. dev.: $4.3x10^{-5}$
mean SO_2: $2.4x10^{17}$
mean BrO: $4.9x10^{13}$



28 June 2018	$6.2x10^{17}$	$8.7x10^{13}$	$1.5x10^{-4}$	$8.9x10^{-6}$
4 July 2018	$2.3x10^{17}$	$4.7x10^{13}$	$9.6x10^{-5}$	$2.5x10^{-5}$
9 July 2018	$7.9x10^{16}$	$2.6x10^{13}$	$1.2x10^{-4}$	$3.7x10^{-5}$
15 July 2018	$1.8x10^{17}$	$6.5x10^{13}$	$2.1x10^{-4}$	$3.2x10^{-5}$
30 July 2018	$7.8x10^{16}$	$1.9x10^{13}$	$1.0x10^{-4}$	$6.5x10^{-5}$

Raung, Indonesia

date	SO_2 VCD max. [molecules cm^{-2}]	BrO VCD	BrO/SO_2 fitted	BrO/SO_2 error

Raung, Indonesia

Type: arc
longitude: 114.05° E
latitude: 8.12° S
Events: 17
$BrO > 2\sigma$: 4
BrO/SO_2: $1.0x10^{-4}$
std. dev.: $4.9x10^{-5}$
mean SO_2: $1.2x10^{17}$
mean BrO: $3.1x10^{13}$



31 May 2019	$1.3x10^{17}$	$1.7x10^{13}$	$6.5x10^{-5}$	$4.8x10^{-5}$
1 July 2019	$1.1x10^{17}$	$2.1x10^{13}$	$1.4x10^{-5}$	$7.3x10^{-5}$
25 July 2020	$1.1x10^{17}$	$4.1x10^{13}$	$1.7x10^{-5}$	$1.2x10^{-4}$
7 Feb 2021	$1.3x10^{17}$	$4.8x10^{13}$	$1.6x10^{-4}$	$2.2x10^{-5}$
11 Feb 2021	$7.1x10^{16}$	$2.2x10^{13}$	$1.4x10^{-4}$	$2.1x10^{-5}$
12 Feb 2021	$7.5x10^{16}$	$2.5x10^{13}$	$1.4x10^{-4}$	$2.2x10^{-5}$
3 May 2021	$9.3x10^{16}$	$3.3x10^{13}$	$1.1x10^{-4}$	$4.9x10^{-5}$
9 May 2021	$1.5x10^{17}$	$3.2x10^{13}$	$5.6x10^{-5}$	$3.9x10^{-5}$
24 May 2021	$1.0x10^{17}$	$2.8x10^{13}$	$5.8x10^{-5}$	$4.2x10^{-5}$
25 May 2021	$8.3x10^{16}$	$2.9x10^{13}$	$9.7x10^{-5}$	$3.9x10^{-5}$
28 Aug 2021	$1.2x10^{17}$	$4.3x10^{13}$	$1.5x10^{-4}$	$4.8x10^{-5}$
29 Aug 2021	$9.0x10^{16}$	$2.7x10^{13}$	$9.1x10^{-5}$	$4.0x10^{-5}$
9 Sept 2021	$1.4x10^{17}$	$3.4x10^{13}$	$6.5x10^{-5}$	$5.1x10^{-5}$
25 Sept 2021	$1.2x10^{17}$	$3.6x10^{13}$	$1.4x10^{-4}$	$3.7x10^{-5}$
6 Oct 2021	$1.6x10^{17}$	$3.4x10^{13}$	$8.4x10^{-5}$	$2.4x10^{-5}$
10 Oct 2021	$1.1x10^{17}$	$3.3x10^{13}$	$1.5x10^{-4}$	$5.4x10^{-5}$
11 Oct 2021	$1.4x10^{17}$	$2.8x10^{13}$	$7.5x10^{-5}$	$3.8x10^{-5}$

Semeru, Indonesia

Type: arc
longitude: 112.92° E
latitude: 8.11° S
Events: 13
$BrO > 2\sigma$: 3
BrO/SO_2: $1.2x10^{-4}$
std. dev.: $4.3x10^{-5}$
mean SO_2: $9.9x10^{16}$
mean BrO: $3.0x10^{13}$



7 Feb 2019	$1.1x10^{17}$	$2.1x10^{13}$	$1.5x10^{-4}$	$4.5x10^{-5}$
27 Mar 2019	$7.8x10^{16}$	$2.6x10^{13}$	$1.5x10^{-4}$	$5.0x10^{-5}$
1 April 2019	$1.4x10^{17}$	$2.4x10^{13}$	$2.0x10^{-5}$	$4.0x10^{-5}$
18 Mar 2020	$7.0x10^{16}$	$2.7x10^{13}$	$9.5x10^{-5}$	$4.2x10^{-5}$
24 Mar 2020	$8.6x10^{16}$	$3.2x10^{13}$	$1.1x10^{-4}$	$5.9x10^{-5}$
9 April 2020	$7.7x10^{16}$	$2.8x10^{13}$	$1.7x10^{-4}$	$6.7x10^{-5}$
26 Mar 2021	$7.6x10^{16}$	$2.6x10^{13}$	$6.5x10^{-5}$	$4.9x10^{-5}$
7 Aug 2021	$1.2x10^{17}$	$4.0x10^{13}$	$1.5x10^{-4}$	$4.8x10^{-5}$
15 Oct 2021	$6.8x10^{16}$	$2.9x10^{13}$	$7.1x10^{-5}$	$3.4x10^{-5}$
7 Dec 2021	$1.0x10^{17}$	$3.5x10^{13}$	$1.4x10^{-4}$	$3.1x10^{-5}$
8 Dec 2021	$1.6x10^{17}$	$4.6x10^{13}$	$1.6x10^{-4}$	$4.1x10^{-5}$
9 Dec 2021	$9.1x10^{16}$	$2.6x10^{13}$	$9.9x10^{-5}$	$5.2x10^{-5}$
12 Dec 2021	$1.0x10^{17}$	$3.2x10^{13}$	$1.6x10^{-4}$	$3.5x10^{-5}$

Anak Krakatau, Indonesia

Type: arc
longitude: 105.42° E
latitude: 6.10° S
Events: 19
$BrO > 2\sigma$: 6
BrO/SO_2: $3.4x10^{-5}$
std. dev.: $6.8x10^{-5}$
mean SO_2: $2.4x10^{17}$
mean BrO: $2.9x10^{13}$



12 July 2018	$8.7x10^{16}$	$2.8x10^{13}$	$1.6x10^{-4}$	$3.6x10^{-5}$
13 July 2018	$1.0x10^{17}$	$2.6x10^{13}$	$9.4x10^{-5}$	$2.2x10^{-5}$
4 Aug 2018	$7.9x10^{16}$	$2.6x10^{13}$	$1.7x10^{-4}$	$3.8x10^{-5}$
8 Sept 2018	$5.5x10^{17}$	$8.3x10^{13}$	$1.2x10^{-4}$	$7.3x10^{-6}$
18 Nov 2018	$3.3x10^{17}$	$4.3x10^{13}$	$1.4x10^{-4}$	$1.1x10^{-5}$
25 Dec 2018	$4.3x10^{17}$	$2.3x10^{13}$	$5.7x10^{-6}$	$2.7x10^{-6}$
26 Dec 2018	$7.9x10^{17}$	$2.1x10^{13}$	$2.5x10^{-6}$	$1.9x10^{-6}$
27 Dec 2018	$2.4x10^{17}$	$2.6x10^{13}$	$6.4x10^{-7}$	$2.3x10^{-6}$

Anak Krakatau, Indonesia

date	SO_2 VCD max. [molecules cm^{-2}]	BrO VCD	BrO/SO_2 fitted	BrO/SO_2 error
28 Dec 2018	$1.9x10^{17}$	$2.8x10^{13}$	$2.1x10^{-5}$	$3.2x10^{-6}$
3 Jan 2019	$3.0x10^{17}$	$1.7x10^{13}$	$1.5x10^{-5}$	$7.2x10^{-6}$
4 Jan 2019	$3.6x10^{17}$	$2.3x10^{13}$	$1.3x10^{-5}$	$6.3x10^{-6}$
6 Jan 2019	$9.6x10^{16}$	$2.2x10^{13}$	$4.4x10^{-5}$	$1.1x10^{-5}$
29 Dec 2019	$1.2x10^{17}$	$2.4x10^{13}$	$5.2x10^{-5}$	$2.5x10^{-5}$
20 April 2021	$7.6x10^{16}$	$2.3x10^{13}$	$1.1x10^{-4}$	$3.6x10^{-5}$
18 June 2021	$2.2x10^{17}$	$4.1x10^{13}$	$1.5x10^{-4}$	$2.4x10^{-5}$
29 June 2021	$9.5x10^{16}$	$2.5x10^{13}$	$1.7x10^{-4}$	$4.7x10^{-5}$
20 July 2021	$9.1x10^{16}$	$2.1x10^{13}$	$1.2x10^{-4}$	$4.0x10^{-5}$
31 July 2021	$1.1x10^{17}$	$3.1x10^{13}$	$2.2x10^{-4}$	$4.7x10^{-5}$
1 Aug 2021	$2.3x10^{17}$	$2.6x10^{13}$	$1.2x10^{-4}$	$2.4x10^{-5}$

Kerinci, Indonesia

Type: arc
longitude: 101.26° E
latitude: 1.70° S
Events: 5
$BrO > 2\sigma$: 2
BrO/SO_2: $6.3x10^{-5}$
std. dev.: $7.2x10^{-5}$
mean SO_2: $1.4x10^{17}$
mean BrO: $2.6x10^{13}$



26 Oct 2018	$1.7x10^{17}$	$2.3x10^{13}$	$1.1x10^{-4}$	$1.7x10^{-5}$
10 July 2019	$1.1x10^{17}$	$2.6x10^{13}$	$1.9x10^{-4}$	$3.5x10^{-5}$
16 Dec 2019	$1.0x10^{17}$	$3.1x10^{13}$	$2.8x10^{-5}$	$5.3x10^{-5}$
13 April 2020	$6.5x10^{16}$	$3.1x10^{13}$	$1.6x10^{-6}$	$1.6x10^{-5}$
1 May 2021	$2.8x10^{17}$	$2.1x10^{13}$	$3.3x10^{-6}$	$4.6x10^{-5}$

Sinabung, Indonesia

Type: arc
longitude: 98.39° E
latitude: 3.17° N
Events: 20
$BrO > 2\sigma$: 3
BrO/SO_2: $2.2x10^{-5}$
std. dev.: $3.3x10^{-5}$
mean SO_2: $2.3x10^{17}$
mean BrO: $2.5x10^{13}$



7 Feb 2018	$1.0x10^{17}$	$3.0x10^{13}$	$7.8x10^{-5}$	$2.7x10^{-5}$
19 Feb 2018	$1.6x10^{18}$	$2.6x10^{13}$	$6.3x10^{-6}$	$1.2x10^{-6}$
22 Feb 2018	$7.4x10^{16}$	$2.0x10^{13}$	$5.2x10^{-5}$	$4.3x10^{-5}$
7 April 2018	$1.7x10^{17}$	$3.2x10^{13}$	$3.6x10^{-5}$	$9.2x10^{-6}$
7 May 2019	$1.0x10^{17}$	$2.0x10^{13}$	$6.4x10^{-5}$	$2.5x10^{-5}$
27 May 2019	$9.3x10^{16}$	$1.4x10^{13}$	$1.3x10^{-6}$	$3.4x10^{-5}$
10 Aug 2020	$2.1x10^{17}$	$2.0x10^{13}$	$2.6x10^{-5}$	$1.3x10^{-5}$
17 Aug 2020	$1.6x10^{17}$	$3.2x10^{13}$	$1.5x10^{-5}$	$1.7x10^{-5}$
18 Aug 2020	$2.2x10^{17}$	$3.8x10^{13}$	$4.6x10^{-5}$	$1.3x10^{-5}$
19 Aug 2020	$1.6x10^{17}$	$2.1x10^{13}$	$4.4x10^{-5}$	$2.9x10^{-5}$
22 Aug 2020	$1.3x10^{17}$	$1.7x10^{13}$	$9.8x10^{-5}$	$2.7x10^{-5}$
23 Aug 2020	$2.0x10^{17}$	$2.8x10^{13}$	$5.4x10^{-5}$	$2.0x10^{-5}$
27 Aug 2020	$8.0x10^{16}$	$2.3x10^{13}$	$5.7x10^{-5}$	$2.7x10^{-5}$
28 Aug 2020	$1.5x10^{17}$	$2.7x10^{13}$	$8.5x10^{-5}$	$2.5x10^{-5}$
29 Aug 2020	$9.5x10^{16}$	$3.1x10^{13}$	$3.7x10^{-6}$	$2.9x10^{-5}$
3 Sept 2020	$8.4x10^{16}$	$2.4x10^{13}$	$2.7x10^{-5}$	$3.8x10^{-5}$
8 Sept 2020	$9.2x10^{16}$	$3.2x10^{13}$	$1.7x10^{-5}$	$3.7x10^{-5}$
23 Dec 2020	$9.4x10^{16}$	$2.0x10^{13}$	$1.2x10^{-4}$	$5.5x10^{-5}$
2 Mar 2021	$6.0x10^{17}$	$2.7x10^{13}$	$2.5x10^{-6}$	$4.3x10^{-6}$
28 July 2021	$1.2x10^{17}$	$8.0x10^{12}$	$9.3x10^{-6}$	$3.0x10^{-5}$

Mayon, Philippines

Type: arc
longitude: 123.69° E
latitude: 13.26° N
Events: 15
$BrO > 2\sigma$: 5
BrO/SO_2: $9.6x10^{-5}$
std. dev.: $5.3x10^{-5}$
mean SO_2: $1.4x10^{17}$
mean BrO: $4.2x10^{13}$



29 Jan 2018	$3.4x10^{17}$	$6.0x10^{13}$	$1.7x10^{-4}$	$1.5x10^{-5}$
2 Feb 2018	$2.6x10^{17}$	$5.7x10^{13}$	$1.4x10^{-4}$	$1.4x10^{-5}$

Mayon, Philippines

date	SO_2 VCD max. [molecules cm^{-2}]	BrO VCD	BrO/SO_2 fitted	BrO/SO_2 error
7 Feb 2018	$1.9x10^{17}$	$5.8x10^{13}$	$1.5x10^{-4}$	$2.1x10^{-5}$
28 Feb 2018	$9.0x10^{16}$	$2.5x10^{13}$	$6.9x10^{-5}$	$4.2x10^{-5}$
10 Mar 2018	$1.2x10^{17}$	$3.2x10^{13}$	$1.6x10^{-4}$	$2.7x10^{-5}$
16 Mar 2018	$1.7x10^{17}$	$2.5x10^{13}$	$1.9x10^{-5}$	$2.6x10^{-5}$
22 Mar 2018	$1.2x10^{17}$	$2.7x10^{13}$	$6.9x10^{-5}$	$4.4x10^{-5}$
18 April 2018	$6.5x10^{16}$	$2.7x10^{13}$	$8.7x10^{-5}$	$3.4x10^{-5}$
19 April 2018	$7.7x10^{16}$	$2.1x10^{13}$	$3.8x10^{-5}$	$4.3x10^{-5}$
25 May 2018	$9.0x10^{16}$	$2.5x10^{13}$	$1.8x10^{-5}$	$4.1x10^{-5}$
29 Aug 2018	$1.2x10^{17}$	$2.8x10^{13}$	$5.4x10^{-5}$	$4.0x10^{-5}$
9 Sept 2018	$1.2x10^{17}$	$1.8x10^{14}$	$1.5x10^{-4}$	$1.5x10^{-4}$
10 Oct 2018	$1.0x10^{17}$	$2.5x10^{13}$	$4.6x10^{-5}$	$3.3x10^{-5}$
23 May 2019	$1.1x10^{17}$	$2.1x10^{13}$	$4.1x10^{-5}$	$3.5x10^{-5}$
23 Sept 2019	$1.3x10^{17}$	$2.3x10^{13}$	$3.7x10^{-5}$	$5.6x10^{-5}$

Taal, Philippines

Type: arc
longitude: 120.99° E
latitude: 14.00° N
Events: 57
$BrO > 2\sigma$: 8
BrO/SO_2: $6.4x10^{-5}$
std. dev.: $3.5x10^{-5}$
mean SO_2: $1.2x10^{17}$
mean BrO: $2.6x10^{13}$



25 April 2021	$8.8x10^{16}$	$2.8x10^{13}$	$1.6x10^{-4}$	$4.8x10^{-5}$
27 May 2021	$7.1x10^{16}$	$3.6x10^{13}$	$7.9x10^{-5}$	$5.4x10^{-5}$
12 June 2021	$7.5x10^{16}$	$3.2x10^{13}$	$1.6x10^{-4}$	$5.1x10^{-5}$
13 June 2021	$1.3x10^{17}$	$3.4x10^{13}$	$1.0x10^{-4}$	$6.4x10^{-5}$
17 June 2021	$1.2x10^{17}$	$3.5x10^{13}$	$1.4x10^{-4}$	$2.6x10^{-5}$
18 June 2021	$8.9x10^{16}$	$2.6x10^{13}$	$4.3x10^{-5}$	$3.4x10^{-5}$
22 June 2021	$7.6x10^{16}$	$1.8x10^{13}$	$4.7x10^{-5}$	$3.9x10^{-5}$
23 June 2021	$9.7x10^{16}$	$1.7x10^{13}$	$8.5x10^{-5}$	$3.8x10^{-5}$
27 June 2021	$1.1x10^{17}$	$3.8x10^{13}$	$5.8x10^{-5}$	$1.2x10^{-5}$
28 June 2021	$2.4x10^{17}$	$3.8x10^{13}$	$7.6x10^{-5}$	$9.6x10^{-6}$
30 June 2021	$1.5x10^{17}$	$2.5x10^{13}$	$9.0x10^{-5}$	$1.5x10^{-5}$
1 July 2021	$1.8x10^{17}$	$1.5x10^{13}$	$4.2x10^{-5}$	$1.9x10^{-5}$
3 July 2021	$9.6x10^{16}$	$1.4x10^{13}$	$2.6x10^{-5}$	$1.1x10^{-5}$
4 July 2021	$1.6x10^{17}$	$2.3x10^{13}$	$2.7x10^{-5}$	$4.3x10^{-5}$
5 July 2021	$1.0x10^{17}$	$1.8x10^{13}$	$7.4x10^{-5}$	$3.2x10^{-5}$
7 July 2021	$7.7x10^{16}$	$2.4x10^{13}$	$5.9x10^{-5}$	$4.3x10^{-5}$
8 July 2021	$6.7x10^{16}$	$2.8x10^{13}$	$3.9x10^{-5}$	$6.0x10^{-5}$
14 July 2021	$1.3x10^{17}$	$3.2x10^{13}$	$6.8x10^{-5}$	$3.9x10^{-5}$
11 Aug 2021	$6.8x10^{16}$	$2.2x10^{13}$	$7.5x10^{-5}$	$4.1x10^{-5}$
14 Aug 2021	$2.2x10^{17}$	$3.3x10^{13}$	$4.6x10^{-5}$	$8.8x10^{-6}$
15 Aug 2021	$1.2x10^{17}$	$3.9x10^{13}$	$1.1x10^{-4}$	$2.4x10^{-5}$
16 Aug 2021	$1.9x10^{17}$	$2.9x10^{13}$	$4.3x10^{-5}$	$2.0x10^{-5}$
21 Aug 2021	$1.9x10^{17}$	$4.1x10^{13}$	$2.5x10^{-5}$	$2.1x10^{-5}$
22 Aug 2021	$1.2x10^{17}$	$2.3x10^{13}$	$3.6x10^{-5}$	$2.5x10^{-5}$
25 Aug 2021	$1.9x10^{17}$	$2.3x10^{13}$	$4.9x10^{-5}$	$1.4x10^{-5}$
30 Aug 2021	$1.7x10^{17}$	$2.1x10^{13}$	$6.3x10^{-5}$	$3.0x10^{-5}$
1 Sept 2021	$8.3x10^{16}$	$2.3x10^{13}$	$2.4x10^{-5}$	$2.4x10^{-5}$
2 Sept 2021	$1.1x10^{17}$	$2.1x10^{13}$	$7.0x10^{-5}$	$3.3x10^{-5}$
4 Sept 2021	$1.3x10^{17}$	$1.3x10^{13}$	$3.6x10^{-5}$	$2.6x10^{-5}$
5 Sept 2021	$1.9x10^{17}$	$2.8x10^{13}$	$7.1x10^{-5}$	$2.7x10^{-5}$
10 Sept 2021	$6.2x10^{16}$	$1.8x10^{13}$	$1.5x10^{-4}$	$2.8x10^{-5}$
14 Sept 2021	$9.4x10^{16}$	$1.8x10^{13}$	$6.8x10^{-5}$	$2.5x10^{-5}$
16 Sept 2021	$8.7x10^{16}$	$2.9x10^{13}$	$7.3x10^{-5}$	$2.6x10^{-5}$
17 Sept 2021	$1.4x10^{17}$	$2.7x10^{13}$	$6.5x10^{-5}$	$4.5x10^{-5}$
21 Sept 2021	$2.1x10^{17}$	$3.3x10^{13}$	$2.8x10^{-5}$	$1.9x10^{-5}$
22 Sept 2021	$7.5x10^{16}$	$2.2x10^{13}$	$7.5x10^{-5}$	$3.2x10^{-5}$
23 Sept 2021	$7.6x10^{16}$	$1.3x10^{13}$	$1.3x10^{-5}$	$3.9x10^{-5}$
26 Sept 2021	$1.0x10^{17}$	$1.8x10^{13}$	$2.7x10^{-5}$	$2.6x10^{-5}$
28 Sept 2021	$2.0x10^{17}$	$2.8x10^{13}$	$1.0x10^{-4}$	$1.2x10^{-5}$
29 Sept 2021	$6.3x10^{16}$	$3.4x10^{13}$	$7.0x10^{-5}$	$4.3x10^{-5}$
1 Oct 2021	$1.1x10^{17}$	$2.1x10^{13}$	$2.9x10^{-5}$	$2.8x10^{-5}$
2 Oct 2021	$2.0x10^{17}$	$3.6x10^{13}$	$2.9x10^{-5}$	$1.1x10^{-5}$
3 Oct 2021	$9.0x10^{16}$	$2.3x10^{13}$	$4.6x10^{-5}$	$5.7x10^{-5}$
8 Oct 2021	$9.3x10^{16}$	$2.2x10^{13}$	$7.7x10^{-5}$	$2.8x10^{-5}$
13 Oct 2021	$6.5x10^{16}$	$2.6x10^{13}$	$1.6x10^{-4}$	$6.7x10^{-5}$
16 Oct 2021	$8.9x10^{16}$	$1.6x10^{13}$	$5.9x10^{-5}$	$2.1x10^{-5}$
17 Oct 2021	$7.7x10^{16}$	$2.1x10^{13}$	$6.1x10^{-5}$	$2.0x10^{-5}$

Taal, Philippines

date	SO_2 VCD max. [molecules cm^{-2}]	BrO VCD	BrO/SO_2 fitted	BrO/SO_2 error
19 Oct 2021	$1.2x10^{17}$	$3.5x10^{13}$	$6.9x10^{-5}$	$2.0x10^{-5}$
22 Oct 2021	$7.6x10^{16}$	$1.8x10^{13}$	$8.0x10^{-5}$	$4.2x10^{-5}$
8 Nov 2021	$8.3x10^{16}$	$2.6x10^{13}$	$9.3x10^{-5}$	$5.3x10^{-5}$
13 Nov 2021	$9.0x10^{16}$	$2.3x10^{13}$	$7.5x10^{-5}$	$4.5x10^{-5}$
14 Nov 2021	$1.9x10^{17}$	$2.9x10^{13}$	$6.0x10^{-5}$	$1.7x10^{-5}$
15 Nov 2021	$9.2x10^{16}$	$2.5x10^{13}$	$6.8x10^{-5}$	$3.9x10^{-5}$
19 Nov 2021	$1.0x10^{17}$	$2.7x10^{13}$	$9.1x10^{-5}$	$2.0x10^{-5}$
30 Nov 2021	$7.6x10^{16}$	$2.3x10^{13}$	$9.6x10^{-5}$	$5.2x10^{-5}$
20 Dec 2021	$9.1x10^{16}$	$3.2x10^{13}$	$5.9x10^{-5}$	$4.4x10^{-5}$
21 Dec 2021	$8.3x10^{16}$	$2.3x10^{13}$	$5.9x10^{-5}$	$3.1x10^{-5}$

Nishinoshima, Japan

Type: arc
longitude: 140.87° E
latitude: 27.25° N
Events: 37
$BrO > 2\sigma$: 19
BrO/SO_2: $5.4x10^{-5}$
std. dev.: $4.0x10^{-5}$
mean SO_2: $3.6x10^{17}$
mean BrO: $3.7x10^{13}$



30 May 2020	$9.8x10^{16}$	$4.0x10^{13}$	$2.0x10^{-4}$	$2.2x10^{-5}$
8 June 2020	$9.3x10^{16}$	$4.1x10^{13}$	$1.7x10^{-4}$	$4.0x10^{-5}$
12 June 2020	$6.2x10^{16}$	$2.1x10^{13}$	$1.6x10^{-4}$	$2.8x10^{-5}$
19 June 2020	$1.6x10^{17}$	$3.7x10^{13}$	$8.5x10^{-5}$	$7.3x10^{-6}$
20 June 2020	$1.5x10^{17}$	$3.0x10^{13}$	$8.3x10^{-5}$	$8.0x10^{-6}$
26 June 2020	$6.5x10^{17}$	$5.1x10^{13}$	$7.4x10^{-5}$	$1.9x10^{-6}$
27 June 2020	$4.0x10^{17}$	$4.6x10^{13}$	$8.6x10^{-5}$	$2.0x10^{-6}$
29 June 2020	$1.6x10^{17}$	$1.9x10^{13}$	$7.2x10^{-5}$	$1.1x10^{-5}$
30 June 2020	$8.8x10^{17}$	$9.2x10^{13}$	$6.6x10^{-5}$	$1.6x10^{-6}$
2 July 2020	$4.4x10^{17}$	$5.6x10^{13}$	$8.8x10^{-5}$	$1.8x10^{-6}$
3 July 2020	$2.8x10^{17}$	$3.5x10^{13}$	$8.7x10^{-5}$	$2.2x10^{-6}$
12 July 2020	$7.1x10^{17}$	$4.0x10^{13}$	$6.6x10^{-5}$	$1.8x10^{-6}$
14 July 2020	$4.1x10^{17}$	$5.1x10^{13}$	$7.6x10^{-5}$	$1.6x10^{-6}$
15 July 2020	$1.7x10^{18}$	$1.2x10^{14}$	$6.2x10^{-5}$	$1.1x10^{-6}$
19 July 2020	$1.1x10^{18}$	$5.1x10^{13}$	$5.8x10^{-5}$	$2.1x10^{-6}$
20 July 2020	$3.7x10^{17}$	$3.0x10^{13}$	$1.3x10^{-5}$	$2.2x10^{-6}$
21 July 2020	$1.3x10^{18}$	$3.1x10^{13}$	$1.1x10^{-5}$	$1.3x10^{-6}$
23 July 2020	$2.9x10^{17}$	$3.8x10^{13}$	$4.2x10^{-5}$	$2.6x10^{-6}$
25 July 2020	$3.4x10^{17}$	$3.0x10^{13}$	$3.8x10^{-5}$	$1.9x10^{-6}$
27 July 2020	$3.0x10^{17}$	$3.2x10^{13}$	$4.6x10^{-5}$	$2.3x10^{-6}$
28 July 2020	$2.0x10^{17}$	$3.2x10^{13}$	$5.5x10^{-5}$	$2.9x10^{-6}$
30 July 2020	$4.5x10^{17}$	$3.5x10^{13}$	$4.8x10^{-5}$	$2.2x10^{-6}$
8 Aug 2020	$3.4x10^{17}$	$3.9x10^{13}$	$2.6x10^{-5}$	$1.3x10^{-6}$
9 Aug 2020	$2.3x10^{17}$	$3.3x10^{13}$	$3.1x10^{-5}$	$2.0x10^{-6}$
10 Aug 2020	$1.2x10^{17}$	$2.8x10^{13}$	$4.5x10^{-5}$	$2.5x10^{-6}$
13 Aug 2020	$1.7x10^{17}$	$2.5x10^{13}$	$6.8x10^{-5}$	$1.1x10^{-5}$
15 Aug 2020	$8.9x10^{16}$	$2.1x10^{13}$	$5.0x10^{-5}$	$1.2x10^{-5}$
16 Aug 2020	$3.0x10^{17}$	$3.9x10^{13}$	$3.6x10^{-5}$	$6.0x10^{-6}$
17 Aug 2020	$2.0x10^{17}$	$2.7x10^{13}$	$5.0x10^{-5}$	$9.2x10^{-6}$
18 Aug 2020	$1.9x10^{17}$	$2.6x10^{13}$	$3.7x10^{-5}$	$9.4x10^{-6}$
19 Aug 2020	$1.6x10^{17}$	$1.5x10^{13}$	$2.6x10^{-5}$	$1.9x10^{-5}$
21 Aug 2020	$1.5x10^{17}$	$2.1x10^{13}$	$4.2x10^{-5}$	$2.2x10^{-5}$
22 Aug 2020	$2.4x10^{17}$	$3.3x10^{13}$	$3.0x10^{-5}$	$1.4x10^{-5}$
23 Aug 2020	$1.1x10^{17}$	$2.1x10^{13}$	$5.0x10^{-5}$	$2.1x10^{-5}$
24 Aug 2020	$7.4x10^{16}$	$2.4x10^{13}$	$4.6x10^{-5}$	$4.1x10^{-5}$
28 Aug 2020	$1.0x10^{17}$	$3.0x10^{13}$	$6.3x10^{-5}$	$2.1x10^{-5}$
18 Oct 2021	$1.4x10^{17}$	$2.5x10^{13}$	$6.1x10^{-5}$	$2.9x10^{-5}$

Raikoke, Russia

Type: arc
longitude: 153.24° E
latitude: 48.29° N
Events: 1
$BrO > 2\sigma$: 1
BrO/SO_2: $4.6x10^{-5}$
std. dev.: N/A
mean SO_2: $2.0x10^{17}$
mean BrO: $2.8x10^{13}$



10 July 2019	$2.0x10^{17}$	$2.8x10^{13}$	$4.6x10^{-5}$	$1.7x10^{-6}$

Lemonosov, Russia

date	SO_2 VCD max. [molecules cm^{-2}]	BrO VCD	BrO/SO_2 fitted	BrO/SO_2 error

Lemonosov, Russia

Type: arc
longitude: 155.43° E
latitude: 50.25° N
Events: 24
$BrO > 2\sigma$: 4
BrO/SO_2: $4.5x10^{-5}$
std. dev.: $4.9x10^{-5}$
mean SO_2: $1.5x10^{17}$
mean BrO: $2.2x10^{13}$



18 June 2018	$1.1x10^{17}$	$1.1x10^{13}$	$0.8x10^{-5}$	$3.5x10^{-5}$
16 Aug 2018	$9.8x10^{16}$	$2.3x10^{13}$	$9.3x10^{-6}$	$3.3x10^{-5}$
26 Aug 2018	$1.2x10^{17}$	$1.7x10^{13}$	$7.0x10^{-6}$	$2.0x10^{-5}$
3 Sept 2018	$3.4x10^{17}$	$1.1x10^{13}$	$7.1x10^{-6}$	$1.9x10^{-5}$
8 June 2019	$6.5x10^{16}$	$1.2x10^{13}$	$1.4x10^{-5}$	$3.2x10^{-5}$
12 June 2019	$1.3x10^{17}$	$2.7x10^{13}$	$3.8x10^{-5}$	$7.4x10^{-5}$
23 Aug 2019	$1.4x10^{17}$	$1.6x10^{13}$	$2.5x10^{-5}$	$3.8x10^{-5}$
26 Aug 2019	$1.6x10^{17}$	$1.3x10^{13}$	$2.6x10^{-5}$	$3.8x10^{-5}$
30 Mar 2020	$8.4x10^{16}$	$2.4x10^{13}$	$0.7x10^{-6}$	$2.3x10^{-5}$
10 April 2020	$2.1x10^{17}$	$3.1x10^{13}$	$8.2x10^{-5}$	$1.3x10^{-5}$
14 April 2020	$8.1x10^{16}$	$3.0x10^{13}$	$1.1x10^{-4}$	$2.0x10^{-5}$
17 April 2020	$2.2x10^{17}$	$5.3x10^{13}$	$1.8x10^{-4}$	$1.5x10^{-5}$
13 May 2020	$1.4x10^{17}$	$2.7x10^{13}$	$6.2x10^{-5}$	$2.3x10^{-5}$
26 May 2020	$6.7x10^{16}$	$1.4x10^{13}$	$3.8x10^{-6}$	$3.3x10^{-5}$
21 July 2020	$1.7x10^{17}$	$2.2x10^{13}$	$4.4x10^{-5}$	$3.0x10^{-5}$
1 July 2021	$1.1x10^{17}$	$1.4x10^{13}$	$3.8x10^{-6}$	$2.5x10^{-5}$
7 July 2021	$6.7x10^{16}$	$1.8x10^{13}$	$2.0x10^{-5}$	$5.2x10^{-5}$
21 July 2021	$6.4x10^{16}$	$9.8x10^{12}$	$0.8x10^{-5}$	$3.2x10^{-5}$
16 Aug 2021	$1.0x10^{17}$	$2.9x10^{13}$	$1.6x10^{-4}$	$2.4x10^{-5}$
17 Aug 2021	$2.1x10^{17}$	$1.8x10^{13}$	$7.8x10^{-5}$	$3.2x10^{-5}$
20 Aug 2021	$1.2x10^{17}$	$2.2x10^{13}$	$3.6x10^{-5}$	$1.5x10^{-5}$
23 Aug 2021	$4.8x10^{17}$	$3.1x10^{13}$	$3.7x10^{-5}$	$5.9x10^{-6}$
24 Aug 2021	$1.4x10^{17}$	$2.0x10^{13}$	$1.7x10^{-5}$	$8.6x10^{-6}$
25 Aug 2021	$8.6x10^{16}$	$3.0x10^{13}$	$4.4x10^{-5}$	$1.8x10^{-5}$

South Kamchatka, Russia

Type: arc
longitude: 158.27° E
latitude: 52.49° N
Events: 47
$BrO > 2\sigma$: 5
BrO/SO_2: $3.5x10^{-5}$
std. dev.: $4.2x10^{-5}$
mean SO_2: $1.5x10^{17}$
mean BrO: $2.0x10^{13}$



25 Mar 2018	$1.8x10^{17}$	$1.5x10^{13}$	$4.7x10^{-5}$	$2.8x10^{-5}$
26 Mar 2018	$1.8x10^{17}$	$2.3x10^{13}$	$6.7x10^{-5}$	$2.2x10^{-5}$
27 Mar 2018	$1.6x10^{17}$	$1.2x10^{13}$	$8.0x10^{-6}$	$5.3x10^{-5}$
5 April 2018	$1.1x10^{17}$	$2.1x10^{13}$	$6.5x10^{-5}$	$3.0x10^{-5}$
22 April 2018	$1.2x10^{17}$	$2.4x10^{13}$	$8.8x10^{-5}$	$1.4x10^{-5}$
7 May 2018	$1.2x10^{17}$	$1.2x10^{13}$	$1.7x10^{-5}$	$6.3x10^{-5}$
24 May 2018	$2.9x10^{17}$	$3.9x10^{13}$	$5.8x10^{-5}$	$2.1x10^{-5}$
29 May 2018	$2.2x10^{17}$	$1.7x10^{13}$	$1.3x10^{-5}$	$4.9x10^{-5}$
19 June 2018	$1.7x10^{17}$	$1.5x10^{13}$	$5.4x10^{-6}$	$1.6x10^{-5}$
20 June 2018	$2.5x10^{17}$	$2.5x10^{13}$	$2.4x10^{-5}$	$2.2x10^{-5}$
21 June 2018	$1.3x10^{17}$	$3.1x10^{13}$	$2.3x10^{-5}$	$5.3x10^{-5}$
17 July 2018	$1.2x10^{17}$	$2.7x10^{13}$	$6.9x10^{-5}$	$3.5x10^{-5}$
5 Aug 2018	$1.1x10^{17}$	$1.3x10^{13}$	$3.5x10^{-5}$	$5.1x10^{-5}$
6 Aug 2018	$1.2x10^{17}$	$1.9x10^{13}$	$6.1x10^{-5}$	$3.0x10^{-5}$
7 Aug 2018	$1.0x10^{17}$	$2.9x10^{13}$	$3.7x10^{-5}$	$2.4x10^{-5}$
8 Aug 2018	$7.8x10^{16}$	$2.3x10^{13}$	$6.5x10^{-6}$	$1.7x10^{-5}$
23 Aug 2018	$2.6x10^{17}$	$2.2x10^{13}$	$3.4x10^{-5}$	$3.7x10^{-5}$
20 April 2019	$9.0x10^{16}$	$2.4x10^{13}$	$1.6x10^{-4}$	$4.9x10^{-5}$
16 Aug 2019	$9.6x10^{16}$	$3.3x10^{13}$	$8.4x10^{-5}$	$4.0x10^{-5}$
19 June 2020	$8.6x10^{16}$	$2.0x10^{13}$	$2.1x10^{-6}$	$3.7x10^{-5}$
5 Feb 2021	$7.1x10^{16}$	$2.4x10^{13}$	$0.7x10^{-4}$	$1.8x10^{-5}$
14 Feb 2021	$1.6x10^{17}$	$1.3x10^{13}$	$4.3x10^{-6}$	$2.9x10^{-5}$
15 Feb 2021	$1.1x10^{17}$	$1.7x10^{13}$	$3.6x10^{-5}$	$6.6x10^{-5}$
16 Feb 2021	$1.3x10^{17}$	$7.0x10^{12}$	$1.4x10^{-5}$	$3.9x10^{-5}$
25 Feb 2021	$2.1x10^{17}$	$2.2x10^{13}$	$9.8x10^{-5}$	$1.8x10^{-5}$

South Kamchatka, Russia

date	SO_2 VCD max. [molecules cm^{-2}]	BrO VCD	BrO/SO_2 fitted	BrO/SO_2 error
3 April 2021	$1.9x10^{17}$	$1.4x10^{13}$	$1.2x10^{-5}$	$4.2x10^{-5}$
6 April 2021	$1.6x10^{17}$	$2.1x10^{13}$	$3.7x10^{-5}$	$3.1x10^{-5}$
7 April 2021	$1.1x10^{17}$	$2.0x10^{13}$	$6.1x10^{-5}$	$6.8x10^{-5}$
10 April 2021	$1.4x10^{17}$	$1.3x10^{13}$	$2.9x10^{-5}$	$3.1x10^{-5}$
16 April 2021	$1.2x10^{17}$	$1.5x10^{13}$	$4.0x10^{-6}$	$6.3x10^{-5}$
23 April 2021	$8.7x10^{16}$	$1.9x10^{13}$	$1.0x10^{-6}$	$4.6x10^{-5}$
30 April 2021	$1.0x10^{17}$	$2.0x10^{13}$	$5.2x10^{-5}$	$3.8x10^{-5}$
6 May 2021	$2.4x10^{17}$	$1.8x10^{13}$	$3.7x10^{-5}$	$2.0x10^{-5}$
10 May 2021	$2.4x10^{17}$	$1.7x10^{13}$	$2.8x10^{-5}$	$2.3x10^{-5}$
11 May 2021	$1.3x10^{17}$	$1.8x10^{13}$	$5.3x10^{-5}$	$4.0x10^{-5}$
15 May 2021	$2.1x10^{17}$	$1.7x10^{13}$	$1.6x10^{-5}$	$3.3x10^{-5}$
29 May 2021	$8.7x10^{16}$	$1.1x10^{13}$	$5.8x10^{-5}$	$3.3x10^{-5}$
28 June 2021	$9.4x10^{16}$	$1.8x10^{13}$	$2.5x10^{-5}$	$6.4x10^{-5}$
29 June 2021	$6.6x10^{16}$	$2.0x10^{13}$	$2.2x10^{-5}$	$4.0x10^{-5}$
30 June 2021	$8.6x10^{16}$	$2.0x10^{13}$	$4.7x10^{-6}$	$5.0x10^{-5}$
8 July 2021	$9.3x10^{16}$	$2.4x10^{13}$	$2.9x10^{-5}$	$2.3x10^{-5}$
20 July 2021	$1.7x10^{17}$	$2.8x10^{13}$	$7.0x10^{-6}$	$1.6x10^{-5}$
23 July 2021	$1.1x10^{17}$	$2.5x10^{13}$	$3.8x10^{-5}$	$1.2x10^{-5}$
9 Aug 2021	$1.1x10^{17}$	$1.5x10^{13}$	$6.9x10^{-5}$	$5.2x10^{-5}$
31 Aug 2021	$3.1x10^{17}$	$2.8x10^{13}$	$6.8x10^{-5}$	$1.4x10^{-5}$
4 Sept 2021	$6.1x10^{16}$	$1.9x10^{13}$	$6.7x10^{-5}$	$2.5x10^{-5}$
5 Sept 2021	$3.1x10^{17}$	$2.8x10^{13}$	$6.6x10^{-5}$	$1.7x10^{-5}$

Karymsky, Russia

Type: arc
longitude: 159.45° E
latitude: 54.05° N
Events: 20
BrO > 2σ: 11
BrO/SO_2: $1.1x10^{-4}$
std. dev.: $6.9x10^{-5}$
mean SO_2: $1.4x10^{17}$
mean BrO: $2.9x10^{13}$



25 June 2018	$1.0x10^{17}$	$2.9x10^{13}$	$5.8x10^{-5}$	$7.1x10^{-5}$
15 July 2018	$1.5x10^{17}$	$2.5x10^{13}$	$1.4x10^{-4}$	$1.7x10^{-5}$
21 Feb 2019	$6.4x10^{16}$	$1.8x10^{13}$	$6.0x10^{-5}$	$6.8x10^{-5}$
22 April 2020	$8.3x10^{16}$	$4.2x10^{13}$	$2.3x10^{-4}$	$2.7x10^{-5}$
2 May 2020	$2.0x10^{17}$	$5.3x10^{13}$	$2.3x10^{-4}$	$2.9x10^{-5}$
25 May 2020	$2.2x10^{17}$	$3.4x10^{13}$	$1.5x10^{-4}$	$1.6x10^{-5}$
27 May 2020	$3.0x10^{17}$	$2.5x10^{13}$	$8.6x10^{-5}$	$1.9x10^{-5}$
16 July 2020	$8.9x10^{16}$	$2.9x10^{13}$	$1.1x10^{-4}$	$2.2x10^{-5}$
2 Nov 2020	$1.8x10^{17}$	$2.1x10^{13}$	$1.0x10^{-4}$	$2.9x10^{-5}$
8 June 2021	$9.2x10^{16}$	$1.6x10^{13}$	$8.4x10^{-5}$	$2.7x10^{-5}$
19 July 2021	$2.2x10^{17}$	$2.5x10^{13}$	$9.0x10^{-5}$	$1.2x10^{-5}$
25 July 2021	$9.7x10^{16}$	$2.8x10^{13}$	$8.8x10^{-5}$	$2.0x10^{-5}$
10 Aug 2021	$1.2x10^{17}$	$3.0x10^{13}$	$2.3x10^{-6}$	$3.4x10^{-5}$
15 Aug 2021	$7.3x10^{16}$	$2.9x10^{13}$	$7.5x10^{-5}$	$3.9x10^{-5}$
21 Aug 2021	$1.9x10^{17}$	$4.6x10^{13}$	$1.7x10^{-4}$	$3.6x10^{-5}$
22 Aug 2021	$8.9x10^{16}$	$2.3x10^{13}$	$6.3x10^{-5}$	$2.8x10^{-5}$
28 Aug 2021	$1.0x10^{17}$	$3.6x10^{13}$	$1.4x10^{-4}$	$1.7x10^{-5}$
1 Sept 2021	$1.8x10^{17}$	$2.2x10^{13}$	$6.8x10^{-5}$	$1.1x10^{-5}$
23 Sept 2021	$8.5x10^{16}$	$3.8x10^{13}$	$2.9x10^{-4}$	$5.0x10^{-5}$
26 Sept 2021	$1.1x10^{17}$	$2.1x10^{13}$	$6.2x10^{-5}$	$4.4x10^{-5}$

Bezymianny, Russia

Type: arc
longitude: 160.59° E
latitude: 55.98° N
Events: 37
BrO > 2σ: 18
BrO/SO_2: $1.1x10^{-4}$
std. dev.: $6.2x10^{-5}$
mean SO_2: $1.3x10^{17}$
mean BrO: $2.8x10^{13}$



18 Mar 2018	$2.1x10^{17}$	$2.2x10^{13}$	$7.4x10^{-5}$	$2.7x10^{-5}$
23 Mar 2018	$6.3x10^{16}$	$2.5x10^{13}$	$0.7x10^{-5}$	$5.6x10^{-5}$
7 April 2018	$2.1x10^{17}$	$2.9x10^{13}$	$9.3x10^{-5}$	$1.6x10^{-5}$
9 April 2018	$1.7x10^{17}$	$2.3x10^{13}$	$1.4x10^{-4}$	$1.8x10^{-5}$
14 April 2018	$6.1x10^{16}$	$2.0x10^{13}$	$1.3x10^{-5}$	$3.3x10^{-5}$
15 April 2018	$1.4x10^{17}$	$2.6x10^{13}$	$1.2x10^{-4}$	$1.5x10^{-5}$
24 April 2018	$1.4x10^{17}$	$2.4x10^{13}$	$1.4x10^{-4}$	$3.4x10^{-5}$

Bezymianny, Russia

date	SO_2 VCD max. [molecules cm^{-2}]	BrO VCD	BrO/SO_2 fitted	BrO/SO_2 error
25 April 2018	$9.3x10^{16}$	$2.3x10^{13}$	$8.9x10^{-5}$	$3.8x10^{-5}$
14 May 2018	$1.2x10^{17}$	$3.4x10^{13}$	$6.0x10^{-5}$	$3.2x10^{-5}$
15 Feb 2019	$7.6x10^{16}$	$2.5x10^{13}$	$2.3x10^{-4}$	$5.4x10^{-5}$
26 Mar 2019	$1.7x10^{17}$	$3.9x10^{13}$	$2.5x10^{-4}$	$3.5x10^{-5}$
28 Mar 2019	$6.9x10^{16}$	$2.2x10^{13}$	$1.9x10^{-4}$	$4.2x10^{-5}$
10 April 2019	$1.7x10^{17}$	$4.2x10^{13}$	$1.8x10^{-4}$	$2.8x10^{-5}$
11 April 2019	$2.0x10^{17}$	$4.9x10^{13}$	$1.5x10^{-4}$	$2.3x10^{-5}$
14 June 2019	$2.0x10^{17}$	$3.6x10^{13}$	$1.1x10^{-4}$	$3.3x10^{-5}$
1 Aug 2019	$2.2x10^{17}$	$3.9x10^{13}$	$1.6x10^{-4}$	$3.1x10^{-5}$
29 Feb 2020	$1.1x10^{17}$	$2.3x10^{13}$	$1.3x10^{-4}$	$3.5x10^{-5}$
1 Mar 2020	$1.0x10^{17}$	$2.5x10^{13}$	$1.1x10^{-4}$	$3.2x10^{-5}$
9 April 2020	$8.8x10^{16}$	$2.4x10^{13}$	$1.4x10^{-4}$	$2.2x10^{-5}$
13 April 2020	$1.3x10^{17}$	$3.4x10^{13}$	$1.2x10^{-4}$	$2.2x10^{-5}$
30 April 2020	$1.3x10^{17}$	$3.0x10^{13}$	$1.7x10^{-4}$	$2.4x10^{-5}$
8 May 2020	$2.0x10^{17}$	$3.6x10^{13}$	$2.0x10^{-4}$	$1.6x10^{-5}$
9 May 2020	$6.2x10^{16}$	$2.1x10^{13}$	$2.0x10^{-4}$	$4.7x10^{-5}$
10 May 2020	$2.0x10^{17}$	$2.4x10^{13}$	$1.0x10^{-4}$	$1.7x10^{-5}$
14 May 2020	$7.1x10^{16}$	$2.6x10^{13}$	$1.1x10^{-4}$	$3.3x10^{-5}$
18 May 2020	$9.9x10^{16}$	$2.2x10^{13}$	$3.5x10^{-5}$	$3.0x10^{-5}$
19 May 2020	$6.5x10^{16}$	$3.0x10^{13}$	$1.1x10^{-4}$	$3.5x10^{-5}$
20 May 2020	$8.6x10^{16}$	$2.2x10^{13}$	$1.3x10^{-4}$	$5.3x10^{-5}$
22 May 2020	$7.2x10^{16}$	$2.1x10^{13}$	$1.2x10^{-4}$	$4.2x10^{-5}$
23 May 2020	$1.3x10^{17}$	$2.5x10^{13}$	$1.1x10^{-4}$	$1.9x10^{-5}$
29 May 2020	$2.7x10^{17}$	$3.1x10^{13}$	$8.5x10^{-5}$	$1.7x10^{-5}$
31 May 2020	$1.2x10^{17}$	$3.3x10^{13}$	$1.0x10^{-4}$	$3.2x10^{-5}$
10 June 2020	$1.1x10^{17}$	$3.9x10^{13}$	$6.2x10^{-5}$	$9.3x10^{-5}$
21 Mar 2021	$7.8x10^{16}$	$1.9x10^{13}$	$1.8x10^{-5}$	$5.7x10^{-5}$
28 Mar 2021	$6.5x10^{16}$	$1.2x10^{13}$	$8.2x10^{-6}$	$1.5x10^{-5}$
4 April 2021	$2.1x10^{17}$	$2.6x10^{13}$	$5.8x10^{-5}$	$9.3x10^{-6}$
26 July 2021	$5.6x10^{16}$	$2.2x10^{13}$	$6.0x10^{-5}$	$2.0x10^{-5}$

Klyuchevskoy, Russia

Type: arc
longitude: 160.64° E
latitude: 56.06° N
Events: 29
BrO > 2σ: 16
BrO/SO_2: $1.1x10^{-4}$
std. dev.: $5.1x10^{-5}$
mean SO_2: $1.4x10^{17}$
mean BrO: $3.4x10^{13}$



17 Mar 2018	$1.4x10^{17}$	$2.2x10^{13}$	$8.0x10^{-5}$	$2.2x10^{-5}$
21 Mar 2018	$1.0x10^{17}$	$1.7x10^{13}$	$6.7x10^{-5}$	$3.6x10^{-5}$
22 Mar 2018	$1.2x10^{17}$	$1.8x10^{13}$	$1.4x10^{-7}$	$2.2x10^{-5}$
11 April 2018	$3.3x10^{17}$	$2.5x10^{13}$	$8.6x10^{-5}$	$1.5x10^{-5}$
13 April 2018	$3.8x10^{17}$	$2.6x10^{13}$	$4.6x10^{-5}$	$9.0x10^{-6}$
2 May 2018	$9.6x10^{16}$	$1.9x10^{13}$	$1.1x10^{-4}$	$2.4x10^{-5}$
3 May 2018	$1.3x10^{17}$	$1.9x10^{13}$	$1.5x10^{-4}$	$2.4x10^{-5}$
22 Feb 2019	$1.4x10^{17}$	$2.3x10^{13}$	$6.4x10^{-5}$	$3.3x10^{-5}$
23 Feb 2019	$1.5x10^{17}$	$1.8x10^{13}$	$1.0x10^{-4}$	$2.9x10^{-5}$
24 Feb 2019	$6.9x10^{16}$	$3.3x10^{13}$	$2.4x10^{-4}$	$4.6x10^{-5}$
22 April 2019	$1.0x10^{17}$	$3.9x10^{13}$	$1.5x10^{-4}$	$3.1x10^{-5}$
27 Aug 2019	$1.1x10^{17}$	$3.2x10^{13}$	$9.9x10^{-5}$	$4.3x10^{-5}$
1 Sept 2019	$9.9x10^{16}$	$6.6x10^{13}$	$1.2x10^{-4}$	$1.1x10^{-4}$
2 Mar 2020	$1.5x10^{17}$	$2.5x10^{13}$	$1.0x10^{-4}$	$2.0x10^{-5}$
8 April 2020	$1.4x10^{17}$	$3.0x10^{13}$	$1.1x10^{-4}$	$1.8x10^{-5}$
11 April 2020	$1.6x10^{17}$	$3.9x10^{13}$	$1.1x10^{-4}$	$2.0x10^{-5}$
15 April 2020	$8.6x10^{16}$	$3.5x10^{13}$	$1.5x10^{-4}$	$4.0x10^{-5}$
16 April 2020	$1.2x10^{17}$	$4.0x10^{13}$	$1.6x10^{-4}$	$3.0x10^{-5}$
1 May 2020	$1.3x10^{17}$	$2.2x10^{13}$	$9.1x10^{-5}$	$1.1x10^{-5}$
4 May 2020	$1.7x10^{17}$	$8.0x10^{13}$	$2.2x10^{-4}$	$2.3x10^{-5}$
6 May 2020	$9.1x10^{16}$	$1.7x10^{13}$	$1.2x10^{-4}$	$2.8x10^{-5}$
7 May 2020	$2.7x10^{17}$	$3.2x10^{13}$	$1.1x10^{-4}$	$6.9x10^{-6}$
21 May 2020	$1.2x10^{17}$	$4.1x10^{13}$	$8.9x10^{-5}$	$5.7x10^{-5}$
26 May 2020	$1.3x10^{17}$	$3.4x10^{13}$	$7.9x10^{-5}$	$1.6x10^{-5}$
6 June 2020	$1.2x10^{17}$	$5.6x10^{13}$	$1.9x10^{-4}$	$2.4x10^{-5}$
8 June 2020	$1.5x10^{17}$	$2.9x10^{13}$	$1.3x10^{-4}$	$1.1x10^{-5}$
16 June 2020	$2.1x10^{17}$	$3.4x10^{13}$	$8.2x10^{-5}$	$1.9x10^{-5}$
21 June 2020	$9.8x10^{16}$	$5.6x10^{13}$	$1.6x10^{-4}$	$4.8x10^{-5}$
1 July 2020	$6.9x10^{16}$	$4.6x10^{13}$	$1.7x10^{-4}$	$5.5x10^{-5}$

Sheveluch, Russia

date	SO_2 VCD max. [molecules cm^{-2}]	BrO VCD	BrO/SO_2 fitted	BrO/SO_2 error

Sheveluch, Russia

Type:	arc
longitude:	161.36° E
latitude:	56.65° N
Events:	30
$BrO > 2\sigma$:	19
BrO/SO_2:	$1.4x10^{-4}$
std. dev.:	$1.1x10^{-4}$
mean SO_2:	$1.2x10^{17}$
mean BrO:	$2.9x10^{13}$



19 Mar 2018	$6.6x10^{16}$	$1.2x10^{13}$	$9.6x10^{-5}$	$3.5x10^{-5}$
8 April 2018	$1.2x10^{17}$	$2.2x10^{13}$	$8.9x10^{-5}$	$2.4x10^{-5}$
12 April 2018	$3.2x10^{17}$	$4.6x10^{13}$	$9.4x10^{-5}$	$1.4x10^{-5}$
19 April 2018	$1.3x10^{17}$	$1.4x10^{13}$	$3.4x10^{-5}$	$4.4x10^{-5}$
20 April 2018	$1.7x10^{17}$	$2.3x10^{13}$	$7.7x10^{-5}$	$1.1x10^{-5}$
30 April 2018	$2.2x10^{17}$	$2.2x10^{13}$	$1.1x10^{-4}$	$1.9x10^{-5}$
1 May 2018	$8.5x10^{16}$	$1.2x10^{13}$	$5.0x10^{-5}$	$1.7x10^{-5}$
5 May 2018	$1.2x10^{17}$	$1.5x10^{13}$	$3.2x10^{-5}$	$4.4x10^{-5}$
15 May 2018	$7.1x10^{16}$	$2.0x10^{13}$	$8.9x10^{-5}$	$2.3x10^{-5}$
17 June 2018	$1.4x10^{17}$	$3.3x10^{13}$	$5.8x10^{-5}$	$2.4x10^{-5}$
22 June 2018	$1.4x10^{17}$	$2.1x10^{13}$	$8.3x10^{-5}$	$3.6x10^{-5}$
22 July 2018	$1.2x10^{17}$	$2.2x10^{13}$	$5.7x10^{-5}$	$2.9x10^{-5}$
4 Sept 2018	$1.7x10^{17}$	$2.8x10^{13}$	$1.3x10^{-4}$	$3.9x10^{-5}$
5 Sept 2018	$1.2x10^{17}$	$1.7x10^{13}$	$1.2x10^{-4}$	$2.8x10^{-5}$
9 Mar 2019	$7.7x10^{16}$	$1.8x10^{13}$	$1.7x10^{-4}$	$5.0x10^{-5}$
11 Mar 2019	$1.4x10^{17}$	$4.4x10^{13}$	$2.4x10^{-4}$	$1.2x10^{-5}$
17 Mar 2019	$6.0x10^{16}$	$2.5x10^{13}$	$2.4x10^{-4}$	$4.1x10^{-5}$
12 April 2019	$1.7x10^{17}$	$3.2x10^{13}$	$1.4x10^{-4}$	$1.7x10^{-5}$
17 April 2019	$9.1x10^{16}$	$4.7x10^{13}$	$3.2x10^{-4}$	$4.0x10^{-5}$
18 April 2019	$8.1x10^{16}$	$3.3x10^{13}$	$3.4x10^{-4}$	$3.0x10^{-5}$
3 June 2019	$1.3x10^{17}$	$6.7x10^{13}$	$4.7x10^{-4}$	$2.4x10^{-5}$
4 June 2019	$1.4x10^{17}$	$6.9x10^{13}$	$3.6x10^{-4}$	$3.1x10^{-5}$
6 Aug 2019	$1.6x10^{17}$	$3.0x10^{13}$	$4.8x10^{-5}$	$2.9x10^{-5}$
6 Oct 2019	$1.3x10^{17}$	$2.8x10^{13}$	$1.7x10^{-4}$	$2.6x10^{-5}$
9 Oct 2019	$1.2x10^{17}$	$3.8x10^{13}$	$2.0x10^{-4}$	$2.8x10^{-5}$
17 Mar 2020	$6.9x10^{16}$	$3.0x10^{13}$	$2.2x10^{-4}$	$5.9x10^{-5}$
19 Mar 2020	$9.4x10^{16}$	$1.9x10^{13}$	$1.1x10^{-4}$	$1.5x10^{-5}$
19 April 2020	$6.4x10^{16}$	$2.0x10^{13}$	$8.9x10^{-5}$	$4.0x10^{-5}$
23 April 2020	$1.2x10^{17}$	$2.7x10^{13}$	$7.6x10^{-5}$	$1.1x10^{-5}$
3 May 2020	$8.5x10^{16}$	$2.6x10^{13}$	$1.3x10^{-4}$	$1.8x10^{-5}$

Shishaldin, USA

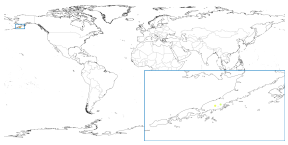
Type:	arc
longitude:	163.97° W
latitude:	54.76° N
Events:	5
$BrO > 2\sigma$:	2
BrO/SO_2:	$1.0x10^{-4}$
std. dev.:	$7.8x10^{-5}$
mean SO_2:	$1.1x10^{17}$
mean BrO:	$2.0x10^{13}$



19 April 2018	$1.2x10^{17}$	$1.5x10^{13}$	$7.0x10^{-5}$	$3.8x10^{-5}$
31 May 2018	$9.0x10^{16}$	$1.1x10^{13}$	$7.9x10^{-5}$	$3.7x10^{-5}$
22 Oct 2019	$1.8x10^{17}$	$1.9x10^{13}$	$6.9x10^{-5}$	$6.6x10^{-6}$
28 Oct 2019	$8.7x10^{16}$	$2.7x10^{13}$	$2.8x10^{-4}$	$3.1x10^{-5}$
5 May 2020	$8.8x10^{16}$	$2.6x10^{13}$	$1.2x10^{-4}$	$5.4x10^{-5}$

Veniaminof, USA

Type:	arc
longitude:	159.39° W
latitude:	56.20° N
Events:	3
$BrO > 2\sigma$:	1
BrO/SO_2:	$7.8x10^{-5}$
std. dev.:	$4.4x10^{-5}$
mean SO_2:	$1.9x10^{17}$
mean BrO:	$2.0x10^{13}$



25 Sept 2018	$2.0x10^{17}$	$2.0x10^{13}$	$9.1x10^{-5}$	$1.5x10^{-5}$
23 Oct 2018	$2.9x10^{17}$	$2.6x10^{13}$	$1.0x10^{-4}$	$3.1x10^{-5}$
21 Mar 2021	$9.1x10^{16}$	$1.3x10^{13}$	$4.6x10^{-6}$	$4.3x10^{-5}$

Kilauea, USA

date	SO_2 VCD max. [molecules cm^{-2}]	BrO VCD	BrO/SO_2 fitted	BrO/SO_2 error

Kilauea, USA

Type:	hot spot
longitude:	155.29° W
latitude:	19.42° N
Events:	110
$BrO > 2\sigma$:	28
BrO/SO_2:	$2.4x10^{-5}$
std. dev.:	$2.8x10^{-5}$
mean SO_2:	$4.5x10^{17}$
mean BrO:	$2.9x10^{13}$



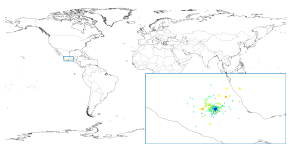
28 Jan 2018	$6.8x10^{16}$	$2.4x10^{13}$	$3.7x10^{-5}$	$2.0x10^{-5}$
8 Feb 2018	$3.7x10^{17}$	$4.0x10^{13}$	$1.7x10^{-5}$	$1.1x10^{-5}$
18 Feb 2018	$1.9x10^{17}$	$2.0x10^{13}$	$3.1x10^{-5}$	$1.1x10^{-5}$
19 Feb 2018	$7.1x10^{16}$	$1.8x10^{13}$	$1.3x10^{-5}$	$5.0x10^{-5}$
20 Feb 2018	$1.0x10^{17}$	$2.2x10^{13}$	$5.6x10^{-6}$	$5.6x10^{-5}$
24 Feb 2018	$2.0x10^{17}$	$1.9x10^{13}$	$4.6x10^{-6}$	$1.3x10^{-5}$
28 Feb 2018	$9.7x10^{16}$	$2.9x10^{13}$	$2.3x10^{-5}$	$3.1x10^{-5}$
7 Mar 2018	$4.5x10^{17}$	$2.5x10^{13}$	$1.0x10^{-5}$	$9.1x10^{-6}$
8 Mar 2018	$5.4x10^{17}$	$1.7x10^{13}$	$9.3x10^{-6}$	$1.3x10^{-5}$
11 Mar 2018	$7.1x10^{16}$	$1.2x10^{13}$	$3.0x10^{-5}$	$3.5x10^{-5}$
16 Mar 2018	$7.9x10^{17}$	$2.6x10^{13}$	$2.2x10^{-5}$	$9.6x10^{-6}$
17 Mar 2018	$3.7x10^{17}$	$3.4x10^{13}$	$6.3x10^{-6}$	$1.2x10^{-5}$
18 Mar 2018	$5.4x10^{17}$	$2.4x10^{13}$	$2.0x10^{-6}$	$1.3x10^{-5}$
21 Mar 2018	$9.4x10^{16}$	$1.8x10^{13}$	$3.0x10^{-5}$	$2.8x10^{-5}$
22 Mar 2018	$2.7x10^{17}$	$2.5x10^{13}$	$1.1x10^{-5}$	$1.2x10^{-5}$
23 Mar 2018	$1.9x10^{17}$	$2.3x10^{13}$	$3.2x10^{-5}$	$2.2x10^{-5}$
27 Mar 2018	$8.9x10^{16}$	$2.0x10^{13}$	$3.5x10^{-5}$	$2.0x10^{-5}$
28 Mar 2018	$1.7x10^{17}$	$2.7x10^{13}$	$3.2x10^{-6}$	$2.1x10^{-5}$
29 Mar 2018	$1.6x10^{17}$	$2.1x10^{13}$	$1.3x10^{-5}$	$2.7x10^{-5}$
31 Mar 2018	$1.3x10^{17}$	$1.6x10^{13}$	$1.4x10^{-5}$	$2.7x10^{-5}$
3 April 2018	$3.1x10^{17}$	$3.4x10^{13}$	$1.1x10^{-5}$	$2.4x10^{-5}$
4 April 2018	$1.4x10^{17}$	$1.7x10^{13}$	$4.8x10^{-6}$	$2.3x10^{-5}$
5 April 2018	$1.6x10^{17}$	$1.2x10^{13}$	$0.8x10^{-6}$	$2.3x10^{-5}$
6 April 2018	$3.9x10^{17}$	$2.3x10^{13}$	$1.6x10^{-5}$	$7.1x10^{-6}$
7 April 2018	$1.1x10^{17}$	$2.0x10^{13}$	$9.2x10^{-6}$	$1.9x10^{-5}$
8 April 2018	$2.4x10^{17}$	$2.7x10^{13}$	$2.9x10^{-6}$	$1.4x10^{-5}$
13 April 2018	$1.9x10^{17}$	$2.3x10^{13}$	$2.6x10^{-5}$	$2.0x10^{-5}$
18 April 2018	$1.3x10^{17}$	$2.1x10^{13}$	$1.4x10^{-5}$	$4.2x10^{-5}$
23 April 2018	$8.2x10^{16}$	$2.2x10^{13}$	$2.6x10^{-5}$	$2.4x10^{-5}$
24 April 2018	$1.5x10^{17}$	$2.8x10^{13}$	$2.9x10^{-5}$	$4.7x10^{-5}$
29 April 2018	$3.7x10^{17}$	$1.7x10^{13}$	$4.3x10^{-5}$	$7.9x10^{-6}$
1 May 2018	$1.6x10^{17}$	$1.2x10^{13}$	$4.6x10^{-5}$	$1.7x10^{-5}$
2 May 2018	$1.3x10^{17}$	$1.5x10^{13}$	$4.2x10^{-5}$	$1.5x10^{-5}$
3 May 2018	$2.7x10^{17}$	$2.9x10^{13}$	$2.7x10^{-5}$	$1.3x10^{-5}$
4 May 2018	$1.2x10^{18}$	$4.5x10^{13}$	$1.4x10^{-5}$	$4.5x10^{-6}$
5 May 2018	$8.8x10^{17}$	$3.0x10^{13}$	$1.5x10^{-5}$	$5.9x10^{-6}$
6 May 2018	$2.1x10^{17}$	$1.6x10^{13}$	$1.0x10^{-5}$	$1.5x10^{-5}$
8 May 2018	$1.8x10^{17}$	$2.1x10^{13}$	$1.0x10^{-5}$	$1.4x10^{-5}$
10 May 2018	$3.8x10^{17}$	$2.6x10^{13}$	$2.7x10^{-5}$	$5.4x10^{-6}$
11 May 2018	$8.1x10^{16}$	$1.3x10^{13}$	$4.1x10^{-5}$	$1.8x10^{-5}$
13 May 2018	$1.1x10^{17}$	$1.6x10^{13}$	$0.9x10^{-6}$	$1.9x10^{-5}$
16 May 2018	$5.8x10^{17}$	$2.4x10^{13}$	$3.3x10^{-5}$	$5.7x10^{-6}$
17 May 2018	$1.9x10^{17}$	$2.2x10^{13}$	$3.2x10^{-5}$	$7.4x10^{-6}$
20 May 2018	$9.1x10^{17}$	$4.0x10^{13}$	$2.3x10^{-5}$	$2.3x10^{-6}$
21 May 2018	$4.8x10^{17}$	$3.6x10^{13}$	$2.8x10^{-5}$	$5.7x10^{-6}$
25 May 2018	$8.2x10^{17}$	$4.0x10^{13}$	$2.9x10^{-5}$	$2.8x10^{-6}$
26 May 2018	$8.4x10^{17}$	$3.7x10^{13}$	$1.8x10^{-5}$	$2.7x10^{-6}$
29 May 2018	$2.3x10^{17}$	$2.2x10^{13}$	$5.3x10^{-5}$	$9.9x10^{-6}$
31 May 2018	$6.9x10^{17}$	$3.4x10^{13}$	$2.2x10^{-5}$	$4.1x10^{-6}$
1 June 2018	$1.2x10^{17}$	$1.6x10^{13}$	$2.8x10^{-5}$	$1.7x10^{-5}$
2 June 2018	$4.1x10^{17}$	$2.1x10^{13}$	$2.2x10^{-5}$	$5.0x10^{-6}$
4 June 2018	$5.9x10^{17}$	$3.6x10^{13}$	$3.3x10^{-5}$	$2.5x10^{-6}$
5 June 2018	$1.1x10^{18}$	$3.3x10^{13}$	$3.1x10^{-5}$	$3.2x10^{-6}$
6 June 2018	$8.8x10^{17}$	$4.7x10^{13}$	$5.2x10^{-5}$	$6.3x10^{-6}$
11 June 2018	$1.7x10^{18}$	$7.9x10^{13}$	$3.6x10^{-5}$	$2.2x10^{-6}$
16 June 2018	$4.1x10^{18}$	$1.6x10^{14}$	$4.1x10^{-5}$	$1.1x10^{-6}$
17 June 2018	$1.4x10^{18}$	$8.1x10^{13}$	$4.7x10^{-5}$	$2.3x10^{-6}$
22 June 2018	$1.1x10^{18}$	$3.8x10^{13}$	$3.0x10^{-5}$	$2.8x10^{-6}$
23 June 2018	$2.5x10^{17}$	$3.4x10^{13}$	$5.1x10^{-5}$	$2.8x10^{-6}$
27 June 2018	$1.1x10^{18}$	$5.1x10^{13}$	$3.6x10^{-5}$	$2.6x10^{-6}$

Kilauea, USA

date	SO_2 VCD max. [molecules cm^{-2}]	BrO VCD	BrO/SO_2 fitted	BrO/SO_2 error
1 July 2018	$1.5x10^{18}$	$8.2x10^{13}$	$5.1x10^{-5}$	$2.1x10^{-6}$
2 July 2018	$1.5x10^{18}$	$5.6x10^{13}$	$1.2x10^{-5}$	$1.2x10^{-6}$
4 July 2018	$3.7x10^{17}$	$2.9x10^{13}$	$4.9x10^{-5}$	$4.3x10^{-6}$
7 July 2018	$2.2x10^{18}$	$5.3x10^{13}$	$1.4x10^{-5}$	$1.5x10^{-6}$
13 July 2018	$1.1x10^{18}$	$3.8x10^{13}$	$2.2x10^{-5}$	$3.8x10^{-6}$
14 July 2018	$8.3x10^{17}$	$3.8x10^{13}$	$2.7x10^{-5}$	$4.0x10^{-6}$
17 July 2018	$7.5x10^{17}$	$3.0x10^{13}$	$2.7x10^{-5}$	$3.6x10^{-6}$
18 July 2018	$1.5x10^{18}$	$5.7x10^{13}$	$2.1x10^{-5}$	$2.2x10^{-6}$
19 July 2018	$2.3x10^{17}$	$2.9x10^{13}$	$2.7x10^{-5}$	$8.1x10^{-6}$
23 July 2018	$1.9x10^{18}$	$4.2x10^{13}$	$2.7x10^{-5}$	$1.8x10^{-6}$
24 July 2018	$5.4x10^{17}$	$4.4x10^{13}$	$4.8x10^{-5}$	$3.9x10^{-6}$
26 July 2018	$9.7x10^{16}$	$1.9x10^{13}$	$2.8x10^{-5}$	$8.6x10^{-6}$
27 July 2018	$5.2x10^{17}$	$4.0x10^{13}$	$3.6x10^{-5}$	$3.5x10^{-6}$
28 July 2018	$1.1x10^{18}$	$5.7x10^{13}$	$2.7x10^{-5}$	$2.7x10^{-6}$
29 July 2018	$1.0x10^{18}$	$4.0x10^{13}$	$2.0x10^{-5}$	$3.3x10^{-6}$
3 Aug 2018	$2.9x10^{17}$	$2.6x10^{13}$	$3.1x10^{-5}$	$7.5x10^{-6}$
4 Aug 2018	$2.3x10^{17}$	$1.6x10^{13}$	$2.6x10^{-6}$	$1.4x10^{-5}$
21 Dec 2020	$1.6x10^{17}$	$1.9x10^{13}$	$2.8x10^{-5}$	$1.0x10^{-5}$
22 Dec 2020	$1.9x10^{17}$	$2.1x10^{13}$	$1.8x10^{-5}$	$9.3x10^{-6}$
23 Dec 2020	$6.5x10^{17}$	$4.1x10^{13}$	$2.5x10^{-5}$	$5.0x10^{-6}$
24 Dec 2020	$3.5x10^{17}$	$3.4x10^{13}$	$2.7x10^{-5}$	$6.7x10^{-6}$
25 Dec 2020	$1.9x10^{17}$	$2.7x10^{13}$	$9.6x10^{-6}$	$1.3x10^{-5}$
29 Dec 2020	$7.0x10^{16}$	$2.3x10^{13}$	$2.0x10^{-5}$	$3.5x10^{-5}$
4 Jan 2021	$1.5x10^{17}$	$2.0x10^{13}$	$1.3x10^{-5}$	$4.2x10^{-5}$
9 Jan 2021	$8.6x10^{16}$	$3.2x10^{13}$	$6.3x10^{-6}$	$5.3x10^{-5}$
13 Jan 2021	$9.0x10^{16}$	$9.4x10^{12}$	$4.0x10^{-5}$	$4.2x10^{-5}$
15 Jan 2021	$1.2x10^{17}$	$3.5x10^{13}$	$3.8x10^{-5}$	$3.4x10^{-5}$
30 Sept 2021	$6.8x10^{17}$	$2.8x10^{13}$	$2.1x10^{-5}$	$5.6x10^{-6}$
1 Oct 2021	$8.8x10^{16}$	$1.9x10^{13}$	$1.5x10^{-5}$	$2.2x10^{-5}$
2 Oct 2021	$1.8x10^{17}$	$2.9x10^{13}$	$3.8x10^{-5}$	$9.0x10^{-6}$
3 Oct 2021	$1.4x10^{17}$	$2.1x10^{13}$	$6.2x10^{-6}$	$1.3x10^{-5}$
4 Oct 2021	$1.2x10^{17}$	$3.0x10^{13}$	$3.7x10^{-5}$	$3.1x10^{-5}$
12 Oct 2021	$1.0x10^{17}$	$1.4x10^{13}$	$2.1x10^{-5}$	$3.4x10^{-5}$
14 Oct 2021	$1.1x10^{17}$	$2.0x10^{13}$	$3.2x10^{-5}$	$4.8x10^{-5}$
18 Oct 2021	$2.0x10^{17}$	$2.1x10^{13}$	$2.1x10^{-5}$	$3.6x10^{-5}$
19 Oct 2021	$1.7x10^{17}$	$2.8x10^{13}$	$4.1x10^{-6}$	$2.8x10^{-5}$
20 Oct 2021	$1.1x10^{17}$	$2.7x10^{13}$	$1.4x10^{-5}$	$3.4x10^{-5}$
28 Oct 2021	$8.6x10^{16}$	$1.1x10^{13}$	$3.0x10^{-6}$	$3.2x10^{-5}$
29 Oct 2021	$1.2x10^{17}$	$1.7x10^{13}$	$2.0x10^{-5}$	$4.0x10^{-5}$
30 Oct 2021	$1.9x10^{17}$	$4.1x10^{13}$	$1.7x10^{-5}$	$3.5x10^{-5}$
31 Oct 2021	$9.7x10^{16}$	$2.1x10^{13}$	$1.9x10^{-6}$	$5.1x10^{-5}$
9 Nov 2021	$1.3x10^{17}$	$2.1x10^{13}$	$1.3x10^{-5}$	$4.3x10^{-5}$
15 Nov 2021	$1.3x10^{17}$	$2.2x10^{13}$	$2.4x10^{-6}$	$4.1x10^{-5}$
16 Nov 2021	$9.6x10^{16}$	$2.3x10^{13}$	$8.3x10^{-6}$	$6.1x10^{-5}$
19 Nov 2021	$1.2x10^{17}$	$2.4x10^{13}$	$2.9x10^{-5}$	$4.9x10^{-5}$
24 Nov 2021	$1.4x10^{17}$	$1.2x10^{13}$	$2.0x10^{-5}$	$2.7x10^{-5}$
25 Nov 2021	$8.3x10^{16}$	$1.9x10^{13}$	$1.9x10^{-5}$	$4.1x10^{-5}$
2 Dec 2021	$9.5x10^{16}$	$1.4x10^{13}$	$3.8x10^{-5}$	$4.1x10^{-5}$
7 Dec 2021	$8.3x10^{16}$	$2.2x10^{13}$	$3.3x10^{-5}$	$3.4x10^{-5}$
17 Dec 2021	$1.4x10^{17}$	$2.8x10^{13}$	$4.0x10^{-6}$	$2.4x10^{-5}$

Popocatepetl, Mexico

Type:	arc
longitude:	98.62° W
latitude:	19.03° N
Events:	467
$BrO > 2\sigma$:	84
BrO/SO_2:	$5.9x10^{-5}$
std. dev.:	$4.5x10^{-5}$
mean SO_2:	$1.9x10^{17}$
mean BrO:	$3.1x10^{13}$



3 Jan 2018	$6.8x10^{16}$	$2.7x10^{13}$	$1.3x10^{-6}$	$3.9x10^{-5}$
4 Jan 2018	$9.0x10^{16}$	$1.6x10^{13}$	$6.3x10^{-5}$	$4.2x10^{-5}$
3 Feb 2018	$9.2x10^{16}$	$2.3x10^{13}$	$1.5x10^{-4}$	$2.1x10^{-5}$
9 Feb 2018	$1.1x10^{17}$	$4.1x10^{13}$	$4.7x10^{-5}$	$6.1x10^{-5}$
19 Feb 2018	$2.5x10^{17}$	$3.2x10^{13}$	$7.7x10^{-5}$	$2.2x10^{-5}$
20 Feb 2018	$2.4x10^{17}$	$3.0x10^{13}$	$1.0x10^{-4}$	$3.0x10^{-5}$
23 Feb 2018	$7.4x10^{16}$	$1.4x10^{13}$	$5.6x10^{-5}$	$2.6x10^{-5}$
24 Feb 2018	$8.1x10^{17}$	$6.5x10^{13}$	$7.3x10^{-5}$	$1.6x10^{-5}$
25 Feb 2018	$2.2x10^{17}$	$2.1x10^{13}$	$1.6x10^{-6}$	$1.8x10^{-5}$
7 Mar 2018	$9.6x10^{16}$	$2.6x10^{13}$	$1.5x10^{-5}$	$2.2x10^{-5}$

Popocatepetl, Mexico

date	SO_2 VCD max. [molecules cm^{-2}]	BrO VCD	BrO/SO_2 fitted	BrO/SO_2 error
8 Mar 2018	$1.7x10^{17}$	$2.8x10^{13}$	$4.8x10^{-5}$	$2.3x10^{-5}$
23 Mar 2018	$1.5x10^{17}$	$3.5x10^{13}$	$1.2x10^{-5}$	$4.5x10^{-5}$
24 Mar 2018	$1.2x10^{17}$	$4.4x10^{13}$	$8.2x10^{-5}$	$3.6x10^{-5}$
25 Mar 2018	$1.6x10^{17}$	$2.8x10^{13}$	$8.5x10^{-5}$	$2.3x10^{-5}$
30 Mar 2018	$1.6x10^{17}$	$3.2x10^{13}$	$7.1x10^{-5}$	$1.8x10^{-5}$
2 April 2018	$1.7x10^{17}$	$2.5x10^{13}$	$7.7x10^{-5}$	$2.0x10^{-5}$
3 April 2018	$4.2x10^{17}$	$2.9x10^{13}$	$1.4x10^{-5}$	$2.0x10^{-5}$
4 April 2018	$4.4x10^{17}$	$3.2x10^{13}$	$8.2x10^{-5}$	$2.8x10^{-5}$
9 April 2018	$2.5x10^{17}$	$3.4x10^{13}$	$4.3x10^{-5}$	$2.6x10^{-5}$
10 April 2018	$2.8x10^{17}$	$3.3x10^{13}$	$7.8x10^{-5}$	$1.8x10^{-5}$
15 April 2018	$1.7x10^{17}$	$4.2x10^{13}$	$6.1x10^{-5}$	$2.7x10^{-5}$
16 April 2018	$7.6x10^{16}$	$1.7x10^{13}$	$1.7x10^{-5}$	$4.4x10^{-5}$
18 April 2018	$9.5x10^{16}$	$2.3x10^{13}$	$3.9x10^{-5}$	$2.5x10^{-5}$
21 April 2018	$1.7x10^{17}$	$2.9x10^{13}$	$9.1x10^{-5}$	$4.2x10^{-5}$
23 April 2018	$7.1x10^{16}$	$1.5x10^{13}$	$2.6x10^{-6}$	$4.3x10^{-5}$
24 April 2018	$9.9x10^{16}$	$2.0x10^{13}$	$1.2x10^{-5}$	$3.2x10^{-5}$
25 April 2018	$1.4x10^{17}$	$2.9x10^{13}$	$2.0x10^{-6}$	$2.1x10^{-5}$
28 April 2018	$1.3x10^{17}$	$3.0x10^{13}$	$6.0x10^{-5}$	$2.7x10^{-5}$
29 April 2018	$1.7x10^{17}$	$2.7x10^{13}$	$9.1x10^{-6}$	$2.1x10^{-5}$
30 April 2018	$1.8x10^{17}$	$2.5x10^{13}$	$3.6x10^{-5}$	$2.7x10^{-5}$
1 May 2018	$5.2x10^{17}$	$2.7x10^{13}$	$2.7x10^{-5}$	$1.8x10^{-5}$
3 May 2018	$9.6x10^{16}$	$1.1x10^{13}$	$4.7x10^{-5}$	$2.8x10^{-5}$
4 May 2018	$5.4x10^{17}$	$2.6x10^{13}$	$2.9x10^{-5}$	$1.4x10^{-5}$
5 May 2018	$2.4x10^{17}$	$2.8x10^{13}$	$5.7x10^{-5}$	$1.8x10^{-5}$
6 May 2018	$5.3x10^{17}$	$4.7x10^{13}$	$7.9x10^{-5}$	$1.5x10^{-5}$
7 May 2018	$4.9x10^{17}$	$2.8x10^{13}$	$6.8x10^{-5}$	$1.2x10^{-5}$
9 May 2018	$1.5x10^{17}$	$3.2x10^{13}$	$1.2x10^{-4}$	$3.4x10^{-5}$
10 May 2018	$5.6x10^{17}$	$4.3x10^{13}$	$6.9x10^{-5}$	$1.6x10^{-5}$
11 May 2018	$3.7x10^{17}$	$4.0x10^{13}$	$4.6x10^{-5}$	$1.5x10^{-5}$
12 May 2018	$2.1x10^{17}$	$1.9x10^{13}$	$3.2x10^{-6}$	$3.1x10^{-5}$
15 May 2018	$2.0x10^{17}$	$5.3x10^{13}$	$6.8x10^{-5}$	$2.3x10^{-5}$
17 May 2018	$4.9x10^{17}$	$2.6x10^{13}$	$2.0x10^{-5}$	$1.2x10^{-5}$
20 May 2018	$7.1x10^{16}$	$1.9x10^{13}$	$2.9x10^{-5}$	$3.0x10^{-5}$
22 May 2018	$8.2x10^{16}$	$3.0x10^{13}$	$2.2x10^{-5}$	$3.6x10^{-5}$
1 June 2018	$6.7x10^{16}$	$2.5x10^{13}$	$6.1x10^{-5}$	$4.4x10^{-5}$
5 June 2018	$1.8x10^{17}$	$2.0x10^{13}$	$5.7x10^{-5}$	$2.1x10^{-5}$
6 June 2018	$1.4x10^{17}$	$2.7x10^{13}$	$6.1x10^{-5}$	$2.0x10^{-5}$
7 June 2018	$1.5x10^{17}$	$4.5x10^{13}$	$5.5x10^{-5}$	$2.4x10^{-5}$
10 June 2018	$1.4x10^{17}$	$3.2x10^{13}$	$8.2x10^{-5}$	$4.5x10^{-5}$
11 June 2018	$1.8x10^{17}$	$2.6x10^{13}$	$3.1x10^{-5}$	$1.9x10^{-5}$
12 June 2018	$7.2x10^{16}$	$2.2x10^{13}$	$1.5x10^{-5}$	$3.2x10^{-5}$
15 June 2018	$1.6x10^{17}$	$1.6x10^{13}$	$3.1x10^{-5}$	$1.8x10^{-5}$
16 June 2018	$3.7x10^{17}$	$3.9x10^{13}$	$5.5x10^{-5}$	$1.6x10^{-5}$
17 June 2018	$2.8x10^{17}$	$3.9x10^{13}$	$3.4x10^{-5}$	$2.7x10^{-5}$
18 June 2018	$2.6x10^{17}$	$2.2x10^{13}$	$5.5x10^{-5}$	$1.4x10^{-5}$
21 June 2018	$1.9x10^{17}$	$2.6x10^{13}$	$4.6x10^{-5}$	$2.4x10^{-5}$
22 June 2018	$1.5x10^{17}$	$2.9x10^{13}$	$4.3x10^{-5}$	$3.9x10^{-5}$
23 June 2018	$1.1x10^{17}$	$2.4x10^{13}$	$2.6x10^{-5}$	$2.6x10^{-5}$
24 June 2018	$2.2x10^{17}$	$3.3x10^{13}$	$3.0x10^{-5}$	$3.1x10^{-5}$
26 June 2018	$8.0x10^{16}$	$2.5x10^{13}$	$1.8x10^{-6}$	$3.6x10^{-5}$
27 June 2018	$8.9x10^{16}$	$4.3x10^{13}$	$8.1x10^{-6}$	$4.0x10^{-5}$
1 July 2018	$6.8x10^{16}$	$2.6x10^{13}$	$4.1x10^{-5}$	$3.1x10^{-5}$
2 July 2018	$1.2x10^{17}$	$4.6x10^{13}$	$7.5x10^{-5}$	$1.9x10^{-5}$
4 July 2018	$1.1x10^{17}$	$3.4x10^{13}$	$5.3x10^{-5}$	$4.3x10^{-5}$
8 July 2018	$1.6x10^{17}$	$3.6x10^{13}$	$1.1x10^{-5}$	$3.2x10^{-5}$
9 July 2018	$1.4x10^{17}$	$5.2x10^{13}$	$1.7x10^{-4}$	$3.7x10^{-5}$
13 July 2018	$1.8x10^{17}$	$4.1x10^{13}$	$5.0x10^{-5}$	$3.6x10^{-5}$
14 July 2018	$1.1x10^{17}$	$2.5x10^{13}$	$5.4x10^{-5}$	$3.7x10^{-5}$
19 July 2018	$9.5x10^{16}$	$2.8x10^{13}$	$7.9x10^{-5}$	$4.4x10^{-5}$
29 July 2018	$2.2x10^{17}$	$4.0x10^{13}$	$1.1x10^{-4}$	$3.7x10^{-5}$
30 July 2018	$1.6x10^{17}$	$3.4x10^{13}$	$5.0x10^{-5}$	$2.2x10^{-5}$
31 July 2018	$1.4x10^{17}$	$3.1x10^{13}$	$5.8x10^{-5}$	$1.9x10^{-5}$
2 Aug 2018	$1.0x10^{17}$	$1.7x10^{13}$	$3.6x10^{-5}$	$4.2x10^{-5}$
3 Aug 2018	$1.7x10^{17}$	$1.6x10^{13}$	$4.5x10^{-5}$	$2.8x10^{-5}$
8 Aug 2018	$2.0x10^{17}$	$4.1x10^{13}$	$1.1x10^{-4}$	$5.1x10^{-5}$
9 Aug 2018	$2.2x10^{17}$	$5.6x10^{13}$	$1.1x10^{-4}$	$3.3x10^{-5}$
10 Aug 2018	$2.6x10^{17}$	$2.2x10^{13}$	$6.9x10^{-5}$	$2.6x10^{-5}$
13 Aug 2018	$9.1x10^{16}$	$3.0x10^{13}$	$1.0x10^{-4}$	$2.9x10^{-5}$
14 Aug 2018	$2.1x10^{17}$	$3.2x10^{13}$	$6.6x10^{-5}$	$2.2x10^{-5}$
15 Aug 2018	$1.2x10^{17}$	$3.3x10^{13}$	$1.0x10^{-4}$	$6.1x10^{-5}$
16 Aug 2018	$1.2x10^{17}$	$3.0x10^{13}$	$6.7x10^{-5}$	$7.2x10^{-5}$

Popocatepetl, Mexico

date	SO_2 VCD max. [molecules cm^{-2}]	BrO VCD	BrO/SO_2 fitted	BrO/SO_2 error
19 Aug 2018	$2.2x10^{17}$	$2.5x10^{13}$	$4.8x10^{-5}$	$2.1x10^{-5}$
20 Aug 2018	$9.9x10^{16}$	$2.8x10^{13}$	$9.7x10^{-5}$	$5.7x10^{-5}$
24 Aug 2018	$1.0x10^{17}$	$1.9x10^{13}$	$6.1x10^{-5}$	$5.5x10^{-5}$
25 Aug 2018	$1.4x10^{17}$	$3.9x10^{13}$	$2.3x10^{-5}$	$2.2x10^{-5}$
26 Aug 2018	$1.1x10^{17}$	$3.0x10^{13}$	$3.2x10^{-5}$	$7.8x10^{-5}$
30 Aug 2018	$1.4x10^{17}$	$3.8x10^{13}$	$4.9x10^{-5}$	$2.9x10^{-5}$
31 Aug 2018	$2.3x10^{17}$	$4.2x10^{13}$	$5.1x10^{-5}$	$1.6x10^{-5}$
1 Sept 2018	$7.8x10^{16}$	$2.3x10^{13}$	$6.8x10^{-5}$	$6.1x10^{-5}$
4 Sept 2018	$2.0x10^{17}$	$3.9x10^{13}$	$8.3x10^{-5}$	$3.7x10^{-5}$
5 Sept 2018	$2.2x10^{17}$	$3.0x10^{13}$	$3.0x10^{-5}$	$2.2x10^{-5}$
6 Sept 2018	$2.1x10^{17}$	$3.0x10^{13}$	$8.0x10^{-5}$	$2.8x10^{-5}$
9 Sept 2018	$1.2x10^{17}$	$2.8x10^{13}$	$3.0x10^{-5}$	$2.5x10^{-5}$
10 Sept 2018	$2.8x10^{17}$	$2.9x10^{13}$	$3.4x10^{-5}$	$2.4x10^{-5}$
12 Sept 2018	$1.7x10^{17}$	$2.0x10^{13}$	$2.6x10^{-5}$	$1.9x10^{-5}$
14 Sept 2018	$1.2x10^{17}$	$2.4x10^{13}$	$4.8x10^{-5}$	$5.0x10^{-5}$
15 Sept 2018	$2.6x10^{17}$	$3.4x10^{13}$	$3.3x10^{-5}$	$1.6x10^{-5}$
16 Sept 2018	$8.5x10^{17}$	$4.5x10^{13}$	$2.9x10^{-5}$	$7.1x10^{-6}$
17 Sept 2018	$3.8x10^{17}$	$3.0x10^{13}$	$3.8x10^{-5}$	$2.0x10^{-5}$
19 Sept 2018	$4.8x10^{17}$	$3.8x10^{13}$	$6.5x10^{-5}$	$7.9x10^{-6}$
20 Sept 2018	$1.9x10^{17}$	$2.8x10^{13}$	$4.8x10^{-5}$	$1.0x10^{-5}$
21 Sept 2018	$3.5x10^{17}$	$4.1x10^{13}$	$3.5x10^{-5}$	$1.9x10^{-5}$
24 Sept 2018	$1.5x10^{17}$	$1.7x10^{13}$	$9.6x10^{-5}$	$2.2x10^{-5}$
25 Sept 2018	$2.0x10^{17}$	$2.6x10^{13}$	$2.4x10^{-5}$	$1.8x10^{-5}$
26 Sept 2018	$3.4x10^{17}$	$4.0x10^{13}$	$2.9x10^{-5}$	$2.0x10^{-5}$
29 Sept 2018	$9.7x10^{16}$	$1.7x10^{13}$	$1.0x10^{-4}$	$3.1x10^{-5}$
30 Sept 2018	$1.6x10^{17}$	$2.7x10^{13}$	$7.1x10^{-5}$	$3.3x10^{-5}$
1 Oct 2018	$2.2x10^{17}$	$3.9x10^{13}$	$6.5x10^{-5}$	$2.0x10^{-5}$
6 Oct 2018	$9.7x10^{16}$	$1.7x10^{13}$	$1.1x10^{-4}$	$3.4x10^{-5}$
7 Oct 2018	$1.1x10^{17}$	$2.9x10^{13}$	$3.2x10^{-5}$	$4.5x10^{-5}$
8 Oct 2018	$1.0x10^{17}$	$2.7x10^{13}$	$2.7x10^{-5}$	$3.1x10^{-5}$
12 Oct 2018	$1.1x10^{17}$	$3.8x10^{13}$	$1.6x10^{-4}$	$4.8x10^{-5}$
24 Oct 2018	$6.3x10^{16}$	$2.3x10^{13}$	$6.7x10^{-5}$	$7.8x10^{-5}$
29 Oct 2018	$1.7x10^{17}$	$2.7x10^{13}$	$6.1x10^{-5}$	$3.3x10^{-5}$
2 Nov 2018	$1.1x10^{17}$	$1.4x10^{13}$	$3.7x10^{-5}$	$3.2x10^{-5}$
7 Nov 2018	$2.0x10^{17}$	$1.9x10^{13}$	$1.2x10^{-5}$	$2.5x10^{-5}$
8 Nov 2018	$3.6x10^{17}$	$3.1x10^{13}$	$2.4x10^{-5}$	$2.0x10^{-5}$
20 Nov 2018	$1.0x10^{17}$	$2.8x10^{13}$	$7.7x10^{-5}$	$9.2x10^{-6}$
23 Nov 2018	$7.8x10^{17}$	$7.1x10^{13}$	$6.5x10^{-5}$	$1.1x10^{-5}$
24 Nov 2018	$2.4x10^{17}$	$3.3x10^{13}$	$3.4x10^{-5}$	$1.8x10^{-5}$
4 Dec 2018	$1.1x10^{17}$	$1.8x10^{13}$	$2.2x10^{-5}$	$1.5x10^{-5}$
5 Dec 2018	$2.0x10^{17}$	$2.8x10^{13}$	$3.6x10^{-5}$	$1.7x10^{-5}$
9 Dec 2018	$3.2x10^{17}$	$2.3x10^{13}$	$6.8x10^{-5}$	$2.5x10^{-5}$
11 Dec 2018	$1.3x10^{17}$	$2.4x10^{13}$	$1.4x10^{-4}$	$3.8x10^{-5}$
15 Dec 2018	$6.3x10^{16}$	$2.4x10^{13}$	$2.2x10^{-6}$	$1.8x10^{-5}$
16 Dec 2018	$8.2x10^{16}$	$2.2x10^{13}$	$1.2x10^{-4}$	$5.1x10^{-5}$
17 Jan 2019	$1.1x10^{17}$	$1.7x10^{13}$	$4.0x10^{-5}$	$3.8x10^{-5}$
12 Feb 2019	$1.2x10^{17}$	$3.4x10^{13}$	$6.7x10^{-5}$	$5.0x10^{-5}$
15 Feb 2019	$8.4x10^{16}$	$1.5x10^{13}$	$3.6x10^{-5}$	$1.5x10^{-5}$
16 Feb 2019	$2.1x10^{17}$	$2.7x10^{13}$	$4.4x10^{-5}$	$1.1x10^{-5}$
17 Feb 2019	$1.7x10^{17}$	$4.3x10^{13}$	$8.7x10^{-5}$	$6.9x10^{-6}$
23 Feb 2019	$1.7x10^{17}$	$3.4x10^{13}$	$7.1x10^{-5}$	$1.3x10^{-5}$
24 Feb 2019	$1.6x10^{17}$	$3.1x10^{13}$	$4.7x10^{-5}$	$2.6x10^{-5}$
28 Feb 2019	$1.1x10^{17}$	$3.3x10^{13}$	$1.7x10^{-4}$	$3.0x10^{-5}$
1 Mar 2019	$1.5x10^{17}$	$3.6x10^{13}$	$1.5x10^{-5}$	$2.4x10^{-5}$
5 Mar 2019	$1.4x10^{17}$	$3.6x10^{13}$	$7.7x10^{-5}$	$1.9x10^{-5}$
6 Mar 2019	$1.9x10^{17}$	$3.3x10^{13}$	$1.1x10^{-4}$	$1.8x10^{-5}$
7 Mar 2019	$1.9x10^{17}$	$3.8x10^{13}$	$1.1x10^{-4}$	$2.1x10^{-5}$
9 Mar 2019	$2.7x10^{17}$	$4.4x10^{13}$	$9.3x10^{-5}$	$1.6x10^{-5}$
10 Mar 2019	$1.6x10^{17}$	$3.3x10^{13}$	$1.2x10^{-4}$	$1.5x10^{-5}$
11 Mar 2019	$1.1x10^{17}$	$2.8x10^{13}$	$6.8x10^{-5}$	$1.4x10^{-5}$
14 Mar 2019	$6.8x10^{16}$	$2.1x10^{13}$	$1.0x10^{-4}$	$4.1x10^{-5}$
16 Mar 2019	$1.1x10^{17}$	$3.5x10^{13}$	$4.0x10^{-5}$	$9.1x10^{-6}$
20 Mar 2019	$6.1x10^{16}$	$1.8x10^{13}$	$1.3x10^{-5}$	$2.6x10^{-5}$
21 Mar 2019	$1.3x10^{17}$	$2.7x10^{13}$	$1.2x10^{-4}$	$1.5x10^{-5}$
22 Mar 2019	$1.0x10^{17}$	$2.9x10^{13}$	$5.9x10^{-5}$	$2.6x10^{-5}$
31 Mar 2019	$9.1x10^{16}$	$1.3x10^{13}$	$9.6x10^{-6}$	$4.1x10^{-5}$
6 April 2019	$2.6x10^{17}$	$4.3x10^{13}$	$3.2x10^{-5}$	$4.6x10^{-5}$
11 April 2019	$8.5x10^{16}$	$2.0x10^{13}$	$2.7x10^{-6}$	$2.5x10^{-5}$
16 April 2019	$1.3x10^{17}$	$2.5x10^{13}$	$9.2x10^{-5}$	$1.5x10^{-5}$
17 April 2019	$1.2x10^{17}$	$2.5x10^{13}$	$4.6x10^{-6}$	$2.5x10^{-5}$
18 April 2019	$1.7x10^{17}$	$2.1x10^{13}$	$1.8x10^{-6}$	$2.1x10^{-5}$

Popocatepetl, Mexico

date	SO_2 VCD max. [molecules cm^{-2}]	BrO VCD	BrO/SO_2 fitted	BrO/SO_2 error
22 April 2019	$8.5x10^{16}$	$2.7x10^{13}$	$6.4x10^{-5}$	$4.3x10^{-5}$
23 April 2019	$1.3x10^{17}$	$1.9x10^{13}$	$5.7x10^{-6}$	$2.2x10^{-5}$
27 April 2019	$7.3x10^{16}$	$2.1x10^{13}$	$5.0x10^{-5}$	$3.3x10^{-5}$
28 April 2019	$6.9x10^{16}$	$1.9x10^{13}$	$9.8x10^{-6}$	$4.3x10^{-5}$
29 April 2019	$1.3x10^{17}$	$1.7x10^{13}$	$3.1x10^{-5}$	$2.6x10^{-5}$
3 May 2019	$8.8x10^{16}$	$2.5x10^{13}$	$1.2x10^{-5}$	$4.9x10^{-5}$
4 May 2019	$1.3x10^{17}$	$2.1x10^{13}$	$2.5x10^{-9}$	$3.0x10^{-5}$
15 May 2019	$9.2x10^{16}$	$2.6x10^{13}$	$1.2x10^{-5}$	$3.2x10^{-5}$
24 May 2019	$1.8x10^{17}$	$2.4x10^{13}$	$1.3x10^{-5}$	$2.9x10^{-5}$
28 May 2019	$1.7x10^{17}$	$1.8x10^{13}$	$1.5x10^{-5}$	$2.5x10^{-5}$
29 May 2019	$1.7x10^{17}$	$2.1x10^{13}$	$2.5x10^{-5}$	$3.5x10^{-5}$
30 May 2019	$9.6x10^{16}$	$1.9x10^{13}$	$1.9x10^{-6}$	$6.1x10^{-5}$
3 June 2019	$2.0x10^{17}$	$3.8x10^{13}$	$4.4x10^{-5}$	$1.3x10^{-5}$
4 June 2019	$5.6x10^{17}$	$2.3x10^{13}$	$2.1x10^{-5}$	$1.8x10^{-5}$
5 June 2019	$2.9x10^{17}$	$3.4x10^{13}$	$3.9x10^{-5}$	$1.6x10^{-5}$
6 June 2019	$1.0x10^{17}$	$1.3x10^{13}$	$2.0x10^{-5}$	$4.7x10^{-5}$
9 June 2019	$7.7x10^{16}$	$2.9x10^{13}$	$3.5x10^{-5}$	$2.3x10^{-5}$
14 June 2019	$4.3x10^{17}$	$3.7x10^{13}$	$6.0x10^{-5}$	$7.0x10^{-6}$
15 June 2019	$8.5x10^{16}$	$2.1x10^{13}$	$5.0x10^{-5}$	$3.2x10^{-5}$
19 June 2019	$2.3x10^{17}$	$3.9x10^{13}$	$2.2x10^{-5}$	$2.4x10^{-5}$
20 June 2019	$3.7x10^{17}$	$3.5x10^{13}$	$3.6x10^{-5}$	$1.2x10^{-5}$
24 June 2019	$1.1x10^{17}$	$1.3x10^{13}$	$2.1x10^{-5}$	$4.7x10^{-5}$
26 June 2019	$3.0x10^{17}$	$4.2x10^{13}$	$2.5x10^{-6}$	$2.0x10^{-5}$
29 June 2019	$2.0x10^{17}$	$2.2x10^{13}$	$4.0x10^{-5}$	$1.8x10^{-5}$
30 June 2019	$1.5x10^{17}$	$5.5x10^{13}$	$3.3x10^{-5}$	$2.1x10^{-5}$
1 July 2019	$2.8x10^{17}$	$2.2x10^{13}$	$1.8x10^{-5}$	$1.6x10^{-5}$
6 July 2019	$1.5x10^{17}$	$3.7x10^{13}$	$6.4x10^{-5}$	$2.8x10^{-5}$
10 July 2019	$1.0x10^{17}$	$2.1x10^{13}$	$4.1x10^{-5}$	$6.3x10^{-5}$
11 July 2019	$1.0x10^{17}$	$2.0x10^{13}$	$4.0x10^{-5}$	$3.6x10^{-5}$
12 July 2019	$2.4x10^{17}$	$3.1x10^{13}$	$4.1x10^{-6}$	$1.4x10^{-5}$
16 July 2019	$6.4x10^{16}$	$2.7x10^{13}$	$4.6x10^{-5}$	$3.0x10^{-5}$
17 July 2019	$1.7x10^{17}$	$1.5x10^{13}$	$2.1x10^{-5}$	$3.1x10^{-5}$
22 July 2019	$2.3x10^{17}$	$2.9x10^{13}$	$2.2x10^{-5}$	$2.5x10^{-5}$
23 July 2019	$3.1x10^{17}$	$2.4x10^{13}$	$5.6x10^{-6}$	$2.2x10^{-5}$
26 July 2019	$1.4x10^{17}$	$2.4x10^{13}$	$2.3x10^{-5}$	$1.4x10^{-5}$
27 July 2019	$1.4x10^{17}$	$3.1x10^{13}$	$4.7x10^{-5}$	$4.2x10^{-5}$
28 July 2019	$2.2x10^{17}$	$1.6x10^{13}$	$1.5x10^{-5}$	$2.7x10^{-5}$
31 July 2019	$1.0x10^{17}$	$1.8x10^{13}$	$5.4x10^{-5}$	$5.6x10^{-5}$
1 Aug 2019	$1.7x10^{17}$	$3.8x10^{13}$	$5.4x10^{-5}$	$2.8x10^{-5}$
2 Aug 2019	$2.6x10^{17}$	$2.7x10^{13}$	$2.9x10^{-5}$	$2.3x10^{-5}$
3 Aug 2019	$3.1x10^{17}$	$2.1x10^{13}$	$1.9x10^{-5}$	$1.7x10^{-5}$
6 Aug 2019	$1.2x10^{17}$	$2.9x10^{13}$	$1.2x10^{-6}$	$3.1x10^{-5}$
7 Aug 2019	$2.6x10^{17}$	$2.0x10^{13}$	$5.4x10^{-5}$	$4.9x10^{-5}$
8 Aug 2019	$8.0x10^{16}$	$4.2x10^{13}$	$7.1x10^{-5}$	$6.5x10^{-5}$
12 Aug 2019	$1.2x10^{17}$	$3.8x10^{13}$	$1.3x10^{-5}$	$3.3x10^{-5}$
13 Aug 2019	$1.5x10^{17}$	$1.8x10^{13}$	$1.3x10^{-5}$	$4.0x10^{-5}$
16 Aug 2019	$1.1x10^{17}$	$3.3x10^{13}$	$7.8x10^{-5}$	$3.4x10^{-5}$
17 Aug 2019	$1.5x10^{17}$	$4.6x10^{13}$	$9.4x10^{-6}$	$2.2x10^{-5}$
22 Aug 2019	$3.7x10^{17}$	$3.2x10^{13}$	$9.1x10^{-6}$	$1.7x10^{-5}$
23 Aug 2019	$4.7x10^{17}$	$9.2x10^{13}$	$2.6x10^{-5}$	$1.1x10^{-5}$
24 Aug 2019	$7.2x10^{16}$	$3.1x10^{13}$	$1.1x10^{-4}$	$3.7x10^{-5}$
1 Sept 2019	$1.2x10^{17}$	$2.2x10^{13}$	$9.1x10^{-5}$	$2.8x10^{-5}$
2 Sept 2019	$1.5x10^{17}$	$4.8x10^{13}$	$3.9x10^{-5}$	$2.1x10^{-5}$
3 Sept 2019	$4.8x10^{17}$	$4.9x10^{13}$	$3.2x10^{-5}$	$1.9x10^{-5}$
7 Sept 2019	$1.8x10^{17}$	$3.5x10^{13}$	$7.7x10^{-7}$	$2.2x10^{-5}$
8 Sept 2019	$3.2x10^{17}$	$3.3x10^{13}$	$2.6x10^{-5}$	$1.8x10^{-5}$
9 Sept 2019	$2.0x10^{17}$	$3.9x10^{13}$	$1.6x10^{-5}$	$2.6x10^{-5}$
11 Sept 2019	$9.7x10^{16}$	$1.8x10^{13}$	$9.4x10^{-5}$	$4.3x10^{-5}$
12 Sept 2019	$1.2x10^{17}$	$2.3x10^{13}$	$4.1x10^{-5}$	$2.4x10^{-5}$
13 Sept 2019	$4.7x10^{17}$	$3.1x10^{13}$	$4.1x10^{-6}$	$1.9x10^{-5}$
14 Sept 2019	$1.4x10^{17}$	$2.3x10^{13}$	$4.1x10^{-6}$	$4.8x10^{-5}$
18 Sept 2019	$5.9x10^{17}$	$3.8x10^{13}$	$1.7x10^{-5}$	$1.6x10^{-5}$
19 Sept 2019	$2.3x10^{17}$	$3.5x10^{13}$	$3.1x10^{-5}$	$3.3x10^{-5}$
22 Sept 2019	$1.2x10^{17}$	$2.3x10^{13}$	$4.5x10^{-5}$	$3.5x10^{-5}$
23 Sept 2019	$2.2x10^{17}$	$2.4x10^{13}$	$3.1x10^{-5}$	$2.5x10^{-5}$
24 Sept 2019	$3.0x10^{17}$	$3.4x10^{13}$	$4.0x10^{-5}$	$3.6x10^{-5}$
25 Sept 2019	$1.3x10^{17}$	$3.0x10^{13}$	$3.5x10^{-5}$	$2.6x10^{-5}$
26 Sept 2019	$8.9x10^{16}$	$2.4x10^{13}$	$6.2x10^{-5}$	$2.4x10^{-5}$
29 Sept 2019	$1.8x10^{17}$	$1.4x10^{13}$	$5.2x10^{-6}$	$2.5x10^{-5}$
30 Sept 2019	$1.3x10^{17}$	$2.9x10^{13}$	$1.4x10^{-5}$	$3.9x10^{-5}$
4 Oct 2019	$4.2x10^{17}$	$3.0x10^{13}$	$2.9x10^{-5}$	$2.3x10^{-5}$

Popocatepetl, Mexico

date	SO_2 VCD max. [molecules cm^{-2}]	BrO VCD	BrO/SO_2 fitted	BrO/SO_2 error
5 Oct 2019	$2.9x10^{17}$	$3.3x10^{13}$	$5.7x10^{-5}$	$2.1x10^{-5}$
10 Oct 2019	$1.6x10^{17}$	$3.6x10^{13}$	$4.5x10^{-5}$	$3.2x10^{-5}$
11 Oct 2019	$1.0x10^{17}$	$4.2x10^{13}$	$8.8x10^{-5}$	$3.8x10^{-5}$
14 Oct 2019	$1.1x10^{17}$	$2.9x10^{13}$	$1.9x10^{-4}$	$5.3x10^{-5}$
15 Oct 2019	$8.2x10^{16}$	$3.4x10^{13}$	$9.7x10^{-5}$	$6.4x10^{-5}$
21 Oct 2019	$1.8x10^{17}$	$2.4x10^{13}$	$2.6x10^{-5}$	$3.3x10^{-5}$
26 Oct 2019	$2.1x10^{17}$	$4.5x10^{13}$	$2.5x10^{-6}$	$2.8x10^{-5}$
27 Oct 2019	$1.4x10^{17}$	$2.1x10^{13}$	$4.0x10^{-5}$	$4.3x10^{-5}$
30 Oct 2019	$1.4x10^{17}$	$3.1x10^{13}$	$1.5x10^{-5}$	$2.2x10^{-5}$
31 Oct 2019	$8.7x10^{16}$	$2.1x10^{13}$	$6.0x10^{-6}$	$4.4x10^{-5}$
1 Nov 2019	$1.6x10^{17}$	$2.6x10^{13}$	$1.1x10^{-4}$	$5.2x10^{-5}$
2 Nov 2019	$4.2x10^{17}$	$5.8x10^{13}$	$1.2x10^{-4}$	$1.4x10^{-5}$
4 Nov 2019	$8.8x10^{16}$	$2.5x10^{13}$	$6.2x10^{-5}$	$2.8x10^{-5}$
5 Nov 2019	$1.3x10^{17}$	$3.8x10^{13}$	$2.8x10^{-6}$	$3.4x10^{-5}$
9 Nov 2019	$8.7x10^{16}$	$2.6x10^{13}$	$1.6x10^{-4}$	$4.2x10^{-5}$
10 Nov 2019	$1.1x10^{17}$	$2.8x10^{13}$	$1.4x10^{-4}$	$3.6x10^{-5}$
15 Nov 2019	$1.8x10^{17}$	$2.5x10^{13}$	$7.9x10^{-5}$	$3.9x10^{-5}$
16 Nov 2019	$2.0x10^{17}$	$2.2x10^{13}$	$2.0x10^{-5}$	$2.4x10^{-5}$
17 Nov 2019	$1.1x10^{17}$	$4.5x10^{13}$	$8.5x10^{-5}$	$3.2x10^{-5}$
21 Nov 2019	$3.3x10^{17}$	$3.6x10^{13}$	$7.3x10^{-5}$	$1.8x10^{-5}$
22 Nov 2019	$1.8x10^{17}$	$3.8x10^{13}$	$7.7x10^{-5}$	$4.0x10^{-5}$
2 Dec 2019	$1.3x10^{17}$	$2.3x10^{13}$	$8.1x10^{-5}$	$4.8x10^{-5}$
3 Dec 2019	$3.0x10^{17}$	$4.5x10^{13}$	$7.8x10^{-5}$	$1.8x10^{-5}$
25 Dec 2019	$1.3x10^{17}$	$1.5x10^{13}$	$2.0x10^{-5}$	$4.3x10^{-5}$
20 Jan 2020	$8.8x10^{16}$	$2.4x10^{13}$	$2.5x10^{-5}$	$4.5x10^{-5}$
14 Feb 2020	$1.3x10^{17}$	$3.4x10^{13}$	$5.3x10^{-5}$	$3.0x10^{-5}$
15 Feb 2020	$1.2x10^{17}$	$3.4x10^{13}$	$8.9x10^{-5}$	$3.3x10^{-5}$
21 Feb 2020	$1.6x10^{17}$	$2.2x10^{13}$	$1.7x10^{-5}$	$2.6x10^{-5}$
6 Mar 2020	$7.9x10^{16}$	$1.9x10^{13}$	$2.1x10^{-5}$	$3.7x10^{-5}$
8 Mar 2020	$1.1x10^{17}$	$2.3x10^{13}$	$8.8x10^{-7}$	$4.3x10^{-5}$
12 Mar 2020	$8.1x10^{16}$	$2.1x10^{13}$	$1.3x10^{-5}$	$3.9x10^{-5}$
18 Mar 2020	$3.0x10^{17}$	$4.5x10^{13}$	$7.0x10^{-5}$	$2.2x10^{-5}$
21 Mar 2020	$1.0x10^{17}$	$2.2x10^{13}$	$8.9x10^{-5}$	$4.4x10^{-5}$
22 Mar 2020	$1.5x10^{17}$	$2.7x10^{13}$	$6.8x10^{-5}$	$2.6x10^{-5}$
23 Mar 2020	$6.8x10^{16}$	$4.1x10^{13}$	$7.0x10^{-5}$	$5.2x10^{-5}$
2 April 2020	$1.5x10^{17}$	$2.9x10^{13}$	$9.5x10^{-5}$	$4.3x10^{-5}$
3 April 2020	$2.1x10^{17}$	$3.3x10^{13}$	$2.2x10^{-6}$	$3.7x10^{-5}$
4 April 2020	$6.8x10^{16}$	$3.8x10^{13}$	$7.9x10^{-6}$	$5.3x10^{-5}$
6 May 2020	$8.7x10^{16}$	$3.5x10^{13}$	$2.1x10^{-6}$	$5.9x10^{-5}$
11 May 2020	$8.6x10^{16}$	$2.8x10^{13}$	$4.2x10^{-5}$	$6.5x10^{-5}$
15 May 2020	$6.8x10^{16}$	$1.5x10^{13}$	$0.7x10^{-6}$	$4.2x10^{-5}$
21 May 2020	$9.2x10^{16}$	$2.3x10^{13}$	$7.7x10^{-5}$	$4.2x10^{-5}$
26 May 2020	$8.6x10^{16}$	$2.9x10^{13}$	$4.2x10^{-5}$	$4.5x10^{-5}$
6 June 2020	$9.9x10^{16}$	$4.6x10^{13}$	$5.6x10^{-5}$	$7.6x10^{-5}$
15 June 2020	$1.1x10^{17}$	$2.7x10^{13}$	$8.6x10^{-5}$	$4.0x10^{-5}$
16 June 2020	$1.6x10^{17}$	$2.2x10^{13}$	$3.2x10^{-5}$	$2.5x10^{-5}$
17 June 2020	$1.2x10^{17}$	$3.3x10^{13}$	$3.3x10^{-5}$	$2.4x10^{-5}$
21 June 2020	$9.2x10^{16}$	$2.2x10^{13}$	$1.2x10^{-5}$	$5.0x10^{-5}$
26 June 2020	$1.1x10^{17}$	$4.5x10^{13}$	$1.6x10^{-4}$	$5.7x10^{-5}$
12 July 2020	$7.6x10^{16}$	$4.6x10^{13}$	$3.2x10^{-5}$	$5.8x10^{-5}$
13 July 2020	$1.1x10^{17}$	$4.1x10^{13}$	$1.9x10^{-7}$	$4.2x10^{-5}$
14 July 2020	$1.1x10^{17}$	$3.8x10^{13}$	$1.3x10^{-4}$	$6.4x10^{-5}$
19 July 2020	$1.7x10^{17}$	$2.8x10^{13}$	$2.2x10^{-5}$	$3.6x10^{-5}$
22 July 2020	$2.2x10^{17}$	$3.5x10^{13}$	$9.9x10^{-5}$	$1.6x10^{-5}$
23 July 2020	$3.1x10^{17}$	$5.0x10^{13}$	$9.5x10^{-5}$	$9.6x10^{-6}$
24 July 2020	$6.2x10^{17}$	$6.4x10^{13}$	$9.8x10^{-5}$	$6.6x10^{-6}$
25 July 2020	$5.8x10^{17}$	$8.2x10^{13}$	$9.2x10^{-5}$	$8.5x10^{-6}$
26 July 2020	$2.0x10^{17}$	$3.8x10^{13}$	$1.0x10^{-4}$	$1.7x10^{-5}$
27 July 2020	$8.7x10^{16}$	$2.0x10^{13}$	$8.2x10^{-5}$	$2.2x10^{-5}$
28 July 2020	$7.0x10^{17}$	$5.1x10^{13}$	$9.3x10^{-5}$	$6.5x10^{-6}$
29 July 2020	$7.6x10^{17}$	$8.2x10^{13}$	$1.0x10^{-4}$	$5.5x10^{-6}$
30 July 2020	$6.0x10^{17}$	$9.9x10^{13}$	$1.1x10^{-4}$	$1.2x10^{-5}$
31 July 2020	$9.6x10^{16}$	$3.5x10^{13}$	$1.5x10^{-4}$	$2.8x10^{-5}$
1 Aug 2020	$1.6x10^{17}$	$2.5x10^{13}$	$7.7x10^{-5}$	$2.6x10^{-5}$
3 Aug 2020	$4.5x10^{17}$	$8.1x10^{13}$	$1.2x10^{-4}$	$5.1x10^{-6}$
4 Aug 2020	$8.7x10^{17}$	$1.0x10^{14}$	$1.2x10^{-4}$	$6.7x10^{-6}$
5 Aug 2020	$2.8x10^{17}$	$4.6x10^{13}$	$1.2x10^{-4}$	$1.9x10^{-5}$
8 Aug 2020	$1.3x10^{17}$	$2.9x10^{13}$	$9.5x10^{-5}$	$3.3x10^{-5}$
9 Aug 2020	$8.4x10^{17}$	$9.5x10^{13}$	$8.7x10^{-5}$	$7.5x10^{-6}$
10 Aug 2020	$2.0x10^{17}$	$4.1x10^{13}$	$1.5x10^{-4}$	$3.3x10^{-5}$
15 Aug 2020	$1.3x10^{17}$	$4.1x10^{13}$	$1.5x10^{-4}$	$6.1x10^{-5}$

Popocatepetl, Mexico

date	SO_2 VCD max. [molecules cm^{-2}]	BrO VCD	BrO/SO_2 fitted	BrO/SO_2 error
18 Aug 2020	$3.2x10^{17}$	$4.4x10^{13}$	$1.1x10^{-4}$	$2.8x10^{-5}$
19 Aug 2020	$8.9x10^{17}$	$4.9x10^{13}$	$5.3x10^{-5}$	$1.1x10^{-5}$
20 Aug 2020	$2.2x10^{17}$	$2.9x10^{13}$	$4.6x10^{-5}$	$1.6x10^{-5}$
21 Aug 2020	$2.4x10^{17}$	$3.7x10^{13}$	$4.3x10^{-5}$	$1.7x10^{-5}$
23 Aug 2020	$2.4x10^{17}$	$5.4x10^{13}$	$1.2x10^{-4}$	$2.4x10^{-5}$
24 Aug 2020	$1.2x10^{17}$	$3.5x10^{13}$	$6.9x10^{-5}$	$1.8x10^{-5}$
25 Aug 2020	$1.4x10^{17}$	$4.2x10^{13}$	$9.2x10^{-5}$	$2.3x10^{-5}$
29 Aug 2020	$1.7x10^{17}$	$3.6x10^{13}$	$6.4x10^{-5}$	$2.3x10^{-5}$
30 Aug 2020	$3.7x10^{17}$	$3.9x10^{13}$	$1.0x10^{-4}$	$1.9x10^{-5}$
5 Sept 2020	$1.3x10^{17}$	$1.9x10^{13}$	$6.4x10^{-5}$	$2.0x10^{-5}$
8 Sept 2020	$1.7x10^{17}$	$3.2x10^{13}$	$1.5x10^{-4}$	$3.1x10^{-5}$
9 Sept 2020	$2.6x10^{17}$	$4.5x10^{13}$	$1.0x10^{-4}$	$4.3x10^{-5}$
10 Sept 2020	$1.1x10^{17}$	$3.0x10^{13}$	$1.3x10^{-4}$	$5.1x10^{-5}$
13 Sept 2020	$1.1x10^{17}$	$2.0x10^{13}$	$6.8x10^{-5}$	$2.5x10^{-5}$
14 Sept 2020	$1.9x10^{17}$	$3.1x10^{13}$	$9.3x10^{-5}$	$1.3x10^{-5}$
15 Sept 2020	$2.5x10^{17}$	$4.1x10^{13}$	$9.7x10^{-5}$	$1.5x10^{-5}$
16 Sept 2020	$5.0x10^{17}$	$4.4x10^{13}$	$9.0x10^{-5}$	$9.4x10^{-6}$
17 Sept 2020	$2.5x10^{17}$	$2.4x10^{13}$	$7.0x10^{-5}$	$1.3x10^{-5}$
19 Sept 2020	$2.5x10^{17}$	$2.6x10^{13}$	$8.2x10^{-5}$	$8.9x10^{-6}$
20 Sept 2020	$2.4x10^{17}$	$4.1x10^{13}$	$2.1x10^{-5}$	$2.1x10^{-5}$
21 Sept 2020	$2.2x10^{17}$	$3.8x10^{13}$	$5.3x10^{-5}$	$2.2x10^{-5}$
22 Sept 2020	$1.3x10^{17}$	$2.8x10^{13}$	$0.7x10^{-5}$	$3.9x10^{-5}$
25 Sept 2020	$3.2x10^{17}$	$1.3x10^{13}$	$3.2x10^{-5}$	$1.9x10^{-5}$
26 Sept 2020	$1.4x10^{17}$	$2.8x10^{13}$	$6.9x10^{-5}$	$2.5x10^{-5}$
27 Sept 2020	$2.0x10^{17}$	$2.9x10^{13}$	$6.3x10^{-5}$	$1.5x10^{-5}$
30 Sept 2020	$1.7x10^{17}$	$2.8x10^{13}$	$9.3x10^{-5}$	$2.4x10^{-5}$
1 Oct 2020	$4.0x10^{17}$	$4.7x10^{13}$	$1.1x10^{-4}$	$1.7x10^{-5}$
2 Oct 2020	$1.1x10^{17}$	$2.6x10^{13}$	$8.8x10^{-5}$	$2.8x10^{-5}$
5 Oct 2020	$8.5x10^{16}$	$2.1x10^{13}$	$1.1x10^{-4}$	$3.1x10^{-5}$
7 Oct 2020	$2.2x10^{17}$	$4.1x10^{13}$	$1.2x10^{-4}$	$2.1x10^{-5}$
8 Oct 2020	$1.0x10^{17}$	$4.6x10^{13}$	$9.4x10^{-5}$	$4.3x10^{-5}$
10 Oct 2020	$1.2x10^{17}$	$2.3x10^{13}$	$1.4x10^{-4}$	$3.1x10^{-5}$
11 Oct 2020	$1.1x10^{17}$	$3.4x10^{13}$	$7.7x10^{-5}$	$2.9x10^{-5}$
12 Oct 2020	$1.6x10^{17}$	$3.7x10^{13}$	$7.0x10^{-5}$	$3.7x10^{-5}$
13 Oct 2020	$1.5x10^{17}$	$3.4x10^{13}$	$1.3x10^{-4}$	$3.0x10^{-5}$
17 Oct 2020	$3.6x10^{17}$	$5.3x10^{13}$	$1.2x10^{-4}$	$3.2x10^{-5}$
18 Oct 2020	$1.7x10^{17}$	$3.2x10^{13}$	$8.6x10^{-5}$	$2.1x10^{-5}$
19 Oct 2020	$1.1x10^{17}$	$2.7x10^{13}$	$1.0x10^{-4}$	$4.3x10^{-5}$
21 Oct 2020	$9.9x10^{16}$	$3.1x10^{13}$	$1.2x10^{-4}$	$3.6x10^{-5}$
22 Oct 2020	$3.6x10^{17}$	$6.6x10^{13}$	$1.2x10^{-4}$	$1.4x10^{-5}$
23 Oct 2020	$1.5x10^{17}$	$4.0x10^{13}$	$8.1x10^{-5}$	$2.4x10^{-5}$
28 Oct 2020	$1.0x10^{17}$	$3.3x10^{13}$	$1.1x10^{-4}$	$5.8x10^{-5}$
6 Nov 2020	$1.3x10^{17}$	$2.3x10^{13}$	$5.9x10^{-5}$	$5.3x10^{-5}$
30 Nov 2020	$1.0x10^{17}$	$2.5x10^{13}$	$1.3x10^{-5}$	$3.9x10^{-5}$
9 Dec 2020	$9.4x10^{16}$	$2.9x10^{13}$	$1.2x10^{-5}$	$4.3x10^{-5}$
16 Jan 2021	$9.7x10^{16}$	$3.7x10^{13}$	$1.3x10^{-4}$	$2.1x10^{-5}$
21 Jan 2021	$2.6x10^{17}$	$3.1x10^{13}$	$7.6x10^{-5}$	$2.5x10^{-5}$
26 Jan 2021	$6.1x10^{16}$	$2.3x10^{13}$	$1.3x10^{-4}$	$2.7x10^{-5}$
28 Jan 2021	$1.2x10^{17}$	$2.8x10^{13}$	$1.5x10^{-4}$	$5.4x10^{-5}$
31 Jan 2021	$1.6x10^{17}$	$2.5x10^{13}$	$1.3x10^{-4}$	$2.9x10^{-5}$
1 Feb 2021	$1.5x10^{17}$	$3.5x10^{13}$	$1.0x10^{-4}$	$4.5x10^{-5}$
2 Feb 2021	$8.3x10^{16}$	$2.3x10^{13}$	$8.9x10^{-5}$	$5.5x10^{-5}$
7 Feb 2021	$9.2x10^{16}$	$3.1x10^{13}$	$4.3x10^{-5}$	$3.5x10^{-5}$
21 Feb 2021	$7.6x10^{16}$	$2.2x10^{13}$	$6.4x10^{-5}$	$4.7x10^{-5}$
22 Feb 2021	$1.5x10^{17}$	$3.4x10^{13}$	$6.0x10^{-5}$	$2.7x10^{-5}$
5 Mar 2021	$1.1x10^{17}$	$2.4x10^{13}$	$8.2x10^{-5}$	$2.7x10^{-5}$
1 April 2021	$1.5x10^{17}$	$4.4x10^{13}$	$1.2x10^{-4}$	$2.9x10^{-5}$
2 April 2021	$3.4x10^{17}$	$5.6x10^{13}$	$9.7x10^{-5}$	$2.5x10^{-5}$
4 April 2021	$1.0x10^{17}$	$2.5x10^{13}$	$8.4x10^{-5}$	$4.0x10^{-5}$
5 April 2021	$8.8x10^{16}$	$2.3x10^{13}$	$4.9x10^{-5}$	$4.1x10^{-5}$
7 April 2021	$7.7x10^{16}$	$2.6x10^{13}$	$1.1x10^{-4}$	$4.7x10^{-5}$
11 April 2021	$1.9x10^{17}$	$2.3x10^{13}$	$2.3x10^{-5}$	$3.3x10^{-5}$
15 April 2021	$9.4x10^{16}$	$1.6x10^{13}$	$4.6x10^{-6}$	$6.8x10^{-5}$
16 April 2021	$1.5x10^{17}$	$2.6x10^{13}$	$9.9x10^{-5}$	$2.6x10^{-5}$
21 April 2021	$1.5x10^{17}$	$4.0x10^{13}$	$5.6x10^{-5}$	$2.9x10^{-5}$
22 April 2021	$2.7x10^{17}$	$2.9x10^{13}$	$1.3x10^{-5}$	$2.4x10^{-5}$
24 April 2021	$1.1x10^{17}$	$1.9x10^{13}$	$1.0x10^{-4}$	$4.2x10^{-5}$
27 April 2021	$2.5x10^{17}$	$3.7x10^{13}$	$7.6x10^{-5}$	$2.6x10^{-5}$
28 April 2021	$1.3x10^{17}$	$2.9x10^{13}$	$5.7x10^{-5}$	$7.5x10^{-5}$
29 April 2021	$8.2x10^{16}$	$1.3x10^{13}$	$4.5x10^{-5}$	$4.4x10^{-5}$
1 May 2021	$1.3x10^{17}$	$3.4x10^{13}$	$1.4x10^{-4}$	$4.0x10^{-5}$

Popocatepetl, Mexico

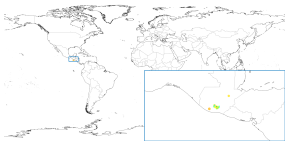
date	SO_2 VCD max. [molecules cm^{-2}]	BrO VCD	BrO/SO_2 fitted	BrO/SO_2 error
2 May 2021	$1.1x10^{17}$	$3.5x10^{13}$	$7.0x10^{-5}$	$2.6x10^{-5}$
3 May 2021	$1.5x10^{17}$	$3.6x10^{13}$	$5.6x10^{-5}$	$2.5x10^{-5}$
4 May 2021	$2.9x10^{17}$	$4.5x10^{13}$	$1.1x10^{-4}$	$2.2x10^{-5}$
7 May 2021	$1.9x10^{17}$	$3.2x10^{13}$	$5.9x10^{-5}$	$1.7x10^{-5}$
8 May 2021	$3.7x10^{17}$	$4.5x10^{13}$	$4.7x10^{-5}$	$1.7x10^{-5}$
9 May 2021	$3.0x10^{17}$	$4.7x10^{13}$	$6.4x10^{-5}$	$1.5x10^{-5}$
12 May 2021	$1.1x10^{17}$	$2.1x10^{13}$	$0.9x10^{-5}$	$3.5x10^{-5}$
14 May 2021	$1.7x10^{17}$	$3.4x10^{13}$	$7.7x10^{-5}$	$1.8x10^{-5}$
15 May 2021	$6.7x10^{16}$	$2.0x10^{13}$	$6.0x10^{-6}$	$4.3x10^{-5}$
18 May 2021	$1.2x10^{17}$	$3.3x10^{13}$	$2.8x10^{-5}$	$3.9x10^{-5}$
19 May 2021	$6.3x10^{16}$	$2.3x10^{13}$	$0.9x10^{-5}$	$3.8x10^{-5}$
23 May 2021	$7.1x10^{16}$	$2.4x10^{13}$	$1.0x10^{-5}$	$3.3x10^{-5}$
24 May 2021	$2.8x10^{17}$	$4.1x10^{13}$	$6.9x10^{-5}$	$2.4x10^{-5}$
25 May 2021	$1.3x10^{17}$	$2.6x10^{13}$	$7.0x10^{-5}$	$4.5x10^{-5}$
29 May 2021	$1.9x10^{17}$	$3.5x10^{13}$	$5.0x10^{-5}$	$3.8x10^{-5}$
2 June 2021	$2.2x10^{17}$	$2.1x10^{13}$	$7.3x10^{-5}$	$2.7x10^{-5}$
4 June 2021	$2.1x10^{17}$	$3.6x10^{13}$	$1.0x10^{-4}$	$2.2x10^{-5}$
8 June 2021	$8.1x10^{16}$	$2.0x10^{13}$	$1.5x10^{-5}$	$5.2x10^{-5}$
9 June 2021	$1.1x10^{17}$	$3.2x10^{13}$	$8.3x10^{-5}$	$4.6x10^{-5}$
10 June 2021	$1.8x10^{17}$	$2.9x10^{13}$	$1.3x10^{-4}$	$3.5x10^{-5}$
13 June 2021	$2.0x10^{17}$	$2.9x10^{13}$	$1.0x10^{-4}$	$4.2x10^{-5}$
14 June 2021	$2.6x10^{17}$	$3.5x10^{13}$	$5.3x10^{-5}$	$2.6x10^{-5}$
15 June 2021	$1.0x10^{17}$	$2.5x10^{13}$	$3.4x10^{-5}$	$5.2x10^{-5}$
17 June 2021	$7.2x10^{16}$	$1.5x10^{13}$	$8.6x10^{-5}$	$4.0x10^{-5}$
20 June 2021	$2.2x10^{17}$	$3.7x10^{13}$	$2.8x10^{-5}$	$4.0x10^{-5}$
21 June 2021	$2.1x10^{17}$	$3.9x10^{13}$	$1.3x10^{-4}$	$3.6x10^{-5}$
25 June 2021	$2.2x10^{17}$	$4.4x10^{13}$	$6.0x10^{-5}$	$4.4x10^{-5}$
26 June 2021	$3.2x10^{17}$	$2.2x10^{13}$	$6.8x10^{-5}$	$2.4x10^{-5}$
29 June 2021	$1.6x10^{17}$	$2.2x10^{13}$	$7.2x10^{-5}$	$2.8x10^{-5}$
30 June 2021	$2.6x10^{17}$	$3.1x10^{13}$	$7.3x10^{-5}$	$2.0x10^{-5}$
1 July 2021	$1.1x10^{17}$	$4.3x10^{13}$	$9.0x10^{-5}$	$3.5x10^{-5}$
4 July 2021	$1.5x10^{17}$	$2.3x10^{13}$	$1.2x10^{-6}$	$3.8x10^{-5}$
5 July 2021	$1.7x10^{17}$	$4.1x10^{13}$	$1.0x10^{-4}$	$3.2x10^{-5}$
6 July 2021	$1.8x10^{17}$	$3.3x10^{13}$	$1.3x10^{-5}$	$2.3x10^{-5}$
11 July 2021	$1.1x10^{17}$	$3.9x10^{13}$	$1.0x10^{-5}$	$5.8x10^{-5}$
15 July 2021	$1.2x10^{17}$	$2.2x10^{13}$	$4.5x10^{-5}$	$3.3x10^{-5}$
16 July 2021	$1.8x10^{17}$	$4.2x10^{13}$	$6.5x10^{-5}$	$3.5x10^{-5}$
17 July 2021	$1.7x10^{17}$	$3.1x10^{13}$	$9.6x10^{-5}$	$1.9x10^{-5}$
20 July 2021	$9.9x10^{16}$	$1.7x10^{13}$	$2.4x10^{-6}$	$4.6x10^{-5}$
21 July 2021	$1.1x10^{17}$	$3.2x10^{13}$	$4.1x10^{-5}$	$8.8x10^{-5}$
22 July 2021	$6.8x10^{16}$	$2.7x10^{13}$	$2.4x10^{-5}$	$1.3x10^{-4}$
25 July 2021	$9.1x10^{16}$	$1.9x10^{13}$	$6.1x10^{-5}$	$4.0x10^{-5}$
26 July 2021	$1.0x10^{17}$	$2.7x10^{13}$	$3.7x10^{-5}$	$5.9x10^{-5}$
27 July 2021	$1.6x10^{17}$	$4.7x10^{13}$	$8.4x10^{-5}$	$2.0x10^{-5}$
28 July 2021	$2.0x10^{17}$	$3.8x10^{13}$	$1.0x10^{-4}$	$3.7x10^{-5}$
31 July 2021	$9.8x10^{16}$	$1.6x10^{13}$	$3.7x10^{-5}$	$5.8x10^{-5}$
1 Aug 2021	$1.3x10^{17}$	$4.0x10^{13}$	$8.4x10^{-5}$	$4.8x10^{-5}$
2 Aug 2021	$1.6x10^{17}$	$2.8x10^{13}$	$9.5x10^{-5}$	$6.2x10^{-5}$
6 Aug 2021	$1.7x10^{17}$	$4.6x10^{13}$	$1.4x10^{-4}$	$5.8x10^{-5}$
11 Aug 2021	$1.2x10^{17}$	$5.5x10^{13}$	$8.0x10^{-5}$	$6.6x10^{-5}$
13 Aug 2021	$1.6x10^{17}$	$2.8x10^{13}$	$5.1x10^{-5}$	$3.3x10^{-5}$
16 Aug 2021	$2.1x10^{17}$	$3.3x10^{13}$	$1.1x10^{-5}$	$2.7x10^{-5}$
17 Aug 2021	$1.4x10^{17}$	$3.0x10^{13}$	$2.5x10^{-6}$	$4.3x10^{-5}$
28 Aug 2021	$8.2x10^{16}$	$3.0x10^{13}$	$6.5x10^{-5}$	$4.5x10^{-5}$
31 Aug 2021	$8.9x10^{16}$	$1.5x10^{13}$	$2.8x10^{-5}$	$2.5x10^{-5}$
1 Sept 2021	$7.6x10^{17}$	$4.2x10^{13}$	$2.6x10^{-5}$	$9.4x10^{-6}$
2 Sept 2021	$2.4x10^{17}$	$3.6x10^{13}$	$1.3x10^{-5}$	$2.3x10^{-5}$
3 Sept 2021	$1.2x10^{17}$	$2.6x10^{13}$	$3.8x10^{-5}$	$3.9x10^{-5}$
4 Sept 2021	$9.4x10^{16}$	$4.2x10^{13}$	$1.1x10^{-4}$	$5.5x10^{-5}$
6 Sept 2021	$1.4x10^{17}$	$2.5x10^{13}$	$1.8x10^{-5}$	$4.0x10^{-5}$
7 Sept 2021	$3.4x10^{17}$	$2.6x10^{13}$	$1.1x10^{-5}$	$2.4x10^{-5}$
8 Sept 2021	$6.7x10^{17}$	$4.2x10^{13}$	$2.4x10^{-5}$	$1.3x10^{-5}$
9 Sept 2021	$2.8x10^{17}$	$2.2x10^{13}$	$3.5x10^{-5}$	$3.2x10^{-5}$
11 Sept 2021	$9.5x10^{16}$	$2.3x10^{13}$	$6.4x10^{-5}$	$2.9x10^{-5}$
12 Sept 2021	$1.7x10^{17}$	$2.6x10^{13}$	$2.0x10^{-5}$	$2.4x10^{-5}$
13 Sept 2021	$2.2x10^{17}$	$2.3x10^{13}$	$1.5x10^{-5}$	$2.4x10^{-5}$
14 Sept 2021	$9.9x10^{16}$	$3.6x10^{13}$	$8.8x10^{-5}$	$4.3x10^{-5}$
17 Sept 2021	$1.0x10^{17}$	$2.8x10^{13}$	$6.7x10^{-5}$	$2.9x10^{-5}$
23 Sept 2021	$1.4x10^{17}$	$3.1x10^{13}$	$6.5x10^{-5}$	$4.6x10^{-5}$
24 Sept 2021	$2.3x10^{17}$	$2.6x10^{13}$	$3.9x10^{-5}$	$1.8x10^{-5}$
25 Sept 2021	$7.8x10^{16}$	$2.4x10^{13}$	$5.7x10^{-5}$	$3.8x10^{-5}$

Popocatepetl, Mexico

date	SO_2 VCD max. [molecules cm^{-2}]	BrO VCD	BrO/SO_2 fitted	BrO/SO_2 error
28 Sept 2021	$1.7x10^{17}$	$2.2x10^{13}$	$2.6x10^{-5}$	$4.5x10^{-5}$
29 Sept 2021	$2.0x10^{17}$	$3.0x10^{13}$	$4.5x10^{-6}$	$3.6x10^{-5}$
3 Oct 2021	$1.2x10^{17}$	$2.5x10^{13}$	$1.2x10^{-4}$	$4.4x10^{-5}$
4 Oct 2021	$1.5x10^{17}$	$2.9x10^{13}$	$7.1x10^{-5}$	$6.1x10^{-5}$
5 Oct 2021	$9.5x10^{16}$	$3.9x10^{13}$	$1.0x10^{-4}$	$4.2x10^{-5}$
20 Oct 2021	$3.7x10^{17}$	$2.6x10^{13}$	$1.6x10^{-5}$	$1.9x10^{-5}$
21 Oct 2021	$8.6x10^{16}$	$3.0x10^{13}$	$5.7x10^{-5}$	$5.3x10^{-5}$
22 Oct 2021	$1.1x10^{17}$	$2.9x10^{13}$	$1.2x10^{-4}$	$4.2x10^{-5}$
26 Oct 2021	$2.9x10^{17}$	$3.1x10^{13}$	$1.5x10^{-5}$	$3.4x10^{-5}$
31 Oct 2021	$9.1x10^{16}$	$3.0x10^{13}$	$7.0x10^{-5}$	$3.3x10^{-5}$
5 Nov 2021	$1.2x10^{17}$	$3.6x10^{13}$	$3.6x10^{-5}$	$2.5x10^{-5}$
11 Nov 2021	$2.4x10^{17}$	$3.4x10^{13}$	$4.6x10^{-5}$	$3.5x10^{-5}$
12 Nov 2021	$7.8x10^{16}$	$1.6x10^{13}$	$8.7x10^{-5}$	$4.0x10^{-5}$
14 Nov 2021	$1.2x10^{17}$	$1.8x10^{13}$	$6.7x10^{-5}$	$3.2x10^{-5}$
15 Nov 2021	$6.7x10^{16}$	$2.5x10^{13}$	$1.2x10^{-4}$	$6.0x10^{-5}$
16 Nov 2021	$8.0x10^{16}$	$2.8x10^{13}$	$8.2x10^{-5}$	$3.1x10^{-5}$
20 Nov 2021	$2.4x10^{17}$	$2.5x10^{13}$	$5.2x10^{-5}$	$3.5x10^{-5}$
21 Nov 2021	$1.8x10^{17}$	$3.8x10^{13}$	$9.1x10^{-5}$	$4.1x10^{-5}$
22 Nov 2021	$9.5x10^{16}$	$2.8x10^{13}$	$9.7x10^{-5}$	$5.1x10^{-5}$
26 Nov 2021	$1.0x10^{17}$	$2.8x10^{13}$	$1.2x10^{-4}$	$6.3x10^{-5}$
27 Nov 2021	$9.5x10^{16}$	$3.5x10^{13}$	$9.9x10^{-5}$	$2.1x10^{-5}$
1 Dec 2021	$1.1x10^{17}$	$2.9x10^{13}$	$1.1x10^{-4}$	$2.5x10^{-5}$
2 Dec 2021	$1.4x10^{17}$	$3.4x10^{13}$	$1.5x10^{-4}$	$4.1x10^{-5}$
3 Dec 2021	$1.5x10^{17}$	$2.8x10^{13}$	$1.2x10^{-4}$	$1.9x10^{-5}$
7 Dec 2021	$1.5x10^{17}$	$2.9x10^{13}$	$1.1x10^{-4}$	$3.9x10^{-5}$
8 Dec 2021	$1.9x10^{17}$	$3.2x10^{13}$	$1.2x10^{-4}$	$3.1x10^{-5}$
12 Dec 2021	$8.0x10^{16}$	$2.2x10^{13}$	$1.0x10^{-5}$	$5.5x10^{-5}$
13 Dec 2021	$1.4x10^{17}$	$3.8x10^{13}$	$1.7x10^{-4}$	$3.7x10^{-5}$
16 Dec 2021	$8.9x10^{16}$	$2.0x10^{13}$	$1.5x10^{-4}$	$3.1x10^{-5}$
18 Dec 2021	$9.5x10^{16}$	$4.3x10^{13}$	$4.0x10^{-5}$	$2.4x10^{-5}$
24 Dec 2021	$1.5x10^{17}$	$2.8x10^{13}$	$1.1x10^{-4}$	$2.8x10^{-5}$

Fuego, Guatemala

Type:	arc
longitude:	90.88° W
latitude:	14.47° N
Events:	18
$BrO > 2\sigma$:	5
BrO/SO_2:	$9.8x10^{-5}$
std. dev.:	$4.1x10^{-5}$
mean SO_2:	$1.4x10^{17}$
mean BrO:	$2.9x10^{13}$



1 Feb 2018	$1.9x10^{17}$	$3.3x10^{13}$	$1.3x10^{-4}$	$1.1x10^{-5}$
20 Mar 2018	$1.0x10^{17}$	$4.5x10^{13}$	$1.2x10^{-4}$	$5.5x10^{-5}$
23 May 2018	$9.7x10^{16}$	$2.0x10^{13}$	$9.1x10^{-5}$	$3.1x10^{-5}$
7 April 2019	$1.4x10^{17}$	$3.3x10^{13}$	$1.4x10^{-4}$	$5.6x10^{-5}$
9 May 2019	$1.0x10^{17}$	$2.0x10^{13}$	$4.9x10^{-5}$	$5.9x10^{-5}$
11 Dec 2020	$7.3x10^{16}$	$3.2x10^{13}$	$1.6x10^{-4}$	$4.2x10^{-5}$
8 Feb 2021	$7.6x10^{16}$	$2.6x10^{13}$	$1.6x10^{-4}$	$6.2x10^{-5}$
18 Feb 2021	$2.0x10^{17}$	$3.0x10^{13}$	$1.3x10^{-4}$	$3.5x10^{-5}$
16 Mar 2021	$1.8x10^{17}$	$2.6x10^{13}$	$1.1x10^{-4}$	$4.0x10^{-5}$
21 Mar 2021	$2.0x10^{17}$	$3.6x10^{13}$	$4.9x10^{-5}$	$2.3x10^{-5}$
22 Mar 2021	$9.4x10^{16}$	$3.1x10^{13}$	$1.6x10^{-4}$	$5.4x10^{-5}$
23 Mar 2021	$1.2x10^{17}$	$2.6x10^{13}$	$5.3x10^{-5}$	$5.3x10^{-5}$
28 Mar 2021	$1.1x10^{17}$	$2.6x10^{13}$	$8.3x10^{-5}$	$2.5x10^{-5}$
6 April 2021	$1.8x10^{17}$	$3.0x10^{13}$	$1.2x10^{-4}$	$2.8x10^{-5}$
8 April 2021	$1.1x10^{17}$	$2.1x10^{13}$	$7.9x10^{-5}$	$3.0x10^{-5}$
12 April 2021	$3.1x10^{17}$	$4.5x10^{13}$	$8.4x10^{-5}$	$1.9x10^{-5}$
13 April 2021	$1.2x10^{17}$	$2.0x10^{13}$	$6.1x10^{-5}$	$2.7x10^{-5}$
18 April 2021	$1.1x10^{17}$	$2.2x10^{13}$	$1.8x10^{-5}$	$4.6x10^{-5}$

Masaya, Nicaragua

date	SO_2 VCD max. [molecules cm^{-2}]	BrO VCD	BrO/SO_2 fitted	BrO/SO_2 error

Masaya, Nicaragua

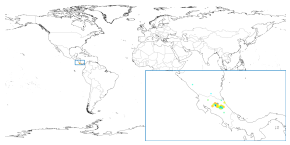
Type:	arc
longitude:	86.15° W
latitude:	11.98° N
Events:	2
BrO > 2σ:	1
BrO/SO_2:	$4.4x10^{-5}$
std. dev.:	$4.1x10^{-5}$
mean SO_2:	$3.5x10^{17}$
mean BrO:	$4.1x10^{13}$



28 June 2021	$5.4x10^{17}$	$5.1x10^{13}$	$2.7x10^{-5}$	$8.2x10^{-6}$
28 Oct 2021	$1.6x10^{17}$	$3.1x10^{13}$	$1.1x10^{-4}$	$3.0x10^{-5}$

Poas, Costa Rica

Type:	arc
longitude:	84.23° W
latitude:	10.20° N
Events:	69
BrO > 2σ:	27
BrO/SO_2:	$8.5x10^{-5}$
std. dev.:	$4.5x10^{-5}$
mean SO_2:	$1.8x10^{17}$
mean BrO:	$2.9x10^{13}$



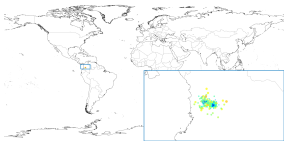
11 Feb 2018	$1.9x10^{17}$	$2.4x10^{13}$	$2.0x10^{-5}$	$2.7x10^{-5}$
20 Mar 2018	$1.9x10^{17}$	$3.7x10^{13}$	$1.6x10^{-4}$	$2.9x10^{-5}$
21 Mar 2018	$2.3x10^{17}$	$3.3x10^{13}$	$7.2x10^{-5}$	$1.7x10^{-5}$
30 Mar 2018	$2.4x10^{17}$	$3.2x10^{13}$	$1.1x10^{-4}$	$1.9x10^{-5}$
31 Mar 2018	$2.4x10^{17}$	$5.4x10^{13}$	$6.1x10^{-5}$	$1.4x10^{-5}$
1 April 2018	$3.5x10^{17}$	$3.5x10^{13}$	$7.8x10^{-5}$	$2.4x10^{-5}$
5 April 2018	$2.0x10^{17}$	$2.1x10^{13}$	$4.8x10^{-5}$	$3.8x10^{-5}$
6 April 2018	$2.5x10^{17}$	$3.9x10^{13}$	$1.0x10^{-4}$	$1.5x10^{-5}$
11 April 2018	$1.1x10^{17}$	$2.2x10^{13}$	$1.6x10^{-4}$	$2.0x10^{-5}$
15 April 2018	$2.7x10^{17}$	$5.0x10^{13}$	$1.0x10^{-4}$	$1.4x10^{-5}$
17 April 2018	$2.3x10^{17}$	$4.6x10^{13}$	$1.3x10^{-4}$	$5.0x10^{-5}$
18 April 2018	$1.1x10^{17}$	$2.6x10^{13}$	$9.3x10^{-5}$	$3.7x10^{-5}$
26 April 2018	$1.3x10^{17}$	$2.4x10^{13}$	$1.4x10^{-4}$	$1.9x10^{-5}$
28 April 2018	$2.2x10^{17}$	$3.4x10^{13}$	$1.4x10^{-4}$	$3.0x10^{-5}$
2 May 2018	$5.7x10^{17}$	$5.6x10^{13}$	$9.6x10^{-5}$	$1.7x10^{-5}$
3 May 2018	$1.6x10^{17}$	$3.3x10^{13}$	$1.0x10^{-4}$	$3.9x10^{-5}$
7 May 2018	$2.1x10^{17}$	$3.9x10^{13}$	$1.1x10^{-4}$	$1.8x10^{-5}$
8 May 2018	$3.5x10^{17}$	$5.1x10^{13}$	$9.0x10^{-5}$	$2.1x10^{-5}$
11 May 2018	$8.8x10^{16}$	$1.5x10^{13}$	$1.4x10^{-4}$	$3.9x10^{-5}$
14 May 2018	$2.7x10^{17}$	$4.3x10^{13}$	$1.8x10^{-4}$	$3.3x10^{-5}$
17 May 2018	$1.0x10^{17}$	$2.7x10^{13}$	$1.4x10^{-4}$	$3.5x10^{-5}$
23 May 2018	$9.8x10^{16}$	$2.0x10^{13}$	$3.8x10^{-5}$	$3.3x10^{-5}$
29 May 2018	$2.8x10^{17}$	$3.6x10^{13}$	$1.0x10^{-4}$	$1.6x10^{-5}$
30 May 2018	$5.0x10^{17}$	$4.7x10^{13}$	$1.2x10^{-4}$	$1.2x10^{-5}$
4 June 2018	$9.3x10^{16}$	$2.6x10^{13}$	$1.9x10^{-6}$	$8.6x10^{-6}$
14 June 2018	$1.7x10^{17}$	$2.7x10^{13}$	$1.1x10^{-4}$	$2.8x10^{-5}$
15 June 2018	$1.1x10^{17}$	$3.6x10^{13}$	$6.3x10^{-5}$	$2.6x10^{-5}$
20 June 2018	$2.1x10^{17}$	$5.9x10^{13}$	$1.3x10^{-4}$	$2.2x10^{-5}$
21 June 2018	$1.3x10^{17}$	$3.0x10^{13}$	$1.7x10^{-4}$	$4.9x10^{-5}$
30 June 2018	$1.1x10^{17}$	$2.5x10^{13}$	$3.4x10^{-5}$	$7.0x10^{-5}$
4 July 2018	$1.9x10^{17}$	$2.3x10^{13}$	$9.6x10^{-5}$	$2.9x10^{-5}$
2 Aug 2018	$1.2x10^{17}$	$2.4x10^{13}$	$1.3x10^{-4}$	$2.6x10^{-5}$
13 Sept 2018	$1.6x10^{17}$	$2.5x10^{13}$	$1.2x10^{-4}$	$3.5x10^{-5}$
28 Sept 2018	$1.3x10^{17}$	$2.4x10^{13}$	$1.7x10^{-4}$	$3.0x10^{-5}$
29 Sept 2018	$2.6x10^{17}$	$4.6x10^{13}$	$1.6x10^{-4}$	$2.9x10^{-5}$
9 Oct 2018	$1.7x10^{17}$	$2.9x10^{13}$	$4.8x10^{-5}$	$1.9x10^{-5}$
1 Nov 2018	$1.2x10^{17}$	$2.5x10^{13}$	$8.0x10^{-5}$	$3.5x10^{-5}$
1 Dec 2018	$9.9x10^{16}$	$1.3x10^{13}$	$1.2x10^{-4}$	$4.1x10^{-5}$
2 Dec 2018	$1.1x10^{17}$	$2.4x10^{13}$	$5.4x10^{-5}$	$2.6x10^{-5}$
12 Dec 2018	$8.4x10^{16}$	$1.6x10^{13}$	$4.2x10^{-6}$	$6.0x10^{-5}$
19 Dec 2018	$1.1x10^{17}$	$3.4x10^{13}$	$1.4x10^{-4}$	$5.1x10^{-5}$
8 Jan 2019	$1.0x10^{17}$	$2.0x10^{13}$	$9.3x10^{-5}$	$3.1x10^{-5}$
19 Jan 2019	$2.9x10^{17}$	$1.3x10^{13}$	$7.1x10^{-6}$	$4.3x10^{-5}$
24 Jan 2019	$1.0x10^{17}$	$2.5x10^{13}$	$3.6x10^{-5}$	$3.5x10^{-5}$
29 Jan 2019	$9.1x10^{16}$	$2.3x10^{13}$	$4.6x10^{-5}$	$5.1x10^{-5}$
4 Feb 2019	$1.5x10^{17}$	$3.0x10^{13}$	$5.1x10^{-5}$	$4.8x10^{-5}$
2 Mar 2019	$1.1x10^{17}$	$1.8x10^{13}$	$2.7x10^{-5}$	$4.8x10^{-5}$

Poas, Costa Rica

date	SO_2 VCD max. [molecules cm^{-2}]	BrO VCD	BrO/SO_2 fitted	BrO/SO_2 error
3 Mar 2019	$1.2x10^{17}$	$2.6x10^{13}$	$5.4x10^{-5}$	$7.4x10^{-5}$
14 Mar 2019	$1.1x10^{17}$	$3.2x10^{13}$	$1.7x10^{-4}$	$5.0x10^{-5}$
19 Mar 2019	$1.3x10^{17}$	$2.4x10^{13}$	$9.3x10^{-5}$	$1.8x10^{-5}$
24 Mar 2019	$1.5x10^{17}$	$2.6x10^{13}$	$6.5x10^{-5}$	$4.7x10^{-5}$
29 Mar 2019	$1.3x10^{17}$	$1.5x10^{13}$	$2.1x10^{-5}$	$4.5x10^{-5}$
9 April 2019	$1.1x10^{17}$	$2.4x10^{13}$	$9.0x10^{-5}$	$4.8x10^{-5}$
20 Sept 2019	$5.3x10^{17}$	$2.7x10^{13}$	$5.7x10^{-5}$	$1.1x10^{-5}$
21 Sept 2019	$9.7x10^{16}$	$2.4x10^{13}$	$4.2x10^{-5}$	$1.9x10^{-5}$
22 Sept 2019	$1.4x10^{17}$	$3.2x10^{13}$	$6.9x10^{-5}$	$4.4x10^{-5}$
26 Sept 2019	$3.6x10^{17}$	$2.4x10^{13}$	$3.4x10^{-5}$	$1.2x10^{-5}$
27 Sept 2019	$2.3x10^{17}$	$3.6x10^{13}$	$7.2x10^{-5}$	$1.2x10^{-5}$
28 Sept 2019	$1.0x10^{17}$	$2.2x10^{13}$	$1.1x10^{-4}$	$4.2x10^{-5}$
1 Oct 2019	$1.4x10^{17}$	$2.4x10^{13}$	$5.0x10^{-5}$	$2.7x10^{-5}$
2 Oct 2019	$1.2x10^{17}$	$2.7x10^{13}$	$5.5x10^{-5}$	$2.8x10^{-5}$
6 Oct 2019	$1.2x10^{17}$	$2.5x10^{13}$	$9.0x10^{-5}$	$3.3x10^{-5}$
6 Feb 2020	$8.3x10^{16}$	$2.6x10^{13}$	$9.4x10^{-5}$	$4.6x10^{-5}$
7 Feb 2020	$1.3x10^{17}$	$3.7x10^{13}$	$7.0x10^{-5}$	$1.7x10^{-5}$
4 Mar 2020	$1.1x10^{17}$	$2.6x10^{13}$	$3.7x10^{-5}$	$5.8x10^{-5}$
23 May 2020	$1.2x10^{17}$	$2.1x10^{13}$	$1.5x10^{-5}$	$6.1x10^{-5}$
14 June 2020	$9.0x10^{16}$	$2.7x10^{13}$	$5.4x10^{-5}$	$3.4x10^{-5}$
23 Mar 2021	$1.6x10^{17}$	$2.0x10^{13}$	$9.3x10^{-5}$	$2.6x10^{-5}$
24 April 2021	$7.8x10^{16}$	$2.4x10^{13}$	$1.1x10^{-4}$	$3.6x10^{-5}$

Nevado del Ruiz, Colombia

Type:	arc
longitude:	75.32° W
latitude:	4.88° N
Events:	467
BrO > 2σ:	113
BrO/SO_2:	$7.5x10^{-5}$
std. dev.:	$3.3x10^{-5}$
mean SO_2:	$1.8x10^{17}$
mean BrO:	$3.1x10^{13}$



1 Jan 2018	$1.3x10^{17}$	$2.2x10^{13}$	$5.9x10^{-5}$	$2.9x10^{-5}$
3 Feb 2018	$1.4x10^{17}$	$2.7x10^{13}$	$9.1x10^{-5}$	$3.3x10^{-5}$
13 Feb 2018	$1.2x10^{17}$	$1.8x10^{13}$	$6.5x10^{-5}$	$4.7x10^{-5}$
18 Feb 2018	$1.5x10^{17}$	$2.1x10^{13}$	$6.2x10^{-5}$	$3.1x10^{-5}$
24 Feb 2018	$1.0x10^{17}$	$1.9x10^{13}$	$1.1x10^{-4}$	$3.6x10^{-5}$
10 Mar 2018	$6.9x10^{16}$	$1.4x10^{13}$	$6.1x10^{-5}$	$3.1x10^{-5}$
17 Mar 2018	$2.5x10^{17}$	$3.1x10^{13}$	$4.8x10^{-5}$	$1.8x10^{-5}$
18 Mar 2018	$2.0x10^{17}$	$2.6x10^{13}$	$4.6x10^{-5}$	$1.9x10^{-5}$
23 Mar 2018	$3.5x10^{17}$	$4.3x10^{13}$	$8.0x10^{-5}$	$3.0x10^{-5}$
28 Mar 2018	$1.1x10^{17}$	$2.1x10^{13}$	$6.0x10^{-5}$	$3.2x10^{-5}$
2 April 2018	$2.5x10^{17}$	$3.4x10^{13}$	$7.6x10^{-5}$	$1.9x10^{-5}$
3 April 2018	$1.9x10^{17}$	$2.6x10^{13}$	$4.8x10^{-5}$	$2.5x10^{-5}$
7 April 2018	$1.6x10^{17}$	$3.1x10^{13}$	$1.1x10^{-4}$	$1.6x10^{-5}$
11 April 2018	$9.6x10^{16}$	$1.3x10^{13}$	$4.3x10^{-5}$	$2.6x10^{-5}$
13 April 2018	$2.6x10^{17}$	$2.7x10^{13}$	$9.1x10^{-5}$	$2.2x10^{-5}$
14 April 2018	$2.1x10^{17}$	$2.9x10^{13}$	$9.9x10^{-5}$	$3.0x10^{-5}$
24 April 2018	$8.5x10^{16}$	$2.1x10^{13}$	$4.1x10^{-5}$	$4.5x10^{-5}$
9 May 2018	$1.1x10^{17}$	$3.4x10^{13}$	$6.3x10^{-5}$	$2.7x10^{-5}$
10 May 2018	$1.7x10^{17}$	$2.4x10^{13}$	$6.5x10^{-5}$	$2.6x10^{-5}$
13 May 2018	$1.0x10^{17}$	$1.8x10^{13}$	$5.4x10^{-5}$	$2.5x10^{-5}$
14 May 2018	$1.1x10^{17}$	$1.8x10^{13}$	$7.8x10^{-5}$	$4.7x10^{-5}$
15 May 2018	$1.5x10^{17}$	$5.6x10^{13}$	$5.5x10^{-5}$	$2.8x10^{-5}$
19 May 2018	$8.7x10^{16}$	$3.0x10^{13}$	$1.3x10^{-4}$	$2.4x10^{-5}$
20 May 2018	$1.9x10^{17}$	$2.7x10^{13}$	$7.2x10^{-5}$	$1.8x10^{-5}$
21 May 2018	$1.1x10^{17}$	$2.4x10^{13}$	$5.9x10^{-5}$	$3.0x10^{-5}$
31 May 2018	$8.7x10^{16}$	$2.9x10^{13}$	$5.7x10^{-6}$	$4.4x10^{-5}$
10 June 2018	$1.1x10^{17}$	$1.8x10^{13}$	$6.9x10^{-5}$	$1.7x10^{-5}$
11 June 2018	$1.3x10^{17}$	$2.7x10^{13}$	$6.3x10^{-5}$	$2.8x10^{-5}$
16 June 2018	$7.2x10^{16}$	$2.5x10^{13}$	$6.1x10^{-5}$	$3.1x10^{-5}$
26 June 2018	$1.1x10^{17}$	$3.1x10^{13}$	$7.8x10^{-5}$	$3.1x10^{-5}$
1 July 2018	$1.3x10^{17}$	$3.1x10^{13}$	$5.6x10^{-5}$	$2.4x10^{-5}$
2 July 2018	$3.0x10^{17}$	$4.0x10^{13}$	$1.0x10^{-4}$	$2.6x10^{-5}$
7 July 2018	$1.3x10^{17}$	$2.6x10^{13}$	$6.2x10^{-5}$	$5.1x10^{-5}$
12 July 2018	$1.4x10^{17}$	$3.5x10^{13}$	$2.2x10^{-5}$	$1.8x10^{-5}$
13 July 2018	$6.8x10^{16}$	$1.9x10^{13}$	$2.6x10^{-5}$	$3.3x10^{-5}$
23 July 2018	$7.9x10^{16}$	$2.8x10^{13}$	$2.3x10^{-5}$	$2.5x10^{-5}$
27 July 2018	$8.1x10^{16}$	$2.2x10^{13}$	$6.7x10^{-5}$	$3.5x10^{-5}$
28 July 2018	$1.5x10^{17}$	$3.0x10^{13}$	$6.7x10^{-5}$	$2.5x10^{-5}$

Nevado del Ruiz, Colombia

date	SO_2 VCD max. [molecules cm^{-2}]	BrO VCD max. [molecules cm^{-2}]	BrO/SO_2 fitted	BrO/SO_2 error
1 Aug 2018	$9.8x10^{16}$	$2.7x10^{13}$	$1.0x10^{-4}$	$2.9x10^{-5}$
3 Aug 2018	$1.1x10^{17}$	$3.3x10^{13}$	$8.6x10^{-5}$	$2.8x10^{-5}$
14 Aug 2018	$1.6x10^{17}$	$2.3x10^{13}$	$7.7x10^{-5}$	$2.1x10^{-5}$
19 Aug 2018	$1.6x10^{17}$	$2.8x10^{13}$	$6.9x10^{-5}$	$2.7x10^{-5}$
20 Aug 2018	$9.1x10^{16}$	$2.5x10^{13}$	$9.5x10^{-5}$	$5.9x10^{-5}$
24 Aug 2018	$8.7x10^{16}$	$3.0x10^{13}$	$3.4x10^{-5}$	$5.3x10^{-5}$
3 Sept 2018	$1.1x10^{17}$	$3.7x10^{13}$	$8.3x10^{-5}$	$4.3x10^{-5}$
13 Sept 2018	$1.7x10^{17}$	$3.1x10^{13}$	$1.5x10^{-4}$	$3.4x10^{-5}$
14 Sept 2018	$1.6x10^{17}$	$3.3x10^{13}$	$9.3x10^{-5}$	$2.0x10^{-5}$
15 Sept 2018	$2.0x10^{17}$	$3.1x10^{13}$	$7.5x10^{-5}$	$2.6x10^{-5}$
19 Sept 2018	$1.4x10^{17}$	$2.6x10^{13}$	$7.5x10^{-5}$	$2.5x10^{-5}$
20 Sept 2018	$9.1x10^{16}$	$3.1x10^{13}$	$7.0x10^{-5}$	$2.9x10^{-5}$
21 Sept 2018	$9.4x10^{16}$	$1.3x10^{13}$	$5.6x10^{-5}$	$3.7x10^{-5}$
25 Sept 2018	$1.1x10^{17}$	$2.1x10^{13}$	$1.9x10^{-5}$	$3.5x10^{-5}$
1 Oct 2018	$1.3x10^{17}$	$2.5x10^{13}$	$1.1x10^{-4}$	$3.8x10^{-5}$
4 Oct 2018	$1.1x10^{17}$	$2.6x10^{13}$	$1.3x10^{-4}$	$4.1x10^{-5}$
5 Oct 2018	$4.0x10^{17}$	$4.8x10^{13}$	$9.4x10^{-5}$	$1.1x10^{-5}$
7 Oct 2018	$1.1x10^{17}$	$2.6x10^{13}$	$5.8x10^{-5}$	$2.4x10^{-5}$
10 Oct 2018	$4.0x10^{17}$	$5.1x10^{13}$	$1.0x10^{-4}$	$1.2x10^{-5}$
11 Oct 2018	$2.6x10^{17}$	$3.5x10^{13}$	$1.1x10^{-4}$	$1.7x10^{-5}$
12 Oct 2018	$2.5x10^{17}$	$3.0x10^{13}$	$9.8x10^{-5}$	$2.4x10^{-5}$
16 Oct 2018	$8.6x10^{16}$	$2.2x10^{13}$	$1.3x10^{-4}$	$2.2x10^{-5}$
17 Oct 2018	$8.7x10^{16}$	$2.7x10^{13}$	$1.1x10^{-4}$	$3.6x10^{-5}$
21 Oct 2018	$9.8x10^{16}$	$1.9x10^{13}$	$1.5x10^{-4}$	$3.2x10^{-5}$
23 Oct 2018	$1.2x10^{17}$	$1.5x10^{13}$	$6.0x10^{-5}$	$4.1x10^{-5}$
26 Oct 2018	$1.6x10^{17}$	$3.5x10^{13}$	$1.3x10^{-4}$	$2.3x10^{-5}$
31 Oct 2018	$7.3x10^{16}$	$1.8x10^{13}$	$5.6x10^{-5}$	$4.0x10^{-5}$
1 Nov 2018	$8.7x10^{16}$	$3.1x10^{13}$	$1.1x10^{-4}$	$3.6x10^{-5}$
3 Nov 2018	$8.8x10^{16}$	$2.2x10^{13}$	$1.3x10^{-4}$	$4.2x10^{-5}$
22 Nov 2018	$1.2x10^{17}$	$1.8x10^{13}$	$6.6x10^{-5}$	$4.6x10^{-5}$
23 Nov 2018	$1.5x10^{17}$	$2.3x10^{13}$	$1.0x10^{-4}$	$3.5x10^{-5}$
29 Nov 2018	$1.6x10^{17}$	$3.6x10^{13}$	$8.1x10^{-5}$	$3.2x10^{-5}$
3 Dec 2018	$1.1x10^{17}$	$2.4x10^{13}$	$1.7x10^{-5}$	$2.8x10^{-5}$
4 Dec 2018	$1.5x10^{17}$	$3.6x10^{13}$	$1.5x10^{-4}$	$3.4x10^{-5}$
5 Dec 2018	$1.2x10^{17}$	$2.0x10^{13}$	$8.1x10^{-5}$	$2.6x10^{-5}$
7 Dec 2018	$1.6x10^{17}$	$2.2x10^{13}$	$1.2x10^{-4}$	$2.2x10^{-5}$
8 Dec 2018	$7.9x10^{16}$	$2.5x10^{13}$	$8.2x10^{-6}$	$3.1x10^{-5}$
9 Dec 2018	$2.0x10^{17}$	$3.1x10^{13}$	$7.5x10^{-5}$	$3.2x10^{-5}$
13 Dec 2018	$1.0x10^{17}$	$2.1x10^{13}$	$6.2x10^{-5}$	$2.8x10^{-5}$
14 Dec 2018	$2.7x10^{17}$	$3.9x10^{13}$	$1.1x10^{-4}$	$2.2x10^{-5}$
20 Dec 2018	$1.1x10^{17}$	$2.1x10^{13}$	$9.5x10^{-5}$	$5.5x10^{-5}$
30 Dec 2018	$1.1x10^{17}$	$2.2x10^{13}$	$5.3x10^{-5}$	$5.0x10^{-5}$
9 Jan 2019	$1.8x10^{17}$	$2.6x10^{13}$	$8.4x10^{-5}$	$1.4x10^{-5}$
10 Jan 2019	$2.1x10^{17}$	$3.6x10^{13}$	$9.6x10^{-5}$	$1.6x10^{-5}$
11 Jan 2019	$1.3x10^{17}$	$2.2x10^{13}$	$4.0x10^{-5}$	$3.0x10^{-5}$
14 Jan 2019	$2.7x10^{17}$	$3.2x10^{13}$	$7.3x10^{-5}$	$1.2x10^{-5}$
15 Jan 2019	$4.8x10^{17}$	$5.0x10^{13}$	$6.9x10^{-5}$	$9.5x10^{-6}$
20 Jan 2019	$1.3x10^{17}$	$2.3x10^{13}$	$5.0x10^{-5}$	$2.4x10^{-5}$
21 Jan 2019	$1.1x10^{17}$	$2.6x10^{13}$	$5.3x10^{-5}$	$3.5x10^{-5}$
25 Jan 2019	$1.8x10^{17}$	$1.6x10^{13}$	$2.4x10^{-5}$	$2.9x10^{-5}$
26 Jan 2019	$8.1x10^{16}$	$3.0x10^{13}$	$3.8x10^{-5}$	$4.6x10^{-5}$
30 Jan 2019	$9.9x10^{16}$	$2.6x10^{13}$	$7.8x10^{-5}$	$1.9x10^{-5}$
5 Feb 2019	$2.6x10^{17}$	$3.5x10^{13}$	$8.9x10^{-5}$	$2.9x10^{-5}$
10 Feb 2019	$1.4x10^{17}$	$2.3x10^{13}$	$7.8x10^{-5}$	$3.0x10^{-5}$
15 Feb 2019	$8.3x10^{16}$	$2.3x10^{13}$	$8.7x10^{-5}$	$3.9x10^{-5}$
16 Feb 2019	$1.9x10^{17}$	$3.0x10^{13}$	$4.1x10^{-5}$	$3.6x10^{-5}$
17 Feb 2019	$2.2x10^{17}$	$2.1x10^{13}$	$6.8x10^{-6}$	$2.1x10^{-5}$
18 Feb 2019	$1.0x10^{17}$	$2.4x10^{13}$	$6.6x10^{-5}$	$3.3x10^{-5}$
21 Feb 2019	$9.3x10^{16}$	$3.0x10^{13}$	$5.1x10^{-7}$	$4.5x10^{-5}$
22 Feb 2019	$1.8x10^{17}$	$2.1x10^{13}$	$4.0x10^{-5}$	$3.5x10^{-5}$
26 Feb 2019	$2.6x10^{17}$	$2.7x10^{13}$	$8.1x10^{-5}$	$1.4x10^{-5}$
3 Mar 2019	$1.4x10^{17}$	$1.9x10^{13}$	$3.1x10^{-5}$	$2.5x10^{-5}$
5 Mar 2019	$1.6x10^{17}$	$1.7x10^{13}$	$2.9x10^{-5}$	$3.7x10^{-5}$
9 Mar 2019	$1.0x10^{17}$	$2.2x10^{13}$	$2.0x10^{-5}$	$2.3x10^{-5}$
10 Mar 2019	$1.0x10^{17}$	$2.7x10^{13}$	$7.5x10^{-5}$	$3.9x10^{-5}$
15 Mar 2019	$2.2x10^{17}$	$3.2x10^{13}$	$2.8x10^{-5}$	$1.3x10^{-5}$
16 Mar 2019	$2.0x10^{17}$	$2.3x10^{13}$	$4.6x10^{-5}$	$3.5x10^{-5}$
20 Mar 2019	$4.6x10^{17}$	$3.2x10^{13}$	$4.9x10^{-5}$	$1.2x10^{-5}$
21 Mar 2019	$1.8x10^{17}$	$1.4x10^{13}$	$8.9x10^{-6}$	$4.4x10^{-5}$
22 Mar 2019	$1.5x10^{17}$	$1.7x10^{13}$	$6.7x10^{-5}$	$2.6x10^{-5}$
24 Mar 2019	$1.3x10^{17}$	$2.4x10^{13}$	$1.1x10^{-4}$	$1.9x10^{-5}$

Nevado del Ruiz, Colombia

date	SO_2 VCD max. [molecules cm^{-2}]	BrO VCD max. [molecules cm^{-2}]	BrO/SO_2 fitted	BrO/SO_2 error
25 Mar 2019	$1.7x10^{17}$	$2.8x10^{13}$	$5.2x10^{-5}$	$2.0x10^{-5}$
27 Mar 2019	$2.0x10^{17}$	$2.0x10^{13}$	$7.6x10^{-5}$	$2.3x10^{-5}$
30 Mar 2019	$1.7x10^{17}$	$3.8x10^{13}$	$3.9x10^{-5}$	$1.6x10^{-5}$
31 Mar 2019	$2.2x10^{17}$	$3.1x10^{13}$	$7.7x10^{-5}$	$1.1x10^{-5}$
1 April 2019	$1.1x10^{17}$	$2.0x10^{13}$	$6.2x10^{-5}$	$3.0x10^{-5}$
3 April 2019	$7.7x10^{16}$	$2.2x10^{13}$	$6.5x10^{-5}$	$1.8x10^{-5}$
5 April 2019	$5.6x10^{17}$	$6.3x10^{13}$	$9.4x10^{-5}$	$1.1x10^{-5}$
6 April 2019	$2.7x10^{17}$	$3.9x10^{13}$	$7.2x10^{-5}$	$2.5x10^{-5}$
10 April 2019	$2.8x10^{17}$	$3.5x10^{13}$	$4.4x10^{-5}$	$2.5x10^{-5}$
11 April 2019	$2.5x10^{17}$	$5.0x10^{13}$	$7.5x10^{-5}$	$2.5x10^{-5}$
15 April 2019	$2.2x10^{17}$	$3.4x10^{13}$	$5.6x10^{-5}$	$1.1x10^{-5}$
16 April 2019	$5.6x10^{17}$	$5.8x10^{13}$	$8.8x10^{-5}$	$9.2x10^{-6}$
17 April 2019	$1.9x10^{17}$	$1.9x10^{13}$	$9.2x10^{-6}$	$2.0x10^{-5}$
20 April 2019	$3.3x10^{17}$	$3.7x10^{13}$	$8.0x10^{-5}$	$1.3x10^{-5}$
21 April 2019	$3.8x10^{17}$	$4.2x10^{13}$	$7.8x10^{-5}$	$1.1x10^{-5}$
22 April 2019	$1.7x10^{17}$	$2.4x10^{13}$	$3.8x10^{-5}$	$1.6x10^{-5}$
25 April 2019	$1.1x10^{17}$	$2.1x10^{13}$	$9.5x10^{-5}$	$1.5x10^{-5}$
27 April 2019	$8.5x10^{16}$	$2.5x10^{13}$	$9.9x10^{-5}$	$2.6x10^{-5}$
1 May 2019	$8.0x10^{16}$	$2.5x10^{13}$	$8.0x10^{-5}$	$3.2x10^{-5}$
2 May 2019	$9.2x10^{16}$	$2.0x10^{13}$	$9.0x10^{-5}$	$1.9x10^{-5}$
11 May 2019	$6.2x10^{16}$	$2.2x10^{13}$	$6.7x10^{-5}$	$4.5x10^{-5}$
12 May 2019	$1.2x10^{17}$	$2.4x10^{13}$	$7.3x10^{-5}$	$2.2x10^{-5}$
18 May 2019	$1.3x10^{17}$	$2.3x10^{13}$	$8.0x10^{-5}$	$3.7x10^{-5}$
19 May 2019	$8.8x10^{16}$	$1.8x10^{13}$	$6.7x10^{-5}$	$3.3x10^{-5}$
8 June 2019	$7.2x10^{16}$	$3.5x10^{13}$	$1.2x10^{-4}$	$4.0x10^{-5}$
26 June 2019	$8.4x10^{16}$	$1.7x10^{13}$	$5.5x10^{-5}$	$4.1x10^{-5}$
4 July 2019	$2.8x10^{17}$	$3.4x10^{13}$	$6.7x10^{-5}$	$1.9x10^{-5}$
5 July 2019	$1.6x10^{17}$	$4.3x10^{13}$	$6.8x10^{-5}$	$2.4x10^{-5}$
9 July 2019	$8.2x10^{16}$	$2.6x10^{13}$	$2.5x10^{-6}$	$3.4x10^{-5}$
15 July 2019	$1.1x10^{17}$	$3.4x10^{13}$	$8.2x10^{-5}$	$3.7x10^{-5}$
25 July 2019	$1.7x10^{17}$	$2.3x10^{13}$	$4.0x10^{-5}$	$2.0x10^{-5}$
26 July 2019	$1.3x10^{17}$	$3.9x10^{13}$	$7.3x10^{-5}$	$3.3x10^{-5}$
27 July 2019	$8.8x10^{16}$	$2.8x10^{13}$	$7.4x10^{-5}$	$2.9x10^{-5}$
30 July 2019	$1.1x10^{17}$	$2.2x10^{13}$	$3.0x10^{-5}$	$1.7x10^{-5}$
31 July 2019	$1.6x10^{17}$	$3.6x10^{13}$	$6.7x10^{-6}$	$2.0x10^{-5}$
1 Aug 2019	$1.2x10^{17}$	$3.5x10^{13}$	$6.3x10^{-5}$	$2.4x10^{-5}$
4 Aug 2019	$8.9x10^{16}$	$2.0x10^{13}$	$4.4x10^{-5}$	$3.4x10^{-5}$
5 Aug 2019	$1.8x10^{17}$	$2.9x10^{13}$	$4.6x10^{-5}$	$1.6x10^{-5}$
6 Aug 2019	$2.4x10^{17}$	$4.1x10^{13}$	$1.3x10^{-4}$	$2.0x10^{-5}$
10 Aug 2019	$1.4x10^{17}$	$2.7x10^{13}$	$7.4x10^{-5}$	$2.7x10^{-5}$
11 Aug 2019	$1.1x10^{17}$	$3.5x10^{13}$	$1.4x10^{-5}$	$5.0x10^{-5}$
12 Aug 2019	$1.2x10^{17}$	$3.0x10^{13}$	$1.1x10^{-4}$	$3.1x10^{-5}$
15 Aug 2019	$8.7x10^{16}$	$2.2x10^{13}$	$3.2x10^{-5}$	$3.2x10^{-5}$
16 Aug 2019	$1.0x10^{17}$	$4.0x10^{13}$	$9.8x10^{-5}$	$4.9x10^{-5}$
17 Aug 2019	$1.7x10^{17}$	$2.6x10^{13}$	$4.2x10^{-5}$	$2.6x10^{-5}$
21 Aug 2019	$1.1x10^{17}$	$3.5x10^{13}$	$1.1x10^{-4}$	$3.9x10^{-5}$
22 Aug 2019	$2.2x10^{17}$	$4.4x10^{13}$	$4.9x10^{-6}$	$2.7x10^{-5}$
26 Aug 2019	$1.0x10^{17}$	$2.7x10^{13}$	$6.6x10^{-5}$	$1.8x10^{-5}$
27 Aug 2019	$7.6x10^{16}$	$4.2x10^{13}$	$4.7x10^{-5}$	$3.8x10^{-5}$
1 Sept 2019	$2.0x10^{17}$	$3.4x10^{13}$	$9.6x10^{-5}$	$2.8x10^{-5}$
2 Sept 2019	$1.3x10^{17}$	$2.2x10^{13}$	$8.8x10^{-5}$	$2.6x10^{-5}$
3 Sept 2019	$9.9x10^{16}$	$2.3x10^{13}$	$9.2x10^{-5}$	$2.9x10^{-5}$
6 Sept 2019	$1.6x10^{17}$	$3.2x10^{13}$	$1.1x10^{-4}$	$2.2x10^{-5}$
7 Sept 2019	$5.7x10^{17}$	$6.0x10^{13}$	$9.2x10^{-5}$	$1.1x10^{-5}$
11 Sept 2019	$3.3x10^{17}$	$3.5x10^{13}$	$1.2x10^{-4}$	$1.8x10^{-5}$
12 Sept 2019	$2.9x10^{17}$	$3.3x10^{13}$	$8.9x10^{-5}$	$2.4x10^{-5}$
13 Sept 2019	$1.4x10^{17}$	$3.2x10^{13}$	$9.5x10^{-5}$	$2.8x10^{-5}$
17 Sept 2019	$2.1x10^{17}$	$3.7x10^{13}$	$1.1x10^{-4}$	$2.7x10^{-5}$
22 Sept 2019	$1.4x10^{17}$	$3.3x10^{13}$	$1.2x10^{-4}$	$2.7x10^{-5}$
23 Sept 2019	$1.6x10^{17}$	$3.5x10^{13}$	$8.5x10^{-5}$	$2.7x10^{-5}$
2 Oct 2019	$1.1x10^{17}$	$2.9x10^{13}$	$1.1x10^{-4}$	$2.5x10^{-5}$
3 Oct 2019	$7.5x10^{16}$	$2.8x10^{13}$	$1.1x10^{-4}$	$3.2x10^{-5}$
4 Oct 2019	$1.4x10^{17}$	$2.5x10^{13}$	$3.6x10^{-5}$	$2.4x10^{-5}$
9 Oct 2019	$1.8x10^{17}$	$3.4x10^{13}$	$1.3x10^{-4}$	$2.3x10^{-5}$
12 Oct 2019	$1.3x10^{17}$	$2.8x10^{13}$	$3.9x10^{-5}$	$3.4x10^{-5}$
13 Oct 2019	$2.1x10^{17}$	$3.1x10^{13}$	$1.2x10^{-4}$	$1.4x10^{-5}$
14 Oct 2019	$2.5x10^{17}$	$4.3x10^{13}$	$8.8x10^{-5}$	$1.4x10^{-5}$
15 Oct 2019	$2.1x10^{17}$	$3.1x10^{13}$	$8.7x10^{-5}$	$2.1x10^{-5}$
18 Oct 2019	$2.0x10^{17}$	$4.3x10^{13}$	$8.1x10^{-5}$	$1.5x10^{-5}$
19 Oct 2019	$2.9x10^{17}$	$3.8x10^{13}$	$7.3x10^{-5}$	$1.1x10^{-5}$
20 Oct 2019	$2.6x10^{17}$	$3.5x10^{13}$	$1.0x10^{-4}$	$1.7x10^{-5}$

Nevado del Ruiz, Colombia

date	SO_2 VCD max. [molecules cm^{-2}]	BrO VCD	BrO/SO_2 fitted	BrO/SO_2 error
21 Oct 2019	$1.2x10^{17}$	$2.6x10^{13}$	$1.3x10^{-4}$	$3.1x10^{-5}$
24 Oct 2019	$1.7x10^{17}$	$2.1x10^{13}$	$4.6x10^{-5}$	$2.0x10^{-5}$
25 Oct 2019	$3.0x10^{17}$	$3.7x10^{13}$	$7.8x10^{-5}$	$3.3x10^{-5}$
26 Oct 2019	$1.0x10^{17}$	$3.3x10^{13}$	$1.0x10^{-4}$	$3.3x10^{-5}$
30 Oct 2019	$1.3x10^{17}$	$3.7x10^{13}$	$6.5x10^{-5}$	$1.8x10^{-5}$
31 Oct 2019	$2.4x10^{17}$	$3.1x10^{13}$	$1.1x10^{-4}$	$2.6x10^{-5}$
3 Nov 2019	$3.3x10^{17}$	$6.6x10^{13}$	$1.4x10^{-4}$	$2.3x10^{-5}$
4 Nov 2019	$2.3x10^{17}$	$2.7x10^{13}$	$1.8x10^{-5}$	$2.6x10^{-5}$
5 Nov 2019	$3.3x10^{17}$	$5.5x10^{13}$	$9.3x10^{-5}$	$1.5x10^{-5}$
6 Nov 2019	$1.1x10^{17}$	$3.1x10^{13}$	$1.4x10^{-4}$	$2.3x10^{-5}$
8 Nov 2019	$1.4x10^{17}$	$2.7x10^{13}$	$1.2x10^{-4}$	$2.3x10^{-5}$
9 Nov 2019	$1.9x10^{17}$	$3.7x10^{13}$	$6.4x10^{-5}$	$1.4x10^{-5}$
10 Nov 2019	$3.8x10^{17}$	$5.9x10^{13}$	$1.1x10^{-4}$	$1.5x10^{-5}$
11 Nov 2019	$3.7x10^{17}$	$4.6x10^{13}$	$1.2x10^{-4}$	$2.4x10^{-5}$
13 Nov 2019	$1.9x10^{17}$	$3.1x10^{13}$	$1.4x10^{-4}$	$2.3x10^{-5}$
14 Nov 2019	$3.8x10^{17}$	$3.1x10^{13}$	$7.6x10^{-5}$	$9.9x10^{-6}$
15 Nov 2019	$5.1x10^{17}$	$4.3x10^{13}$	$7.7x10^{-5}$	$6.0x10^{-6}$
17 Nov 2019	$1.4x10^{17}$	$2.4x10^{13}$	$6.5x10^{-5}$	$2.4x10^{-5}$
19 Nov 2019	$2.5x10^{17}$	$2.6x10^{13}$	$8.5x10^{-5}$	$1.8x10^{-5}$
20 Nov 2019	$2.8x10^{17}$	$7.1x10^{13}$	$9.7x10^{-5}$	$1.3x10^{-5}$
21 Nov 2019	$2.6x10^{17}$	$3.8x10^{13}$	$7.8x10^{-5}$	$1.6x10^{-5}$
22 Nov 2019	$3.1x10^{17}$	$3.2x10^{13}$	$9.6x10^{-5}$	$1.7x10^{-5}$
24 Nov 2019	$1.6x10^{17}$	$3.4x10^{13}$	$1.1x10^{-4}$	$1.7x10^{-5}$
25 Nov 2019	$2.6x10^{17}$	$2.8x10^{13}$	$9.2x10^{-5}$	$1.8x10^{-5}$
26 Nov 2019	$1.3x10^{17}$	$3.7x10^{13}$	$8.5x10^{-5}$	$4.1x10^{-5}$
30 Nov 2019	$2.4x10^{17}$	$3.4x10^{13}$	$1.0x10^{-4}$	$1.1x10^{-5}$
1 Dec 2019	$4.7x10^{17}$	$6.3x10^{13}$	$9.3x10^{-5}$	$1.2x10^{-5}$
2 Dec 2019	$2.6x10^{17}$	$3.6x10^{13}$	$6.3x10^{-5}$	$1.4x10^{-5}$
5 Dec 2019	$1.3x10^{17}$	$3.3x10^{13}$	$7.7x10^{-5}$	$1.6x10^{-5}$
6 Dec 2019	$1.4x10^{17}$	$3.3x10^{13}$	$8.1x10^{-5}$	$2.1x10^{-5}$
7 Dec 2019	$1.2x10^{17}$	$3.6x10^{13}$	$1.9x10^{-4}$	$2.1x10^{-5}$
13 Dec 2019	$1.3x10^{17}$	$4.5x10^{13}$	$8.2x10^{-5}$	$4.4x10^{-5}$
17 Dec 2019	$2.0x10^{17}$	$4.5x10^{13}$	$7.3x10^{-5}$	$1.6x10^{-5}$
28 Dec 2019	$1.3x10^{17}$	$2.5x10^{13}$	$8.3x10^{-5}$	$3.1x10^{-5}$
2 Jan 2020	$1.6x10^{17}$	$3.2x10^{13}$	$8.6x10^{-5}$	$2.4x10^{-5}$
7 Jan 2020	$7.3x10^{16}$	$2.9x10^{13}$	$7.1x10^{-5}$	$4.8x10^{-5}$
8 Jan 2020	$8.5x10^{16}$	$3.1x10^{13}$	$2.9x10^{-5}$	$3.6x10^{-5}$
12 Jan 2020	$3.0x10^{17}$	$2.8x10^{13}$	$2.6x10^{-5}$	$2.0x10^{-5}$
13 Jan 2020	$1.3x10^{17}$	$3.5x10^{13}$	$2.3x10^{-5}$	$2.8x10^{-5}$
18 Jan 2020	$2.1x10^{17}$	$3.1x10^{13}$	$1.2x10^{-5}$	$3.4x10^{-5}$
23 Jan 2020	$3.5x10^{17}$	$4.0x10^{13}$	$1.0x10^{-4}$	$1.3x10^{-5}$
24 Jan 2020	$2.0x10^{17}$	$3.0x10^{13}$	$5.1x10^{-5}$	$2.1x10^{-5}$
25 Jan 2020	$1.2x10^{17}$	$2.8x10^{13}$	$1.3x10^{-4}$	$3.2x10^{-5}$
27 Jan 2020	$1.7x10^{17}$	$2.4x10^{13}$	$1.1x10^{-4}$	$3.3x10^{-5}$
28 Jan 2020	$1.2x10^{17}$	$3.0x10^{13}$	$5.6x10^{-5}$	$1.7x10^{-5}$
29 Jan 2020	$1.6x10^{17}$	$2.7x10^{13}$	$7.7x10^{-5}$	$2.7x10^{-5}$
30 Jan 2020	$3.2x10^{17}$	$3.9x10^{13}$	$8.6x10^{-5}$	$1.7x10^{-5}$
2 Feb 2020	$1.6x10^{17}$	$2.3x10^{13}$	$9.1x10^{-5}$	$2.5x10^{-5}$
3 Feb 2020	$9.2x10^{16}$	$2.7x10^{13}$	$6.0x10^{-5}$	$2.2x10^{-5}$
4 Feb 2020	$1.3x10^{17}$	$3.3x10^{13}$	$4.6x10^{-5}$	$2.9x10^{-5}$
8 Feb 2020	$4.0x10^{17}$	$4.4x10^{13}$	$6.4x10^{-5}$	$2.0x10^{-5}$
9 Feb 2020	$4.2x10^{17}$	$4.0x10^{13}$	$6.9x10^{-5}$	$1.5x10^{-5}$
13 Feb 2020	$1.4x10^{17}$	$3.2x10^{13}$	$5.5x10^{-5}$	$1.6x10^{-5}$
14 Feb 2020	$1.8x10^{17}$	$3.6x10^{13}$	$7.4x10^{-5}$	$1.9x10^{-5}$
15 Feb 2020	$1.8x10^{17}$	$2.0x10^{13}$	$2.1x10^{-5}$	$3.3x10^{-5}$
19 Feb 2020	$1.1x10^{17}$	$3.0x10^{13}$	$4.6x10^{-5}$	$2.4x10^{-5}$
23 Feb 2020	$2.0x10^{17}$	$2.9x10^{13}$	$8.7x10^{-5}$	$9.3x10^{-6}$
24 Feb 2020	$6.7x10^{17}$	$3.8x10^{13}$	$4.8x10^{-5}$	$6.9x10^{-6}$
25 Feb 2020	$2.0x10^{17}$	$3.6x10^{13}$	$7.5x10^{-5}$	$1.5x10^{-5}$
26 Feb 2020	$3.0x10^{17}$	$3.7x10^{13}$	$1.1x10^{-4}$	$1.2x10^{-5}$
28 Feb 2020	$1.3x10^{17}$	$3.1x10^{13}$	$1.4x10^{-4}$	$2.2x10^{-5}$
29 Feb 2020	$2.3x10^{17}$	$3.5x10^{13}$	$7.0x10^{-5}$	$1.3x10^{-5}$
1 Mar 2020	$1.8x10^{17}$	$3.0x10^{13}$	$0.8x10^{-6}$	$2.1x10^{-5}$
2 Mar 2020	$2.4x10^{17}$	$3.1x10^{13}$	$4.5x10^{-5}$	$1.4x10^{-5}$
4 Mar 2020	$8.4x10^{16}$	$1.4x10^{13}$	$6.0x10^{-5}$	$3.1x10^{-5}$
5 Mar 2020	$1.4x10^{17}$	$4.2x10^{13}$	$8.2x10^{-5}$	$3.5x10^{-5}$
6 Mar 2020	$2.6x10^{17}$	$3.9x10^{13}$	$3.7x10^{-5}$	$1.7x10^{-5}$
7 Mar 2020	$1.0x10^{17}$	$2.7x10^{13}$	$2.9x10^{-5}$	$2.5x10^{-5}$
8 Mar 2020	$3.0x10^{17}$	$2.9x10^{13}$	$6.3x10^{-5}$	$1.4x10^{-5}$
11 Mar 2020	$2.2x10^{17}$	$3.4x10^{13}$	$7.5x10^{-5}$	$1.3x10^{-5}$
12 Mar 2020	$3.9x10^{17}$	$3.5x10^{13}$	$6.5x10^{-5}$	$1.1x10^{-5}$

Nevado del Ruiz, Colombia

date	SO_2 VCD max. [molecules cm^{-2}]	BrO VCD	BrO/SO_2 fitted	BrO/SO_2 error
13 Mar 2020	$1.5x10^{17}$	$2.0x10^{13}$	$4.8x10^{-5}$	$2.7x10^{-5}$
15 Mar 2020	$1.1x10^{17}$	$2.1x10^{13}$	$1.4x10^{-4}$	$3.3x10^{-5}$
16 Mar 2020	$6.5x10^{16}$	$2.7x10^{13}$	$6.5x10^{-5}$	$1.8x10^{-5}$
17 Mar 2020	$4.6x10^{17}$	$6.0x10^{13}$	$1.1x10^{-4}$	$1.4x10^{-5}$
18 Mar 2020	$1.5x10^{17}$	$2.1x10^{13}$	$8.5x10^{-5}$	$3.8x10^{-5}$
21 Mar 2020	$2.5x10^{17}$	$4.5x10^{13}$	$2.8x10^{-5}$	$2.8x10^{-5}$
22 Mar 2020	$3.0x10^{17}$	$4.7x10^{13}$	$2.8x10^{-5}$	$1.3x10^{-5}$
23 Mar 2020	$1.6x10^{17}$	$3.4x10^{13}$	$0.8x10^{-5}$	$1.4x10^{-5}$
26 Mar 2020	$1.1x10^{17}$	$2.0x10^{13}$	$6.8x10^{-5}$	$1.8x10^{-5}$
27 Mar 2020	$2.8x10^{17}$	$4.5x10^{13}$	$8.7x10^{-5}$	$1.1x10^{-5}$
29 Mar 2020	$3.5x10^{17}$	$1.7x10^{13}$	$4.1x10^{-5}$	$1.4x10^{-5}$
1 April 2020	$1.3x10^{17}$	$1.6x10^{13}$	$7.5x10^{-5}$	$3.7x10^{-5}$
2 April 2020	$1.6x10^{17}$	$4.6x10^{13}$	$6.3x10^{-5}$	$2.0x10^{-5}$
6 April 2020	$9.2x10^{16}$	$1.5x10^{13}$	$6.4x10^{-5}$	$4.0x10^{-5}$
7 April 2020	$8.5x10^{16}$	$3.6x10^{13}$	$6.7x10^{-5}$	$4.9x10^{-5}$
8 April 2020	$1.4x10^{17}$	$3.4x10^{13}$	$4.1x10^{-5}$	$2.5x10^{-5}$
12 April 2020	$3.9x10^{17}$	$5.4x10^{13}$	$1.1x10^{-4}$	$1.4x10^{-5}$
13 April 2020	$2.3x10^{17}$	$3.4x10^{13}$	$8.7x10^{-5}$	$2.0x10^{-5}$
16 April 2020	$9.3x10^{16}$	$2.6x10^{13}$	$7.6x10^{-5}$	$3.0x10^{-5}$
18 April 2020	$3.0x10^{17}$	$3.5x10^{13}$	$6.7x10^{-5}$	$1.1x10^{-5}$
24 April 2020	$2.6x10^{17}$	$4.2x10^{13}$	$7.6x10^{-5}$	$2.7x10^{-5}$
28 April 2020	$1.9x10^{17}$	$3.7x10^{13}$	$5.9x10^{-5}$	$2.3x10^{-5}$
29 April 2020	$2.8x10^{17}$	$3.6x10^{13}$	$7.7x10^{-5}$	$2.5x10^{-5}$
3 May 2020	$1.2x10^{17}$	$3.3x10^{13}$	$9.5x10^{-5}$	$2.3x10^{-5}$
4 May 2020	$1.1x10^{17}$	$2.1x10^{13}$	$2.1x10^{-5}$	$3.6x10^{-5}$
14 May 2020	$6.2x10^{16}$	$3.8x10^{13}$	$1.2x10^{-4}$	$5.6x10^{-5}$
24 May 2020	$7.5x10^{16}$	$1.6x10^{13}$	$9.1x10^{-5}$	$3.1x10^{-5}$
29 May 2020	$1.1x10^{17}$	$3.5x10^{13}$	$6.7x10^{-5}$	$3.4x10^{-5}$
30 May 2020	$8.6x10^{16}$	$3.4x10^{13}$	$6.7x10^{-5}$	$3.4x10^{-5}$
31 May 2020	$1.6x10^{17}$	$2.6x10^{13}$	$1.1x10^{-4}$	$3.2x10^{-5}$
10 June 2020	$4.5x10^{17}$	$5.0x10^{13}$	$1.1x10^{-4}$	$1.6x10^{-5}$
11 June 2020	$3.9x10^{17}$	$4.1x10^{13}$	$1.0x10^{-4}$	$1.5x10^{-5}$
12 June 2020	$1.0x10^{17}$	$3.9x10^{13}$	$4.7x10^{-5}$	$9.3x10^{-6}$
16 June 2020	$1.0x10^{17}$	$2.4x10^{13}$	$1.2x10^{-4}$	$3.9x10^{-5}$
19 June 2020	$1.5x10^{17}$	$2.1x10^{13}$	$6.7x10^{-5}$	$1.9x10^{-5}$
20 June 2020	$1.3x10^{17}$	$2.7x10^{13}$	$1.8x10^{-5}$	$2.3x10^{-5}$
21 June 2020	$9.1x10^{16}$	$2.7x10^{13}$	$6.7x10^{-5}$	$3.1x10^{-5}$
25 June 2020	$1.2x10^{17}$	$2.3x10^{13}$	$6.5x10^{-5}$	$2.3x10^{-5}$
26 June 2020	$8.2x10^{16}$	$2.8x10^{13}$	$6.3x10^{-5}$	$2.8x10^{-5}$
27 June 2020	$6.0x10^{16}$	$2.0x10^{13}$	$2.2x10^{-5}$	$3.4x10^{-5}$
29 June 2020	$9.1x10^{16}$	$1.9x10^{13}$	$1.1x10^{-4}$	$2.1x10^{-5}$
30 June 2020	$1.3x10^{17}$	$2.8x10^{13}$	$7.9x10^{-5}$	$2.3x10^{-5}$
1 July 2020	$1.1x10^{17}$	$3.7x10^{13}$	$8.9x10^{-5}$	$2.0x10^{-5}$
2 July 2020	$9.2x10^{16}$	$2.9x10^{13}$	$1.5x10^{-4}$	$3.3x10^{-5}$
7 July 2020	$1.5x10^{17}$	$3.3x10^{13}$	$1.9x10^{-4}$	$5.4x10^{-5}$
23 July 2020	$2.5x10^{17}$	$2.5x10^{13}$	$6.9x10^{-5}$	$3.1x10^{-5}$
27 July 2020	$1.1x10^{17}$	$2.8x10^{13}$	$8.8x10^{-5}$	$1.8x10^{-5}$
28 July 2020	$8.7x10^{16}$	$3.4x10^{13}$	$1.5x10^{-4}$	$3.9x10^{-5}$
29 July 2020	$1.7x10^{17}$	$3.3x10^{13}$	$7.7x10^{-5}$	$2.3x10^{-5}$
1 Aug 2020	$1.1x10^{17}$	$3.7x10^{13}$	$4.5x10^{-5}$	$2.8x10^{-5}$
2 Aug 2020	$1.9x10^{17}$	$3.7x10^{13}$	$6.4x10^{-5}$	$1.9x10^{-5}$
7 Aug 2020	$9.3x10^{16}$	$2.9x10^{13}$	$6.2x10^{-6}$	$1.8x10^{-5}$
8 Aug 2020	$1.7x10^{17}$	$4.1x10^{13}$	$2.0x10^{-5}$	$1.9x10^{-5}$
9 Aug 2020	$1.3x10^{17}$	$2.4x10^{13}$	$8.3x10^{-6}$	$3.1x10^{-5}$
13 Aug 2020	$1.9x10^{17}$	$3.5x10^{13}$	$7.4x10^{-5}$	$2.6x10^{-5}$
14 Aug 2020	$8.9x10^{16}$	$2.1x10^{13}$	$8.6x10^{-5}$	$3.1x10^{-5}$
18 Aug 2020	$1.7x10^{17}$	$3.8x10^{13}$	$1.2x10^{-4}$	$2.7x10^{-5}$
19 Aug 2020	$1.7x10^{17}$	$3.8x10^{13}$	$1.1x10^{-4}$	$2.7x10^{-5}$
23 Aug 2020	$2.2x10^{17}$	$3.8x10^{13}$	$8.4x10^{-5}$	$1.6x10^{-5}$
24 Aug 2020	$1.1x10^{17}$	$4.6x10^{13}$	$9.5x10^{-5}$	$5.5x10^{-5}$
29 Aug 2020	$1.3x10^{17}$	$2.9x10^{13}$	$8.1x10^{-5}$	$3.2x10^{-5}$
2 Sept 2020	$4.4x10^{17}$	$2.8x10^{13}$	$4.3x10^{-5}$	$1.6x10^{-5}$
3 Sept 2020	$3.9x10^{17}$	$4.1x10^{13}$	$7.0x10^{-5}$	$1.6x10^{-5}$
9 Sept 2020	$1.5x10^{17}$	$3.2x10^{13}$	$1.1x10^{-4}$	$2.1x10^{-5}$
10 Sept 2020	$1.1x10^{17}$	$1.9x10^{13}$	$6.1x10^{-5}$	$4.6x10^{-5}$
19 Sept 2020	$2.4x10^{17}$	$3.4x10^{13}$	$8.7x10^{-5}$	$1.2x10^{-5}$
20 Sept 2020	$9.5x10^{16}$	$3.8x10^{13}$	$5.4x10^{-5}$	$3.3x10^{-5}$
21 Sept 2020	$8.2x10^{16}$	$1.5x10^{13}$	$4.9x10^{-5}$	$3.6x10^{-5}$
29 Sept 2020	$9.8x10^{16}$	$3.2x10^{13}$	$8.4x10^{-5}$	$1.8x10^{-5}$
30 Sept 2020	$1.7x10^{17}$	$3.5x10^{13}$	$7.0x10^{-5}$	$2.3x10^{-5}$
1 Oct 2020	$1.0x10^{17}$	$2.7x10^{13}$	$6.9x10^{-5}$	$3.2x10^{-5}$

Nevado del Ruiz, Colombia

date	SO_2 VCD max. [molecules cm^{-2}]	BrO VCD max. [molecules cm^{-2}]	BrO/SO_2 fitted	BrO/SO_2 error
2 Oct 2020	$9.3x10^{16}$	$2.8x10^{13}$	$1.5x10^{-4}$	$2.3x10^{-5}$
4 Oct 2020	$8.5x10^{16}$	$2.4x10^{13}$	$1.1x10^{-4}$	$3.8x10^{-5}$
5 Oct 2020	$1.8x10^{17}$	$4.1x10^{13}$	$9.6x10^{-5}$	$1.0x10^{-5}$
6 Oct 2020	$7.2x10^{16}$	$2.6x10^{13}$	$1.5x10^{-4}$	$4.0x10^{-5}$
10 Oct 2020	$1.1x10^{17}$	$4.2x10^{13}$	$9.1x10^{-5}$	$2.3x10^{-5}$
11 Oct 2020	$2.0x10^{17}$	$3.4x10^{13}$	$1.1x10^{-4}$	$2.5x10^{-5}$
12 Oct 2020	$1.4x10^{17}$	$2.7x10^{13}$	$6.6x10^{-5}$	$2.4x10^{-5}$
14 Oct 2020	$6.9x10^{16}$	$1.7x10^{13}$	$1.1x10^{-4}$	$2.0x10^{-5}$
17 Oct 2020	$1.4x10^{17}$	$2.2x10^{13}$	$8.3x10^{-5}$	$1.9x10^{-5}$
18 Oct 2020	$1.3x10^{17}$	$1.7x10^{13}$	$6.4x10^{-5}$	$3.2x10^{-5}$
20 Oct 2020	$1.3x10^{17}$	$2.1x10^{13}$	$6.1x10^{-5}$	$3.0x10^{-5}$
28 Oct 2020	$8.5x10^{16}$	$2.2x10^{13}$	$7.4x10^{-5}$	$2.1x10^{-5}$
31 Oct 2020	$1.3x10^{17}$	$2.8x10^{13}$	$7.2x10^{-5}$	$2.2x10^{-5}$
1 Nov 2020	$3.0x10^{17}$	$4.0x10^{13}$	$7.0x10^{-5}$	$8.4x10^{-6}$
2 Nov 2020	$2.2x10^{17}$	$4.0x10^{13}$	$6.2x10^{-5}$	$2.8x10^{-5}$
3 Nov 2020	$7.7x10^{16}$	$1.7x10^{13}$	$9.1x10^{-5}$	$7.3x10^{-5}$
6 Nov 2020	$5.6x10^{17}$	$7.5x10^{13}$	$1.1x10^{-4}$	$7.4x10^{-6}$
8 Nov 2020	$1.6x10^{17}$	$3.2x10^{13}$	$7.3x10^{-5}$	$2.1x10^{-5}$
10 Nov 2020	$8.0x10^{16}$	$1.9x10^{13}$	$8.4x10^{-5}$	$2.1x10^{-5}$
11 Nov 2020	$2.5x10^{17}$	$3.1x10^{13}$	$1.0x10^{-4}$	$1.2x10^{-5}$
12 Nov 2020	$3.0x10^{17}$	$3.6x10^{13}$	$7.6x10^{-5}$	$1.2x10^{-5}$
13 Nov 2020	$3.7x10^{17}$	$5.2x10^{13}$	$1.1x10^{-4}$	$1.9x10^{-5}$
18 Nov 2020	$5.6x10^{17}$	$5.7x10^{13}$	$8.9x10^{-5}$	$8.6x10^{-6}$
19 Nov 2020	$3.3x10^{17}$	$3.7x10^{13}$	$1.0x10^{-4}$	$1.7x10^{-5}$
23 Nov 2020	$1.1x10^{17}$	$3.0x10^{13}$	$8.7x10^{-5}$	$2.4x10^{-5}$
24 Nov 2020	$7.2x10^{16}$	$2.4x10^{13}$	$1.3x10^{-4}$	$3.8x10^{-5}$
29 Nov 2020	$1.2x10^{17}$	$3.1x10^{13}$	$7.6x10^{-5}$	$2.6x10^{-5}$
1 Dec 2020	$7.7x10^{16}$	$1.9x10^{13}$	$1.2x10^{-4}$	$2.6x10^{-5}$
3 Dec 2020	$2.8x10^{17}$	$5.4x10^{13}$	$8.0x10^{-5}$	$1.1x10^{-5}$
4 Dec 2020	$1.1x10^{17}$	$2.4x10^{13}$	$2.8x10^{-5}$	$2.8x10^{-5}$
14 Dec 2020	$1.6x10^{17}$	$2.8x10^{13}$	$1.0x10^{-4}$	$9.8x10^{-6}$
15 Dec 2020	$1.3x10^{17}$	$2.7x10^{13}$	$1.3x10^{-4}$	$5.0x10^{-5}$
18 Dec 2020	$1.1x10^{17}$	$2.8x10^{13}$	$7.9x10^{-5}$	$2.4x10^{-5}$
31 Dec 2020	$2.3x10^{17}$	$2.8x10^{13}$	$7.6x10^{-5}$	$1.1x10^{-5}$
30 Jan 2021	$2.4x10^{17}$	$3.0x10^{13}$	$2.3x10^{-5}$	$2.1x10^{-5}$
31 Jan 2021	$9.6x10^{16}$	$3.6x10^{13}$	$1.4x10^{-5}$	$3.4x10^{-5}$
1 Feb 2021	$1.0x10^{17}$	$2.0x10^{13}$	$6.3x10^{-5}$	$6.0x10^{-5}$
4 Feb 2021	$1.0x10^{17}$	$2.8x10^{13}$	$6.4x10^{-5}$	$2.5x10^{-5}$
5 Feb 2021	$4.7x10^{17}$	$2.6x10^{13}$	$6.3x10^{-5}$	$1.0x10^{-5}$
6 Feb 2021	$2.8x10^{17}$	$3.1x10^{13}$	$4.9x10^{-5}$	$1.6x10^{-5}$
7 Feb 2021	$2.2x10^{17}$	$2.3x10^{13}$	$9.3x10^{-5}$	$1.7x10^{-5}$
9 Feb 2021	$1.2x10^{17}$	$2.4x10^{13}$	$9.4x10^{-5}$	$3.9x10^{-5}$
17 Feb 2021	$1.5x10^{17}$	$2.7x10^{13}$	$1.0x10^{-4}$	$3.8x10^{-5}$
22 Feb 2021	$1.3x10^{17}$	$3.1x10^{13}$	$8.8x10^{-5}$	$2.2x10^{-5}$
26 Feb 2021	$4.2x10^{17}$	$3.3x10^{13}$	$5.6x10^{-5}$	$1.2x10^{-5}$
27 Feb 2021	$4.0x10^{17}$	$4.7x10^{13}$	$1.0x10^{-4}$	$2.7x10^{-5}$
28 Feb 2021	$8.0x10^{16}$	$1.4x10^{13}$	$4.9x10^{-5}$	$3.3x10^{-5}$
3 Mar 2021	$4.7x10^{17}$	$6.1x10^{13}$	$6.5x10^{-5}$	$5.4x10^{-6}$
4 Mar 2021	$7.5x10^{17}$	$8.0x10^{13}$	$6.2x10^{-5}$	$5.4x10^{-6}$
5 Mar 2021	$4.3x10^{17}$	$3.4x10^{13}$	$5.1x10^{-5}$	$7.5x10^{-6}$
14 Mar 2021	$2.3x10^{17}$	$3.3x10^{13}$	$1.0x10^{-4}$	$1.8x10^{-5}$
15 Mar 2021	$2.8x10^{17}$	$2.3x10^{13}$	$4.5x10^{-5}$	$1.4x10^{-5}$
19 Mar 2021	$2.8x10^{17}$	$3.9x10^{13}$	$5.2x10^{-5}$	$1.4x10^{-5}$
20 Mar 2021	$8.6x10^{17}$	$7.3x10^{13}$	$7.4x10^{-5}$	$5.1x10^{-6}$
21 Mar 2021	$2.1x10^{17}$	$3.9x10^{13}$	$4.8x10^{-5}$	$1.9x10^{-5}$
22 Mar 2021	$1.6x10^{17}$	$2.5x10^{13}$	$1.3x10^{-4}$	$1.7x10^{-5}$
10 April 2021	$1.3x10^{17}$	$3.3x10^{13}$	$7.7x10^{-5}$	$2.6x10^{-5}$
11 April 2021	$1.3x10^{17}$	$2.7x10^{13}$	$1.2x10^{-4}$	$4.7x10^{-5}$
16 April 2021	$1.1x10^{17}$	$2.7x10^{13}$	$7.7x10^{-5}$	$3.4x10^{-5}$
22 April 2021	$8.7x10^{16}$	$3.5x10^{13}$	$1.2x10^{-4}$	$2.7x10^{-5}$
25 April 2021	$2.4x10^{17}$	$3.4x10^{13}$	$5.3x10^{-5}$	$1.5x10^{-5}$
26 April 2021	$2.0x10^{17}$	$3.3x10^{13}$	$9.8x10^{-5}$	$2.9x10^{-5}$
27 April 2021	$3.3x10^{17}$	$3.7x10^{13}$	$7.5x10^{-5}$	$1.7x10^{-5}$
1 May 2021	$2.3x10^{17}$	$2.5x10^{13}$	$4.3x10^{-5}$	$2.4x10^{-5}$
2 May 2021	$1.9x10^{17}$	$3.2x10^{13}$	$4.8x10^{-5}$	$2.3x10^{-5}$
3 May 2021	$1.3x10^{17}$	$2.4x10^{13}$	$7.8x10^{-5}$	$2.6x10^{-5}$
8 May 2021	$1.7x10^{17}$	$3.4x10^{13}$	$6.5x10^{-5}$	$3.7x10^{-5}$
13 May 2021	$9.2x10^{16}$	$2.9x10^{13}$	$4.6x10^{-5}$	$4.5x10^{-5}$
17 May 2021	$2.1x10^{17}$	$3.5x10^{13}$	$2.9x10^{-5}$	$9.7x10^{-6}$
18 May 2021	$2.9x10^{17}$	$4.5x10^{13}$	$8.2x10^{-5}$	$2.9x10^{-5}$
19 May 2021	$1.4x10^{17}$	$2.6x10^{13}$	$9.4x10^{-5}$	$2.3x10^{-5}$

Nevado del Ruiz, Colombia

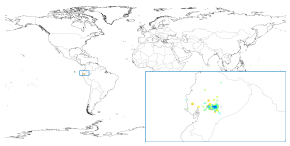
date	SO_2 VCD max. [molecules cm^{-2}]	BrO VCD max. [molecules cm^{-2}]	BrO/SO_2 fitted	BrO/SO_2 error
22 May 2021	$6.4x10^{16}$	$1.8x10^{13}$	$5.1x10^{-5}$	$2.4x10^{-5}$
27 May 2021	$7.7x10^{16}$	$2.5x10^{13}$	$2.3x10^{-5}$	$3.1x10^{-5}$
28 May 2021	$4.6x10^{17}$	$3.7x10^{13}$	$7.3x10^{-5}$	$1.1x10^{-5}$
29 May 2021	$2.4x10^{17}$	$3.3x10^{13}$	$6.1x10^{-5}$	$1.7x10^{-5}$
30 May 2021	$1.5x10^{17}$	$2.5x10^{13}$	$1.2x10^{-4}$	$3.8x10^{-5}$
2 June 2021	$1.2x10^{17}$	$2.4x10^{13}$	$4.4x10^{-5}$	$3.3x10^{-5}$
3 June 2021	$7.6x10^{16}$	$2.0x10^{13}$	$5.4x10^{-5}$	$2.7x10^{-5}$
9 June 2021	$1.4x10^{17}$	$2.3x10^{13}$	$1.0x10^{-4}$	$2.4x10^{-5}$
13 June 2021	$2.4x10^{17}$	$3.4x10^{13}$	$7.6x10^{-5}$	$8.7x10^{-6}$
14 June 2021	$1.7x10^{17}$	$3.0x10^{13}$	$5.3x10^{-5}$	$2.1x10^{-5}$
18 June 2021	$8.4x10^{16}$	$2.7x10^{13}$	$1.4x10^{-5}$	$3.4x10^{-5}$
19 June 2021	$1.1x10^{17}$	$3.2x10^{13}$	$4.2x10^{-5}$	$3.8x10^{-5}$
23 June 2021	$1.5x10^{17}$	$2.9x10^{13}$	$6.9x10^{-5}$	$2.4x10^{-5}$
24 June 2021	$7.0x10^{16}$	$2.9x10^{13}$	$8.5x10^{-5}$	$5.1x10^{-5}$
29 June 2021	$2.4x10^{17}$	$3.0x10^{13}$	$5.3x10^{-5}$	$1.8x10^{-5}$
30 June 2021	$7.8x10^{16}$	$2.6x10^{13}$	$2.2x10^{-5}$	$3.1x10^{-5}$
4 July 2021	$1.3x10^{17}$	$4.5x10^{13}$	$1.1x10^{-4}$	$3.5x10^{-5}$
5 July 2021	$1.3x10^{17}$	$2.9x10^{13}$	$1.7x10^{-5}$	$2.4x10^{-5}$
15 July 2021	$1.3x10^{17}$	$3.3x10^{13}$	$6.8x10^{-5}$	$2.6x10^{-5}$
20 July 2021	$6.9x10^{16}$	$3.3x10^{13}$	$3.0x10^{-6}$	$3.9x10^{-5}$
26 July 2021	$8.2x10^{16}$	$3.5x10^{13}$	$7.0x10^{-5}$	$3.3x10^{-5}$
31 July 2021	$3.2x10^{17}$	$5.5x10^{13}$	$1.1x10^{-4}$	$2.5x10^{-5}$
1 Aug 2021	$1.1x10^{17}$	$1.4x10^{13}$	$8.0x10^{-5}$	$1.7x10^{-5}$
4 Aug 2021	$6.9x10^{16}$	$2.2x10^{13}$	$4.7x10^{-5}$	$4.0x10^{-5}$
6 Aug 2021	$1.3x10^{17}$	$3.5x10^{13}$	$9.2x10^{-5}$	$3.4x10^{-5}$
16 Aug 2021	$1.7x10^{17}$	$2.4x10^{13}$	$8.0x10^{-5}$	$2.0x10^{-5}$
20 Aug 2021	$3.0x10^{17}$	$3.8x10^{13}$	$1.3x10^{-4}$	$1.6x10^{-5}$
25 Aug 2021	$1.3x10^{17}$	$1.9x10^{13}$	$1.0x10^{-4}$	$2.6x10^{-5}$
26 Aug 2021	$1.2x10^{17}$	$2.6x10^{13}$	$6.6x10^{-5}$	$1.5x10^{-5}$
31 Aug 2021	$1.3x10^{17}$	$3.3x10^{13}$	$9.7x10^{-5}$	$2.1x10^{-5}$
1 Sept 2021	$1.2x10^{17}$	$3.1x10^{13}$	$1.3x10^{-4}$	$3.7x10^{-5}$
2 Sept 2021	$1.0x10^{17}$	$3.7x10^{13}$	$1.1x10^{-4}$	$4.2x10^{-5}$
5 Sept 2021	$2.2x10^{17}$	$3.2x10^{13}$	$9.0x10^{-5}$	$1.9x10^{-5}$
6 Sept 2021	$4.1x10^{17}$	$4.8x10^{13}$	$1.1x10^{-4}$	$1.2x10^{-5}$
7 Sept 2021	$1.4x10^{17}$	$4.2x10^{13}$	$1.1x10^{-4}$	$2.3x10^{-5}$
11 Sept 2021	$9.9x10^{16}$	$3.2x10^{13}$	$1.0x10^{-4}$	$2.0x10^{-5}$
12 Sept 2021	$7.3x10^{16}$	$2.6x10^{13}$	$6.1x10^{-5}$	$3.4x10^{-5}$
17 Sept 2021	$1.7x10^{17}$	$4.5x10^{13}$	$6.8x10^{-5}$	$6.6x10^{-5}$
22 Sept 2021	$2.0x10^{17}$	$4.5x10^{13}$	$1.0x10^{-4}$	$2.3x10^{-5}$
24 Sept 2021	$9.3x10^{16}$	$2.1x10^{13}$	$5.7x10^{-5}$	$4.1x10^{-5}$
26 Sept 2021	$8.1x10^{16}$	$2.3x10^{13}$	$1.2x10^{-4}$	$4.1x10^{-5}$
27 Sept 2021	$1.7x10^{17}$	$3.6x10^{13}$	$7.1x10^{-5}$	$1.8x10^{-5}$
28 Sept 2021	$1.4x10^{17}$	$2.6x10^{13}$	$7.7x10^{-5}$	$1.5x10^{-5}$
29 Sept 2021	$1.9x10^{17}$	$3.2x10^{13}$	$6.7x10^{-5}$	$3.0x10^{-5}$
3 Oct 2021	$1.8x10^{17}$	$4.6x10^{13}$	$1.1x10^{-4}$	$2.0x10^{-5}$
4 Oct 2021	$1.1x10^{17}$	$3.6x10^{13}$	$8.4x10^{-5}$	$2.5x10^{-5}$
8 Oct 2021	$1.3x10^{17}$	$3.8x10^{13}$	$1.4x10^{-4}$	$5.3x10^{-5}$
9 Oct 2021	$1.4x10^{17}$	$1.9x10^{13}$	$4.9x10^{-5}$	$1.8x10^{-5}$
10 Oct 2021	$1.3x10^{17}$	$2.5x10^{13}$	$1.0x10^{-4}$	$2.2x10^{-5}$
19 Oct 2021	$2.3x10^{17}$	$3.9x10^{13}$	$5.8x10^{-5}$	$1.9x10^{-5}$
23 Oct 2021	$1.5x10^{17}$	$2.4x10^{13}$	$8.1x10^{-5}$	$1.6x10^{-5}$
24 Oct 2021	$3.2x10^{17}$	$4.6x10^{13}$	$9.8x10^{-5}$	$1.9x10^{-5}$
25 Oct 2021	$2.6x10^{17}$	$3.3x10^{13}$	$9.2x10^{-5}$	$1.3x10^{-5}$
26 Oct 2021	$1.0x10^{17}$	$2.6x10^{13}$	$1.1x10^{-4}$	$2.7x10^{-5}$
29 Oct 2021	$1.8x10^{17}$	$3.3x10^{13}$	$9.4x10^{-5}$	$3.0x10^{-5}$
30 Oct 2021	$2.2x10^{17}$	$4.1x10^{13}$	$1.2x10^{-4}$	$1.4x10^{-5}$
31 Oct 2021	$1.9x10^{17}$	$4.2x10^{13}$	$1.1x10^{-4}$	$2.5x10^{-5}$
3 Nov 2021	$4.0x10^{17}$	$4.6x10^{13}$	$6.0x10^{-5}$	$1.1x10^{-5}$
4 Nov 2021	$3.2x10^{17}$	$4.5x10^{13}$	$7.0x10^{-5}$	$1.1x10^{-5}$
5 Nov 2021	$1.7x10^{17}$	$3.7x10^{13}$	$1.0x10^{-4}$	$2.7x10^{-5}$
7 Nov 2021	$6.0x10^{16}$	$2.0x10^{13}$	$1.1x10^{-4}$	$3.8x10^{-5}$
8 Nov 2021	$6.9x10^{16}$	$2.8x10^{13}$	$7.2x10^{-5}$	$3.3x10^{-5}$
9 Nov 2021	$2.8x10^{17}$	$3.5x10^{13}$	$6.6x10^{-5}$	$9.5x10^{-6}$
10 Nov 2021	$3.3x10^{17}$	$3.0x10^{13}$	$5.4x10^{-5}$	$1.1x10^{-5}$
11 Nov 2021	$1.3x10^{17}$	$3.3x10^{13}$	$1.0x10^{-4}$	$2.4x10^{-5}$
13 Nov 2021	$6.7x10^{16}$	$2.2x10^{13}$	$1.4x10^{-4}$	$3.5x10^{-5}$
15 Nov 2021	$2.2x10^{17}$	$3.7x10^{13}$	$6.8x10^{-5}$	$1.5x10^{-5}$
20 Nov 2021	$3.2x10^{17}$	$3.7x10^{13}$	$9.2x10^{-5}$	$9.8x10^{-6}$
21 Nov 2021	$1.4x10^{17}$	$2.6x10^{13}$	$7.1x10^{-5}$	$2.2x10^{-5}$
24 Nov 2021	$1.2x10^{17}$	$2.6x10^{13}$	$7.1x10^{-5}$	$2.4x10^{-5}$
25 Nov 2021	$3.5x10^{17}$	$3.4x10^{13}$	$4.7x10^{-5}$	$8.7x10^{-6}$

Nevado del Ruiz, Colombia

date	SO_2 VCD max. [molecules cm^{-2}]	BrO VCD	BrO/SO_2 fitted	BrO/SO_2 error
26 Nov 2021	$2.1x10^{17}$	$3.8x10^{13}$	$7.1x10^{-5}$	$2.3x10^{-5}$
27 Nov 2021	$1.8x10^{17}$	$3.0x10^{13}$	$5.5x10^{-5}$	$1.4x10^{-5}$
23 Dec 2021	$1.6x10^{17}$	$3.2x10^{13}$	$8.3x10^{-5}$	$1.9x10^{-5}$

Sangay, Ecuador

Type: arc
longitude: 78.34° W
latitude: 2.00° S
Events: 230
$BrO > 2\sigma$: 55
BrO/SO_2: $6.0x10^{-5}$
std. dev.: $3.3x10^{-5}$
mean SO_2: $2.0x10^{17}$
mean BrO: $3.0x10^{13}$



16 Mar 2018	$1.0x10^{17}$	$1.9x10^{13}$	$6.7x10^{-5}$	$3.3x10^{-5}$
28 April 2018	$9.9x10^{16}$	$1.3x10^{13}$	$1.0x10^{-5}$	$7.3x10^{-5}$
22 May 2019	$6.5x10^{16}$	$2.4x10^{13}$	$1.4x10^{-4}$	$2.7x10^{-5}$
28 Sept 2019	$1.1x10^{17}$	$5.0x10^{13}$	$1.0x10^{-4}$	$2.4x10^{-5}$
7 Oct 2019	$1.3x10^{17}$	$3.2x10^{13}$	$1.3x10^{-4}$	$1.9x10^{-5}$
8 Oct 2019	$1.8x10^{17}$	$3.7x10^{13}$	$1.0x10^{-4}$	$1.6x10^{-5}$
12 Oct 2019	$1.6x10^{17}$	$2.6x10^{13}$	$8.5x10^{-5}$	$1.8x10^{-5}$
23 Oct 2019	$8.1x10^{16}$	$2.6x10^{13}$	$9.6x10^{-5}$	$2.8x10^{-5}$
24 Oct 2019	$7.8x10^{16}$	$3.1x10^{13}$	$1.5x10^{-4}$	$5.4x10^{-5}$
29 Oct 2019	$2.7x10^{17}$	$5.1x10^{13}$	$8.3x10^{-5}$	$1.8x10^{-5}$
30 Oct 2019	$1.8x10^{17}$	$3.1x10^{13}$	$1.8x10^{-4}$	$2.7x10^{-5}$
2 Nov 2019	$7.1x10^{16}$	$2.6x10^{13}$	$4.7x10^{-5}$	$3.5x10^{-5}$
13 Nov 2019	$1.8x10^{17}$	$2.8x10^{13}$	$9.4x10^{-5}$	$2.5x10^{-5}$
29 Nov 2019	$7.9x10^{16}$	$2.3x10^{13}$	$1.4x10^{-4}$	$3.4x10^{-5}$
4 Dec 2019	$1.7x10^{17}$	$2.9x10^{13}$	$1.0x10^{-4}$	$1.8x10^{-5}$
10 Dec 2019	$1.9x10^{17}$	$3.4x10^{13}$	$1.2x10^{-4}$	$2.2x10^{-5}$
11 Dec 2019	$1.4x10^{17}$	$2.4x10^{13}$	$4.3x10^{-5}$	$2.1x10^{-5}$
15 Dec 2019	$1.7x10^{17}$	$2.8x10^{13}$	$1.1x10^{-4}$	$2.5x10^{-5}$
16 Dec 2019	$1.9x10^{17}$	$3.9x10^{13}$	$1.1x10^{-4}$	$1.3x10^{-5}$
1 Jan 2020	$1.8x10^{17}$	$3.6x10^{13}$	$7.9x10^{-5}$	$1.9x10^{-5}$
6 Jan 2020	$6.8x10^{16}$	$5.3x10^{13}$	$8.6x10^{-5}$	$3.3x10^{-5}$
7 Jan 2020	$7.4x10^{16}$	$2.4x10^{13}$	$4.1x10^{-6}$	$5.4x10^{-5}$
6 Feb 2020	$1.3x10^{17}$	$3.3x10^{13}$	$1.2x10^{-4}$	$2.7x10^{-5}$
18 Feb 2020	$1.5x10^{17}$	$2.9x10^{13}$	$1.7x10^{-5}$	$4.0x10^{-5}$
22 Feb 2020	$9.2x10^{16}$	$1.9x10^{13}$	$8.2x10^{-5}$	$3.9x10^{-5}$
27 Feb 2020	$1.6x10^{17}$	$2.7x10^{13}$	$1.0x10^{-4}$	$1.3x10^{-5}$
9 Mar 2020	$6.5x10^{16}$	$1.6x10^{13}$	$5.0x10^{-5}$	$1.8x10^{-5}$
15 Mar 2020	$1.4x10^{17}$	$2.5x10^{13}$	$1.3x10^{-4}$	$3.3x10^{-5}$
16 Mar 2020	$1.2x10^{17}$	$2.9x10^{13}$	$9.4x10^{-5}$	$3.6x10^{-5}$
31 Mar 2020	$1.7x10^{17}$	$2.6x10^{13}$	$7.3x10^{-5}$	$2.2x10^{-5}$
1 April 2020	$2.4x10^{17}$	$3.6x10^{13}$	$1.0x10^{-4}$	$1.8x10^{-5}$
11 April 2020	$1.0x10^{17}$	$2.1x10^{13}$	$7.9x10^{-5}$	$2.1x10^{-5}$
26 April 2020	$1.3x10^{17}$	$2.0x10^{13}$	$1.2x10^{-4}$	$3.0x10^{-5}$
13 May 2020	$1.9x10^{17}$	$2.6x10^{13}$	$1.3x10^{-4}$	$2.2x10^{-5}$
20 May 2020	$8.8x10^{16}$	$1.8x10^{13}$	$8.2x10^{-5}$	$6.4x10^{-5}$
3 June 2020	$1.3x10^{17}$	$2.7x10^{13}$	$8.3x10^{-5}$	$2.8x10^{-5}$
4 June 2020	$3.4x10^{17}$	$2.9x10^{13}$	$7.7x10^{-5}$	$1.4x10^{-5}$
8 June 2020	$9.8x10^{16}$	$3.5x10^{13}$	$1.0x10^{-4}$	$4.3x10^{-5}$
30 June 2020	$1.6x10^{17}$	$8.8x10^{13}$	$1.1x10^{-4}$	$1.7x10^{-5}$
5 July 2020	$1.2x10^{17}$	$3.1x10^{13}$	$1.1x10^{-4}$	$1.4x10^{-5}$
6 July 2020	$1.7x10^{17}$	$3.1x10^{13}$	$7.7x10^{-5}$	$1.3x10^{-5}$
11 July 2020	$1.6x10^{17}$	$3.5x10^{13}$	$1.2x10^{-4}$	$1.5x10^{-5}$
16 July 2020	$6.8x10^{16}$	$5.3x10^{13}$	$1.6x10^{-4}$	$4.5x10^{-5}$
20 July 2020	$1.3x10^{17}$	$2.4x10^{13}$	$6.7x10^{-5}$	$1.8x10^{-5}$
31 July 2020	$8.6x10^{16}$	$1.8x10^{13}$	$4.8x10^{-5}$	$2.0x10^{-5}$
6 Aug 2020	$1.3x10^{17}$	$1.1x10^{13}$	$1.1x10^{-5}$	$5.0x10^{-5}$
7 Aug 2020	$1.2x10^{17}$	$2.7x10^{13}$	$6.3x10^{-5}$	$4.9x10^{-5}$
11 Aug 2020	$1.2x10^{17}$	$3.7x10^{13}$	$2.4x10^{-5}$	$2.4x10^{-5}$
12 Aug 2020	$3.0x10^{17}$	$4.3x10^{13}$	$3.0x10^{-5}$	$1.9x10^{-5}$
16 Aug 2020	$7.6x10^{16}$	$2.4x10^{13}$	$9.9x10^{-5}$	$1.4x10^{-5}$
22 Aug 2020	$9.3x10^{16}$	$3.0x10^{13}$	$1.3x10^{-4}$	$2.5x10^{-5}$
27 Aug 2020	$1.4x10^{17}$	$2.9x10^{13}$	$7.7x10^{-5}$	$2.2x10^{-5}$
28 Aug 2020	$1.7x10^{17}$	$3.9x10^{13}$	$3.1x10^{-5}$	$4.8x10^{-5}$
31 Aug 2020	$1.7x10^{17}$	$2.3x10^{13}$	$9.1x10^{-5}$	$1.6x10^{-5}$
1 Sept 2020	$8.1x10^{16}$	$2.1x10^{13}$	$7.0x10^{-5}$	$1.7x10^{-5}$
7 Sept 2020	$2.0x10^{17}$	$2.1x10^{13}$	$2.5x10^{-5}$	$1.3x10^{-5}$
12 Sept 2020	$1.0x10^{17}$	$2.1x10^{13}$	$3.0x10^{-5}$	$2.3x10^{-5}$

Sangay, Ecuador

date	SO_2 VCD max. [molecules cm^{-2}]	BrO VCD	BrO/SO_2 fitted	BrO/SO_2 error
14 Sept 2020	$1.0x10^{17}$	$1.3x10^{13}$	$2.7x10^{-5}$	$3.3x10^{-5}$
17 Sept 2020	$1.2x10^{17}$	$2.9x10^{13}$	$8.4x10^{-5}$	$9.5x10^{-6}$
18 Sept 2020	$2.0x10^{17}$	$3.9x10^{13}$	$4.1x10^{-5}$	$8.1x10^{-6}$
20 Sept 2020	$1.4x10^{17}$	$1.8x10^{13}$	$4.2x10^{-5}$	$3.3x10^{-5}$
23 Sept 2020	$1.4x10^{17}$	$2.4x10^{13}$	$1.1x10^{-5}$	$2.5x10^{-5}$
24 Sept 2020	$1.4x10^{17}$	$2.6x10^{13}$	$8.7x10^{-5}$	$2.6x10^{-5}$
28 Sept 2020	$1.4x10^{17}$	$2.8x10^{13}$	$1.3x10^{-4}$	$2.7x10^{-5}$
30 Sept 2020	$1.2x10^{17}$	$3.9x10^{13}$	$4.3x10^{-5}$	$2.3x10^{-5}$
3 Oct 2020	$7.3x10^{16}$	$1.8x10^{13}$	$8.5x10^{-5}$	$3.1x10^{-5}$
4 Oct 2020	$2.4x10^{17}$	$2.6x10^{13}$	$1.1x10^{-4}$	$1.3x10^{-5}$
8 Oct 2020	$6.8x10^{16}$	$1.2x10^{13}$	$7.1x10^{-5}$	$3.1x10^{-5}$
14 Oct 2020	$9.8x10^{16}$	$2.5x10^{13}$	$9.3x10^{-7}$	$4.8x10^{-5}$
15 Oct 2020	$2.7x10^{17}$	$4.0x10^{13}$	$7.8x10^{-5}$	$7.7x10^{-6}$
19 Oct 2020	$3.8x10^{17}$	$2.7x10^{13}$	$7.9x10^{-5}$	$1.4x10^{-5}$
20 Oct 2020	$6.5x10^{17}$	$5.6x10^{13}$	$6.2x10^{-5}$	$8.9x10^{-6}$
24 Oct 2020	$1.6x10^{17}$	$1.9x10^{13}$	$1.2x10^{-4}$	$1.8x10^{-5}$
26 Oct 2020	$3.5x10^{17}$	$5.0x10^{13}$	$6.1x10^{-5}$	$7.7x10^{-6}$
27 Oct 2020	$7.2x10^{16}$	$3.4x10^{13}$	$9.7x10^{-5}$	$2.3x10^{-5}$
4 Nov 2020	$2.2x10^{17}$	$3.5x10^{13}$	$7.7x10^{-5}$	$2.0x10^{-5}$
5 Nov 2020	$1.7x10^{17}$	$3.2x10^{13}$	$2.1x10^{-5}$	$2.0x10^{-5}$
10 Nov 2020	$2.0x10^{17}$	$3.5x10^{13}$	$6.9x10^{-5}$	$1.2x10^{-5}$
17 Nov 2020	$3.2x10^{17}$	$3.8x10^{13}$	$1.1x10^{-4}$	$9.6x10^{-6}$
20 Nov 2020	$8.5x10^{16}$	$1.6x10^{13}$	$7.6x10^{-5}$	$3.2x10^{-5}$
21 Nov 2020	$2.1x10^{17}$	$3.8x10^{13}$	$9.8x10^{-5}$	$1.3x10^{-5}$
5 Dec 2020	$1.3x10^{17}$	$1.3x10^{13}$	$7.3x10^{-5}$	$1.8x10^{-5}$
6 Dec 2020	$1.5x10^{17}$	$3.3x10^{13}$	$6.6x10^{-5}$	$1.7x10^{-5}$
8 Dec 2020	$2.5x10^{17}$	$4.3x10^{13}$	$4.6x10^{-5}$	$1.4x10^{-5}$
9 Dec 2020	$1.2x10^{17}$	$2.9x10^{13}$	$6.4x10^{-5}$	$2.6x10^{-5}$
10 Dec 2020	$1.7x10^{17}$	$2.8x10^{13}$	$1.4x10^{-4}$	$1.4x10^{-5}$
11 Dec 2020	$3.0x10^{17}$	$2.5x10^{13}$	$6.3x10^{-5}$	$7.8x10^{-6}$
12 Dec 2020	$2.8x10^{17}$	$3.2x10^{13}$	$3.2x10^{-5}$	$8.7x10^{-6}$
13 Dec 2020	$1.7x10^{17}$	$4.7x10^{13}$	$7.8x10^{-5}$	$1.7x10^{-5}$
17 Dec 2020	$7.8x10^{16}$	$2.9x10^{13}$	$2.4x10^{-5}$	$1.6x10^{-5}$
19 Dec 2020	$2.6x10^{17}$	$3.3x10^{13}$	$8.7x10^{-5}$	$2.3x10^{-5}$
23 Dec 2020	$6.0x10^{17}$	$4.6x10^{13}$	$8.4x10^{-5}$	$1.1x10^{-5}$
24 Dec 2020	$1.6x10^{17}$	$1.9x10^{13}$	$6.2x10^{-5}$	$6.7x10^{-6}$
25 Dec 2020	$2.4x10^{17}$	$2.2x10^{13}$	$8.2x10^{-5}$	$1.3x10^{-5}$
28 Dec 2020	$3.8x10^{17}$	$2.2x10^{13}$	$6.4x10^{-5}$	$8.3x10^{-6}$
29 Dec 2020	$1.1x10^{18}$	$6.3x10^{13}$	$4.7x10^{-5}$	$4.1x10^{-6}$
30 Dec 2020	$2.7x10^{17}$	$2.8x10^{13}$	$6.0x10^{-5}$	$8.8x10^{-6}$
2 Jan 2021	$1.1x10^{17}$	$2.5x10^{13}$	$8.0x10^{-5}$	$2.2x10^{-5}$
3 Jan 2021	$2.7x10^{17}$	$3.7x10^{13}$	$9.0x10^{-5}$	$9.0x10^{-6}$
4 Jan 2021	$3.3x10^{17}$	$2.8x10^{13}$	$2.9x10^{-5}$	$1.4x10^{-5}$
5 Jan 2021	$4.2x10^{17}$	$3.7x10^{13}$	$9.1x10^{-5}$	$6.0x10^{-6}$
7 Jan 2021	$1.4x10^{17}$	$3.3x10^{13}$	$8.5x10^{-5}$	$3.8x10^{-5}$
8 Jan 2021	$1.5x10^{17}$	$3.4x10^{13}$	$7.7x10^{-5}$	$1.8x10^{-5}$
9 Jan 2021	$1.7x10^{17}$	$2.5x10^{13}$	$6.3x10^{-5}$	$1.0x10^{-5}$
13 Jan 2021	$2.2x10^{17}$	$3.3x10^{13}$	$9.8x10^{-5}$	$1.2x10^{-5}$
14 Jan 2021	$2.1x10^{17}$	$2.8x10^{13}$	$5.2x10^{-5}$	$2.4x10^{-5}$
15 Jan 2021	$1.2x10^{17}$	$4.1x10^{13}$	$1.2x10^{-4}$	$2.8x10^{-5}$
18 Jan 2021	$2.2x10^{17}$	$2.3x10^{13}$	$4.7x10^{-5}$	$1.1x10^{-5}$
19 Jan 2021	$1.2x10^{17}$	$3.2x10^{13}$	$2.9x10^{-5}$	$2.7x10^{-5}$
23 Jan 2021	$4.1x10^{17}$	$3.9x10^{13}$	$7.8x10^{-5}$	$5.3x10^{-6}$
24 Jan 2021	$1.4x10^{17}$	$3.0x10^{13}$	$5.3x10^{-5}$	$2.9x10^{-5}$
29 Jan 2021	$1.7x10^{17}$	$2.3x10^{13}$	$2.9x10^{-5}$	$2.4x10^{-5}$
8 Feb 2021	$6.2x10^{16}$	$2.7x10^{13}$	$1.0x10^{-4}$	$1.6x10^{-5}$
9 Feb 2021	$1.6x10^{17}$	$2.6x10^{13}$	$4.4x10^{-5}$	$1.8x10^{-5}$
10 Feb 2021	$2.7x10^{17}$	$3.8x10^{13}$	$6.2x10^{-5}$	$1.2x10^{-5}$
11 Feb 2021	$3.0x10^{17}$	$3.2x10^{13}$	$5.6x10^{-5}$	$1.3x10^{-5}$
13 Feb 2021	$1.4x10^{17}$	$1.9x10^{13}$	$6.7x10^{-5}$	$2.9x10^{-5}$
14 Feb 2021	$3.5x10^{17}$	$4.3x10^{13}$	$5.2x10^{-5}$	$1.1x10^{-5}$
15 Feb 2021	$4.8x10^{17}$	$3.1x10^{13}$	$4.3x10^{-5}$	$6.7x10^{-6}$
16 Feb 2021	$1.8x10^{17}$	$3.3x10^{13}$	$3.8x10^{-5}$	$1.6x10^{-5}$
18 Feb 2021	$1.3x10^{17}$	$2.3x10^{13}$	$7.8x10^{-5}$	$7.9x10^{-6}$
19 Feb 2021	$2.2x10^{17}$	$2.7x10^{13}$	$4.1x10^{-5}$	$1.7x10^{-5}$
20 Feb 2021	$8.3x10^{17}$	$4.6x10^{13}$	$4.9x10^{-5}$	$4.7x10^{-6}$
23 Feb 2021	$1.3x10^{17}$	$1.7x10^{13}$	$2.8x10^{-5}$	$1.5x10^{-5}$
24 Feb 2021	$1.1x10^{17}$	$2.4x10^{13}$	$1.5x10^{-5}$	$1.4x10^{-5}$
25 Feb 2021	$2.9x10^{17}$	$2.8x10^{13}$	$1.8x10^{-5}$	$1.4x10^{-5}$
1 Mar 2021	$2.5x10^{17}$	$2.4x10^{13}$	$7.2x10^{-5}$	$1.2x10^{-5}$
2 Mar 2021	$5.3x10^{17}$	$3.1x10^{13}$	$4.5x10^{-5}$	$5.5x10^{-6}$

Sangay, Ecuador

date	SO_2 VCD max. [molecules cm^{-2}]	BrO VCD	BrO/SO_2 fitted	BrO/SO_2 error
6 Mar 2021	$6.0x10^{17}$	$5.0x10^{13}$	$7.2x10^{-5}$	$4.1x10^{-6}$
8 Mar 2021	$6.3x10^{17}$	$3.6x10^{13}$	$6.4x10^{-5}$	$1.2x10^{-5}$
9 Mar 2021	$6.4x10^{17}$	$5.7x10^{13}$	$4.7x10^{-5}$	$5.8x10^{-6}$
12 Mar 2021	$1.3x10^{17}$	$9.7x10^{13}$	$2.0x10^{-5}$	$4.9x10^{-6}$
13 Mar 2021	$2.5x10^{17}$	$3.2x10^{13}$	$9.3x10^{-5}$	$1.5x10^{-5}$
14 Mar 2021	$4.5x10^{17}$	$3.7x10^{13}$	$2.8x10^{-5}$	$1.1x10^{-5}$
18 Mar 2021	$1.9x10^{17}$	$2.6x10^{13}$	$6.6x10^{-5}$	$1.3x10^{-5}$
22 Mar 2021	$1.8x10^{17}$	$1.1x10^{13}$	$4.6x10^{-5}$	$1.7x10^{-5}$
23 Mar 2021	$2.6x10^{17}$	$3.1x10^{13}$	$3.1x10^{-5}$	$1.2x10^{-5}$
24 Mar 2021	$5.3x10^{17}$	$3.6x10^{13}$	$5.4x10^{-5}$	$8.0x10^{-6}$
25 Mar 2021	$2.7x10^{17}$	$3.3x10^{13}$	$5.5x10^{-5}$	$1.6x10^{-5}$
28 Mar 2021	$1.3x10^{17}$	$2.5x10^{13}$	$3.6x10^{-5}$	$1.1x10^{-5}$
29 Mar 2021	$1.4x10^{17}$	$4.3x10^{13}$	$5.6x10^{-5}$	$2.0x10^{-5}$
30 Mar 2021	$1.6x10^{17}$	$3.3x10^{13}$	$6.0x10^{-5}$	$2.4x10^{-5}$
3 April 2021	$1.9x10^{17}$	$1.8x10^{13}$	$1.9x10^{-5}$	$3.0x10^{-5}$
4 April 2021	$3.1x10^{17}$	$2.8x10^{13}$	$5.8x10^{-5}$	$1.0x10^{-5}$
8 April 2021	$9.3x10^{16}$	$2.4x10^{13}$	$3.3x10^{-5}$	$2.6x10^{-5}$
9 April 2021	$1.1x10^{17}$	$2.9x10^{13}$	$3.8x10^{-6}$	$2.1x10^{-5}$
14 April 2021	$1.6x10^{17}$	$3.6x10^{13}$	$4.3x10^{-5}$	$1.5x10^{-5}$
15 April 2021	$1.7x10^{17}$	$3.2x10^{13}$	$5.7x10^{-5}$	$1.3x10^{-5}$
18 April 2021	$1.7x10^{17}$	$2.6x10^{13}$	$4.7x10^{-5}$	$1.6x10^{-5}$
19 April 2021	$2.4x10^{17}$	$2.7x10^{13}$	$4.6x10^{-5}$	$1.1x10^{-5}$
20 April 2021	$3.1x10^{17}$	$3.5x10^{13}$	$5.3x10^{-5}$	$7.0x10^{-6}$
21 April 2021	$5.1x10^{17}$	$3.9x10^{13}$	$6.3x10^{-5}$	$1.0x10^{-5}$
28 April 2021	$1.2x10^{17}$	$1.5x10^{13}$	$3.7x10^{-5}$	$2.0x10^{-5}$
29 April 2021	$1.5x10^{17}$	$3.4x10^{13}$	$3.0x10^{-5}$	$2.3x10^{-5}$
5 May 2021	$7.2x10^{16}$	$2.5x10^{13}$	$1.5x10^{-5}$	$2.4x10^{-5}$
7 May 2021	$1.7x10^{18}$	$3.9x10^{13}$	$1.4x10^{-5}$	$1.4x10^{-6}$
16 May 2021	$7.4x10^{17}$	$4.2x10^{13}$	$3.6x10^{-5}$	$2.9x10^{-6}$
20 May 2021	$9.6x10^{16}$	$2.1x10^{13}$	$4.3x10^{-5}$	$2.2x10^{-5}$
21 May 2021	$2.9x10^{17}$	$3.0x10^{13}$	$4.2x10^{-5}$	$6.9x10^{-6}$
22 May 2021	$1.2x10^{17}$	$2.4x10^{13}$	$4.0x10^{-5}$	$1.0x10^{-5}$
23 May 2021	$1.8x10^{17}$	$2.7x10^{13}$	$3.6x10^{-5}$	$1.8x10^{-5}$
26 May 2021	$8.3x10^{16}$	$2.0x10^{13}$	$2.2x10^{-5}$	$2.3x10^{-5}$
27 May 2021	$9.8x10^{16}$	$2.3x10^{13}$	$7.5x10^{-5}$	$1.6x10^{-5}$
2 June 2021	$3.2x10^{17}$	$4.9x10^{13}$	$9.8x10^{-5}$	$1.4x10^{-5}$
5 June 2021	$1.1x10^{17}$	$2.9x10^{13}$	$6.9x10^{-5}$	$1.6x10^{-5}$
6 June 2021	$1.7x10^{17}$	$2.8x10^{13}$	$3.2x10^{-5}$	$7.9x10^{-6}$
7 June 2021	$3.0x10^{17}$	$3.1x10^{13}$	$3.4x10^{-5}$	$1.1x10^{-5}$
8 June 2021	$2.3x10^{17}$	$3.4x10^{13}$	$6.9x10^{-5}$	$1.8x10^{-5}$
12 June 2021	$2.1x10^{17}$	$4.1x10^{13}$	$7.9x10^{-5}$	$1.4x10^{-5}$
16 June 2021	$2.2x10^{17}$	$3.4x10^{13}$	$8.9x10^{-5}$	$2.6x10^{-5}$
17 June 2021	$1.2x10^{17}$	$6.1x10^{13}$	$8.2x10^{-5}$	$1.1x10^{-5}$
21 June 2021	$1.0x10^{17}$	$1.9x10^{13}$	$5.1x10^{-5}$	$2.8x10^{-5}$
27 June 2021	$1.1x10^{17}$	$2.7x10^{13}$	$1.7x10^{-5}$	$5.7x10^{-5}$
7 July 2021	$9.3x10^{16}$	$1.8x10^{13}$	$9.7x10^{-6}$	$1.6x10^{-5}$
8 July 2021	$1.4x10^{17}$	$2.4x10^{13}$	$1.3x10^{-5}$	$2.1x10^{-5}$
9 July 2021	$1.0x10^{17}$	$2.8x10^{13}$	$2.0x10^{-5}$	$3.8x10^{-5}$
14 July 2021	$9.3x10^{16}$	$3.1x10^{13}$	$8.7x10^{-5}$	$4.1x10^{-5}$
24 July 2021	$9.1x10^{16}$	$2.7x10^{13}$	$6.0x10^{-5}$	$1.3x10^{-5}$
25 July 2021	$2.5x10^{17}$	$2.8x10^{13}$	$4.3x10^{-5}$	$8.0x10^{-6}$
26 July 2021	$9.0x10^{16}$	$1.3x10^{13}$	$1.9x10^{-5}$	$3.3x10^{-5}$
28 July 2021	$9.3x10^{16}$	$1.4x10^{13}$	$9.4x10^{-5}$	$2.5x10^{-5}$
29 July 2021	$1.9x10^{17}$	$2.1x10^{13}$	$4.7x10^{-5}$	$9.2x10^{-6}$
30 July 2021	$2.1x10^{17}$	$2.6x10^{13}$	$7.0x10^{-5}$	$7.4x10^{-6}$
31 July 2021	$1.0x10^{17}$	$2.5x10^{13}$	$1.0x10^{-4}$	$3.0x10^{-5}$
4 Aug 2021	$2.2x10^{17}$	$4.7x10^{13}$	$8.4x10^{-5}$	$1.3x10^{-5}$
5 Aug 2021	$1.7x10^{17}$	$2.8x10^{13}$	$3.9x10^{-5}$	$1.7x10^{-5}$
9 Aug 2021	$1.1x10^{17}$	$2.8x10^{13}$	$7.7x10^{-5}$	$1.1x10^{-5}$
14 Aug 2021	$9.5x10^{16}$	$2.2x10^{13}$	$3.7x10^{-5}$	$1.9x10^{-5}$
15 Aug 2021	$2.2x10^{17}$	$2.4x10^{13}$	$4.3x10^{-5}$	$1.8x10^{-5}$
19 Aug 2021	$1.0x10^{17}$	$2.0x10^{13}$	$8.1x10^{-5}$	$2.0x10^{-5}$
20 Aug 2021	$2.6x10^{17}$	$4.5x10^{13}$	$6.9x10^{-5}$	$1.8x10^{-5}$
25 Aug 2021	$1.2x10^{17}$	$2.6x10^{13}$	$2.1x10^{-5}$	$3.2x10^{-5}$
30 Aug 2021	$1.1x10^{17}$	$2.2x10^{13}$	$8.1x10^{-5}$	$3.2x10^{-5}$
10 Sept 2021	$1.0x10^{17}$	$2.9x10^{13}$	$6.6x10^{-5}$	$4.1x10^{-5}$
11 Sept 2021	$1.6x10^{17}$	$3.0x10^{13}$	$1.1x10^{-4}$	$2.1x10^{-5}$
20 Sept 2021	$6.4x10^{16}$	$1.5x10^{13}$	$7.5x10^{-5}$	$1.8x10^{-5}$
21 Sept 2021	$1.1x10^{17}$	$2.1x10^{13}$	$6.5x10^{-5}$	$4.3x10^{-5}$
1 Oct 2021	$1.1x10^{17}$	$2.0x10^{13}$	$1.1x10^{-4}$	$4.1x10^{-5}$
7 Oct 2021	$1.1x10^{17}$	$5.3x10^{13}$	$7.8x10^{-5}$	$3.3x10^{-5}$

Sangay, Ecuador

date	SO_2 VCD max. [molecules cm^{-2}]	BrO VCD	BrO/SO_2 fitted	BrO/SO_2 error
8 Oct 2021	$1.1x10^{17}$	$3.9x10^{13}$	$8.9x10^{-5}$	$3.3x10^{-5}$
13 Oct 2021	$1.1x10^{17}$	$4.2x10^{13}$	$9.2x10^{-5}$	$3.3x10^{-5}$
18 Oct 2021	$1.1x10^{17}$	$2.7x10^{13}$	$7.5x10^{-5}$	$1.9x10^{-5}$
28 Oct 2021	$8.7x10^{16}$	$3.0x10^{13}$	$1.0x10^{-4}$	$3.7x10^{-5}$
29 Oct 2021	$1.5x10^{17}$	$3.1x10^{13}$	$8.9x10^{-5}$	$3.0x10^{-5}$
2 Nov 2021	$9.9x10^{16}$	$2.0x10^{13}$	$7.6x10^{-5}$	$3.4x10^{-5}$
8 Nov 2021	$1.7x10^{17}$	$3.1x10^{13}$	$7.1x10^{-5}$	$2.7x10^{-5}$
12 Nov 2021	$7.5x10^{16}$	$1.9x10^{13}$	$7.7x10^{-5}$	$4.2x10^{-5}$
13 Nov 2021	$2.6x10^{17}$	$2.6x10^{13}$	$3.6x10^{-5}$	$1.9x10^{-5}$
14 Nov 2021	$2.6x10^{17}$	$2.9x10^{13}$	$7.0x10^{-5}$	$1.4x10^{-5}$
18 Nov 2021	$4.2x10^{17}$	$5.0x10^{13}$	$8.3x10^{-5}$	$1.1x10^{-5}$
19 Nov 2021	$2.6x10^{17}$	$3.2x10^{13}$	$6.8x10^{-5}$	$1.1x10^{-5}$
23 Nov 2021	$1.4x10^{17}$	$2.4x10^{13}$	$7.0x10^{-5}$	$1.6x10^{-5}$
24 Nov 2021	$2.7x10^{17}$	$3.0x10^{13}$	$4.2x10^{-5}$	$9.6x10^{-6}$
28 Nov 2021	$9.2x10^{16}$	$2.2x10^{13}$	$3.5x10^{-5}$	$2.0x10^{-5}$
29 Nov 2021	$9.1x10^{16}$	$1.4x10^{13}$	$2.5x10^{-5}$	$2.0x10^{-5}$
30 Nov 2021	$3.4x10^{17}$	$2.6x10^{13}$	$4.9x10^{-5}$	$1.1x10^{-5}$
1 Dec 2021	$4.0x10^{17}$	$4.9x10^{13}$	$6.8x10^{-5}$	$1.0x10^{-5}$
3 Dec 2021	$1.5x10^{17}$	$2.0x10^{13}$	$9.2x10^{-5}$	$2.3x10^{-5}$
4 Dec 2021	$2.1x10^{17}$	$2.4x10^{13}$	$5.3x10^{-5}$	$1.0x10^{-5}$
5 Dec 2021	$4.1x10^{17}$	$3.9x10^{13}$	$6.5x10^{-5}$	$8.0x10^{-6}$
6 Dec 2021	$3.9x10^{17}$	$4.6x10^{13}$	$4.3x10^{-5}$	$1.1x10^{-5}$
9 Dec 2021	$1.8x10^{17}$	$2.1x10^{13}$	$6.6x10^{-5}$	$1.3x10^{-5}$
10 Dec 2021	$3.0x10^{17}$	$3.3x10^{13}$	$3.6x10^{-5}$	$7.0x10^{-6}$
12 Dec 2021	$2.7x10^{17}$	$3.2x10^{13}$	$4.0x10^{-5}$	$1.8x10^{-5}$
16 Dec 2021	$1.6x10^{17}$	$1.7x10^{13}$	$3.5x10^{-5}$	$1.9x10^{-5}$
17 Dec 2021	$1.2x10^{17}$	$1.7x10^{13}$	$6.4x10^{-6}$	$3.7x10^{-5}$
19 Dec 2021	$1.1x10^{17}$	$2.2x10^{13}$	$5.9x10^{-5}$	$1.5x10^{-5}$
20 Dec 2021	$1.8x10^{17}$	$2.3x10^{13}$	$3.2x10^{-5}$	$1.1x10^{-5}$
21 Dec 2021	$1.9x10^{17}$	$2.9x10^{13}$	$3.2x10^{-5}$	$1.8x10^{-5}$
22 Dec 2021	$2.9x10^{17}$	$4.0x10^{13}$	$4.7x10^{-5}$	$1.1x10^{-5}$

Fernandina, Ecuador

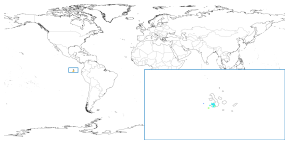
Type:	hot spot
longitude:	91.55° W
latitude:	0.37° S
Events:	2
$BrO > 2\sigma$:	2
BrO/SO_2:	$4.6x10^{-5}$
std. dev.:	$1.6x10^{-5}$
mean SO_2:	$4.0x10^{18}$
mean BrO:	$2.4x10^{14}$



16 June 2018	$4.7x10^{18}$	$3.3x10^{14}$	$7.3x10^{-5}$	$3.7x10^{-6}$
17 June 2018	$3.4x10^{18}$	$1.5x10^{14}$	$4.0x10^{-5}$	$8.3x10^{-7}$

Sierra Negra, Ecuador

Type:	hot spot
longitude:	91.17° W
latitude:	0.83° S
Events:	18
$BrO > 2\sigma$:	16
BrO/SO_2:	$3.9x10^{-5}$
std. dev.:	$1.5x10^{-5}$
mean SO_2:	$1.1x10^{18}$
mean BrO:	$6.3x10^{13}$



26 June 2018	$5.2x10^{18}$	$2.0x10^{14}$	$3.5x10^{-5}$	$4.3x10^{-6}$
3 July 2018	$9.8x10^{17}$	$6.9x10^{13}$	$3.9x10^{-5}$	$1.2x10^{-6}$
7 July 2018	$4.1x10^{17}$	$2.6x10^{13}$	$4.3x10^{-5}$	$6.4x10^{-6}$
9 July 2018	$2.5x10^{18}$	$1.3x10^{14}$	$3.9x10^{-5}$	$9.1x10^{-7}$
14 July 2018	$1.7x10^{18}$	$3.6x10^{13}$	$2.2x10^{-5}$	$9.4x10^{-7}$
15 July 2018	$1.6x10^{18}$	$8.2x10^{13}$	$4.0x10^{-5}$	$2.3x10^{-6}$
16 July 2018	$3.7x10^{17}$	$5.1x10^{13}$	$7.8x10^{-5}$	$6.1x10^{-6}$
21 July 2018	$1.2x10^{18}$	$7.0x10^{13}$	$4.6x10^{-5}$	$3.0x10^{-6}$
23 July 2018	$6.1x10^{17}$	$5.0x10^{13}$	$5.5x10^{-5}$	$3.6x10^{-6}$
24 July 2018	$1.0x10^{18}$	$5.7x10^{13}$	$4.7x10^{-5}$	$2.3x10^{-6}$
25 July 2018	$2.1x10^{18}$	$9.9x10^{13}$	$4.3x10^{-5}$	$1.7x10^{-6}$
26 July 2018	$4.1x10^{17}$	$7.1x10^{13}$	$5.0x10^{-5}$	$6.5x10^{-6}$
28 July 2018	$2.1x10^{17}$	$2.6x10^{13}$	$7.9x10^{-5}$	$8.3x10^{-6}$
29 July 2018	$7.9x10^{17}$	$3.2x10^{13}$	$3.1x10^{-5}$	$3.9x10^{-6}$
9 Aug 2018	$8.1x10^{17}$	$6.6x10^{13}$	$3.1x10^{-5}$	$1.9x10^{-6}$
14 Aug 2018	$1.8x10^{17}$	$1.7x10^{13}$	$5.0x10^{-5}$	$8.9x10^{-6}$

Sierra Negra, Ecuador

date	SO_2 VCD max. [molecules cm^{-2}]	BrO VCD	BrO/SO_2 fitted	BrO/SO_2 error
15 Aug 2018	$3.6x10^{17}$	$2.3x10^{13}$	$4.3x10^{-5}$	$1.4x10^{-5}$
16 Aug 2018	$1.6x10^{17}$	$3.4x10^{13}$	$6.4x10^{-5}$	$3.3x10^{-5}$

List of Figures

1.1 Volcanism, Earth's structure, and plate tectonic. . . . 6
1.2 Influence of volcanic degassing on the Earth's climate. . . . 8
1.3 Bromine evolution inside the plume after release. . . . 10
1.4 Volcanic bromine evolution and the *bromine explosion* cycle. . . . 11
1.5 Time evolution of the BrO/SO_2 ratio inside the volcanic plume. . . . 12
1.6 Evolution with depth of the ratios of different volcanic gases at Stromboli volcano. . . . 14

2.1 Attenuation of light intensity in the atmosphere due to aerosol and Rayleigh scattering as well as differential effects. . . . 21
2.2 Schematic view of a satellite measurement of a volcanic plume. . . . 25

3.1 Spectral specifications of the TROPOMI detectors. . . . 27
3.2 Overview of the TROPOMI Scanning procedure. . . . 28
3.3 Comparison of the pixel area of different satellite Instruments. . . . 29
3.4 Satellite viewing geometry. . . . 30

4.1 BrO distribution and RMS comparison between irradiance and earthshine references. 32
4.2 Absorption cross section of SO_2. . . . 34
4.3 Absorption cross section of BrO and HCHO. . . . 36
4.4 Global map of the BrO geometric VCD on 1 October 2018. . . . 39
4.5 Maps of the MICRU cloud fraction, FRESCO cloud top height and BrO VCD over the equatorial Pacific. . . . 40
4.6 BrO dependency on CF and CTH in the pacific equatorial region. . . . 40
4.7 BrO dependency on CF and CTH for all latitudes. . . . 41
4.8 Global map of the BrO VCD for different correction schemes. . . . 44
4.9 Overview of the BrO VCD dependency on CTH and CF for different latitudes and correction schemes. . . . 45
4.10 Systematic influence of clouds onto the BrO retrieval with latitude. . . . 46
4.11 Total systematic influence onto the BrO retrieval with latitude. . . . 47
4.12 Maps of the auxiliary data and the BrO VCD over the African biomass burning region on 1 October 2018. . . . 48
4.13 Mean BrO SCD as a function cloud fraction and HCHO SCD bins for the African biomass region on 1 October 2018. . . . 49
4.14 Mean BrO SCD as a function cloud fraction and HCHO SCD bins for the African biomass region on 1 October 2018 for cloud free scenes. . . . 50
4.15 Statistical uncertainty of the eight BrO fits. . . . 51
4.16 Latitudinal variation of the statistical uncertainty. . . . 52

5.1 Aquisition time for the orbits on the 25 December 2018. . . . 58
5.2 Aquisition time in h UTC for the orbits on 24 to 26 December 2018. . . . 59
5.3 Map of the global SO_2 VCD on 25 December 2018. . . . 60
5.4 Global map of SO_2 VCD on 25 December 2018 including the event grid boxes. . . . 63
5.5 SO_2 VCD of the example event of the plume of Anak Krakatau, 25 December 2018. 64
5.6 Overview of the processing of the BrO VCD of a volcanic event. . . . 67

5.7 Overview of the processing of the SO_2 VCD of a volcanic event. 68
5.8 Modelled BrO-SO_2 data-sets for different σ_{BrO} and BrO/SO_2 ratios, N = 1000. . . . 71
5.9 SQE, SQT, and R^2 as a function of the BrO/SO_2 ratio for different σ_{BrO}. 72
5.10 SQE, SQT, and R^2 as a function of the BrO/SO_2 ratio for different maximal SO_2. . 72
5.11 SQE, SQT, and R^2 as a function of the BrO/SO_2 ratio for different number of points. 73
5.12 Absolute and relative fit error for different σ_{BrO} and BrO/SO_2 ratios. 74
5.13 Absolute and relative fit error for different maximal SO_2 and BrO/SO_2 ratios. 74
5.14 Absolute (top) and relative (bottom) fit error for different number of points and BrO/SO_2 ratios. 75
5.15 Dependency of the fit error on the variation of various parameter. 75
5.16 Distribution of the BrO VCD and SO_2 VCD of different linearity for events of Mt. Etna. 76

6.1 Overview of the maximum SO_2 VCD and BrO VCD of the volcanic plume events over the four-year time-series. 80
6.2 Global map of the linear BrO/SO_2 ratios. 83
6.3 Global map of the weakly non-linear BrO/SO_2 ratios. 84
6.4 Global map of the highly non-linear BrO/SO_2 ratios. 85
6.5 Eruption of Sheveluch, Kamchatka, Russia, on 18 April 2019. 86
6.6 Eruption of Mt. Etna, Italy, on 23 March 2020. 87
6.7 Eruption of Ambrym volcano, Vanuatu, on 30 September 2018.. 88
6.8 Eruption of Mount Etna, Italy, on 29 January 2019. 89
6.9 Eruption of Fernandina, Galapagos, Ecuador, on 17 June 2018. 90
6.10 Eruption of Ambrym, Vanuatu, on 15/16 December 2018. 92
6.11 Eruption of Mount Etna, Italy, on 25 December 2018. 94
6.12 Eruption of Raikoke volcano, Kuril islands, Russia, on 22 June 2019. 96
6.13 Separated plume parts of the Raikoke volcano, Kuril islands, Russia, on 22 June 2019. 97
6.14 RGB image of the Raikoke plume on 22 June 2019. 98
6.15 Global map of the BrO/SO_2 ratio for all events derived by the plume algorithm which have a linear BrO-SO_2 relation. 100
6.16 Zoom into major volcanic regions. Map of events with linear BrO/SO_2 ratio. 101
6.17 Map of the assignment to volcanoes within the BrO/SO_2 ratio catalogue. 102
6.18 Number of events for each volcano of the catalogue. 104
6.19 Global map of the mean BrO/SO_2 ratio for the 43 volcanoes of the catalogue. 106
6.20 Mean BrO/SO_2 ratio of the 43 volcanoes of the catalogue considering all data. . . . 107
6.21 Mean BrO/SO_2 ratio of the 43 volcanoes of the catalogue considering only events with a rel. error, of the BrO/SO_2 ratio below 20 %. 108
6.22 Mean BrO/SO_2 ratio of the 43 volcanoes of the catalogue considering only events, where a clear BrO signal is detected. 109
6.23 Mean BrO/SO_2 ratio of the 43 volcanoes of the catalogue for all three data-sets: . . 110
6.24 Dependencies of the BrO/SO_2 ratio on the max. SO_2 VCD for the linear BrO/SO_2 ratios within the catalogue. 111
6.25 BrO/SO_2 ratios within the catalogue as a function of solar zenith angle, viewing zenith angle, and latitude. 111
6.26 Histogram of the BrO/SO_2 ratios of the individual events of the catalogue separated by volcano type: arc, hot spot, and rift volcanoes. 115
6.27 Comparison of BrO/SO_2 ratios of the catalogue with BrO/SO_2 ratio derived from GOME-2 satellite. 116
6.28 Comparison of BrO/SO_2 ratios of the catalogue with BrO/SO_2 ratio derived from ground-based measurements. 117
6.29 The BrO/SO_2 ratios as a function of the distance from the vent of Mt. Etna measured from ground-based instruments as well as TROPOMI 118
6.30 Comparison of simultaneous measurements of the BrO/SO_2 ratio from TROPOMI and ground-based instruments of Manam, Papua New Guinea. 119
6.31 Time series of the BrO/SO_2 ratio for Fagradalsfjall, Iceland, Mt. Etna, Italy, Nyiragongo, DR Congo, and **d** Piton de la Fournaise, France. 122

6.32 Time series of the BrO/SO_2 ratio for **a** Yasur, **b** Ambrym, both Vanuatu, **c** Bagana, and **d** Manam, both Papua New Guinea. Events, where BrO is above detection, are marked in blue. . . . 123
6.33 Time series of the BrO/SO_2 ratio for Dukono, Anak Krakatau, both Indonesia, Taal, Philippines, and Nishinoshima, Japan. . . . 125
6.34 Time series of the BrO/SO_2 ratio for Popocatepetl, Mexico, Poas, Costa Rica, Nevado del Ruiz, Colombia, and Sangay, Ecuador. . . . 126
6.35 Time series of the BrO/SO_2 ratio for »South Kamchatka«, Bezymianny, both Russia, and Kilauea, USA. . . . 128
6.36 BrO/SO_2 ratios as a function of distance of the maximal SO_2 VCD from the volcanic vent for all events attributed to Mt. Etna. . . . 129
6.37 BrO/SO_2 ratios as a function of distance of the maximal SO_2 VCD from the volcanic vent for all events attributed to Nishinoshima (Japan), Sierra Negra (Ecuador), and Fagradalsfjall (Iceland). . . . 130
6.38 BrO/SO_2 ratios as a function of distance of the maximal SO_2 VCD from the volcanic vent for all events attributed to Ambrym, and Ambae, both Vanuatu. . . . 131

7.1 Sketch of the conceptual model. . . . 134
7.2 Results of the conceptual model: O_3 concentration at the center of the plume and the radial fraction of the mixed plume as a function of the plume radius. . . . 137
7.3 Map of SO_2 VCD of the eruption of Mount Etna on 25 December 2018. . . . 138
7.4 Rotated maps of the SO_2 VCD, BrO VCD and BrO/SO_2 ratio of the eruption of Mount Etna on 25 December 2018. . . . 139
7.5 Rotated map of SO_2 VCDs of the eruption of Mount Etna on 25 December 2018 on the bases along and perpendicular to the plume. . . . 140
7.6 Rotated maps of the averaged SO_2 VCD, BrO VCD and BrO/SO_2 ratio of the eruption of Mount Etna on 25 December 2018. . . . 141
7.7 Sketch of the empirical model of a plume slice. . . . 142
7.8 Sketch of the elliptical coordinate system. . . . 145
7.9 Workflow of the empirical model. . . . 146
7.10 Results of the empirical model. . . . 148
7.11 Output of the empirical model parameter σ_y, f_x,f_y, and the mixed BrO/SO_2 ratio. . . 150
7.12 Model results for plume slice 30. . . . 151
7.13 Model results for plume slice 720. . . . 151
7.14 Measured BrO VCD and the BrO/SO_2 ratio. . . . 152

List of Tables

1.1 Volcanic gas constituents and global estimated source strength. 7

4.1 Selection criteria for the SO_2 multiple fit range algorithm. 33
4.2 Fit settings for the four SO_2 DOAS retrievals. 35
4.3 Fit settings for the eight BrO DOAS retrievals. 37
4.4 Cloud/O_3 correction schemes. 42
4.5 Fit settings for the selected BrO DOAS retrieval. 53
4.6 Overview of the different systematic influence contributions. 55

5.1 List of the latitude and longitude boundaries of the different exclusion areas. 61
5.2 Variables used to calculate synthetic BrO-SO_2 distributions. 71

6.1 Overview of the events detected by the automated plume algorithm categorized by their maximal SO_2 VCD. 81
6.2 Overview of the events detected by the automated plume algorithm categorized by the classification. 82
6.3 List of the 43 volcanoes of the BrO/SO_2 catalogue. Name, country, location, as well as the number of events within 300 km distance are listed. Additionally the number of events who have a rel. BrO/SO_2 error below 20 % or who have a clear detection of BrO are given. 103

7.1 Initialization of the four input parameter of the least-square fit of the empirical model. 147

Bibliography

Global Volcanism Program, 2013. Eyjafjallajökull, volcano number 372020, in: Volcanoes of the World, v. 4.10.6 (24 Mar 2022), edited by Venzke, E., Smithsonian Institution, URL `https://volcano.si.edu/volcano.cfm?vn=372020`, 2013a.

Global Volcanism Program, 2013. Erebus, volcano number 390020, in: Volcanoes of the World, v. 4.10.6 (24 Mar 2022), edited by Venzke, E., Smithsonian Institution, URL `https://volcano.si.edu/volcano.cfm?vn=390020`, 2013b.

Global Volcanism Program, 2010. Report on Agung (Indonesia), Bulletin of the Global Volcanism Network, 43, https://doi.org/10.5479/si.gvp.bgvn201801-264020, 2018a.

Global Volcanism Program, 2010. Report on Agung (Indonesia), Bulletin of the Global Volcanism Network, 43, https://doi.org/10.5479/si.gvp.bgvn201808-264020, 2018b.

Global Volcanism Program, 2010. Report on Fernandina (Ecuador), Bulletin of the Global Volcanism Network, 43, https://doi.org/10.5479/si.gvp.bgvn201808-353010, 2018c.

Global Volcanism Program, 2010. Report on Karymsky (Russia), Bulletin of the Global Volcanism Network, 43, https://doi.org/10.5479/si.gvp.bgvn201808-300130, 2018d.

Global Volcanism Program, 2010. Report on Mayon (Philippines), Bulletin of the Global Volcanism Network, 43, https://doi.org/10.5479/si.gvp.bgvn201804-273030, 2018e.

Global Volcanism Program, 2010. Report on Sierra Negra (Ecuador), Weekly Volcanic Activity Report, 29 August – 4 September 2018, 2018f.

Global Volcanism Program, 2010. Report on Ambrym (Vanuatu), Bulletin of the Global Volcanism Network, 44, https://doi.org/10.5479/si.gvp.bgvn201901-257040, 2019a.

Global Volcanism Program, 2010. Report on Etna (Italy), Bulletin of the Global Volcanism Network, 44, https://doi.org/10.5479/si.gvp.bgvn201904-211060, 2019b.

Global Volcanism Program, 2010. Report on Kerinci (Indonesia), Bulletin of the Global Volcanism Network, 44, https://doi.org/10.5479/si.gvp.bgvn201902-261170, 2019c.

Global Volcanism Program, 2010. Report on Kerinci (Indonesia), Bulletin of the Global Volcanism Network, 44, https://doi.org/10.5479/si.gvp.bgvn201912-261170, 2019d.

Global Volcanism Program, 2010. Report on Krakatau (Indonesia), Bulletin of the Global Volcanism Network, 44, https://doi.org/10.5479/si.gvp.bgvn201903-262000, 2019e.

Global Volcanism Program, 2010. Report on Manam (Papua New Guinea), Bulletin of the Global Volcanism Network, 44, https://doi.org/10.5479/si.gvp.bgvn201902-251020, 2019f.

Global Volcanism Program, 2010. Report on Raikoke (Russia), weekly volcanic activity report, 19 June – 25 June 2019, 2019g.

Global Volcanism Program, 2010. Report on Soputan (Indonesia), Bulletin of the Global Volcanism Network, 44, https://doi.org/10.5479/si.gvp.bgvn201901-266030, 2019h.

Global Volcanism Program, 2010. Report on Ulawun (Papua New Guinea), Bulletin of the Global Volcanism Network, 44, https://doi.org/10.5479/si.gvp.bgvn201909-252120, 2019i.

Global Volcanism Program, 2010. Report on Yasur (Vanuatu), Bulletin of the Global Volcanism Network, 44, https://doi.org/10.5479/si.gvp.bgvn201906-257100, 2019j.

Global Volcanism Program, 2010. Report on Karymsky (Russia), Bulletin of the Global Volcanism Network, 45, https://doi.org/10.5479/si.gvp.bgvn202010-300130, 2020a.

Global Volcanism Program, 2010. Report on Nishinoshima (Japan), Bulletin of the Global Volcanism Network, 45, https://doi.org/10.5479/si.gvp.bgvn202009-284096, 2020b.

Global Volcanism Program, 2010. Report on Semeru (Indonesia), Bulletin of the Global Volcanism Network, 45, https://doi.org/10.5479/si.gvp.bgvn202004-263300, 2020c.

Global Volcanism Program, 2010. Report on Lewotolok (Indonesia), Bulletin of the Global Volcanism Network, 46, https://doi.org/10.5479/si.gvp.bgvn202102-264230, 2021a.

Global Volcanism Program, 2010. Report on Raung (Indonesia), Bulletin of the Global Volcanism Network, 46, https://doi.org/10.5479/si.gvp.bgvn202107-263340, 2021b.

Global Volcanism Program, 2010. Report on Soufriere St. Vincent (Saint Vincent and the Grenadines), Bulletin of the Global Volcanism Network, 46, https://doi.org/10.5479/si.gvp.bgvn202105-360150, 2021c.

Global Volcanism Program, 2010. Report on Taal (Philippines), Bulletin of the Global Volcanism Network, 46, https://doi.org/10.5479/si.GVP.BGVN202110-273070, 2021d.

Copernicus Sentinel-5P (processed by ESA), 2021, TROPOMI Level 2 Nitrogen Dioxide total column products. Version 02. European Space Agency, 2021.

Afe, O. T., Richter, A., Sierk, B., Wittrock, F., and Burrows, J. P.: BrO emission from volcanoes: A survey using GOME and SCIAMACHY measurements, Geophysical Research Letters, 31, https://doi.org/10.1029/2004GL020994, 2004.

Aiuppa, A.: Degassing of halogens from basaltic volcanism: Insights from volcanic gas observations, Chemical Geology, 263, 99 – 109, https://doi.org/10.1016/j.chemgeo.2008.08.022, halogens in Volcanic Systems and Their Environmental Impacts, 2009.

Aiuppa, A., Federico, C., Antonio, P., Giovannella, P., and Mariano, V.: S, Cl and F degassing as an indicator of volcanic dynamics: The 2001 eruption of Mount Etna, Geophysical Research Letters, 29, 54–1–54–4, https://doi.org/10.1029/2002GL015032, 2002.

Aiuppa, A., Federico, C., Giudice, G., Gurrieri, S., Paonita, A., and Valenza, M.: Plume chemistry provides insights into mechanisms of sulfur and halogen degassing in basaltic volcanoes, Earth and Planetary Science Letters, 222, 469 – 483, https://doi.org/10.1016/j.epsl.2004.03.020, 2004.

Aiuppa, A., Federico, C., Franco, A., Giudice, G., Gurrieri, S., Inguaggiato, S., Liuzzo, M., McGonigle, A. J. S., and Valenza, M.: Emission of bromine and iodine from Mount Etna volcano, Geochemistry, Geophysics, Geosystems, 6, https://doi.org/10.1029/2005GC000965, 2005.

Aliwell, S. R., Van Roozendael, M., Johnston, P. V., Richter, A., Wagner, T., Arlander, D. W., Burrows, J. P., Fish, D. J., Jones, R. L., Tørnkvist, K. K., Lambert, J.-C., Pfeilsticker, K., and Pundt, I.: Analysis for BrO in zenith-sky spectra: An intercomparison exercise for analysis improvement, Journal of Geophysical Research: Atmospheres, 107, ACH 10–1–ACH 10–20, https://doi.org/10.1029/2001JD000329, 2002.

Allard, P., Burton, M., and Muré, F.: Spectroscopic evidence for a lava fountain driven by previously accumulated magmatic gas, Nature, 433, 407–410, https://doi.org/10.1038/nature03246, 2005.

Alletti, M., Baker, D. R., Scaillet, B., Aiuppa, A., Moretti, R., and Ottolini, L.: Chlorine partitioning between a basaltic melt and H_2O–CO_2 fluids at Mount Etna, Chemical Geology, 263, 37 – 50, https://doi.org/10.1016/j.chemgeo.2009.04.003, halogens in Volcanic Systems and Their Environmental Impacts, 2009.

Anderson, H. and Jackson, J.: The deep seismicity of the Tyrrhenian Sea, Geophysical Journal International, 91, 613–637, https://doi.org/10.1111/j.1365-246x.1987.tb01661.x, 1987.

Andújar, J., Martel, C., Pichavant, M., Samaniego, P., Scaillet, B., and Molina, I.: Structure of the Plumbing System at Tungurahua Volcano, Ecuador: Insights from Phase Equilibrium Experiments on July–August 2006 Eruption Products, Journal of Petrology, 58, 1249–1278, https://doi.org/10.1093/petrology/egx054, 2017.

Anscombe, F. J.: Graphs in Statistical Analysis, The American Statistician, 27, 17–21, https://doi.org/10.2307/2682899, 1973.

Arellano, S. R., Hall, M., Samaniego, P., Pennec, J.-L. L., Ruiz, A., Molina, I., and Yepes, H.: Degassing patterns of Tungurahua volcano (Ecuador) during the 1999–2006 eruptive period, inferred from remote spectroscopic measurements of SO_2 emissions, Journal of Volcanology and Geothermal Research, 176, 151 – 162, https://doi.org/10.1016/j.jvolgeores.2008.07.007, recent and active volcanism in the Ecuadorian Andes, 2008.

Bablon, M., Quidelleur, X., Samaniego, P., Le Pennec, J.-L., Lahitte, P., Liorzou, C., Bustillos, J. E., and Hidalgo, S.: Eruptive chronology of Tungurahua volcano (Ecuador) revisited based on new K-Ar ages and geomorphological reconstructions, Journal of Volcanology and Geothermal Research, 357, 378–398, https://doi.org/10.1016/j.jvolgeores.2018.05.007, 2018.

Bagnato, E., Aiuppa, A., Bertagnini, A., Bonadonna, C., Cioni, R., Pistolesi, M., Pedone, M., and Hoskuldsson, A.: Scavenging of sulphur, halogens and trace metals by volcanic ash: The 2010 Eyjafjallajökull eruption, Geochimica et Cosmochimica Acta, 103, 138 – 160, https://doi.org/10.1016/j.gca.2012.10.048, 2013.

Bakker, D. C. E., Bange, H. W., Gruber, N., Johannessen, T., Upstill-Goddard, R. C., Borges, A. V., Delille, B., Löscher, C. R., Naqvi, S. W. A., Omar, A. M., and Santana-Casiano, J. M.: Air-Sea Interactions of Natural Long-Lived Greenhouse Gases (CO2, N2O, CH4) in a Changing Climate, pp. 113–169, Springer Berlin Heidelberg, Berlin, Heidelberg, https://doi.org/10.1007/978-3-642-25643-1_3, 2014.

Bani, P., Oppenheimer, C., Tsanev, V. I., Carn, S. A., Cronin, S. J., Crimp, R., Calkins, J. A., Charley, D., Lardy, M., and Roberts, T. R.: Surge in sulphur and halogen degassing from Ambrym volcano, Vanuatu, Bulletin of Volcanology, 71, 1159–1168, https://doi.org/10.1007/s00445-009-0293-7, 2009.

Beermann, O., Botcharnikov, R. E., and Nowak, M.: Partitioning of sulfur and chlorine between aqueous fluid and basaltic melt at 1050°C, 100 and 200 MPa, Chemical Geology, 418, 132 – 157, https://doi.org/10.1016/j.chemgeo.2015.08.008, 2015.

Begoin, M., Richter, A., Weber, M., Kaleschke, L., Tian-Kunze, X., Stohl, A., Theys, N., and Burrows, J. P.: Satellite observations of long range transport of a large BrO plume in the Arctic, Atmospheric Chemistry and Physics, 10, 6515–6526, https://doi.org/10.5194/acp-10-6515-2010, 2010.

Behrendt, J. C., LeMasurier, W. E., Cooper, A. K., Tessensohn, F., Tréhu, A., and Damaske, D.: Geophysical studies of the West Antarctic Rift System, Tectonics, 10, 1257–1273, https://doi.org/10.1029/91tc00868, 1991.

Beirle, S., Sihler, H., and Wagner, T.: Linearisation of the effects of spectral shift and stretch in DOAS analysis, Atmospheric Measurement Techniques, 6, 661–675, https://doi.org/10.5194/amt-6-661-2013, 2013.

Beirle, S., Hörmann, C., Penning de Vries, M., Dörner, S., Kern, C., and Wagner, T.: Estimating the volcanic emission rate and atmospheric lifetime of SO_2 from space: a case study for Kilauea volcano, Hawaii, Atmospheric Chemistry and Physics, 14, 8309–8322, https://doi.org/10.5194/acp-14-8309-2014, 2014.

Beirle, S., Lampel, J., Lerot, C., Sihler, H., and Wagner, T.: Parameterizing the instrumental spectral response function and its changes by a super-Gaussian and its derivatives, Atmospheric Measurement Techniques, 10, 581–598, https://doi.org/10.5194/amt-10-581-2017, 2017.

Berresheim, H., Wine, P. H., and Davis, D. D.: Composition, Cemistry, and Climate of the Atmosphere, chap. Sulfur in the atmosphere, H. B. Singh,Van Nostrand Reinhold, New York, 1995.

Bobrowski, N.: Volcanic Gas Studies by Multi Axis Differential Absorption Spectroscopy, Ph.D. thesis, Heidelberg University, https://doi.org/10.11588/HEIDOK.00006052, 2005.

Bobrowski, N. and Giuffrida, G.: Bromine monoxide / sulphur dioxide ratios in relation to volcanological observations at Mt. Etna 2006 - 2009, Solid Earth, 3, 433–445, https://doi.org/10.5194/se-3-433-2012, 2012.

Bobrowski, N. and Platt, U.: SO_2/BrO ratios studied in five volcanic plumes, Journal of Volcanology and Geothermal Research, 166, 147 – 160, https://doi.org/10.1016/j.jvolgeores.2007.07.003, 2007.

Bobrowski, N., Hönniger, G., Galle, B., and Platt, U.: Detection of bromine monoxide in a volcanic plume, Nature, 423, 273–276, https://doi.org/10.1038/nature01625, 2003.

Bobrowski, N., von Glasow, R., Aiuppa, A., Inguaggiato, S., Louban, I., Ibrahim, O. W., and Platt, U.: Reactive halogen chemistry in volcanic plumes, Journal of Geophysical Research, 112, https://doi.org/10.1029/2006JD007206, 2007.

Bobrowski, N., Kern, C., Platt, U., Hörmann, C., and Wagner, T.: Novel SO_2 spectral evaluation scheme using the 360–390 nm wavelength range, Atmospheric Measurement Techniques, 3, 879–891, https://doi.org/10.5194/amt-3-879-2010, 2010.

Bobrowski, N., von Glasow, R., Giuffrida, G. B., Tedesco, D., Aiuppa, A., Yalire, M., Arellano, S., Johansson, M., and Galle, B.: Gas emission strength and evolution of the molar ratio of BrO/SO_2 in the plume of Nyiragongo in comparison to Etna, Journal of Geophysical Research: Atmospheres, 120, 277–291, https://doi.org/10.1002/2013jd021069, 2015.

Bobrowski, N., Giuffrida, G. B., Yalire, M., Lübcke, P., Arellano, S., Balagizi, C., Calabrese, S., Galle, B., and Tedesco, D.: Multi-component gas emission measurements of the active lava lake of Nyiragongo, DR Congo, Journal of African Earth Sciences, 134, 856 – 865, https://doi.org/10.1016/j.jafrearsci.2016.07.010, 2017.

Bogumil, K., Orphal, J., Homann, T., Voigt, S., Spietz, P., Fleischmann, O. C., Vogel, A., Hartmann, M., Kromminga, H., Bovensmann, H., Frerick, J., and Burrows, J. P.: Measurements of molecular absorption spectra with the SCIAMACHY pre-flight model: instrument characterization and reference data for atmospheric remote-sensing in the 230–2380 nm region, Journal of Photochemistry and Photobiology A: Chemistry, 157, 167–184, https://doi.org/10.1016/S1010-6030(03)00062-5, atmospheric Photochemistry, 2003.

Boichu, M., Oppenheimer, C., Roberts, T. J., Tsanev, V., and Kyle, P. R.: On bromine, nitrogen oxides and ozone depletion in the tropospheric plume of Erebus volcano (Antarctica), Atmospheric Environment, 45, 3856 – 3866, https://doi.org/10.1016/j.atmosenv.2011.03.027, 2011.

Brenna, H., Kutterolf, S., and Krüger, K.: Global ozone depletion and increase of UV radiation caused by pre-industrial tropical volcanic eruptions, Scientific Reports, 9, https://doi.org/10.1038/s41598-019-45630-0, 2019.

Bureau, H., Keppler, H., and Métrich, N.: Volcanic degassing of bromine and iodine: experimental fluid/melt partitioning data and applications to stratospheric chemistry, Earth and Planetary Science Letters, 183, 51 – 60, https://doi.org/10.1016/S0012-821X(00)00258-2, 2000.

Bureau, H., Foy, E., Raepsaet, C., Somogyi, A., Munsch, P., Simon, G., and Kubsky, S.: Bromine cycle in subduction zones through in situ Br monitoring in diamond anvil cells, Geochimica et Cosmochimica Acta, 74, 3839 – 3850, https://doi.org/10.1016/j.gca.2010.04.001, 2010.

Bureau, H., Auzende, A.-L., Marocchi, M., Raepsaet, C., Munsch, P., Testemale, D., Mézouar, M., Kubsky, S., Carrière, M., Ricolleau, A., and Fiquet, G.: Modern and past volcanic degassing of iodine, Geochimica et Cosmochimica Acta, 173, 114 – 125, https://doi.org/10.1016/j.gca.2015.10.017, 2016.

Burrows, J. P., Richter, A., Dehn, A., Deters, B., Himmelmann, S., Voigt, S., and Orphal, J.: ATMOSPHERIC REMOTE-SENSING REFERENCE DATA FROM GOME-2. TEMPERATURE-DEPENDENT ABSORPTION CROSS SECTIONS OF O_3 IN THE 231-794 NM RANGE, Journal of Quantitative Spectroscopy and Radiative Transfer, 61, 509 – 517, https://doi.org/10.1016/S0022-4073(98)00037-5, 1999.

Burton, M., Allard, P., Muré, F., and Spina, A. L.: Magmatic Gas Composition Reveals the Source Depth of Slug-Driven Strombolian Explosive Activity, Science, 317, 227–230, https://doi.org/10.1126/science.1141900, 2007.

Cadoux, A., Iacono-Marziano, G., Scaillet, B., Aiuppa, A., Mather, T. A., Pyle, D. M., Deloule, E., Gennaro, E., and Paonita, A.: The role of melt composition on aqueous fluid vs. silicate melt partitioning of bromine in magmas, Earth and Planetary Science Letters, 498, 450 – 463, https://doi.org/10.1016/j.epsl.2018.06.038, 2018.

Calvari, S., Bilotta, G., Bonaccorso, A., Caltabiano, T., Cappello, A., Corradino, C., Negro, C. D., Ganci, G., Neri, M., Pecora, E., Salerno, G. G., and Spampinato, L.: The VEI 2 Christmas 2018 Etna Eruption: A Small But Intense Eruptive Event or the Starting Phase of a Larger One?, Remote Sensing, 12, 905, https://doi.org/10.3390/rs12060905, 2020.

Cantrell, C. A.: Technical Note: Review of methods for linear least-squares fitting of data and application to atmospheric chemistry problems, Atmospheric Chemistry and Physics, 8, 5477–5487, https://doi.org/10.5194/acp-8-5477-2008, 2008.

Carn, S. A., Krueger, A., Arellano, S., Krotkov, N., and Yang, K.: Daily monitoring of Ecuadorian volcanic degassing from space, Journal of Volcanology and Geothermal Research, 176, 141 – 150, https://doi.org/10.1016/j.jvolgeores.2008.01.029, recent and active volcanism in the Ecuadorian Andes, 2008.

Carn, S. A., Fioletov, V. E., McLinden, C. A., Li, C., and Krotkov, N. A.: A decade of global volcanic SO2 emissions measured from space, Scientific Reports, 7, https://doi.org/10.1038/srep44095, 2017.

Carroll, M. R. and Holloway, J. R., eds.: Volatiles in Magmas, De Gruyter, https://doi.org/doi:10.1515/9781501509674, 2018.

Carroll, M. R. and Webster, J. D.: SOLUBILITIES OF SULFUR, NOBLE GASES, NITROGEN, CHLORINE, AND FLUORINE IN MAGMAS, in: Volatiles in Magmas, edited by und John R. Holloway, M. R. C., no. 30 in Reviews in Mineralogy, pp. 231–280, De Gruyter, https://doi.org/10.1515/9781501509674-013, 1994.

Chance, K.: Analysis of BrO measurements from the Global Ozone Monitoring Experiment, Geophysical Research Letters, 25, 3335–3338, https://doi.org/10.1029/98GL52359, 1998.

Chance, K.: Algorithm Theoretical Basis Document - Volume IV, Tech. rep., Smithsonian Astrophysical Observatory, Cambridge, MA, USA, 2002.

Clarke, T.: Etna in identity crisis, Nature, https://doi.org/10.1038/news010830-10, 2001.

Cochain, B., Sanloup, C., de Grouchy, C., Crépisson, C., Bureau, H., Leroy, C., Kantor, I., and Irifune, T.: Bromine speciation in hydrous silicate melts at high pressure, Chemical Geology, 404, 18 – 26, https://doi.org/10.1016/j.chemgeo.2015.03.015, 2015.

Compernolle, S., Argyrouli, A., Lutz, R., Sneep, M., Lambert, J.-C., Fjæraa, A. M., Hubert, D., Keppens, A., Loyola, D., O'Connor, E., Romahn, F., Stammes, P., Verhoelst, T., and Wang, P.: Validation of the Sentinel-5 Precursor TROPOMI cloud data with Cloudnet, Aura OMI O_2–O_2, MODIS, and Suomi-NPP VIIRS, Atmospheric Measurement Techniques, 14, 2451–2476, https://doi.org/10.5194/amt-14-2451-2021, 2021.

Crutzen, P. J. and Arnold, F.: Nitric acid cloud formation in the cold Antarctic stratosphere: a major cause for the springtime 'ozone hole', Nature, 324, 651–655, https://doi.org/10.1038/324651a0, 1986.

De Smedt, I., Van Roozendael, M., Stavrakou, T., Müller, J.-F., Lerot, C., Theys, N., Valks, P., Hao, N., and van der A, R.: Improved retrieval of global tropospheric formaldehyde columns from GOME-2/MetOp-A addressing noise reduction and instrumental degradation issues, Atmospheric Measurement Techniques, 5, 2933–2949, https://doi.org/10.5194/amt-5-2933-2012, 2012.

De Smedt, I., Theys, N., Yu, H., Danckaert, T., Lerot, C., Compernolle, S., Van Roozendael, M., Richter, A., Hilboll, A., Peters, E., Pedergnana, M., Loyola, D., Beirle, S., Wagner, T., Eskes, H., van Geffen, J., Boersma, K. F., and Veefkind, P.: Algorithm theoretical baseline for formaldehyde retrievals from S5P TROPOMI and from the QA4ECV project, Atmospheric Measurement Techniques, 11, 2395–2426, https://doi.org/10.5194/amt-11-2395-2018, 2018.

Delmelle, P., Lambert, M., Dufrene, Y., Gerin, P., and Oskarsson, N.: Gas/aerosol–ash interaction in volcanic plumes: New insights from surface analyses of fine ash particles, Earth and Planetary Science Letters, 259, 159 – 170, https://doi.org/10.1016/j.epsl.2007.04.052, 2007.

Deutschmann, T., Beirle, S., Frieß, U., Grzegorski, M., Kern, C., Kritten, L., Platt, U., Prados-Román, C., Puķīte, J., Wagner, T., Werner, B., and Pfeilsticker, K.: The Monte Carlo atmospheric radiative transfer model McArtim: Introduction and validation of jacobians and 3D features, Journal of Quantitative Spectroscopy and Radiative Transfer, 112, 1119–1137, https://doi.org/10.1016/j.jqsrt.2010.12.009, 2011.

Dinger, F., Bobrowski, N., Warnach, S., Bredemeyer, S., Hidalgo, S., Arellano, S., Galle, B., Platt, U., and Wagner, T.: Periodicity in the BrO/SO_2 molar ratios in the volcanic gas plume of Cotopaxi and its correlation with the Earth tides during the eruption in 2015, Solid Earth, 9, 247–266, https://doi.org/10.5194/se-9-247-2018, 2018.

Edmonds, M., Gerlach, T. M., and Herd, R. A.: Halogen degassing during ascent and eruption of water-poor basaltic magma, Chemical Geology, 263, 122 – 130, https://doi.org/10.1016/j.chemgeo.2008.09.022, halogens in Volcanic Systems and Their Environmental Impacts, 2009.

Eisinger, M. and Burrows, J. P.: Tropospheric sulfur dioxide observed by the ERS-2 GOME instrument, Geophysical Research Letters, 25, 4177–4180, https://doi.org/https://doi.org/10.1029/1998GL900128, 1998.

Fleischmann, O. C., Hartmann, M., Burrows, J. P., and Orphal, J.: New ultraviolet absorption cross-sections of BrO at atmospheric temperatures measured by time-windowing Fourier transform spectroscopy, Journal of Photochemistry and Photobiology A: Chemistry, 168, 117–132, https://doi.org/10.1016/j.jphotochem.2004.03.026, 2004.

Francis, P. and Oppenheimer, C.: Volcanoes, Oxford University Press, 2004.

Galle, B., Johansson, M., Rivera, C., Zhang, Y., Kihlman, M., Kern, C., Lehmann, T., Platt, U., and Hidalgo, S.: Network for Observation of Volcanic and Atmospheric Change (NOVAC) - A global network for volcanic gas monitoring: Network layout and instrument description, Journal of Geophysical Research, 115, https://doi.org/10.1029/2009JD011823, 2010.

General, S., Bobrowski, N., Pöhler, D., Weber, K., Fischer, C., and Platt, U.: Airborne I-DOAS measurements at Mt. Etna: BrO and OClO evolution in the plume, Journal of Volcanology and Geothermal Research, 300, 175–186, https://doi.org/10.1016/j.jvolgeores.2014.05.012, 2015.

Gerlach, T.: Volcanic versus anthropogenic carbon dioxide, Eos, Transactions American Geophysical Union, 92, 201–202, https://doi.org/10.1029/2011eo240001, 2011.

Gerlach, T. M.: Volcanic sources of tropospheric ozone-depleting trace gases, Geochemistry, Geophysics, Geosystems, 5, https://doi.org/10.1029/2004GC000747, 2004.

Girina, O., Melnikov, D., Manevich, A., Nuzhdaev, A., and Petrova, E.: The 2018 activity of Kamchatka volcanoes and danger to aviation, 2019.

Gliß, J., Bobrowski, N., Vogel, L., Pöhler, D., and Platt, U.: OClO and BrO observations in the volcanic plume of Mt. Etna – implications on the chemistry of chlorine and bromine species in volcanic plumes, Atmospheric Chemistry and Physics, 15, 5659–5681, https://doi.org/10.5194/acp-15-5659-2015, 2015.

Global Volcanism Program: Smithsonian Institution, URL `https://volcano.si.edu/`.

Grainger, J. F. and Ring, J.: Anomalous Fraunhofer Line Profiles, Nature, 193, https://doi.org/10.1038/193762a0, 1962.

Gutmann, A., Bobrowski, N., Roberts, T. J., Rüdiger, J., and Hoffmann, T.: Advances in Bromine Speciation in Volcanic Plumes, Frontiers in Earth Science, 6, 213, https://doi.org/10.3389/feart.2018.00213, 2018.

Hall, M. L., Robin, C., Beate, B., Mothes, P., and Monzier, M.: Tungurahua Volcano, Ecuador: structure, eruptive history and hazards, Journal of Volcanology and Geothermal Research, 91, 1 – 21, https://doi.org/10.1016/S0377-0273(99)00047-5, 1999.

Halmer, M. M., Schmincke, H.-U., and Graf, H.-F.: The annual volcanic gas input into the atmosphere, in particular into the stratosphere: a global data set for the past 100 years, Journal of Volcanology and Geothermal Research, 115, 511–528, https://doi.org/10.1016/S0377-0273(01)00318-3, 2002.

Hamling, I. J., Cevuard, S., and Garaebiti, E.: Large-Scale Drainage of a Complex Magmatic System: Observations From the 2018 Eruption of Ambrym Volcano, Vanuatu, Geophysical Research Letters, 46, 4609–4617, https://doi.org/10.1029/2019gl082606, 2019.

Hausmann, M. and Platt, U.: Spectroscopic measurement of bromine oxide and ozone in the high Arctic during Polar Sunrise Experiment 1992, Journal of Geophysical Research, 99, 25 399, https://doi.org/10.1029/94jd01314, 1994.

Hedelt, P., Efremenko, D. S., Loyola, D. G., Spurr, R., and Clarisse, L.: Sulfur dioxide layer height retrieval from Sentinel-5 Precursor/TROPOMI using FP_ILM, Atmospheric Measurement Techniques, 12, 5503–5517, https://doi.org/10.5194/amt-12-5503-2019, 2019.

Hegels, E., Crutzen, P. J., Klüpfel, T., Perner, D., and Burrows, J. P.: Global distribution of atmospheric bromine-monoxide from GOME on Earth Observing Satellite ERS-2, Geophysical Research Letters, 25, 3127–3130, https://doi.org/10.1029/98GL02417, 1998.

Helmig, D., Boylan, P., Johnson, B., Oltmans, S., Fairall, C., Staebler, R., Weinheimer, A., Orlando, J., Knapp, D. J., Montzka, D. D., Flocke, F., Frieß, U., Sihler, H., and Shepson, P. B.: Ozone dynamics and snow-atmosphere exchanges during ozone depletion events at Barrow, Alaska, Journal of Geophysical Research: Atmospheres, 117, https://doi.org/10.1029/2012jd017531, 2012.

Hermans, C., Vandaele, A. C., Fally, S., Carleer, M., Colin, R., Coquart, B., Jenouvrier, A., and Merienne, M.-F.: Absorption Cross-section of the Collision-Induced Bands of Oxygen from the UV to the NIR, in: Weakly Interacting Molecular Pairs: Unconventional Absorbers of Radiation in the Atmosphere, edited by Camy-Peyret, C. and Vigasin, A., vol. 27 of *NATO Science Series*, pp. 193–202, Springer Netherlands, https://doi.org/10.1007/978-94-010-0025-3_16, 2003.

Heue, K.-P., Brenninkmeijer, C. A. M., Baker, A. K., Rauthe-Schöch, A., Walter, D., Wagner, T., Hörmann, C., Sihler, H., Dix, B., Frieß, U., Platt, U., Martinsson, B. G., van Velthoven, P. F. J., Zahn, A., and Ebinghaus, R.: SO_2 and BrO observation in the plume of the Eyjafjallajökull volcano 2010: CARIBIC and GOME-2 retrievals, Atmospheric Chemistry and Physics, 11, 2973–2989, https://doi.org/10.5194/acp-11-2973-2011, 2011.

Hidalgo, S., Battaglia, J., Arellano, S., Steele, A., Bernard, B., Bourquin, J., Galle, B., Arrais, S., and Vásconez, F.: SO_2 degassing at Tungurahua volcano (Ecuador) between 2007 and 2013: Transition from continuous to episodic activity, Journal of Volcanology and Geothermal Research, 298, 1 – 14, https://doi.org/10.1016/j.jvolgeores.2015.03.022, 2015.

Hidalgo, S., Battaglia, J., Arellano, S., Sierra, D., Bernard, B., Parra, R., Kelly, P., Dinger, F., Barrington, C., and Samaniego, P.: Evolution of the 2015 Cotopaxi Eruption Revealed by Combined Geochemical & Seismic Observations, Geochemistry, Geophysics, Geosystems, 0, https://doi.org/10.1029/2018GC007514, 2018.

Hörmann, C., Sihler, H., Bobrowski, N., Beirle, S., Penning de Vries, M., Platt, U., and Wagner, T.: Systematic investigation of bromine monoxide in volcanic plumes from space by using the GOME-2 instrument, Atmospheric Chemistry and Physics, 13, 4749–4781, https://doi.org/10.5194/acp-13-4749-2013, 2013.

Hörmann, C., Sihler, H., Beirle, S., Penning de Vries, M., Platt, U., and Wagner, T.: Seasonal variation of tropospheric bromine monoxide over the Rann of Kutch salt marsh seen from space, Atmospheric Chemistry and Physics, 16, 13 015–13 034, https://doi.org/10.5194/acp-16-13015-2016, 2016.

Hörmann, C.: Space-based monitoring of volcanic emissions using the GOME-2 instrument, Ph.D. thesis, Heidelberg University, https://doi.org/10.11588/HEIDOK.00014536, 2013.

IPCC: Intergovernmental panel on climate change: Climate change 2013: the physical science basis. Contribution of working group I to the fifth assessment report of the intergovernmental panel on climate change, Cambridge University Press; Stocker, TF and Qin, D and Plattner, GK and Tignor, M and Allen, SK and Boschung, J and Nauels, A and Xia, Y and Bex, B and Midgley, BM, 2013.

Johnson, J. B.: Generation and propagation of infrasonic airwaves from volcanic explosions, Journal of Volcanology and Geothermal Research, 121, 1 – 14, https://doi.org/10.1016/S0377-0273(02)00408-0, 2003.

Johnston, P. V.: Studies on the I0-effect, 1996.

Kelly, P. J., Kern, C., Roberts, T. J., Lopez, T., Werner, C., and Aiuppa, A.: Rapid chemical evolution of tropospheric volcanic emissions from Redoubt Volcano, Alaska, based on observations of ozone and halogen-containing gases, Journal of Volcanology and Geothermal Research, 259, 317 – 333, https://doi.org/10.1016/j.jvolgeores.2012.04.023, the 2009 Eruption of Redoubt Volcano, Alaska, 2013.

Kern, C.: Spectroscopic measurements of volcanic gas emissions in the ultra-violet wavelength region, Ph.D. thesis, University of Heidelberg, 2009.

Kern, C., Sihler, H., Vogel, L., Rivera, C., Herrera, M., and Platt, U.: Halogen oxide measurements at Masaya Volcano, Nicaragua using active long path differential optical absorption spectroscopy, Bulletin of Volcanology, 71, 659–670, https://doi.org/10.1007/s00445-008-0252-8, 2009.

Khokhar, M. F., Frankenberg, C., Van Roozendael, M., Beirle, S., Kühl, S., Richter, A., Platt, U., and Wagner, T.: Satellite observations of atmospheric SO2 from volcanic eruptions during the time-period of 1996–2002, Advances in Space Research, 36, 879–887, https://doi.org/10.1016/j.asr.2005.04.114, atmospheric Remote Sensing: Earth's Surface, Troposphere, Stratosphere and Mesosphere- I, 2005.

Kim, K., Lees, J. M., and Ruiz, M. C.: Source mechanism of vulcanian eruption at Tungurahua volcano, Ecuador, derived fromseismic moment tensor inversions, Journal of Geophysical Research: Solid Earth, 119, https://doi.org/10.1002/2013JB010590, 2014.

Kraus, S. G.: DOASIS - a framework design for DOAS, Ph.D. thesis, University of Mannheim, 2006.

Kuhn, J.: Novel approaches to the analysis of volcanic degassing, Ph.D. thesis, Heidelberg University, 2022.

Kumagai, H., Placios, P., Ruiz, M., Yepes, H., and Kozono, T.: Ascending seismic source during an explosive eruption at Tungurahua volcano, Ecuador, Geophysical Research Letters, 38, https://doi.org/10.1029/2010GL045944, 2011.

Kurucz, R. L., Furenlid, I., Brault, J., and Testerman, L.: Solar fluxatlas from 296 to 1300 nm, National Solar Observatory Atlas, Sunspot, National Solar Observatory, https://doi.org/10.1007/978-3-642-25643-1_3, 1984.

Kutterolf, S., Hansteen, T. H., Freundt, A., Wehrmann, H., Appel, K., Krüger, K., and Pérez, W.: Bromine and chlorine emissions from Plinian eruptions along the Central American Volcanic Arc: From source to atmosphere, Earth and Planetary Science Letters, 429, 234 – 246, https://doi.org/10.1016/j.epsl.2015.07.064, 2015.

Liu, E. J., Aiuppa, A., Alan, A., Arellano, S., Bitetto, M., Bobrowski, N., Carn, S., Clarke, R., Corrales, E., de Moor, J. M., Diaz, J. A., Edmonds, M., Fischer, T. P., Freer, J., Fricke, G. M., Galle, B., Gerdes, G., Giudice, G., Gutmann, A., Hayer, C., Itikarai, I., Jones, J., Mason, E., Kilbride, B. T. M., Mulina, K., Nowicki, S., Rahilly, K., Richardson, T., Rüdiger, J., Schipper, C. I., Watson, I. M., and Wood, K.: Aerial strategies advance volcanic gas measurements at inaccessible, strongly degassing volcanoes, Science Advances, 6, https://doi.org/10.1126/sciadv.abb9103, 2020.

Lübcke, P.: Optical remote sensing measurements of bromine and sulphur emissions: Investigating their potential as trace of volcanic activity, Ph.D. thesis, Universität Heidelberg, https://doi.org/10.11588/heidok.00016879, 2014.

Lübcke, P., Bobrowski, N., Arellano, S., Galle, B., Garzón, G., Vogel, L., and Platt, U.: BrO/SO_2 molar ratios from scanning DOAS measurements in the NOVAC network, Solid Earth, 5, 409–424, https://doi.org/10.5194/se-5-409-2014, 2014.

Malinconico, L. L.: Fluctuations in SO_2 emission during recent eruptions of Etna, Nature, pp. 43–45, https://doi.org/10.1038/278043a0, 1979.

McCormick, B. T., Herzog, M., Yang, J., Edmonds, M., Mather, T. A., Carn, S. A., Hidalgo, S., and Langmann, B.: A comparison of satellite- and ground-based measurements of SO2 emissions from Tungurahua volcano, Ecuador, Journal of Geophysical Research: Atmospheres, 119, 4264–4285, https://doi.org/10.1002/2013JD019771, 2014.

McCormick, M. P., Thomason, L. W., and Trepte, C. R.: Atmospheric effects of the Mt. Pinatubo eruption, Nature, 373, 399–404, https://doi.org/10.1038/373399a0, 1995.

Meller, R. and Moortgat, G. K.: Temperature dependence of the absorption cross sections of formaldehyde between 223 and 323 K in the wavelength range 225 - 375 nm, Journal of Geophysical Research: Atmospheres, 105, 7089–7101, https://doi.org/10.1029/1999JD901074, 2000.

Menyailov, I. A.: Prediction of eruptions using changes in composition of volcanic gases, Bulletin Volcanologique, 39, 112–125, https://doi.org/10.1007/BF02596951, 1975.

Miles, G. M., Siddans, R., Kerridge, B. J., Latter, B. G., and Richards, N. A. D.: Tropospheric ozone and ozone profiles retrieved from GOME-2 and their validation, Atmospheric Measurement Techniques, 8, 385–398, https://doi.org/10.5194/amt-8-385-2015, 2015.

Munro, R., Lang, R., Klaes, D., Poli, G., Retscher, C., Lindstrot, R., Huckle, R., Lacan, A., Grzegorski, M., Holdak, A., Kokhanovsky, A., Livschitz, J., and Eisinger, M.: The GOME-2 instrument on the Metop series of satellites: instrument design, calibration, and level 1 data processing – an overview, Atmospheric Measurement Techniques, 9, 1279–1301, https://doi.org/10.5194/amt-9-1279-2016, 2016.

Muraoka, H., Nasution, A., Simanjuntak, J., Dwipa, S., Takahashi, M., Takahashi, H., Matsuda, K., and Sueyoshi, Y.: Geology and Geothermal Systems in the Bajawa Volcanic Rift Zone, Flores, Eastern Indonesia, 2005.

Myers, M. L., Geist, D. J., Rowe, M. C., Harpp, K. S., Wallace, P. J., and Dufek, J.: Replenishment of volatile-rich mafic magma into a degassed chamber drives mixing and eruption of Tungurahua volcano, Bulletin of Volcanology, 76, 872, https://doi.org/10.1007/s00445-014-0872-0, 2014.

Noguchi, K. and Kamiya, H.: Prediction of volcanic eruption by measuring the chemical composition and amounts of gases, Bulletin Volcanologique, 26, 367–378, https://doi.org/10.1007/BF02597298, 1963.

Olmos, R., Barrancos, J., Rivera, C., Barahona, F., López, D. L., Henriquez, B., Hernández, A., Benitez, E., Hernández, P. A., Pérez, N. M., and Galle, B.: Anomalous Emissions of SO_2 During the Recent Eruption of Santa Ana Volcano, El Salvador, Central America, Pure and Applied Geophysics, 164, 2489–2506, https://doi.org/10.1007/s00024-007-0276-6, 2007.

Oppenheimer, C.: Volcanic Degassing, in: Treatise on Geochemistry, edited by Holland, H. D. and Turekian, K. K., pp. 123–166, Pergamon, Oxford, https://doi.org/10.1016/b0-08-043751-6/03020-6, 2003.

Oppenheimer, C., Tsanev, V. I., Braban, C. F., Cox, R. A., Adams, J. W., Aiuppa, A., Bobrowski, N., Delmelle, P., Barclay, J., and McGonigle, A. J. S.: BrO formation in volcanic plumes, Geochimica et Cosmochimica Acta, 70, 2935 – 2941, https://doi.org/10.1016/j.gca.2006.04.001, 2006.

Pennec, J.-L. L., Jaya, D., Samaniego, P., Ramón, P., Yánez, S. M., Egred, J., and van der Plicht, J.: The AD 1300–1700 eruptive periods at Tungurahua volcano, Ecuador, revealed by historical narratives, stratigraphy and radiocarbon dating, Journal of Volcanology and Geothermal Research, 176, 70 – 81, https://doi.org/10.1016/j.jvolgeores.2008.05.019, recent and active volcanism in the Ecuadorian Andes, 2008.

Pennisi, M. and Cloarec, M.-F. L.: Variations of Cl, F, and S in Mount Etna's plume, Italy, between 1992 and 1995, Journal of Geophysical Research: Solid Earth, 103, https://doi.org/10.1029/97JB03011, 1998.

Perner, D. and Platt, U.: Detection of nitrous acid in the atmosphere by differential optical absorption, Geophysical Research Letters, 6, 917–920, https://doi.org/10.1029/GL006i012p00917, 1979.

Platt, U. and Bobrowski, N.: Quantification of volcanic reactive halogen emissions, p. 115–132, Cambridge University Press, https://doi.org/10.1017/CBO9781107415683.011, 2015.

Platt, U. and Hönninger, G.: The role of halogen species in the troposphere, Chemosphere, 52, 325–338, https://doi.org/10.1016/s0045-6535(03)00216-9, 2003.

Platt, U. and Lehrer, E.: Arctic Tropospheric Ozone Chemistry, ARCTOC Final Report to the European Union, 1997.

Platt, U. and Stutz, J.: Differential Optical Absorption Spectroscopy, in: Differential Optical Absorption Spectroscopy, Physics of Earth and Space Environments, pp. 135–174, Springer Berlin Heidelberg, https://doi.org/10.1007/978-3-540-75776-4_6, 2008.

Puķīte, J. and Wagner, T.: Quantification and parametrization of non-linearity effects by higher-order sensitivity terms in scattered light differential optical absorption spectroscopy, Atmospheric Measurement Techniques, 9, 2147–2177, https://doi.org/10.5194/amt-9-2147-2016, 2016.

Puķīte, J., Kühl, S., Deutschmann, T., Platt, U., and Wagner, T.: Extending differential optical absorption spectroscopy for limb measurements in the UV, Atmospheric Measurement Techniques, 3, 631–653, https://doi.org/10.5194/amt-3-631-2010, 2010.

Pyle, D. M. and Mather, T. A.: Halogens in igneous processes and their fluxes to the atmosphere and oceans from volcanic activity: A review, Chemical Geology, 263, 110–121, https://doi.org/10.1016/j.chemgeo.2008.11.013, 2009.

Rashidov, V. A., Girina, O., Ozerov, A. Y., and Pavlov, N. N.: THE JUNE 2019. ERUPTION OF RAIKOKE VOLCANO (THE KURILE ISLANDS), Bulletin of Kamchatka Regional Association «Educational-Scientific Center». Earth Sciences, pp. 5–8, https://doi.org/10.31431/1816-5524-2019-2-42-5-8, 2019.

Richter, A. and the S5-P/TROPOMI verification team: S-5P/TROPOMI Science Verification Report, Tech. rep., ESA, URL `https://sentinels.copernicus.eu/web/sentinel/user-guides/sentinel-5p-tropomi/document-library/-/asset_publisher/w9Mnd6VPjXlc/content/sentinel-5p-tropomi-science-verification-report`, 2015.

Richter, A., Wittrock, F., Eisinger, M., and Burrows, J. P.: GOME observations of tropospheric BrO in northern hemispheric spring and summer 1997, Geophysical Research Letters, 25, 2683–2686, https://doi.org/10.1029/98GL52016, 1998.

Richter, A., Wittrock, F., Ladstätter-Weißenmayer, A., and Burrows, J. P.: Gome measurements of stratospheric and tropospheric BrO, Advances in Space Research, 29, 1667–1672, https://doi.org/10.1016/S0273-1177(02)00123-0, 2002.

Rix, M., Valks, P., Hao, N., Loyola, D., Schlager, H., Huntrieser, H., Flemming, J., Koehler, U., Schumann, U., and Inness, A.: Volcanic SO2, BrO and plume height estimations using GOME-2 satellite measurements during the eruption of Eyjafjallajökull in May 2010, Journal of Geophysical Research: Atmospheres, 117, https://doi.org/10.1029/2011JD016718, 2012.

Roberts, T., Dayma, G., and Oppenheimer, C.: Reaction Rates Control High-Temperature Chemistry of Volcanic Gases in Air, Frontiers in Earth Science, 7, https://doi.org/10.3389/feart.2019.00154, 2019.

Roberts, T. J., Martin, R. S., and Jourdain, L.: Reactive bromine chemistry in Mount Etna's volcanic plume: the influence of total Br, high-temperature processing, aerosol loading and plume–air mixing, Atmospheric Chemistry and Physics, 14, 11 201–11 219, https://doi.org/10.5194/acp-14-11201-2014, 2014.

Robock, A.: Volcanic eruptions and climate, Reviews of Geophysics, 38, 191–219, https://doi.org/10.1029/1998rg000054, 2000.

Salawitch, R. J., Canty, T., Kurosu, T., Chance, K., Liang, Q., da Silva, A., Pawson, S., Nielsen, J. E., Rodriguez, J. M., Bhartia, P. K., Liu, X., Huey, L. G., Liao, J., Stickel, R. E., Tanner, D. J., Dibb, J. E., Simpson, W. R., Donohoue, D., Weinheimer, A., Flocke, F., Knapp, D., Montzka, D., Neuman, J. A., Nowak, J. B., Ryerson, T. B., Oltmans, S., Blake, D. R., Atlas, E. L., Kinnison, D. E., Tilmes, S., Pan, L. L., Hendrick, F., Van Roozendael, M., Kreher, K., Johnston, P. V., Gao, R. S., Johnson, B., Bui, T. P., Chen, G., Pierce, R. B., Crawford, J. H., and Jacob, D. J.: A new interpretation of total column BrO during Arctic spring, Geophysical Research Letters, 37, https://doi.org/10.1029/2010GL043798, 2010.

Samaniego, P., Pennec, J.-L. L., Robin, C., and Hidalgo, S.: Petrological analysis of the pre-eruptive magmatic process prior to the 2006 explosive eruptions at Tungurahua volcano (Ecuador), Journal of Volcanology and Geothermal Research, 199, 69 – 84, https://doi.org/10.1016/j.jvolgeores.2010.10.010, 2011.

Scandone, R., Cashman, K. V., and Malone, S. D.: Magma supply, magma ascent and the style of volcanic eruptions, Earth and Planetary Science Letters, 253, 513 – 529, https://doi.org/10.1016/j.epsl.2006.11.016, 2007.

Schiano, P., Clocchiatti, R., Ottolini, L., and Busà, T.: Transition of mount Etna lavas from a mantle-plume to an island-arc magmatic source, Nature, 412, 900–904, https://doi.org/10.1038/35091056, 2001.

Schmincke, H.-U.: Volcanism, Springer Berlin Heidelberg, https://doi.org/10.1007/978-3-642-18952-4, 2004.

Self, S., Zhao, J.-X., Holasek, R. E., Torres, R. C., and King, A. J.: The atmospheric impact of the 1991 mount Pinatubo eruption, NASA Reports, 1993.

Seo, J. H. and Zajacz, Z.: Fractionation of Cl/Br during fluid phase separation in magmatic–hydrothermal fluids, Geochimica et Cosmochimica Acta, 183, 125 – 137, https://doi.org/10.1016/j.gca.2016.04.009, 2016.

Seo, S., Richter, A., Blechschmidt, A.-M., Bougoudis, I., and Burrows, J. P.: First high-resolution BrO column retrievals from TROPOMI, Atmospheric Measurement Techniques, 12, 2913–2932, https://doi.org/10.5194/amt-12-2913-2019, 2019.

Serdyuchenko, A., Gorshelev, V., Weber, M., Chehade, W., and Burrows, J. P.: High spectral resolution ozone absorption cross-sections – part 2: Temperature dependence, Atmospheric Measurement Techniques, 7, 625–636, https://doi.org/10.5194/amt-7-625-2014, 2014.

Sihler, H., Platt, U., Beirle, S., Marbach, T., Kühl, S., Dörner, S., Verschaeve, J., Frieß, U., Pöhler, D., Vogel, L., Sander, R., and Wagner, T.: Tropospheric BrO column densities in the Arctic derived from satellite: retrieval and comparison to ground-based measurements, Atmospheric Measurement Techniques, 5, 2779–2807, https://doi.org/10.5194/amt-5-2779-2012, 2012.

Sihler, H., Beirle, S., Dörner, S., Gutenstein-Penning de Vries, M., Hörmann, C., Borger, C., Warnach, S., and Wagner, T.: MICRU background map and effective cloud fraction algorithms designed for UV/vis satellite instruments with large viewing angles, Atmospheric Measurement Techniques Discussions, 2020, 1–58, https://doi.org/10.5194/amt-2020-182, 2020.

Spilliaert, N., Métrich, N., and Allard, P.: S–C–F degassing pattern of water-rich alkali basalt: Modelling and relationship with eruption styles on Mount Etna volcano, Earth and Planetary Science Letters, 248, 772 – 786, https://doi.org/10.1016/j.epsl.2006.06.031, 2006.

Spina, A. L., Burton, M., Allard, P., Alparone, S., and Muré, F.: Open-path FTIR spectroscopy of magma degassing processes during eight lava fountains on Mount Etna, Earth and Planetary Science Letters, 413, 123 – 134, https://doi.org/10.1016/j.epsl.2014.12.038, 2015.

Spinetti, C. and Buongiorno, M. F.: Volcanic aerosol optical characteristics of Mt. Etna tropospheric plume retrieved by means of airborne multispectral images, Journal of Atmospheric and Solar-Terrestrial Physics, 69, 981 – 994, https://doi.org/10.1016/j.jastp.2007.03.014, 2007.

Spurr, R. J. D.: VLIDORT: A linearized pseudo-spherical vector discrete ordinate radiative transfer code for forward model and retrieval studies in multilayer multiple scattering media, Journal of Quantitative Spectroscopy and Radiative Transfer, 102, 316–342, https://doi.org/https://doi.org/10.1016/j.jqsrt.2006.05.005, 2006.

Suleiman, R. M., Chance, K., Liu, X., González Abad, G., Kurosu, T. P., Hendrick, F., and Theys, N.: OMI total bromine monoxide (OMBRO) data product: algorithm, retrieval and measurement comparisons, Atmospheric Measurement Techniques, 12, 2067–2084, https://doi.org/10.5194/amt-12-2067-2019, 2019.

Sun, C.: Explicit Equations to Transform from Cartesian to Elliptic Coordinates, Mathematical Modelling and Applications, 2, 43, https://doi.org/10.11648/j.mma.20170204.12, 2017.

Surl, L., Roberts, T., and Bekki, S.: Observation and modelling of ozone-destructive halogen chemistry in a passively degassing volcanic plume, Atmospheric Chemistry and Physics, 21, 12 413–12 441, https://doi.org/10.5194/acp-21-12413-2021, 2021.

Tamura, Y., Ishizuka, O., Sato, T., and Nichols, A. R. L.: Nishinoshima volcano in the Ogasawara Arc: New continent from the ocean?, Island Arc, 28, e12 285, https://doi.org/10.1111/iar.12285, 2018.

Tanguy, J.-C., Condomines, M., and Kieffer, G.: Evolution of the Mount Etna magma: Constraints on the present feeding system and eruptive mechanism, Journal of Volcanology and Geothermal Research, 75, 221–250, https://doi.org/10.1016/s0377-0273(96)00065-0, 1997.

Textor, C., Graf, H.-F., Timmreck, C., and Robock, A.: Emissions from volcanoes, in: Emissions of Atmospheric Trace Compounds, edited by Granier, C., Artaxo, P., and Reeves, C., vol. 18 of *Advances in Global Change Research*, pp. 269–303, Springer Netherlands, https://doi.org/10.1007/978-1-4020-2167-1_7, 2004.

Thalman, R. and Volkamer, R.: Temperature dependent absorption cross-sections of O2–O2 collision pairs between 340 and 630 nm and at atmospherically relevant pressure, Phys. Chem. Chem. Phys., 15, 15 371–15 381, https://doi.org/10.1039/C3CP50968K, 2013.

Theys, N., Roozendael, M. V., Dils, B., Hendrick, F., Hao, N., and Mazière, M. D.: First satellite detection of volcanic bromine monoxide emission after the Kasatochi eruption, Geophysical Research Letters, 36, https://doi.org/10.1029/2008GL036552, 2009.

Theys, N., Van Roozendael, M., Hendrick, F., Yang, X., De Smedt, I., Richter, A., Begoin, M., Errera, Q., Johnston, P. V., Kreher, K., and De Mazière, M.: Global observations of tropospheric BrO columns using GOME-2 satellite data, Atmospheric Chemistry and Physics, 11, 1791–1811, https://doi.org/10.5194/acp-11-1791-2011, 2011.

Theys, N., De Smedt, I., van Gent, J., Danckaert, T., Wang, T., Hendrick, F., Stavrakou, T., Bauduin, S., Clarisse, L., Li, C., Krotkov, N., Yu, H., Brenot, H., and Van Roozendael, M.: Sulfur dioxide vertical column DOAS retrievals from the Ozone Monitoring Instrument: Global observations and comparison to ground-based and satellite data, Journal of Geophysical Research: Atmospheres, 120, 2470–2491, https://doi.org/10.1002/2014JD022657, 2015.

Theys, N., De Smedt, I., Yu, H., Danckaert, T., van Gent, J., Hörmann, C., Wagner, T., Hedelt, P., Bauer, H., Romahn, F., Pedergnana, M., Loyola, D., and Van Roozendael, M.: Sulfur dioxide retrievals from TROPOMI onboard Sentinel-5 Precursor: algorithm theoretical basis, Atmospheric Measurement Techniques, 10, 119–153, https://doi.org/10.5194/amt-10-119-2017, 2017.

Theys, N., de Smedt, I., Lerot, C., Yu, H., and van Roozendael, M.: S5P/TROPOMI SO2 ATBD, Tech. rep., ESA, URL `https://sentinels.copernicus.eu/web/sentinel/user-guides/document-library/-/asset_publisher/xlslt4309D5h/content/sentinel-5p-tropomi-so2-atbd`, 2021.

Thomas, W., Erbertseder, T., Ruppert, T., Roozendael, M. V., Verdebout, J., Balis, D., Meleti, C., and Zerefos, C.: On the Retrieval of Volcanic Sulfur Dioxide Emissions from GOME Backscatter Measurements, Journal of Atmospheric Chemistry, 50, 295–320, https://doi.org/10.1007/s10874-005-5544-1, 2005.

Valks, P., Loyola, D., Hao, N., and Rix, M.: Algorithm Theoretical Basis Document for GOME-2 Total Column Products of Ozone, Minor Trace Gases, and Cloud Properties, techreport, Deutsches Zentrum für Luft und Raumfahrt, Oberpfaffenhofen, Germany, 2009.

van de Hulst, H. C.: Light scattering by small particles., Quarterly Journal of the Royal Meteorological Society, 84, 198–199, https://doi.org/10.1002/qj.49708436025, 1958.

van Geffen, J., Eskes, H. J., Boersma, K. F., and Veefkind, J. P.: TROPOMI ATBD of thetotal and tropospheric NO2 data products, resreport, KNMI, URL `https://sentinel.esa.int/documents/247904/2476257/Sentinel-5P-TROPOMI-ATBD-NO2-data-products`, report S5P-KNMI-L2-0005-RP, 2021.

van Roozendael, M. and the Sentinel 5 Verification team: Sentinel 5 verification report.

Vandaele, A. C., Hermans, C., Simon, P. C., Carleer, M., Colin, R., Fally, S., Merienne, M. F., Jenouvrier, A., and Coquart, B.: Measurements of the NO_2 absorption cross-section from 42 000 cm^{-1} to 10 000 cm^{-1} (238-1000 nm) at 220 K and 294 K, Journal of Quantitative Spectroscopy and Radiative Transfer, 59, 171 – 184, https://doi.org/10.1016/S0022-4073(97)00168-4, atmospheric Spectroscopy Applications 96, 1998.

Vandaele, A. C., Hermans, C., and Fally, S.: Fourier transform measurements of SO_2 absorption cross sections: II.: Temperature dependence in the 29 000 - 44 000 cm^{-1} (227 - 345 nm) region, Journal of Quantitative Spectroscopy and Radiative Transfer, 110, 2115 – 2126, https://doi.org/10.1016/j.jqsrt.2009.05.006, 2009.

Veefkind, J. P., Aben, I., McMullan, K., Förster, H., de Vries, J., Otter, G., Claas, J., Eskes, H. J., de Haan, J. F., Kleipool, Q., van Weele, M., Hasekamp, O., Hoogeveen, R., Landgraf, J., Snel, R., Tol, P., Ingmann, P., Voors, R., Kruizinga, B., Vink, R., Visser, H., and Levelt, P. F.: TROPOMI on the ESA Sentinel-5 Precursor: A GMES mission for global observations of the atmospheric composition for climate, air quality and ozone layer applications, Remote Sensing of Environment, 120, 70–83, https://doi.org/10.1016/j.rse.2011.09.027, 2012.

Villemant, B. and Boudon, G.: H_2O and halogen (F, Cl, Br) behaviour during shallow magma degassing processes, Earth and Planetary Science Letters, 168, 271 – 286, https://doi.org/10.1016/S0012-821X(99)00058-8, 1999.

Villemant, B., Mouatt, J., and Michel, A.: Andesitic magma degassing investigated through H_2O vapour–melt partitioning of halogens at Soufrière Hills volcano, Montserrat (Lesser Antilles), Earth and Planetary Science Letters, 269, 212 – 229, https://doi.org/10.1016/j.epsl.2008.02.014, 2008.

Vogel, L.: Volcanic plumes: Evaluation of spectroscopic measurements, early detection, an bromine chemistry, phdthesis, Universität Heidelberg, https://doi.org/10.11588/heidok.00013219, 2011.

Vogel, L., Sihler, H., Lampel, J., Wagner, T., and Platt, U.: Retrieval interval mapping: a tool to visualize the impact of the spectral retrieval range on differential optical absorption spectroscopy evaluations, Atmospheric Measurement Techniques, 6, 275–299, https://doi.org/10.5194/amt-6-275-2013, 2013.

von Glasow, R.: Atmospheric chemistry in volcanic plumes, Proceedings of the National Academy of Sciences, 107, https://doi.org/10.1073/pnas.0913164107, 2010.

Wagner, T. and Platt, U.: Satellite mapping of enhanced BrO concentrations in the troposphere, Nature, 395, 486–490, https://doi.org/10.1038/26723, 1998.

Wagner, T. and the Sentinel 4 Verification team: Sentinel 4 verification report.

Wagner, T., Otten, C., Pfeilsticker, K., Pundt, I., and Platt, U.: DOAS moonlight observation of atmospheric NO3 in the Arctic winter, Geophysical Research Letters, 27, 3441–3444, https://doi.org/10.1029/1999GL011153, 2000.

Wagner, T., Chance, K., Frieß, U., Gil, M., Goutail, F., Hönninger, G., Johnston, P., Karlsen-Tørnkvist, K., Kostadinov, I., Leser, H., Petritoli, A., Richter, A., Van Roozendael, M., and Platt, U.: Correction of the Ring effect and I0-effect for DOAS observations of scattered sunlight, Proc. of the 1st DOAS Workshop, 2001.

Wagner, T., Beirle, S., Deutschmann, T., Eigemeier, E., Frankenberg, C., Grzegorski, M., Liu, C., Marbach, T., Platt, U., and Penning de Vries, M.: Monitoring of atmospheric trace gases, clouds, aerosols and surface properties from UV/vis/NIR satellite instruments, Journal of Optics A: Pure and Applied Optics, 10, 104019, https://doi.org/10.1088/1464-4258/10/10/104019, 2008.

Wagner, T., Beirle, S., and Deutschmann, T.: Three-dimensional simulation of the Ring effect in observations of scattered sun light using Monte Carlo radiative transfer models, Atmospheric Measurement Techniques, 2, 113–124, https://doi.org/10.5194/amt-2-113-2009, 2009.

Warnach, S.: Improvements of BrO and SO_2 retrievals of NOVAC data - Tungurahua volcanoas a case study, Master's thesis, University Heidelberg, 2015.

Warnach, S., Bobrowski, N., Hidalgo, S., Arellano, S., Sihler, H., Dinger, F., Lübcke, P., Battaglia, J., Steele, A., Galle, B., Platt, U., and Wagner, T.: Variation of the BrO/SO_2 Molar Ratio in the Plume of Tungurahua Volcano Between 2007 and 2017 and Its Relationship to Volcanic Activity, Frontiers in Earth Science, 7, 132, https://doi.org/10.3389/feart.2019.00132, 2019.

Webster, J. D., Sintoni, M. F., and De Vivo, B.: The partitioning behavior of Cl, S, and H_2O in aqueous vapor- saline-liquid saturated phonolitic and trachytic melts at 200 MPa, Chemical Geology, 263, 19 – 36, https://doi.org/10.1016/j.chemgeo.2008.10.017, halogens in Volcanic Systems and Their Environmental Impacts, 2009.

Webster, J. D., Baker, D. R., and Aiuppa, A.: Halogens in Mafic and Intermediate-Silica Content Magmas, in: Springer Geochemistry, pp. 307–430, Springer International Publishing, https://doi.org/10.1007/978-3-319-61667-4_6, 2018.

Wennberg, P.: Bromine explosion, Nature, 397, 299–301, https://doi.org/10.1038/16805, 1999.

Wright, H. M. N., Cashman, K. V., Mothes, P. A., Hall, M. L., Ruiz, A. G., and Le Pennec, J.: Estimating rates of decompression from textures of erupted ash particles produced by 1999–2006 eruptions of Tungurahua volcano, Ecuador, Geology, 40, 619, https://doi.org/10.1130/G32948.1, 2012.

Zajacz, Z., Candela, P. A., Piccoli, P. M., and Sanchez-Valle, C.: The partitioning of sulfur and chlorine between andesite melts and magmatic volatiles and the exchange coefficients of major cations, Geochimica et Cosmochimica Acta, 89, 81 – 101, https://doi.org/10.1016/j.gca.2012.04.039, 2012.

Zielcke, J.: Direct moonlight studies of volcanic plumes using differential opticalabsorption spectroscopy, Master's thesis, University Heidelberg, 2010.

Danksagungen – Acknowledgements

Mein größter Dank geht an meinen Doktorvater Prof. Thomas Wagner, dafür, dass er diese Arbeit ermöglicht hat und mich auf dem Weg vom Satelliten zu den Vulkanen betreut hat. Er hat mir dabei immer die richtige Richtung aufgezeigt, auch wenn es nicht die Richtung war, die ich ursprünglich vorhatte einzuschlagen. Besonders dankbar bin ich zudem für die größtmögliche Freiheit, welche es mir ermöglicht hat den TROPOMI Datensatz nach allen erdenklichen Schätzen zu durchforsten, sowie das fortwährende Vertrauen in meine Arbeit auch Abseits der Arbeitsgruppe, sei es in den ESA Projekten oder den Vertretungsaufgaben für die Gruppe.
Desweiteren möchte ich mich bei folgenden Personen bedanken:

Besonderer Dank gilt auch meinem Betreuer Holger Sihler, der mir stets mit Rat und Tat in allen Lebenslagen beiseite stand. Egal ob ich morgens beim gemeinsamen Pendeln noch an meinem Vortrag für das SatSem gefeilt habe, eine Parametrisierung in elliptischen Koordinaten ausklamüsert habe, oder einfach über das Leben reden wollte, Holger hatte immer Zeit und guten Sachverstand über BrO, Wolken, Mathematik. Er war mir in der gesamten Zeit eine große Stütze; das gemeinsame Pendeln von Heidelberg nach Mainz wird mir fehlen. Im Nachhinein sehr zu schätzen weiß ich auch sein fortwährendes Plädoyer für gutes Programmieren.

Desweiteren möchte ich mich bei den Mitbetreuern Prof. Ulrich Platt, Steffen Beirle und Nicole Bobrowski bedanken. Mein Dank gilt Steffen Beirle dafür, dass er immer im Blick behalten hat, welche Fragen als nächstes in der Arbeit wichtig sind, prägnante Fragen bei allen meetings gestellt hat, und für sein Engagement für die gute Gruppenatmosphäre in Mainz. Bei Nicole Bobrowski möchte ich mich dafür bedanken, dass sie mir die Vulkane näher gebracht hat und zu jeder Vulkanfrage eine Antwort hatte. Außerdem ist es ihr unschätzbarer Verdienst, dass sie in Heidelberg eine so freudige und vertraute Vulkangemeinschaft aufgebaut und kultiviert hat. Prof. Ulrich Platt möchte ich dafür danken, dass er mir in der DOAS-Gruppe in Heidelberg ein zweites Basislager für die Doktorarbeit gegeben hat und immer prägnante Vorschläge, wie zum Beispiel die wertvollen Überlegungen zum Fahnenmodel, sowie bestärkende Kommentare zu meinen Ergebnissen hatte.

Jonas Kuhn möchte ich danken dafür, dass ich zusammen mit ihm auf den Weg (1) durch die Doktorarbeit und (2) durch die Vulkanfernerkundung gehen durfte. Die vielen Gesprächen über Vulkane, das Doktorieren und alles andere in der Mensa, der institutionalisierten Kaffepause oder einfach so war ein fester Anker gerade in Zeiten von Corona.

Mein Dank gilt Christian Borger für das Programmieren der Infrastruktur für die Satellitenauswertung, die ohne ihn nicht möglich gewesen wäre. Vor allem aber bin ich ihm

für seine Geduld und Mühe bei allen meinen diesbezüglichen und auch sonstigen Anfragen dankbar. Seine immer positive Einstellung, die gemeinsamen Bürounterhaltungen und die Kaffepausen haben mir das Mainzer Büro A.5.02 heimelig gemacht.

I would like to thank the complete Satellite group in Mainz for giving me a wonderful scientific home, fun board game nights, interesting Mensa conversations, and above all a great place. Namely Steffen Dörner, whose attentive, kind and warmhearted mindset lightened up the whole group spirit, Marloes Penning de Vries, whose kind spirit and outlooking nature I highly valued and lastly, Christoph Hörmann, whose ideas where the start of the data I present here.

Auch danken möchte ich der gesammten DOAS Gruppe in Heidelberg, von denen ich viel gelernt habe. Neben den bereits erwähnten danke ich besonders Lukas Tirpitz für gute Gespräche über Gott und die Welt und Christopher Fuchs fürs chillige Miteinander und die gute Laune.

Jonas Kuhn und Nicole Bobrowski möchte ich danken, dass sie mich als »Datenauswerter« einen Monat mit zum Vulkan genommen haben.

Ich möchte mich bei Rüdiger Sörensen bedanken, dass er die IT Infrastruktur wunderbar aufgebaut und gemanaged hat, immer meine unqualifizierten IT Fragen ertragen hat und Dresden genau bis zur Abgabe meiner Doktorarbeit am Laufen gehalten hat.

Die Vulkanologengruppe war eine Gemeinschaft, die mich in vielen Probevorträgen das gute Präsentieren gelehrt hat und eine Gemeinschaft für sich war. Ich bin dankbar ein Teil davon sein zu dürfen.

Fürs Korrekturlesen bedanke ich mich besonders bei Thomas Wagner, Steffen Beirle, Dietlind von der Trenck, Benjamin Delarue und Marie-Luise Knott; außerdem bei Nicole Bobrowski, Jonas Kuhn, Dominik Neuenfeld und Ulrich Platt. Danke, dass ihr meine Aversion dem englischen Plural und Artikeln gegenüber ertragen habt.

I would like to thank Karin Sulsky and the Paul Crutzen Graduate school for giving me a framework for my PhD thesis and assisting me with valuable advice throughout my thesis.

Dank gilt Prof. Thomas Leisner für die Übernahme der Zweitkorrektur trotz seines vollgepackten Terminkalenders. Außerdem danke ich Prof. Schulz-Coulon and Prof. Thilman Plehn dafür, dass sie sich als weitere Prüfer in der Doktorprüfung bereiterklärt haben.

Thanks is in order for ESA, KNMI and the TROPOMI L1B team for their great work on TROPOMI.

Meinen Eltern danke ich für die Unterstützung in ferner Vergangenheit und naher Gegenwart.

Am meisten danke ich Dietlind – fürs Anstubsen, Motivieren, Zuhören, Ertragen und mich zum Lachen bringen. Immer.